

DK: 621.4

2000 0556

**McGraw-Hill Series in Mechanical Engineering**

Jack P. Holman, *Southern Methodist University*  
Consulting Editor

- Anderson: *Modern Compressible Flow: With Historical Perspective*  
Dieter: *Engineering Design: A Materials and Processing Approach*  
Eckert and Drake: *Analysis of Heat and Mass Transfer*  
Heywood: *Internal Combustion Engine Fundamentals*  
Hinze: *Turbulence, 2/e*  
Hutton: *Applied Mechanical Vibrations*  
Juvinall: *Engineering Considerations of Stress, Strain, and Strength*  
Kane and Levinson: *Dynamics: Theory and Applications*  
Kays and Crawford: *Convective Heat and Mass Transfer*  
Martin: *Kinematics and Dynamics of Machines*  
Phelan: *Dynamics of Machinery*  
Phelan: *Fundamentals of Mechanical Design, 3/e*  
Pierce: *Acoustics: An Introduction to Its Physical Principles and Applications*  
Raven: *Automatic Control Engineering, 4/e*  
Rosenberg and Karnopp: *Introduction to Physics*  
Schlichting: *Boundary-Layer Theory, 7/e*  
Shames: *Mechanics of Fluids, 2/e*  
Shigley: *Kinematic Analysis of Mechanisms, 2/e*  
Shigley and Mitchell: *Mechanical Engineering Design, 4/e*  
Shigley and Uicker: *Theory of Machines and Mechanisms*  
Stoecker and Jones: *Refrigeration and Air Conditioning, 2/e*  
Vanderplaats: *Numerical Optimization Techniques for Engineering Design:  
With Applications*

**INTERNAL  
COMBUSTION  
ENGINE  
FUNDAMENTALS**

**John B. Heywood**

Professor of Mechanical Engineering  
Director, Sloan Automotive Laboratory  
Massachusetts Institute of Technology

Dauerleih an: FV/SLE4 (S)

Änderung nur über  
Fachbibliothek BFV21 (SF)

McGraw-Hill, Inc.  
New York St. Louis San Francisco Auckland Bogotá  
Caracas Lisbon London Madrid Mexico City Milan  
Montreal New Delhi San Juan Singapore  
Sydney Tokyo Toronto

## **INTERNAL COMBUSTION ENGINE FUNDAMENTALS**

This book was set in Times Roman.

The editors were Anne Duffy and John M. Morris; the designer was Joan E. O'Connor; the production supervisor was Denise L. Puryear. New drawings were done by ANCO. Project Supervision was done by Santype International Ltd. R. R. Donnelley & Sons Company was printer and binder.

See acknowledgements on page xxi.

Copyright © 1988 by McGraw-Hill, Inc. All rights reserved.  
Printed in the United States of America. Except as permitted under the  
United States Copyright Act of 1976, no part of this publication may be  
reproduced or distributed in any form or by any means, or stored in a data  
base or retrieval system, without the prior written permission  
of the publisher.

14 15 16 17 DOC/DOC 9 9 8

ISBN 0-07-028637-X

### **Library of Congress Cataloging-in-Publication Data**

Heywood, John B.

Internal combustion engine fundamentals.

(McGraw-Hill series in mechanical engineering)

Bibliography: p.

Includes index.

I. Internal combustion engines. I. Title. II. Series.

TJ755.H45 1988 621.43 87-15251

This book is printed on acid-free paper.

## **ABOUT THE AUTHOR**

Dr. John B. Heywood received the Ph.D. degree in mechanical engineering from the Massachusetts Institute of Technology in 1965. Following an additional post-doctoral year of research at MIT, he worked as a research officer at the Central Electricity Generating Board's Research Laboratory in England on magneto-hydrodynamic power generation. In 1968 he joined the faculty at MIT where he is Professor of Mechanical Engineering. At MIT he is Director of the Sloan Automotive Laboratory. He is currently Head of the Fluid and Thermal Science Division of the Mechanical Engineering Department, and the Transportation Energy Program Director in the MIT Energy Laboratory. He is faculty advisor to the MIT Sports Car Club.

Professor Heywood's teaching and research interests lie in the areas of thermodynamics, combustion, energy, power, and propulsion. During the past two decades, his research activities have centered on the operating characteristics and fuels requirements of automotive and aircraft engines. A major emphasis has been on computer models which predict the performance, efficiency, and emissions of spark-ignition, diesel, and gas turbine engines, and in carrying out experiments to develop and validate these models. He is also actively involved in technology assessments and policy studies related to automotive engines, automobile fuel utilization, and the control of air pollution. He consults frequently in the automotive and petroleum industries, and for the U.S. Government.

His extensive research in the field of engines has been supported by the U.S. Army, Department of Energy, Environmental Protection Agency, NASA, National Science Foundation, automobile and diesel engine manufacturers, and petroleum companies. He has presented or published over a hundred papers on

his research in technical conferences and journals. He has co-authored two previous books: *Open-Cycle MHD Power Generation* published by Pergamon Press in 1969 and *The Automobile and the Regulation of Its Impact on the Environment* published by University of Oklahoma Press in 1975.

He is a member of the American Society of Mechanical Engineers, an associate fellow of the American Institute of Aeronautics and Astronautics, a fellow of the British Institution of Mechanical Engineers, and in 1982 was elected a Fellow of the U.S. Society of Automotive Engineers for his technical contributions to automotive engineering. He is a member of the editorial boards of the journals *Progress in Energy and Combustion Science* and the *International Journal of Vehicle Design*.

His research publications on internal combustion engines, power generation, and gas turbine combustion have won numerous awards. He was awarded the Ayreton Premium in 1969 by the British Institution of Electrical Engineers. Professor Heywood received a Ralph R. Teetor Award as an outstanding young engineering educator from the Society of Automotive Engineers in 1971. He has twice been the recipient of an SAE Arch T. Colwell Merit Award for an outstanding technical publication (1973 and 1981). He received SAE's Horning Memorial Award for the best paper on engines and fuels in 1984. In 1984 he received the Sc.D. degree from Cambridge University for his published contributions to engineering research. He was selected as the 1986 American Society of Mechanical Engineers Freeman Scholar for a major review of "Fluid Motion within the Cylinder of Internal Combustion Engines."

THIS BOOK IS DEDICATED TO MY FATHER,  
Harold Heywood:

*I have followed many of the paths he took.*

---

---

## **CONTENTS**

---

Preface	xvii
Commonly Used Symbols, Subscripts, and Abbreviations	xxiii
<b>Chapter 1 Engine Types and Their Operation</b>	1
1.1 Introduction and Historical Perspective	1
1.2 Engine Classifications	7
1.3 Engine Operating Cycles	9
1.4 Engine Components	12
1.5 Spark-Ignition Engine Operation	15
1.6 Examples of Spark-Ignition Engines	19
1.7 Compression-Ignition Engine Operation	25
1.8 Examples of Diesel Engines	31
1.9 Stratified-Charge Engines	37
<b>Chapter 2 Engine Design and Operating Parameters</b>	42
2.1 Important Engine Characteristics	42
2.2 Geometrical Properties of Reciprocating Engines	43
2.3 Brake Torque and Power	45
2.4 Indicated Work Per Cycle	46
2.5 Mechanical Efficiency	48
2.6 Road-Load Power	49
2.7 Mean Effective Pressure	50
2.8 Specific Fuel Consumption and Efficiency	51
2.9 Air/Fuel and Fuel/Air Ratios	53

2.10 Volumetric Efficiency	53
2.11 Engine Specific Weight and Specific Volume	54
2.12 Correction Factors for Power and Volumetric Efficiency	54
2.13 Specific Emissions and Emissions Index	56
2.14 Relationships between Performance Parameters	56
2.15 Engine Design and Performance Data	57
<b>Chapter 3 Thermochemistry of Fuel-Air Mixtures</b>	<b>62</b>
3.1 Characterization of Flames	62
3.2 Ideal Gas Model	64
3.3 Composition of Air and Fuels	64
3.4 Combustion Stoichiometry	68
3.5 The First Law of Thermodynamics and Combustion	72
3.5.1 Energy and Enthalpy Balances	72
3.5.2 Enthalpies of Formation	76
3.5.3 Heating Values	78
3.5.4 Adiabatic Combustion Processes	80
3.5.5 Combustion Efficiency of an Internal Combustion Engine	81
3.6 The Second Law of Thermodynamics Applied to Combustion	83
3.6.1 Entropy	83
3.6.2 Maximum Work from an Internal Combustion Engine and Efficiency	83
3.7 Chemically Reacting Gas Mixtures	85
3.7.1 Chemical Equilibrium	86
3.7.2 Chemical Reaction Rates	92
<b>Chapter 4 Properties of Working Fluids</b>	<b>100</b>
4.1 Introduction	100
4.2 Unburned Mixture Composition	102
4.3 Gas Property Relationships	107
4.4 A Simple Analytic Ideal Gas Model	109
4.5 Thermodynamic Charts	112
4.5.1 Unburned Mixture Charts	112
4.5.2 Burned Mixture Charts	116
4.5.3 Relation between Unburned and Burned Mixture Charts	123
4.6 Tables of Properties and Composition	127
4.7 Computer Routines for Property and Composition Calculations	130
4.7.1 Unburned Mixtures	130
4.7.2 Burned Mixtures	135
4.8 Transport Properties	141
4.9 Exhaust Gas Composition	145
4.9.1 Species Concentration Data	145
4.9.2 Equivalence Ratio Determination from Exhaust Gas Constituents	148
4.9.3 Effects of Fuel/Air Ratio Nonuniformity	152
4.9.4 Combustion Inefficiency	154

<b>Chapter 5 Ideal Models of Engine Cycles</b>	<b>161</b>
Introduction	161
5.2 Ideal Models of Engine Processes	162
Thermodynamic Relations for Engine Processes	164
Cycle Analysis with Ideal Gas Working Fluid with $c_v$ and $c_p$ Constant	169
5.4.1 Constant-Volume Cycle	169
5.4.2 Limited- and Constant-Pressure Cycles	172
5.4.3 Cycle Comparison	173
Fuel-Air Cycle Analysis	177
5.5.1 SI Engine Cycle Simulation	178
5.5.2 CI Engine Cycle Simulation	180
5.5.3 Results of Cycle Calculations	181
Overexpanded Engine Cycles	183
5.7 Availability Analysis of Engine Processes	186
5.7.1 Availability Relationships	186
5.7.2 Entropy Changes in Ideal Cycles	188
5.7.3 Availability Analysis of Ideal Cycles	189
5.7.4 Effect of Equivalence Ratio	192
Comparison with Real Engine Cycles	193
<b>Chapter 6 Gas Exchange Processes</b>	<b>205</b>
6.1 Inlet and Exhaust Processes in the Four-Stroke Cycle	206
6.2 Volumetric Efficiency	209
6.2.1 Quasi-Static Effects	209
6.2.2 Combined Quasi-Static and Dynamic Effects	212
6.2.3 Variation with Speed, and Valve Area, Lift, and Timing	216
6.3 Flow Through Valves	220
6.3.1 Poppet Valve Geometry and Timing	220
6.3.2 Flow Rate and Discharge Coefficients	225
6.4 Residual Gas Fraction	230
6.5 Exhaust Gas Flow Rate and Temperature Variation	231
6.6 Scavenging in Two-Stroke Cycle Engines	235
6.6.1 Two-Stroke Engine Configurations	235
6.6.2 Scavenging Parameters and Models	237
6.6.3 Actual Scavenging Processes	240
6.7 Flow Through Ports	245
6.8 Supercharging and Turbocharging	248
6.8.1 Methods of Power Boosting	248
6.8.2 Basic Relationships	249
6.8.3 Compressors	255
6.8.4 Turbines	263
6.8.5 Wave-Compression Devices	270
<b>Chapter 7 SI Engine Fuel Metering and Manifold Phenomena</b>	<b>279</b>
7.1 Spark-Ignition Engine Mixture Requirements	279
Carburetors	282

7.2.1 Carburetor Fundamentals	282	9.6.2 Knock Fundamentals	457	
7.2.2 Modern Carburetor Design	285	9.6.3 Fuel Factors	470	
<b>7.3 Fuel-Injection Systems</b>	<b>294</b>	<b>Chapter 10</b>	<b>Combustion in Compression-Ignition Engines</b>	<b>491</b>
7.3.1 Multipoint Port Injection	294	10.1 Essential Features of Process	491	
7.3.2 Single-Point Throttle-Body Injection	299	10.2 Types of Diesel Combustion Systems	493	
<b>7.4 Feedback Systems</b>	<b>301</b>	10.2.1 Direct-Injection Systems	493	
<b>7.5 Flow Past Throttle Plate</b>	<b>304</b>	10.2.2 Indirect-Injection Systems	494	
<b>7.6 Flow in Intake Manifolds</b>	<b>308</b>	10.2.3 Comparison of Different Combustion Systems	495	
7.6.1 Design Requirements	308	Phenomenological Model of Compression-Ignition Engine		
7.6.2 Air-Flow Phenomena	309	Combustion	497	
7.6.3 Fuel-Flow Phenomena	314	10.3.1 Photographic Studies of Engine Combustion	497	
<b>Chapter 8 Charge Motion within the Cylinder</b>	<b>326</b>	10.3.2 Combustion in Direct-Injection, Multispray Systems	503	
8.1 Intake Jet Flow	326	10.3.3 Application of Model to Other Combustion Systems	506	
8.2 Mean Velocity and Turbulence Characteristics	330	Analysis of Cylinder Pressure Data	508	
8.2.1 Definitions	330	10.4.1 Combustion Efficiency	509	
8.2.2 Application to Engine Velocity Data	336	10.4.2 Direct-Injection Engines	509	
<b>8.3 Swirl</b>	<b>342</b>	10.4.3 Indirect-Injection Engines	514	
8.3.1 Swirl Measurement	343	10.5 Fuel Spray Behavior	517	
8.3.2 Swirl Generation during Induction	345	10.5.1 Fuel Injection	517	
8.3.3 Swirl Modification within the Cylinder	349	10.5.2 Overall Spray Structure	522	
8.4 Squish	353	10.5.3 Atomization	525	
8.5 Prechamber Engine Flows	357	10.5.4 Spray Penetration	529	
8.6 Crevice Flows and Blowby	360	10.5.5 Droplet Size Distribution	532	
8.7 Flows Generated by Piston–Cylinder Wall Interaction	365	10.5.6 Spray Evaporation	535	
<b>Chapter 9 Combustion in Spark-Ignition Engines</b>	<b>371</b>	10.6 Ignition Delay	539	
9.1 Essential Features of Process	371	10.6.1 Definition and Discussion	539	
9.2 Thermodynamic Analysis of SI Engine Combustion	376	10.6.2 Fuel Ignition Quality	541	
9.2.1 Burned and Unburned Mixture States	376	10.6.3 Autoignition Fundamentals	542	
9.2.2 Analysis of Cylinder Pressure Data	383	10.6.4 Physical Factors Affecting Delay	546	
9.2.3 Combustion Process Characterization	389	10.6.5 Effect of Fuel Properties	550	
<b>9.3 Flame Structure and Speed</b>	<b>390</b>	10.6.6 Correlations for Ignition Delay in Engines	553	
9.3.1 Experimental Observations	390	Mixing-Controlled Combustion	555	
9.3.2 Flame Structure	395	10.7.1 Background	555	
9.3.3 Laminar Burning Speeds	402	10.7.2 Spray and Flame Structure	555	
9.3.4 Flame Propagation Relations	406	10.7.3 Fuel-Air Mixing and Burning Rates	558	
<b>9.4 Cyclic Variations in Combustion, Partial Burning, and Misfire</b>	<b>413</b>	<b>Chapter 11 Pollutant Formation and Control</b>	<b>567</b>	
9.4.1 Observations and Definitions	413	11.1 Nature and Extent of Problem	567	
9.4.2 Causes of Cycle-by-Cycle and Cylinder-to-Cylinder		11.2 Nitrogen Oxides	572	
Variations	419	11.2.1 Kinetics of NO Formation	572	
9.4.3 Partial Burning, Misfire, and Engine Stability	424	11.2.2 Formation of NO <sub>2</sub>	577	
<b>9.5 Spark Ignition</b>	<b>427</b>	11.2.3 NO Formation in Spark-Ignition Engines	578	
9.5.1 Ignition Fundamentals	427	11.2.4 NO <sub>x</sub> Formation in Compression-Ignition Engines	586	
9.5.2 Conventional Ignition Systems	437	11.3 Carbon Monoxide	592	
9.5.3 Alternative Ignition Approaches	443	11.4 Unburned Hydrocarbon Emissions	596	
<b>9.6 Abnormal Combustion: Knock and Surface Ignition</b>	<b>450</b>	11.4.1 Background	596	
9.6.1 Description of Phenomena	450	11.4.2 Flame Quenching and Oxidation Fundamentals	599	

	11.4.3 HC Emissions from Spark-Ignition Engines	601		13.3.1 Lubricated Friction	715
	11.4.4 Hydrocarbon Emission Mechanisms in Diesel Engines	620		13.3.2 Turbulent Dissipation	719
11.5	Particulate Emissions	626		13.3.3 Total Friction	719
	11.5.1 Spark-Ignition Engine Particulates	626	13.4	Measurement Methods	719
	11.5.2 Characteristics of Diesel Particulates	626	13.5	Engine Friction Data	722
	11.5.3 Particulate Distribution within the Cylinder	631		13.5.1 SI Engines	722
	11.5.4 Soot Formation Fundamentals	635		13.5.2 Diesel Engines	724
	11.5.5 Soot Oxidation	642	13.6	Engine Friction Components	725
	11.5.6 Adsorption and Condensation	646		13.6.1 Motored Engine Breakdown Tests	725
11.6	Exhaust Gas Treatment	648		13.6.2 Pumping Friction	726
	11.6.1 Available Options	648		13.6.3 Piston Assembly Friction	729
	11.6.2 Catalytic Converters	649		13.6.4 Crankshaft Bearing Friction	734
	11.6.3 Thermal Reactors	657	13.7	13.6.5 Valve Train Friction	737
	11.6.4 Particulate Traps	659		Accessory Power Requirements	739
<b>Chapter 12</b>	<b>Engine Heat Transfer</b>	<b>668</b>		Lubrication	740
12.1	Importance of Heat Transfer	668		13.8.1 Lubrication System	740
12.2	Modes of Heat Transfer	670		13.8.2 Lubricant Requirements	741
	12.2.1 Conduction	670	<b>Chapter 14</b>	<b>Modeling Real Engine Flow and Combustion Processes</b>	<b>748</b>
	12.2.2 Convection	670		Purpose and Classification of Models	748
	12.2.3 Radiation	671		Governing Equations for Open Thermodynamic System	750
	12.2.4 Overall Heat-Transfer Process	671	14.2	14.2.1 Conservation of Mass	750
12.3	Heat Transfer and Engine Energy Balance	673		14.2.2 Conservation of Energy	751
12.4	Convective Heat Transfer	676	14.3	Intake and Exhaust Flow Models	753
	12.4.1 Dimensional Analysis	676		14.3.1 Background	753
	12.4.2 Correlations for Time-Averaged Heat Flux	677		14.3.2 Quasi-Steady Flow Models	753
	12.4.3 Correlations for Instantaneous Spatial Average Coefficients	678		14.3.3 Filling and Emptying Methods	754
	12.4.4 Correlations for Instantaneous Local Coefficients	681		14.3.4 Gas Dynamic Models	756
	12.4.5 Intake and Exhaust System Heat Transfer	682	14.4	Thermodynamic-Based In-Cylinder Models	762
12.5	Radiative Heat Transfer	683		14.4.1 Background and Overall Model Structure	762
	12.5.1 Radiation from Gases	683		14.4.2 Spark-Ignition Engine Models	766
	12.5.2 Flame Radiation	684		14.4.3 Direct-Injection Engine Models	778
	12.5.3 Prediction Formulas	688		14.4.4 Prechamber Engine Models	784
12.6	Measurements of Instantaneous Heat-Transfer Rates	689		14.4.5 Multicylinder and Complex Engine System Models	789
	12.6.1 Measurement Methods	689		14.4.6 Second Law Analysis of Engine Processes	792
	12.6.2 Spark-Ignition Engine Measurements	690	14.5	Fluid-Mechanic-Based Multidimensional Models	797
	12.6.3 Diesel Engine Measurements	692		14.5.1 Basic Approach and Governing Equations	797
	12.6.4 Evaluation of Heat-Transfer Correlations	694		14.5.2 Turbulence Models	800
	12.6.5 Boundary-Layer Behavior	697		14.5.3 Numerical Methodology	803
12.7	Thermal Loading and Component Temperatures	698		14.5.4 Flow Field Predictions	807
	12.7.1 Component Temperature Distributions	698		14.5.5 Fuel Spray Modeling	813
	12.7.2 Effect of Engine Variables	701		14.5.6 Combustion Modeling	816
<b>Chapter 13</b>	<b>Engine Friction and Lubrication</b>	<b>712</b>	<b>Chapter 15</b>	<b>Engine Operating Characteristics</b>	<b>823</b>
13.1	Background	712	15.1	Engine Performance Parameters	823
13.2	Definitions	714	15.2	Indicated and Brake Power and MEP	824
13.3	Friction Fundamentals	715			

15.3	Operating Variables That Affect SI Engine Performance, Efficiency, and Emissions	827
15.3.1	Spark Timing	827
15.3.2	Mixture Composition	829
15.3.3	Load and Speed	839
15.3.4	Compression Ratio	841
15.4	SI Engine Combustion Chamber Design	844
15.4.1	Design Objectives and Options	844
15.4.2	Factors That Control Combustion	846
15.4.3	Factors That Control Performance	850
15.4.4	Chamber Octane Requirement	852
15.4.5	Chamber Optimization Strategy	857
15.5	Variables That Affect CI Engine Performance, Efficiency, and Emissions	858
15.5.1	Load and Speed	858
15.5.2	Fuel-Injection Parameters	863
15.5.3	Air Swirl and Bowl-in-Piston Design	866
15.6	Supercharged and Turbocharged Engine Performance	869
15.6.1	Four-Stroke Cycle SI Engines	869
15.6.2	Four-Stroke Cycle CI Engines	874
15.6.3	Two-Stroke Cycle SI Engines	881
15.6.4	Two-Stroke Cycle CI Engines	883
15.7	Engine Performance Summary	886
 Appendixes		
A	Unit Conversion Factors	899
B	Ideal Gas Relationships	902
B.1	Ideal Gas Law	902
B.2	The Mole	903
B.3	Thermodynamic Properties	903
B.4	Mixtures of Ideal Gases	905
C	Equations for Fluid Flow through a Restriction	906
C.1	Liquid Flow	907
C.2	Gas Flow	907
D	Data on Working Fluids	911
Index		917

## PREFACE

Internal combustion engines date back to 1876 when Otto first developed the spark-ignition engine and 1892 when Diesel invented the compression-ignition engine. Since that time these engines have continued to develop as our knowledge of engine processes has increased, as new technologies became available, as demand for new types of engine arose, and as environmental constraints on engine use changed. Internal combustion engines, and the industries that develop and manufacture them and support their use, now play a dominant role in the fields of power, propulsion, and energy. The last twenty-five years or so have seen an explosive growth in engine research and development as the issues of air pollution, fuel cost, and market competitiveness have become increasingly important. An enormous technical literature on engines now exists which has yet to be adequately organized and summarized.

This book has been written as a text and a professional reference in response to that need. It contains a broadly based and extensive review of the fundamental principles which govern internal combustion engine design and operation. It attempts to provide a simplifying framework for the vast and complex mass of technical material that now exists on spark-ignition and compression-ignition engines, and at the same time to include sufficient detail to convey the real world dimensions of this pragmatic engineering field. It is the author's conviction that a sound knowledge of the relevant fundamentals in the many disciplines that contribute to this field, as well as an awareness of the extensive practical knowledge base which has been built up over many decades, are essential tools for engine research, development, and design. Of course, no one text can include everything about engines. The emphasis here is on the thermodynamics, combustion physics and chemistry, fluid flow, heat transfer, friction, and lubrication processes relevant to internal combustion engine design, performance, efficiency, emissions, and fuels requirements.

From a fundamental point of view, how the fuel-air mixture within an internal combustion engine cylinder is ignited appropriately organizes the field. From the method of ignition—spark-ignition or compression-ignition—follows each type of engine's important features: fuel requirements, method of mixture preparation, combustion chamber design, details of the combustion process, method of load control, emission formation mechanisms, and performance and efficiency characteristics. While many engine processes (such as intake and exhaust flows, convective heat transfer, and friction) are similar in both types of engines, this distinction is fundamental and lies behind the overall organization of the book.

The book is arranged in four major sections. The first (Chapters 1 to 5) provides an introduction to, and overview of, the major characteristics of spark-ignition and compression-ignition engines, defines the parameters used to describe engine operation, and develops the necessary thermodynamics and combustion theory required for a quantitative analysis of engine behavior. It concludes with an integrated treatment of the various methods of analyzing idealized models of internal combustion engine cycles. The second section (Chapters 6 to 8) focuses on engine flow phenomena. The details of the gas exchange process—intake and exhaust processes in four-stroke and scavenging in two-stroke cycles—and the various methods of supercharging engines—are reviewed. Fuel metering methods for spark-ignition engines and air- and fuel-flow phenomena in intake manifolds are described. The essential features of the various types of fluid motion within the engine cylinder are then developed. These flow processes control the amount of air an engine will induct (and therefore its power), and largely govern the rate at which the fuel-air mixture will burn during combustion.

The third section of the book focuses on engine combustion phenomena. These chapters (9, 10, and 11) are especially important. The combustion process releases the fuel's energy within the engine cylinder for eventual conversion to useful work. What fraction of the fuel's energy is converted depends strongly on how combustion takes place. The spark-ignition and compression-ignition engine combustion processes (Chapters 9 and 10, respectively) therefore influence essentially all aspects of engine behavior. Air pollutants are undesirable byproducts of combustion. Our extensive knowledge of how the major pollutants form during these combustion processes and how such emissions can be controlled is reviewed in Chapter 11.

The last section of the book focuses on engine operating characteristics. First, the fundamentals of engine heat transfer and friction, both of which detract from engine performance, are developed in Chapters 12 and 13. Chapter 14 then focuses on the methods available for predicting important aspects of engine behavior based on realistic models of engine flow and combustion processes. Since the various thermodynamic-based and fluid-mechanic-based models which have been developed over the past fifteen years or so are increasingly used in engine research and development, a knowledge of their basic structure and capabilities is most important. Then, Chapter 15 presents a summary of how the operating characteristics—power, efficiency, and emissions—of spark-ignition and compression-ignition engines depend on the major engine design and oper-

ating variables. These final two chapters effectively integrate the analytical understanding and practical knowledge of individual engine processes together to describe overall spark-ignition and compression-ignition engine behavior. Material on internal combustion engine fuels is distributed appropriately throughout the book. Each chapter is extensively illustrated and referenced, and includes problems for both undergraduate and graduate level courses.

While this book contains much advanced material on engine design and operation intended for the practitioner, each major topic is developed from its beginnings and the more sophisticated chapters have introductory sections to facilitate their use in undergraduate courses. The chapters are extensively cross-referenced and indexed. Thus several arrangements of the material for a course on engines can be followed. For example, an introductory course on internal combustion engines could begin with Chapters 1 and 2, which review the different types of engines and how their performance is characterized, and continue with the parts of Chapters 3 and 5, which introduce the key combustion concepts necessary to understand the effects of fuel/air ratio, and ideal cycle analysis. Selections from the introductory sections of Chapters 6, 9, 10, 11, and 15 could then be used to explain several of the practical and design aspects of spark-ignition and diesel engine intake and exhaust processes, combustion, emissions, and performance. A more advanced course would review this introductory material more rapidly, and then move on to those sections of Chapters 4 and 5, which cover fuel-air cycle analysis, a more extensive discussion of engine breathing using additional sections of Chapter 6, and more in-depth treatment of engine combustion and emissions processes based on the appropriate sections of Chapters 9, 10, and 11. Material on engine heat transfer and friction selected from Chapters 12 and 13 could be included next. While Chapter 14 on modeling the thermodynamics and fluid dynamics of real engine processes is primarily intended for the professional scientist and engineer, material from this chapter along with selections from Chapter 15 could be used to illustrate the performance, efficiency, and emissions characteristics of the different types of internal combustion engines. I have also used much of the more sophisticated material in Chapters 6 through 15 for review seminars on individual engine topics and more extensive courses for professional engineers, an additional important educational and reference opportunity.

Many individuals and organizations have assisted me in various ways as I have worked on this book over the past ten or so years. I am especially indebted to my colleagues in the Sloan Automotive Laboratory at M.I.T., Professors Wai K. Cheng, Ahmed F. Ghoniem, and James C. Keck, and Drs. Jack A. Ekchian, David P. Hoult, Joe M. Rife, and Victor W. Wong, for providing a stimulating environment in which to carry out engine research and for assuming additional burdens as a result of my writing. Many of the Sloan Automotive Laboratory's students have made significant contributions to this text through their research; their names appear in the reference lists. The U.S. Department of Energy provided support during the early stages of the text development and funded the work on engine cycle simulation used extensively in Chapters 14 and 15. I am grateful

to Churchill College, Cambridge University, for a year spent as a Richard C. Mellon Visiting Fellow, 1977-78, and the Engineering Department, Cambridge University, for acting as my host while I developed the outline and earlier chapters of the book. The M.I.T. sabbatical leave fund supported my full-time writing for eight months in 1983, and the Mechanical Engineering Department at Imperial College graciously acted as host.

I also want to acknowledge several individuals and organizations who have provided major inputs to this book beyond those cited in the references. Members of General Motors Research Laboratories have interacted extensively with the Sloan Automotive Laboratory over many years and provided valuable advice on engine research developments. Engineers from the Engine Research and Fluid Mechanics Departments at General Motors Research Laboratories reviewed and critiqued the final draft manuscript for me. Charles A. Amann, Head of the Engine Research Department, made especially helpful inputs on engine performance. John J. Brogan of the U.S. Department of Energy provided valuable assistance with the initial organization of this effort. My regular interactions over the years with the Advanced Powertrain Engineering Office and Scientific Research Laboratories of the Ford Motor Company have given me a broad exposure to the practical side of engine design and operation. A long-term relationship with Mobil Research and Development Corporation has provided comparable experiences in the area of engine-fuels interactions. Many organizations and individuals supplied specific material and illustrations for the text. I am especially grateful to those who made available the high-quality photographs and line drawings which I have used and acknowledged.

McGraw-Hill and the author would like to express their thanks to the following reviewers for their useful comments and suggestions: Jay A. Bolt, University of Michigan; Gary L. Borman and William L. Brown, University of Wisconsin at Madison; Dwight Bushnell, Oregon State University; Jerald A. Caton, Texas A & M University; David E. Cole, University of Michigan; Lawrence W. Evers, Michigan Technological University; Samuel S. Lestz, Pennsylvania State University; Willard Pulkrabek, University of Wisconsin; Robert F. Sawyer, University of California at Berkeley; Joseph E. Shepherd, Rensselaer Polytechnic Institute; and Spencer C. Sorenson, The Technical University of Denmark.

Special thanks are due to my secretaries for their faithful and thoughtful assistance with the manuscript over these many years, beyond the "call of duty"; Linda Pope typed an earlier draft of the book, and Karla Stryker was responsible for producing and coordinating subsequent drafts and the final manuscript. My wife Peggy, and sons James, Stephen, and Ben have encouraged me throughout this long and time-consuming project which took many hours away from them. Without their continuing support it would never have been finished; for their patience, and faith that it would ultimately come to fruition, I will always be grateful.

*John B. Heywood*

## ACKNOWLEDGMENTS

The author wishes to acknowledge the following organizations and publishers for permission to reproduce figures and tables from their publications in this text: The American Chemical Society; American Institute of Aeronautics & Astronautics; American Society of Mechanical Engineers; Robert Bosch GmbH, CIMAC, Cambridge University Press; The Combustion Institute; Elsevier Science Publishing Company; G. T. Foulis & Co. Ltd.; General Motors Corporation; Gordon & Breach Science Publishers; The Institution of Mechanical Engineers; The Japan Society of Mechanical Engineers; M.I.T. Press; Macmillan Press Ltd.; McGraw-Hill Book Company; Mir Publishers; Mobil Oil Corporation; Morgan-Grampian Publishers; Pergamon Journals, Inc.; Plenum Press Corporation; The Royal Society of London; Scientific Publications Limited; Society of Automotive Engineers; Society of Automotive Engineers of Japan, Inc.; Society of Tribologists and Lubrications Engineers; Department of Mechanical Engineering, Stanford University.

---

## COMMONLY USED SYMBOLS, SUBSCRIPTS, AND ABBREVIATIONS<sup>†</sup>

---

### 1. SYMBOLS

$a$	Crank radius
	Sound speed
	Specific availability
$a$	Acceleration
$A$	Area
$A_c$	Valve curtain area
$A_{ch}$	Cylinder head area
$A_e$	Exhaust port area
$A_E$	Effective area of flow restriction
$A_i$	Inlet port area
$A_p$	Piston crown area
$B$	Cylinder bore
	Steady-flow availability
$c$	Specific heat
$c_p$	Specific heat at constant pressure
$c_s$	Soot concentration (mass/volume)
$c_v$	Specific heat at constant volume
$C$	Absolute gas velocity

---

<sup>†</sup> Nomenclature specific to a section or chapter is defined in that section or chapter.

$C_s$	Swirl coefficient
$C_D$	Discharge coefficient
$V$	Vehicle drag coefficient
$d$	Diameter
$d_n$	Fuel-injection-nozzle orifice diameter
$D$	Diameter
$D_d$	Diffusion coefficient
$D_{SM}$	Droplet diameter
$D_v$	Sauter mean droplet diameter
$e$	Valve diameter
$E_A$	Radiative emissive power
$f$	Specific energy
$F$	Activation energy
$g$	Coefficient of friction
$G$	Fuel mass fraction
$h$	Force
$h$	Gravitational acceleration
$h$	Specific Gibbs free energy
$h$	Gibbs free energy
$h$	Clearance height
$h_c$	Oil film thickness
$h_p$	Specific enthalpy
$h_s$	Heat-transfer coefficient
$H$	Port open height
$I$	Sensible specific enthalpy
$J$	Enthalpy
$k$	Moment of inertia
$k^+, k^-$	Flux
$K$	Thermal conductivity
$K_i$	Turbulent kinetic energy
$K$	Forward, backward, rate constants for $i$ th reaction
$K_c$	Constant
$K_p$	Equilibrium constant expressed in concentrations
$l$	Equilibrium constant expressed in partial pressures
$l_T$	Characteristic length scale
$L$	Connecting rod length
$L_n$	Characteristic length scale of turbulent flame
$L_v$	Piston stroke
$m$	Fuel-injection-nozzle orifice length
$\dot{m}$	Valve lift
$m_r$	Mass
$M$	Mass flow rate
	Mass of residual gas
	Mach number
	Molecular weight

$n$	Number of moles
$n_R$	Polytropic exponent
$N$	Number of crank revolutions per power stroke
$p$	Crankshaft rotational speed
$q$	Soot particle number density
$Q$	Turbocharger shaft speed
$Q$	Cylinder pressure
$P$	Pressure
$q$	Power
$Q$	Heat-transfer rate per unit area
$Q$	Heat-transfer rate per unit mass of fluid
$Q_{ch}$	Heat transfer
$Q_{hv}$	Heat-transfer rate
$Q_n$	Fuel chemical energy release or gross heat release
$r$	Fuel heating value
$r_c$	Net heat release
$R$	Radius
$R^+, R^-$	Compression ratio
$R_s$	Connecting rod length/crank radius
$s$	Gas constant
$S$	Radius
$S_b$	One-way reaction rates
$S_L$	Swirl ratio
$S_p$	Crank axis to piston pin distance
$t$	Specific entropy
$T$	Entropy
$u$	Spray penetration
$u'$	Turbulent burning speed
$u_s$	Laminar flame speed
$u_T$	Piston speed
$U$	Time
$v$	Temperature
$v$	Torque
$v$	Velocity
$v_{ps}$	Specific internal energy
$v$	Velocity
$v$	Turbulence intensity
$v$	Sensible specific internal energy
$v$	Characteristic turbulent velocity
$v$	Compressor/turbine impellor tangential velocity
$v$	Fluid velocity
$v$	Internal energy
$v$	Specific volume
$v$	Velocity
$v$	Velocity
$v_{ps}$	Velocity
$v_{ps}$	Valve pseudo-flow velocity

$v_{sq}$	Squish velocity
$V$	Cylinder volume
$V$	Volume
$V_c$	Clearance volume
$V_d$	Displaced cylinder volume
$w$	Relative gas velocity
	Soot surface oxidation rate
$W$	Work transfer
$W_c$	Work per cycle
$W_p$	Pumping work
$x, y, z$	Spatial coordinates
$x$	Mass fraction
$\tilde{x}$	Mole fraction
$x_b$	Burned mass fraction
$x_r$	Residual mass fraction
$y$	H/C ratio of fuel
	Volume fraction
$Y_\alpha$	Concentration of species $\alpha$ per unit mass
$Z$	Inlet Mach index
$\alpha$	Angle
	Thermal diffusivity $k/(\rho c)$
$\beta$	Angle
$\gamma$	Specific heat ratio $c_p/c_v$
$\Gamma_c$	Angular momentum of charge
$\delta$	Boundary-layer thickness
$\delta_L$	Laminar flame thickness
$\Delta h_{f,i}^\circ$	Molal enthalpy of formation of species $i$
$\Delta\theta_b$	Rapid burning angle
$\Delta\theta_d$	Flame development angle
$\varepsilon$	$4/(4+y)$ : $y = \text{H/C ratio of fuel}$
	Turbulent kinetic energy dissipation rate
$\eta_a$	Availability conversion efficiency
$\eta_c$	Combustion efficiency
$\eta_C$	Compressor isentropic efficiency
$\eta_{ch}$	Charging efficiency
$\eta_f$	Fuel conversion efficiency
$\eta_m$	Mechanical efficiency
$\eta_{sc}$	Scavenging efficiency
$\eta_t$	Thermal conversion efficiency
$\eta_T$	Turbine isentropic efficiency
$\eta_{tr}$	Trapping efficiency
$\eta_v$	Volumetric efficiency
$\theta$	Crank angle
$\lambda$	Relative air/fuel ratio
$\Lambda$	Delivery ratio

$\mu$	Dynamic viscosity
$\mu_i$	Chemical potential of species $i$
$\nu$	Kinematic viscosity $\mu/\rho$
$v_i$	Stoichiometric coefficient of species $i$
$\xi$	Flow friction coefficient
$\rho$	Density
$\rho_{a,0}, \rho_{a,i}$	Air density at standard, inlet conditions
$\sigma$	Normal stress
	Standard deviation
	Stefan-Boltzmann constant
	Surface tension
$\tau$	Characteristic time
	Induction time
	Shear stress
$\tau_{id}$	Ignition delay time
$\phi$	Fuel/air equivalence ratio
$\Phi$	Flow compressibility function [Eq. (C.11)]
	Isentropic compression function [Eq. (4.15b)]
$\psi$	Molar N/O ratio
	Throttle plate open angle
$\Psi$	Isentropic compression function [Eq. (4.15a)]
$\omega$	Angular velocity
	Frequency

## 2. SUBSCRIPTS

$a$	Air
$b$	Burned gas
$c$	Coolant
$C$	Cylinder
	Compression stroke
	Compressor
$cr$	Crevice
$e$	Equilibrium
	Exhaust
$E$	Expansion stroke
$f$	Flame
	Friction
	Fuel
$g$	Gas
$i$	Indicated
	Intake
	Species $i$
$ig$	Gross indicated
$in$	Net indicated

<i>l</i>	Liquid
<i>L</i>	Laminar
<i>p</i>	Piston
<i>P</i>	Port
<i>P</i>	Prechamber
<i>r, θ, z</i>	<i>r, θ, z</i> components
<i>R</i>	Reference value
<i>s</i>	Isentropic
	Stoichiometric
<i>T</i>	Nozzle or orifice throat
	Turbine
	Turbulent
<i>u</i>	Unburned
<i>v</i>	Valve
<i>w</i>	Wall
<i>x, y, z</i>	<i>x, y, z</i> components
0	Reference value
	Stagnation value

ON	Fuel octane number
Re	Reynolds number $\rho u L / \mu$
sfc	Specific fuel consumption
TC, ATC, BTC	Top-center crank position, after TC, before TC
We	Weber number $\rho_i u^2 D / \sigma$

### 3. NOTATION

Δ	Difference
—	Average or mean value
~	Value per mole
[ ]	Concentration, moles/vol
{ }	Mass fraction
.	Rate of change with time

### 4. ABBREVIATIONS

(A/F)	Air/fuel ratio
BC, ABC, BBC	Bottom-center crank position, after BC, before BC
CN	Fuel cetane number
Da	Damköhler number $\tau_T / \tau_L$
EGR	Exhaust gas recycle
EI	Emission index
EPC, EPO	Exhaust port closing, opening
EVC, EVO	Exhaust valve closing, opening
(F/A)	Fuel/air ratio
(G/F)	Gas/fuel ratio
IPC, IPO	Inlet port closing, opening
IVC, IVO	Inlet valve closing, opening
mep	Mean effective pressure
Nu	Nusselt number $h_c l / k$

---

# CHAPTER

# 1

---

## ENGINE TYPES AND THEIR OPERATION

### 1.1 INTRODUCTION AND HISTORICAL PERSPECTIVE

The purpose of internal combustion engines is the production of mechanical power from the chemical energy contained in the fuel. In *internal* combustion engines, as distinct from *external* combustion engines, this energy is released by burning or oxidizing the fuel *inside* the engine. The fuel-air mixture before combustion and the burned products after combustion are the actual working fluids. The work transfers which provide the desired power output occur directly between these working fluids and the mechanical components of the engine. The internal combustion engines which are the subject of this book are spark-ignition engines (sometimes called Otto engines, or gasoline or petrol engines, though other fuels can be used) and compression-ignition or diesel engines.<sup>†</sup> Because of their simplicity, ruggedness and high power/weight ratio, these two types of engine have found wide application in transportation (land, sea, and air) and power generation. It is the fact that combustion takes place inside the work-

---

<sup>†</sup> The gas turbine is also, by this definition, an "internal combustion engine." Conventionally, however, the term is used for spark-ignition and compression-ignition engines. The operating principles of gas turbines are fundamentally different, and they are not discussed as separate engines in this book.

producing part of these engines that makes their design and operating characteristics fundamentally different from those of other types of engine.

Practical heat engines have served mankind for over two and a half centuries. For the first 150 years, water, raised to steam, was interposed between the combustion gases produced by burning the fuel and the work-producing piston-in-cylinder expander. It was not until the 1860s that the internal combustion engine became a practical reality.<sup>1, 2</sup> The early engines developed for commercial use burned coal-gas air mixtures at atmospheric pressure—there was no compression before combustion. J. J. E. Lenoir (1822–1900) developed the first marketable engine of this type. Gas and air were drawn into the cylinder during the first half of the piston stroke. The charge was then ignited with a spark, the pressure increased, and the burned gases then delivered power to the piston for the second half of the stroke. The cycle was completed with an exhaust stroke. Some 5000 of these engines were built between 1860 and 1865 in sizes up to six horsepower. Efficiency was at best about 5 percent.

A more successful development—an atmospheric engine introduced in 1867 by Nicolaus A. Otto (1832–1891) and Eugen Langen (1833–1895)—used the pressure rise resulting from combustion of the fuel-air charge early in the outward stroke to accelerate a free piston and rack assembly so its momentum would generate a vacuum in the cylinder. Atmospheric pressure then pushed the piston inward, with the rack engaged through a roller clutch to the output shaft. Production engines, of which about 5000 were built, obtained thermal efficiencies of up to 11 percent. A slide valve controlled intake, ignition by a gas flame, and exhaust.

To overcome this engine's shortcomings of low thermal efficiency and excessive weight, Otto proposed an engine cycle with four piston strokes: an intake stroke, then a compression stroke before ignition, an expansion or power stroke where work was delivered to the crankshaft, and finally an exhaust stroke. He also proposed incorporating a stratified-charge induction system, though this was not achieved in practice. His prototype four-stroke engine first ran in 1876. A comparison between the Otto engine and its atmospheric-type predecessor indicates the reason for its success (see Table 1.1): the enormous reduction in engine weight and volume. This was the breakthrough that effectively founded the internal combustion engine industry. By 1890, almost 50,000 of these engines had been sold in Europe and the United States.

In 1884, an unpublished French patent issued in 1862 to Alphonse Beau de Rochas (1815–1893) was found which described the principles of the four-stroke cycle. This chance discovery cast doubt on the validity of Otto's own patent for this concept, and in Germany it was declared invalid. Beau de Rochas also outlined the conditions under which maximum efficiency in an internal combustion engine could be achieved. These were:

1. The largest possible cylinder volume with the minimum boundary surface
2. The greatest possible working speed

TABLE 1.1  
Comparison of Otto four-stroke cycle and Otto-Langen engines<sup>2</sup>

	Otto and Langen	Otto four-stroke
Brake horsepower	2	2
Weight, lb, approx.	4000	1250
Piston displacement, in <sup>3</sup>	4900	310
Power strokes per min	28	80
Shaft speed, rev/min	90	160
Mechanical efficiency, %	68	84
Overall efficiency, %	11	14
Expansion ratio	10	2.5

3. The greatest possible expansion ratio
4. The greatest possible pressure at the beginning of expansion

The first two conditions hold heat losses from the charge to a minimum. The third condition recognizes that the greater the expansion of the postcombustion gases, the greater the work extracted. The fourth condition recognizes that higher initial pressures make greater expansion possible, and give higher pressures throughout the process, both resulting in greater work transfer. Although Beau de Rochas' unpublished writings predate Otto's developments, he never reduced these ideas to practice. Thus Otto, in the broader sense, was the inventor of the modern internal combustion engine as we know it today.

Further developments followed fast once the full impact of what Otto had achieved became apparent. By the 1880s several engineers (e.g., Dugald Clerk, 1854–1913; and James Robson, 1833–1913, in England and Karl Benz, 1844–1929, in Germany) had successfully developed two-stroke internal combustion engines where the exhaust and intake processes occur during the end of the power stroke and the beginning of the compression stroke. James Atkinson (1846–1914) in England made an engine with a longer expansion than compression stroke, which had a high efficiency for the times but mechanical weaknesses. It was recognized that efficiency was a direct function of expansion ratio, yet compression ratios were limited to less than four if serious knock problems were to be avoided with the available fuels. Substantial carburetor and ignition system developments were required, and occurred, before high-speed gasoline engines suitable for automobiles became available in the late 1880s. Stationary engine progress also continued. By the late 1890s, large single-cylinder engines of 1.3-m bore fueled by low-energy blast furnace gas produced 600 bhp at 90 rev/min. In Britain, legal restrictions on volatile fuels turned their engine builders toward kerosene. Low compression ratio "oil" engines with heated external fuel vaporizers and electric ignition were developed with efficiencies comparable to those of gas engines (14 to 18 percent). The Hornsby-Ackroyd engine became the most

popular oil engine in Britain, and was also built in large numbers in the United States.<sup>2</sup>

In 1892, the German engineer Rudolf Diesel (1858–1913) outlined in his patent a new form of internal combustion engine. His concept of initiating combustion by injecting a liquid fuel into air heated solely by compression permitted a doubling of efficiency over other internal combustion engines. Much greater expansion ratios, without detonation or knock, were now possible. However, even with the efforts of Diesel and the resources of M.A.N. in Ausburg combined, it took five years to develop a practical engine.

Engine developments, perhaps less fundamental but nonetheless important to the steadily widening internal combustion engine markets, have continued ever since.<sup>2–4</sup> One more recent major development has been the rotary internal combustion engine. Although a wide variety of experimental rotary engines have been proposed over the years,<sup>5</sup> the first practical rotary internal combustion engine, the Wankel, was not successfully tested until 1957. That engine, which evolved through many years of research and development, was based on the designs of the German inventor Felix Wankel.<sup>6, 7</sup>

Fuels have also had a major impact on engine development. The earliest engines used for generating mechanical power burned gas. Gasoline, and lighter fractions of crude oil, became available in the late 1800s and various types of carburetors were developed to vaporize the fuel and mix it with air. Before 1905 there were few problems with gasoline; though compression ratios were low (4 or less) to avoid knock, the highly volatile fuel made starting easy and gave good cold weather performance. However, a serious crude oil shortage developed, and to meet the fivefold increase in gasoline demand between 1907 and 1915, the yield from crude had to be raised. Through the work of William Burton (1865–1954) and his associates of Standard Oil of Indiana, a thermal cracking process was developed whereby heavier oils were heated under pressure and decomposed into less complex more volatile compounds. These thermally cracked gasolines satisfied demand, but their higher boiling point range created cold weather starting problems. Fortunately, electrically driven starters, introduced in 1912, came along just in time.

On the farm, kerosene was the logical fuel for internal combustion engines since it was used for heat and light. Many early farm engines had heated carburetors or vaporizers to enable them to operate with such a fuel.

The period following World War I saw a tremendous advance in our understanding of how fuels affect combustion, and especially the problem of knock. The antiknock effect of tetraethyl lead was discovered at General Motors,<sup>4</sup> and it became commercially available as a gasoline additive in the United States in 1923. In the late 1930s, Eugene Houdry found that vaporized oils passed over an activated catalyst at 450 to 480°C were converted to high-quality gasoline in much higher yields than was possible with thermal cracking. These advances, and others, permitted fuels with better and better antiknock properties to be produced in large quantities; thus engine compression ratios steadily increased, improving power and efficiency.

During the past three decades, new factors for change have become important and now significantly affect engine design and operation. These factors are, first, the need to control the automotive contribution to urban air pollution and, second, the need to achieve significant improvements in automotive fuel consumption.

The automotive air-pollution problem became apparent in the 1940s in the Los Angeles basin. In 1952, it was demonstrated by Prof. A. J. Haagen-Smit that the smog problem there resulted from reactions between oxides of nitrogen and hydrocarbon compounds in the presence of sunlight.<sup>8</sup> In due course it became clear that the automobile was a major contributor to hydrocarbon and oxides of nitrogen emissions, as well as the prime cause of high carbon monoxide levels in urban areas. Diesel engines are a significant source of small soot or smoke particles, as well as hydrocarbons and oxides of nitrogen. Table 1.2 outlines the dimensions of the problem. As a result of these developments, emission standards for automobiles were introduced first in California, then nationwide in the United States, starting in the early 1960s. Emission standards in Japan and Europe, and for other engine applications, have followed. Substantial reductions in emissions from spark-ignition and diesel engines have been achieved. Both the use of catalysts in spark-ignition engine exhaust systems for emissions control and concern over the toxicity of lead antiknock additives have resulted in the reappearance of unleaded gasoline as a major part of the automotive fuels market. Also, the maximum lead content in leaded gasoline has been substantially reduced. The emission-control requirements and these fuel developments have produced significant changes in the way internal combustion engines are designed and operated.

Internal combustion engines are also an important source of noise. There are several sources of engine noise: the exhaust system, the intake system, the fan used for cooling, and the engine block surface. The noise may be generated by aerodynamic effects, may be due to forces that result from the combustion process, or may result from mechanical excitation by rotating or reciprocating engine components. Vehicle noise legislation to reduce emissions to the environment was first introduced in the early 1970s.

During the 1970s the price of crude petroleum rose rapidly to several times its cost (in real terms) in 1970, and concern built up regarding the longer-term availability of petroleum. Pressures for substantial improvements in internal combustion engine efficiency (in all its many applications) have become very substantial indeed. Yet emission-control requirements have made improving engine fuel consumption more difficult, and the removal and reduction of lead in gasoline has forced spark-ignition engine compression ratios to be reduced. Much work is being done on the use of alternative fuels to gasoline and diesel. Of the non-petroleum-based fuels, natural gas, and methanol and ethanol (methyl and ethyl alcohols) are receiving the greatest attention, while synthetic gasoline and diesel made from shale oil or coal, and hydrogen could be longer-term possibilities.

It might be thought that after over a century of development, the internal

**TABLE 1.2**  
The automotive urban air-pollution problem

Pollutant	Impact	Automobile emissions		Truck emissions††		
		Mobile source emissions as % of total†	Uncontrolled vehicles, g/km‡	Reduction in new vehicles, % ¶	SI engines, g/km	Diesel, g/km
Oxides of nitrogen (NO and NO <sub>2</sub> )	Reactant in photochemical smog; NO <sub>2</sub> is toxic	40–60	2.5	75	7	12
Carbon monoxide (CO)	Toxic	90	65	95	150	17
Unburned hydrocarbons (HC, many hydrocarbon compounds)	Reactant in photochemical smog	30–50	10	90	17††	3
Particulates (soot and absorbed hydrocarbon compounds)	Reduces visibility; some of HC compounds mutagenic	50	0.5§	40§	n	0.5

† Depends on type of urban area and source mix.

‡ Average values for pre-1968 automobiles which had no emission controls, determined by U.S. test procedure which simulates typical urban and highway driving. Exhaust emissions, except for HC where 55 percent are exhaust emissions, 20 percent are evaporative emissions from fuel tank and carburetor, and 25 percent are crankcase blowby gases.

§ Diesel engine automobiles only. Particulate emissions from spark-ignition engines are negligible.

¶ Compares emissions from new spark-ignition engine automobiles with uncontrolled automobile levels in previous column. Varies from country to country. The United States, Canada, Western Europe, and Japan have standards with different degrees of severity. The United States, Europe, and Japan have different test procedures. Standards are strictest in the United States and Japan.

†† Representative average emission levels for trucks.

‡‡ With 95 percent exhaust emissions and 5 percent evaporative emissions.

n = negligible.

combustion engine has reached its peak and little potential for further improvement remains. Such is not the case. Conventional spark-ignition and diesel engines continue to show substantial improvements in efficiency, power, and degree of emission control. New materials now becoming available offer the possibilities of reduced engine weight, cost, and heat losses, and of different and more efficient internal combustion engine systems. Alternative types of internal combustion engines, such as the stratified-charge (which combines characteristics normally associated with either the spark-ignition or diesel) with its wider fuel tolerance, may become sufficiently attractive to reach large-scale production. The engine development opportunities of the future are substantial. While they

present a formidable challenge to automotive engineers, they will be made possible in large part by the enormous expansion of our knowledge of engine processes which the last twenty years has witnessed.

## 1.2 ENGINE CLASSIFICATIONS

There are many different types of internal combustion engines. They can be classified by:

1. *Application.* Automobile, truck, locomotive, light aircraft, marine, portable power system, power generation
2. *Basic engine design.* Reciprocating engines (in turn subdivided by arrangement of cylinders: e.g., in-line, V, radial, opposed), rotary engines (Wankel and other geometries)
3. *Working cycle.* Four-stroke cycle: naturally aspirated (admitting atmospheric air), supercharged (admitting precompressed fresh mixture), and turbocharged (admitting fresh mixture compressed in a compressor driven by an exhaust turbine), two-stroke cycle: crankcase scavenged, supercharged, and turbocharged
4. *Valve or port design and location.* Overhead (or I-head) valves, underhead (or L-head) valves, rotary valves, cross-scavenged porting (inlet and exhaust ports on opposite sides of cylinder at one end), loop-scavenged porting (inlet and exhaust ports on same side of cylinder at one end), through- or uniflow-scavenged (inlet and exhaust ports or valves at different ends of cylinder)
5. *Fuel.* Gasoline (or petrol), fuel oil (or diesel fuel), natural gas, liquid petroleum gas, alcohols (methanol, ethanol), hydrogen, dual fuel
6. *Method of mixture preparation.* Carburetion, fuel injection into the intake ports or intake manifold, fuel injection into the engine cylinder
7. *Method of ignition.* Spark ignition (in conventional engines where the mixture is uniform and in stratified-charge engines where the mixture is non-uniform), compression ignition (in conventional diesels, as well as ignition in gas engines by pilot injection of fuel oil)
8. *Combustion chamber design.* Open chamber (many designs: e.g., disc, wedge, hemisphere, bowl-in-piston), divided chamber (small and large auxiliary chambers; many designs: e.g., swirl chambers, prechambers)
9. *Method of load control.* Throttling of fuel and air flow together so mixture composition is essentially unchanged, control of fuel flow alone, a combination of these
10. *Method of cooling.* Water cooled, air cooled, uncooled (other than by natural convection and radiation)

All these distinctions are important and they illustrate the breadth of engine designs available. Because this book approaches the operating and emissions

**TABLE 1.3**  
Classification of reciprocating engines by application

Class	Service	Approximate engine power range, kW	Predominant type		
			D or SI	Cycle	Cooling
Road vehicles	Motorcycles, scooters	0.75–70	SI	2, 4	A
	Small passenger cars	15–75	SI	4	A, W
	Large passenger cars	75–200	SI	4	W
	Light commercial	35–150	SI, D	4	W
	Heavy (long-distance) commercial	120–400	D	4	W
Off-road vehicles	Light vehicles (factory, airport, etc.)	1.5–15	SI	2, 4	A, W
	Agricultural	3–150	SI, D	2, 4	A, W
	Earth moving	40–750	D	2, 4	W
Railroad	Military	40–2000	D	2, 4	A, W
	Rail cars	150–400	D	2, 4	W
Marine	Locomotives	400–3000	D	2, 4	W
	Outboard	0.4–75	SI	2	W
	Inboard motorcrafts	4–750	SI, D	4	W
Airborne vehicles	Light naval craft	30–2200	D	2, 4	W
	Ships	3500–22,000	D	2, 4	W
	Ships' auxiliaries	75–750	D	4	W
Home use	Airplanes	45–2700	SI	4	A
	Helicopters	45–1500	SI	4	A
Stationary	Lawn mowers	0.7–3	SI	2, 4	A
	Snow blowers	2–5	SI	2, 4	A
	Light tractors	2–8	SI	4	A
Stationary	Building service	7–400	D	2, 4	W
	Electric power	35–22,000	D	2, 4	W
	Gas pipeline	750–5000	SI	2, 4	W

SI = spark-ignition; D = diesel; A = air cooled; W = water cooled.

Source: Adapted from Taylor.<sup>9</sup>

characteristics of internal combustion engines from a fundamental point of view, the method of ignition has been selected as the primary classifying feature. From the method of ignition—spark-ignition or compression-ignition<sup>†</sup>—follow the important characteristics of the fuel used, method of mixture preparation, combustion chamber design, method of load control, details of the combustion process, engine emissions, and operating characteristics. Some of the other classifications are used as subcategories within this basic classification. The engine operating cycle—four-stroke or two-stroke—is next in importance; the principles of these two cycles are described in the following section.

Table 1.3 shows the most common applications of internal combustion

<sup>†</sup> In the remainder of the book, these terms will often be abbreviated by SI and CI, respectively.

engines, the predominant type of engine used in each classification listed, and the approximate engine power range in each type of service.

### 1.3 ENGINE OPERATING CYCLES

Most of this book is about reciprocating engines, where the piston moves back and forth in a cylinder and transmits power through a connecting rod and crank mechanism to the drive shaft as shown in Fig. 1-1. The steady rotation of the crank produces a cyclical piston motion. The piston comes to rest at the top-center (TC) crank position and bottom-center (BC) crank position when the cylinder volume is a minimum or maximum, respectively.<sup>†</sup> The minimum cylinder volume is called the clearance volume  $V_c$ . The volume swept out by the

<sup>†</sup> These crank positions are also referred to as top-dead-center (TDC) and bottom-dead-center (BDC).

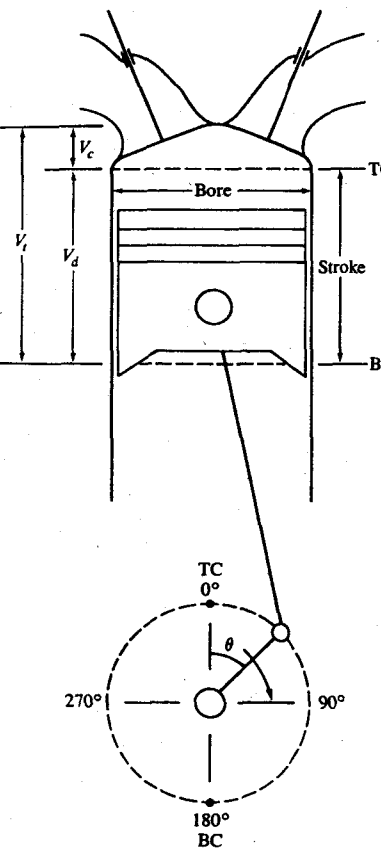


**FIGURE 1-1**

Basic geometry of the reciprocating internal combustion engine.  $V_t$ ,  $V_d$  and  $V_c$  indicate clearance, displaced, and total cylinder volumes.

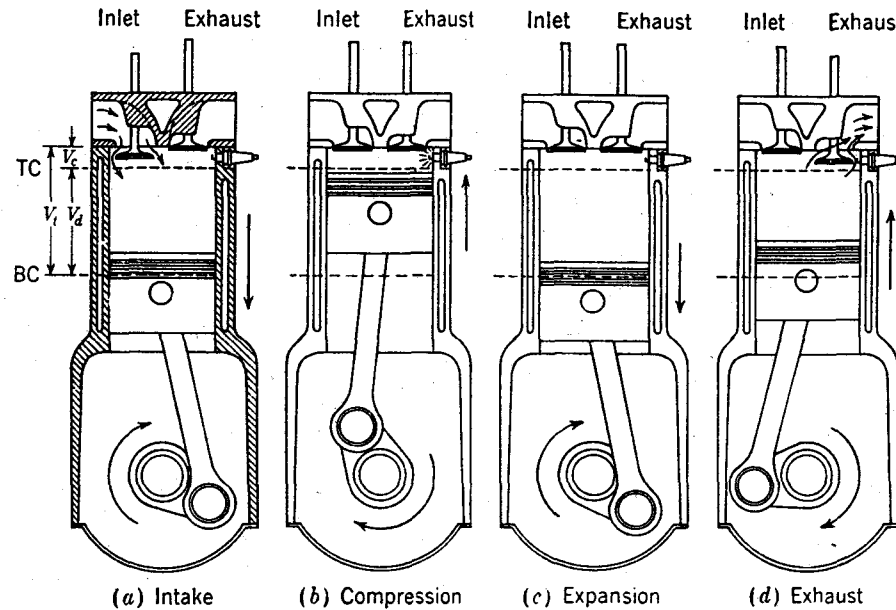


FIGURE 1-2  
The four-stroke operating cycle.<sup>10</sup>

piston, the difference between the maximum or total volume  $V_t$  and the clearance volume, is called the displaced or swept volume  $V_d$ . The ratio of maximum volume to minimum volume is the compression ratio  $r_c$ . Typical values of  $r_c$  are 8 to 12 for SI engines and 12 to 24 for CI engines.

The majority of reciprocating engines operate on what is known as the *four-stroke cycle*. Each cylinder requires four strokes of its piston—two revolutions of the crankshaft—to complete the sequence of events which produces one power stroke. Both SI and CI engines use this cycle which comprises (see Fig. 1-2):

1. An *intake stroke*, which starts with the piston at TC and ends with the piston at BC, which draws fresh mixture into the cylinder. To increase the mass induced, the inlet valve opens shortly before the stroke starts and closes after it ends.
2. A *compression stroke*, when both valves are closed and the mixture inside the cylinder is compressed to a small fraction of its initial volume. Toward the end of the compression stroke, combustion is initiated and the cylinder pressure rises more rapidly.
3. A *power stroke*, or *expansion stroke*, which starts with the piston at TC and ends at BC as the high-temperature, high-pressure, gases push the piston down and force the crank to rotate. About five times as much work is done on the piston during the power stroke as the piston had to do during compression.

As the piston approaches BC the exhaust valve opens to initiate the exhaust process and drop the cylinder pressure to close to the exhaust pressure.

4. An *exhaust stroke*, where the remaining burned gases exit the cylinder: first, because the cylinder pressure may be substantially higher than the exhaust pressure; then as they are swept out by the piston as it moves toward TC. As the piston approaches TC the inlet valve opens. Just after TC the exhaust valve closes and the cycle starts again.

Though often called the Otto cycle after its inventor, Nicolaus Otto, who built the first engine operating on these principles in 1876, the more descriptive four-stroke nomenclature is preferred.

The four-stroke cycle requires, for each engine cylinder, two crankshaft revolutions for each power stroke. To obtain a higher power output from a given engine size, and a simpler valve design, the *two-stroke cycle* was developed. The two-stroke cycle is applicable to both SI and CI engines.

Figure 1-3 shows one of the simplest types of two-stroke engine designs. Ports in the cylinder liner, opened and closed by the piston motion, control the exhaust and inlet flows while the piston is close to BC. The two strokes are:

1. A *compression stroke*, which starts by closing the inlet and exhaust ports, and then compresses the cylinder contents and draws fresh charge into the crankcase. As the piston approaches TC, combustion is initiated.

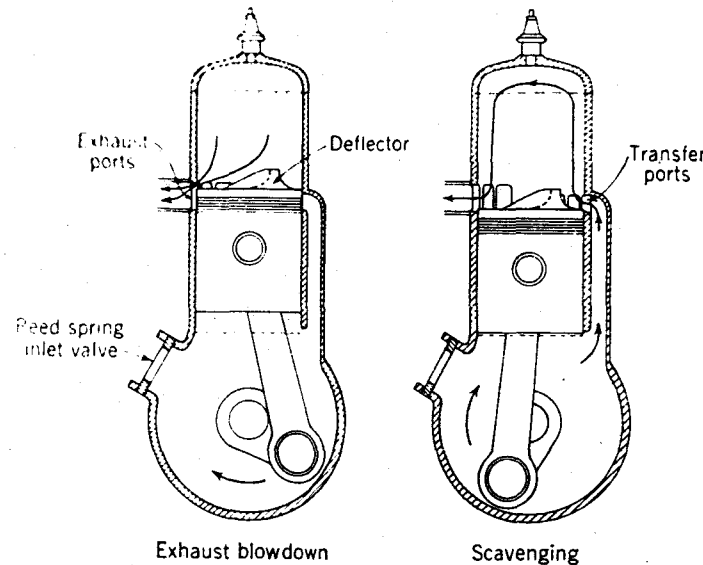


FIGURE 1-3  
The two-stroke operating cycle. A crankcase-scavenged engine is shown.<sup>10</sup>

2. A power or expansion stroke, similar to that in the four-stroke cycle until the piston approaches BC, when first the exhaust ports and then the intake ports are uncovered (Fig. 1-3). Most of the burnt gases exit the cylinder in an exhaust blowdown process. When the inlet ports are uncovered, the fresh charge which has been compressed in the crankcase flows into the cylinder. The piston and the ports are generally shaped to deflect the incoming charge from flowing directly into the exhaust ports and to achieve effective scavenging of the residual gases.

Each engine cycle with one power stroke is completed in one crankshaft revolution. However, it is difficult to fill completely the displaced volume with fresh charge, and some of the fresh mixture flows directly out of the cylinder during the scavenging process.<sup>†</sup> The example shown is a *cross-scavenged* design; other approaches use *loop-scavenging* or *uniflow* systems (see Sec. 6.6).

#### 1.4 ENGINE COMPONENTS

Labeled cutaway drawings of a four-stroke SI engine and a two-stroke CI engine are shown in Figs. 1-4 and 1-5, respectively. The spark-ignition engine is a four-cylinder in-line automobile engine. The diesel is a large V eight-cylinder design with a uniflow scavenging process. The function of the major components of these engines and their construction materials will now be reviewed.

The engine cylinders are contained in the engine block. The block has traditionally been made of gray cast iron because of its good wear resistance and low cost. Passages for the cooling water are cast into the block. Heavy-duty and truck engines often use removable cylinder sleeves pressed into the block that can be replaced when worn. These are called *wet liners* or *dry liners* depending on whether the sleeve is in direct contact with the cooling water. Aluminum is being used increasingly in smaller SI engine blocks to reduce engine weight. Iron cylinder liners may be inserted at the casting stage, or later on in the machining and assembly process. The crankcase is often integral with the cylinder block.

The crankshaft has traditionally been a steel forging; nodular cast iron crankshafts are also accepted normal practice in automotive engines. The crankshaft is supported in main bearings. The maximum number of main bearings is one more than the number of cylinders; there may be less. The crank has eccentric portions (crank throws); the connecting rod big-end bearings attach to the crank pin on each throw. Both main and connecting rod bearings use steel-backed precision inserts with bronze, babbitt, or aluminum as the bearing materials. The crankcase is sealed at the bottom with a pressed-steel or cast aluminum oil pan which acts as an oil reservoir for the lubricating system.

<sup>†</sup> It is primarily for this reason that two-stroke SI engines are at a disadvantage because the lost fresh charge contains fuel and air.

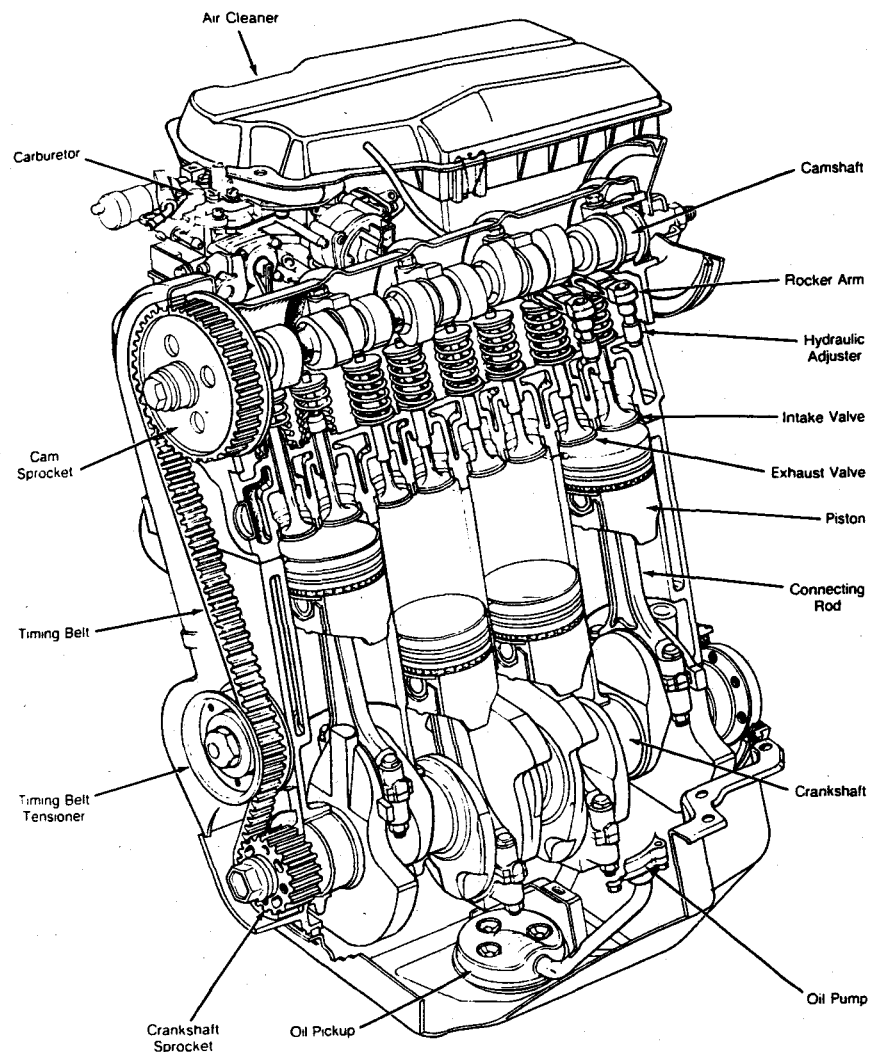


FIGURE 1-4

Cutaway drawing of Chrysler 2.2-liter displacement four-cylinder spark-ignition engine.<sup>11</sup> Bore 87.5 mm, stroke 92 mm, compression ratio 8.9, maximum power 65 kW at 5000 rev/min.

Pistons are made of aluminum in small engines or cast iron in larger slower-speed engines. The piston both seals the cylinder and transmits the combustion-generated gas pressure to the crank pin via the connecting rod. The connecting rod, usually a steel or alloy forging (though sometimes aluminum in small engines), is fastened to the piston by means of a steel piston pin through the rod upper end. The piston pin is usually hollow to reduce its weight.

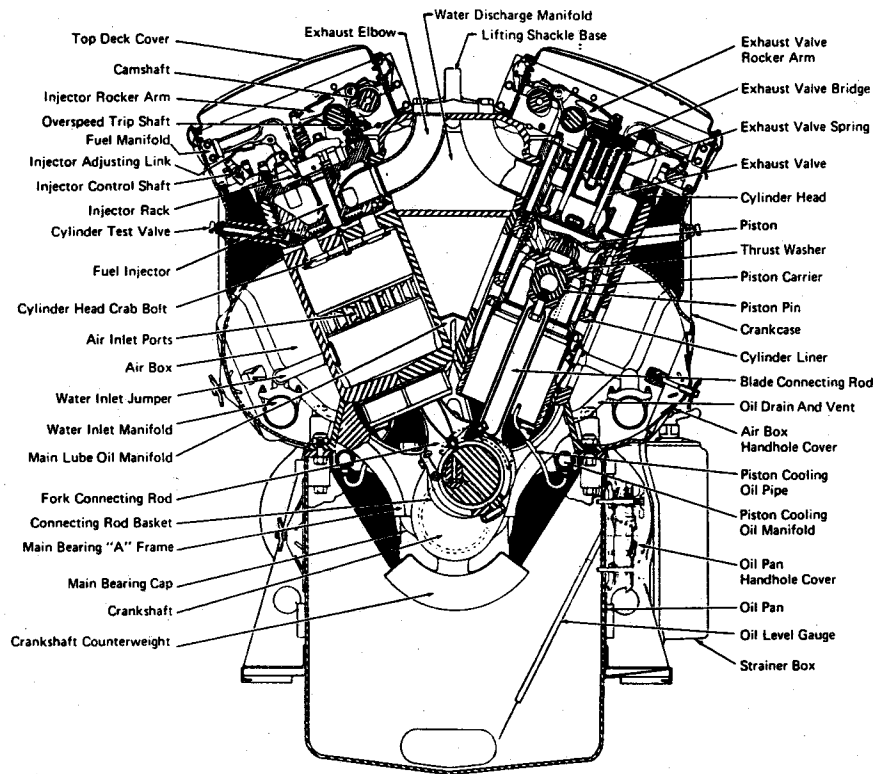


FIGURE 1-5

Cross-section drawing of an Electro-Motive two-stroke cycle diesel engine. This engine uses a uniflow scavenging process with inlet ports in the cylinder liner and four exhaust valves in the cylinder head. Bore 230.2 mm, stroke 254 mm, displaced volume per cylinder 10.57 liters, rated speed 750–900 rev/min. (Courtesy Electro-Motive Division, General Motors Corporation.)

The oscillating motion of the connecting rod exerts an oscillating force on the cylinder walls via the piston skirt (the region below the piston rings). The piston skirt is usually shaped to provide appropriate thrust surfaces. The piston is fitted with rings which ride in grooves cut in the piston head to seal against gas leakage and control oil flow. The upper rings are compression rings which are forced outward against the cylinder wall and downward onto the groove face. The lower rings scrape the surplus oil from the cylinder wall and return it to the crankcase. The crankcase must be ventilated to remove gases which blow by the piston rings, to prevent pressure buildup.

The cylinder head (or heads in V engines) seals off the cylinders and is made of cast iron or aluminum. It must be strong and rigid to distribute the gas forces acting on the head as uniformly as possible through the engine block. The cylinder head contains the spark plug (for an SI engine) or fuel injector (for a CI engine), and, in overhead valve engines, parts of the valve mechanism.

The valves shown in Fig. 1-4 are poppet valves, the valve type normally used in four-stroke engines. Valves are made from forged alloy steel; the cooling of the exhaust valve which operates at about 700°C may be enhanced by using a hollow stem partially filled with sodium which through evaporation and condensation carries heat from the hot valve head to the cooler stem. Most modern spark-ignition engines have overhead valve locations (sometimes called valve-in-head or I-head configurations) as shown in Fig. 1-4. This geometry leads to a compact combustion chamber with minimum heat losses and flame travel time, and improves the breathing capacity. Previous geometries such as the L head where valves are to one side of the cylinder are now only used in small engines.

The valve stem moves in a valve guide, which can be an integral part of the cylinder head (or engine block for L-head engines), or may be a separate unit pressed into the head (or block). The valve seats may be cut in the head or block metal (if cast iron) or hard steel inserts may be pressed into the head or block. A valve spring, attached to the valve stem with a spring washer and split keeper, holds the valve closed. A valve rotator turns the valves a few degrees on opening to wipe the valve seat, avoid local hot spots, and prevent deposits building up in the valve guide.

A camshaft made of cast iron or forged steel with one cam per valve is used to open and close the valves. The cam surfaces are hardened to obtain adequate life. In four-stroke cycle engines, camshafts turn at one-half the crankshaft speed. Mechanical or hydraulic lifters or tappets slide in the block and ride on the cam. Depending on valve and camshaft location, additional members are required to transmit the tappet motion to the valve stem; e.g., in in-head valve engines with the camshaft at the side, a push rod and rocker arm are used. A recent trend in automotive engines is to mount the camshaft over the head with the cams acting either directly or through a pivoted follower on the valve. Camshafts are gear, belt, or chain driven from the crankshaft.

An intake manifold (aluminum or cast iron) and an exhaust manifold (generally of cast iron) complete the SI engine assembly. Other engine components specific to spark-ignition engines—carburetor, fuel injectors, ignition systems—are described more fully in the remaining sections in this chapter.

The two-stroke cycle CI engine shown in Fig. 1-5 is of the uniflow scavenged design. The burned gases exhaust through four valves in the cylinder head. These valves are controlled through cam-driven rocker arms. Fresh air is compressed and fed to the air box by a Roots blower. The air inlet ports at the bottom of each cylinder liner are uncovered by the descending piston, and the scavenging air flows upward along the cylinder axis. The fuel injectors are mounted in the cylinder head and are driven by the camshaft through rocker arms. Diesel fuel-injection systems are discussed in more detail in Sec. 1.7.

## 1.5 SPARK-IGNITION ENGINE OPERATION

In SI engines the air and fuel are usually mixed together in the intake system prior to entry to the engine cylinder, using a carburetor (Fig. 1-6) or fuel-injection system (Fig. 1-7). In automobile applications, the temperature of the air entering

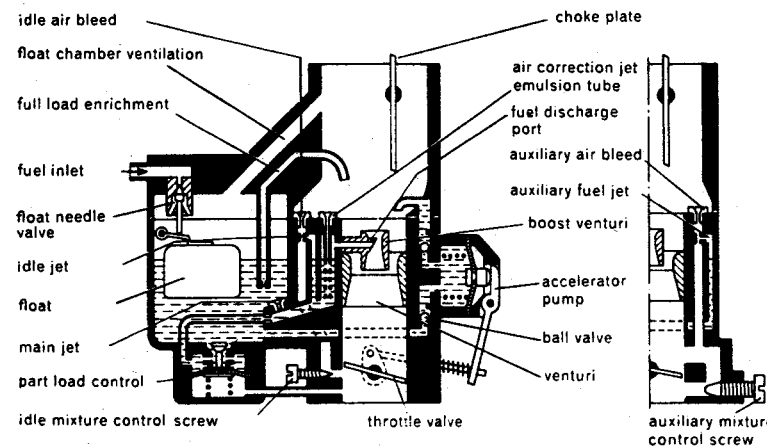


**FIGURE 1-6**  
Cross section of single-barrel downdraft carburetor.<sup>12</sup> (Courtesy Robert Bosch GmbH and SAE.)

the intake system is controlled by mixing ambient air with air heated by contact with the exhaust manifold. The ratio of mass flow of air to mass flow of fuel must be held approximately constant at about 15 to ensure reliable combustion. The

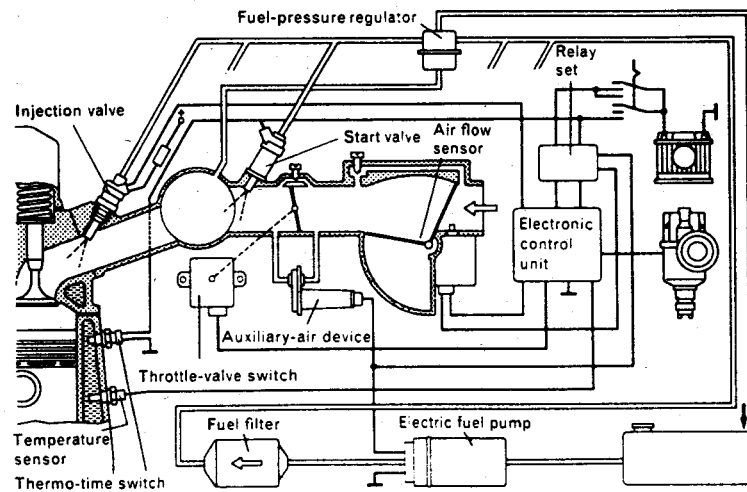


**FIGURE 1-7**  
Schematic drawing of L-Jetronic port electronic fuel-injection system.<sup>12</sup> (Courtesy Robert Bosch GmbH and SAE.)

carburetor meters an appropriate fuel flow for the engine air flow in the following manner. The air flow through the venturi (a converging-diverging nozzle) sets up a pressure difference between the venturi inlet and throat which is used to meter an appropriate amount of fuel from the float chamber, through a series of orifices, into the air flow at the venturi throat. Just downstream of the venturi is a throttle valve or plate which controls the combined air and fuel flow, and thus the engine output. The intake flow is throttled to below atmospheric pressure by reducing the flow area when the power required (at any engine speed) is below the maximum which is obtained when the throttle is wide open. The intake manifold is usually heated to promote faster evaporation of the liquid fuel and obtain more uniform fuel distribution between cylinders.

Fuel injection into the intake manifold or inlet port is an increasingly common alternative to a carburetor. With port injection, fuel is injected through individual injectors from a low-pressure fuel supply system into each intake port. There are several different types of systems: mechanical injection using an injection pump driven by the engine; mechanical, driveless, continuous injection; electronically controlled, driveless, injection. Figure 1-7 shows an example of an electronically controlled system. In this system, the air flow rate is measured directly; the injection valves are actuated twice per cam shaft revolution by injection pulses whose duration is determined by the electronic control unit to provide the desired amount of fuel per cylinder per cycle.<sup>12</sup> An alternative approach is to use a single fuel injector located above the throttle plate in the position normally occupied by the carburetor. This approach permits electronic control of the fuel flow at reduced cost.

The sequence of events which take place inside the engine cylinder is illustrated in Fig. 1-8. Several variables are plotted against crank angle through the entire four-stroke cycle. Crank angle is a useful independent variable because engine processes occupy almost constant crank angle intervals over a wide range of engine speeds. The figure shows the valve timing and volume relationship for a typical automotive spark-ignition engine. To maintain high mixture flows at high engine speeds (and hence high power outputs) the inlet valve, which opens before TC, closes substantially after BC. During intake, the inducted fuel and air mix in the cylinder with the residual burned gases remaining from the previous cycle. After the intake valve closes, the cylinder contents are compressed to above atmospheric pressure and temperature as the cylinder volume is reduced. Some heat transfer to the piston, cylinder head, and cylinder walls occurs but the effect on unburned gas properties is modest.

Between 10 and 40 crank angle degrees before TC an electrical discharge across the spark plug starts the combustion process. A distributor, a rotating switch driven off the camshaft, interrupts the current from the battery through the primary circuit of the ignition coil. The secondary winding of the ignition coil, connected to the spark plug, produces a high voltage across the plug electrodes as the magnetic field collapses. Traditionally, cam-operated breaker points have been used; in most automotive engines, the switching is now done electronically. A turbulent flame develops from the spark discharge, propagates

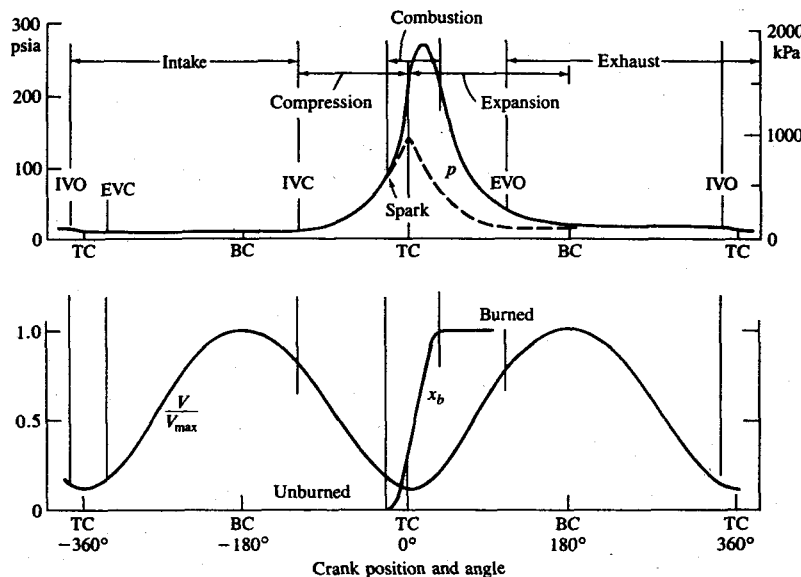


FIGURE 1-8

Sequence of events in four-stroke spark-ignition engine operating cycle. Cylinder pressure  $p$  (solid line, firing cycle; dashed line, motored cycle), cylinder volume  $V/V_{\max}$ , and mass fraction burned  $x_b$  are plotted against crank angle.

across the mixture of air, fuel, and residual gas in the cylinder, and extinguishes at the combustion chamber wall. The duration of this burning process varies with engine design and operation, but is typically 40 to 60 crank angle degrees, as shown in Fig. 1-8. As fuel-air mixture burns in the flame, the cylinder pressure in Fig. 1-8 (solid line) rises above the level due to compression alone (dashed line). This latter curve—called the motored cylinder pressure—is the pressure trace obtained from a motored or nonfiring engine.<sup>†</sup> Note that due to differences in the flow pattern and mixture composition between cylinders, and within each cylinder cycle-by-cycle, the development of each combustion process differs somewhat. As a result, the shape of the pressure versus crank angle curve in each cylinder, and cycle-by-cycle, is not exactly the same.

There is an optimum spark timing which, for a given mass of fuel and air inside the cylinder, gives maximum torque. More advanced (earlier) timing or retarded (later) timing than this optimum gives lower output. Called *maximum*

<sup>†</sup> In practice, the intake and compression processes of a firing engine and a motored engine are not exactly the same due to the presence of burned gases from the previous cycle under firing conditions.

*brake-torque (MBT)* timing,<sup>†</sup> this optimum timing is an empirical compromise between starting combustion too early in the compression stroke (when the work transfer is to the cylinder gases) and completing combustion too late in the expansion stroke (and so lowering peak expansion stroke pressures).

About two-thirds of the way through the expansion stroke, the exhaust valve starts to open. The cylinder pressure is greater than the exhaust manifold pressure and a *blowdown* process occurs. The burned gases flow through the valve into the exhaust port and manifold until the cylinder pressure and exhaust pressure equilibrate. The duration of this process depends on the pressure level in the cylinder. The piston then *displaces* the burned gases from the cylinder into the manifold during the exhaust stroke. The exhaust valve opens before the end of the expansion stroke to ensure that the blowdown process does not last too far into the exhaust stroke. The actual timing is a compromise which balances reduced work transfer to the piston before BC against reduced work transfer to the cylinder contents after BC.

The exhaust valve remains open until just after TC; the intake opens just before TC. The valves are opened and closed slowly to avoid noise and excessive cam wear. To ensure the valves are fully open when piston velocities are at their highest, the valve open periods often overlap. If the intake flow is throttled to below exhaust manifold pressure, then backflow of burned gases into the intake manifold occurs when the intake valve is first opened.

## 1.6 EXAMPLES OF SPARK-IGNITION ENGINES

This section presents examples of production spark-ignition engines to illustrate the different types of engines in common use.

Small SI engines are used in many applications: in the home (e.g., lawn mowers, chain saws), in portable power generation, as outboard motorboat engines, and in motorcycles. These are often single-cylinder engines. In the above applications, light weight, small bulk, and low cost in relation to the power generated are the most important characteristics; fuel consumption, engine vibration, and engine durability are less important. A single-cylinder engine gives only one power stroke per revolution (two-stroke cycle) or two revolutions (four-stroke cycle). Hence, the torque pulses are widely spaced, and engine vibration and smoothness are significant problems.

Multicylinder engines are invariably used in automotive practice. As rated power increases, the advantages of smaller cylinders in regard to size, weight, and improved engine balance and smoothness point toward increasing the number of

<sup>†</sup> MBT timing has traditionally been defined as the minimum spark advance for best torque. Since the torque first increases and then decreases as spark timing is advanced, the definition used here is more precise.

cylinders per engine. An upper limit on cylinder size is dictated by dynamic considerations: the inertial forces that are created by accelerating and decelerating the reciprocating masses of the piston and connecting rod would quickly limit the maximum speed of the engine. Thus, the displaced volume is spread out amongst several smaller cylinders. The increased frequency of power strokes with a multi-cylinder engine produces much smoother torque characteristics. Multicylinder engines can also achieve a much better state of balance than single-cylinder engines. A force must be applied to the piston to accelerate it during the first half of its travel from bottom-center or top-center. The piston then exerts a force as it decelerates during the second part of the stroke. It is desirable to cancel these inertia forces through the choice of number and arrangement of cylinders to achieve a *primary balance*. Note, however, that the motion of the piston is more rapid during the upper half of its stroke than during the lower half (a consequence of the connecting rod and crank mechanism evident from Fig. 1-1; see also Sec. 2.2). The resulting inequality in piston acceleration and deceleration produces corresponding differences in inertia forces generated. Certain combinations of cylinder number and arrangement will balance out these secondary inertia force effects.

Four-cylinder in-line engines are the most common arrangements for automobile engines up to about 2.5-liter displacement. An example of this in-line arrangement was shown in Fig. 1-4. It is compact—an important consideration for small passenger cars. It provides two torque pulses per revolution of the crankshaft and primary inertia forces (though not secondary forces) are balanced. V engines and opposed-piston engines are occasionally used with this number of cylinders.

The V arrangement, with two banks of cylinders set at  $90^\circ$  or a more acute angle to each other, provides a compact block and is used extensively for larger displacement engines. Figure 1-9 shows a V-6 engine, the six cylinders being arranged in two banks of three with a  $60^\circ$  angle between their axis. Six cylinders are usually used in the 2.5- to 4.5-liter displacement range. Six-cylinder engines provide smoother operation with three torque pulses per revolution. The in-line arrangement results in a long engine, however, giving rise to crankshaft torsional vibration and making even distribution of air and fuel to each cylinder more difficult. The V-6 arrangement is much more compact, and the example shown provides primary balance of the reciprocating components. With the V engine, however, a rocking moment is imposed on the crankshaft due to the secondary inertia forces, which results in the engine being less well balanced than the in-line version. The V-8 and V-12 arrangements are also commonly used to provide compact, smooth, low-vibration, larger-displacement, spark-ignition engines.

Turbochargers are used to increase the maximum power that can be obtained from a given displacement engine. The work transfer to the piston per cycle, in each cylinder, which controls the power the engine can deliver, depends on the amount of fuel burned per cylinder per cycle. This depends on the amount of fresh air that is inducted each cycle. Increasing the air density prior to entry into the engine thus increases the maximum power that an engine of given dis-

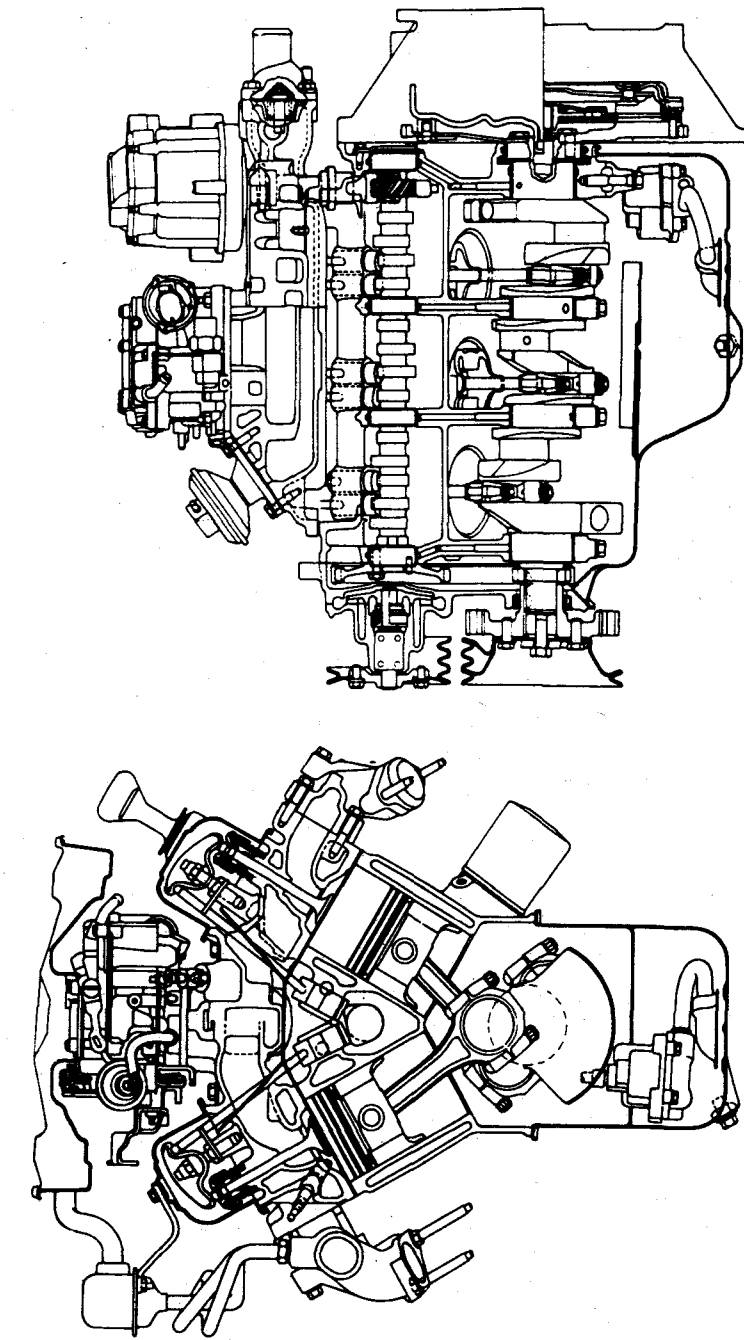


FIGURE 1-9  
Cross-section drawings of General Motors 60 degree V-6 spark-ignition engine.<sup>13</sup> Displacement 2.8 liter, bore 89 mm, stroke 76 mm, compression ratio 8.5, maximum power 86 kW at 4800 rev/min.

placement can deliver. Figure 1-10 shows an example of a turbocharged four-cylinder spark-ignition engine. The turbocharger, a compressor-turbine combination, uses the energy available in the engine exhaust stream to achieve compression of the intake flow. The air flow passes through the compressor (2), intercooler (3), carburetor (4), manifold (5), and inlet valve (6) as shown. Engine inlet pressures (or boost) of up to about 100 kPa above atmospheric pressure are typical. The exhaust flow through the valve (7) and manifold (8) drives the turbine (9) which powers the compressor. A wastegate (valve) just upstream of the turbine bypasses some of the exhaust gas flow when necessary to prevent the boost pressure becoming too high. The wastegate linkage (11) is controlled by a boost pressure regulator. While this turbocharged engine configuration has the carburetor downstream of the compressor, some turbocharged spark-ignition engines have the carburetor upstream of the compressor so that it operates at or below atmospheric pressure. Figure 1-11 shows a cutaway drawing of a small automotive turbocharger. The arrangements of the compressor and turbine

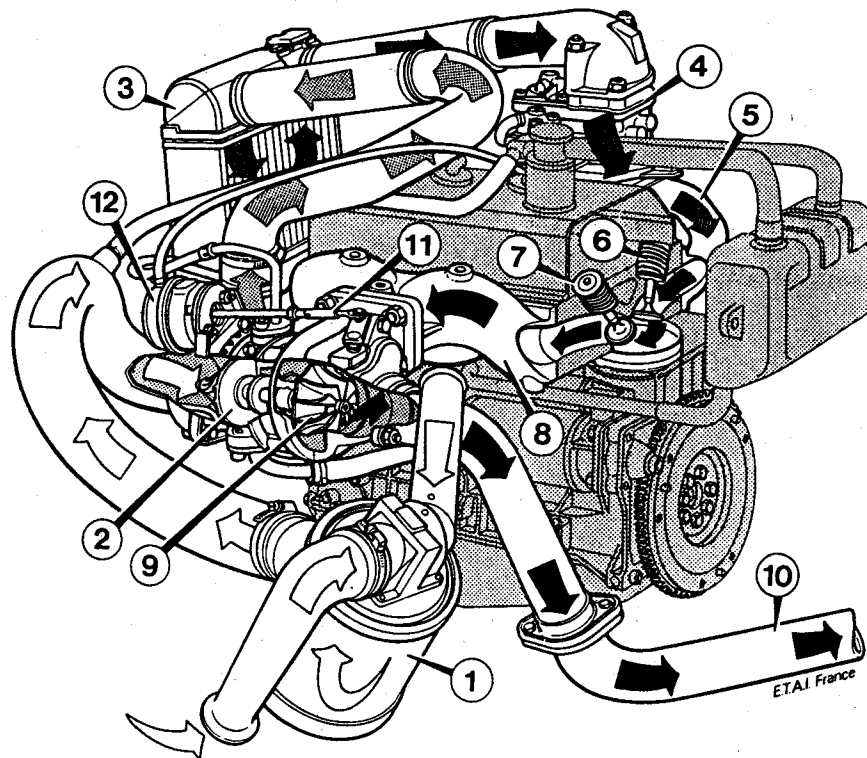


FIGURE 1-10  
Turbocharged four-cylinder automotive spark-ignition engine. (Courtesy Regie Nationale des Usines.)

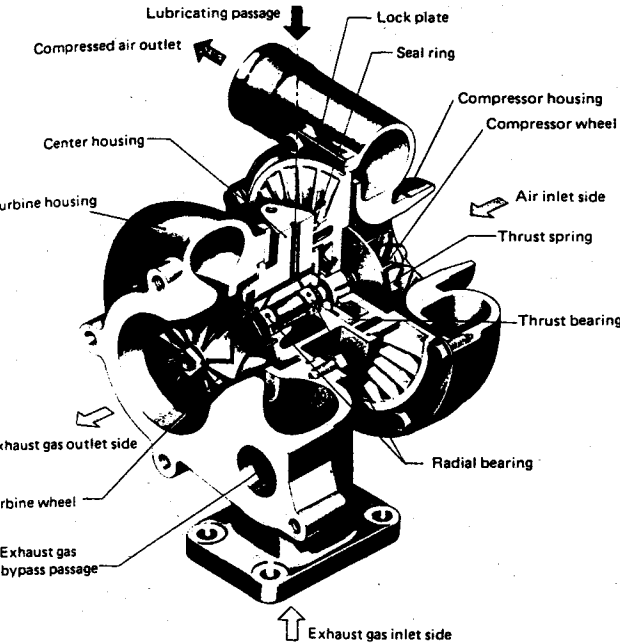
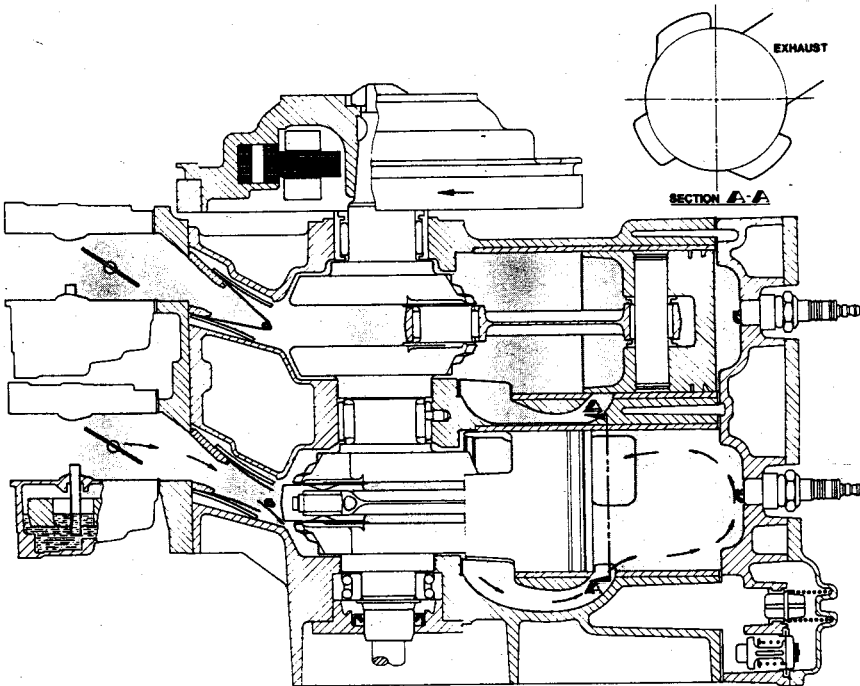


FIGURE 1-11  
Cutaway view of small automotive engine turbocharger. (Courtesy Nissan Motor Co., Ltd.)

rotors connected via the central shaft and of the turbine and compressor flow passages are evident.

Figure 1-12 shows a two-stroke cycle spark-ignition engine. The two-stroke cycle spark-ignition engine is used for small-engine applications where low cost and weight/power ratio are important and when the use factor is low. Examples of such applications are outboard motorboat engines, motorcycles, and chain saws. All such engines are of the carburetor crankcase-compression type which is one of the simplest prime movers available. It has three moving parts per cylinder: the piston, connecting rod, and the crank. The prime advantage of the two-stroke cycle spark-ignition engine relative to the four-stroke cycle engine is its higher power per unit displaced volume due to twice the number of power strokes per crank revolution. This is offset by the lower fresh charge density achieved by the two-stroke cycle gas-exchange process and the loss of fresh mixture which goes straight through the engine during scavenging. Also, oil consumption is higher in two-stroke cycle engines due to the need to add oil to the fuel to lubricate the piston ring and piston surfaces.

The Wankel rotary engine is an alternative to the reciprocating engine geometry of the engines illustrated above. It is used when its compactness and higher engine speed (which result in high power/weight and power/volume ratios), and inherent balance and smoothness, offset its higher heat transfer, and



**FIGURE 1-12**  
Cutaway drawing of two-cylinder two-stroke cycle loop-scavenged marine spark-ignition engine. Displaced volume  $737 \text{ cm}^3$ , maximum power  $41 \text{ kW}$  at  $5500 \text{ rev/min}$ . (Courtesy Outboard Marine Corporation.)

its sealing and leakage problems. Figure 1-13 shows the major mechanical parts of a simple single-rotor Wankel engine and illustrates its geometry. There are two rotating parts: the triangular-shaped rotor and the output shaft with its integral eccentric. The rotor revolves directly on the eccentric. The rotor has an internal timing gear which meshes with the fixed timing gear on one side housing to maintain the correct phase relationship between the rotor and eccentric shaft rotations. Thus the rotor rotates and orbits around the shaft axis. Breathing is through ports in the center housing (and sometimes the side housings). The combustion chamber lies between the center housing and rotor surface and is sealed by seals at the apex of the rotor and around the perimeters of the rotor sides. Figure 1-13 also shows how the Wankel rotary geometry operates with the four-stroke cycle. The figure shows the induction, compression, power, and exhaust processes of the four-stroke cycle for the chamber defined by rotor surface AB. The remaining two chambers defined by the other rotor surfaces undergo exactly the same sequence. As the rotor makes one complete rotation, during which the eccentric shaft rotates through three revolutions, each chamber produces one power "stroke." Three power pulses occur, therefore, for each rotor revolution;

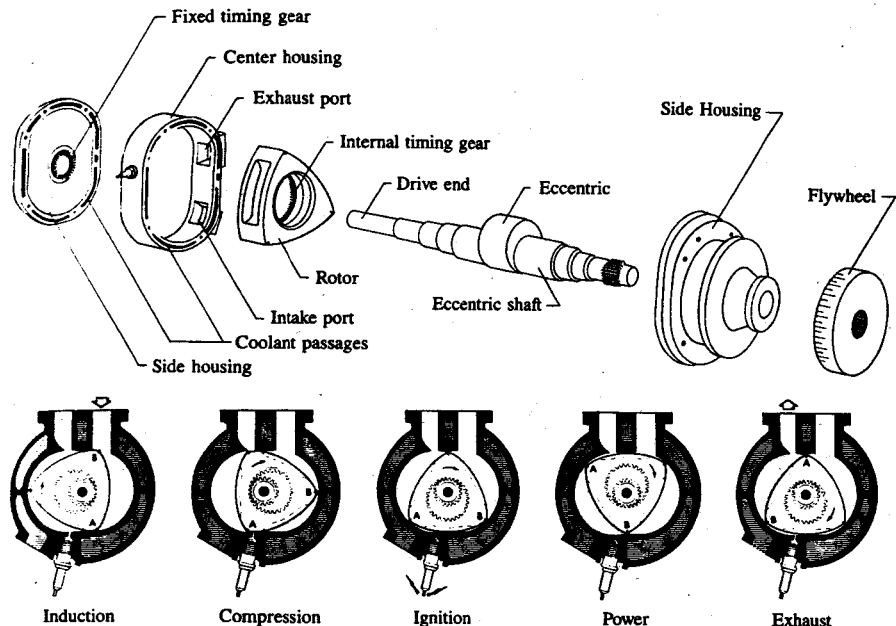


**FIGURE 1-13**  
(a) Major components of the Wankel rotary engine; (b) induction, compression, power, and exhaust processes of the four-stroke cycle for the chamber defined by rotor surface AB. (From Mobil Technical Bulletin, Rotary Engines, © Mobil Oil Corporation, 1971.)

thus for each eccentric (output) shaft revolution there is one power pulse. Figure 1-14 shows a cutaway drawing of a two-rotor automobile Wankel engine. The two rotors are out of phase to provide a greater number of torque pulses per shaft revolution. Note the combustion chamber cut out in each rotor face, the rotor apex, and side seals. Two spark plugs per firing chamber are often used to obtain a faster combustion process.

## 1.7 COMPRESSION-IGNITION ENGINE OPERATION

In compression-ignition engines, air alone is inducted into the cylinder. The fuel (in most applications a light fuel oil, though heated residual fuel is used in marine and power-generation applications) is injected directly into the engine cylinder just before the combustion process is required to start. Load control is achieved by varying the amount of fuel injected each cycle; the air flow at a given engine speed is essentially unchanged. There are a great variety of CI engine designs in use in a wide range of applications—automobile, truck, locomotive, marine, power generation. Naturally aspirated engines where atmospheric air is inducted, turbocharged engines where the inlet air is compressed by an exhaust-driven

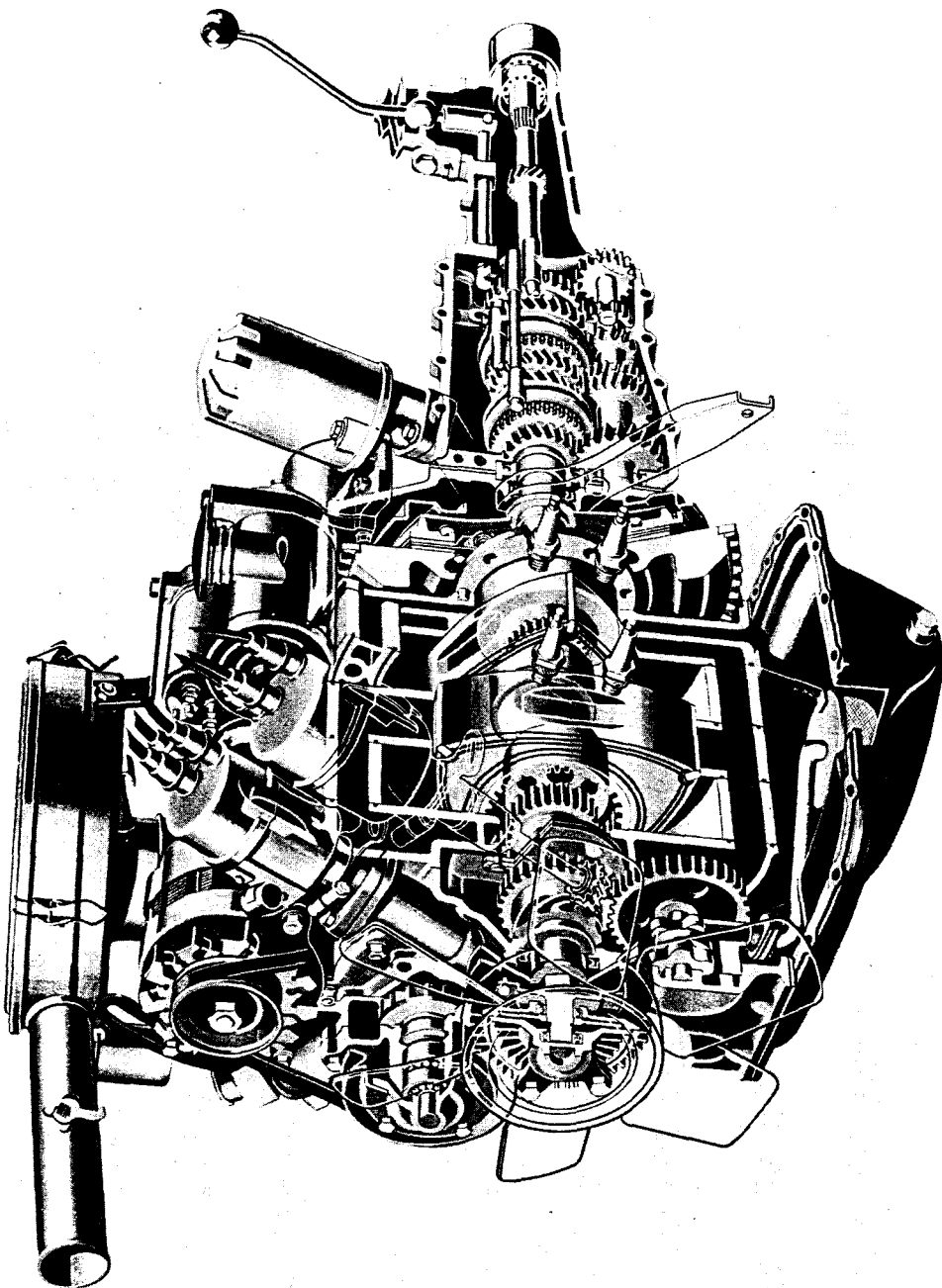


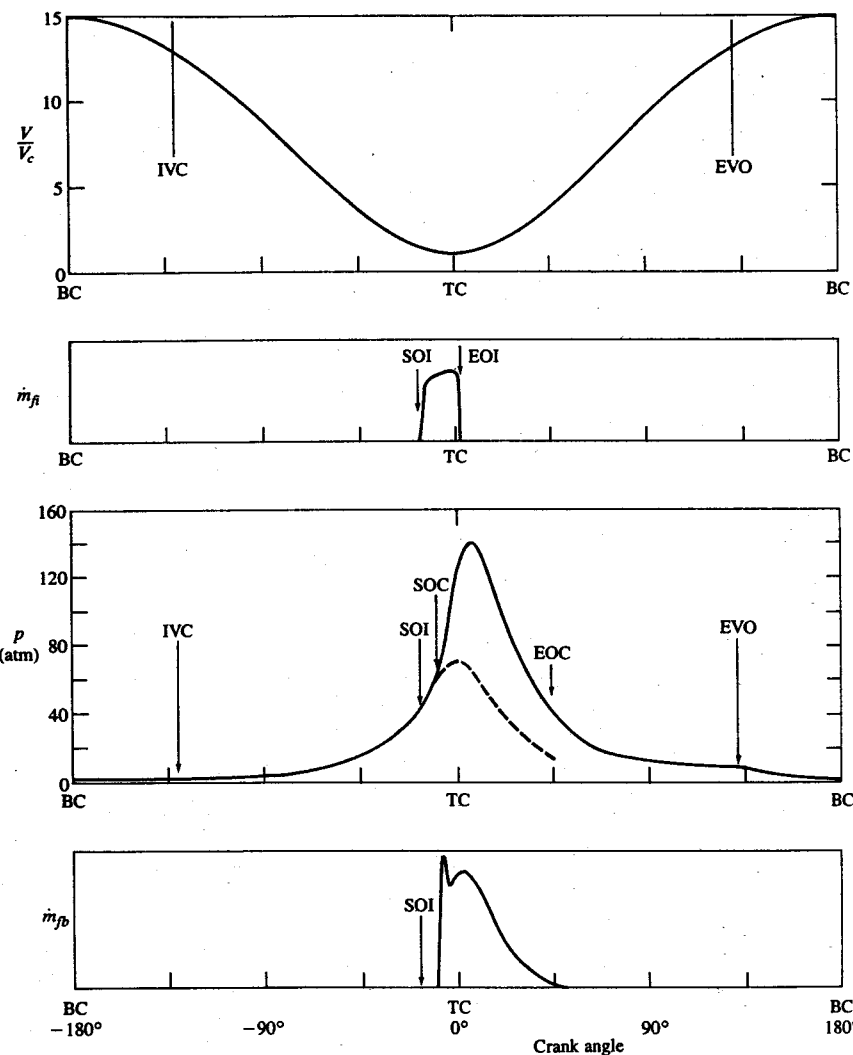
FIGURE 1-14 Cutaway drawing of two-rotor Wankel spark-ignition engine. Displacement of each working chamber 573 cm<sup>3</sup>, compression ratio 9.4, maximum cylinder diameter 45 mm at 7000 rev/min. (Courtesy of Texaco Research Laboratories)

turbine-compressor combination, and supercharged engines where the air is compressed by a mechanically driven pump or blower are common. Turbocharging and supercharging increase engine output by increasing the air mass flow per unit displaced volume, thereby allowing an increase in fuel flow. These methods are used, usually in larger engines, to reduce engine size and weight for a given power output. Except in smaller engine sizes, the two-stroke cycle is competitive with the four-stroke cycle, in large part because, with the diesel cycle, only air is lost in the cylinder scavenging process.

The operation of a typical four-stroke naturally aspirated CI engine is illustrated in Fig. 1-15. The compression ratio of diesels is much higher than typical SI engine values, and is in the range 12 to 24, depending on the type of diesel engine and whether the engine is naturally aspirated or turbocharged. The valve timings used are similar to those of SI engines. Air at close-to-atmospheric pressure is inducted during the intake stroke and then compressed to a pressure of about 4 MPa (600 lb/in<sup>2</sup>) and temperature of about 800 K (1000°F) during the compression stroke. At about 20° before TC, fuel injection into the engine cylinder commences; a typical rate of injection profile is shown in Fig. 1-15b. The liquid fuel jet atomizes into drops and entrains air. The liquid fuel evaporates; fuel vapor then mixes with air to within combustible proportions. The air temperature and pressure are above the fuel's ignition point. Therefore after a short *delay period*, spontaneous ignition (autoignition) of parts of the nonuniform fuel-air mixture initiates the combustion process, and the cylinder pressure (solid line in Fig. 1-15c) rises above the nonfiring engine level. The flame spreads rapidly through that portion of the injected fuel which has already mixed with sufficient air to burn. As the expansion process proceeds, mixing between fuel, air, and burning gases continues, accompanied by further combustion (see Fig. 1-15d). At full load, the mass of fuel injected is about 5 percent of the mass of air in the cylinder. Increasing levels of black smoke in the exhaust limit the amount of fuel that can be burned efficiently. The exhaust process is similar to that of the four-stroke SI engine. At the end of the exhaust stroke, the cycle starts again.

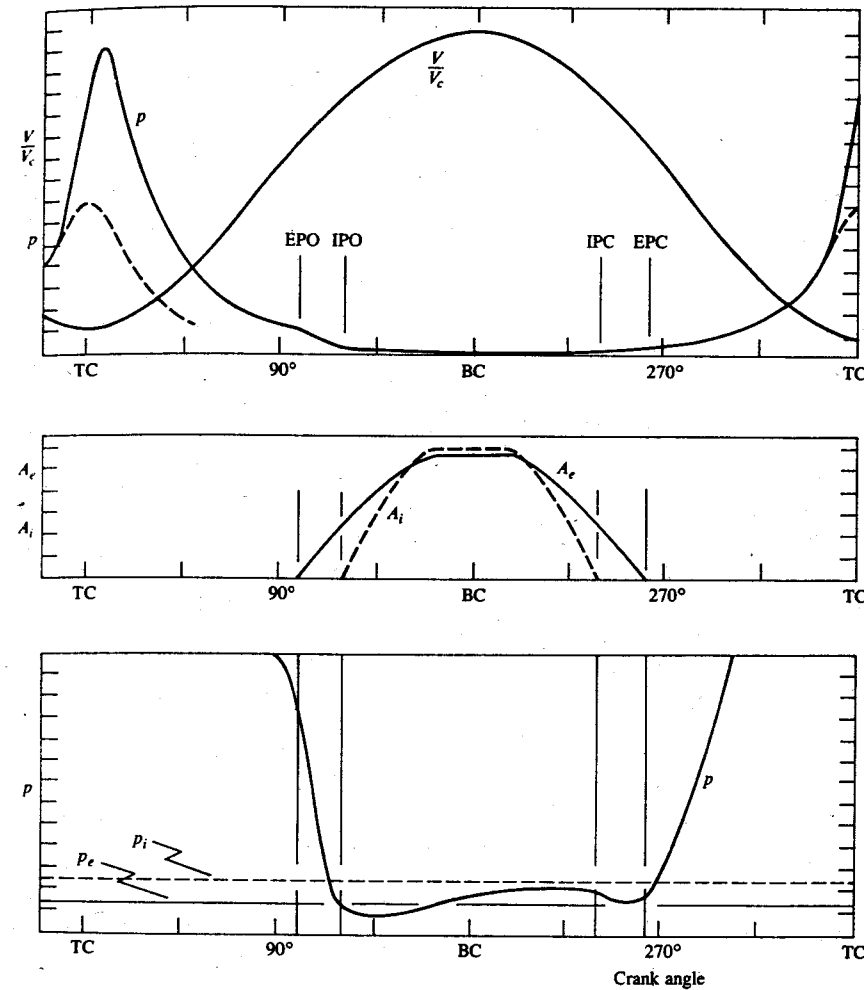
In the two-stroke CI engine cycle, compression, fuel injection, combustion, and expansion processes are similar to the equivalent four-stroke cycle processes; it is the intake and exhaust pressure which are different. The sequence of events in a loop-scavenged two-stroke engine is illustrated in Fig. 1-16. In loop-scavenged engines both exhaust and inlet ports are at the same end of the cylinder and are uncovered as the piston approaches BC (see Fig. 1-16a). After the exhaust ports open, the cylinder pressure  $p$  falls rapidly in a blowdown process (Fig. 1-16b). The inlet ports then open, and once the cylinder pressure  $p$  falls below the inlet pressure  $p_i$ , air flows into the cylinder. The burned gases, displaced by this fresh air, continue to flow out of the exhaust port (along with some of the fresh air). Once the ports close as the piston starts the compression stroke, compression, fuel-injection, fuel-air mixing, combustion and expansion processes proceed as in the four-stroke CI engine cycle.

The diesel fuel-injection system consists of an injection pump, delivery pipes, and fuel injector nozzles. Several different types of injection pumps and

**FIGURE 1-15**

Sequence of events during compression, combustion, and expansion processes of a naturally aspirated compression-ignition engine operating cycle. Cylinder volume/clearance volume  $V/V_c$ , rate of fuel injection  $\dot{m}_{fi}$ , cylinder pressure  $p$  (solid line, firing cycle; dashed line, motored cycle), and rate of fuel burning (or fuel chemical energy release rate)  $\dot{m}_{fb}$  are plotted against crank angle.

nozzles are used. In one common fuel pump (an in-line pump design shown in Fig. 1-17) a set of cam-driven plungers (one for each cylinder) operate in closely fitting barrels. Early in the stroke of the plunger, the inlet port is closed and the fuel trapped above the plunger is forced through a check valve into the injection

**FIGURE 1-16**

Sequence of events during expansion, gas exchange, and compression processes in a loop-scavenged two-stroke cycle compression-ignition engine. Cylinder volume/clearance volume  $V/V_c$ , cylinder pressure  $p$ , exhaust port open area  $A_e$ , and intake port open area  $A_i$  are plotted against crank angle.

line. The injection nozzle (Fig. 1-18) has one or more holes through which the fuel sprays into the cylinder. A spring-loaded valve closes these holes until the pressure in the injection line, acting on part of the valve surface, overcomes the spring force and opens the valve. Injection starts shortly after the line pressure begins to rise. Thus, the phase of the pump camshaft relative to the engine crank-shaft controls the start of injection. Injection is stopped when the inlet port of the pump is uncovered by a helical groove in the pump plunger, because the high

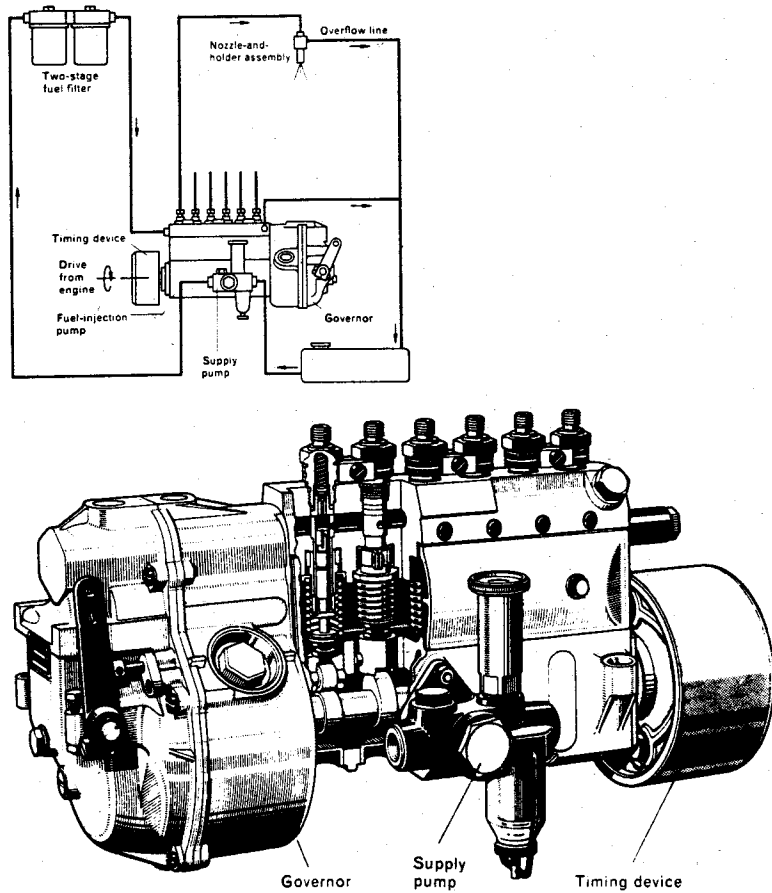


**FIGURE 1-17**  
Diesel fuel system with in-line fuel-injection pump (type PE).<sup>12</sup> (Courtesy Robert Bosch GmbH.)

pressure above the plunger is then released (Fig. 1-18). The amount of fuel injected (which controls the load) is determined by the injection pump cam design and the position of the helical groove. Thus for a given cam design, rotating the plunger and its helical groove varies the load.

Distributor-type pumps have only one pump plunger and barrel, which meters and distributes the fuel to all the injection nozzles. A schematic of a distributor-type pump is shown in Fig. 1-19. The unit contains a low-pressure fuel pump (on left), a high-pressure injection pump (on right), an overspeed governor, and an injection timer. High pressure is generated by the plunger which is made to describe a combined rotary and stroke movement by the rotating eccentric disc or cam plate; the rotary motion distributes the fuel to the individual injection nozzles.

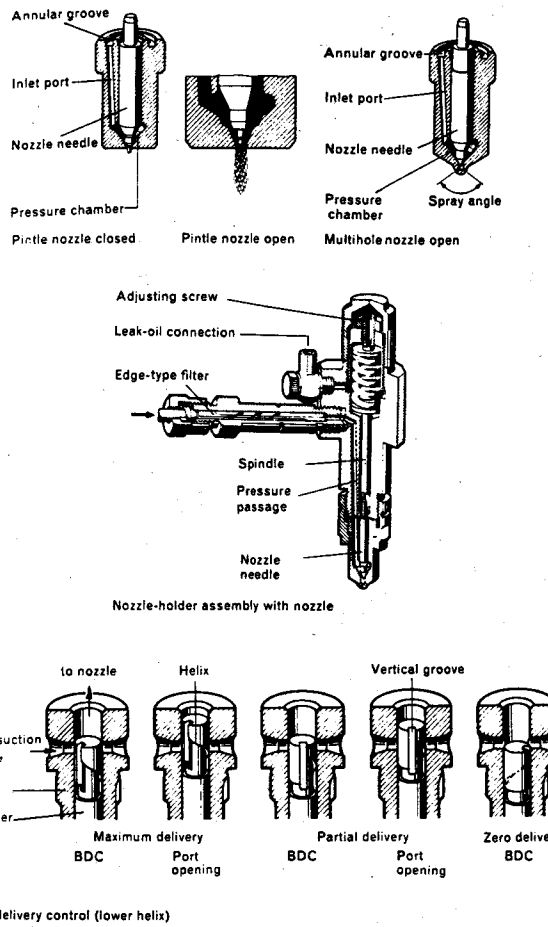


**FIGURE 1-18**  
Details of fuel-injection nozzles, nozzle holder assembly and fuel-delivery control.<sup>12</sup> (Courtesy Robert Bosch GmbH.)

Distributor pumps can operate at higher speed and take up less space than in-line pumps. They are normally used on smaller diesel engines. In-line pumps are used in the mid-engine-size range. In the larger diesels, individual single-barrel injection pumps, close mounted to each cylinder with an external drive as shown in Fig. 1-5, are normally used.

## 1.8 EXAMPLES OF DIESEL ENGINES

A large number of diesel engine configurations and designs are in common use. The very large marine and stationary power-generating diesels are two-stroke

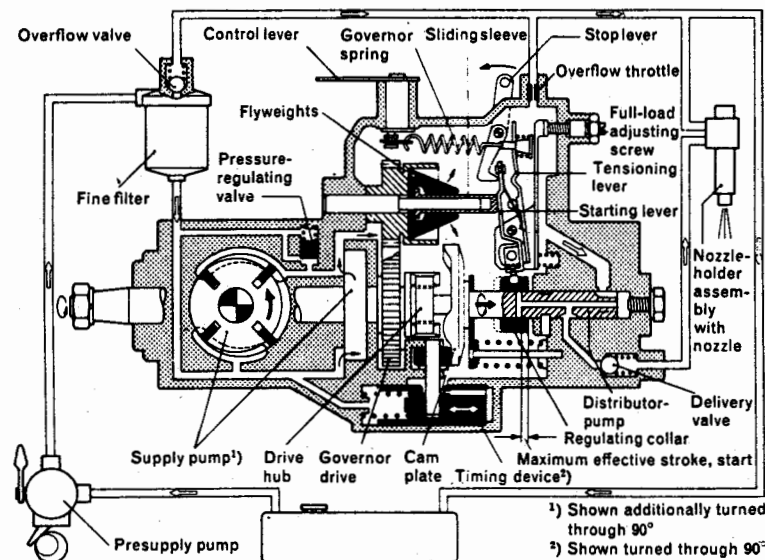


FIGURE 1-19

Diesel fuel system with distributor-type fuel-injection pump with mechanical governor.<sup>12</sup> (Courtesy Robert Bosch GmbH.)

cycle engines. Small- and medium-size engines use the four-stroke cycle. Because air capacity is an important constraint on the amount of fuel that can be burned in the diesel engine, and therefore on the engine's power, turbocharging is used extensively. All large engines are turbocharged. The majority of smaller diesels are not turbocharged, though they can be turbocharged and many are. The details of the engine design also vary significantly over the diesel size range. In particular, different combustion chamber geometries and fuel-injection characteristics are required to deal effectively with a major diesel engine design problem—achieving sufficiently rapid fuel-air mixing rates to complete the fuel-burning process in the time available. A wide variety of inlet port geometries, cylinder head and piston shapes, and fuel-injection patterns are used to accomplish this over the diesel size range.

Figure 1-20 shows a diesel engine typical of the medium-duty truck application. The design shown is a six-cylinder in-line engine. The drawing indicates that diesel engines are generally substantially heavier than spark-ignition engines because stress levels are higher due to the significantly higher pressure levels of the diesel cycle. The engine shown has a displacement of 10 liters, a compression ratio of 16.3, and is usually turbocharged. The engine has pressed-in cylinder liners to achieve better cylinder wear characteristics. This type of diesel is called a *direct-injection* diesel. The fuel is injected into a combustion chamber directly above the piston crown. The combustion chamber shown is a "bowl-in-piston" design, which puts most of the clearance volume into a compact shape. With this

size of diesel engine, it is often necessary to use a swirling air flow rotating about the cylinder axis, which is created by suitable design of the inlet port and valve, to achieve adequate fuel-air mixing and fuel burning rates. The fuel injector, shown left-of-center in the drawing, has a multi-hole nozzle, typically with three to five holes. The fuel jets move out radially from the center of the piston bowl into the (swirling) air flow. The in-line fuel-injection pump is normally used with this type of diesel engine.

Figure 1-21 shows a four-cylinder in-line overhead-valve-cam design automobile diesel engine. The smallest diesels such as this operate at higher engine speed than larger engines; hence the time available for burning the fuel is less and the fuel-injection and combustion system must achieve faster fuel-air mixing rates. This is accomplished by using an *indirect-injection* type of diesel. Fuel is injected into an auxiliary combustion chamber which is separated from the main combustion chamber above the piston by a flow restriction or nozzle. During the latter stages of the compression process, air is forced through this nozzle from the

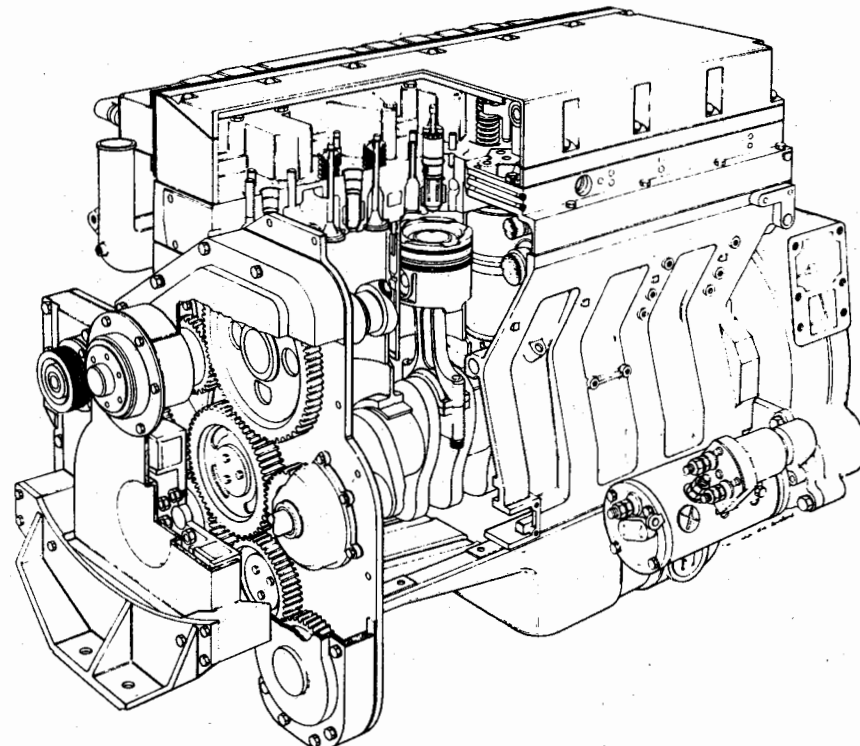
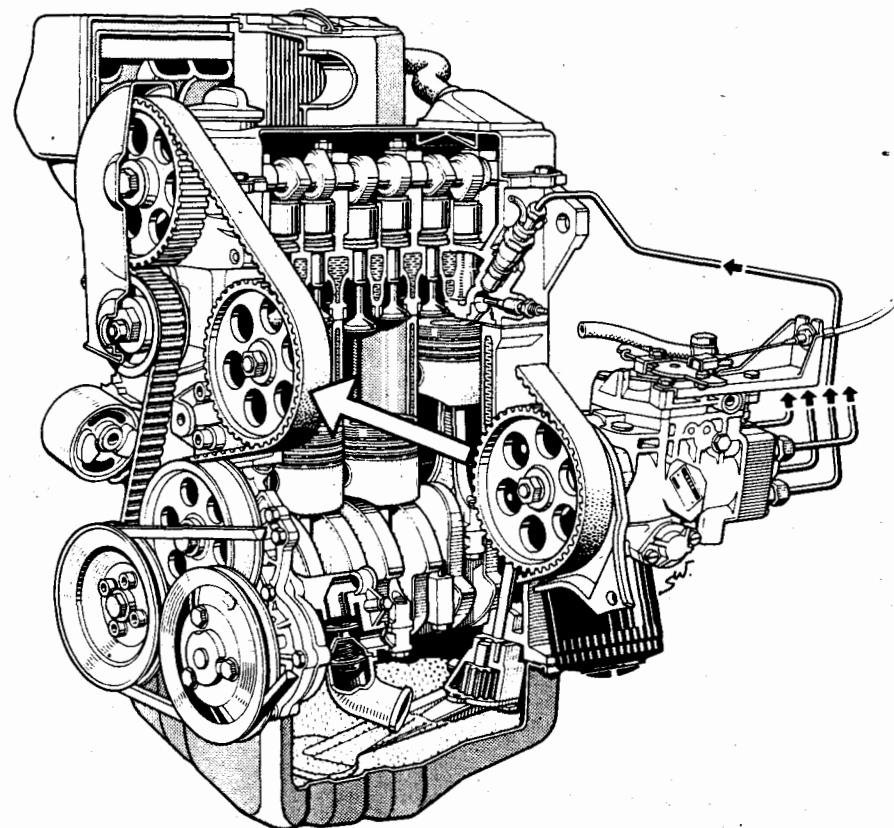


FIGURE 1-20

Direct-injection four-stroke cycle six-cylinder turbocharged Cummins diesel engine. Displaced volume 10 liters, bore 125 mm, stroke 136 mm, compression ratio 16.3, maximum power 168 to 246 kW at rated speed of 2100 rev/min. (Courtesy Cummins Engine Company, Inc.)

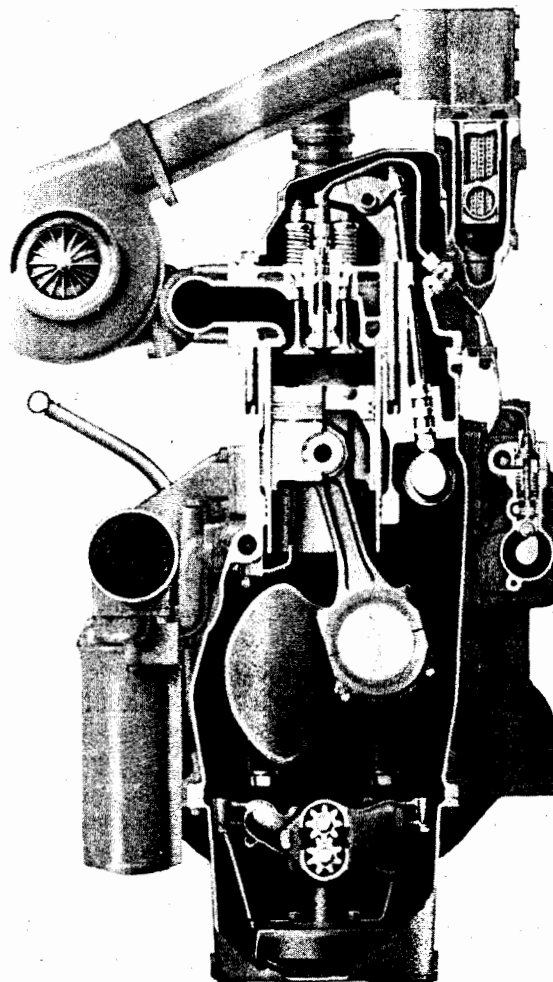
**FIGURE 1-21**

Four-cylinder naturally aspirated indirect-injection automobile Volkswagen diesel engine.<sup>14</sup> Displaced volume 1.47 liters, bore 76.5 mm, stroke 80 mm, maximum power 37 kW at 5000 rev/min.

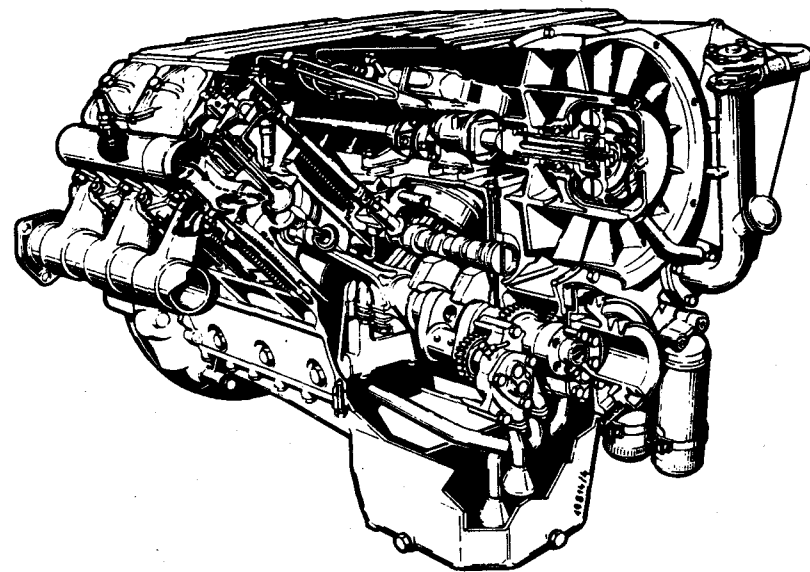
cylinder into the prechamber at high velocity. Fuel is injected into this highly turbulent and often rapidly swirling flow in this auxiliary or prechamber, and very high mixing rates are achieved. Combustion starts in the prechamber, and the resulting pressure rise in the prechamber forces burning gases, fuel, and air into the main chamber. Since this outflow is also extremely vigorous, rapid mixing then occurs in the main chamber as the burning jet mixes with the remaining air and combustion is completed. A distributor-type fuel pump, which is normally used in this engine size range, driven off the camshaft at half the crankshaft speed by a toothed belt, is shown on the right of the figure. It supplies high-pressure fuel pulses to the pintle-type injector nozzles in turn. A glow plug is also shown in the auxiliary chamber; this plug is electrically heated prior to and during cold engine start-up to raise the temperature of the air charge and the fuel sufficiently to achieve autoignition. The compression ratio of this engine is 23. Indirect-injection diesel engines require higher compression ratios than direct-injection engines to start adequately when cold.

Diesel engines are turbocharged to achieve higher power/weight ratios. By increasing the density of the inlet air, a given displaced volume can induct more air. Hence more fuel can be injected and burned, and more power delivered, while avoiding excessive black smoke in the exhaust. All the larger diesels are turbocharged; smaller diesels can be and often are. Figure 1-22 shows how a turbocharger connects to a direct-injection diesel.

All the above diesels are water cooled; some production diesels are air cooled. Figure 1-23 shows a V-8 air-cooled direct-injection naturally aspirated

**FIGURE 1-22**

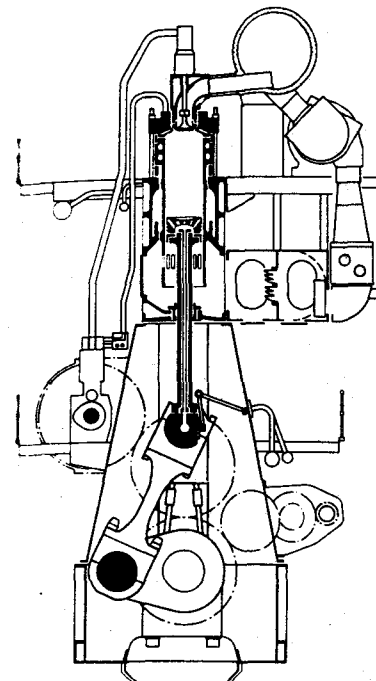
Turbocharged aftercooled direct-injection four-stroke cycle Caterpillar six-cylinder in-line heavy-duty truck diesel engine. Bore 137.2 mm, stroke 165.1 mm, rated power 200–300 kW and rated speed of 1600–2100 rev/min depending on application. (Courtesy Caterpillar Tractor Company.)

**FIGURE 1-23**

V-8 air-cooled direct-injection naturally aspirated diesel engine. Displacement 13.4 liter, bore 128 mm, stroke 130 mm, compression ratio 17, maximum rated power 188 kW at rated speed of 2300 rev/min. (Courtesy Klöcker-Humboldt-Deutz AG.<sup>15</sup>)

diesel. The primary advantage compared to the water-cooled engines is lower engine weight. The fins on the cylinder block and head are necessary to increase the external heat-transfer surface area to achieve the required heat rejection. An air blower, shown on the right of the cutaway drawing, provides forced air convection over the block. The blower is driven off the injection pump shaft, which in turn is driven off the camshaft. The in-line injection pump is placed between the two banks of cylinders. The injection nozzles are located at an angle to the cylinder axis. The combustion chamber and fuel-injection characteristics are similar to those of the engine in Fig. 1-22. The nozzle shown injects four fuel sprays into a reentrant bowl-in-piston combustion chamber.

Diesels are also made in very large engine sizes. These large engines are used for marine propulsion and electrical power generation and operate on the two-stroke cycle in contrast to the small- and medium-size diesels illustrated above. Figure 1-24 shows such a two-stroke cycle marine engine, available with from 4 to 12 cylinders, with a maximum bore of 0.6–0.9 m and stroke of 2–3 m, which operates at speeds of about 100 rev/min. These engines are normally of the crosshead type to reduce side forces on the cylinder. The gas exchange between cycles is controlled by first opening the exhaust valves, and then the piston uncovering inlet ports in the cylinder liner. Expanding exhaust gases leave the cylinder via the exhaust valves and manifold and pass through the turbocharger

**FIGURE 1-24**

Large Sulzer two-stroke turbocharged marine diesel engine. Bore 840 mm, stroke 2900 mm, rated power 1.9 MW per cylinder at 78 rev/min, 4 to 12 cylinders. (Courtesy Sulzer Brothers Ltd.)

turbine. Compressed air enters via the inlet ports and induces forced scavenging; air is supplied from the turbocharger and cooler. At part load electrically driven blowers cut in to compress the scavenge air. Because these large engines operate at low speed, the motion induced by the centrally injected fuel jets is sufficient to mix the fuel with air and burn it in the time available. A simple open combustion chamber shape can be used, therefore, which achieves efficient combustion even with the low-quality heavy fuels used with these types of engines. The pistons are water cooled in these very large engines. The splash oil piston cooling used in medium- and small-size diesels is not adequate.

## 1.9 STRATIFIED-CHARGE ENGINES

Since the 1920s, attempts have been made to develop a hybrid internal combustion engine that combines the best features of the spark-ignition engine and the diesel. The goals have been to operate such an engine at close to the optimum compression ratio for efficiency (in the 12 to 15 range) by: (1) injecting the fuel directly into the combustion chamber during the compression process (and thereby avoid the knock or spontaneous ignition problem that limits conventional spark-ignition engines with their premixed charge); (2) igniting the fuel as it mixes with air with a spark plug to provide direct control of the ignition process

(and thereby avoid the fuel ignition-quality requirement of the diesel); (3) controlling the engine power level by varying the amount of fuel injected per cycle (with the air flow unthrottled to minimize work done pumping the fresh charge into the cylinder). Such engines are often called *stratified-charge engines* from the need to produce in the mixing process between the fuel jet and the air in the cylinder a "stratified" fuel-air mixture, with an easily ignitable composition at the spark plug at the time of ignition. Because such engines avoid the spark-ignition engine requirement for fuels with a high antiknock quality and the diesel requirement for fuels with high ignition quality, they are usually fuel-tolerant and will operate with a wide range of liquid fuels.

Many different types of stratified-charge engine have been proposed, and some have been partially or fully developed. A few have even been used in practice in automotive applications. The operating principles of those that are truly fuel-tolerant or multifuel engines are illustrated in Fig. 1-25. The combustion chamber is usually a bowl-in-piston design, and a high degree of air swirl is created during intake and enhanced in the piston bowl during compression to achieve rapid fuel-air mixing. Fuel is injected into the cylinder, tangentially into the bowl, during the latter stages of compression. A long-duration spark discharge ignites the developing fuel-air jet as it passes the spark plug. The flame spreads downstream, and envelopes and consumes the fuel-air mixture. Mixing continues, and the final stages of combustion are completed during expansion. Most successful designs of this type of engine have used the four-stroke cycle. This concept is usually called a *direct-injection stratified-charge engine*. The engine can be turbocharged to increase its power density.

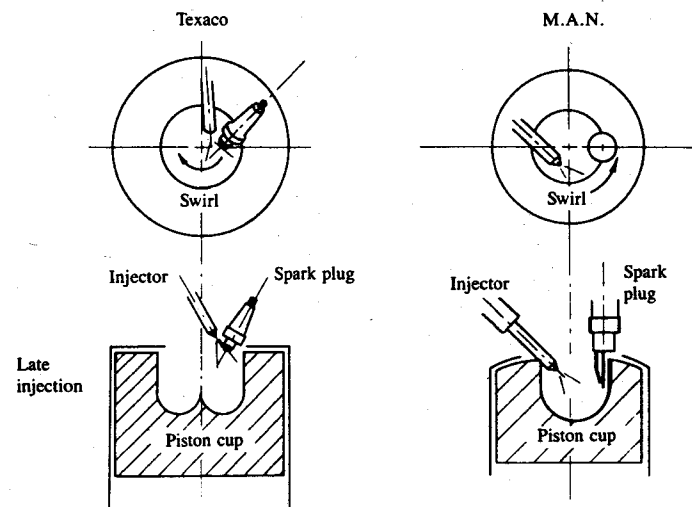


**FIGURE 1-25**  
Two multifuel stratified-charge engines which have been used in commercial practice: the Texaco Controlled Combustion System (TCCS)<sup>16</sup> and the M.A.N.-FM System.<sup>17</sup>

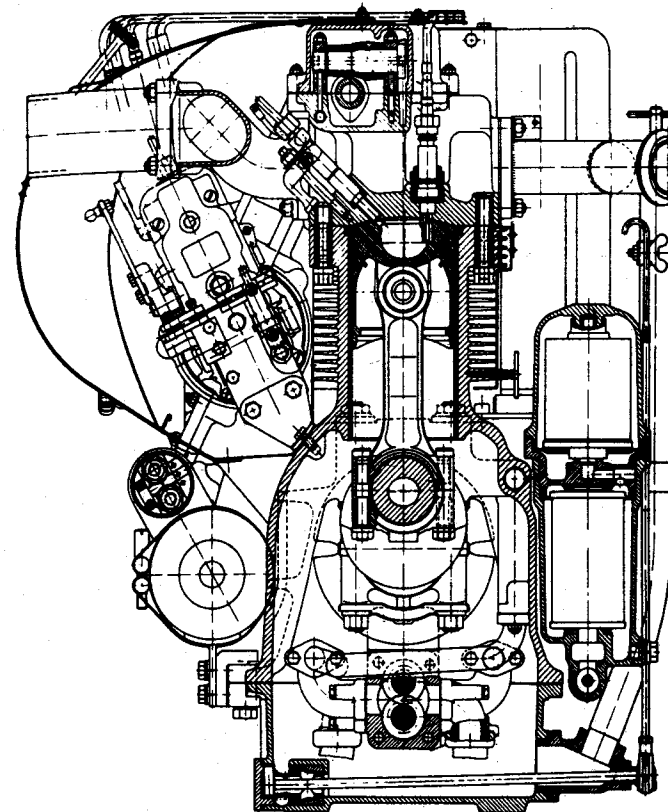


**FIGURE 1-26**  
Sectional drawing of M.A.N. high-speed multifuel four-cylinder direct-injection stratified-charge engine. Bore 94.5 mm, stroke 100 mm, displacement 2.65 liters, compression ratio 16.5, rated power 52 kW at 3800 rev/min.<sup>17</sup>

A commercial multifuel engine is shown in Fig. 1-26. In this particular design, the fuel injector comes diagonally through the cylinder head from the upper left and injects the fuel onto the hot wall of the deep spherical piston bowl. The fuel is carried around the wall of the bowl by the swirling flow, evaporated off the wall, mixed with air, and then ignited by the discharge at the spark plug which enters the chamber vertically on the right. This particular engine is air cooled, so the cylinder block and head are finned to increase surface area.

An alternative stratified-charge engine concept, which has also been mass produced, uses a small *prechamber* fed during intake with an auxiliary fuel system to obtain an easily ignitable mixture around the spark plug. This concept, first proposed by Ricardo in the 1920s and extensively developed in the Soviet Union and Japan, is often called a *jet-ignition* or *torch-ignition* stratified-charge engine. Its operating principles are illustrated in Fig. 1-27 which shows a three-valve

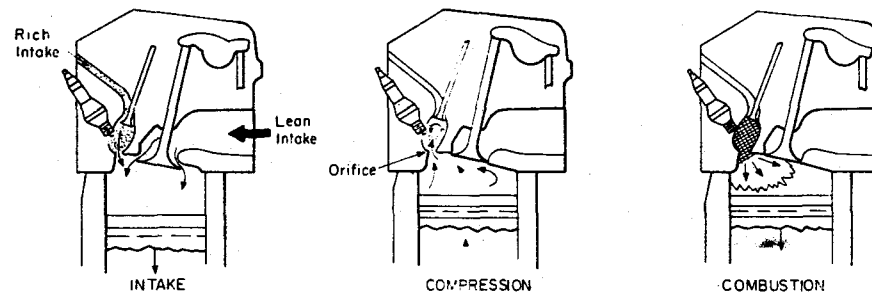


**FIGURE 1-27**  
Schematic of three-valve torch-ignition stratified-charge spark-ignition engine.

carbureted version of the concept.<sup>18</sup> A separate carburetor and intake manifold feeds a fuel-rich mixture (which contains fuel beyond the amount that can be burned with the available air) through a separate small intake valve into the prechamber which contains the spark plug. At the same time, a very lean mixture (which contains excess air beyond that required to burn the fuel completely) is fed to the main combustion chamber through the main carburetor and intake manifold. During intake the rich prechamber flow fully purges the prechamber volume. After intake valve closing, lean mixture from the main chamber is compressed into the prechamber bringing the mixture at the spark plug to an easily ignitable, slightly rich, composition. After combustion starts in the prechamber, rich burning mixture issues as a jet through the orifice into the main chamber, entraining and igniting the lean main chamber charge. Though called a stratified-charge engine, this engine is really a jet-ignition concept whose primary function is to extend the operating limit of conventionally ignited spark-ignition engines to mixtures leaner than could normally be burned.

## PROBLEMS

- 1.1. Describe the major functions of the following reciprocating engine components: piston, connecting rod, crankshaft, cams and camshaft, valves, intake and exhaust manifolds.
- 1.2. Indicate on an appropriate sketch the different forces that act on the piston, and the direction of these forces, during the engine's expansion stroke with the piston, connecting rod, and crank in the positions shown in Fig. 1-1.
- 1.3. List five important differences between the design and operating characteristics of spark-ignition and compression-ignition (diesel) engines.
- 1.4. Indicate the approximate crank angle at which the following events in the four-stroke and two-stroke internal combustion engine cycles occur on a line representing the full cycle ( $720^\circ$  for the four-stroke cycle;  $360^\circ$  for the two-stroke cycle): bottom- and top-center crank positions, inlet and exhaust valve or port opening and closing, start of combustion process, end of combustion process, maximum cylinder pressure.

- 1.5. The two-stroke cycle has twice as many power strokes per crank revolution as the four-stroke cycle. However, two-stroke cycle engine power outputs per unit displaced volume are less than twice the power output of an equivalent four-stroke cycle engine at the same engine speed. Suggest reasons why this potential advantage of the two-stroke cycle is offset in practice.
- 1.6. Suggest reasons why multicylinder engines prove more attractive than single-cylinder engines once the total engine displaced volume exceeds a few hundred cubic centimeters.
- 1.7. The Wankel rotary spark-ignition engine, while lighter and more compact than a reciprocating spark-ignition engine of equal maximum power, typically has worse efficiency due to significantly higher gas leakage from the combustion chamber and higher total heat loss from the hot combustion gases to the chamber walls. Based on the design details in Figs. 1-4, 1-13, and 1-14 suggest reasons for these higher losses.

## REFERENCES

1. Cummins, Jr., C. L.: *Internal Fire*, Carnot Press, Lake Oswego, Oreg., 1976.
2. Cummins, Jr., C. L.: "Early IC and Automotive Engines," SAE paper 760604 in *A History of the Automotive Internal Combustion Engine*, SP-409, SAE Trans., vol. 85, 1976.
3. Hempson, J. G. G.: "The Automobile Engine 1920-1950," SAE paper 760605 in *A History of the Automotive Internal Combustion Engine*, SP-409, SAE, 1976.
4. Agnew, W. G.: "Fifty Years of Combustion Research at General Motors," *Progress in Energy and Combustion Science*, vol. 4, pp. 115-156, 1978.
5. Wankel, F.: *Rotary Piston Machines*, Iliffe Books, London, 1965.
6. Ansdale, R. F.: *The Wankel RC Engine Design and Performance*, Iliffe Books, London, 1968.
7. Yamamoto, K.: *Rotary Engine*, Toyo Kogyo Co. Ltd., Hiroshima, 1969.
8. Haagen-Smit, A. J.: "Chemistry and Physiology of Los Angeles Smog," *Ind. Eng. Chem.*, vol. 44, p. 1342, 1952.
9. Taylor, C. F.: *The Internal Combustion Engine in Theory and Practice*, vol. 2, table 10-1, MIT Press, Cambridge, Mass., 1968.
10. Rogowski, A. R.: *Elements of Internal Combustion Engines*, McGraw-Hill, 1953.
11. Weertman, W. L., and Dean, J. W.: "Chrysler Corporation's New 2.2 Liter 4 Cylinder Engine," SAE paper 810007, 1981.
12. Bosch: *Automotive Handbook*, 1st English edition, Robert Bosch GmbH, 1976.
13. Martens, D. A.: "The General Motors 2.8 Liter 60° V-6 Engine Designed by Chevrolet," SAE paper 790697, 1979.
14. Hofbauer, P., and Sator, K.: "Advanced Automotive Power Systems—Part 2: A Diesel for a Subcompact Car," SAE paper 770113, SAE Trans., vol. 86, 1977.
15. Garthe, H.: "The Deutz BF8L 513 Aircooled Diesel Engine for Truck and Bus Application," SAE paper 852321, 1985.
16. Alperstein, M., Schafer, G. H., and Villforth, F. J.: "Texaco's Stratified Charge Engine—Multifuel, Efficient, Clean, and Practical," SAE paper 740563, 1974.
17. Urlaub, A. G., and Chmela, F. G.: "High-Speed, Multifuel Engine: L9204 FMV," SAE paper 740122, 1974.
18. Date, T., and Yagi, S.: "Research and Development of the Honda CVCC Engine," SAE paper 740605, 1974.

# CHAPTER 2

## ENGINE DESIGN AND OPERATING PARAMETERS

### 2.1 IMPORTANT ENGINE CHARACTERISTICS

In this chapter, some basic geometrical relationships and the parameters commonly used to characterize engine operation are developed. The factors important to an engine user are:

1. The engine's performance over its operating range
2. The engine's fuel consumption within this operating range and the cost of the required fuel
3. The engine's noise and air pollutant emissions within this operating range
4. The initial cost of the engine and its installation
5. The reliability and durability of the engine, its maintenance requirements, and how these affect engine availability and operating costs

These factors control total engine operating costs—usually the primary consideration of the user—and whether the engine in operation can satisfy environmental regulations. This book is concerned primarily with the performance, efficiency, and emissions characteristics of engines; the omission of the other factors listed above does not, in any way, reduce their great importance.

Engine performance is more precisely defined by:

1. The maximum power (or the maximum torque) available at each speed within the useful engine operating range
2. The range of speed and power over which engine operation is satisfactory

The following performance definitions are commonly used:

*Maximum rated power.* The highest power an engine is allowed to develop for short periods of operation.

*Normal rated power.* The highest power an engine is allowed to develop in continuous operation.

*Rated speed.* The crankshaft rotational speed at which rated power is developed.

### 2.2 GEOMETRICAL PROPERTIES OF RECIPROCATING ENGINES

The following parameters define the basic geometry of a reciprocating engine (see Fig. 2-1):

Compression ratio  $r_c$ :

$$r_c = \frac{\text{maximum cylinder volume}}{\text{minimum cylinder volume}} = \frac{V_d + V_c}{V_c} \quad (2.1)$$

where  $V_d$  is the displaced or swept volume and  $V_c$  is the clearance volume.

Ratio of cylinder bore to piston stroke:

$$R_{bs} = \frac{B}{L} \quad (2.2)$$

Ratio of connecting rod length to crank radius:

$$R = \frac{l}{a} \quad (2.3)$$

In addition, the stroke and crank radius are related by

$$L = 2a$$

Typical values of these parameters are:  $r_c = 8$  to 12 for SI engines and  $r_c = 12$  to 24 for CI engines;  $B/L = 0.8$  to 1.2 for small- and medium-size engines, decreasing to about 0.5 for large slow-speed CI engines;  $R = 3$  to 4 for small- and medium-size engines, increasing to 5 to 9 for large slow-speed CI engines.

The cylinder volume  $V$  at any crank position  $\theta$  is

$$V = V_c + \frac{\pi B^2}{4} (l + a - s) \quad (2.4)$$

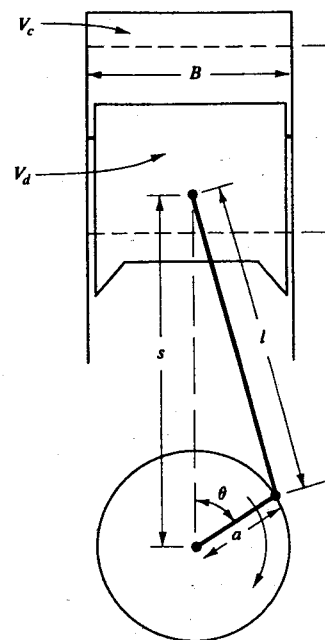


FIGURE 2-1

Geometry of cylinder, piston, connecting rod, and crankshaft where  $B$  = bore,  $L$  = stroke,  $l$  = connecting rod length,  $a$  = crank radius,  $\theta$  = crank angle.

where  $s$  is the distance between the crank axis and the piston pin axis (Fig. 2-1), and is given by

$$s = a \cos \theta + (l^2 - a^2 \sin^2 \theta)^{1/2} \quad (2.5)$$

The angle  $\theta$ , defined as shown in Fig. 2-1, is called the *crank angle*. Equation (2.4) with the above definitions can be rearranged:

$$\frac{V}{V_c} = 1 + \frac{1}{2} (r_e - 1) [R + 1 - \cos \theta - (R^2 - \sin^2 \theta)^{1/2}] \quad (2.6)$$

The combustion chamber surface area  $A$  at any crank position  $\theta$  is given by

$$A = A_{ch} + A_p + \pi B(l + a - s) \quad (2.7)$$

where  $A_{ch}$  is the cylinder head surface area and  $A_p$  is the piston crown surface area. For flat-topped pistons,  $A_p = \pi B^2/4$ . Using Eq. (2.5), Eq. (2.7) can be rearranged:

$$A = A_{ch} + A_p + \frac{\pi B L}{2} [R + 1 - \cos \theta - (R^2 - \sin^2 \theta)^{1/2}] \quad (2.8)$$

An important characteristic speed is the *mean piston speed*  $\bar{S}_p$ :

$$\bar{S}_p = 2LN \quad (2.9)$$

where  $N$  is the rotational speed of the crankshaft. Mean piston speed is often a

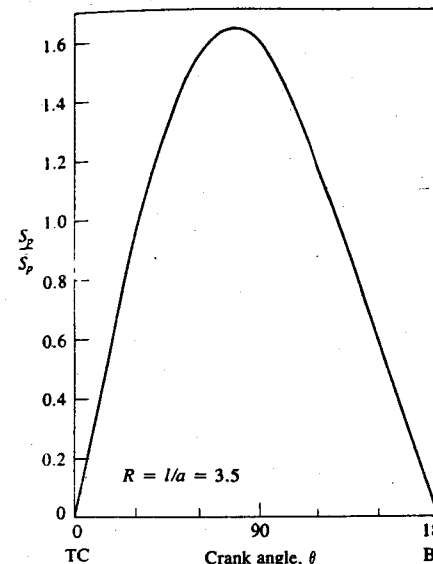


FIGURE 2-2

Instantaneous piston speed/mean piston speed as a function of crank angle for  $R = 3.5$ .

more appropriate parameter than crank rotational speed for correlating engine behavior as a function of speed. For example, gas-flow velocities in the intake and the cylinder all scale with  $\bar{S}_p$ . The *instantaneous* piston velocity  $S_p$  is obtained from

$$S_p = \frac{ds}{dt} \quad (2.10)$$

The piston velocity is zero at the beginning of the stroke, reaches a maximum near the middle of the stroke, and decreases to zero at the end of the stroke. Differentiation of Eq. (2.5) and substitution gives

$$\frac{S_p}{\bar{S}_p} = \frac{\pi}{2} \sin \theta \left[ 1 + \frac{\cos \theta}{(R^2 - \sin^2 \theta)^{1/2}} \right] \quad (2.11)$$

Figure 2-2 shows how  $S_p$  varies over each stroke for  $R = 3.5$ .

Resistance to gas flow into the engine or stresses due to the inertia of the moving parts limit the maximum mean piston speed to within the range 8 to 15 m/s (1500 to 3000 ft/min). Automobile engines operate at the higher end of this range; the lower end is typical of large marine diesel engines.

### 2.3 BRAKE TORQUE AND POWER

Engine torque is normally measured with a dynamometer.<sup>1</sup> The engine is clamped on a test bed and the shaft is connected to the dynamometer rotor. Figure 2-3 illustrates the operating principle of a dynamometer. The rotor is

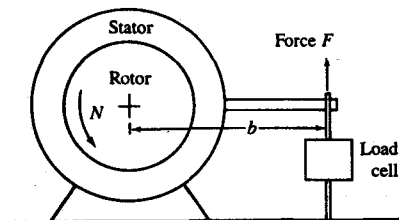


FIGURE 2-3  
Schematic of principle of operation of dynamometer.

coupled electromagnetically, hydraulically, or by mechanical friction to a stator, which is supported in low friction bearings. The stator is balanced with the rotor stationary. The torque exerted on the stator with the rotor turning is measured by balancing the stator with weights, springs, or pneumatic means.

Using the notation in Fig. 2-3, if the torque exerted by the engine is  $T$ :

$$T = Fb \quad (2.12)$$

The power  $P$  delivered by the engine and absorbed by the dynamometer is the product of torque and angular speed:

$$P = 2\pi NT \quad (2.13a)$$

where  $N$  is the crankshaft rotational speed. In SI units:

$$P(\text{kW}) = 2\pi N(\text{rev/s}) T(\text{N} \cdot \text{m}) \times 10^{-3} \quad (2.13b)$$

or in U.S. units:

$$P(\text{hp}) = \frac{N(\text{rev/min}) T(\text{lbf} \cdot \text{ft})}{5252} \quad (2.13c)$$

Note that torque is a measure of an engine's ability to do work; power is the rate at which work is done.

The value of engine power measured as described above is called *brake power*  $P_b$ . This power is the usable power delivered by the engine to the load—in this case, a “brake.”

## 2.4 INDICATED WORK PER CYCLE

Pressure data for the gas in the cylinder over the operating cycle of the engine can be used to calculate the work transfer from the gas to the piston. The cylinder pressure and corresponding cylinder volume throughout the engine cycle can be plotted on a  $p$ - $V$  diagram as shown in Fig. 2-4. The *indicated work per cycle*  $W_{c,i}$ † (per cylinder) is obtained by integrating around the curve to obtain the

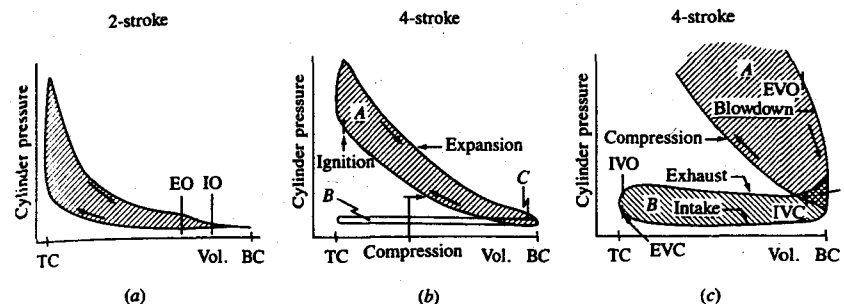


FIGURE 2-4  
Examples of  $p$ - $V$  diagrams for (a) a two-stroke cycle engine, (b) a four-stroke cycle engine; (c) a four-stroke cycle spark-ignition engine exhaust and intake strokes (pumping loop) at part load.

area enclosed on the diagram:

$$W_{c,i} = \oint p \, dV \quad (2.14)$$

With two-stroke cycles (Fig. 2-4a), the application of Eq. (2.14) is straightforward. With the addition of inlet and exhaust strokes for the four-stroke cycle, some ambiguity is introduced as two definitions of indicated output are in common use. These will be defined as:

*Gross indicated work per cycle*  $W_{c,ig}$ . Work delivered to the piston over the compression and expansion strokes only.

*Net indicated work per cycle*  $W_{c,in}$ . Work delivered to the piston over the entire four-stroke cycle.

In Fig. 2-4b and c,  $W_{c,ig}$  is (area  $A +$  area  $C$ ) and  $W_{c,in}$  is (area  $A +$  area  $C$ ) – (area  $B +$  area  $C$ ), which equals (area  $A -$  area  $B$ ), where each of these areas is regarded as a positive quantity. Area  $B +$  area  $C$  is the work transfer between the piston and the cylinder gases during the inlet and exhaust strokes and is called the *pumping work*  $W_p$  (see Chaps. 5 and 13). The pumping work transfer will be *to* the cylinder gases if the pressure during the intake stroke is less than the pressure during the exhaust stroke. This is the situation with naturally aspirated engines. The pumping work transfer will be *from* the cylinder gases to the piston if the exhaust stroke pressure is lower than the intake pressure, which is normally the case with highly loaded turbocharged engines.†

† The term indicated is used because such  $p$ - $V$  diagrams used to be generated directly with a device called an engine indicator.

† With some two-stroke engine concepts there is a piston pumping work term associated with compressing the scavenging air in the crankcase.

The power per cylinder is related to the indicated work per cycle by

$$P_i = \frac{W_{c,i} N}{n_R} \quad (2.15)$$

where  $n_R$  is the number of crank revolutions for each power stroke per cylinder. For four-stroke cycles,  $n_R$  equals 2; for two-stroke cycles,  $n_R$  equals 1. This power is the indicated power; i.e., the rate of work transfer from the gas within the cylinder to the piston. It differs from the brake power by the power absorbed in overcoming engine friction, driving engine accessories, and (in the case of gross indicated power) the pumping power.

In discussing indicated quantities of the four-stroke cycle engine, such as work per cycle or power, the definition used for "indicated" (i.e., gross or net) should always be explicitly stated. The gross indicated output, the definition most commonly used, will be chosen where possible in this book for the following reasons. Indicated quantities are used primarily to identify the impact of the compression, combustion, and expansion processes on engine performance, etc. The gross indicated output is, therefore, the most appropriate definition. It represents the sum of the useful work available at the shaft and the work required to overcome all the engine losses. Furthermore, the standard engine test codes<sup>2</sup> define procedures for measuring brake power and friction power (the friction power test provides a close approximation to the total lost power in the engine). The sum of brake power and friction power provides an alternative way of estimating indicated power; the value obtained is a close approximation to the gross indicated power.

The terms brake and indicated are used to describe other parameters such as mean effective pressure, specific fuel consumption, and specific emissions (see the following sections) in a manner similar to that used for work per cycle and power.

## 2.5 MECHANICAL EFFICIENCY

We have seen that part of the gross indicated work per cycle or power is used to expel exhaust gases and induct fresh charge. An additional portion is used to overcome the friction of the bearings, pistons, and other mechanical components of the engine, and to drive the engine accessories. All of these power requirements are grouped together and called *friction power*  $P_f$ .<sup>†</sup> Thus:

$$P_{ig} = P_b + P_f \quad (2.16)$$

Friction power is difficult to determine accurately. One common approach for high-speed engines is to drive or motor the engine with a dynamometer (i.e., operate the engine without firing it) and measure the power which has to be

<sup>†</sup> The various components of friction power are examined in detail in Chap. 13.

supplied by the dynamometer to overcome all these frictional losses. The engine speed, throttle setting, oil and water temperatures, and ambient conditions are kept the same in the motored test as under firing conditions. The major sources of inaccuracy with this method are that gas pressure forces on the piston and rings are lower in the motored test than when the engine is firing and that the oil temperatures on the cylinder wall are also lower under motoring conditions.

The ratio of the brake (or useful) power delivered by the engine to the indicated power is called the *mechanical efficiency*  $\eta_m$ :

$$\eta_m = \frac{P_b}{P_{ig}} = 1 - \frac{P_f}{P_{ig}} \quad (2.17)$$

Since the friction power includes the power required to pump gas into and out of the engine, mechanical efficiency depends on throttle position as well as engine design and engine speed. Typical values for a modern automotive engine at wide-open or full throttle are 90 percent at speeds below about 30 to 40 rev/s (1800 to 2400 rev/min), decreasing to 75 percent at maximum rated speed. As the engine is throttled, mechanical efficiency decreases, eventually to zero at idle operation.

## 2.6 ROAD-LOAD POWER

A part-load power level useful as a reference point for testing automobile engines is the power required to drive a vehicle on a level road at a steady speed. Called *road-load power*, this power overcomes the rolling resistance which arises from the friction of the tires and the aerodynamic drag of the vehicle. Rolling resistance and drag coefficients,  $C_R$  and  $C_D$ , respectively, are determined empirically. An approximate formula for road-load power  $P_r$  is

$$P_r = (C_R M_v g + \frac{1}{2} \rho_a C_D A_v S_v^2) S_v \quad (2.18a)$$

where  $C_R$  = coefficient of rolling resistance ( $0.012 < C_R < 0.015$ )<sup>3</sup>

$M_v$  = mass of vehicle [for passenger cars: curb mass plus passenger load of 68 kg (150 lbm); in U.S. units  $W_v$  = vehicle weight in lbf]

$g$  = acceleration due to gravity

$\rho_a$  = ambient air density

$C_D$  = drag coefficient (for cars:  $0.3 < C_D \lesssim 0.5$ )<sup>3</sup>

$A_v$  = frontal area of vehicle

$S_v$  = vehicle speed

With the quantities in the units indicated:

$$P_r(\text{kW}) = [2.73 C_R M_v(\text{kg}) + 0.0126 C_D A_v(\text{m}^2) S_v(\text{km/h})^2] S_v(\text{km/h}) \times 10^{-3} \quad (2.18b)$$

$$\text{or } P_r(\text{hp}) = [C_R W_v(\text{lbf}) + 0.0025 C_D A_v(\text{ft}^2) S_v(\text{mi/h})^2] S_v(\text{mi/h}) \quad (2.18c)$$

## 2.7 MEAN EFFECTIVE PRESSURE

While torque is a valuable measure of a particular engine's ability to do work, it depends on engine size. A more useful relative engine performance measure is obtained by dividing the work per cycle by the cylinder volume displaced per cycle. The parameter so obtained has units of force per unit area and is called the *mean effective pressure* (mep). Since, from Eq. (2.15),

$$\text{Work per cycle} = \frac{Pn_R}{N}$$

where  $n_R$  is the number of crank revolutions for each power stroke per cylinder (two for four-stroke cycles; one for two-stroke cycles), then

$$\text{mep} = \frac{Pn_R}{V_d N} \quad (2.19a)$$

For SI and U.S. units, respectively,

$$\text{mep(kPa)} = \frac{P(\text{kW})n_R \times 10^3}{V_d(\text{dm}^3)N(\text{rev/s})} \quad (2.19b)$$

$$\text{mep(lb/in}^2\text{)} = \frac{P(\text{hp})n_R \times 396,000}{V_d(\text{in}^3)N(\text{rev/min})} \quad (2.19c)$$

Mean effective pressure can also be expressed in terms of torque by using Eq. (2.13):

$$\text{mep(kPa)} = \frac{6.28n_R T(\text{N} \cdot \text{m})}{V_d(\text{dm}^3)} \quad (2.20a)$$

or  $\text{mep(lb/in}^2\text{)} = \frac{75.4n_R T(\text{lbf} \cdot \text{ft})}{V_d(\text{in}^3)}$  (2.20b)

The maximum brake mean effective pressure of good engine designs is well established, and is essentially constant over a wide range of engine sizes. Thus, the actual bmepl that a particular engine develops can be compared with this norm, and the effectiveness with which the engine designer has used the engine's displaced volume can be assessed. Also, for design calculations, the engine displacement required to provide a given torque or power, at a specified speed, can be estimated by assuming appropriate values for bmepl for that particular application.

Typical values for bmepl are as follows. For naturally aspirated spark-ignition engines, maximum values are in the range 850 to 1050 kPa (~ 125 to 150 lb/in<sup>2</sup>) at the engine speed where maximum torque is obtained (about 3000 rev/min). At the maximum rated power, bmepl values are 10 to 15 percent lower. For turbocharged automotive spark-ignition engines the maximum bmepl is in the 1250 to 1700 kPa (180 to 250 lb/in<sup>2</sup>) range. At the maximum rated power, bmepl is in the 900 to 1400 kPa (130 to 200 lb/in<sup>2</sup>) range. For naturally aspirated four-stroke diesels, the maximum bmepl is in the 700 to 900 kPa (100 to 130

lb/in<sup>2</sup>) range, with the bmepl at the maximum rated power of about 700 kPa (100 lb/in<sup>2</sup>). Turbocharged four-stroke diesel maximum bmepl values are typically in the range 1000 to 1200 kPa (145 to 175 lb/in<sup>2</sup>); for turbocharged aftercooled engines this can rise to 1400 kPa. At maximum rated power, bmepl is about 850 to 950 kPa (125 to 140 lb/in<sup>2</sup>). Two-stroke cycle diesels have comparable performance to four-stroke cycle engines. Large low-speed two-stroke cycle engines can achieve bmepl values of about 1600 kPa.

An example of how the above engine performance parameters can be used to initiate an engine design is given below.

**Example.** A four-cylinder automotive spark-ignition engine is being designed to provide a maximum brake torque of 150 N·m (110 lbf·ft) in the mid-speed range (~ 3000 rev/min). Estimate the required engine displacement, bore and stroke, and the maximum brake power the engine will deliver.

Equation (2.20a) relates torque and mep. Assume that 925 kPa is an appropriate value for bmepl at the maximum engine torque point. Equation (2.20a) gives

$$V(\text{dm}^3) = \frac{6.28n_R T_{\max}(\text{N} \cdot \text{m})}{\text{bmepl}_{\max}(\text{kPa})} = \frac{6.28 \times 2 \times 150}{925} = 2 \text{ dm}^3$$

For a four-cylinder engine, the displaced volume, bore, and stroke are related by

$$V_d = 4 \times \frac{\pi}{4} B^2 L$$

Assume  $B = L$ ; this gives  $B = L = 86$  mm.

The maximum rated engine speed can be estimated from an appropriate value for the maximum mean piston speed, 15 m/s (see Sec. 2.2):

$$\bar{s}_{\max} = 2LN_{\max} \rightarrow N_{\max} = 87 \text{ rev/s (5200 rev/min)}$$

The maximum brake power can be estimated from the typical bmepl value at maximum power, 800 kPa (116 lb/in<sup>2</sup>), using Eq. (2.19b):

$$P_{\max}(\text{kW}) = \frac{\text{bmepl}(\text{kPa})V(\text{dm}^3)N_{\max}(\text{rev/s})}{n_R \times 10^3} = \frac{800 \times 2 \times 87}{2 \times 10^3} = 70 \text{ kW}$$

## 2.8 SPECIFIC FUEL CONSUMPTION AND EFFICIENCY

In engine tests, the fuel consumption is measured as a flow rate—mass flow per unit time  $\dot{m}_f$ . A more useful parameter is the *specific fuel consumption* (sfc)—the fuel flow rate per unit power output. It measures how efficiently an engine is using the fuel supplied to produce work:

$$\text{sfc} = \frac{\dot{m}_f}{P} \quad (2.21)$$

With units,

$$\text{sfc}(\text{mg/J}) = \frac{\dot{m}_f(\text{g/s})}{P(\text{kW})} \quad (2.22a)$$

or  $\text{sfc}(\text{g/kW}\cdot\text{h}) = \frac{\dot{m}_f(\text{g/h})}{P(\text{kW})} = 608.3 \text{ sfc(lbm/hp}\cdot\text{h)} \quad (2.22b)$

or  $\text{sfc(lbm/hp}\cdot\text{h)} = \frac{\dot{m}_f(\text{lbm/h})}{P(\text{hp})} = 1.644 \times 10^3 \text{ sfc(g/kW}\cdot\text{h)} \quad (2.22c)$

Low values of sfc are obviously desirable. For SI engines typical best values of brake specific fuel consumption are about  $75 \mu\text{g/J} = 270 \text{ g/kW}\cdot\text{h} = 0.47 \text{ lbm/hp}\cdot\text{h}$ . For CI engines, best values are lower and in large engines can go below  $55 \mu\text{g/J} = 200 \text{ g/kW}\cdot\text{h} = 0.32 \text{ lbm/hp}\cdot\text{h}$ .

The specific fuel consumption has units. A dimensionless parameter that relates the desired engine output (work per cycle or power) to the necessary input (fuel flow) would have more fundamental value. The ratio of the work produced per cycle to the amount of fuel energy supplied per cycle that can be released in the combustion process is commonly used for this purpose. It is a measure of the engine's efficiency. The fuel energy supplied which can be released by combustion is given by the mass of fuel supplied to the engine per cycle times the heating value of the fuel. The heating value of a fuel,  $Q_{\text{HV}}$ , defines its energy content. It is determined in a standardized test procedure in which a known mass of fuel is fully burned with air, and the thermal energy released by the combustion process is absorbed by a calorimeter as the combustion products cool down to their original temperature.

This measure of an engine's "efficiency," which will be called the *fuel conversion efficiency*  $\eta_f$ ,† is given by

$$\eta_f = \frac{W_c}{m_f Q_{\text{HV}}} = \frac{(Pn_R/N)}{(\dot{m}_f n_R/N)Q_{\text{HV}}} = \frac{P}{\dot{m}_f Q_{\text{HV}}} \quad (2.23)$$

where  $m_f$  is the mass of fuel inducted per cycle. Substitution for  $P/\dot{m}_f$  from Eq. (2.21) gives

$$\eta_f = \frac{1}{\text{sfc } Q_{\text{HV}}} \quad (2.24a)$$

or with units:

$$\eta_f = \frac{1}{\text{sfc}(\text{mg/J})Q_{\text{HV}}(\text{MJ/kg})} \quad (2.24b)$$

$$\eta_f = \frac{3600}{\text{sfc}(\text{g/kW}\cdot\text{h})Q_{\text{HV}}(\text{MJ/kg})} \quad (2.24c)$$

$$\eta_f = \frac{2545}{\text{sfc(lbm/hp}\cdot\text{h)}Q_{\text{HV}}(\text{Btu/lbm})} \quad (2.24d)$$

Typical heating values for the commercial hydrocarbon fuels used in engines are in the range 42 to 44 MJ/kg (18,000 to 19,000 Btu/lbm). Thus, specific fuel consumption is inversely proportional to fuel conversion efficiency for normal hydrocarbon fuels.

Note that the fuel energy supplied to the engine per cycle is not fully released as thermal energy in the combustion process because the actual combustion process is incomplete. When enough air is present in the cylinder to oxidize the fuel completely, almost all (more than about 96 percent) of this fuel energy supplied is transferred as thermal energy to the working fluid. When insufficient air is present to oxidize the fuel completely, lack of oxygen prevents this fuel energy supplied from being fully released. This topic is discussed in more detail in Secs. 3.5 and 4.9.4.

## 2.9 AIR/FUEL AND FUEL/AIR RATIOS

In engine testing, both the air mass flow rate  $\dot{m}_a$  and the fuel mass flow rate  $\dot{m}_f$  are normally measured. The ratio of these flow rates is useful in defining engine operating conditions:

$$\text{Air/fuel ratio (A/F)} = \frac{\dot{m}_a}{\dot{m}_f} \quad (2.25)$$

$$\text{Fuel/air ratio (F/A)} = \frac{\dot{m}_f}{\dot{m}_a} \quad (2.26)$$

The normal operating range for a conventional SI engine using gasoline fuel is  $12 \leq A/F \leq 18$  ( $0.056 \leq F/A \leq 0.083$ ); for CI engines with diesel fuel, it is  $18 \leq A/F \leq 70$  ( $0.014 \leq F/A \leq 0.056$ ).

## 2.10 VOLUMETRIC EFFICIENCY

The intake system—the air filter, carburetor, and throttle plate (in a spark-ignition engine), intake manifold, intake port, intake valve—restricts the amount of air which an engine of given displacement can induct. The parameter used to measure the effectiveness of an engine's induction process is the *volumetric efficiency*  $\eta_v$ . Volumetric efficiency is only used with four-stroke cycle engines which have a distinct induction process. It is defined as the volume flow rate of air into

† This empirically defined engine efficiency has previously been called thermal efficiency or enthalpy efficiency. The term fuel conversion efficiency is preferred because it describes this quantity more precisely, and distinguishes it clearly from other definitions of engine efficiency which will be developed in Sec. 3.6. Note that there are several different definitions of heating value (see Sec. 3.5). The numerical values do not normally differ by more than a few percent, however. In this text, the lower heating value at constant pressure is used in evaluating the fuel conversion efficiency.

the intake system divided by the rate at which volume is displaced by the piston:

$$\eta_v = \frac{2\dot{m}_a}{\rho_{a,i} V_d N} \quad (2.27a)$$

where  $\rho_{a,i}$  is the inlet air density. An alternative equivalent definition for volumetric efficiency is

$$\eta_v = \frac{\dot{m}_a}{\rho_{a,i} V_d} \quad (2.27b)$$

where  $\dot{m}_a$  is the mass of air inducted into the cylinder per cycle.

The inlet density may either be taken as atmosphere air density (in which case  $\eta_v$  measures the pumping performance of the entire inlet system) or may be taken as the air density in the inlet manifold (in which case  $\eta_v$  measures the pumping performance of the inlet port and valve only). Typical maximum values of  $\eta_v$  for naturally aspirated engines are in the range 80 to 90 percent. The volumetric efficiency for diesels is somewhat higher than for SI engines. Volumetric efficiency is discussed more fully in Sec. 6.2.

## 2.11 ENGINE SPECIFIC WEIGHT AND SPECIFIC VOLUME

Engine weight and bulk volume for a given rated power are important in many applications. Two parameters useful for comparing these attributes from one engine to another are:

$$\text{Specific weight} = \frac{\text{engine weight}}{\text{rated power}} \quad (2.28)$$

$$\text{Specific volume} = \frac{\text{engine volume}}{\text{rated power}} \quad (2.29)$$

For these parameters to be useful in engine comparisons, a consistent definition of what components and auxiliaries are included in the term "engine" must be adhered to. These parameters indicate the effectiveness with which the engine designer has used the engine materials and packaged the engine components.<sup>4</sup>

## 2.12 CORRECTION FACTORS FOR POWER AND VOLUMETRIC EFFICIENCY

The pressure, humidity, and temperature of the ambient air inducted into an engine, at a given engine speed, affect the air mass flow rate and the power output. Correction factors are used to adjust measured wide-open-throttle power and volumetric efficiency values to standard atmospheric conditions to provide a more accurate basis for comparisons between engines. Typical standard ambient

conditions used are:

Dry air pressure	Water vapour pressure	Temperature
736.6 mmHg 29.00 inHg	9.65 mmHg 0.38 inHg	29.4°C 85°F

The basis for the correction factor is the equation for one-dimensional steady compressible flow through an orifice or flow restriction of effective area  $A_E$  (see App. C):

$$\dot{m} = \frac{A_E p_0}{\sqrt{RT_0}} \left\{ \frac{2\gamma}{\gamma - 1} \left[ \left( \frac{p}{p_0} \right)^{2/\gamma} - \left( \frac{p}{p_0} \right)^{(1+\gamma)/\gamma} \right] \right\}^{1/2} \quad (2.30)$$

In deriving this equation, it has been assumed that the fluid is an ideal gas with gas constant  $R$  and that the ratio of specific heats ( $c_p/c_v = \gamma$ ) is a constant;  $p_0$  and  $T_0$  are the total pressure and temperature upstream of the restriction and  $p$  is the pressure at the throat of the restriction.

If, in the engine,  $p/p_0$  is assumed constant at wide-open throttle, then for a given intake system and engine, the mass flow rate of dry air  $\dot{m}_a$  varies as

$$\dot{m}_a \propto \frac{p_0}{\sqrt{T_0}} \quad (2.31)$$

For mixtures containing the proper amount of fuel to use all the air available (and thus provide maximum power), the indicated power at full throttle  $P_i$  will be proportional to  $\dot{m}_a$ , the dry air flow rate. Thus if

$$P_{i,s} = C_F P_{i,m} \quad (2.32)$$

where the subscripts  $s$  and  $m$  denote values at the standard and measured conditions, respectively, the correction factor  $C_F$  is given by

$$C_F = \frac{p_{s,d}}{p_m - p_{v,m}} \left( \frac{T_m}{T_s} \right)^{1/2} \quad (2.33)$$

where  $p_{s,d}$  = standard dry-air absolute pressure

$p_m$  = measured ambient-air absolute pressure

$p_{v,m}$  = measured ambient-water vapour partial pressure

$T_m$  = measured ambient temperature, K

$T_s$  = standard ambient temperature, K

The rated *brake* power is corrected by using Eq. (2.33) to correct the *indicated* power and making the assumption that friction power is unchanged. Thus

$$P_{b,s} = C_F P_{i,m} - P_{f,m} \quad (2.34)$$

Volumetric efficiency is proportional to  $\dot{m}_a/\rho_a$  [see Eq. (2.27)]. Since  $\rho_a$  is proportional to  $p/T$ , the correction factor for volumetric efficiency,  $C'_F$ , is

$$C'_F = \frac{\eta_{v,s}}{\eta_{v,m}} = \left( \frac{T_s}{T_m} \right)^{1/2} \quad (2.35)$$

## 2.13 SPECIFIC EMISSIONS AND EMISSIONS INDEX

Levels of emissions of oxides of nitrogen (nitric oxide, NO, and nitrogen dioxide, NO<sub>2</sub>, usually grouped together as NO<sub>x</sub>), carbon monoxide (CO), unburned hydrocarbons (HC), and particulates are important engine operating characteristics.

The concentrations of gaseous emissions in the engine exhaust gases are usually measured in parts per million or percent by volume (which corresponds to the mole fraction multiplied by 10<sup>6</sup> or by 10<sup>2</sup>, respectively). Normalized indicators of emissions levels are more useful, however, and two of these are in common use. *Specific emissions* are the mass flow rate of pollutant per unit power output:

$$s\text{NO}_x = \frac{\dot{m}_{\text{NO}_x}}{P} \quad (2.36a)$$

$$s\text{CO} = \frac{\dot{m}_{\text{CO}}}{P} \quad (2.36b)$$

$$s\text{HC} = \frac{\dot{m}_{\text{HC}}}{P} \quad (2.36c)$$

$$s\text{Part} = \frac{\dot{m}_{\text{part}}}{P} \quad (2.36d)$$

Indicated and brake specific emissions can be defined. Units in common use are  $\mu\text{g}/\text{J}$ ,  $\text{g}/\text{kW}\cdot\text{h}$ , and  $\text{g}/\text{hp}\cdot\text{h}$ .

Alternatively, emission rates can be normalized by the fuel flow rate. An *emission index* (EI) is commonly used: e.g.,

$$\text{EI}_{\text{NO}_x} = \frac{\dot{m}_{\text{NO}_x}(\text{g}/\text{s})}{\dot{m}_f(\text{kg}/\text{s})} \quad (2.37)$$

with similar expressions for CO, HC, and particulates.

## 2.14 RELATIONSHIPS BETWEEN PERFORMANCE PARAMETERS

The importance of the parameters defined in Secs. 2.8 to 2.10 to engine performance becomes evident when power, torque, and mean effective pressure are expressed in terms of these parameters. From the definitions of engine power [Eq. (2.13)], mean effective pressure [Eq. (2.19)], fuel conversion efficiency [Eq. (2.23)], fuel/air ratio [Eq. (2.26)], and volumetric efficiency [Eq. (2.27)], the following relationships between engine performance parameters can be developed. For power  $P$ :

$$P = \frac{\eta_f m_a N Q_{\text{HV}}(F/A)}{n_R} \quad (2.38)$$

For four-stroke cycle engines, volumetric efficiency can be introduced:

$$P = \frac{\eta_f \eta_v N V_d Q_{\text{HV}} \rho_{a,i}(F/A)}{2} \quad (2.39)$$

For torque  $T$ :

$$T = \frac{\eta_f \eta_v V_d Q_{\text{HV}} \rho_{a,i}(F/A)}{4\pi} \quad (2.40)$$

For mean effective pressure:

$$\text{mep} = \eta_f \eta_v Q_{\text{HV}} \rho_{a,i}(F/A) \quad (2.41)$$

The power per unit piston area, often called the *specific power*, is a measure of the engine designer's success in using the available piston area regardless of cylinder size. From Eq. (2.39), the specific power is

$$\frac{P}{A_p} = \frac{\eta_f \eta_v N L Q_{\text{HV}} \rho_{a,i}(F/A)}{2} \quad (2.42)$$

Mean piston speed can be introduced with Eq. (2.9) to give

$$\frac{P}{A_p} = \frac{\eta_f \eta_v \bar{S}_p Q_{\text{HV}} \rho_{a,i}(F/A)}{4} \quad (2.43)$$

Specific power is thus proportional to the product of mean effective pressure and mean piston speed.

These relationships illustrate the direct importance to engine performance of:

1. High fuel conversion efficiency
2. High volumetric efficiency
3. Increasing the output of a given displacement engine by increasing the inlet air density
4. Maximum fuel/air ratio that can be usefully burned in the engine
5. High mean piston speed

## 2.15 ENGINE DESIGN AND PERFORMANCE DATA

Engine ratings usually indicate the highest power at which manufacturers expect their products to give satisfactory economy, reliability, and durability under service conditions. Maximum torque, and the speed at which it is achieved, is usually given also. Since both of these quantities depend on displaced volume, for comparative analyses between engines of different displacements in a given engine category normalized performance parameters are more useful. The following measures, at the operating points indicated, have most significance:<sup>4</sup>

TABLE 2.1  
Typical design and operating data for internal combustion engines

	Operating cycle	Compression ratio	Bore, m	Stroke/bore	Rated maximum		Weight/power best bfc, g/kW·h
					Speed, rev/min	bmep, atm	
<i>Spark-ignition engines:</i>							
Small (e.g., motorcycles)	2S,4S	6-11	0.05-0.085	1.2-0.9	4500-7500	4-10	20-60
Passenger cars	4S	8-10	0.07-0.1	1.1-0.9	4500-6500	7-10	20-50
Trucks	4S	7-9	0.09-0.13	1.2-0.7	3600-5000	6.5-7	25-30
Large gas engines	2S,4S	8-12	0.22-0.45	1.1-1.4	300-900	6.8-12	3-7
Wankel engines	4S	≈ 9	0.57 dm <sup>3</sup> per chamber	6000-8000	9.5-10.5	35-45	1.6-0.9
<i>Diesel engines:</i>							
Passenger cars	4S	17-23	0.075-0.1	1.2-0.9	4000-5000	5-7.5	18-22
Trucks (NA)	4S	16-22	0.1-0.15	1.3-0.8	2100-4000	6-9	15-22
Trucks (TC)	4S	14-20	0.1-0.15	1.3-0.8	2100-4000	12-18	18-26
Locomotive,	4S,2S	12-18	0.15-0.4	1.1-1.3	425-1800	7-23	5-20
Industrial, marine							6-18
Large engines, marine and stationary	2S	10-12	0.4-1	1.2-3	110-400	9-17	2-8
							12-50
							180

- At maximum or normal rated point:

*Mean piston speed.* Measures comparative success in handling loads due to inertia of the parts, resistance to air flow, and/or engine friction.

*Brake mean effective pressure.* In naturally aspirated engines bmep is not stress limited. It then reflects the product of volumetric efficiency (ability to induct air), fuel/air ratio (effectiveness of air utilization in combustion), and fuel conversion efficiency. In supercharged engines bmep indicates the degree of success in handling higher gas pressures and thermal loading.

*Power per unit piston area.* Measures the effectiveness with which the piston area is used, regardless of cylinder size.

*Specific weight.* Indicates relative economy with which materials are used.

*Specific volume.* Indicates relative effectiveness with which engine space has been utilized.

- At all speeds at which the engine will be used with full throttle or with maximum fuel-pump setting:

*Brake mean effective pressure.* Measures ability to obtain/provide high air flow and use it effectively over the full range.

- At all useful regimes of operation and particularly in those regimes where the engine is run for long periods of time:

*Brake specific fuel consumption or fuel conversion efficiency.*

*Brake specific emissions.*

Typical performance data for spark-ignition and diesel engines over the normal production size range are summarized in Table 2.1.<sup>4</sup> The four-stroke cycle dominates except in the smallest and largest engine sizes. The larger engines are turbocharged or supercharged. The maximum rated engine speed decreases as engine size increases, maintaining the maximum mean piston speed in the range of about 8 to 15 m/s. The maximum brake mean effective pressure for turbocharged and supercharged engines is higher than for naturally aspirated engines. Because the maximum fuel/air ratio for spark-ignition engines is higher than for diesels, their naturally aspirated maximum bmep levels are higher. As engine size increases, brake specific fuel consumption decreases and fuel conversion efficiency increases, due to reduced importance of heat losses and friction. For the largest diesel engines, brake fuel conversion efficiencies of about 50 percent and indicated fuel conversion efficiencies of over 55 percent can be obtained.

## PROBLEMS

- Explain why the brake mean effective pressure of a naturally aspirated diesel engine is lower than that of a naturally aspirated spark-ignition engine. Explain why the bmep is lower at the maximum rated power for a given engine than the bmep at the maximum torque.

- 2.2. Describe the impact on air flow, maximum torque, and maximum power of changing a spark-ignition engine cylinder head from 2 valves per cylinder to 4 valves (2 inlet and 2 exhaust) per cylinder.
- 2.3. Calculate the mean piston speed, bmepl, and specific power of the spark-ignition engines in Figs. 1-4, 1-9, and 1-12 at their maximum rated power.
- 2.4. Calculate the mean piston speed, bmepl, and specific power of the diesel engines in Figs. 1-20, 1-21, 1-22, 1-23, and 1-24 at their maximum rated power. Briefly explain any significant differences.
- 2.5. Develop an equation for the power required to drive a vehicle at constant speed up a hill of angle  $\alpha$ , in terms of vehicle speed, mass, frontal area, drag coefficient, coefficient of rolling resistance,  $\alpha$ , and acceleration due to gravity. Calculate this power when the car mass is 1500 kg, the hill angle is 15 degrees, and the vehicle speed is 50 mi/h.
- 2.6. The spark-ignition engine in Fig. 1-4 is operating at a mean piston speed of 10 m/s. The measured air flow is 60 g/s. Calculate the volumetric efficiency based on atmospheric conditions.
- 2.7. The diesel engine of Fig. 1-20 is operating with a mean piston speed of 8 m/s. Calculate the air flow if the volumetric efficiency is 0.92. If  $(F/A)$  is 0.05 what is the fuel flow rate, and the mass of fuel injected per cylinder per cycle?
- 2.8. The brake fuel conversion efficiency of a spark-ignition engine is 0.3, and varies little with fuel type. Calculate the brake specific fuel consumption for iso-octane, gasoline, methanol, and hydrogen (relevant data are in App. D).
- 2.9. You are doing a preliminary design study of a turbocharged four-stroke diesel engine. The maximum rated power is limited by stress considerations to a brake mean effective pressure of 1200 kPa and maximum value of the mean piston speed of 12 m/s.
  - (a) Derive an equation relating the engine inlet pressure (pressure in the inlet manifold at the turbocharger compressor exit) to the fuel/air ratio at this maximum rated power operating point. Other reciprocating engine parameters (e.g., volumetric efficiency, fuel conversion efficiency, bmepl, etc.) appear in this equation also.
  - (b) The maximum rated brake power requirement for this engine is 400 kW. Estimate sensible values for number of cylinders, cylinder bore, stroke, and determine the maximum rated speed of this preliminary engine design.
  - (c) If the pressure ratio across the compressor is 2, estimate the overall fuel/air and air/fuel ratios at the maximum rated power. Assume appropriate values for any other parameters you may need.
- 2.10. In the reciprocating engine, during the power or expansion stroke, the gas pressure force acting on the piston is transmitted to the crankshaft via the connecting rod. List the forces acting on the piston during this part of the operating cycle. Show the direction of the forces acting on the piston on a sketch of the piston, cylinder, connecting rod, crank arrangement. Write out the force balance for the piston (a) along the cylinder axis and (b) transverse to the cylinder axis in the plane containing the connecting rod. (You are not asked to manipulate or solve these equations.)
- 2.11. You are designing a four-stroke cycle diesel engine to provide a brake power of 300 kW naturally aspirated at its maximum rated speed. Based on typical values for brake mean effective pressure and maximum mean piston speed, estimate the required engine displacement, and the bore and stroke for sensible cylinder geometry and number of engine cylinders. What is the maximum rated engine speed (rev/min)

- for your design? What would be the brake torque ( $N \cdot m$ ) and the fuel flow rate ( $g/h$ ) at this maximum speed? Assume a maximum mean piston speed of 12 m/s is typical of good engine designs.
- 2.12. The power per unit piston area  $P/A_p$  (often called the specific power) is a measure of the designer's success in using the available piston area regardless of size.
    - (a) Derive an expression for  $P/A_p$  in terms of mean effective pressure and mean piston speed for two-stroke and four-stroke engine cycles.
    - (b) Compute typical maximum values of  $P/A_p$  for a spark-ignition engine (e.g., Fig. 1-4), a turbocharged four-stroke cycle diesel engine (e.g., Fig. 1-22), and a large marine diesel (Fig. 1-24). Table 2-1 may be helpful. State your assumptions clearly.
  - 2.13. Several velocities, time, and length scales are useful in understanding what goes on inside engines. Make estimates of the following quantities for a 1.6-liter displacement four-cylinder spark-ignition engine, operating at wide-open throttle at 2500 rev/min.
    - (a) The mean piston speed and the maximum piston speed.
    - (b) The maximum charge velocity in the intake port (the port area is about 20 percent of the piston area).
    - (c) The time occupied by one engine operating cycle, the intake process, the compression process, the combustion process, the expansion process, and the exhaust process. (Note: The word *process* is used here not the word *stroke*.)
    - (d) The average velocity with which the flame travels across the combustion chamber.
    - (e) The length of the intake system (the intake port, the manifold runner, etc.) which is filled by one cylinder charge just before the intake valve opens and this charge enters the cylinder (i.e., how far back from the intake valve, in centimeters, one cylinder volume extends in the intake system).
    - (f) The length of exhaust system filled by one cylinder charge after it exits the cylinder (assume an average exhaust gas temperature of 425°C).

You will have to make several appropriate geometric assumptions. The calculations are straightforward, and only approximate answers are required.
  - 2.14. The values of mean effective pressure at rated speed, maximum mean piston speed, and maximum specific power (engine power/total piston area) are essentially independent of cylinder size for naturally aspirated engines of a given type. If we also assume that engine weight per unit displaced volume is essentially constant, how will the *specific weight* of an engine (engine weight/maximum rated power) at fixed total displaced volume vary with the number of cylinders? Assume the bore and stroke are equal.

## REFERENCES

1. Obert, E.F.: *Internal Combustion Engines and Air Pollution*, chap. 2, Intext Educational Publishers, New York, 1973.
2. SAE Standard: "Engine Test Code—Spark Ignition and Diesel," SAE J816b, SAE Handbook.
3. Bosch: *Automotive Handbook*, 2nd English edition, Robert Bosch GmbH, Stuttgart, 1986.
4. Taylor, C.F.: *The Internal Combustion Engine in Theory and Practice*, vol. II, MIT Press, Cambridge, Mass., 1968.

# CHAPTER

# 3

## THERMOCHEMISTRY OF FUEL-AIR MIXTURES

### 3.1 CHARACTERIZATION OF FLAMES

Combustion of the fuel-air mixture inside the engine cylinder is one of the processes that controls engine power, efficiency, and emissions. Some background in relevant combustion phenomena is therefore a necessary preliminary to understanding engine operation. These combustion phenomena are different for the two main types of engines—spark-ignition and diesel—which are the subject of this book. In spark-ignition engines, the fuel is normally mixed with air in the engine intake system. Following the compression of this fuel-air mixture, an electrical discharge initiates the combustion process; a flame develops from the “kernal” created by the spark discharge and propagates across the cylinder to the combustion chamber walls. At the walls, the flame is “quenched” or extinguished as heat transfer and destruction of active species at the wall become the dominant processes. An undesirable combustion phenomenon—the “spontaneous” ignition of a substantial mass of fuel-air mixture ahead of the flame, before the flame can propagate through this mixture (which is called the end-gas)—can also occur. This autoignition or self-explosion combustion phenomenon is the cause of spark-ignition engine knock which, due to the high pressures generated, can lead to engine damage.

In the diesel engine, the fuel is injected into the cylinder into air already at high pressure and temperature, near the end of the compression stroke. The autoignition, or self-ignition, of portions of the developing mixture of already

injected and vaporized fuel with this hot air starts the combustion process, which spreads rapidly. Burning then proceeds as fuel and air mix to the appropriate composition for combustion to take place. Thus, fuel-air mixing plays a controlling role in the diesel combustion process.

Chapters 3 and 4 focus on the thermochemistry of combustion: i.e., the composition and thermodynamic properties of the pre- and postcombustion working fluids in engines and the energy changes associated with the combustion processes that take place inside the engine cylinder. Later chapters (9 and 10) deal with the phenomenological aspects of engine combustion: i.e., the details of the physical and chemical processes by which the fuel-air mixture is converted to burned products. At this point it is useful to review briefly the key combustion phenomena which occur in engines to provide an appropriate background for the material which follows. More detailed information on these combustion phenomena can be found in texts on combustion such as those of Fristrom and Westenberg<sup>1</sup> and Glassman.<sup>2</sup>

The combustion process is a fast exothermic gas-phase reaction (where oxygen is usually one of the reactants). A flame is a combustion reaction which can propagate subsonically through space; motion of the flame relative to the unburned gas is the important feature. Flame structure does not depend on whether the flame moves relative to the observer or remains stationary as the gas moves through it. The existence of flame motion implies that the reaction is confined to a zone which is small in thickness compared to the dimensions of the apparatus—in our case the engine combustion chamber. The reaction zone is usually called the flame front. This flame characteristic of spatial propagation is the result of the strong coupling between chemical reaction, the transport processes of mass diffusion and heat conduction, and fluid flow. The generation of heat and active species accelerate the chemical reaction; the supply of fresh reactants, governed by the convection velocity, limits the reaction. When these processes are in balance, a steady-state flame results.<sup>1</sup>

Flames are usually classified according to the following overall characteristics. The first of these has to do with the composition of the reactants as they enter the reaction zone. If the fuel and oxidizer are essentially uniformly mixed together, the flame is designated as *premixed*. If the reactants are not premixed and must mix together in the same region where reaction takes place, the flame is called a *diffusion* flame because the mixing must be accomplished by a diffusion process. The second means of classification relates to the basic character of the gas flow through the reaction zone: whether it is *laminar* or *turbulent*. In laminar (or streamlined) flow, mixing and transport are done by molecular processes. Laminar flows only occur at low Reynolds number. The Reynolds number (density × velocity × lengthscale/viscosity) is the ratio of inertial to viscous forces. In turbulent flows, mixing and transport are enhanced (usually by a substantial factor) by the macroscopic relative motion of eddies or lumps of fluid which are the characteristic feature of a turbulent (high Reynolds number) flow. A third area of classification is whether the flame is *steady* or *unsteady*. The distinguishing feature here is whether the flame structure and motion change with

time. The final characterizing feature is the *initial phase* of the reactants—gas, liquid, or solid.

Flames in engines are unsteady, an obvious consequence of the internal combustion engine's operating cycle. Engine flames are turbulent. Only with substantial augmentation of laminar transport processes by the turbulent convection processes can mixing and burning rates and flame-propagation rates be made fast enough to complete the engine combustion process within the time available.

The conventional spark-ignition flame is thus a premixed unsteady turbulent flame, and the fuel-air mixture through which the flame propagates is in the gaseous state. The diesel engine combustion process is predominantly an unsteady turbulent diffusion flame, and the fuel is initially in the liquid phase. Both these flames are extremely complicated because they involve the coupling of the complex chemical mechanism, by which fuel and oxidizer react to form products, with the turbulent convective transport process. The diesel combustion process is even more complicated than the spark-ignition combustion process, because vaporization of liquid fuel and fuel-air mixing processes are involved too. Chapters 9 and 10 contain a more detailed discussion of the spark-ignition engine and diesel combustion processes, respectively. This chapter reviews the basic thermodynamic and chemical composition aspects of engine combustion.

### 3.2 IDEAL GAS MODEL

The gas species that make up the working fluids in internal combustion engines (e.g., oxygen, nitrogen, fuel vapor, carbon dioxide, water vapor, etc.) can usually be treated as ideal gases. The relationships between the thermodynamic properties of an ideal gas and of ideal gas mixtures are reviewed in App. B. There can be found the various forms of the ideal gas law:

$$pV = mRT = m \frac{\tilde{R}}{M} T = n\tilde{R}T \quad (3.1)$$

where  $p$  is the pressure,  $V$  the volume,  $m$  the mass of gas,  $R$  the gas constant for the gas,  $T$  the temperature,  $\tilde{R}$  the universal gas constant,  $M$  the molecular weight, and  $n$  the number of moles. Relations for evaluating the specific internal energy  $u$ , enthalpy  $h$ , and entropy  $s$ , specific heats at constant volume  $c_v$ , and constant pressure  $c_p$ , on a per unit mass basis and on a per mole basis (where the notation  $\tilde{u}$ ,  $\tilde{h}$ ,  $\tilde{s}$ ,  $\tilde{c}_v$ , and  $\tilde{c}_p$  is used) of an ideal gas, are developed. Also given are equations for calculating the thermodynamic properties of mixtures of ideal gases.

### 3.3 COMPOSITION OF AIR AND FUELS

Normally in engines, fuels are burned with air. Dry air is a mixture of gases that has a representative composition by volume of 20.95 percent oxygen, 78.09 percent nitrogen, 0.93 percent argon, and trace amounts of carbon dioxide, neon, helium, methane, and other gases. Table 3.1 shows the relative proportions of the major constituents of dry air.<sup>3</sup>

TABLE 3.1  
Principle constituents of dry air

Gas	ppm by volume	Molecular weight	Mole fraction	Molar ratio
O <sub>2</sub>	209,500	31.998	0.2095	1
N <sub>2</sub>	780,900	28.012	0.7905	3.773
Ar	9,300	39.948		
CO <sub>2</sub>	300	44.009		
Air	1,000,000	28.962	1.0000	4.773

In combustion, oxygen is the reactive component of air. It is usually sufficiently accurate to regard air as consisting of 21 percent oxygen and 79 percent inert gases taken as nitrogen (often called atmospheric or apparent nitrogen). For each mole of oxygen in air there are

$$\frac{1 - 0.2095}{0.2095} = 3.773$$

moles of atmospheric nitrogen. The molecular weight of air is obtained from Table 3.1 with Eq. (B.17) as 28.962, usually approximated by 29. Because atmospheric nitrogen contains traces of other species, its molecular weight is slightly different from that of pure molecular nitrogen, i.e.,

$$M_{\text{aN}_2} = \frac{28.962 - 0.2095 \times 31.998}{1 - 0.2095} = 28.16$$

In the following sections, *nitrogen* will refer to atmospheric nitrogen and a molecular weight of 28.16 will be used. An air composition of 3.773 moles of nitrogen per mole of oxygen will be assumed.

The density of dry air can be obtained from Eq. (3.1) with  $R = 8314.3 \text{ J}/\text{kmol} \cdot \text{K}$  and  $M = 28.962$ :

$$\rho(\text{kg/m}^3) = \frac{3.483 \times 10^{-3} p(\text{Pa})}{T(\text{K})} \quad (3.2a)$$

$$\text{or} \quad \rho(\text{lbm/ft}^3) = \frac{2.699 p(\text{lbf/in}^2)}{T(\text{°R})} \quad (3.2b)$$

Thus, the value for the density of dry air at 1 atmosphere ( $1.0133 \times 10^5 \text{ Pa}$ ,  $14.696 \text{ lbf/in}^2$ ) and  $25^\circ\text{C}$  ( $77^\circ\text{F}$ ) is  $1.184 \text{ kg/m}^3$  ( $0.0739 \text{ lbm/ft}^3$ ).

Actual air normally contains water vapor, the amount depending on temperature and degree of saturation. Typically the proportion by mass is about 1 percent, though it can rise to about 4 percent under extreme conditions. The *relative humidity* compares the water vapor content of air with that required to saturate. It is defined as:

The ratio of the partial pressure of water vapor actually present to the saturation pressure at the same temperature.

Water vapor content is measured with a wet- and dry-bulb psychrometer. This consists of two thermometers exposed to a stream of moist air. The dry-bulb temperature is the temperature of the air. The bulb of the other thermometer is wetted by a wick in contact with a water reservoir. The wet-bulb temperature is lower than the dry-bulb temperature due to evaporation of water from the wick. It is a good approximation to assume that the wet-bulb temperature is the adiabatic saturation temperature. Water vapor pressure can be obtained from observed wet- and dry-bulb temperatures and a psychrometric chart such as Fig. 3-1.<sup>4</sup> The effect of humidity on the properties of air is given in Fig. 3-2.<sup>5</sup>

The fuels most commonly used in internal combustion engines (gasoline or petrol, and diesel fuels) are blends of many different hydrocarbon compounds obtained by refining petroleum or crude oil. These fuels are predominantly carbon and hydrogen (typically about 86 percent carbon and 14 percent hydrogen by weight) though diesel fuels can contain up to about 1 percent sulfur. Other fuels of interest are alcohols (which contain oxygen), gaseous fuels (natural gas and liquid petroleum gas), and single hydrocarbon compounds (e.g., methane, propane, isoctane) which are often used in engine research. Properties of the more common internal combustion engine fuels are summarized in App. D.

Some knowledge of the different classes of organic compounds and their

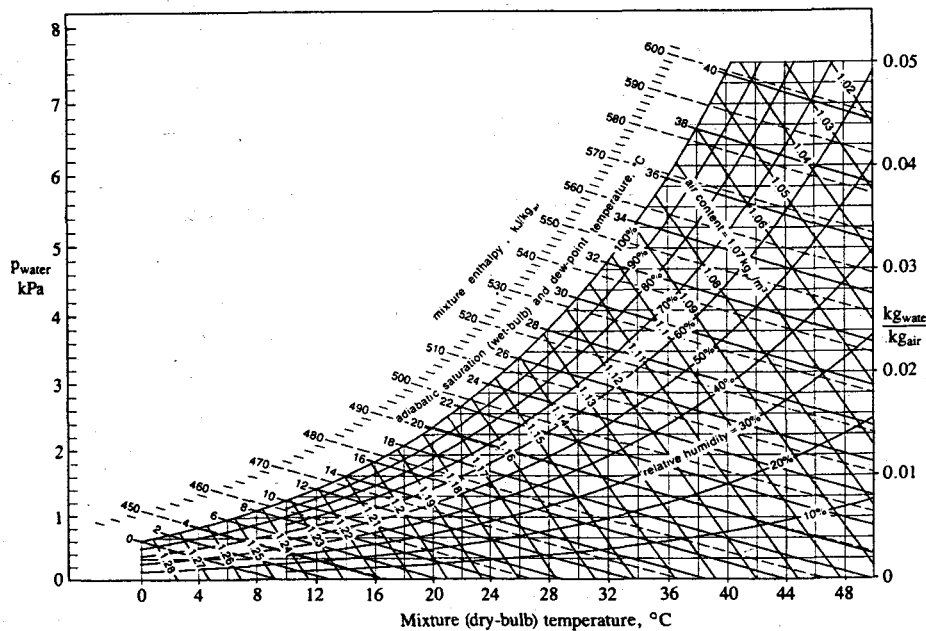


FIGURE 3-1  
Psychrometric chart for air-water mixtures at 1 atmosphere. (From Reynolds.<sup>4</sup>)

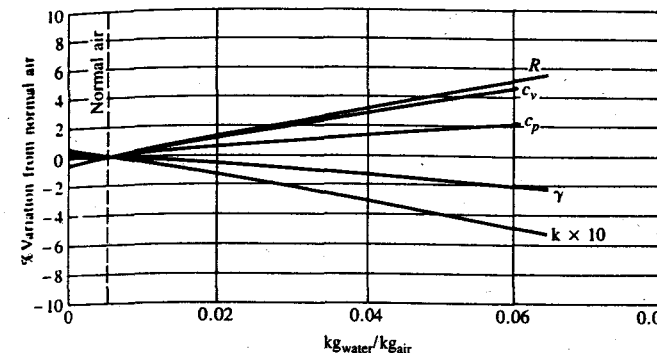


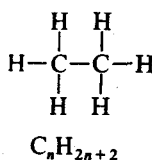
FIGURE 3-2

Effect of humidity on properties of air:  $R$  is the gas constant;  $c_v$  and  $c_p$  are specific heats at constant volume and pressure, respectively;  $\gamma = c_p/c_v$ ;  $k$  is the thermal conductivity. (From Taylor.<sup>5</sup>)

molecular structure is necessary in order to understand combustion mechanisms.<sup>6</sup> The different classes are as follows:

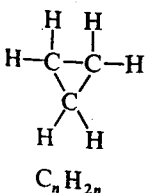
### Alkyl Compounds

#### Paraffins (alkanes)

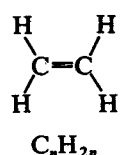


Single-bonded open-chain saturated hydrocarbon molecules: i.e., no more hydrogen can be added. For the larger molecules straight-chain and branched-chain configurations exist. These are called normal (*n*-) and iso compounds, respectively. Examples:  $\text{CH}_4$ , methane;  $\text{C}_2\text{H}_6$ , ethane;  $\text{C}_3\text{H}_8$ , propane;  $\text{C}_8\text{H}_{18}$ , *n*-octane and isoctane. There are several "isoctanes," depending on the relative position of the branches. By isoctane is usually meant 2,2,4-trimethylpentane, indicating five carbon atoms in the straight chain (pentane) with three methyl ( $\text{CH}_3$ ) branches located respectively at C-atoms 2, 2, and 4. Radicals deficient in one hydrogen take the name methyl, ethyl, propyl, etc.

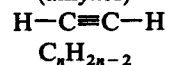
#### Cycloparaffins or napthenes (cyclanes)



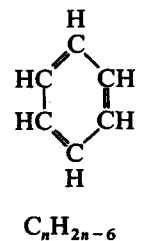
Single bond (no double bond) ring hydrocarbons. Unsaturated, since ring can be broken and additional hydrogen added. Examples:  $\text{C}_3\text{H}_6$ , cyclopropane (three C-atom ring);  $\text{C}_4\text{H}_8$ , cyclobutane (four C-atom ring);  $\text{C}_5\text{H}_{10}$ , cyclopentane (five C-atom ring).

**Olefins  
(alkenes)**

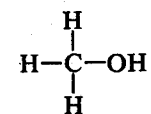
Open-chain hydrocarbons containing a double bond; hence they are unsaturated. Examples are:  $\text{C}_2\text{H}_4$ , ethene (or ethylene);  $\text{C}_3\text{H}_6$ , propene (or propylene);  $\text{C}_4\text{H}_8$ , butene (or butylene); . . . From butene upwards several structural isomers are possible depending on the location of the double bond in the basic carbon chain. Straight- and branched-chain structures exist. Diolefins contain two double bonds.

**Acetylenes  
(alkynes)**

Open-chain unsaturated hydrocarbons containing one carbon-carbon triple bond. First member is acetylene,  $\text{H}-\text{C}\equiv\text{C}-\text{H}$ . Additional members of the alkyne series comprise open-chain molecules, similar to higher alkenes but with each double bond replaced by a triple bond.

**Aromatics**

Building block for aromatic hydrocarbons is the benzene ( $\text{C}_6\text{H}_6$ ) ring structure shown. This ring structure is very stable and accommodates additional  $-\text{CH}_2$  groups in side chains and not by ring expansion. Examples:  $\text{C}_7\text{H}_8$ , toluene;  $\text{C}_8\text{H}_{10}$ , xylene (several structural arrangements); . . . More complex aromatic hydrocarbons incorporate ethyl, propyl, and heavier alkyl side chains in a variety of structural arrangements.

**Alcohols****Monohydric  
alcohols**

In these organic compounds, one hydroxyl ( $-\text{OH}$ ) group is substituted for one hydrogen atom. Thus methane becomes methyl alcohol,  $\text{CH}_3\text{OH}$  (also called methanol); ethane becomes ethyl alcohol,  $\text{C}_2\text{H}_5\text{OH}$  (ethanol); etc.

**3.4 COMBUSTION STOICHIOMETRY**

This section develops relations between the composition of the reactants (fuel and air) of a combustible mixture and the composition of the products. Since these relations depend only on the conservation of mass of each chemical element in the reactants, only the relative elemental composition of the fuel and the relative proportions of fuel and air are needed.

If sufficient oxygen is available, a hydrocarbon fuel can be completely oxidized. The carbon in the fuel is then converted to carbon dioxide  $\text{CO}_2$  and the hydrogen to water  $\text{H}_2\text{O}$ . For example, consider the overall chemical equation for the complete combustion of one mole of propane  $\text{C}_3\text{H}_8$ :

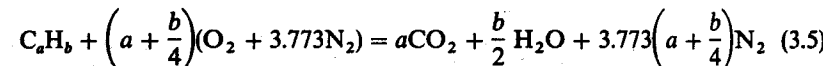


A carbon balance between the reactants and products gives  $b = 3$ . A hydrogen balance gives  $2c = 8$ , or  $c = 4$ . An oxygen balance gives  $2b + c = 10 = 2a$ , or  $a = 5$ . Thus Eq. (3.3) becomes



Note that Eq. (3.4) only relates the elemental composition of the reactant and product species; it does not indicate the process by which combustion proceeds, which is much more complex.

Air contains nitrogen, but when the products are at low temperatures the nitrogen is not significantly affected by the reaction. Consider the complete combustion of a general hydrocarbon fuel of average molecular composition  $\text{C}_a\text{H}_b$  with air. The overall complete combustion equation is



Note that only the *ratios* of the numbers in front of the symbol for each chemical species are defined by Eq. (3.5); i.e., only the relative proportions on a molar basis are obtained. Thus the fuel composition could have been written  $\text{CH}_y$ , where  $y = b/a$ .

Equation (3.5) defines the *stoichiometric* (or chemically correct or theoretical) proportions of fuel and air; i.e., there is just enough oxygen for conversion of all the fuel into completely oxidized products. The stoichiometric air/fuel or fuel/air ratios (see Sec. 2.9) depend on fuel composition. From Eq. (3.5):

$$\begin{aligned} \left(\frac{A}{F}\right)_s &= \left(\frac{F}{A}\right)_s^{-1} = \frac{(1 + y/4)(32 + 3.773 \times 28.16)}{12.011 + 1.008y} \\ &= \frac{34.56(4 + y)}{12.011 + 1.008y} \end{aligned} \quad (3.6)$$

The molecular weights of oxygen, atmospheric nitrogen, atomic carbon, and atomic hydrogen are, respectively, 32, 28.16, 12.011, and 1.008.  $(A/F)_s$  depends only on  $y$ ; Fig. 3-3 shows the variation in  $(A/F)_s$  as  $y$  varies from 1 (e.g., benzene) to 4 (methane).

**Example 3.1.** A hydrocarbon fuel of composition 84.1 percent by mass C and 15.9 percent by mass H has a molecular weight of 114.15. Determine the number of moles of air required for stoichiometric combustion and the number of moles of products produced per mole of fuel. Calculate  $(A/F)_s$ ,  $(F/A)_s$ , and the molecular weights of the reactants and the products.

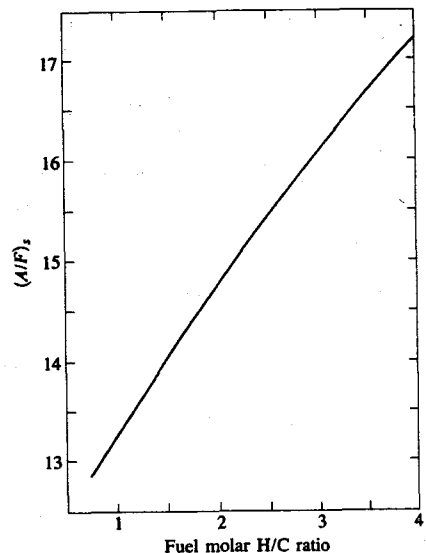


FIGURE 3-3  
Stoichiometric air/fuel ratio for air-hydrocarbon fuel mixtures as a function of fuel molar H/C ratio.

Assume a fuel composition  $C_aH_b$ . The molecular weight relation gives

$$114.15 = 12.011a + 1.008b$$

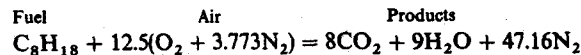
The gravimetric analysis of the fuel gives

$$\frac{b}{a} = \frac{15.9/1.008}{84.1/12.011} = 2.25$$

Thus

$$a = 8 \quad b = 18\ddagger$$

The fuel is octane  $C_8H_{18}$ . Equation (3.5) then becomes



In moles:

$$\begin{array}{rcl} 1 & + 12.5(1 + 3.773) & = 8 + 9 + 47.16 \\ 1 & + 59.66 & = 64.16 \end{array}$$

Relative mass:

$$\begin{array}{rcl} 114.15 + 59.66 \times 28.96 & = 8 \times 44.01 + 9 \times 18.02 + 47.16 \times 28.16 \\ 114.5 + 1727.8 & = 1842.3 \end{array}$$

Per unit mass fuel:

$$1 + 15.14 = 16.14$$

Thus for stoichiometric combustion, 1 mole of fuel requires 59.66 moles of air and produces 64.16 moles of products. The stoichiometric  $(A/F)_s$  is 15.14 and  $(F/A)_s$  is 0.0661.

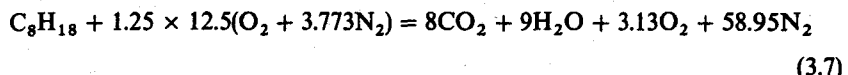
The molecular weights of the reactants  $M_R$  and products  $M_P$  are

$$M_R = \frac{1}{n} \sum n_i M_i = \frac{1}{60.66} (1 \times 114.15 + 59.66 \times 28.96)$$

$$M_P = \frac{1}{n} \sum n_i M_i = \frac{1}{64.16} (8 \times 44.01 + 9 \times 18.02 + 47.16 \times 28.16)$$

$$\text{or} \quad M_R = 30.36 \quad M_P = 28.71$$

Fuel-air mixtures with more than or less than the stoichiometric air requirement can be burned. With excess air or fuel-lean combustion, the extra air appears in the products in unchanged form. For example, the combustion of isoctane with 25 percent excess air, or 1.25 times the stoichiometric air requirement, gives



With less than the stoichiometric air requirement, i.e., with fuel-rich combustion, there is insufficient oxygen to oxidize fully the fuel C and H to  $CO_2$  and  $H_2O$ . The products are a mixture of  $CO_2$  and  $H_2O$  with carbon monoxide CO and hydrogen  $H_2$  (as well as  $N_2$ ). The product composition cannot be determined from an element balance alone and an additional assumption about the chemical composition of the product species must be made (see Secs. 4.2 and 4.9.2).

Because the composition of the combustion products is significantly different for fuel-lean and fuel-rich mixtures, and because the stoichiometric fuel/air ratio depends on fuel composition, the ratio of the actual fuel/air ratio to the stoichiometric ratio (or its inverse) is a more informative parameter for defining mixture composition. The *fuel/air equivalence ratio*  $\phi$ ,

$$\phi = \frac{(F/A)_{\text{actual}}}{(F/A)_s} \quad (3.8)$$

will be used throughout this text for this purpose. The inverse of  $\phi$ , the *relative air/fuel ratio*  $\lambda$ ,

$$\lambda = \phi^{-1} = \frac{(A/F)_{\text{actual}}}{(A/F)_s} \quad (3.9)$$

is also sometimes used.

† Note that for fuels which are mixtures of hydrocarbons,  $a$  and  $b$  need not be integers.

For fuel-lean mixtures:  $\phi < 1, \lambda > 1$

For stoichiometric mixtures:  $\phi = \lambda = 1$

For fuel-rich mixtures:  $\phi > 1, \lambda < 1$

When the fuel contains oxygen (e.g., with alcohols), the procedure for determining the overall combustion equation is the same except that fuel oxygen is included in the oxygen balance between reactants and products. For methyl alcohol (methanol),  $\text{CH}_3\text{OH}$ , the stoichiometric combustion equation is



and  $(A/F)_s = 6.47$ . For ethyl alcohol (ethanol),  $\text{C}_2\text{H}_5\text{OH}$ , the stoichiometric combustion equation is



and  $(A/F)_s = 9.00$ .

If there are significant amounts of sulfur in the fuel, the appropriate oxidation product for determining the stoichiometric air and fuel proportions is sulfur dioxide,  $\text{SO}_2$ .

For hydrogen fuel, the stoichiometric equation is



and the stoichiometric ( $A/F$ ) ratio is 34.3.

Note that the composition of the products of combustion in Eqs. (3.7) and (3.10) to (3.12) may not occur in practice. At normal combustion temperatures significant dissociation of  $\text{CO}_2$  and of  $\text{H}_2\text{O}$  occurs (see Sec. 3.7.1). Whether, at low temperatures, recombination brings the product composition to that indicated by these overall chemical equations depends on the rate of cooling of the product gases. More general relationships for the composition of unburned and burned gas mixtures are developed in Chap. 4.

The stoichiometric ( $A/F$ ) and ( $F/A$ ) ratios of common fuels and representative single hydrocarbon and other compounds are given in App. D along with other fuel data.

### 3.5 THE FIRST LAW OF THERMODYNAMICS AND COMBUSTION†

#### 3.5.1 Energy and Enthalpy Balances

In a combustion process, fuel and oxidizer react to produce products of different composition. The actual path by which this transformation takes place is understood only for simple fuels such as hydrogen and methane. For fuels with more complicated structure, the details are not well defined. Nonetheless, the first law

of thermodynamics can be used to relate the end states of mixtures undergoing a combustion process; its application does not require that the details of the process be known.

The first law of thermodynamics relates changes in internal energy (or enthalpy) to heat and work transfer interactions. In applying the first law to a system whose chemical composition changes, care must be exercised in relating the reference states at which zero internal energy or enthalpy for each species or groups of species are assigned. We are not free, when chemical reactions occur, to choose independently the zero internal energy or enthalpy reference states of chemical substances transformed into each other by reaction.

Consider a system of mass  $m$  which changes its composition from reactants to products by chemical reaction as indicated in Fig. 3-4. Applying the first law to the system between its initial and final states gives

$$Q_{R-P} - W_{R-P} = U_P - U_R \quad (3.13)$$

Heat transfer  $Q_{R-P}$  and work transfer  $W_{R-P}$  due to normal force displacements may occur across the system boundary. The standard thermodynamic sign convention for each energy transfer interaction—positive for heat transfer to the system and positive for work transfer from the system—is used.

We will consider a series of special processes: first, a *constant volume* process where the initial and final temperatures are the same,  $T'$ . Then Eq. (3.13) becomes

$$Q_{R-P} = U'_P - U'_R = (\Delta U)_{V, T'} \quad (3.14)$$

The internal energy of the system has changed by an amount  $(\Delta U)_{V, T'}$  which can be measured or calculated. Combustion processes are exothermic [i.e.,  $Q_{R-P}$  and  $(\Delta U)_{V, T'}$  are negative]; therefore the system's internal energy decreases. If Eq. (3.14) is expressed per mole of fuel, then  $(\Delta U)_{V, T'}$  is known as the increase in

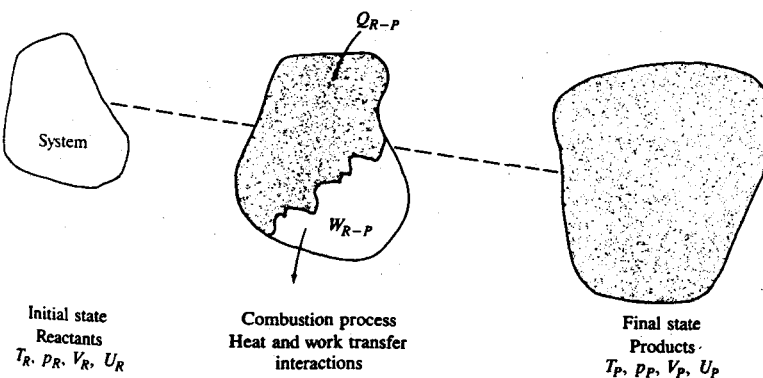
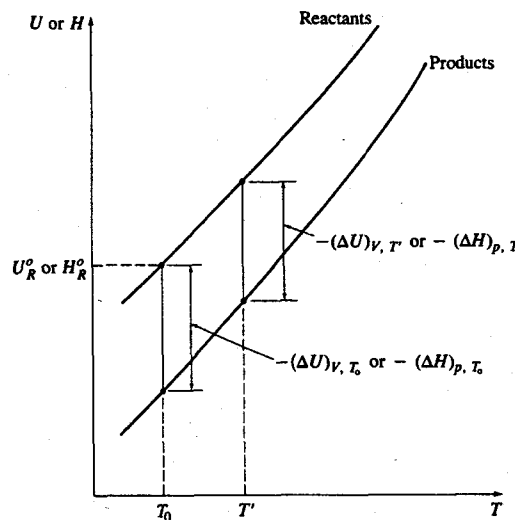


FIGURE 3-4  
System changing from reactants to products for first law analysis.

† The approach used here follows that developed by Spalding and Cole.<sup>7</sup>



**FIGURE 3-5**  
Schematic plot of internal energy ( $U$ ) or enthalpy ( $H$ ) of reactants and products as a function of temperature.

internal energy at constant volume, and  $-(\Delta U)_{V, T'}$  is known as the *heat of reaction at constant volume* at temperature  $T'$ .

Next, consider a *constant pressure* process where the initial and final temperatures are the same,  $T'$ . For a constant pressure process

$$W_{R-P} = \int_R^P p \, dV = p(V_P - V_R) \quad (3.15)$$

so Eq. (3.13) becomes

$$\begin{aligned} Q_{R-P} - p(V_P - V_R) &= U'_P - U'_R \\ \text{or } Q_{R-P} &= (U'_P + pV'_P) - (U'_R + pV'_R) \\ &= H'_P - H'_R = (\Delta H)_{P, T'} \end{aligned} \quad (3.16)$$

The enthalpy of the system has changed by an amount  $(\Delta H)_{P, T'}$ , which can be measured or calculated. Again for combustion reactions,  $(\Delta H)_{P, T'}$  is a negative quantity. If Eq. (3.16) is written per mole of fuel,  $(\Delta H)_{P, T'}$  is called the increase in enthalpy at constant pressure and  $-(\Delta H)_{P, T'}$  is called the *heat of reaction at constant pressure* at  $T'$ .

These processes can be displayed, respectively, on the internal energy or enthalpy versus temperature plot shown schematically in Fig. 3-5. If  $U$  (or  $H$ ) for the reactants is arbitrarily assigned a value  $U_R^o$  (or  $H_R^o$ ) at some reference temperature  $T_0$ , then the value of  $(\Delta U)_{V, T_0}$  [or  $(\Delta H)_{P, T_0}$ ] fixes the relationship between  $U(T)$  or  $H(T)$ , respectively, for the products and the reactants. Note that the slope of these lines (the specific heat at constant volume or pressure if the diagram is expressed per unit mass or per mole) increases with increasing tem-

perature; also, the magnitude of  $(\Delta U)_{V, T'}$  [or  $(\Delta H)_{P, T'}$ ] decreases with increasing temperature because  $c_v$  (or  $c_p$ ) for the products is greater than for the reactants.

The difference between  $(\Delta H)_{P, T'}$  and  $(\Delta U)_{V, T'}$  is

$$(\Delta H)_{P, T'} - (\Delta U)_{V, T'} = p(V_P - V_R) \quad (3.17)$$

Only if the volumes of the products and reactants in the constant pressure process are the same are  $(\Delta H)_{P, T'}$  and  $(\Delta U)_{V, T'}$  equal. If all the reactant and product species are ideal gases, then the ideal gas law Eq. (3.1) gives

$$(\Delta H)_{P, T'} - (\Delta U)_{V, T'} = \tilde{R}(n'_P - n'_R)T' \quad (3.18)$$

Note that any inert gases do not contribute to  $(n'_P - n'_R)$ .

With a hydrocarbon fuel, one of the products,  $\text{H}_2\text{O}$ , can be in the gaseous or liquid phase. The internal energy (or enthalpy) of the products in the constant volume (or constant pressure) processes described above in Fig. 3-5 will depend on the relative proportions of the water in the gaseous and liquid phases. The limiting cases of all vapor and all liquid are shown in Fig. 3-6a for a  $U-T$  plot. The internal energy differences between the curves is

$$|(\Delta U)_{V, T', \text{H}_2\text{O liq}}| - |(\Delta U)_{V, T', \text{H}_2\text{O vap}}| = m_{\text{H}_2\text{O}} u'_{fg, \text{H}_2\text{O}} \quad (3.19)$$

where  $m_{\text{H}_2\text{O}}$  is the mass of water in the products and  $u'_{fg, \text{H}_2\text{O}}$  is the internal energy of vaporization of water at the temperature and pressure of the products. Similar

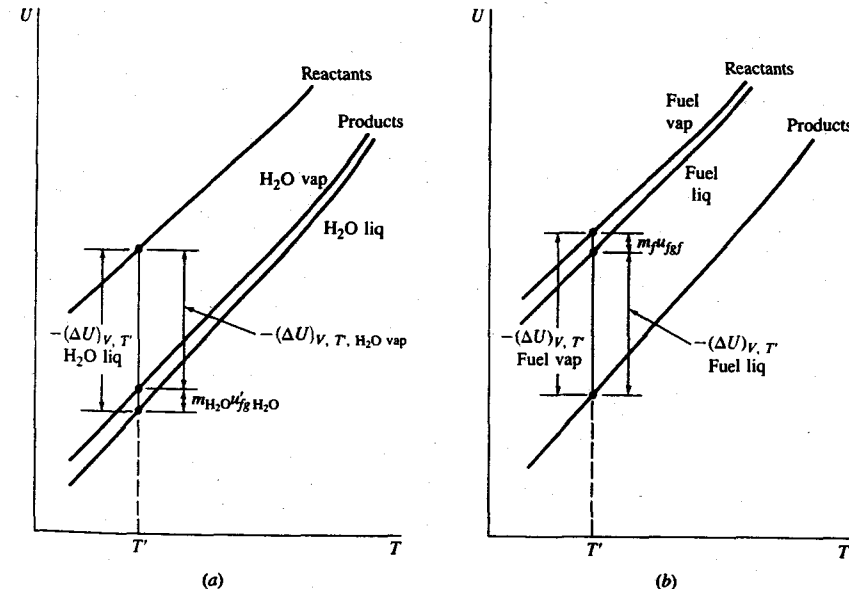


**FIGURE 3-6**  
Schematic plots of internal energy of reactants and products as a function of temperature. (a) Effect of water in products as either vapor or liquid. (b) Effect of fuel in reactants as either vapor or liquid.

curves and relationships apply for enthalpy:

$$|(\Delta H)_{p, T', \text{H}_2\text{O liq}}| - |(\Delta H)_{p, T', \text{H}_2\text{O vap}}| = m_{\text{H}_2\text{O}} h'_{fg} \text{H}_2\text{O} \quad (3.20)$$

For some fuels, the reactants may contain the fuel as either liquid or vapor. The *U-T* (or *H-T*) line for the reactants with the fuel as liquid or as vapor will be different, as indicated in Fig. 3-6b. The vertical distance between the two reactant curves is  $m_f u_{fg}$  (or  $m_f h_{fg}$ ) where the subscript *f* denotes fuel.

### 3.5.2 Enthalpies of Formation

For fuels which are single hydrocarbon compounds, or where the precise fuel composition is known, the internal energies or enthalpies of the reactants and the products can be related through the enthalpies of formation of the reactants and products.

The *enthalpy of formation*  $\tilde{\Delta}h_f^\circ$  of a chemical compound is the enthalpy increase associated with the reaction of forming one mole of the given compound from its elements, with each substance in its thermodynamic standard state at the given temperature.

The *standard state* is the state at one atmosphere pressure and the temperature under consideration. We will denote the standard state by the superscript  $^\circ$ .

Since thermodynamic calculations are made as a difference between an initial and a final state, it is necessary to select a *datum state* to which all other thermodynamic states can be referred. While a number of datum states have been used in the literature, the most common datum is 298.15 K (25°C) and 1 atmosphere. We will use this datum throughout this text. Elements at their *reference state* are arbitrarily assigned zero enthalpy at the datum temperature. The reference state of each element is its stable standard state; e.g., for oxygen at 298.15 K, the reference state is  $\text{O}_2$  gas.

Enthalpies of formation are tabulated as a function of temperature for all commonly occurring species. For inorganic compounds, the *JANAF Thermochemical Tables* are the primary reference source.<sup>8</sup> These tables include values of the molar specific heat at constant pressure, standard entropy, standard Gibbs free energy (called free energy in the tables), standard enthalpy, enthalpy of formation and Gibbs free energy of formation, and  $\log_{10}$  equilibrium constant for the formation of each species from its elements. Some primary references for thermodynamic data on fuel compounds are Maxwell,<sup>9</sup> Rossini *et al.*,<sup>10</sup> and Stull *et al.*<sup>11</sup> Enthalpies of formation of species relevant to hydrocarbon fuel combustion are tabulated in Table 3.2. Selected values of thermodynamic properties of relevant species are tabulated in App. D.

For a given combustion reaction, the enthalpy of the products at the standard state relative to the enthalpy datum is then given by

$$H_p^\circ = \sum_{\text{products}} n_i \tilde{\Delta}h_f^\circ \quad (3.21a)$$

TABLE 3.2  
Standard enthalpies of formation

Species	State†	$\tilde{\Delta}h_f^\circ$ , MJ/kmol
$\text{O}_2$	Gas	0
$\text{N}_2$	Gas	0
$\text{H}_2$	Gas	0
C	Gas	0
$\text{CO}_2$	Gas	-393.52
$\text{H}_2\text{O}$	Gas	-241.83
$\text{H}_2\text{O}$	Liquid	-285.84
CO	Gas	-110.54
$\text{CH}_4$	Gas	-74.87
$\text{C}_3\text{H}_8$	Gas	-103.85
$\text{CH}_3\text{OH}$	Gas	-201.17
$\text{CH}_3\text{OH}$	Liquid	-238.58
$\text{C}_8\text{H}_{18}$	Gas	-208.45
$\text{C}_8\text{H}_{18}$	Liquid	-249.35

† At 298.15 K (25°C) and 1 atm.

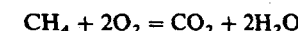
and the enthalpy of the reactants is given by

$$H_R^\circ = \sum_{\text{reactants}} n_i \tilde{\Delta}h_f^\circ \quad (3.21b)$$

The enthalpy increase,  $(\Delta H)_{p, T_0}$ , is then obtained from the difference  $(H_p^\circ - H_R^\circ)$ . The internal energy increase can be obtained with Eq. (3.17).

**Example 3.2.** Calculate the enthalpy of the products and reactants, and the enthalpy increase and internal energy increase of the reaction, of a stoichiometric mixture of methane and oxygen at 298.15 K.

The stoichiometric reaction is



Thus, for  $\text{H}_2\text{O}$  gas, from Table 3.2 and Eq. (3.21a, b):

$$H_p^\circ = -393.52 + 2(-241.83) = -877.18 \text{ MJ/kmol CH}_4$$

For  $\text{H}_2\text{O}$  liquid:

$$H_p^\circ = -393.52 + 2(-285.84) = -965.20 \text{ MJ/kmol CH}_4$$

$$H_R^\circ = -74.87 \text{ MJ/kmol CH}_4$$

Hence for  $\text{H}_2\text{O}$  gas:

$$(\Delta H)_p^\circ = -877.18 + 74.87 = -802.31 \text{ MJ/kmol CH}_4$$

and for  $\text{H}_2\text{O}$  liquid:

$$(\Delta H)_p^\circ = -965.20 + 74.87 = -890.33 \text{ MJ/kmol CH}_4$$

Use Eq. (3.18) to find  $(\Delta U)_v^\circ$ . With  $\text{H}_2\text{O}$  gas, the number of moles of reactants and products are equal, so

$$(\Delta U)_v^\circ = (\Delta H)_p^\circ = -802.3 \text{ MJ/kmol CH}_4$$

For  $\text{H}_2\text{O}$  liquid:

$$(\Delta U)_v^\circ = -890.33 - 8.3143 \times 10^{-3}(1 - 3)298.15 \text{ MJ/kmol CH}_4$$

$$(\Delta U)_v^\circ = -885.4 \text{ MJ/kmol CH}_4$$

Note that the presence of nitrogen in the mixture or oxygen in excess of the stoichiometric amount would not change any of these calculations.

### 3.5.3 Heating Values

For fuels where the precise fuel composition is not known, the enthalpy of the reactants cannot be determined from the enthalpies of formation of the reactant species. The *heating value* of the fuel is then measured directly.

The heating value  $Q_{\text{HV}}$  or calorific value of a fuel is the magnitude of the heat of reaction at constant pressure or at constant volume at a standard temperature [usually 25°C (77°F)] for the complete combustion of unit mass of fuel. Thus

$$Q_{\text{HV}, p} = -(\Delta H)_{p, T_0} \quad (3.22a)$$

and

$$Q_{\text{HV}, v} = -(\Delta U)_{v, T_0} \quad (3.22b)$$

Complete combustion means that all carbon is converted to  $\text{CO}_2$ , all hydrogen is converted to  $\text{H}_2\text{O}$ , and any sulfur present is converted to  $\text{SO}_2$ . The heating value is usually expressed in joules per kilogram or joules per kilomole of fuel (British thermal units per pound-mass or British thermal units per pound-mole). It is therefore unnecessary to specify how much oxidant was mixed with the fuel, though this must exceed the stoichiometric requirement. It is immaterial whether the oxidant is air or oxygen.

For fuels containing hydrogen, we have shown that whether the  $\text{H}_2\text{O}$  in the products is in the liquid or gaseous phase affects the value of the heat of reaction. The term *higher heating value*  $Q_{\text{HHV}}$  (or gross heating value) is used when the  $\text{H}_2\text{O}$  formed is all condensed to the liquid phase; the term *lower heating value*  $Q_{\text{LHV}}$  (or net heating value) is used when the  $\text{H}_2\text{O}$  formed is all in the vapor phase. The two heating values at constant pressure are related by

$$Q_{\text{HHV}, p} = Q_{\text{LHV}, p} + \left( \frac{m_{\text{H}_2\text{O}}}{m_f} \right) h_{fg, \text{H}_2\text{O}} \quad (3.23)$$

where  $(m_{\text{H}_2\text{O}}/m_f)$  is the ratio of mass of  $\text{H}_2\text{O}$  produced to mass of fuel burned. A similar expression with  $u_{fg, \text{H}_2\text{O}}$  replacing  $h_{fg, \text{H}_2\text{O}}$  applies for the higher and lower heating value at constant volume.

The heating value at constant pressure is the more commonly used; often the qualification "at constant pressure" is omitted. The difference between the heating values at constant pressure and constant volume is small.

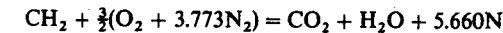
Heating values of fuels are measured in calorimeters. For gaseous fuels, it is most convenient and accurate to use a continuous-flow atmosphere pressure calorimeter. The entering fuel is saturated with water vapor and mixed with sufficient saturated air for complete combustion at the reference temperature. The mixture is burned in a burner and the combustion products cooled with water-cooled metal tube coils to close to the inlet temperature. The heat transferred to the cooling water is calculated from the measured water flow rate and water temperature rise. The heating value determined by this process is the higher heating value at constant pressure.

For liquid and solid fuels, it is more satisfactory to burn the fuel with oxygen under pressure at constant volume in a bomb calorimeter. A sample of the fuel is placed in the bomb calorimeter, which is a stainless-steel container immersed in cooling water at the standard temperature. Sufficient water is placed in the bomb to ensure that the water produced in the combustion process will condense. Oxygen at 30 atmospheres is admitted to the bomb. A length of firing cotton is suspended into the sample from an electrically heated wire filament to act as a source of ignition. When combustion is complete the temperature rise of the bomb and cooling water is measured. The heating value determined by this process is the higher heating value at constant volume.

The heating values of common fuels are tabulated with other fuel data in App. D. The following example illustrates how the enthalpy of a reactant mixture relative to the enthalpy datum we have defined can be determined from the measured heating value of the fuel.

**Example 3.3.** Liquid kerosene fuel of the lower heating value (determined in a bomb calorimeter) of 43.2 MJ/kg and average molar H/C ratio of 2 is mixed with the stoichiometric air requirement at 298.15 K. Calculate the enthalpy of the reactant mixture relative to the datum of zero enthalpy for C,  $\text{O}_2$ ,  $\text{N}_2$ , and  $\text{H}_2$  at 298.15 K.

The combustion equation per mole of C can be written



$$\text{or} \quad \begin{array}{c} 7.160 \text{ kmol} \\ \text{14 kg fuel} \end{array} + \begin{array}{c} 7.66 \text{ kmol} \\ \text{air} \end{array} \rightarrow \begin{array}{c} 221.4 \text{ kg} \\ \text{products} \end{array}$$

where  $M = 28.962$  for atmospheric air.

The heating value given is at constant volume,  $-(\Delta U)_v^\circ$ .  $(\Delta H)_p^\circ$  is obtained from Eq. (3.18), noting that the fuel is in the liquid phase:

$$\begin{aligned} (\Delta H)_p^\circ &= -43.2 + 8.3143 \times 10^{-3} (7.66 - 7.160) \times \frac{298.15}{14} \\ &= -43.2 + 0.09 = -43.1 \text{ MJ/kg fuel} \end{aligned}$$

<sup>†</sup> Standard methods for measuring heating values are defined by the American Society for Testing Materials.

The enthalpy of the products per kilogram of mixture is found from the enthalpies of formation (with H<sub>2</sub>O vapor):

$$h_p = \frac{1(-393.52) + 1(-241.83)}{221.4} \\ = 2.87 \text{ MJ/kg}$$

The enthalpy of the reactants per kilogram of mixture is then

$$h_r = h_p - (\Delta h)_p^{\circ} = 2.87 + \frac{43.1 \times 14}{221.4} = 5.59 \text{ MJ/kg}$$

### 3.5.4 Adiabatic Combustion Processes

We now use the relationships developed above to examine two other special processes important in engine analysis: constant-volume and constant-pressure adiabatic combustion. For an adiabatic constant-volume process, Eq. (3.13) becomes

$$U_p - U_r = 0 \quad (3.24)$$

when  $U_p$  and  $U_r$  are evaluated relative to the same datum (e.g., the enthalpies of C, O<sub>2</sub>, N<sub>2</sub>, and H<sub>2</sub> are zero at 298.15 K, the datum used throughout this text).

Frequently, however, the tables or graphs of internal energy or enthalpy for species and reactant or product mixtures which are available give internal energies or enthalpies relative to the species or mixture value at some reference temperature  $T_0$ , i.e.,  $U(T) - U(T_0)$  or  $H(T) - H(T_0)$  are tabulated. Since

$$U_p(T_0) - U_r(T_0) = (\Delta U)_{V, T_0}$$

it follows from Eq. (3.24) that

$$[U_p(T) - U_p(T_0)] - [U_r(T) - U_r(T_0)] = -(\Delta U)_{V, T_0} \quad (3.25)$$

relates the product and reactant states. Figure 3-7 illustrates the adiabatic constant-volume combustion process on a  $U$ - $T$  diagram. Given the initial state of the reactants ( $T_r, V$ ) we can determine the final state of the products ( $T_p, V$ ).

For an adiabatic constant-pressure combustion process, Eq. (3.13) gives

$$H_p - H_r = 0$$

which combines with Eq. (3.16) to give

$$[H_p(T) - H_p(T_0)] - [H_r(T) - H_r(T_0)] = -(\Delta H)_{P, T_0} \quad (3.26)$$

Figure 3-7 illustrates this process also. Given the initial reactant state ( $T_r, p$ ) we can determine the final product state ( $T_p, p$ ).

Note that while in Figs. 3-5, 3-6, and 3-7 we have shown  $U$  and  $H$  for the reactants and products to be functions of  $T$  only, in practice for the products at high temperature  $U$  and  $H$  will be functions of  $p$  and  $T$ . The analysis presented here is general; however, to determine the final state of the products in an adia-

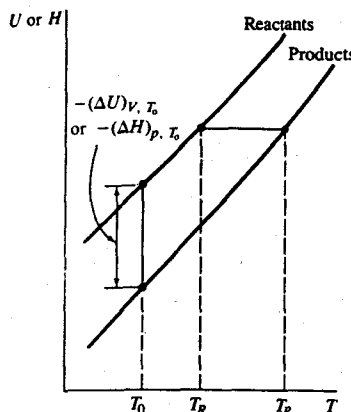


FIGURE 3-7

Adiabatic constant-volume combustion process on  $U$ - $T$  diagram or adiabatic constant-pressure combustion process on  $H$ - $T$  diagram.

batic combustion process, the constant-volume or constant-pressure constraint must also be used explicitly.

The final temperature of the products in an adiabatic combustion process is called the *adiabatic flame temperature*. Examples of typical adiabatic flame temperatures are shown later in Fig. 3-11.

### 3.5.5 Combustion Efficiency of an Internal Combustion Engine

In practice, the exhaust gas of an internal combustion engine contains incomplete combustion products (e.g., CO, H<sub>2</sub>, unburned hydrocarbons, soot) as well as complete combustion products (CO<sub>2</sub> and H<sub>2</sub>O) (see Sec. 4.9). Under lean operating conditions the amounts of incomplete combustion products are small. Under fuel-rich operating conditions these amounts become more substantial since there is insufficient oxygen to complete combustion. Because a fraction of the fuel's chemical energy is not fully released inside the engine during the combustion process, it is useful to define a *combustion efficiency*. The engine can be analyzed as an open system which exchanges heat and work with its surrounding environment (the atmosphere). Reactants (fuel and air) flow into the system; products (exhaust gases) flow out. Consider a mass  $m$  which passes through the control volume surrounding the engine shown in Fig. 3-8; the *net chemical energy release* due to combustion within the engine is given by

$$[H_r(T_A) - H_p(T_A)] = m \left( \sum_{i, \text{ reactants}} n_i \Delta \tilde{h}_{f,i}^{\circ} - \sum_{i, \text{ products}} n_i \Delta \tilde{h}_{f,i}^{\circ} \right)$$

Enthalpy is the appropriate property since  $p_r = p_p = p_{\text{atm}}$ .  $n_i$  is the number of moles of species  $i$  in the reactants or products per unit mass of working fluid and  $\Delta \tilde{h}_{f,i}^{\circ}$  is the standard enthalpy of formation of species  $i$  at ambient temperature  $T_A$ .

The amount of fuel energy supplied to the control volume around the engine which can be released by combustion is  $m_f Q_{\text{HV}}$ . Hence, the *combustion*

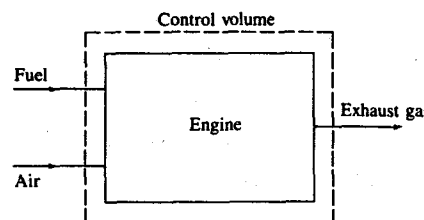


**FIGURE 3-8**  
Control volume surrounding engine.

efficiency—the fraction of the fuel energy supplied which is released in the combustion process—is given by<sup>12</sup>

$$\eta_c = \frac{H_R(T_A) - H_P(T_A)}{m_f Q_{HV}} \quad (3.27)$$

Note that  $m$  and  $m_f$  could be replaced by the average mass flow rates  $\dot{m}$  and  $\dot{m}_f$ .

Figure 3-9 shows how combustion efficiency varies with the fuel/air equivalence ratio for internal combustion engines. For spark-ignition engines, for lean equivalence ratios, the combustion efficiency is usually in the range 95 to 98 percent. For mixtures richer than stoichiometric, lack of oxygen prevents complete combustion of the fuel carbon and hydrogen, and the combustion efficiency steadily decreases as the mixture becomes richer. Combustion efficiency is little affected by other engine operating and design variables, provided the engine com-

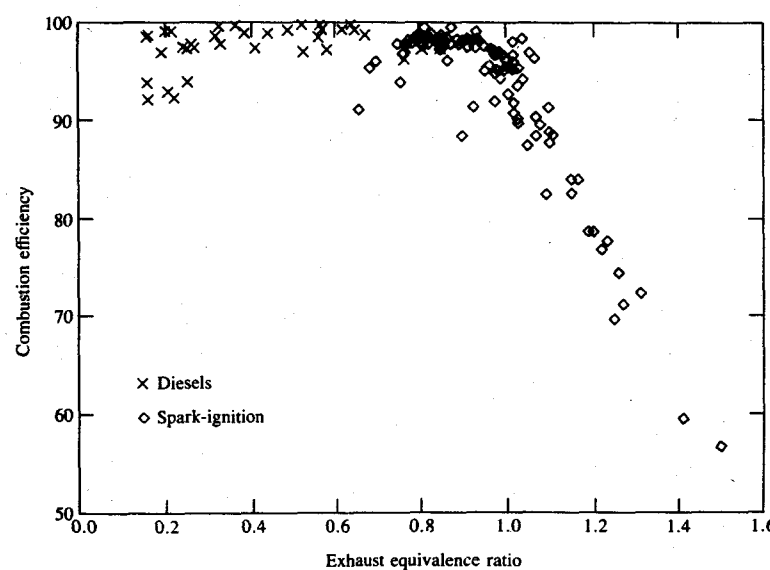


**FIGURE 3-9**  
Variation of engine combustion efficiency with fuel/air equivalence ratio.

bustion process remains stable. For diesel engines, which always operate lean, the combustion efficiency is normally higher—about 98 percent. Details of exhaust gas composition, on which these combustion efficiencies are based, can be found in Sec. 4.9.

### 3.6 THE SECOND LAW OF THERMODYNAMICS APPLIED TO COMBUSTION

#### 3.6.1 Entropy

In App. B, it is shown how the entropy of a mixture of ideal gases of known composition can be calculated. The discussion earlier relating enthalpies (or internal energies) of reactant and product mixtures applies to entropy also. The standard state entropies of chemical species are tabulated in the JANAF tables relative to zero entropy at 0 K. If the entropies of the elements at a datum temperature are arbitrarily set equal to zero, then the values of the entropy of a reactant mixture of given composition and of the resulting product mixture of given composition are both determined.

#### 3.6.2 Maximum Work from an Internal Combustion Engine and Efficiency

An internal combustion engine can be analyzed as an open system which exchanges heat and work with its surrounding environment (the atmosphere). Reactants (fuel and air) flow into the system; products (exhaust gases) flow out. By applying the second law of thermodynamics to a control volume surrounding the engine, as illustrated in Fig. 3-8, we can derive an expression for the maximum useful work that the engine can deliver.

Consider a mass  $m$  of fluid as it passes through the control volume surrounding the engine. The first law gives

$$\Delta Q - \Delta W_U = \Delta H$$

where  $\Delta W_U$  is the useful work transfer (i.e., non- $p$   $dV$  work) to the environment and  $\Delta H = H_P - H_R$ . Since the heat transfer  $\Delta Q$  occurs only with the atmosphere at temperature  $T_A$ , from the second law

$$\frac{\Delta Q}{T_A} \leq \Delta S$$

These equations combine to give

$$\Delta W_U \leq -(\Delta H - T_A \Delta S) = -\Delta B$$

where  $B$  is the steady-flow availability function,  $H - T_A S$ .<sup>13</sup> Usually  $p_R = p_A$  and  $T_R = T_A$ . The maximum work will be obtained when  $p_P = p_A$  and  $T_P = T_A$ .

TABLE 3.3  
Enthalpies and free energies of combustion reactions

Reaction†	$\Delta\tilde{H}_{298}^{\circ}$ , MJ/kmol	$\Delta\tilde{g}_{298}^{\circ}$ , MJ/kmol
$C + O_2 \rightarrow CO_2$	-393.52	-394.40
$H_2 + \frac{1}{2}O_2 \rightarrow H_2O$	-240.91	-232.78
$CH_4 + 2O_2 \rightarrow CO_2 + 2H_2O$	-802.30	-800.76
$CH_4O(l) + \frac{3}{2}O_2 \rightarrow CO_2 + 2H_2O$	-638.59	-685.35
$C_3H_8(g) + 5O_2 \rightarrow 3CO_2 + 4H_2O$	-2044.0	-2074.1
$C_6H_6(l) + \frac{15}{2}O_2 \rightarrow 6CO_2 + 3H_2O$	-3135.2	-3175.1
$C_8H_{18}(l) + \frac{25}{2}O_2 \rightarrow 8CO_2 + 9H_2O$	-5074.6	-5219.9

†  $H_2O$  (gas) in products.

Under these conditions,

$$\Delta W_U \leq -[(H - TS)_{P_{T_A}, P_A} - (H - TS)_{R_{T_A}, P_A}] = -(\Delta G)_{T_A, P_A} \quad (3.28)$$

or  $\Delta W_{U \max} = -(\Delta G)_{T_A, P_A}$

$G$  is the Gibbs free energy,  $H - TS$ , and  $(\Delta G)_{T_A, P_A}$  is the Gibbs free energy increase in the reaction of the fuel-air mixture to products at atmospheric temperature and pressure.  $-(\Delta G)_{T_A, P_A}$  will be a maximum when combustion is complete.

A fundamental measure of the effectiveness of any practical internal combustion engine is the ratio of the actual work delivered compared with this maximum work. This ratio will be called the *availability conversion efficiency*  $\eta_a$ :

$$\eta_a = \frac{\Delta W}{\Delta W_{U \max}} = -\frac{\Delta W}{-(\Delta G)_{T_A, P_A}} \quad (3.29)$$

The property *availability* is the maximum useful work transfer that can be obtained from a system atmosphere (or control-volume atmosphere) combination at a given state. This efficiency therefore defines the fraction of the availability of the unburned fuel and air which, passing through the engine and interacting only with the atmosphere, is actually converted to useful work. Availability analysis of engine operation is proving valuable in identifying where the significant irreversibilities or losses in availability occur. This topic is discussed more fully in Sec. 5.7.

$(\Delta G)_{T_A, P_A}$ , or  $(\Delta g)_{T_A, P_A}$ , is not an easy quantity to evaluate for practical fuels; it is the heating value,  $-(\Delta h)_{T_A}$ , which is usually measured. Values of  $(\Delta g)_{298}^{\circ}$  and  $(\Delta h)_{298}^{\circ}$  for selected fuel combustion reactions are given in Table 3.3. For the pure hydrocarbons they are closely comparable because at 298 K,  $\Delta\tilde{s}^{\circ} \ll \Delta\tilde{h}^{\circ}/T$ . For hydrogen and methanol the differences are larger, however. Because for practical fuels  $-(\Delta h)_{298}^{\circ}$  is measured directly as the heating value of the fuel, it is standard practice to use the following definition of efficiency:

$$\eta_f = \frac{W_c}{m_f Q_{HV}} \quad (3.30)$$

which was defined as the *fuel conversion efficiency* in Sec. 2.8. Note that sometimes the higher heating value is used in Eq. (3.30) and sometimes the lower heating value. Whichever value is used should be explicitly stated. The normal practice in internal combustion engine analysis is to use the lower heating value at constant pressure, since the engine overall is a steady flow device and the water in the exhaust is always in vapor form. We will use  $Q_{HV}$  in Eq. (3.30) throughout this text. The fuel conversion efficiency is the most commonly used definition of engine efficiency because it uses an easily measured quantity, the heating value, to define the usable fuel energy supplied to the engine. For hydrocarbon fuels, since  $\Delta\tilde{h}^{\circ} \approx \Delta\tilde{g}^{\circ}$ , the fuel conversion efficiency and the availability conversion efficiency are closely comparable in value.

In practice, not all the fuel energy supplied to the engine is released by the combustion process since combustion is incomplete: the combustion efficiency [Eq. (3.27)] is less than unity. It is sometimes useful to separate out the effects of incomplete combustion by defining an efficiency which relates the actual work per cycle to the amount of fuel chemical energy released in the combustion process. We will call this the *thermal conversion efficiency*  $\eta_t$ :

$$\eta_t = \frac{W_c}{H_R(T_A) - H_P(T_A)} = -\frac{W_c}{(\Delta H)_{T_A}} = \frac{W_c}{\eta_c m_f Q_{HV}} \quad (3.31)$$

Obviously the fuel conversion, thermal conversion, and combustion efficiencies are related by

$$\eta_f = \eta_c \eta_t \quad (3.32)$$

It is important to understand that there is a fundamental difference between availability conversion efficiency as defined by Eq. (3.29) [and the fuel conversion efficiency for internal combustion engines, Eq. (3.30), which closely approximates it] and the efficiency of a thermodynamic heat engine. The second law limit to the availability conversion efficiency is unity. For a thermodynamic heat engine (which experiences heat-transfer interactions with at least two heat reservoirs) the efficiency is limited to a value substantially less than unity by the temperatures of the heat reservoirs available.<sup>13</sup>

### 3.7 CHEMICALLY REACTING GAS MIXTURES

The working fluids in engines are mixtures of gases. Depending on the problem under consideration and the portion of the engine cycle in which it occurs chemical reactions may: (1) be so slow that they have a negligible effect on mixture composition (the mixture composition is essentially "frozen"); (2) be so rapid that the mixture state changes and the composition remains in chemical equilibrium; (3) be one of the rate-controlling processes that determine how the composition of the mixture changes with time.

### 3.7.1 Chemical Equilibrium

It is a good approximation for performance estimates in engines to regard the burned gases produced by the combustion of fuel and air as in chemical equilibrium.<sup>†</sup> By this we mean that the chemical reactions, by which individual species in the burned gases react together, produce and remove each species at equal rates. No net change in species composition results.

For example, if the temperature of a mass of carbon dioxide gas in a vessel is increased sufficiently, some of the  $\text{CO}_2$  molecules dissociate into  $\text{CO}$  and  $\text{O}_2$  molecules. If the mixture of  $\text{CO}_2$ ,  $\text{CO}$ , and  $\text{O}_2$  is in equilibrium, then  $\text{CO}_2$  molecules are dissociating into  $\text{CO}$  and  $\text{O}_2$  at the same rate as  $\text{CO}$  and  $\text{O}_2$  molecules are recombining in the proportions required to satisfy the equation



In combustion products of hydrocarbon fuels, the major species present at low temperatures are  $\text{N}_2$ ,  $\text{H}_2\text{O}$ ,  $\text{CO}_2$ , and  $\text{O}_2$  or  $\text{CO}$  and  $\text{H}_2$ . At higher temperatures (greater than about 2200 K), these major species dissociate and react to form additional species in significant amounts. For example, the adiabatic combustion of a stoichiometric mixture of a typical hydrocarbon fuel with air produces products with species mole fractions of:  $\text{N}_2 \sim 0.7$ ;  $\text{H}_2\text{O}$ ,  $\text{CO}_2 \sim 0.1$ ;  $\text{CO}$ ,  $\text{OH}$ ,  $\text{O}_2$ ,  $\text{NO}$ ,  $\text{H}_2 \sim 0.01$ ;  $\text{H}, \text{O} \sim 0.001$ ; and other species in lesser amounts.

The second law of thermodynamics defines the criterion for chemical equilibrium as follows. Consider a system of chemically reacting substances undergoing a constant-pressure, constant-temperature process. In the absence of shear work (and electrical work, gravity, motion, capillarity), the first law gives

$$\delta Q = dH$$

The second law gives

$$\delta Q \leq T dS$$

Combining these gives

$$dH - T dS \leq 0$$

Since we are considering constant-temperature processes, this equation holds for finite changes:

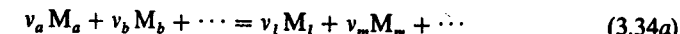
$$\Delta H - T \Delta S = \Delta G \leq 0$$

Thus, reactions can only occur (at constant pressure and temperature) if  $G$  ( $= H - TS$ ) for the products is less than  $G$  for the reactants. Hence at equilibrium

$$(\Delta G)_{p, T} = 0 \quad (3.33)$$

<sup>†</sup> This assumption is not valid late in the expansion stroke and during the exhaust process (see Sec. 4.9). Nor does it take account of pollutant formation processes (see Chap. 11).

Consider a reactive mixture of ideal gases. The reactant species  $M_a$ ,  $M_b$ , etc., and product species  $M_l$ ,  $M_m$ , etc., are related by the general reaction whose stoichiometry is given by



This can be written as

$$\sum_i v_i M_i = 0 \quad (3.34b)$$

where the  $v_i$  are the stoichiometric coefficients and by convention are positive for the product species and negative for the reactant species.

Let an amount  $\delta n_a$  of  $M_a$  react with  $\delta n_b$  of  $M_b$ , etc., and produce  $\delta n_l$  of  $M_l$ ,  $\delta n_m$  of  $M_m$ , etc. These amounts are in proportion:

$$\delta n_i = v_i \delta n \quad (3.35)$$

The change in Gibbs free energy of a mixture of ideal gases, at constant pressure and temperature, as the composition changes is given by

$$(\Delta G)_{p, T} = \sum_i \tilde{\mu}_i \delta n_i \quad (3.36)$$

where  $\delta n_i$  is the change in number of moles of species  $i$  and  $\tilde{\mu}$  is the *chemical potential*. The chemical potential, an intensive property, is defined as

$$\tilde{\mu}_i = \left( \frac{\partial G}{\partial n_i} \right)_{p, T, n_j (j \neq i)} \quad (3.37)$$

It is equal in magnitude to the specific Gibbs free energy at a given temperature and pressure. For an ideal gas, it follows from Eqs. (B.13), (B.15) and (3.37) that

$$\tilde{\mu}_i = \tilde{\mu}_i^\circ(T) + \tilde{R}T \ln \frac{p_i}{p_0} \quad (3.38)$$

where  $\tilde{\mu}_i^\circ$  equals  $\tilde{g}_i^\circ$ , the standard specific Gibbs free energy of formation. The standard state pressure  $p_0$  is usually one atmosphere.

Substitution in Eq. (3.36) gives, at equilibrium,

$$\sum \left( \tilde{\mu}_i^\circ + \tilde{R}T \ln \frac{p_i}{p_0} \right) \delta n_i = 0$$

or

$$\sum \left( \tilde{\mu}_i^\circ + \tilde{R}T \ln \frac{p_i}{p_0} \right) v_i \delta n = 0$$

We can divide by  $\delta n$  and rearrange, to obtain

$$\sum \ln \left( \frac{p_i}{p_0} \right)^{v_i} = - \frac{(\sum \tilde{\mu}_i^\circ v_i)}{\tilde{R}T} = - \frac{\Delta G^\circ}{\tilde{R}T} = \ln K_p \quad (3.39)$$

$K_p$  is the equilibrium constant at constant pressure:

$$K_p = \prod_i \left( \frac{p_i}{p_0} \right)^{v_i} \quad (3.40)$$

It is obtained from the Gibbs free energy of the reaction which can be calculated from the Gibbs free energy of formation of each species in the reaction, as indicated in Eq. (3.39) above. It is a function of temperature only.

In the JANAF tables,<sup>8</sup> to simplify the calculation of equilibrium constants, values of  $\log_{10} (K_p)_i$ , the equilibrium constants of formation of one mole of each species from their elements in their standard states, are tabulated against temperature. The equilibrium constant for a specific reaction is then obtained via the relation

$$\log_{10} (K_p)_{\text{reaction}} = \sum_i v_i \log_{10} (K_p)_i \quad (3.41)$$

With the JANAF table values of  $(K_p)_i$ , the pressures in Eqs. (3.40) and (3.41) must be in atmospheres.

The effect of pressure on the equilibrium composition can be deduced from Eq. (3.40). Substitution of the mole fractions  $\tilde{x}_i$  and mixture pressure  $p$  gives

$$\prod_i \left( \frac{p_i}{p_0} \right)^{v_i} = \prod_i \left( \tilde{x}_i \frac{p}{p_0} \right)^{v_i} = \left( \frac{p}{p_0} \right)^{\sum_i v_i} \prod_i \tilde{x}_i^{v_i} = K_p$$

If  $\sum_i v_i = 0$ , changes in pressure have no effect on the composition. If  $\sum_i v_i > 0$  (dissociation reactions), then the mole fractions of the dissociation products decrease as pressure increases. If  $\sum_i v_i < 0$  (recombination reactions), the converse is true.

An equilibrium constant,  $K_c$ , based on concentrations (usually expressed in gram moles per cubic centimeter) is also used:

$$K_c = \prod_i [M_i]^{v_i} \quad (3.42)$$

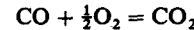
Equation (3.40) can be used to relate  $K_p$  and  $K_c$ :

$$K_p = K_c (\bar{R}T)^{\sum_i v_i} \quad (3.43)$$

for  $p_0 = 1$  atmosphere. For  $\sum_i v_i = 0$ ,  $K_p$  and  $K_c$  are equal.

**Example 3.4.** A stoichiometric mixture of CO and O<sub>2</sub> in a closed vessel, initially at 1 atm and 300 K, is exploded. Calculate the composition of the products of combustion at 2500 K and the gas pressure.

The combustion equation is



The JANAF tables give  $\log_{10} K_p$  (equilibrium constants of formation from the elements in their standard state) at 2500 K of CO<sub>2</sub>, CO, and O<sub>2</sub> as 8.280, 6.840, and 0, respectively. Thus, the equilibrium constant for the CO combustion reaction above is, from Eq. (3.41),

$$\log_{10} K_p = 8.280 - 6.840 = 1.440$$

which gives  $K_p = 27.5$ .

If the degree of dissociation in the products is  $\alpha$  (i.e., a fraction  $\alpha$  of the CO<sub>2</sub> formed by complete combustion is dissociated), the product composition is

$$\text{CO}_2, (1 - \alpha); \quad \text{CO}, \alpha; \quad \text{O}_2, \frac{\alpha}{2}$$

For this mixture, the number of moles of reactants  $n_R$  is  $\frac{1}{2}$ ; the number of moles of products  $n_P$  is  $(1 + \alpha/2)$ .

The ideal gas law gives

$$p_R V = n_R \bar{R} T_R \quad p_P V = n_P \bar{R} T_P$$

Thus

$$\frac{p_P}{n_P} = \frac{1}{1.5} \times \frac{2500}{300} = 5.555 \text{ atm/mol}$$

The equilibrium relation [Eq. (3.40)] gives

$$\frac{1 - \alpha}{\alpha(\alpha/2)^{1/2}} \left( \frac{n_P}{p_P} \right)^{1/2} = 27.5$$

which can be solved to give  $\alpha = 0.074$ .

The composition of the products in mole fractions is, therefore,

$$x_{\text{CO}_2} = \frac{1 - \alpha}{n_P} = 0.893$$

$$x_{\text{CO}} = \frac{\alpha}{n_P} = 0.071$$

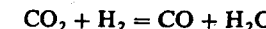
$$x_{\text{O}_2} = \frac{\alpha/2}{n_P} = 0.037$$

The pressure of the product mixture is

$$p = 5.555 n_P = 5.76 \text{ atm}$$

**Example 3.5.** In fuel-rich combustion product mixtures, equilibrium between the species CO<sub>2</sub>, H<sub>2</sub>O, CO, and H<sub>2</sub> is often assumed to determine the burned gas composition. For  $\phi = 1.2$ , for C<sub>8</sub>H<sub>18</sub>-air combustion products, determine the mole fractions of the product species at 1700 K.

The reaction relating these species (often called the water gas reaction) is

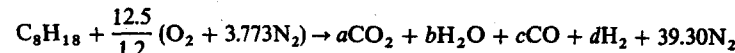


From the JANAF tables,  $\log_{10} K_p$  of formation for these species at 1700 K are: CO<sub>2</sub>, 12.180; H<sub>2</sub>, 0; CO, 8.011; H<sub>2</sub>O(g), 4.699. The equilibrium constant for the above reaction is, from Eq. (3.41),

$$\log_{10} K_p = 8.011 + 4.699 - 12.180 = 0.530$$

from which  $K_p = 3.388$ .

The combustion reaction for C<sub>8</sub>H<sub>18</sub>-air with  $\phi = 1.2$  can be written



A carbon balance gives:  $a + c = 8$

A hydrogen balance gives:  $2b + 2d = 18$

An oxygen balance gives:  $2a + b + c = 20.83$

The equilibrium relation gives  $(bc)/(ad) = 3.388$  (since the equilibrated reaction has the same number of moles as there are reactants or products, the moles of each species can be substituted for the partial pressures).

These four equations can be solved to obtain

$$c^2 - 19.3c + 47.3 = 0$$

which gives  $c = 2.89$ ,  $a = 5.12$ ,  $b = 7.72$ , and  $d = 1.29$ . The total number of moles of products is

$$a + b + c + d + 39.3 = 56.3$$

and the mole fractions of the species in the burned gas mixture are

$$\text{CO}_2, 0.0908; \quad \text{H}_2\text{O}, 0.137; \quad \text{CO}, 0.051; \quad \text{H}_2, 0.023; \quad \text{N}_2, 0.698$$

Our development of the equilibrium relationship for one reaction has placed no restrictions on the occurrence of simultaneous equilibria. Consider a mixture of  $N$  reacting gases in equilibrium. If there are  $C$  chemical elements, conservation of elements will provide  $C$  equations which relate the concentrations of these  $N$  species. Any set of  $(N - C)$  chemical reactions, each in equilibrium, which includes each species at least once will then provide the additional equations required to determine the concentration of each species in the mixture. Unfortunately, this complete set of equations is a coupled set of  $C$  linear and  $(N - C)$  nonlinear equations which is difficult to solve for cases where  $(N - C) > 2$ . For complex systems such as this, the following approach to equilibrium composition calculations is now more widely used.

Standardized computer methods for the calculation of complex chemical equilibrium compositions have been developed. A generally available and well-documented example is the NASA program of this type.<sup>14</sup> The approach taken is to minimize explicitly the Gibbs free energy of the reacting mixture (at constant temperature and pressure) subject to the constraints of element mass conservation. The basic equations for the NASA program are the following.

If the stoichiometric coefficients  $a_{ij}$  are the number of kilomoles of element  $i$  per kilomole of species  $j$ ,  $b_i^*$  is the number of kilomoles of element  $i$  per kilogram of mixture, and  $n_j$  is the number of kilomoles of species  $j$  per kilogram of mixture, element mass balance constraints are

$$\sum_{j=1}^n a_{ij} n_j - b_i^* = 0 \quad \text{for } i = 1, 2, \dots, l \quad (3.44)$$

The Gibbs free energy per kilogram of mixture is

$$g = \sum_{j=1}^n \tilde{\mu}_j n_j \quad (3.45)$$

For gases, the chemical potential  $\tilde{\mu}_j$  is

$$\tilde{\mu}_j = \tilde{\mu}_j^\circ + \tilde{R}T \ln \left( \frac{n_j}{n} \right) + \tilde{R}T \ln p \quad (3.46)$$

where  $\tilde{\mu}_j^\circ$  is the chemical potential in the standard state and  $p$  is the mixture pressure in atmospheres. Using the method of lagrangian multipliers, the term

$$G = g + \sum_{i=1}^l \lambda_i \sum_{j=1}^n (a_{ij} n_j - b_i^*)$$

is defined. The condition for equilibrium then becomes

$$\delta G = \sum_{j=1}^n \left( \mu_j + \sum_{i=1}^l \lambda_i a_{ij} \right) \delta n_j + \sum_{i=1}^l \sum_{j=1}^n (a_{ij} n_j - b_i^*) \delta \lambda_i = 0 \quad (3.47)$$

Treating the variations  $\delta n_j$  and  $\delta \lambda_i$  as independent gives

$$\tilde{\mu}_j + \sum_{i=1}^l \lambda_i a_{ij} = 0 \quad \text{for } j = 1, \dots, n \quad (3.48)$$

and the original mass balance equation (3.44). Equations (3.44) and (3.48) permit the determination of equilibrium compositions for thermodynamic states specified by a temperature  $T$  and pressure  $p$ .

In the NASA program, the thermodynamic state may be specified by other pairs of state variables: enthalpy and pressure (useful for constant-pressure combustion processes); temperature and volume; internal energy and volume (useful for constant-volume combustion processes); entropy and pressure, and entropy and volume (useful for isentropic compressions and expansions). The equations required to obtain mixture composition are not all linear in the composition variables and an iteration procedure is generally required to obtain their solution. Once the composition is determined, additional relations, such as those in App. B which define the thermodynamic properties of gas mixtures, must then be used.

For each species, standard state enthalpies  $\tilde{h}^\circ$  are obtained by combining standard enthalpies of formation at the datum temperature (298.15 K)  $\Delta \tilde{h}_{f,298}^\circ$  with sensible enthalpies  $(\tilde{h}^\circ - \tilde{h}_{298}^\circ)$ , i.e.,

$$\tilde{h}^\circ = \Delta \tilde{h}_{f,298}^\circ + (\tilde{h}^\circ - \tilde{h}_{298}^\circ) \quad (3.49)$$

For the elements in their reference state,  $\Delta \tilde{h}_{f,298}^\circ$  is zero [the elements important in combustion are C (solid, graphite), H<sub>2</sub>(g), O<sub>2</sub>(g), N<sub>2</sub>(g)].

For each species, the thermodynamic quantities specific heat, enthalpy, and entropy as functions of temperature are given in the form:

$$\frac{\tilde{c}_p^\circ}{\tilde{R}} = a_1 + a_2 T + a_3 T^2 + a_4 T^3 + a_5 T^4 \quad (3.50a)$$

$$\frac{\tilde{h}^\circ}{\tilde{R}T} = a_1 + \frac{a_2}{2} T + \frac{a_3}{3} T^2 + \frac{a_4}{4} T^3 + \frac{a_5}{5} T^4 + \frac{a_6}{T} \quad (3.50b)$$

$$\frac{\tilde{s}^o}{R} = a_1 \ln T + a_2 T + \frac{a_3}{2} T^2 + \frac{a_4}{3} T^3 + \frac{a_5}{4} T^4 + a_7 \quad (3.50c)$$

The coefficients are obtained by least-squares matching with thermodynamic property data from the JANAF tables. Usually two sets of coefficients are included for two adjacent temperature intervals (in the NASA program these are 300 to 1000 K and 1000 to 5000 K) (see Sec. 4.7).

In some equilibrium programs, the species to be included in the mixture must be specified as an input to the calculation. In the NASA program, all allowable species are included in the calculation, though species may be specifically omitted from consideration.

For each reactant composition and pair of thermodynamic state variables, the program calculates and prints out the following:

1. *Thermodynamic mixture properties* (obtained from the equilibrium composition and the appropriate gas mixture rule; see App. B).  $p$ ,  $T$ ,  $\rho$ ,  $h$ ,  $s$ ,  $M$ ,  $(\partial \ln V / \partial \ln p)_T$ ,  $(\partial \ln V / \partial \ln T)_p$ ,  $c_p$ ,  $\gamma_s$ , and  $a$  (sound speed)
2. *Equilibrium composition*. Mole fractions of each species (which are present in significant amounts),  $\tilde{x}_i$

Figure 3-10 shows how the equilibrium composition of the products of combustion of isoctane-air mixtures at selected temperatures and 30 atm pressure varies with the equivalence ratio. At low temperatures, the products are  $N_2$ ,  $CO_2$ ,  $H_2O$ , and  $O_2$  for lean mixtures and  $N_2$ ,  $CO_2$ ,  $H_2O$ ,  $CO$ , and  $H_2$  for rich mixtures. As temperature increases, the burned-gas mixture composition becomes much more complex with dissociation products such as  $OH$ ,  $O$ , and  $H$  becoming significant.

Figure 3-11 shows adiabatic flame temperatures for typical engine conditions as a function of the equivalence ratio, obtained with the NASA program using the methodology of Sec. 3.5.4. The isoctane-air unburned mixture state was 700 K and 10 atm. Flame temperatures for adiabatic combustion at constant pressure (where  $p_R$  and  $H_R$  are specified) and at constant volume (where  $V_R$  and  $U_R$  are specified) are shown. Flame temperatures at constant volume are higher, because the final pressure is higher and dissociation is less. Maximum flame temperatures occur slightly rich of stoichiometric.

### 3.7.2 Chemical Reaction Rates

Whether a system is in chemical equilibrium depends on whether the time constants of the controlling chemical reactions are short compared with time scales over which the system conditions (temperature and pressure) change. Chemical processes in engines are often not in equilibrium. Important examples of non-equilibrium phenomena are the flame reaction zone where the fuel is oxidized, and the air-pollutant formation mechanisms. Such nonequilibrium processes are controlled by the rates at which the actual chemical reactions which convert

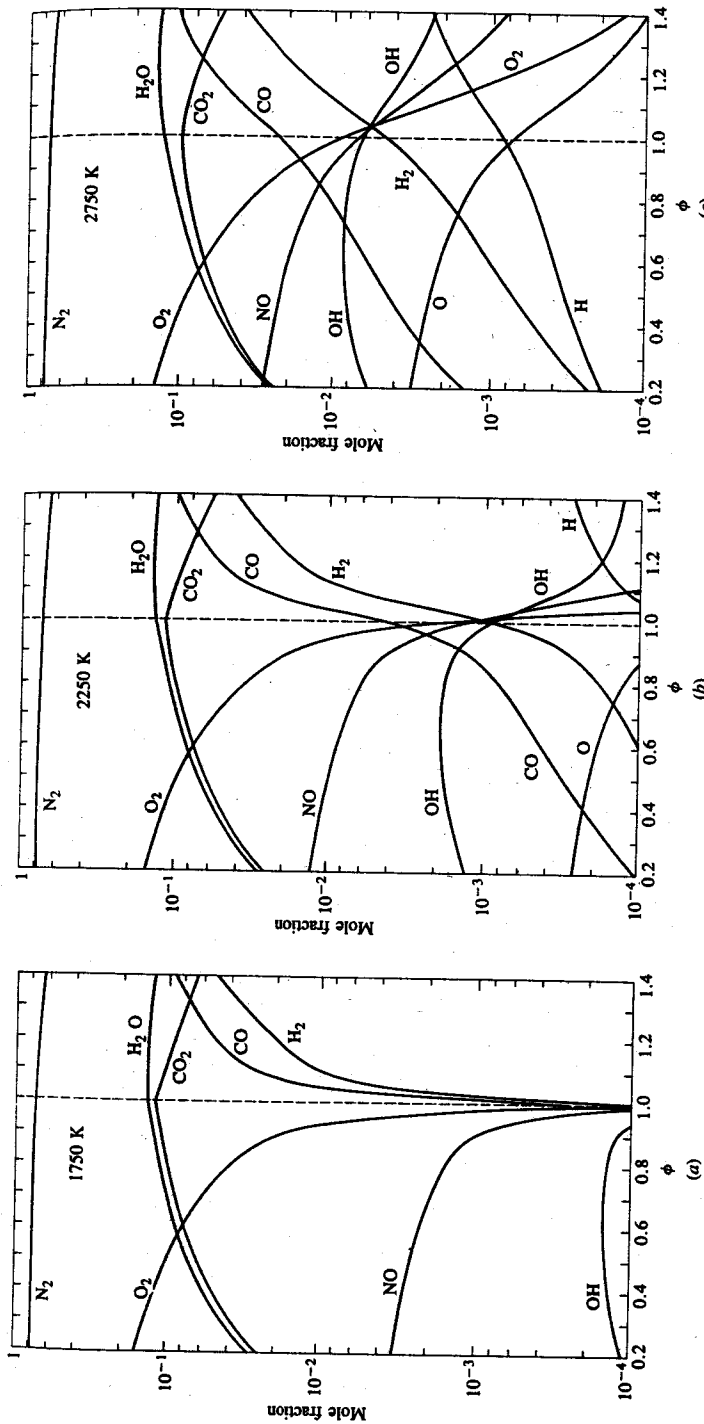


FIGURE 3-10  
Mole fractions of equilibrium combustion products of isoctane-air mixtures as a function of fuel/air equivalence ratio at 30 atmospheres and (a) 1750 K; (b) 2250 K; and (c) 2750 K.

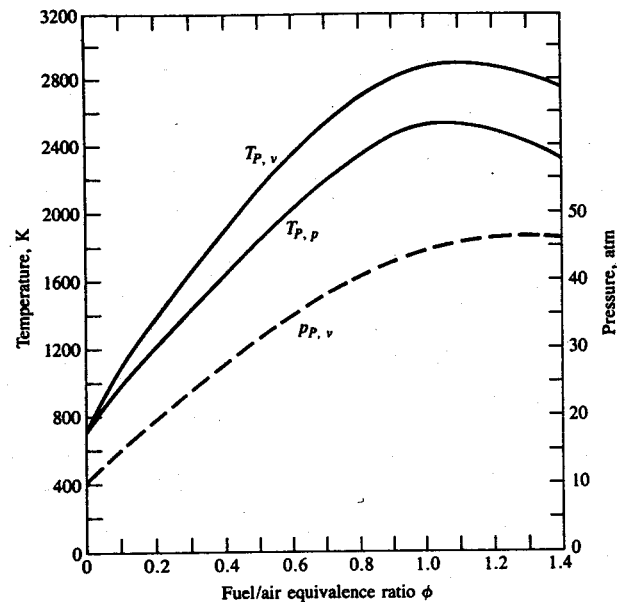


FIGURE 3-11

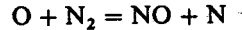
Equilibrium product temperatures for constant-volume ( $T_{P,v}$ ) and constant-pressure ( $T_{P,p}$ ) adiabatic combustion of isoctane-air mixture initially at 700 K and 10 atm, as a function of fuel/air equivalence ratio. Pressure ( $p_{P,v}$ ) is equilibrium pressure for adiabatic constant-volume combustion.

reactants to products occur. The rates at which chemical reactions proceed depend on the concentration of the reactants, temperature, and whether any catalyst is present. This field is called chemical kinetics and some of its basic relations will now be reviewed.<sup>2</sup>

Most of the chemical reactions of interest in combustion are binary reactions, where two reactant molecules,  $M_a$  and  $M_b$ , with the capability of reacting together collide and form two product molecules,  $M_c$  and  $M_d$ ; i.e.,



An important example of such a reaction is the rate-controlling step in the process by which the pollutant nitric oxide, NO, forms:



This is a second-order reaction since the stoichiometric coefficients of the reactants  $v_a$  and  $v_b$  are each unity and sum to 2. (The only first-order reactions are decomposition processes.) Third-order reactions are important in combustion, also. Examples are the recombination reactions by which radical species such as H, O, and OH combine during the final stage of the fuel oxidation process: e.g.,



$M$  is any molecule (such as  $N_2$ ) which takes part in the collision and carries away the excess energy.

The law of mass action states that the rate at which product species are produced and the rate at which reactant species are removed is proportional to the product of the concentrations of reactant species, with the concentration of each species raised to the power of its stoichiometric coefficient  $v_i$ . Thus, for reaction (3.51) above, the reaction rate  $R^+$  in the forward (+) direction, reactants to products, is given by

$$R^+ = -\frac{d[M_a]^+}{dt} = \frac{d[M_c]^+}{dt} = k^+[M_a][M_b] \quad (3.53)$$

If the reaction can also proceed in the reverse (-) direction, then the backward rate  $R^-$  is given by

$$R^- = -\frac{d[M_c]^-}{dt} = \frac{d[M_a]^-}{dt} = k^-[M_c][M_d] \quad (3.54)$$

$k^+$  and  $k^-$  are the rate constants in the forward and reverse directions for this reaction. The net rate of production of products or removal of reactants is, therefore,

$$\begin{aligned} R^+ - R^- &= \frac{d[M_c]^+}{dt} + \frac{d[M_c]^-}{dt} = -\frac{d[M_a]^+}{dt} - \frac{d[M_d]^-}{dt} \\ &= k^+[M_a][M_b] - k^-[M_c][M_d] \end{aligned} \quad (3.55)$$

These results can be stated more generally as follows. Any reaction can be written as

$$\sum_{i=1}^n v_{R,i} M_{R,i} = \sum_{i=1}^m v_{P,i} M_{P,i} \quad (3.56)$$

where  $v_i$  is the stoichiometric coefficient of species  $M_i$ , subscripts  $R$  and  $P$  denote reactants and products, respectively, and there are  $n$  reactant species and  $m$  product species. The forward reaction rate  $R^+$  and the reverse reaction rate  $R^-$  are given by

$$\begin{aligned} R^+ &= k^+ \prod_{i=1}^n [M_{R,i}]^{v_{R,i}} \\ R^- &= k^- \prod_{i=1}^m [M_{P,i}]^{v_{P,i}} \end{aligned} \quad (3.57)$$

The net rate of removal of reactant species  $M_{R,i}$  is

$$-\frac{d[M_{R,i}]}{dt} = v_{R,i}(R^+ - R^-) \quad (3.58a)$$

and the net rate of production of product species  $M_{P_i}$  is

$$\frac{d[M_{P_i}]}{dt} = v_{P_i}(R^+ - R^-) \quad (3.58b)$$

The rate constants,  $k$ , usually follow the Arrhenius form:

$$k = A \exp\left(-\frac{E_A}{RT}\right) \quad (3.59)$$

where  $A$  is called the frequency or preexponential factor and may be a (moderate) function of temperature;  $E_A$  is the activation energy. The Boltzmann factor  $\exp(-E_A/RT)$  defines the fraction of all collisions that have an energy greater than  $E_A$ —i.e., sufficient energy to make the reaction take place. The functional dependence of  $k$  on  $T$  and the constants in the Arrhenius form, Eq. (3.59), if that is appropriate, are determined experimentally.

At equilibrium, the forward and reverse reaction rates are equal. Then, from Eq. (3.55), with  $R^+ - R^- = 0$ :

$$\frac{k^+}{k^-} = \frac{[M_c][M_d]}{[M_a][M_b]} = K_e$$

where  $K_e$  is the equilibrium constant based on concentrations defined by Eq. (3.42). It can be related to  $K_p$ , the equilibrium constant based on partial pressures, by Eq. (3.43).

The chemical reaction mechanisms of importance in combustion are much more complex than the above illustrations of rate-controlled processes. Such mechanisms usually involve both parallel and sequential interdependent reactions. The methodology reviewed above still holds; however, one must sum algebraically the forward and reverse rates of all the reactions which produce (or remove) a species of interest. In such complex mechanisms it is often useful to assume that (some of) the reactive intermediate species or radicals are in *steady state*. That is, these radicals react so quickly once they are formed that their concentrations do not rise but are maintained in steady state with the species with which they react. The net rate at which their concentration changes with time is set equal to zero.

## PROBLEMS

- 3.1. Isooctane is supplied to a four-cylinder spark-ignition engine at 2 g/s. Calculate the air flow rate for stoichiometric combustion. If the engine is operating at 1500 rev/min, estimate the mass of fuel and air entering each cylinder per cycle. The engine displaced volume is 2.4 liters. What is the volumetric efficiency?
- 3.2. Calculate the exhaust gas composition of a butane-fueled spark-ignition engine operating with equivalence ratio of 0.9. Assume the fuel is fully burned within the cylinder. Butane is  $C_4H_{10}$ .

- 3.3. The molar composition of dry exhaust gas of a propane-fueled SI engine is given below (water was removed before the measurement). Calculate the equivalence ratio.

$$CO_2 = 10.8\%, \quad O_2 = 4.5\%, \quad CO = 0\%, \quad H_2 = 0\%$$

- 3.4. Evaluate and compare the lower heating values per unit mass of stoichiometric mixture and per unit volume of stoichiometric mixture (at standard atmospheric conditions) for methane, isoctane, methyl alcohol, and hydrogen. Assume the fuel is fully vaporized.
  - 3.5. The measured engine fuel flow rate is 0.4 g/s, air flow rate is 5.6 g/s, and exhaust gas composition (measured dry) is  $CO_2 = 13.0\%$ ,  $CO = 2.8\%$  with  $O_2$  essentially zero. Unburned hydrocarbon emissions can be neglected. Compare the equivalence ratio calculated from the fuel and air flow with the equivalence ratio calculated from exhaust gas composition. The fuel is gasoline with a H/C ratio of 1.87. Assume a  $H_2$  concentration equal to one-third the  $CO$  concentration.
  - 3.6. The brake fuel conversion efficiency of an engine is 0.3. The mechanical efficiency is 0.8. The combustion efficiency is 0.94. The heat losses to the coolant and oil are 60 kW. The fuel chemical energy entering the engine per unit time,  $\dot{m}_f Q_{hv}$ , is 190 kW. What percentage of this energy becomes (a) brake work; (b) friction work; (c) heat losses; (d) exhaust chemical energy; (e) exhaust sensible energy.
  - 3.7. An upper estimate can be made of the amount of NO formed in an engine from considering the equilibrium of the reaction  $N_2 + O_2 = 2NO$ . Calculate the NO concentration at equilibrium at 2500 K and 30 atm.  $\log_{10} K_p = -1.2$  for this reaction at 2500 K. Assume N/O ratio in the combustion products is 15.  $N_2$ ,  $O_2$ , and NO are the only species present.
  - 3.8. Carbon monoxide reacts with air at 1 atm and 1000 K in an exhaust gas reactor. The mole fractions of the exhaust gas-air mixture flowing into the reactor are  $CO, 3\%$ ;  $O_2, 7\%$ ;  $N_2, 74\%$ ;  $CO_2, 6\%$ ;  $H_2O, 10\%$ .
    - (a) Calculate the concentration of  $CO$  and  $O_2$  in gram moles per  $cm^3$  in the entering mixture.
    - (b) The rate of reaction is given by
- $$\frac{d[CO]}{dt} = -4.3 \times 10^{11} \times [CO][O_2]^{0.25} \exp[-E/(RT)]$$
- [ ] denotes concentration in gram moles per  $cm^3$ ,  $E/R = 20,000$  K. Calculate the initial reaction rate of  $CO$ ,  $d[CO]/dt$ : time is in seconds.
- (c) The equilibrium constant  $K_p$  for the reaction  $CO + \frac{1}{2}O_2 = CO_2$  at 1000 K is  $10^{10}$ . Find the equilibrium  $CO$  concentration.
  - (d) Determine the time to reach this equilibrium concentration of  $CO$  using the initial reaction rate. (The actual time will be longer but this calculation indicates approximately the time required.)
  - 3.9. The exhaust gases of a hydrogen-fueled engine contain 22.3 percent  $H_2O$ , 7.44 percent  $O_2$ , and 70.2 percent  $N_2$ . At what equivalence ratio is it operating?
  - 3.10. Gas is sampled at 1 atmosphere pressure from the exhaust manifold of an internal combustion engine and analyzed. The mole fractions of species in the exhaust are:  
 $H_2O, 0.0468; \quad CO_2, 0.0585; \quad O_2, 0.123; \quad N_2, 0.772$   
 Other species such as  $CO$  and unburned hydrocarbons can be neglected.  
 (a) The fuel is a synthetic fuel derived from coal containing only carbon and hydrogen. What is the ratio of hydrogen atoms to carbon atoms in the fuel?

- (b) Calculate the fuel/air equivalence ratio at which this engine is operating.  
 (c) Is the internal combustion engine a conventional spark-ignition or a diesel engine? Explain.  
 (d) The engine has a displaced volume of 2 liters. Estimate approximately the percentage by which the fuel flow rate would be increased if this engine were operated at its maximum load at this same speed (2000 rev/min). Explain briefly what limits the equivalence ratio at maximum load.
- 3.11. The following are approximate values of the relative molecular mass (molecular weights): oxygen O<sub>2</sub>, 32; nitrogen N<sub>2</sub>, 28; hydrogen H<sub>2</sub>, 2; carbon C, 12. Determine the stoichiometric fuel/air and air/fuel ratios on a mass basis, and the lower heating value per unit mass of stoichiometric mixture for the following fuels:
- Methane (CH<sub>4</sub>), isoctane (C<sub>8</sub>H<sub>18</sub>), benzene (C<sub>6</sub>H<sub>6</sub>), hydrogen (H<sub>2</sub>), methyl alcohol (CH<sub>3</sub>OH)
- Heating values for these fuels are given in App. D.
- 3.12. Liquid petroleum gas (LPG) is used to fuel spark-ignition engines. A typical sample of the fuel consists of

70 percent by volume propane C<sub>3</sub>H<sub>8</sub>  
 5 percent by volume butane C<sub>4</sub>H<sub>10</sub>  
 25 percent by volume propene C<sub>3</sub>H<sub>6</sub>

- The higher heating values of the fuels are: propane, 50.38 MJ/kg; butane, 49.56 MJ/kg; propylene (propene), 48.95 MJ/kg.
- (a) Work out the overall combustion reaction for stoichiometric combustion of 1 mole of LPG with air, and the stoichiometric F/A and A/F.  
 (b) What are the higher and lower heating values for combustion of this fuel with excess air, per unit mass of LPG?
- 3.13. A spark-ignition engine is operated on isoctane fuel (C<sub>8</sub>H<sub>18</sub>). The exhaust gases are cooled, dried to remove water, and then analyzed for CO<sub>2</sub>, CO, H<sub>2</sub>, O<sub>2</sub>. Using the overall combustion reaction for a range of equivalence ratios from 0.5 to 1.5, calculate the mole fractions of CO<sub>2</sub>, CO, H<sub>2</sub>, and O<sub>2</sub> in the dry exhaust gas, and plot the results as a function of equivalence ratio. Assume:
- (a) that all the fuel is burnt inside the engine (almost true) and that the ratio of moles CO to moles H<sub>2</sub> in the exhaust is 3 : 1, and  
 (b) that there is no hydrogen in the exhaust for lean mixtures.
- For high-power engine operation the air/fuel ratio is 14 : 1. What is the exhaust gas composition, in mole fractions, before the water is removed?

## REFERENCES

1. Fristrom, R. M., and Westenberg, A. A.: *Flame Structure*, McGraw-Hill, 1965.
2. Glassman, I.: *Combustion*, Academic Press, 1977.
3. Kaye, G. W. C., and Laby, T. H.: *Tables of Physical and Chemical Constants*, Longmans, London, 1973.
4. Reynolds, W. C.: *Thermodynamic Properties in SI*, Department of Mechanical Engineering, Stanford University, 1979.
5. Taylor, C. F.: *The Internal Combustion Engine in Theory and Practice*, vol. 1, MIT Press, Cambridge, Mass., 1960.

6. Goodger, E. M.: *Hydrocarbon Fuels*, Macmillan, London, 1975.
7. Spalding, D. B., and Cole, E. H.: *Engineering Thermodynamics*, 3d ed., Edward Arnold, 1973.
8. JANAF Thermochemical Tables, National Bureau of Standards Publication NSRDS-NBS37, 1971.
9. Maxwell, J. B.: *Data Book on Hydrocarbons*, Van Nostrand, New York, 1950.
10. Rossini, F. D., Pitzer, K. S., Arnett, R. L., Braun, R. M., and Primentel, G. C.: *Selected Values of Physical and Thermodynamic Properties of Hydrocarbons and Related Compounds*, Carnegie Press, Pittsburgh, Pa., 1953.
11. Stull, D. R., Westrum, E. F., and Sinke, G. C.: *The Chemical Thermodynamics of Organic Compounds*, John Wiley, New York, 1969.
12. Matthews, R. D.: "Relationship of Brake Power to Various Energy Efficiencies and Other Engine Parameters: The Efficiency Rule," *Int. J. of Vehicle Design*, vol. 4, no. 5, pp. 491-500, 1983.
13. Keenan, J. H.: *Thermodynamics*, John Wiley, New York, 1941 (MIT Press, Cambridge, Mass., 1970).
14. Svehla, R. A., and McBride, B. J.: "Fortran IV Computer Program for Calculation of Thermodynamic and Transport Properties of Complex Chemical Systems," NASA Technical Note TN D-7056, NASA Lewis Research Center, 1973.

# CHAPTER

# 4

## PROPERTIES OF WORKING FLUIDS

### 4.1 INTRODUCTION

The study of engine operation through an analysis of the processes that occur inside the engine has a long and productive history. The earliest attempts at this analysis used the constant-volume and constant-pressure ideal cycles as approximations to real engine processes (see Chap. 5). With the development of high-speed digital computers, the simulation of engine processes has become much more sophisticated and accurate (see Chap. 14). All these engine simulations (from the simplest to the most complex) require models for the composition and properties of the working fluids inside the engine, as well as models for the individual processes—induction, compression, combustion, expansion, and exhaust—that make up the engine operating cycle. This chapter deals with models for the working fluid composition, and thermodynamic and transport properties.

The composition of the working fluid, which changes during the engine operating cycle, is indicated in Table 4.1. The unburned mixture for a spark-ignition engine during intake and compression consists of air, fuel, and previously burned gases. It is, therefore, a mixture of  $N_2$ ,  $O_2$ ,  $CO_2$ ,  $H_2O$ ,  $CO$ , and  $H_2$  for fuel-rich mixtures, and fuel (usually vapor). The composition of the unburned mixture does not change significantly during intake and compression. It is suffi-

TABLE 4.1  
Working fluid constituents

Process	Spark-ignition engine	Compression-ignition engine
Intake	Air Fuel† Recycled exhaust‡ Residual gas§	Air Recycled exhaust‡ Residual gas§
Compression	Air Fuel vapor Recycled exhaust Residual gas	Air Recycled exhaust Residual gas
Expansion	Combustion products (mixture of $N_2$ , $H_2O$ , $CO_2$ , $CO$ , $H_2$ , $O_2$ , $NO$ , $OH$ , $O$ , $H$ , ...)	Combustion products (mixture of $N_2$ , $H_2O$ , $CO_2$ , $CO$ , $H_2$ , $O_2$ , $NO$ , $OH$ , $O$ , $H$ , ...)
Exhaust	Combustion products [mainly $N_2$ , $CO_2$ , $H_2O$ , and either $O_2$ ( $\phi < 1$ ) or $CO$ and $H_2$ ( $\phi > 1$ )]	Combustion products [mainly $N_2$ , $CO_2$ , $H_2O$ , and $O_2$ ]

† Liquid and vapor in the intake; mainly vapor within the cylinder.

‡ Sometimes used to control  $NO_x$  emissions (see Secs. 11.2, 15.3.2, and 15.5.1).

§ Within the cylinder.

ciently accurate to assume the composition is *frozen*. For the compression-ignition engine, the unburned mixture prior to injection contains no fuel; it consists of air and previously burned gas.

The combustion products or burned mixture gases, during the combustion process and much of the expansion process, are close to *thermodynamic equilibrium*. The composition of such mixtures has already been discussed (Sec. 3.7.1). As these combustion products cool, recombination occurs as indicated in Fig. 3-10. Towards the end of the expansion process, the gas composition departs from the equilibrium composition; recombination can no longer occur fast enough to maintain the reacting mixture in equilibrium. During the exhaust process, reactions are sufficiently slow so that for calculating thermodynamic properties the composition can be regarded as *frozen*.

The models used for predicting the thermodynamic properties of unburned and burned mixtures can be grouped into the five categories listed in Table 4.2. The first category is only useful for illustrative purposes since the specific heats of unburned and burned mixtures are significantly different. While the specific heats of the working fluids increase with increasing temperature in the range of interest, a constant-specific-heat model can be matched to the thermodynamic data over a limited temperature range. This approach provides a simple *analytic* model which can be useful when moderate accuracy of prediction will suffice. The appropriateness of frozen and equilibrium assumptions has already been discussed above. Approximations to thermodynamic equilibrium calculations are useful because of

**TABLE 4.2**  
Categories of models for thermodynamic properties

Unburned mixture	Burned mixture
1. Single ideal gas throughout operating cycle with $c_v$ (and hence $c_p$ ) constant	
2. Ideal gas; $c_{v,u}$ constant	Ideal gas; $c_{v,b}$ constant
3. Frozen mixture of ideal gases; $c_{v,i}(T)$	Frozen mixture of ideal gases; $c_{v,b}(T)$
4. Frozen mixture of ideal gases; $c_{v,i}(T)$	Approximations fitted to equilibrium thermodynamic properties
5. Frozen mixture of ideal gases; $c_{v,i}(T)$	Mixture of reacting ideal gases in thermodynamic equilibrium

Note: Subscripts  $i$ ,  $u$ , and  $b$  denote species  $i$  in the gas mixture, the unburned mixture, and burned mixture properties, respectively.

the savings in computational time, relative to full equilibrium calculations, which can result from their use.

Values of thermodynamic properties of unburned and burned mixtures relevant to engine calculations are available from charts, tables, and algebraic relationships developed to match tabulated data. A selection of this material is included in this chapter and App. D. The references indicate additional sources.

## 4.2 UNBURNED MIXTURE COMPOSITION

The mass of charge trapped in the cylinder ( $m_c$ ) is the inducted mass per cycle ( $m_i$ ), plus the residual mass ( $m_r$ ) left over from the previous cycle. The residual fraction ( $x_r$ ) is

$$x_r = \frac{m_r}{m_c} \quad (4.1)$$

Typical residual fractions in spark-ignition engines range from 20 percent at light load to 7 percent at full load. In diesels, the residual fraction is smaller (a few percent) due to the higher compression ratio, and in naturally aspirated engines is approximately constant since the intake is unthrottled. If the inducted mixture is fuel and air (or air only), then the *burned gas fraction* ( $x_b$ ) in the unburned mixture during compression equals the residual fraction.

In some engines, a fraction of the engine exhaust gases is recycled to the intake to dilute the fresh mixture for control of  $\text{NO}_x$  emissions (see Sec. 11.2). If

the percent of exhaust gas recycled (%EGR) is defined as the percent of the total intake mixture which is recycled exhaust,<sup>†</sup>

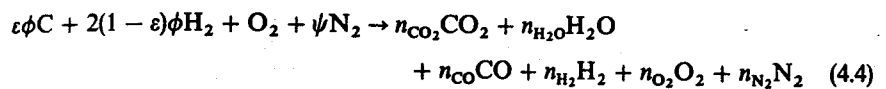
$$\text{EGR}(\%) = \left( \frac{m_{\text{EGR}}}{m_i} \right) \times 100 \quad (4.2)$$

where  $m_{\text{EGR}}$  is the mass of exhaust gas recycled, then the burned gas fraction in the fresh mixture is

$$x_b = \frac{m_{\text{EGR}} + m_r}{m_c} = \left( \frac{\text{EGR}}{100} \right) (1 - x_r) + x_r \quad (4.3)$$

Up to about 30 percent of the exhaust can be recycled; the burned gas fraction during compression can, therefore, approach 30 to 40 percent.

The composition of the burned gas fraction in the unburned mixture can be calculated as follows. The combustion equation for a hydrocarbon fuel of average molar H/C ratio  $y$  [e.g., Eq. (3.5)] can be written per mole  $\text{O}_2$  as



where  $\psi$  = the molar N/O ratio (3.773 for air)

$$\epsilon = \frac{4}{4+y}$$

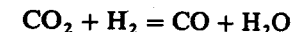
$y$  = the molar H/C ratio of the fuel

$\phi$  = fuel/air equivalence ratio

$n_i$  = moles of species  $i$  per mole  $\text{O}_2$  reactant

The  $n_i$  are determined using the following assumptions:

1. For lean and stoichiometric mixtures ( $\phi \leq 1$ )  $\text{CO}$  and  $\text{H}_2$  can be neglected.
2. For rich and stoichiometric mixtures ( $\phi \geq 1$ )  $\text{O}_2$  can be neglected.
3. For rich mixtures, either (a) the water gas reaction



<sup>†</sup> An alternative definition of percent EGR is also used based on the ratio of EGR to fresh mixture (fuel and air):

$$\text{EGR}^*(\%) = \left( \frac{m_{\text{EGR}}}{m_s + m_f} \right) \times 100$$

The two definitions are related by

$$\frac{\text{EGR}^*}{100} = \frac{\text{EGR}}{100 - \text{EGR}} \quad \text{and} \quad \frac{\text{EGR}}{100} = \frac{\text{EGR}^*}{100 + \text{EGR}^*}$$

can be assumed to be in equilibrium with the equilibrium constant  $K(T)$ :

$$K(T) = \frac{n_{H_2O} n_{CO}}{n_{CO_2} n_{H_2}}$$

where  $K(T)$  can be determined from a curve fit to JANAF table data:<sup>8</sup>

$$\ln K(T) = 2.743 - \frac{1.761 \times 10^3}{T} - \frac{1.611 \times 10^6}{T^2} + \frac{0.2803 \times 10^9}{T^3} \quad (4.5)$$

where  $T$  is in K, or (b)  $K$  can be assumed constant over the normal engine operating range. A value of 3.5 is often assumed (see Sec. 4.9), which corresponds to evaluating the equilibrium constant at 1740 K.

The  $n_i$  obtained from an element balance and the above assumptions are shown in Table 4.3. The value of  $c$  is obtained by solving the quadratic:

$$(K - 1)c^2 - c\{K[2(\phi - 1) + \varepsilon\phi] + 2(1 - \varepsilon\phi)\} + 2K\varepsilon\phi(\phi - 1) = 0 \quad (4.6)$$

The mole fractions are given by

$$\tilde{x}_i = \frac{n_i}{n_b}$$

where  $n_b = \sum_i n_i$  is given in the bottom line of Table 4.3.

While Eq. (4.4) is for a fuel containing C and H only, it can readily be modified for alcohols or alcohol-hydrocarbon blends. For a fuel of molar composition  $CH_y O_z$ , the reactant mixture

$$CH_y O_z + \frac{1}{\phi} \left(1 + \frac{y}{4} - \frac{z}{2}\right) (O_2 + \psi N_2)$$

can be rearranged per mole of  $O_2$  reactant as

$$\zeta \phi \varepsilon C + 2\zeta \phi (1 - \varepsilon) H_2 + O_2 + \left(1 - \frac{\varepsilon z}{2}\right) \zeta \psi N_2 \quad (4.7a)$$

TABLE 4.3  
Burned gas composition under 1700 K

Species	$n_i$ , moles/mole $O_2$ reactant	
	$\phi \leq 1$	$\phi > 1 \dagger$
$CO_2$	$\varepsilon\phi$	$\varepsilon\phi - c$
$H_2O$	$2(1 - \varepsilon)\phi$	$2(1 - \varepsilon\phi) + c$
$CO$	0	$c$
$H_2$	0	$2(\phi - 1) - c$
$O_2$	$1 - \phi$	0
$N_2$	$\psi$	$\psi$
Sum: $n_b$	$(1 - \varepsilon)\phi + 1 + \psi$	$(2 - \varepsilon)\phi + \psi$

<sup>†</sup>  $c$  defined by Eq. (4.6).

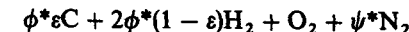
where

$$\zeta = \frac{2}{2 - \varepsilon z(1 - \phi)} \quad (4.7b)$$

If we write

$$\phi^* = \zeta \phi \quad \text{and} \quad \psi^* = \left(1 - \frac{\varepsilon z}{2}\right) \zeta \psi \quad (4.7c)$$

the reactant expression (4.7a) becomes



which is identical in form to the reactant expression for a hydrocarbon fuel (4.4). Thus Table 4.3 can still be used to give the composition of the burned gas residual fraction in the unburned mixture, except that  $\phi^*$  replaces  $\phi$  and  $\psi^*$  replaces  $\psi$  in the expressions for  $n_i$ .

Now consider the unburned mixture. The number of moles of fuel per mole  $O_2$  in the mixture depends on the molecular weight of the fuel,  $M_f$ . If the average molecular formula of the fuel is  $(CH_y)_a$  then

$$M_f = a(12 + y)$$

The fresh fuel-air mixture (not yet diluted with EGR or residual),



then becomes

$$\frac{4}{M_f} (1 + 2\varepsilon)\phi(CH_y)_a + O_2 + \psi N_2$$

The unburned mixture (fuel, air, and a burned gas fraction), per mole  $O_2$  in the mixture, can be written:

$$(1 - x_b) \left[ \frac{4}{M_f} (1 + 2\varepsilon)\phi(CH_y)_a + O_2 + \psi N_2 \right] + x_b(n_{CO_2} + n_{H_2O} + n_{CO} + n_{H_2} + n_{O_2} + n_{N_2})$$

The number of moles of each species in the unburned mixture, per mole  $O_2$ , is summarized in Table 4.4. The mole fractions of each species are obtained by dividing by the total number of moles of unburned mixture  $n_u$ ,

$$n_u = (1 - x_b) \left[ \frac{4(1 + 2\varepsilon)\phi}{M_f} + 1 + \psi \right] + x_b n_b \quad (4.8)$$

where  $n_b$  is given in Table 4.3.

The molecular weights of the (low-temperature) burned and unburned

**TABLE 4.4**  
Unburned mixture composition

Species	$n_i$ , moles/mole $O_2$ reactant	
	$\phi \leq 1$	$\phi > 1$
Fuel	$4(1 - x_b)(1 + 2\varepsilon)\phi/M_f$	
$O_2$	$1 - x_b\phi$	$1 - x_b$
$N_2$	$\psi$	$\psi$
$CO_2$	$x_b\varepsilon\phi$	$x_b(\varepsilon\phi - c)$
$H_2O$	$2x_b(1 - \varepsilon)\phi$	$x_b[2(1 - \varepsilon\phi) + c]$
CO	0	$x_b c$
$H_2$	0	$x_b[2(\phi - 1) - c]$
Sum†	$n_u$	$n_u$

† Given by Eq. (4.8).

mixture can now be determined. The mass of mixture (burned or unburned) per mole  $O_2$  in the mixture,  $m_{RP}$ , is given by

$$m_{RP} = 32 + 4\phi(1 + 2\varepsilon) + 28.16\psi \quad (4.9)$$

The molecular weight of the burned mixture,  $M_b$ , is therefore

$$M_b = \frac{m_{RP}}{n_b} \quad (4.10)$$

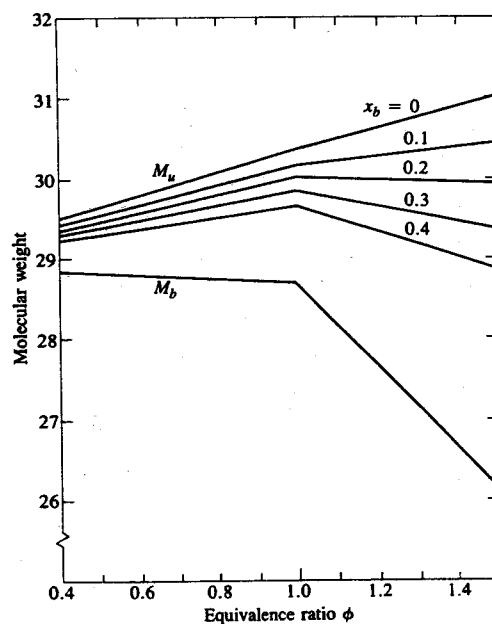


**FIGURE 4-1**  
Molecular weight of unburned and low-temperature burned isooctane-air mixtures as a function of fuel/air equivalence ratio and burned gas fraction.

**TABLE 4.5**  
Factors for relating properties on molar and mass basis

Quantity, per mole $O_2$ in the mixture	General equation‡	Equation for $C_8H_{18}$ -air mixtures
Moles of burned mixture $n_b$	$n_b = (1 - \varepsilon)\phi + 1 + \psi,$ $n_b = (2 - \varepsilon)\phi + \psi,$	$\phi \leq 1 \quad n_b = 0.36\phi + 4.773$ $\phi > 1 \quad n_b = 1.36\phi + 3.773$
Moles of unburned mixture $n_u$	$(1 - x_b) \left[ \frac{4(1 + 2\varepsilon)\phi}{M_f} + 1 + \psi \right] + x_b n_b$	$\begin{cases} \phi \leq 1 \\ \phi > 1 \end{cases} \quad \begin{aligned} n_u &= 0.08\phi + 4.773 \\ &\quad + 0.28x_b\phi \\ n_u &= 0.08\phi + 4.773 \\ &\quad + x_b(1.28\phi - 1) \end{aligned}$
Mass of mixture† (burned or unburned)	$m_{RP} = 32 + 4\phi(1 + 2\varepsilon) + 28.16\psi$	$138.2 + 9.12\phi$
Mass of air†	$32 + 28.16\psi$	$138.2$

† Units: kg/kmol or lbm/lb · mol.

‡ For hydrocarbon fuels,  $\psi$  for air = 3.773; for fuels containing oxygen,  $\phi^*$  and  $\psi^*$  given by Eq. (4.7c) are substituted for  $\phi$  and  $\psi$ , respectively.

The molecular weight of the unburned mixture,  $M_u$ , is

$$M_u = \frac{m_{RP}}{n_u} \quad (4.11)$$

Figure 4-1 gives  $M_u$  and  $M_b$  for a range of  $\phi$  and  $x_b$  for air, isooctane, burned gas mixtures.

Frequently, thermodynamic properties of unburned and burned mixtures are expressed per unit mass of air in the original mixture (for burned mixture this is the mixture before combustion). To obtain properties in these units, we need the mass of original air, per mole  $O_2$  in the mixture, which is

$$(32 + 28.16 \psi)$$

with units of kilograms per kilomole or pound-mass per pound-mole.

Table 4.5 summarizes the factors needed to relate properties expressed on a molar and a mass basis.

### 4.3 GAS PROPERTY RELATIONSHIPS

The individual species in the unburned and burned gas mixtures can with sufficient accuracy be modeled as ideal gases. Ideal gas relationships are reviewed in App. B. The most important relationships for property determination for engine calculations are summarized below.

Since internal energy and enthalpy are functions of temperature only, the specific heats at constant volume and constant pressure are given by

$$c_v = \left( \frac{\partial u}{\partial T} \right)_v = \frac{du}{dT} = c_v(T) \quad (4.12a)$$

$$c_p = \left( \frac{\partial h}{\partial T} \right)_p = \frac{dh}{dT} = c_p(T) \quad (4.12b)$$

and

$$u - u_0 = \int_{T_0}^T c_v dT \quad (4.13a)$$

$$h - h_0 = \int_{T_0}^T c_p dT \quad (4.13b)$$

The entropy  $s(T, v)$  or  $s(T, p)$  is given by

$$s - s_0 = \int_{T_0}^T c_v \frac{dT}{T} + R \ln \frac{v}{v_0} \quad (4.14a)$$

$$s - s_0 = \int_{T_0}^T c_p \frac{dT}{T} - R \ln \frac{p}{p_0} \quad (4.14b)$$

The integrals in Eqs. (4.14a, b) are functions of temperature only, and are useful in evaluating entropy changes and in following isentropic processes. If we define

$$\Psi(T) = \int_{T_0}^T c_v(T) \frac{dT}{T} \quad (4.15a)$$

$$\Phi(T) = \int_{T_0}^T c_p(T) \frac{dT}{T} \quad (4.15b)$$

and

$$s - s_0 = \Psi + R \ln \left( \frac{v}{v_0} \right) \quad (4.16a)$$

$$s - s_0 = \Phi - R \ln \left( \frac{p}{p_0} \right) \quad (4.16b)$$

Thus, for example, the entropy change between states  $(T_1, p_1)$  and  $(T_2, p_2)$  is

$$s_2 - s_1 = \Phi_2 - \Phi_1 - R \ln \left( \frac{p_2}{p_1} \right) \quad (4.17)$$

For an isentropic process,

$$\ln \left( \frac{p_2}{p_1} \right) = \frac{\Phi_2 - \Phi_1}{R} \quad (4.18)$$

In these equations, the units of  $u$  and  $h$  can be on a per unit mass or molar basis [i.e., joules per kilogram (British thermal units per pound-mass) or joules per kilomole (British thermal units per pound-mole)]; similarly,  $s$ ,  $c_v$ ,  $c_p$ ,  $R$ ,  $\Psi$ , and  $\Phi$  can be in joules per kilogram-kelvin (British thermal units per pound-mass-degree Rankine) or joules per kilomole-kelvin (British thermal units per pound-mole-degree Rankine).

For gas mixtures, once the composition is known, mixture properties are determined either on a mass or molar basis from

$$u = \sum x_i u_i \quad \tilde{u} = \sum \tilde{x}_i \tilde{u}_i \quad (4.19a)$$

$$h = \sum x_i h_i \quad \tilde{h} = \sum \tilde{x}_i \tilde{h}_i \quad (4.19b)$$

$$s = \sum x_i s_i \quad \tilde{s} = \sum \tilde{x}_i \tilde{s}_i \quad (4.19c)$$

and

$$c_v = \sum x_i c_{v,i} \quad \tilde{c}_v = \sum \tilde{x}_i \tilde{c}_{v,i} \quad (4.20a)$$

$$c_p = \sum x_i c_{p,i} \quad \tilde{c}_p = \sum \tilde{x}_i \tilde{c}_{p,i} \quad (4.20b)$$

#### 4.4 A SIMPLE ANALYTIC IDEAL GAS MODEL

While the first category of model listed in Table 4.2 is too inaccurate for other than illustrative purposes, the second category—constant but different specific heats for the unburned and burned gas mixtures—can with careful choice of specific heat values be made much more precise. The advantages of a simple analytic model may be important for certain problems.

Figure 4-2 shows an internal energy versus temperature plot for a stoichiometric mixture. It is a quantitative version of Fig. 3-5. The unburned mixture line is for a burned gas fraction of 0.1. The fuel is isoctane. Data to construct such graphs can be obtained from charts or tables or computer programs (see Secs. 4.5 to 4.7). The units for  $u$  are kilojoules per kilogram of air in the original mixture (the units of the charts in Sec. 4.5). The datum is zero enthalpy for  $O_2$ ,  $N_2$ ,  $H_2$ , and C (solid) at 298 K. Note that the specific heats of the unburned and burned mixtures (the slopes of the lines in Fig. 4-2) are a function of temperature; at high temperatures, the internal energy of the burned mixture is a function of temperature and pressure.

However, the temperature range of interest for the unburned mixture in an SI engine is 400 to 900 K (700 to 1600°R); for the burned gas mixture, the extreme end states are approximately 2800 K, 35 atm (5000°R, 500 lb/in<sup>2</sup> abs) and 1200 K, 2 atm (2200°R, 30 lb/in<sup>2</sup> abs). Linear approximations to the unburned and burned mixture curves which minimize the error in  $u$  over the temperature (and pressure) ranges of interest are shown as dashed lines. The error in  $T$  for a given  $u$  is less than 50 K.

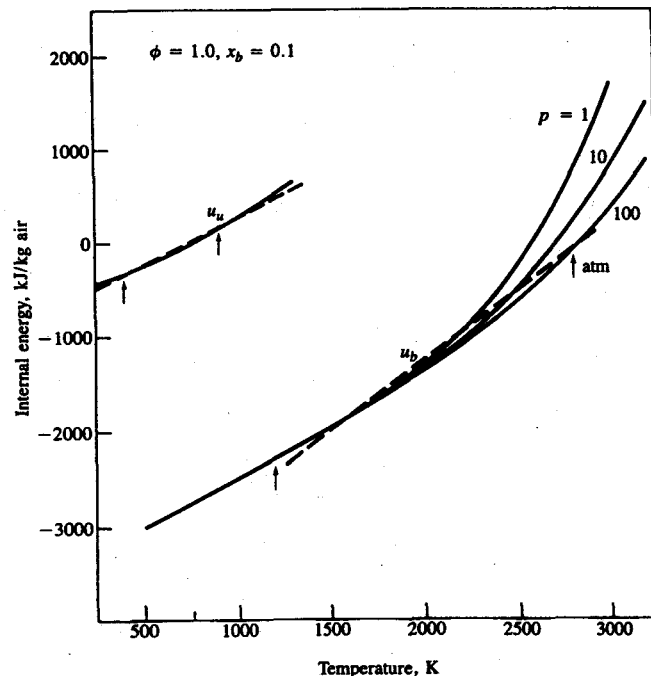


**FIGURE 4-2**  
Internal energy versus temperature plot for stoichiometric unburned and burned gas mixtures: iso-octane fuel; unburned residual fraction 0.1.

The basis for this ideal gas model is

$$u_u = c_{v,u} T_u + h_{f,u} \quad h_u = c_{p,u} T_u + h_{f,u} \quad (4.21a, b)$$

$$u_b = c_{v,b} T_b + h_{f,b} \quad h_b = c_{p,b} T_b + h_{f,b} \quad (4.22a, b)$$

where  $h_{f,u}$  and  $h_{f,b}$  are the enthalpies of formation of unburned and burned gas mixture, respectively, at 0 K.

Then, for a constant-volume adiabatic combustion process,

$$u_u = u_b$$

$$\text{or} \quad c_{v,u} T_u + h_{f,u} = c_{v,b} T_b + h_{f,b}$$

If we solve for  $T_b$  and use the relations  $(R_b/R_u) = (M_u/M_b)$  and  $c_v/R = 1/(\gamma - 1)$ , we obtain

$$T_b = (\gamma_b - 1) \left( \frac{M_b}{M_u} \right) \left( \frac{T_u}{\gamma_u - 1} + \frac{\Delta h_f}{R_u} \right) \quad (4.23)$$

where  $\Delta h_f = h_{f,u} - h_{f,b}$ .

For a constant-pressure adiabatic combustion process,

$$h_u = h_b$$

and it can similarly be shown that

$$T_b = \frac{\gamma_b - 1}{\gamma_b} \left( \frac{M_b}{M_u} \right) \left( \frac{\gamma_u}{\gamma_u - 1} T_u + \frac{\Delta h_f}{R_u} \right) \quad (4.24)$$

To use the model, suitable values of  $\gamma_u$ ,  $\gamma_b$ ,  $M_u$ ,  $(M_b/M_u)$ , and  $\Delta h_f/R_u$  must be determined. Values for  $M_u$  and  $M_b$  can be obtained from Eqs. (4.10) and (4.11).† Values of  $\gamma_u$ ,  $\gamma_b$ , and  $\Delta h_f/R_u$  can be obtained from graphs such as Fig. 4-2 (see Example 4.1 below). Values for  $\gamma_u$ ,  $\gamma_b$ , and  $\Delta h_f/R_u$  are available in the literature (e.g., Refs. 1 and 2) for a range of  $\phi$  and  $x_b$ . However, values used for computations should always be checked over the temperature range of interest, to ensure that the particular linear fit to  $u(T)$  used is appropriate.

**Example 4.1.** Determine the values of  $\gamma_u$ ,  $\gamma_b$ , and  $\Delta h_f/R_u$  which correspond to the straight-line fits for  $u_u(T)$  and  $u_b(T)$  in Fig. 4-2.

Equations for the straight lines in Fig. 4-2 are

$$u_u \text{ (kJ/kg air)} = 0.96T(K) - 700$$

and

$$u_b \text{ (kJ/kg air)} = 1.5T(K) - 4250$$

From Table 4.5, for iso-octane fuel with  $\phi = 1.0$  and  $x_b = 0.1$ , the number of moles of unburned mixture per mole  $O_2$  in the mixture is

$$n_u = 0.08 \times 1 + 4.773 + 0.28 \times 0.1 \times 1 = 4.881$$

The mass of air per mole  $O_2$  in the mixture is 138.2. Thus, the number of moles of unburned mixture per unit mass of air in the original mixture is

$$\frac{4.881}{138.2} = 0.0353$$

The molar specific heat of the unburned mixture  $\tilde{c}_{v,u}$  is therefore

$$\tilde{c}_{v,u} = \frac{0.96}{0.0353} = 27.2 \text{ kJ/kmol} \cdot \text{K}$$

Since  $\tilde{R} = 8.314 \text{ kJ/kmol} \cdot \text{K}$ ,

$$\gamma_u = \frac{27.2 + 8.314}{27.2} = 1.31$$

The number of moles of burned mixture per mole  $O_2$  is (from Table 4.5)

$$n_b = 0.36 \times 1 + 4.773 = 5.133$$

† The error in ignoring the effect of dissociation on  $M_b$  is small.

The number of moles of burned mixture per unit mass of air in the original mixture is

$$\frac{5.133}{138.2} = 0.0371$$

The molar specific heat  $\tilde{c}_{v,b}$  is therefore

$$\tilde{c}_{v,b} = \frac{1.5}{0.0371} = 40.4 \text{ kJ/kmol}\cdot\text{K}$$

and  $\gamma_b$  is

$$\gamma_b = \frac{40.4 + 8.314}{40.4} = 1.21$$

To find  $\Delta h_f/R_u$ ,  $R_u$  is given by

$$R_u = 8.314 \times 0.0353 = 0.293 \text{ kJ/kg air}\cdot\text{K}$$

and so

$$\frac{\Delta h_f}{R_u} = \frac{(-700) - (-4250)}{0.293} = 1.2 \times 10^4 \text{ K}$$

## 4.5 THERMODYNAMIC CHARTS

One method of presenting thermodynamic properties of unburned and burned gas mixtures for internal combustion engine calculations is on charts. Two sets of charts are in common use: those developed by Hottel *et al.*<sup>3</sup> and those developed by Newhall and Starkman.<sup>4,5</sup> Both these sets of charts use U.S. units. We have developed a new set of charts in SI units, following the approach of Newhall and Starkman. Charts are no longer used extensively for engine cycle calculations; computer models for the thermodynamic properties of working fluids have replaced the charts. Nonetheless, charts are useful for illustrative purposes, and afford an easy and accurate method where a limited number of calculations are required. The charts presented below are for isoctane fuel, and the following equivalence ratios:  $\phi = 0.4, 0.6, 0.8, 1.0, 1.2$ .

### 4.5.1 Unburned Mixture Charts

The thermodynamic properties of each unburned fuel-air mixture are represented by two charts. The first chart is designed to relate the mixture temperature, pressure, and volume at the beginning and at the end of the compression process; the second gives the mixture internal energy and enthalpy as functions of temperature.

The following assumptions are made:

1. The compression process is reversible and adiabatic.

TABLE 4.6  
Unburned mixture composition for charts

Equivalence ratio $\phi$	(F/A)	Kilograms of mixture per kilogram of air	Moles of mixture per mole of O <sub>2</sub>	Kilomole of mixture per kilogram of air	$n_u \bar{R}_t$ J/kg air·K
0.4	0.0264	1.0264	4.805 + 0.112x <sub>b</sub>	0.0348 + 0.00081x <sub>b</sub>	289
0.6	0.0396	1.0396	4.821 + 0.168x <sub>b</sub>	0.0349 + 0.00122x <sub>b</sub>	290
0.8	0.0528	1.0528	4.837 + 0.224x <sub>b</sub>	0.0350 + 0.00162x <sub>b</sub>	291
1.0	0.0661	1.0661	4.853 + 0.280x <sub>b</sub>	0.0351 + 0.00203x <sub>b</sub>	292
1.2	0.0792	1.0792	4.869 + 0.536x <sub>b</sub>	0.0352 + 0.00388x <sub>b</sub>	292

† For  $x_b = 0$ . Error in neglecting  $x_b$  is usually small.

2. The fuel is in the vapor phase.
3. The mixture composition is homogeneous and frozen (no reactions between the fuel and air).
4. Each species in the mixture can be modeled as an ideal gas.
5. The burned gas fraction is zero.†

It proves convenient to assign zero internal energy or enthalpy to the unburned mixture at 298.15 K. Internal energy and enthalpies relative to this datum are called *sensible internal energy u<sub>s</sub>* or *sensible enthalpy h<sub>s</sub>*. By sensible we mean changes in *u* or *h* which result from changes in temperature alone, and we exclude changes due to chemical reaction or phase change.

Table 4.6 provides the basic composition data for the unburned mixture charts. Equations (4.13a, b) provide the basis for obtaining the *u<sub>s,u</sub>(T)* and *h<sub>s,u</sub>(T)* curves shown in Fig. 4-3.

Equations (4.15) and (4.16) provide the basis for following a reversible adiabatic (i.e., isentropic) compression process. Between end states 1 and 2, we obtain, per kilogram of air in the mixture,

$$\Psi(T_2) = \Psi(T_1) - n_u \bar{R} \ln \left( \frac{v_2}{v_1} \right) \quad (4.25a)$$

$$\Phi(T_2) = \Phi(T_1) + n_u \bar{R} \ln \left( \frac{p_2}{p_1} \right) \quad (4.25b)$$

where  $n_u$  is the number of moles of unburned mixture per kilogram of air. Values

† This assumption introduces negligible error into calculations of the compression process for mixtures with normal burned gas fractions, since the major constituent of the residual is N<sub>2</sub>. The burned gas fraction must, however, be included when the unburned mixture properties are related to burned mixture properties in a combustion process.

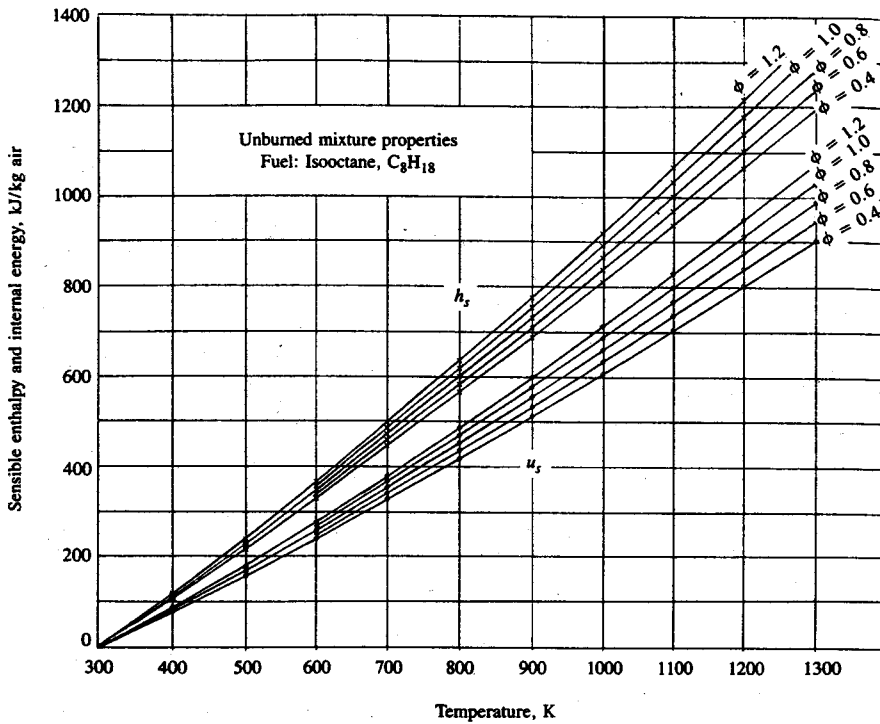


**FIGURE 4-3**  
Sensible enthalpy and internal energy of unburned isoctane-air mixtures as function of temperature.  
Units: kJ/kg air in mixture.

of  $n_u$  and  $n_u \tilde{R}$  are given in Table 4.6.  $\Psi(T)$  and  $\Phi(T)$  are given in Fig. 4-4. Note that  $v$ ,  $p$ , and  $T$  are related by

$$p(\text{Pa})v(\text{m}^3/\text{kg air}) = n_u \tilde{R}(\text{J/kg air} \cdot \text{K})T(\text{K}) \quad (4.26)$$

**Example 4.2.** The compression process in an internal combustion engine can be modeled approximately as adiabatic and reversible (i.e., as an isentropic process). A spark-ignition engine with a compression ratio of 8 operates with a stoichiometric fuel vapor-air mixture which is at 350 K and 1 atm at the start of the compression stroke. Find the temperature, pressure, and volume per unit mass of air at the end of the compression stroke. Calculate the compression stroke work.

Given  $T_1 = 350$  K at the start of compression, find  $T_2$  at the end of compression using the isentropic compression chart, Fig. 4-4, and Eq. (4.25a). For  $T_1 = 350$  K,  $\Psi_1 = 150$  J/kg air · K. From Eq. (4.25a),

$$\Psi_2(T_2) = \Psi_1(T_1) - n_u \tilde{R} \ln\left(\frac{v_2}{v_1}\right) = 150 - 292 \ln\left(\frac{1}{8}\right) = 757 \text{ J/kg air} \cdot \text{K}$$

Figure 4-4 then gives

$$T_2 = 682 \text{ K}$$

The ideal gas law [Eq. (4.26)] gives

$$v_1 = \frac{292 \times 350}{1 \times 1.013 \times 10^5} = 1.0 \text{ m}^3/\text{kg air}$$

and

$$p_2 = p_1 \left( \frac{T_2}{T_1} \right) \left( \frac{v_1}{v_2} \right) = \frac{682}{350} \times 8 = 15.5 \text{ atm}$$

$$v_2 = \frac{1.0}{8} = 0.125 \text{ m}^3/\text{kg air}$$

Note that  $p_2$  can also be obtained from Fig. 4-4 and Eq. (4.25b):

$$\ln\left(\frac{p_2}{p_1}\right) = \frac{\Phi_2 - \Phi_1}{n_u \tilde{R}} = \frac{980 - 180}{292} = 2.74$$

$$p_2 = 15.5 \text{ atm} = 1.57 \text{ MPa}$$

The compression stroke work, assuming the process is adiabatic and using the data in Fig. 4-3, is

$$-W_{1-2} = u_s(T_2) - u_s(T_1) = 350 - 40 = 310 \text{ kJ/kg air}$$

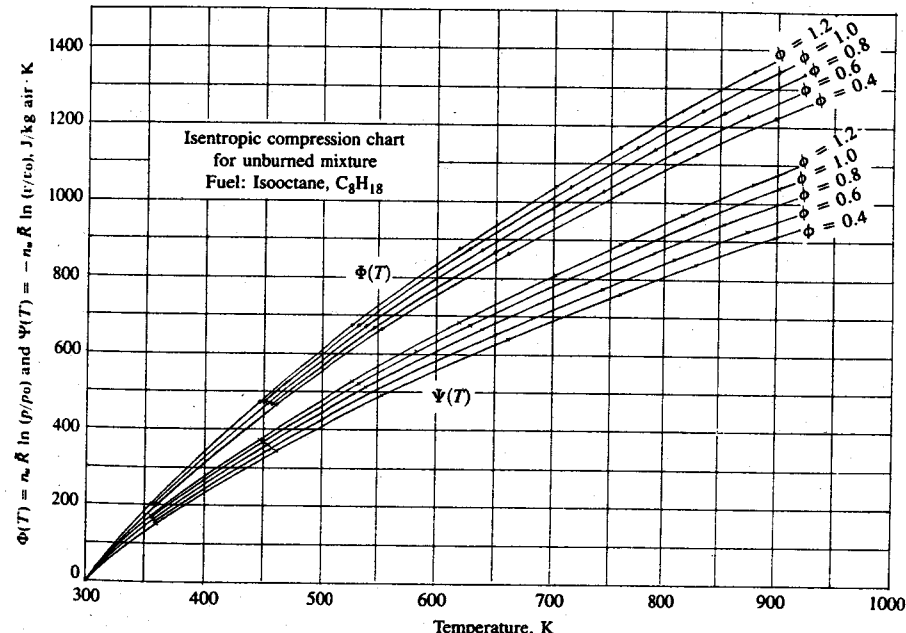


**FIGURE 4-4**  
Isentropic compression functions,  $\Phi$  and  $\Psi$ , as function of temperature for unburned isoctane-air mixtures. Units: J/kg air · K.

#### 4.5.2 Burned Mixture Charts

The primary burned mixture charts are for the products of combustion at high temperatures, i.e., for the working fluid during the expansion process. The following assumptions are made:

1. Each species in the mixture can be modeled as an ideal gas.
2. The mixture is in thermodynamic equilibrium at temperatures above 1700 K; the mixture composition is frozen below 1700 K.
3. *Datum.* At the datum state of 298.15 K (25°C or 77°F) and 1 atm the chemical elements in their naturally occurring form ( $N_2$ ,  $O_2$ ,  $H_2$  as diatomic gases and C as solid graphite) are assigned zero enthalpy and entropy.

The charts were prepared with the NASA equilibrium program described in Sec. 3.7.<sup>9,10</sup> The C/H/O/N ratio of the mixture is specified for each chart. The extensive properties (internal energy, enthalpy, entropy, and specific volume) are all expressed per unit mass of air in the original mixture; i.e., they correspond to the combustion of 1 kg of air with the appropriate mass of fuel. The mass basis for the unburned and burned mixture charts are the same.

Figures 4-5 to 4-9 are property charts for the high-temperature burned gas; each is a plot of internal energy versus entropy for a particular fuel and equivalence ratio. Lines of constant temperature, pressure, and specific volume are drawn on each chart. An illustration of the use of these charts follows.

**Example 4.3.** The expansion process in an internal combustion engine, following completion of combustion, can be modeled approximately as an adiabatic and reversible process (i.e., isentropic). Under full-load operation, the pressure in the cylinder of a spark-ignition engine at top-center immediately following combustion is 7100 kPa. Find the gas state at the end of the expansion stroke and the expansion stroke work. The compression ratio is 8, the mixture is stoichiometric, and the volume per unit mass of air at the start of expansion is  $0.125 \text{ m}^3/\text{kg air}$ .

Locate  $p_1 = 7100 \text{ kPa}$  and  $v_1 = 0.125 \text{ m}^3/\text{kg air}$  on the  $\phi = 1.0$  burned gas chart (Fig. 4-8). This gives  $T_1 = 2825 \text{ K}$ ,  $u_1 = -5 \text{ kJ/kg air}$ , and  $s_1 = 9.33 \text{ kJ/kg air} \cdot \text{K}$ . The gas expands at constant entropy to  $v_2 = 8 \times v_1 = 1 \text{ m}^3/\text{kg air}$ . Following a constant entropy process from state 1 on Fig. 4-8 gives

$$T_2 = 1840 \text{ K}, \quad p_2 = 570 \text{ kPa}, \quad \text{and} \quad u_2 = -1540 \text{ kJ/kg air}$$

The expansion stroke work, assuming the process is adiabatic, is

$$W_{1-2} = -(u_2 - u_1) = 1540 - 5 = 1535 \text{ kJ/kg air}$$

As the burned gases in an engine cylinder cool during the expansion process, the composition eventually "freezes"—becomes fixed in composition—because the chemical reactions become extremely slow. This is usually assumed to occur at about 1700 K (see Sec. 4.9). The equilibrium assumption is then no longer valid. For lean and stoichiometric mixtures this distinction is not important because the mole fractions of dissociated species below this temperature are

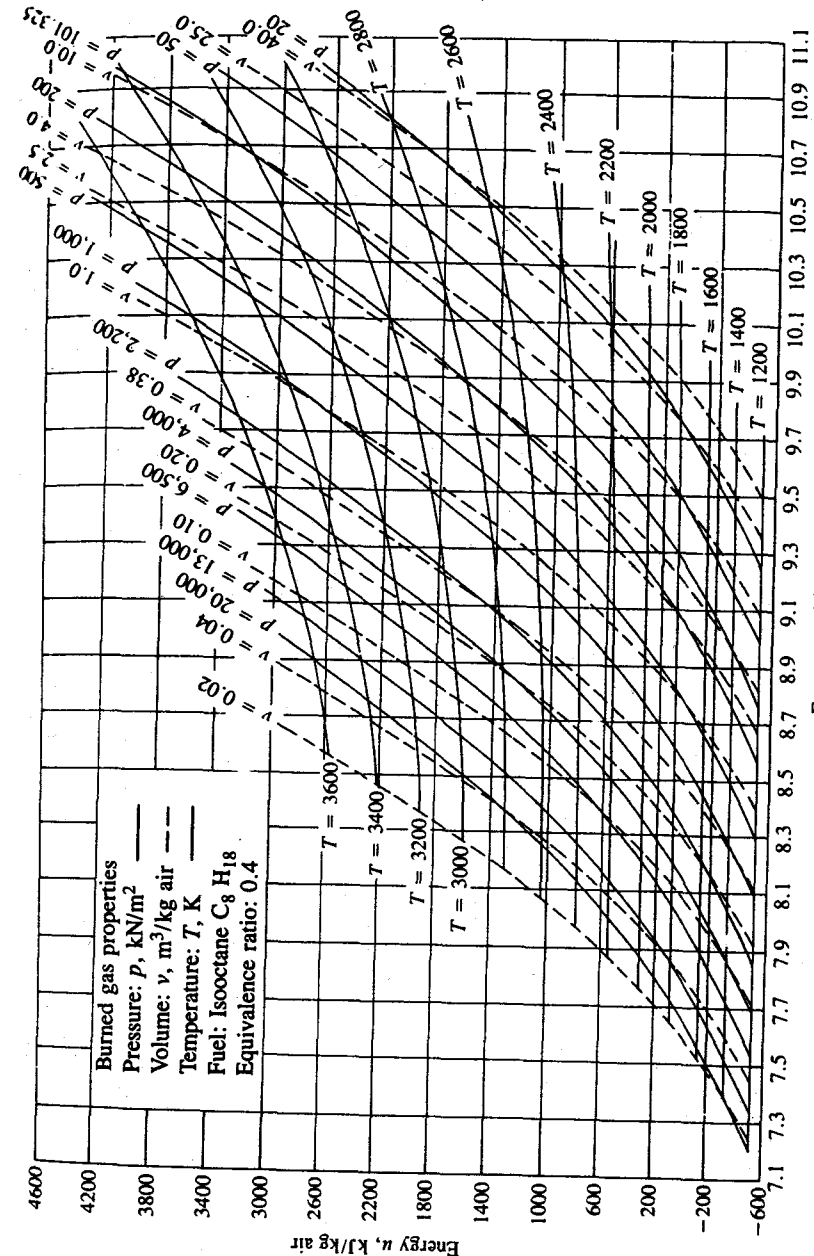
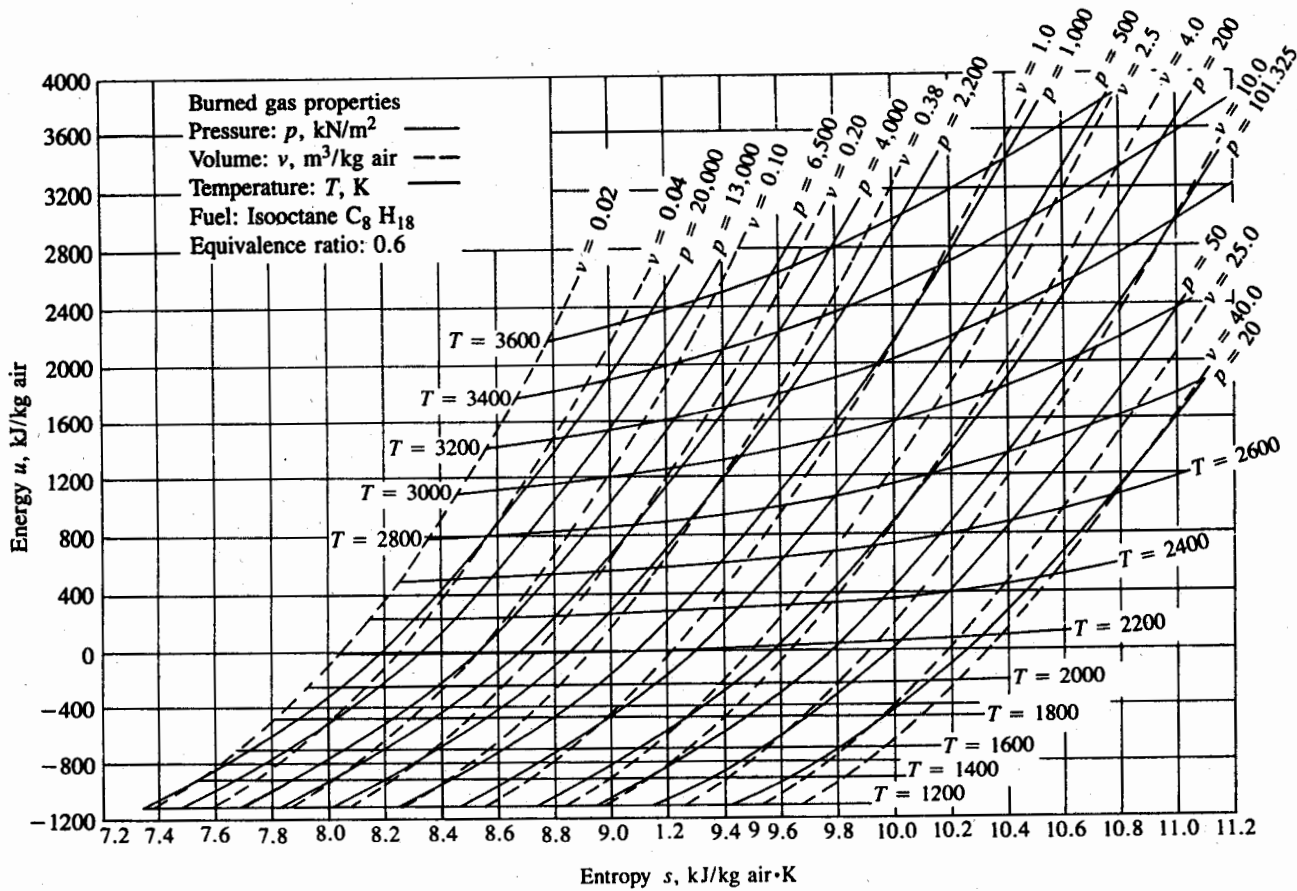
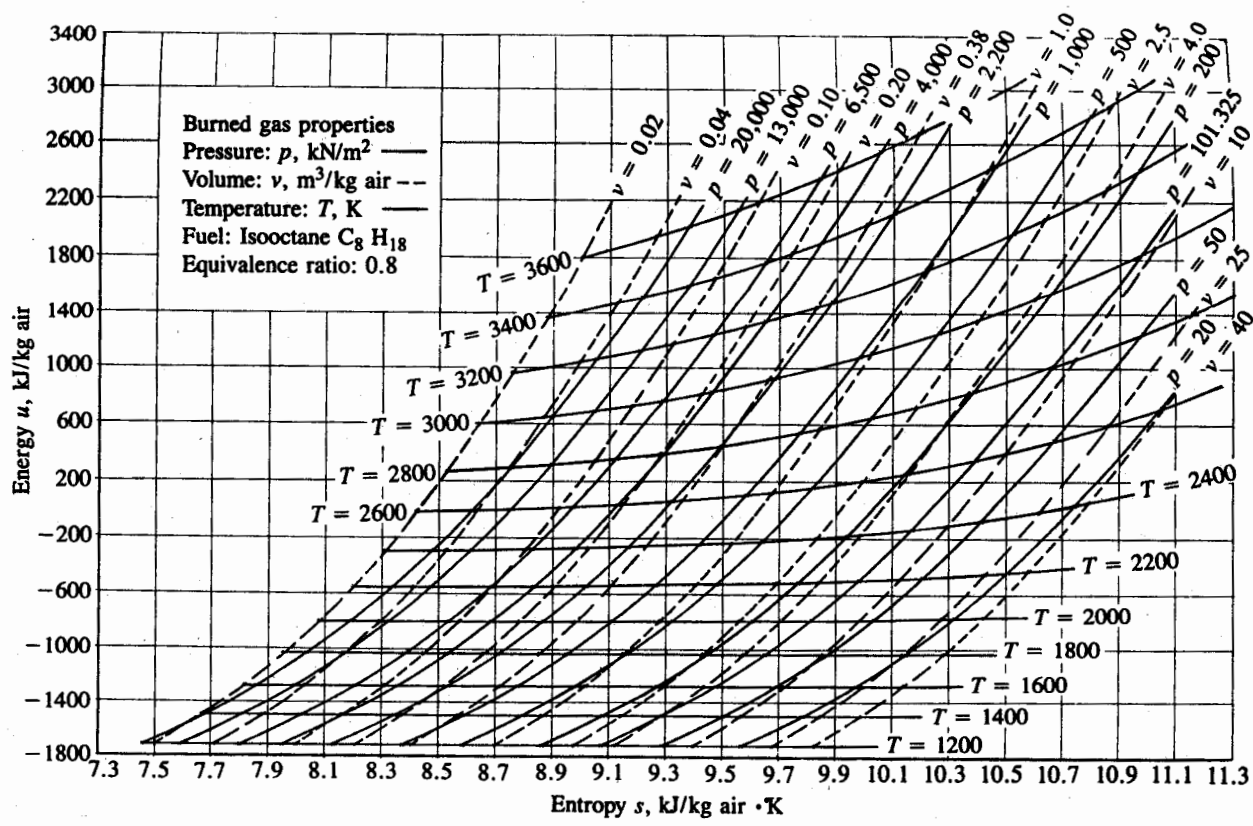


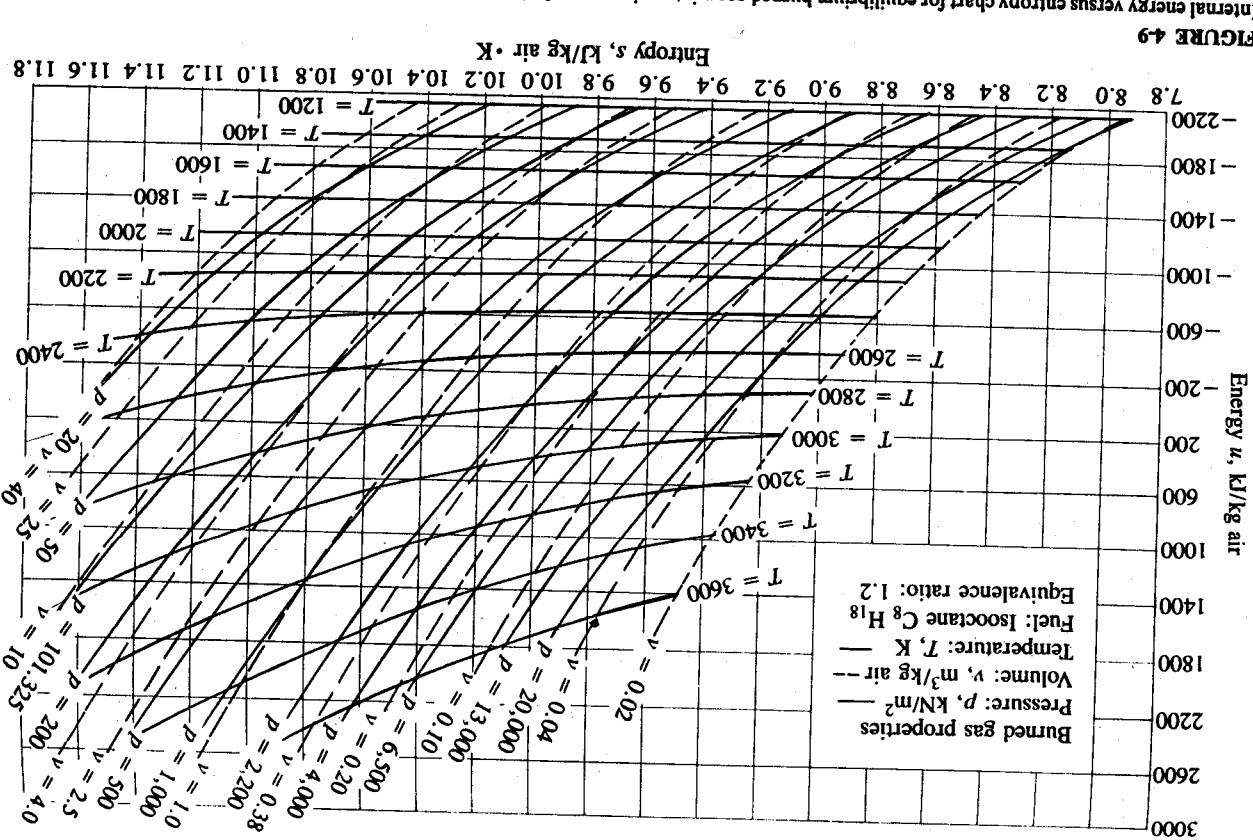
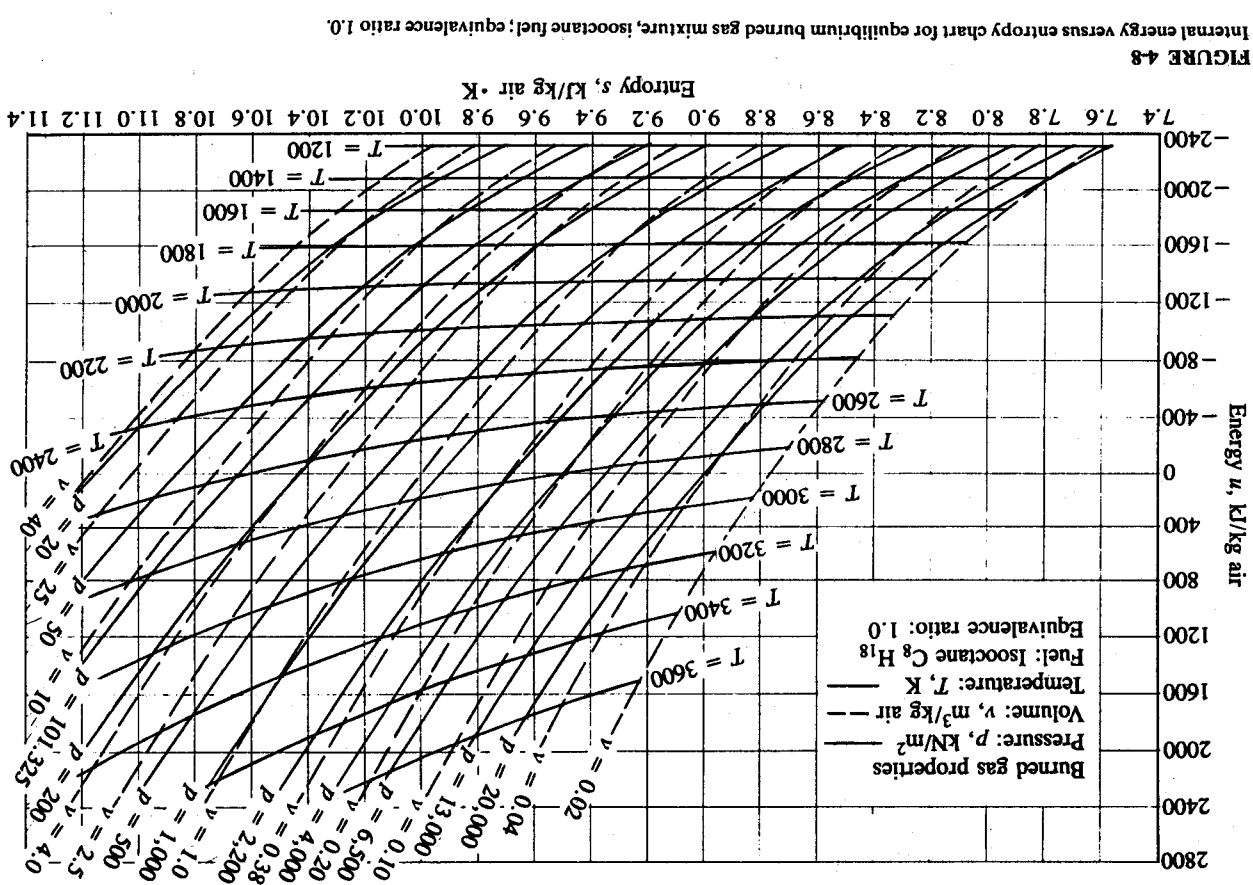
FIGURE 4-5  
Internal energy versus entropy chart for equilibrium burned gas mixture, isoctane fuel; equivalence ratio 0.4.



**FIGURE 4-6**  
 Internal energy versus entropy chart for equilibrium burned gas mixture, isoctane fuel; equivalence ratio 0.6.



**FIGURE 4-7**  
 Internal energy versus entropy chart for equilibrium burned gas mixture, isoctane fuel; equivalence ratio 0.8.



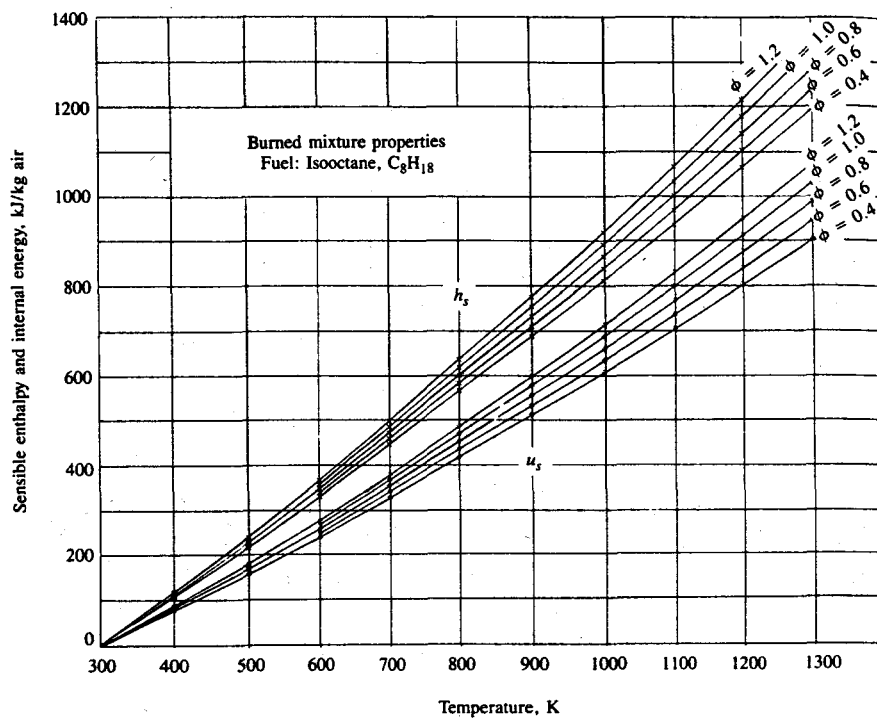


**FIGURE 4-10**  
Sensible enthalpy and internal energy of low-temperature burned gases as function of temperature, isoctane fuel. Units: kJ/kg air in original mixture.

**TABLE 4.7**  
Frozen burned gas composition:  $C_8H_{18}$ -air combustion

$\phi$	$CO_2$	$H_2O$	$CO$	$H_2$	$O_2$	$N_2$	Sum	Units
0.4	0.0521	0.0586	—	—	0.122	0.767	1.000	mole fractions
1.85	2.08	—	—	—	4.34	27.3	35.6	mol/kg air‡
0.6	0.0770	0.0866	—	—	0.0802	0.756	1.000	mole fractions
2.78	3.13	—	—	—	2.89	27.3	36.1	mol/kg air‡
0.8	0.101	0.113	—	—	0.0395	0.746	1.000	mole fractions
3.70	4.14	—	—	—	1.45	27.3	36.6	mol/kg air‡
1.0	0.125	0.140	—	—	—	0.735	1.000	mole fractions
4.64	5.2	—	—	—	—	27.3	37.1	mol/kg air‡
1.2†	0.0905	0.138	0.0516	0.0224	—	0.698	1.000	mole fractions
	3.54	5.38	2.02	0.876	—	27.3	39.1	mol/kg air‡

†  $K(T)$  in Eq. (4.6) evaluated at 1740 K;  $K = 3.5$ .

‡ Note mol/kg air; multiply by  $10^{-3}$  for kmol/kg air.

small. For rich mixtures, a frozen composition must be selected and used because the mole fractions of  $CO_2$ ,  $CO$ ,  $H_2O$ , and  $H_2$  would continue to change if equilibrium is assumed as the temperature decreases. Internal energy and enthalpy, per kilogram of air in the original mixture, of the frozen burned mixture are plotted against temperature in Fig. 4-10. The assumed frozen burned mixture compositions are listed in Table 4.7. These are sensible internal energies and enthalpies, given relative to their values at 298.15 K.

#### 4.5.3 Relation between Unburned and Burned Mixture Charts

We now address the questions: Given unburned mixture at  $T_1$ ,  $p_1$ ,  $v_1$ , what is the state of the burned mixture following (1) constant-volume adiabatic combustion or (2) constant-pressure adiabatic combustion?

The datum for internal energy and enthalpy for the unburned mixture in Fig. 4-3 is different from the datum for internal energy and enthalpy for the burned mixture. For the unburned mixture, zero internal energy and enthalpy for the mixture at 298.15 K was assumed. For the burned mixture, zero enthalpy for the gaseous species  $O_2$ ,  $N_2$ , and  $H_2$ , and C (solid graphite) at 298.15 K was assumed. These data can be related through the enthalpies of formation, from  $O_2$ ,  $N_2$ ,  $H_2$ , and C, of each species in the unburned mixture.

If  $\Delta h_{f,i}^\circ$  is the enthalpy of formation of species  $i$  at 298.15 K, per kilomole, and  $\Delta h_{f,u}^\circ$  is the enthalpy of formation of the unburned mixture at 298.15 K, per kilogram of air in the original mixture, then

$$\Delta h_{f,u}^\circ = \sum_i n_i \Delta h_{f,i}^\circ \quad (4.27)$$

where  $n_i$  is the number of kilomoles of species  $i$  per kilogram of air. The unburned mixture enthalpy  $h_u$ , with the same datum as the burned mixture enthalpy, is therefore given by the sum of the sensible enthalpy  $h_{s,u}$  and  $\Delta h_{f,u}^\circ$ :

$$h_u = h_{s,u} + \Delta h_{f,u}^\circ \quad (4.28)$$

Similarly, the internal energy  $u_u$  is given by

$$u_u = u_{s,u} + \Delta u_{f,u}^\circ \quad (4.29)$$

$\Delta u_{f,u}^\circ$  can be obtained from

$$\Delta u_{f,u}^\circ = \sum_i n_i \Delta \tilde{u}_{f,i}^\circ \quad (4.30)$$

Alternately, Eq. (3.18) can be used to obtain  $\Delta u_{f,u}^\circ$  from  $\Delta h_{f,u}^\circ$ :

$$\Delta u_{f,u}^\circ = \Delta h_{f,u}^\circ - (n_p - n_R) \tilde{R} T \quad (4.31)$$

Enthalpies and internal energies of formation of the relevant burned gas species and individual fuel compounds are given in Table 4.8 and App. D. Values of  $n_i$  are obtained from Tables 4.4 and 4.7. Following the procedure used in Example 4.4 below, expressions for  $\Delta h_{f,u}^\circ$  and  $\Delta u_{f,u}^\circ$  in kilojoules per kilogram of

TABLE 4.8  
Standard enthalpies and internal energies of formation†

	$\Delta\tilde{h}_{f,i}^\circ$ , MJ/kmol	$\Delta\tilde{u}_{f,i}^\circ$ , MJ/kmol
CO <sub>2</sub>	-393.5	-393.5
H <sub>2</sub> O (gas)	-241.8	-240.6
CO	-110.5	-111.7
C <sub>8</sub> H <sub>18</sub> (gas)	-224.1	-204.3

† At 298.15 K.  $\Delta\tilde{h}_{f,i}^\circ$  for O<sub>2</sub>, N<sub>2</sub>, and H<sub>2</sub> are zero by definition.

Sources: JANAF tables,<sup>8</sup> Rossini *et al.*<sup>16</sup>

air can be obtained. For the charts of Figs. 4-3 and 4-5 to 4-9, these expressions are:

$\phi = 0.4$ :

$$\Delta h_{f,u}^\circ = -51.9 - 1181x_b \quad \Delta u_{f,u}^\circ = -47.3 - 1183x_b$$

$\phi = 0.6$ :

$$\Delta h_{f,u}^\circ = -77.8 - 1771x_b \quad \Delta u_{f,u}^\circ = -70.9 - 1774x_b$$

$\phi = 0.8$ :

$$\Delta h_{f,u}^\circ = -103.8 - 2361x_b \quad \Delta u_{f,u}^\circ = -94.6 - 2365x_b \quad (4.32)$$

$\phi = 1.0$ :

$$\Delta h_{f,u}^\circ = -129.7 - 2951x_b \quad \Delta u_{f,u}^\circ = -118.2 - 2956x_b$$

$\phi = 1.2$ :

$$\Delta h_{f,u}^\circ = -155.6 - 2759x_b \quad \Delta u_{f,u}^\circ = -141.9 - 2769x_b$$

**Example 4.4.** Calculate  $\Delta h_{f,u}^\circ$ , the enthalpy of formation of the unburned mixture, and  $\Delta u_{f,u}^\circ$ , the internal energy of formation of the unburned mixture, for a C<sub>8</sub>H<sub>18</sub>-air mixture with  $\phi = 1.0$  and burned gas fraction  $x_b$ .

Table 4.4 gives the moles of each species in the unburned mixture, per mole O<sub>2</sub> with  $\phi = 1.0$ , as

$$\begin{array}{ll} \text{C}_8\text{H}_{18}, 0.08(1-x_b) & \text{CO}_2, 0.64x_b \\ \text{O}_2, 1-x_b & \text{H}_2\text{O}, 0.72x_b \\ \text{N}_2, 3.773 & \text{CO and H}_2, 0 \end{array}$$

Table 4.5 gives the mass of air per mole O<sub>2</sub> as 138.2 kg/kmol. Thus the number of kilomoles of each species per kilogram of air is

$$\begin{array}{ll} \text{C}_8\text{H}_{18}, 5.787 \times 10^{-4}(1-x_b) & \text{CO}_2, 4.629 \times 10^{-3}x_b \\ \text{O}_2, 7.233 \times 10^{-3}(1-x_b) & \text{H}_2\text{O}, 5.208 \times 10^{-3}x_b \\ \text{N}_2, 2.729 \times 10^{-2} & \text{CO and H}_2, 0 \end{array}$$

With  $\Delta\tilde{h}_{f,i}^\circ$  from Table 4.8, Eq. (4.27) gives

$$\begin{aligned} \Delta h_{f,u}^\circ &= 5.787 \times 10^{-4} \times (-224.1 \times 10^6)(1-x_b) \\ &\quad + x_b[4.629 \times 10^{-3} \times (-393.5 \times 10^6) + 5.208 \times 10^{-3} \times (-241.8 \times 10^6)] \end{aligned}$$

$$\Delta h_{f,u}^\circ = (-129.7 - 2951x_b) \times 10^3 \quad \text{J/kg air}$$

With  $\Delta\tilde{u}_{f,i}^\circ$  from Table 4.8, Eq. (4.30) gives

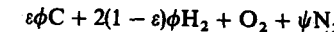
$$\begin{aligned} \Delta u_{f,u}^\circ &= 5.787 \times 10^{-4} \times (-204.3 \times 10^6)(1-x_b) \\ &\quad + x_b[4.629 \times 10^{-3} \times (-393.5 \times 10^6) + 5.208 \times 10^{-3} \times (-240.6 \times 10^6)] \end{aligned}$$

$$\Delta u_{f,u}^\circ = (-118.2 - 2956x_b) \times 10^3 \quad \text{J/kg air}$$

Alternatively, we can determine  $\Delta u_{f,u}^\circ$  from  $\Delta h_{f,u}^\circ$  using Eq. (4.31). For this calculation, the "product" gas is the unburned mixture and the "reactant" gas is the mixture of elements from which the unburned mixture is formed. The number of gaseous moles in the unburned mixture  $n_p$ , per mole O<sub>2</sub> in the original mixture, is (from Table 4.5 for  $\phi \leq 1$ )

$$n_p = (1-x_b) \left[ 4(1+2\varepsilon) \frac{\phi}{M_f} + 1 + \psi \right] + x_b[(1-\varepsilon)\phi + 1 + \psi]$$

The elemental reactant mixture from which the unburned mixture is formed is, from Eq. (4.4),



Thus,  $n_R$ , the moles of *gaseous* elements, is

$$n_R = 2(1-\varepsilon)\phi + 1 + \psi$$

For air,  $\psi = 3.773$ ; for C<sub>8</sub>H<sub>18</sub> fuel,  $\varepsilon = 0.64$  and  $M_f = 114$ . For  $\phi = 1$ ,

$$n_p - n_R = -0.64 + 0.28x_b \quad \text{moles/mole O}_2$$

$$\text{and} \quad (n_p - n_R)\bar{R}T = (-0.64 + 0.28x_b) \times 8.3143 \times 10^3 \times \frac{298.15}{138.2}$$

$$\text{or} \quad (n_p - n_R)\bar{R}T = (-11.5 + 5.0x_b) \times 10^3 \quad \text{J/kg air}$$

Since

$$\Delta u_{f,u}^\circ = \Delta h_{f,u}^\circ - (n_p - n_R)\bar{R}T$$

$$\Delta u_{f,u}^\circ = (-129.7 - 2951x_b) \times 10^3 - (-11.5 + 5.0x_b) \times 10^3$$

$$\Delta u_{f,u}^\circ = (-118.2 - 2956x_b) \times 10^3 \quad \text{J/kg air}$$

The combustion process links the unburned and burned mixture properties as follows:

For an adiabatic constant-volume combustion process,

$$u_b = u_u = u_{s,u} + \Delta u_{f,u}^\circ \quad (4.33)$$

and

$$v_b = v_u$$

Thus, given  $u_{s,u}$  and  $v_u$ , the state of the burned mixture can be determined from the appropriate burned mixture chart.

For an adiabatic constant-pressure combustion process,

$$h_b = h_u = h_{s,u} + \Delta h_{f,u}^o \quad (4.34)$$

Since

$$u_b = h_b - p v_b$$

given  $h_{s,u}$  and  $p$ ,  $u_b$  and  $v_b$  must be found by trial and error along the specified constant-pressure line on the appropriate burned mixture chart.

**Example 4.5.** Calculate the temperature and pressure after constant-volume adiabatic combustion and constant-pressure adiabatic combustion of the unburned mixture (with  $\phi = 1.0$  and  $x_b = 0.08$ ) at the state corresponding to the end of the compression process examined in Example 4.2.

The state of the unburned mixture at the end of the compression process in Example 4.2 was

$$T_u = 682 \text{ K}, \quad u_{s,u} = 350 \text{ kJ/kg air}, \quad p_u = 1.57 \text{ MPa}, \quad v_u = 0.125 \text{ m}^3/\text{kg air}$$

For an adiabatic *constant-volume* combustion process [Eq. (4.33)],

$$u_b = u_u = u_{s,u} + \Delta u_{f,u}^o$$

For  $\phi = 1.0$ ,  $\Delta u_{f,u}^o$  is given by Eq. (4.32) as

$$\Delta u_{f,u}^o = -118.2 - 2956x_b = -118.2 - 236.5 = -355 \text{ kJ/kg air}$$

Hence

$$u_b = 350 - 355 = -5 \text{ kJ/kg air}$$

Also

$$v_b = v_u = 0.125 \text{ m}^3/\text{kg air}$$

Locating ( $u_b$ ,  $v_b$ ) on the burned gas chart (Fig. 4-8) gives

$$T_b = 2825 \text{ K}, \quad p_b = 7100 \text{ kPa}$$

For a *constant-pressure* combustion process [Eq. (4.34)],

$$h_b = h_u = h_{s,u} + \Delta h_{f,u}^o$$

For  $\phi = 1.0$ ,  $\Delta h_{f,u}^o$  is given by Eq. (4.32) as

$$\Delta h_{f,u}^o = -129.7 - 2951x_b = -129.7 - 236 = -366 \text{ kJ/kg air}$$

At  $T_u = 682 \text{ K}$ ,  $h_{s,u} = 465 \text{ kJ/kg air}$ , so

$$h_b = 465 - 366 = 99 \text{ kJ/kg air}$$

Since  $p_b = p_u = 1.57 \text{ MPa}$ , the internal energy  $u_b$  is given by

$$u_b = h_b - p_b v_b = 99 - 1.57 \times 10^3 v_b \quad \text{kJ/kg air}$$

A trial-and-error solution for  $v_b$  and  $u_b$  along the  $p = 1570 \text{ kPa}$  line on Fig. 4-8 gives

$$u_b = -655 \text{ kJ/kg air}, \quad T_b = 2440 \text{ K}, \quad v_b = 0.485 \text{ m}^3/\text{kg air}$$

(Use the ideal gas law to estimate  $p$ ,  $T$ , or  $v$  more accurately.)

## 4.6 TABLES OF PROPERTIES AND COMPOSITION

Tables of thermodynamic properties of air are useful for analysis of motored engine operation, diesels and compressors. Keenan, Chao, and Kaye's *Gas Tables*<sup>6</sup> are the standard reference for the thermodynamic properties of air at low pressures (i.e., at pressures substantially below the critical pressure when the ideal gas law is accurate). These gas tables are in U.S. and SI units. A set of tables for air in SI units has been prepared by Reynolds<sup>7</sup> following the format of the Keenan *et al.* tables. A condensed table of thermodynamic properties of air, derived from Reynolds, is given in App. D. It contains:

$h$  = enthalpy, kJ/kg

$u$  = internal energy, kJ/kg

$$\Psi = \int_0^T \left( \frac{c_v}{T} \right) dT, \text{ kJ/kg} \cdot \text{K}$$

$$\Phi = \int_0^T \left( \frac{c_p}{T} \right) dT, \text{ kJ/kg} \cdot \text{K}$$

$p_r$  = relative pressure

$v_r$  = relative volume

$c_p$  = specific heat at constant pressure, kJ/kg · K

$c_v$  = specific heat at constant volume, kJ/kg · K

$\gamma$  = ratio of specific heats

all as a function of  $T$ (K).

$\Phi$  is the standard state entropy at temperature  $T$  and 1 atm pressure, relative to the entropy at 0 K and 1 atm pressure. The entropy at pressures other than 1 atm is obtained using Eq. (4.14b).

The relative pressure  $p_r$  is defined by

$$\ln p_r = \frac{\Phi}{R} \quad (4.35)$$

and is a function of  $T$  only. Along a given isentropic, it follows from Eq. (4.18) that the ratio of actual pressures  $p_2$  and  $p_1$  corresponding to temperatures  $T_2$  and  $T_1$  is equal to the ratio of relative pressures, i.e.,

$$\left( \frac{p_2}{p_1} \right)_{s=\text{const}} = \left( \frac{p_{r2}}{p_{r1}} \right) \quad (4.36)$$

This affords a means of determining  $T_2$ , for an isentropic process, given  $T_1$  and  $p_2/p_1$  (see Example 4.6).

The relative volume  $v_r$  is defined by

$$v_r = \frac{RT}{p_r} \quad (4.37)$$

The units are selected so that  $v_r$  is in cubic meters per kilogram when  $T$  is in kelvins and  $p_r$  is in pascals. Along a given isentropic, the ratio of actual volumes  $V_2$  and  $V_1$  (for a fixed mass) at temperatures  $T_2$  and  $T_1$ , from Eq. (4.37), is equal to the ratio of relative volumes

$$\left(\frac{V_2}{V_1}\right)_{s=\text{const}} = \left(\frac{v_{r2}}{v_{r1}}\right) \quad (4.38)$$

This affords a means of determining  $T_2$  for an isentropic process, given  $T_1$  and  $V_2/V_1$  (see Example 4.6).

Tables giving the composition and thermodynamic properties of combustion products have been compiled. They are useful sources of property and species concentrations data in burned gas mixtures for a range of equivalence ratios, temperatures, and pressures. Summary information on four generally available sets of tables is given in Table 4.9. The most extensive set of tables of combustion product composition and thermodynamic properties is the AGARD set, *Properties of Air and Combustion Products with Kerosene and Hydrogen Fuels*, by Banes et al.<sup>12</sup> Note, however, that their enthalpy datum differs from the usual datum (enthalpy for O<sub>2</sub>, N<sub>2</sub>, H<sub>2</sub>, and C is zero at 298.15 K). The elements in their reference state at 298.15 K were assigned arbitrary positive values for enthalpy to avoid negative enthalpies for the equilibrium burned gas mixture.

**Example 4.6.** In a diesel engine, the air conditions at the start of compression are  $p_1 = 1$  atm and  $T_1 = 325$  K. At the end of compression  $p_2 = 60$  atm. Find the temperature  $T_2$  and the compression ratio  $V_1/V_2$ .

Air tables (see App. D), at  $T_1 = 325$  K, give

$$p_{r1} = 97.13 \quad \text{and} \quad v_{r1} = 960.6$$

Use Eq. (4.36),

$$\frac{p_{r2}}{p_{r1}} = \frac{p_2}{p_1} = 60$$

to give

$$p_{r2} = 5828$$

Tables then give

$$T_2 = 992 \text{ K} \quad \text{and} \quad v_{r2} = 48.92$$

The compression ratio is given by

$$\frac{V_1}{V_2} = \frac{v_{r1}}{v_{r2}} = \frac{960.6}{48.92} = 19.6$$

TABLE 4.9  
Tables of properties of air and combustion products

Source	Properties P, composition C	Mixture	Units	$\phi$ range	T range	p range	Enthalpy datum
Keenan, Chao, and Kaye <sup>6</sup>	P	Air (CH <sub>2</sub> ) <sub>n</sub> -air	U.S., SI	0.25, 0.5, 1.0	100–3600 K	Low	$h = 0$ at 0 K $h_b = 0$ at 0 K
Reynolds <sup>7</sup> General Electric <sup>11</sup>	P and C	Air-(CH <sub>2</sub> ) <sub>n</sub>	SI U.S.	0.25–4	200–1500 K 600–5000°R	Low 0.01–30 atm	$h$ of C, H <sub>2</sub> , N <sub>2</sub> , O <sub>2</sub> zero at 0°R
AGARD <sup>12</sup>	P and C	Air (CH <sub>2</sub> ) <sub>n</sub> -air H <sub>2</sub> -air	SI	0.2–2 0.2–2	100–6000 K	1–800 atm	Arbitrary, to keep $h_b > 0$

## 4.7 COMPUTER ROUTINES FOR PROPERTY AND COMPOSITION CALCULATIONS

When large numbers of computations are being made or high accuracy is required, engine process calculations are carried out on a computer. Relationships which model the composition and/or thermodynamic properties of unburned and burned gas mixtures have been developed for computer use. These vary considerably in range of application and accuracy.

The most complete models are based on polynomial curve fits to the thermodynamic data for each species in the mixture and the assumptions that (1) the unburned mixture is frozen in composition and (2) the burned mixture is in equilibrium. The approach used as the basis for representing JANAF table thermodynamic data<sup>8</sup> in the NASA equilibrium program<sup>9,10</sup> (see Sec. 3.7) will be summarized here because it is consistent with the approach used throughout to calculate unburned and burned mixture properties.

For each species  $i$  in its standard state at temperature  $T(K)$ , the specific heat  $\tilde{c}_{p,i}$  is approximated by

$$\frac{\tilde{c}_{p,i}}{R} = a_{i1} + a_{i2} T + a_{i3} T^2 + a_{i4} T^3 + a_{i5} T^4 \quad (4.39)$$

The standard state enthalpy of species  $i$  is then given by

$$\frac{\tilde{h}_i}{RT} = a_{i1} + \frac{a_{i2}}{2} T + \frac{a_{i3}}{3} T^2 + \frac{a_{i4}}{4} T^3 + \frac{a_{i5}}{5} T^4 + \frac{a_{i6}}{T} \quad (4.40)$$

The standard state entropy of species  $i$  at temperature  $T(K)$  and pressure 1 atm, from Eq. (4.14), is then

$$\frac{\tilde{s}_i}{R} = a_{i1} \ln T + a_{i2} T + \frac{a_{i3}}{2} T^2 + \frac{a_{i4}}{3} T^3 + \frac{a_{i5}}{4} T^4 + a_{i7} \quad (4.41)$$

Values of the coefficients  $a_{ij}$  for CO<sub>2</sub>, H<sub>2</sub>O, CO, H<sub>2</sub>, O<sub>2</sub>, N<sub>2</sub>, OH, NO, O, and H from the NASA program are given in Table 4.10. Two temperature ranges are given. The 300 to 1000 K range is appropriate for unburned mixture property calculations. The 1000 to 5000 K range is appropriate for burned mixture property calculations. Figure 4-11 gives values of  $c_p/R$  for the major species, CO<sub>2</sub>, H<sub>2</sub>O, O<sub>2</sub>, N<sub>2</sub>, H<sub>2</sub>, and CO, as a function of temperature.

### 4.7.1 Unburned Mixtures

Polynomial functions for various fuels (in the vapor phase) have been fitted to the functional form:<sup>13-15</sup>

$$\tilde{c}_{p,f} = A_{f1} + A_{f2} t + A_{f3} t^2 + A_{f4} t^3 + \frac{A_{f5}}{t^2} \quad (4.42)$$

TABLE 4.10  
Coefficients for species thermodynamic properties

Species	T range, K	$a_{i1}$	$a_{i2}$	$a_{i3}$	$a_{i4}$	$a_{i5}$	$a_{i6}$	$a_{i7}$
CO <sub>2</sub>	1000-5000	0.44608(+1)	0.30982(-2)	-0.12393(-5)	0.22741(-9)	-0.15526(-13)	-0.48961(+5)	-0.98636(0)
	300-1000	0.24008(+1)	0.87351(-2)	-0.66071(-5)	0.20022(-8)	0.63274(-15)	-0.48378(+5)	0.96951(+1)
H <sub>2</sub> O	1000-5000	0.27168(+1)	0.29451(-2)	-0.80224(-6)	0.10227(-9)	-0.48472(-14)	-0.29906(+5)	0.66306(+1)
	300-1000	0.40701(+1)	-0.11084(-2)	0.41521(-5)	-0.29637(-8)	0.80702(-12)	-0.30280(+5)	-0.32270(0)
CO	1000-5000	0.29841(+1)	0.14891(-2)	-0.57900(-6)	0.10365(-9)	-0.69354(-14)	-0.14245(+5)	0.63479(+1)
	300-1000	0.37101(+1)	-0.16191(-2)	0.36924(-5)	-0.20320(-8)	0.23953(-12)	-0.14356(+5)	0.29555(+1)
H <sub>2</sub>	1000-5000	0.31002(+1)	0.51119(-3)	0.52644(-7)	-0.34910(-10)	0.36945(-14)	-0.87738(+3)	-0.19629(+1)
	300-1000	0.30574(+1)	0.26765(-2)	-0.58099(-5)	0.555210(-8)	-0.18123(-11)	-0.98890(+3)	-0.22997(+1)
O <sub>2</sub>	1000-5000	0.36220(+1)	0.75618(-3)	-0.19652(-6)	0.36202(-10)	-0.28946(-14)	-0.12020(+4)	0.36151(+1)
	300-1000	0.36256(+1)	-0.18782(-2)	0.70555(-5)	-0.67635(-8)	0.21556(-11)	-0.10475(+4)	0.43053(+1)
N <sub>2</sub>	1000-5000	0.28963(+1)	0.15155(-2)	-0.57235(-6)	0.99807(-10)	-0.65224(-14)	-0.90586(+3)	0.61615(+1)
	300-1000	0.36748(+1)	-0.12082(-2)	0.23240(-5)	-0.63218(-9)	-0.22577(-12)	-0.10612(+4)	0.23580(+1)
OH	1000-5000	0.29106(+1)	0.95932(-3)	-0.19442(-6)	0.13757(-10)	0.14225(-15)	0.39354(+4)	0.54423(+1)
	300-1000	0.31890(+1)	0.13382(-2)	-0.52899(-6)	0.95919(-10)	-0.64848(-14)	0.98283(+4)	0.67458(+1)
O	1000-5000	0.25421(+1)	-0.27551(-4)	-0.31028(-8)	0.45511(-11)	-0.43681(-15)	0.29231(+5)	0.49203(+1)
	300-1000	0.225(+1)	0.0	0.0	0.0	0.0	0.25472(+5)	-0.46012(0)

Source: NASA Equilibrium Code.<sup>9</sup>

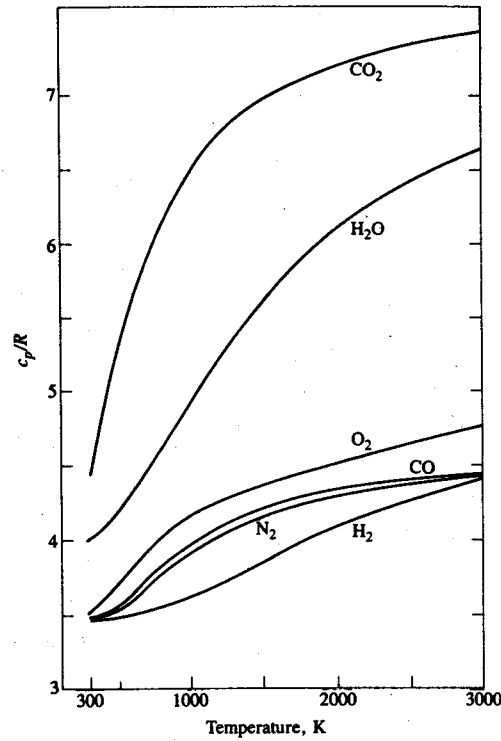


**FIGURE 4-11**  
Specific heat at constant pressure,  $c_p/R$ , as function of temperature for species  $\text{CO}_2$ ,  $\text{H}_2\text{O}$ ,  $\text{O}_2$ ,  $\text{N}_2$ ,  $\text{H}_2$ , and  $\text{CO}$ . (From JANAF tables.<sup>8</sup>)

$$\tilde{h}_f = A_{f1} t + A_{f2} \frac{t^2}{2} + A_{f3} \frac{t^3}{3} + A_{f4} \frac{t^4}{4} - \frac{A_{f5}}{t} + A_{f6} + A_{f8} \quad (4.43)$$

where  $t = T(\text{K})/1000$ .  $A_{f6}$  is the constant for the datum of zero enthalpy for C,  $\text{H}_2$ ,  $\text{O}_2$ , and  $\text{N}_2$  at 298.15 K. For a 0 K datum,  $A_{f8}$  is added to  $A_{f6}$ . For pure hydrocarbon compounds, the coefficients  $A_{fi}$  were found by fitting Eqs. (4.42) and (4.43) to data from Rossini *et al.*<sup>16</sup> Values for relevant pure fuels are given in Table 4.11. The units for  $\tilde{c}_{p,f}$  are cal/gmol·K, and for  $\tilde{h}_f$  are kcal/gmol.

Multicomponent fuel coefficients were determined as follows.<sup>14</sup> Chemical analysis of the fuel was performed to obtain the H/C ratio, average molecular weight, heating value, and the weight percent of aromatics, olefins, and total paraffins (including cycloparaffins). The fuel was then modeled as composed of a representative aromatic, olefin, and paraffin hydrocarbon. From atomic conservation of hydrogen and carbon and the chemical analysis results, component molar fractions and average carbon numbers can be determined. Table 4.11 gives values for the coefficients  $A_{f1}$  to  $A_{f8}$  for typical petroleum-based fuels. The units of the coefficients give  $\tilde{c}_{p,f}$  and  $\tilde{h}_f$  in cal/gmol·K and kcal/gmol, respectively, with  $t = T(\text{K})/1000$ .

**TABLE 4.11**  
Coefficients for polynomials [Eqs. (4.42) and (4.43)] for fuel enthalpy and specific heat

Fuel	Formula	Molecular weight	(A/F) <sub>f</sub>	(F/A) <sub>f</sub>	$A_{f1}$	$A_{f2}$	$A_{f3}$	$A_{f4}$	$A_{f5}$	$A_{f6}$	$A_{f7}$	$A_{f8}$
Methane	$\text{CH}_4$	16.04	17.23	0.0580	-0.29149	26.327	-10.610	1.5656	0.16573	-18.331	4.3000	
Propane	$\text{C}_3\text{H}_8$	44.10	15.67	0.0638	-1.4867	74.339	-39.065	8.0543	0.01219	-27.313	8.852	
Hexane	$\text{C}_6\text{H}_{14}$	86.18	15.24	0.0656	-20.777	210.48	-164.125	52.832	0.56635	-39.836	15.611	
Isooctane	$\text{C}_8\text{H}_{18}$	114.2	15.14	0.0661	-0.55313	181.62	-97.787	20.402	-0.03095	-60.751	20.232	
Methanol	$\text{CH}_3\text{OH}$	32.04	6.47	0.1546	-2.7059	44.168	-27.501	7.2193	0.20299	-48.288	5.3375	
Ethanol	$\text{C}_2\text{H}_5\text{OH}$	46.07	9.00	0.1111	6.990	39.741	-11.926	0	0	-60.214	7.6135	
Gasoline	$\text{C}_{8.26}\text{H}_{15.5}$	114.8	14.64	0.0683	-24.078	256.63	-201.68	64.750	0.5808	-27.562	17.792	
	$\text{C}_{7.76}\text{H}_{13.1}$	106.4	14.37	0.0696	-22.501	227.99	-177.26	56.048	0.4845	-17.578	15.235	
Diesel	$\text{C}_{10.8}\text{H}_{18.7}$	148.6	14.4	0.0694	-9.1063	246.97	-143.74	32.329	0.0518	-50.128	23.514	

Units of  $A_{fi}$  such that  $\tilde{h}_f$  is in kcal/gmol and  $\tilde{c}_{p,f}$  is in cal/gmol·K with  $t = T(\text{K})/1000$ .  $A_{f6}$  gives enthalpy datum at 298.15 K;  $(A_{f6} + A_{f8})$  gives enthalpy datum at 0 K.

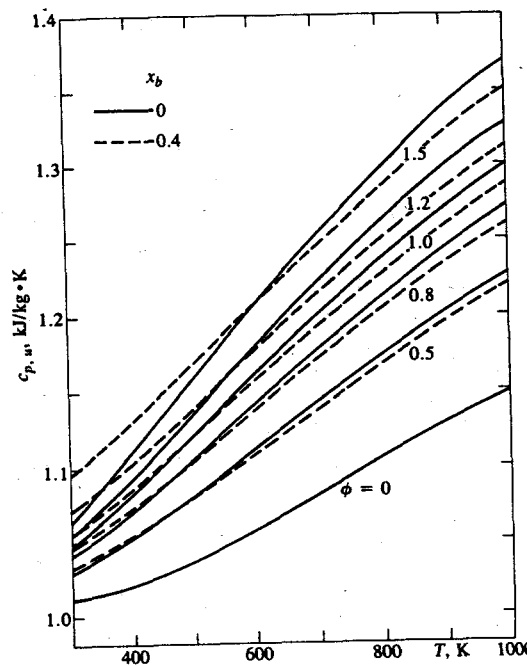


**FIGURE 4-12**  
Specific heat at constant pressure of unburned gasoline, air, burned gas mixtures as function of temperature, equivalence ratio, and burned gas fraction. Units: kJ/kg mixture·K.

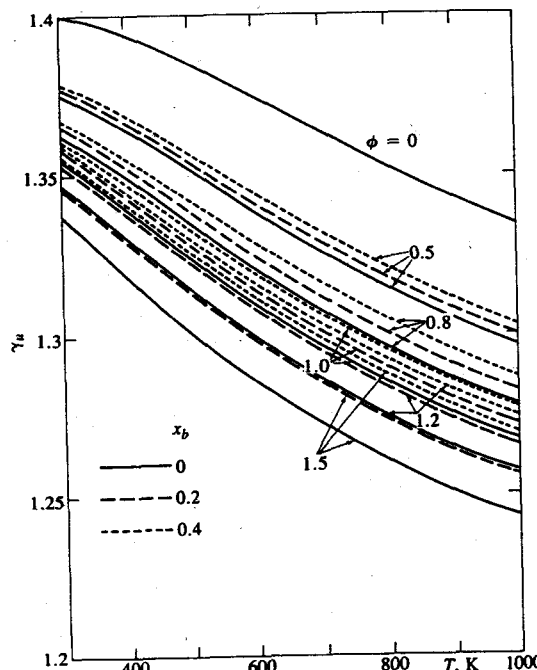


**FIGURE 4-13**  
Ratio of specific heats,  $\gamma_u = c_{p,u}/c_{v,u}$ , of unburned gasoline, air, burned gas mixtures as function of temperature, equivalence ratio, and burned gas fraction.

The thermodynamic properties of the unburned mixture can now be obtained. With the moles of each species per mole  $O_2$ ,  $n_i$ , determined from Table 4.4, and the mass of mixture per mole  $O_2$ ,  $m_{RP}$ , determined from Table 4.5, the unburned mixture properties are given by

$$c_{p,u} = \frac{1}{m_{RP}} \sum_i n_i \tilde{c}_{p,i} \quad (4.44a)$$

$$h_u = \frac{1}{m_{RP}} \sum_i n_i \tilde{h}_i \quad (4.44b)$$

$$s_u = \frac{1}{m_{RP}} \left\{ \sum_i n_i \left[ \tilde{s}_i^\circ - \tilde{R} \ln \left( \frac{n_i}{n_u} \right) \right] - n_u \tilde{R} \ln p \right\} \quad (4.44c)$$

where  $p$  is in atmospheres.

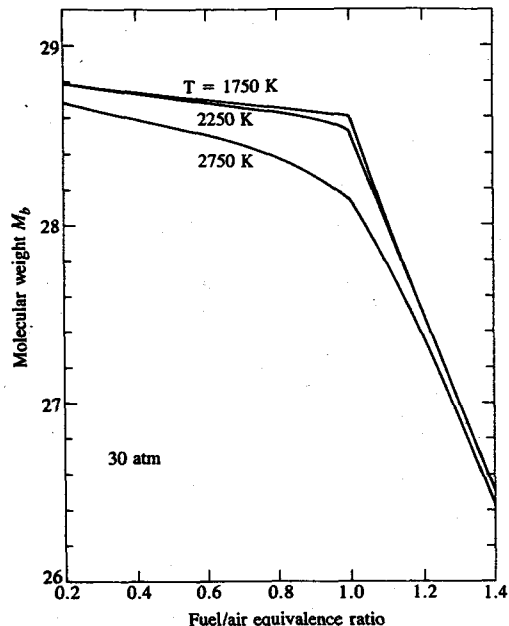
Figures 4-12 and 4-13, obtained with the above relations, show how  $c_{p,u}$  and  $\gamma_u$  ( $= c_{p,u}/c_{v,u}$ ) vary with temperature, equivalence ratio, and burned gas fraction, for a gasoline-air mixture.

#### 4.7.2 Burned Mixtures

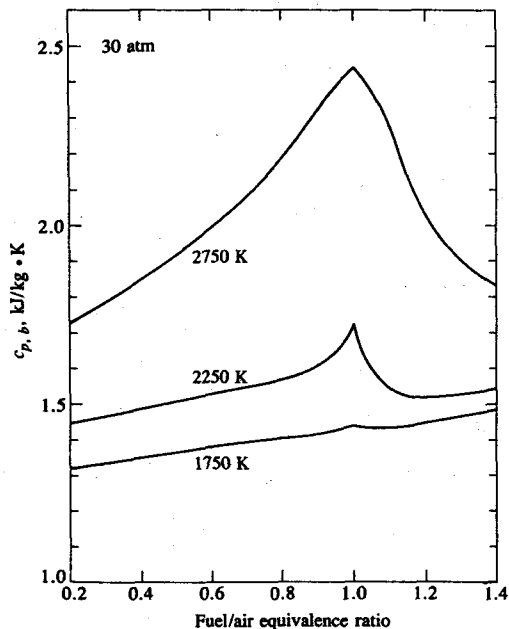
The most accurate approach for burned mixture property and composition calculations is to use a thermodynamic equilibrium program at temperatures above about 1700 K and a frozen composition below 1700 K. The properties of each species at high and low temperatures are given by polynomial functions such as Eqs. (4.39) to (4.41) and their coefficients in Table 4.10. The NASA equilibrium program (see Sec. 3.7) is readily available for this purpose and is well documented.<sup>9,10</sup> The following are examples of its output.

Figure 3-10 showed species concentration data for burned gases as a function of equivalence ratio at 1750, 2250, and 2750 K, at 30 atm. Figure 4-14 shows the burned gas molecular weight  $M_b$ , and Figs. 4-15 and 4-16 give  $c_{p,b}$  and  $\gamma_b$  as functions of equivalence ratio at 1750, 2250, and 2750 K, at 30 atm. Figures 4-17 and 4-18 show  $c_{p,b}$  and  $\gamma_b$  as a function of temperature and pressure for selected equivalence ratios for mixtures lean and rich of stoichiometric.<sup>17</sup> For rich mixtures ( $\phi > 1$ ), for  $T > 2000$  K,  $c_{p,b}$  and  $\gamma_b$  are equilibrium values. For  $1200 \text{ K} \leq T \leq 2000 \text{ K}$ , "frozen" composition data are shown where the gas composition is in equilibrium at the given  $T$  and  $p$  but is frozen as  $c_p$  and  $c_v$  are computed. Below about 1500 K, fixed composition data are shown corresponding to a value of 3.5 for the water-gas equilibrium constant which adequately describes exhaust gases (see Sec. 4.9).

Because the computational time involved in repeated use of a full equilibrium program can be substantial, simpler equilibrium programs and approximate fits to the equilibrium thermodynamic data have been developed. The approach usually used is to estimate the composition and/or properties of undissociated combustion products and then to use iterative procedures or corrections to account for the effects of dissociation.



**FIGURE 4-14**  
Molecular weight of equilibrium burned gases as a function of equivalence ratio at  $T = 1750, 2250$ , and  $2750\text{ K}$ , and  $30\text{ atm}$ . Fuel: isoctane.



**FIGURE 4-15**  
Specific heat at constant pressure of equilibrium burned gases as a function of equivalence ratio at  $T = 1750, 2250$ , and  $2750\text{ K}$ , and  $30\text{ atm}$ . Fuel: isoctane. Units:  $\text{kJ/kg mixture} \cdot \text{K}$ .

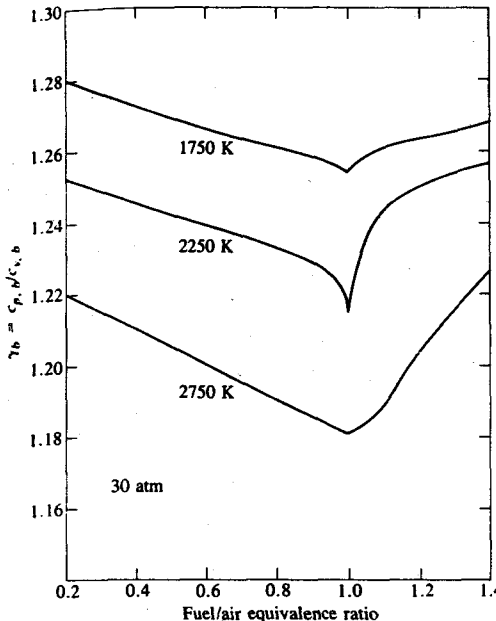
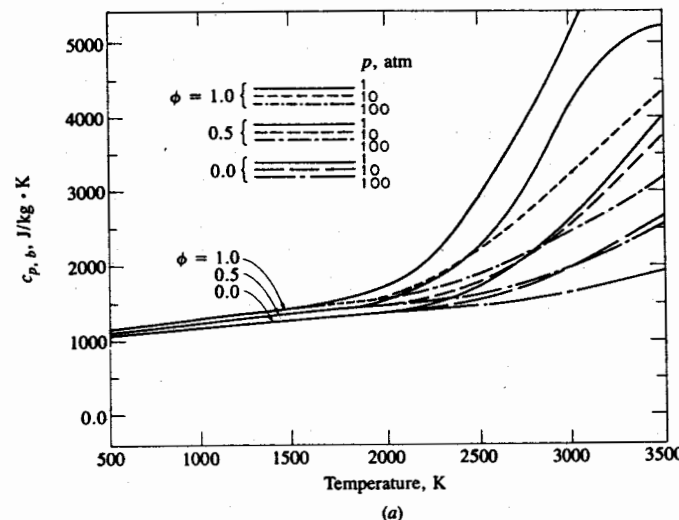


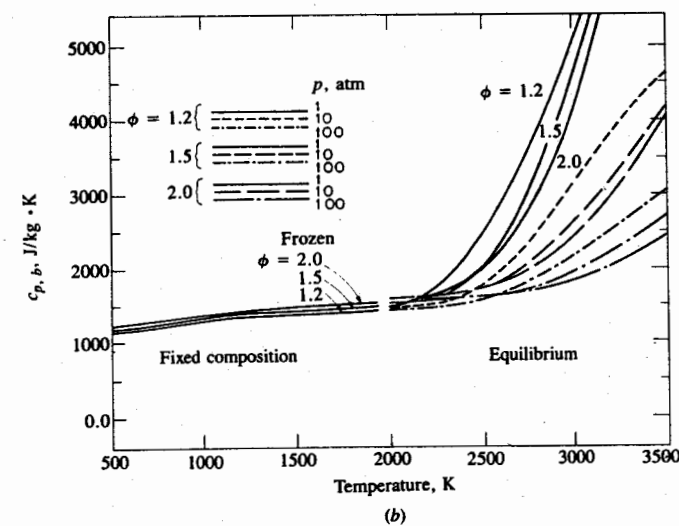
**FIGURE 4-16**  
Ratio of specific heats,  $\gamma_b = c_{p,b}/c_{v,b}$ , for equilibrium burned gases as a function of equivalence ratio at  $T = 1750, 2250$ , and  $2750\text{ K}$ , and  $30\text{ atm}$ . Fuel: isoctane.

A computer program for calculating properties of equilibrium combustion products, designed specifically for use in internal combustion engine applications, has been developed by Olikara and Borman and is readily available.<sup>18</sup> The fuel composition ( $C_nH_mO_lN_k$ ), fuel/air equivalence ratio, and product pressure and temperature are specified. The species included in the product mixture are:  $\text{CO}_2$ ,  $\text{H}_2\text{O}$ ,  $\text{CO}$ ,  $\text{H}_2$ ,  $\text{O}_2$ ,  $\text{N}_2$ ,  $\text{Ar}$ ,  $\text{NO}$ ,  $\text{OH}$ ,  $\text{O}$ ,  $\text{H}$ , and  $\text{N}$ . The element balance equations and equilibrium constants for seven nonredundant reactions provide the set of 11 equations required for solution of these species concentrations (see Sec. 3.7). The equilibrium constants are curve fitted from data in the JANAF tables.<sup>8</sup> The initial estimate of mole fractions to start the iteration procedure is the nondissociated composition. Once the mixture composition is determined, the thermodynamic properties and their derivatives with respect to temperature, pressure, and equivalence ratio are computed. This limited set of species has been found to be sufficiently accurate for engine burned gas calculations, and is much more rapid than the extensive NASA equilibrium program.<sup>9, 10</sup>

Several techniques for estimating the *thermodynamic properties* of high-temperature burned gases for engine applications have been developed. One commonly used approach is that developed by Krieger and Borman.<sup>19</sup> The internal energy and gas constant of undissociated combustion products were first described by polynomials in gas temperature. The second step was to limit the range of  $T$  and  $p$  to values found in internal combustion engines. Then the deviations between the equilibrium thermodynamic property data published by Newhall and Starkman<sup>4, 5</sup> and the calculated nondissociated values were fitted



(a)

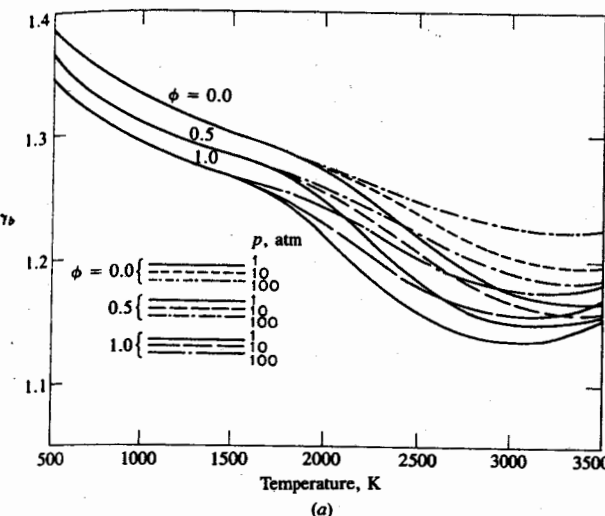


(b)

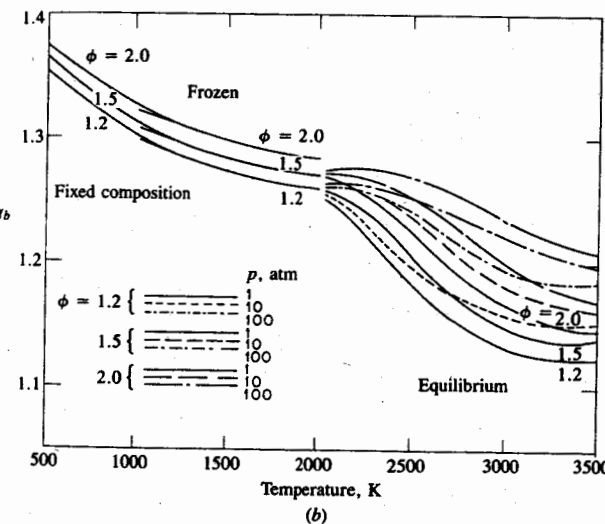
FIGURE 4-17

Specific heat at constant pressure for equilibrium, frozen, and fixed composition burned gases as a function of temperature and pressure: (a) equivalence ratio  $\phi \leq 1.0$ ; (b) equivalence ratio  $\phi > 1$ . Units:  $J/kg$  mixture ·  $K$ . Fuel:  $C_nH_{2n}$ .

by an exponential function of  $T$ ,  $p$ , and  $\phi$ . For  $\phi \leq 1$ , a single set of equations resulted. For  $\phi \geq 1$ , sets of equations were developed, each set applying to a specific value of equivalence ratio (see Ref. 19). In general, the fit for internal energy is within  $2\frac{1}{2}$  percent over the pressure and temperature range of interest, and the error over most of the range is less than 1 percent. For many applica-



(a)



(b)

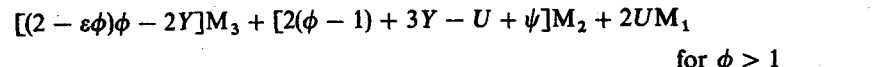
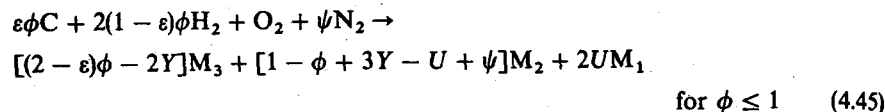
FIGURE 4-18

Ratio of specific heats,  $\gamma_b = c_{p,b}/c_{o,b}$ , for equilibrium, frozen, and fixed composition burned gases as a function of temperature and pressure: (a) equivalence ratio  $\phi \leq 1.0$ ; (b) equivalence ratio  $\phi > 1$ . Fuel:  $C_nH_{2n}$ .

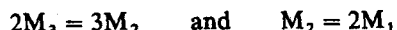
tions, the undissociated equations for thermodynamic properties are sufficiently accurate.

An alternative approach for property calculations, applicable to a wide range of hydrocarbon and alcohol fuels, is used extensively in the author's laboratory.<sup>20</sup> With this method, the products of combustion of hydrocarbon (or

alcohol)-air mixtures are divided into triatomic, diatomic, and monatomic molecules,  $M_3$ ,  $M_2$ , and  $M_1$ , respectively. Then, if  $Y$  is the extra number of moles of diatomic molecules due to dissociation of triatomic molecules and  $U$  is the extra number of monatomic molecules due to dissociation of diatomic molecules, the combustion reaction can be written as



The method is based upon a fitting of data obtained from sets of detailed chemical equilibrium calculations to this functional form. Two general dissociation reactions:



are then used with fitted equilibrium constants  $K_1(T)$  and  $K_2(T)$  to calculate the relative species concentrations. This approach has been developed to give equations for enthalpy which sum the translational, rotational, and vibrational contributions to the specific heat, and the enthalpy of formation:

$$m_{RP} h = \frac{R}{2} (8N_3 + 7N_2 + 5N_1)T + R(3N_3 + N_2) \frac{T_v}{\exp(T_v/T) - 1} + m_{RP} h_f \quad (4.46)$$

where  $N_3$ ,  $N_2$ , and  $N_1$  are the number of moles of triatomic, diatomic, and monatomic molecules respectively per mole  $O_2$  reactant,  $T_v$  is a fitted vibrational temperature,  $m_{RP}$  is the mass of products per mole  $O_2$  reactant [Eq. (4.9)], and  $h_f$  is the average specific enthalpy of formation of the products.

The molecular weight is given by

$$M_b = \frac{m_{RP}}{1 + (1 - \varepsilon)\phi + \psi + Y + U} \quad \text{for } \phi \leq 1 \quad (4.47)$$

$$\text{or} \quad M_b = \frac{m_{RP}}{(2 - \varepsilon)\phi + \psi + Y + U} \quad \text{for } \phi > 1$$

$U$  and  $Y$  are found using an approximate solution to the equations obtained by applying the fitted equilibrium constants to the dissociation reactions;  $h_f$  is obtained by fitting a correction to the undissociated products enthalpy of formation. Equations are presented for the partial derivatives of enthalpy  $h$  and density  $\rho$  with respect to  $T$ ,  $p$ , and  $\phi$ .<sup>20</sup> These relationships have been tested for fuels with H/C ratios of 4 to 0.707, equivalence ratios 0.4 to 1.4, pressures 1 to 30 atm, and temperatures 1000 to 3000 K. The error for burned mixture temperatures relevant to engine calculations is always less than  $\pm 10$  K. The errors in density are less than  $\pm 0.2$  percent.

## 4.8 TRANSPORT PROPERTIES

The processes by which mass, momentum, and energy are transferred from one point in a system to another are called rate processes. In internal combustion engines, examples of such processes are evaporation of liquid fuel, fuel-air mixing, friction at a gas/solid interface, and heat transfer between gas and the walls of the engine combustion chamber. In engines, most of these processes are turbulent and are therefore strongly influenced by the properties of the fluid flow. However, turbulent rate processes are usually characterized by correlations between dimensionless numbers (e.g., Reynolds, Prandtl, Nusselt numbers, etc.), which contain the fluid's transport properties of viscosity, thermal conductivity, and diffusion coefficient as well as the flow properties.

The simplest approach for computing the transport properties is based on the application of kinetic theory to a gas composed of hard-sphere molecules. By analyzing the momentum flux in a plane Couette flow,<sup>†</sup> it can be shown (Chapman and Cowling, Ref. 21, p. 218) that the viscosity  $\mu$  of a monatomic hard-sphere gas [where  $\mu = \tau/(du/dx)$ ,  $\tau$  being the shear stress and  $(du/dx)$  the velocity gradient] is given by

$$\mu = \frac{[5/(16\sqrt{\pi})](m\tilde{k}T)^{1/2}}{d^2} \quad (4.48)$$

where  $m$  is the mass of the gas molecule,  $d$  is the molecular diameter, and  $\tilde{k}$  is Boltzmann's constant,  $1.381 \times 10^{-23}$  J/K.

For such a gas, the viscosity varies as  $T^{1/2}$ , but will not vary with gas pressure or density. Measurements of viscosity show it does only vary with temperature, but generally not proportionally to  $T^{1/2}$ . The measured temperature dependence can only be explained with more sophisticated models for the intermolecular potential energy than that of a hard sphere. Effectively, at higher temperatures, the higher average kinetic energy of a pair of colliding molecules requires that they approach closer to each other and experience a greater repulsive force to be deflected in the collision. As a result, the molecules appear to be smaller spheres as the temperature increases.

An expression for the thermal conductivity  $k$  of a monatomic hard-sphere gas [ $k = \dot{q}/(dT/dx)$ , where  $\dot{q}$  is the heat flux per unit area and  $dT/dx$  is the temperature gradient] can be derived from an analysis of the thermal equivalent of plane Couette flow (Ref. 21, p. 235):

$$k = \frac{[75/(64\sqrt{\pi})](\tilde{k}^3 T/m)^{1/2}}{d^2} \quad (4.49)$$

<sup>†</sup> In Couette flow, the fluid is contained between two infinite plane parallel surfaces, one at rest and one moving with constant velocity. In the absence of pressure gradients, the fluid velocity varies linearly across the distance between the surfaces.

which has the same temperature dependence as  $\mu$ . Equations (4.48) and (4.49) can be combined to give

$$k = \frac{5}{2} \mu c_v$$

since, for a monatomic gas, the specific heat at constant volume is  $3\bar{k}/(2m)$ . This simple equality is in good agreement with measurements of  $\mu$  and  $k$  for monoatomic gases.

The above model does not take into account the vibrational and rotational energy exchange in collisions between polyatomic molecules which contribute to energy transport in gases of interest in engines. Experimental measurements of  $k$  and  $\mu$  show that  $k$  is less than  $\frac{5}{2}\mu c_v$  for such polyatomic gases, where  $c_v$  is the sum of the translational specific heat and the specific heat due to internal degrees of freedom. It was suggested by Eucken that transport of vibrational and rotational energy was slower than that of translational energy. He proposed an empirical expression

$$k = \frac{9\gamma - 5}{4} \mu c_v \quad (4.50)$$

or

$$\text{Pr} = \frac{\mu c_p}{k} = \frac{4\gamma}{9\gamma - 5}$$

where  $\text{Pr}$  is the Prandtl number, which is in good agreement with experimental data.

A similar analysis of a binary diffusion process, where one gas diffuses through another, leads to an expression for the binary diffusion coefficient  $D_{ij}$ .  $D_{ij}$  is a transport property of the gas mixture composed of species  $i$  and  $j$ , defined by Fick's law of molecular diffusion which relates the fluxes of species  $i$  and  $j$ ,  $\Gamma_{xi}$  and  $\Gamma_{xj}$ , in the  $x$  direction to the concentration gradients,  $dn_i/dx$  and  $dn_j/dx$  ( $n$  is the molecular number density):

$$\Gamma_{xi} = -D_{ij} \left( \frac{dn_i}{dx} \right) \quad \Gamma_{xj} = -D_{ij} \left( \frac{dn_j}{dx} \right)$$

The binary diffusion coefficient for a mixture of hard-sphere molecules is (Ref. 21, p. 245)

$$D_{ij} = \frac{3}{16nd^2} \left( \frac{2\bar{k}T}{\pi m_{ij}} \right)^{1/2} \quad (4.51)$$

where  $m_{ij}$  is the reduced mass  $m_i m_j / (m_i + m_j)$ .

A more rigorous treatment of gas transport properties, based on more realistic intermolecular potential energy models, can be found in Hirschfelder *et al.*<sup>22</sup> who also present methods for computing the transport properties of mixtures of gases. The NASA computer program "Thermodynamic and Transport Properties of Complex Chemical Systems"<sup>10</sup> computes the viscosity, thermal conduc-

tivity, and Prandtl number in addition to the thermodynamic calculations described in Secs. 3.7 and 4.7 for high-temperature equilibrium and frozen gas composition mixtures. The procedures used in the NASA program to compute these transport properties are based on the techniques described in Hirschfelder *et al.*<sup>22</sup> The NASA program has been used to compute the transport properties of hydrocarbon-air combustion products.<sup>17</sup> These quantities are functions of temperature  $T$ , equivalence ratio  $\phi$ , and (except for viscosity) pressure  $p$ . Approximate correlations were then fitted to the calculated data of viscosity and Prandtl number. The principal advantage of these correlations is computational speed. For Prandtl number ( $\mu c_p/k$ ), it was found convenient to use  $\gamma$ , the specific heat ratio ( $c_p/c_v$ ), as an independent variable. Values of  $\gamma$  and  $c_p$  then permit determination of the thermal conductivity.

The viscosity of hydrocarbon-air combustion products over the temperature range 500 up to 4000 K, for pressures from 1 up to 100 atm, for  $\phi = 0$  up to  $\phi = 4$  is shown in Fig. 4-19. The viscosity as a function of temperature of hydrocarbon-air combustion products differs little from that of air. Therefore, a power law based on air viscosity data was used to fit the data:

$$\mu_{\text{air}} (\text{kg/m} \cdot \text{s}) = 3.3 \times 10^{-7} \times T^{0.7} \quad (4.52)$$

where  $T$  is in kelvins. The viscosity of combustion products is almost indepen-

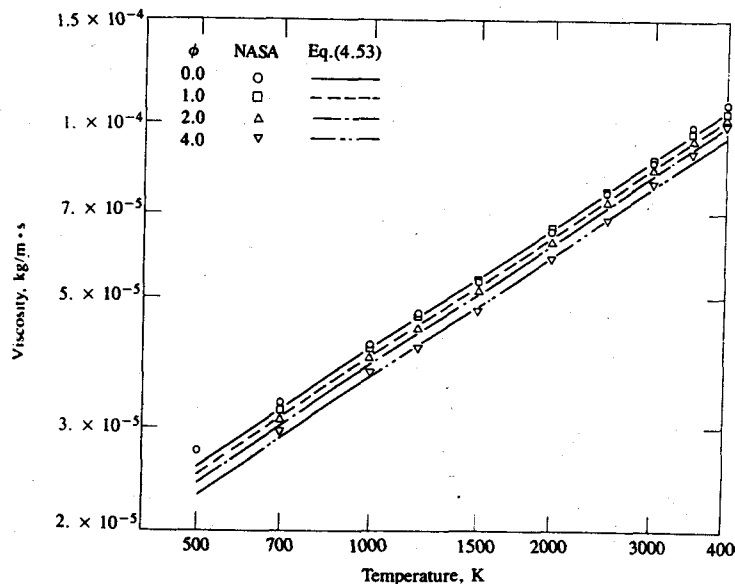


FIGURE 4-19  
Viscosity,  $\text{kg/m} \cdot \text{s}$ , of combustion products as a function of temperature and equivalence ratio. Equations shown are (4.52) and (4.53).

dent of pressure. This correlation was corrected to include the effect of the equivalence ratio  $\phi$  on the viscosity of hydrocarbon-air combustion products:

$$\mu_{\text{prod}} = \frac{\mu_{\text{air}}}{1 + 0.027\phi} \quad (4.53)$$

Figure 4-19 shows that the viscosity predicted using Eqs. (4.52) and (4.53) is very close to the viscosity values calculated with the NASA program. There is less than 4 percent error.

The Prandtl number of hydrocarbon-air combustion products has also been correlated over the above ranges of temperatures, pressures, and equivalence ratios. Since the expression for Prandtl number of a monatomic hard-sphere molecule gas is a function of  $\gamma$ , a second-order polynomial of  $\gamma$  was used to curve-fit the calculated Prandtl number data. A good fit to the data for lean combustion product mixtures was the following:

$$\text{Pr} = 0.05 + 4.2(\gamma - 1) - 6.7(\gamma - 1)^2 \quad \phi \leq 1 \quad (4.54)$$

The values of Pr predicted with Eq. (4.54) are within 5 percent of the equilibrium Pr values calculated with the NASA program. For rich mixtures the following equation is a good fit to the equilibrium values of Pr using equilibrium values of  $\gamma$ , for temperatures greater than 2000 K:

$$\text{Pr} = \frac{0.05 + 4.2(\gamma - 1) - 6.7(\gamma - 1)^2}{1 + 0.015 \times 10^{-6}(\phi T)^2} \quad 1 < \phi \leq 4 \quad (4.55)$$

The predicted values of Pr in this case are also close to the calculated values of Pr, with less than 10 percent error. Equation (4.55) is also a reasonable fit to the frozen values† of Pr for rich mixtures, using frozen values of  $\gamma$ , for the temperature range 1200 to 2000 K. As there are no data for Pr of rich mixtures at low temperatures, we suggest that where a fixed composition for the mixture is appropriate (e.g., during the exhaust process in an internal combustion engine), Eq. (4.55) can also be used with fixed composition values of  $\gamma$ .

The Prandtl number can be obtained from the above relations if  $\gamma$  is known. The thermal conductivity can be obtained from the Prandtl number if values of  $\mu$  and  $c_p$  are known. Values of  $\gamma_b$  and  $c_{p,b}$  as functions of temperature, pressure, and equivalence ratio are given in Figs. 4-15 to 4-18.

Since the fundamental relations for viscosity and thermal conductivity are complicated, various approximate methods have been proposed for evaluating these transport properties for gas mixtures. A good approximation for the vis-

cosity of a multicomponent gas mixture is

$$\mu_{\text{mixt}} = \sum_{i=1}^v \frac{\tilde{x}_i^2}{\tilde{x}_i^2/\mu_i + 1.385 \sum_{j=1, j \neq i}^v \tilde{x}_i \tilde{x}_j (\tilde{R}T/p M_i D_{ij})} \quad (4.56)$$

where  $\tilde{x}_i$  and  $M_i$  are the mole fraction and molecular weight of the  $i$ th species,  $\mu_i$  is the viscosity of the  $i$ th species,  $v$  is the number of species in the mixture, and  $D_{ij}$  is the binary diffusion coefficient for species  $i$  and  $j$ .<sup>22</sup>

## 4.9 EXHAUST GAS COMPOSITION

While the formulas for the products of combustion used in Sec. 3.4 are useful for determining unburned mixture stoichiometry, they do not correspond closely to the actual burned gas composition. At high temperatures (e.g., during combustion and the early part of the expansion stroke) the burned gas composition corresponds closely to the equilibrium composition at the local temperature, pressure, and equivalence ratio. During the expansion process, recombination reactions simplify the burned gas composition. However, late in the expansion stroke and during exhaust blowdown, the recombination reactions are unable to maintain the gases in chemical equilibrium and, in the exhaust process, the composition becomes frozen. In addition, not all the fuel which enters the engine is fully burned inside the cylinder; the combustion inefficiency even when excess air is present is a few percent (see Fig. 3-9). Also, the contents of each cylinder are not necessarily uniform in composition, and the amounts of fuel and air fed to each cylinder of a multicylinder engine are not exactly the same. For all these reasons, the composition of the engine exhaust gases cannot easily be calculated.

It is now routine to measure the composition of engine exhaust gases. This is done to determine engine emissions (e.g., CO, NO<sub>x</sub>, unburned hydrocarbons, and particulates). It is also done to determine the relative proportions of fuel and air which enter the engine so that its operating equivalence ratio can be computed. In this section, typical engine exhaust gas composition will be reviewed, and techniques for calculating the equivalence ratio from exhaust gas composition will be given.

### 4.9.1 Species Concentration Data

Standard instrumentation for measuring the concentrations of the major exhaust gas species has been developed.<sup>23</sup> Normally a small fraction of the engine exhaust gas stream is drawn off into a sample line. Part of this sample is fed directly to the instrument used for unburned hydrocarbon analysis, a flame ionization detector (FID). The hydrocarbons present in the exhaust gas sample are burned in a small hydrogen-air flame, producing ions in an amount proportional to the number of carbon atoms burned. The FID is effectively a carbon atom counter. It is calibrated with sample gases containing known amounts of hydrocarbons. Unburned hydrocarbon concentrations are normally expressed as a mole fraction

† In the NASA program, "frozen" means the gas composition is in equilibrium at the given  $T$  and  $p$ , but is frozen as  $c_p$ ,  $c_v$ , and  $k$  are computed.

or volume fraction in parts per million (ppm) as  $C_1$ . Sometimes results are expressed as ppm propane ( $C_3H_8$ ) or ppm hexane ( $C_6H_{14}$ ); to convert these to ppm  $C_1$  multiply by 3 or 6, respectively. Older measurements of unburned hydrocarbons were often made with a nondispersive infrared (NDIR) analyzer, where the infrared absorption by the hydrocarbons in a sample cell was used to determine their concentration.<sup>23</sup> Values of HC concentrations in engine exhaust gases measured by an FID are about two times the equivalent values measured by an NDIR analyzer (on the same carbon number basis, e.g.,  $C_1$ ). NDIR-obtained concentrations are usually multiplied by 2 to obtain an estimate of actual HC concentrations. Substantial concentrations of oxygen in the exhaust gas affect the FID measurements. Analysis of *unburned* fuel-air mixtures should be done with special care.<sup>23</sup> To prevent condensation of hydrocarbons in the sample line (especially important in diesel exhaust gas), the sample line is often heated.

NDIR analyzers are used for  $CO_2$  and CO concentration measurements. Infrared absorption in a sample cell containing exhaust gas is compared to absorption in a reference cell. The detector contains the gas being measured in two compartments separated by a diaphragm. Radiation not absorbed in the sample cell is absorbed by the gas in the detector on one side of the diaphragm. Radiation not absorbed in the reference cell is absorbed by the gas in the other half of the detector. Different amounts of absorption in the two halves of the detector result in a pressure difference being built up which is measured in terms of diaphragm distention. NDIR detectors are calibrated with sample gases of known composition. Since water vapor IR absorption overlaps  $CO_2$  and CO absorption bands, the exhaust gas sample is dried with an ice bath and chemical dryer before it enters the NDIR instrument.

Oxygen concentrations are usually measured with paramagnetic analyzers. Oxides of nitrogen, either the amount of nitric oxide (NO) or total oxides of nitrogen ( $NO + NO_2$ ,  $NO_x$ ), are measured with a chemiluminescent analyzer. The NO in the exhaust gas sample stream is reacted with ozone in a flow reactor. The reaction produces electronically excited  $NO_2$  molecules which emit radiation as they decay to the ground state. The amount of radiation is measured with a photomultiplier and is proportional to the amount of NO. The instrument can also convert any  $NO_2$  in the sample stream to NO by decomposition in a heated stainless steel tube so that the total  $NO_x$  ( $NO + NO_2$ ) concentration can be determined.<sup>23</sup> Gas chromatography can be used to determine all the inorganic species ( $N_2$ ,  $CO_2$ ,  $O_2$ , CO,  $H_2$ ) or can be used to measure the individual hydrocarbon compounds in the total unburned hydrocarbon mixture. Particulate emissions are measured by filtering the particles from the exhaust gas stream onto a previously weighed filter, drying the filter plus particulate, and reweighing.

**SPARK-IGNITION ENGINE DATA.** Dry exhaust gas composition data, as a function of the fuel/air equivalence ratio, for several different multi- and single-cylinder automotive spark-ignition engines over a range of engine speeds and loads are shown in Fig. 4-20. The fuel compositions (gasolines and isoctane) had H/C ratios ranging from 2.0 to 2.25. Exhaust gas composition is substantially

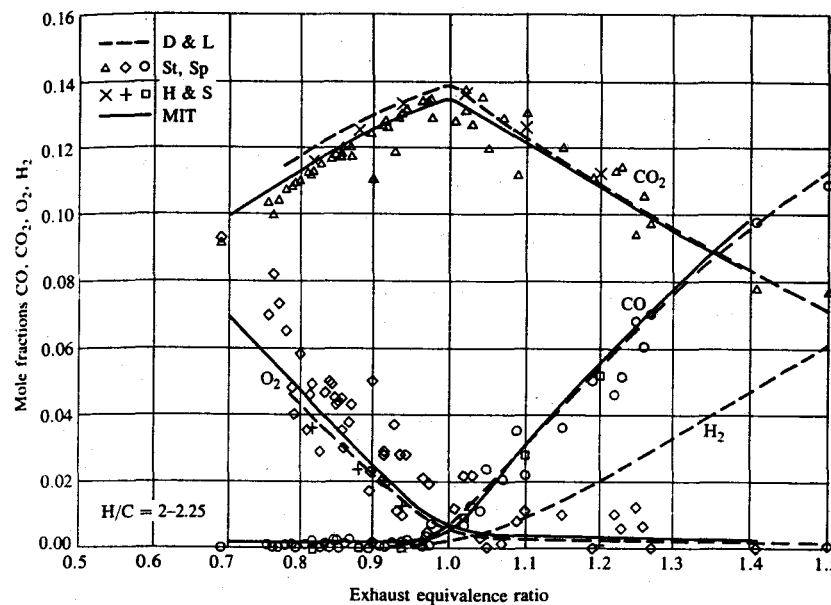


FIGURE 4-20

Spark-ignition engine exhaust gas composition data in mole fractions as a function of fuel/air equivalence ratio. Fuels: gasoline and isoctane, H/C 2 to 2.25. (From D'Alleva and Lovell,<sup>24</sup> Stivender,<sup>25</sup> Harrington and Shishu,<sup>26</sup> Spindt,<sup>27</sup> and data from the author's laboratory at MIT.)

different on the lean and the rich side of the stoichiometric air/fuel or fuel/air ratios; thus, the fuel/air equivalence ratio  $\phi$  (or its inverse, the relative air/fuel ratio  $\lambda$ ) is the appropriate correlating parameter. On the lean side of stoichiometric, as  $\phi$  decreases,  $CO_2$  concentrations fall, oxygen concentrations increase, and CO levels are low but not zero (~0.2 percent). On the rich side of stoichiometric, CO and  $H_2$  concentrations rise steadily as  $\phi$  increases and  $CO_2$  concentrations fall.  $O_2$  levels are low (~0.2 to 0.3 percent) but are not zero. At stoichiometric operation, there is typically half a percent  $O_2$  and three-quarters of a percent CO.

Fuel composition has only a modest effect on the magnitude of the species concentrations shown. Measurements with a wide range of liquid fuels show that CO concentrations depend only on the equivalence ratio or relative fuel/air ratio (see Fig. 11-20).<sup>26</sup> A comparison of exhaust CO concentrations with gasoline, propane ( $C_3H_8$ ), and natural gas (predominantly methane,  $CH_4$ ) show that only with the high H/C ratio of methane, and then only for  $CO \geq 4$  percent, is fuel composition significant.<sup>28</sup> The values of  $CO_2$  concentration at a given  $\phi$  are slightly affected by the fuel H/C ratio. For example, for stoichiometric mixtures with 0.5 percent  $O_2$  and 0.75 percent CO, as the H/C ratio decreases  $CO_2$  concentrations increase from 13.7 percent for isoctane (H/C = 2.25), to 14.2 to 14.5 percent for typical gasolines (H/C in range 2-1.8), to 16 for toluene (H/C = 1.14).<sup>29</sup>

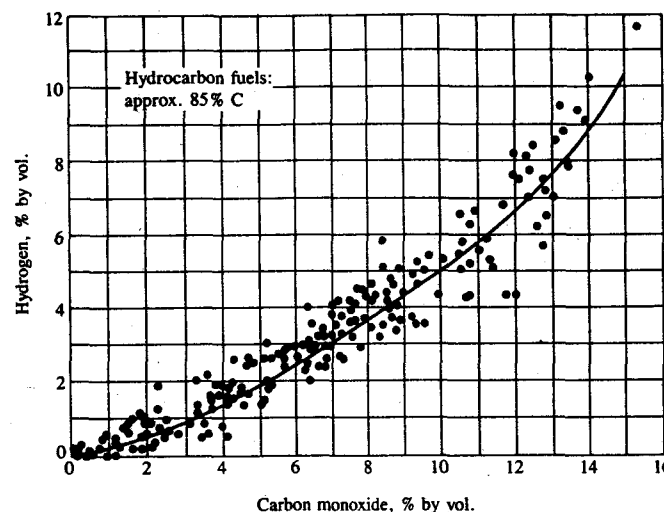


FIGURE 4-21

Hydrogen concentration in spark-ignition engine exhaust as a function of carbon monoxide concentration. Units: percent by volume.<sup>30</sup>

Unburned hydrocarbon exhaust concentrations vary substantially with engine design and operating conditions. Spark-ignition engine exhaust levels in a modern low-emission engine are typically of the order of 2000 ppm C<sub>1</sub> with liquid hydrocarbon fuels, and about half that level with natural gas and propane fuels.

Hydrogen concentrations in engine exhaust are not routinely measured. However, when the mixture is oxygen-deficient—fuel rich—hydrogen is present with CO as an incomplete combustion product. Figure 4-21 summarizes much of the available data on H<sub>2</sub> concentrations plotted as a function of CO.<sup>30</sup>

**DIESEL EXHAUST DATA.** Since diesels normally operate significantly lean of stoichiometric ( $\phi \leq 0.8$ ) and the diesel combustion process is essentially complete (combustion inefficiency is  $\leq 2$  percent), their exhaust gas composition is straightforward. Figure 4-22 shows that O<sub>2</sub> and CO<sub>2</sub> concentrations vary linearly with the fuel/air equivalence ratio over the normal operating range. Diesel emissions of CO and unburned HC are low.

#### 4.9.2 Equivalence Ratio Determination from Exhaust Gas Constituents

Exhaust gas composition depends on the relative proportions of fuel and air fed to the engine, fuel composition, and completeness of combustion. These relationships can be used to determine the operating fuel/air equivalence ratio of an engine from a knowledge of its exhaust gas composition. A general formula for

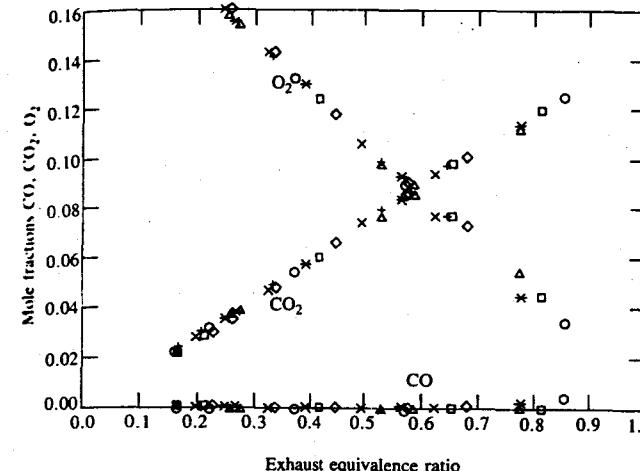


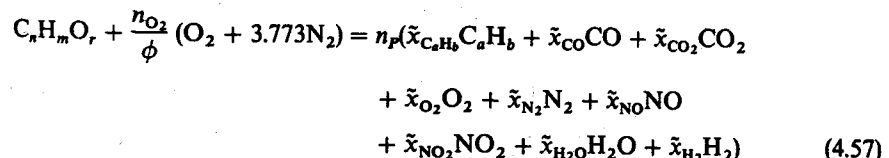
FIGURE 4-22

Exhaust gas composition from several diesel engines in mole fractions on a dry basis as a function of fuel/air equivalence ratio.<sup>31</sup>

the composition of fuel can be represented as C<sub>n</sub>H<sub>m</sub>O<sub>r</sub>. For conventional petroleum-based fuels, oxygen will be absent; for fuels containing alcohols, oxygen will be present. The overall combustion reaction can be written as



The fuel is C<sub>n</sub>H<sub>m</sub>O<sub>r</sub>; the oxidizer is air (O<sub>2</sub> + 3.773N<sub>2</sub>). The products are CO<sub>2</sub>, H<sub>2</sub>O, CO, H<sub>2</sub>, O<sub>2</sub>, NO<sub>x</sub>, N<sub>2</sub>, unburned hydrocarbons (unburned fuel and products of partial fuel reaction), and soot particles (which are mainly solid carbon). The amount of solid carbon present is usually sufficiently small ( $\leq 0.5$  percent of the fuel mass) for it to be omitted from the analysis. The overall combustion reaction can be written explicitly as



where  $\phi$  is the measured equivalence ratio  $[(F/A)_{\text{actual}}/(F/A)_{\text{stoichiometric}}]$ ,  $n_{\text{O}_2}$  is the number of O<sub>2</sub> molecules required for complete combustion ( $n + m/4 - r/2$ ),  $n_p$  is the total number of moles of exhaust products, and  $\tilde{x}_i$  is the mole fraction of the  $i$ th component.

There are several methods for using Eq. (4.57) to determine  $\phi$ , the equivalence ratio, depending on the amount of information available. Normally CO<sub>2</sub>, CO, O<sub>2</sub>, NO<sub>x</sub> concentrations as mole fractions and unburned hydrocarbon (as

mole fraction or ppm C<sub>1</sub>, i.e.,  $\tilde{x}_{\text{CH}_4}$ ) are measured. The concentration of the inorganic gases are usually measured *dry* (i.e., with H<sub>2</sub>O removed) or *partially dry*. Unburned hydrocarbons may be measured *wet* or *dry* or *partially dry*. NO<sub>x</sub> is mainly nitric oxide (NO); its concentration is usually sufficiently low (< 0.5 percent) for its effect on equivalence ratio determination to be negligibly small. Thus, in Eq. (4.57) there are seven unknowns which are:  $\phi$ ,  $\tilde{x}_{\text{H}_2}$ ,  $\tilde{x}_{\text{H}_2\text{O}}$ ,  $\tilde{x}_{\text{N}_2}$ ,  $n_p$ ,  $a$ ,  $b$ . (There will be additional unknowns if the measurements listed above are incomplete.)

To solve for these unknowns we need seven additional equations. We can obtain five equations using an atomic balance for each element and the definition of mole fraction, as follows:

Carbon balance:

$$n = n_p(a\tilde{x}_{\text{C}_6\text{H}_6} + \tilde{x}_{\text{CO}} + \tilde{x}_{\text{CO}_2}) \quad (4.58)$$

Hydrogen balance:

$$m = n_p(b\tilde{x}_{\text{C}_6\text{H}_6} + 2\tilde{x}_{\text{H}_2\text{O}} + 2\tilde{x}_{\text{H}_2}) \quad (4.59)$$

Oxygen balance:

$$r + \frac{2n_{\text{O}_2}}{\phi} = n_p(\tilde{x}_{\text{CO}} + 2\tilde{x}_{\text{CO}_2} + \tilde{x}_{\text{NO}} + 2\tilde{x}_{\text{O}_2} + \tilde{x}_{\text{H}_2\text{O}}) \quad (4.60)$$

Nitrogen balance:

$$\frac{7.546n_{\text{O}_2}}{\phi} = n_p(2\tilde{x}_{\text{N}_2} + \tilde{x}_{\text{NO}}) \quad (4.61)$$

Mole fractions add up to 1:

$$\tilde{x}_{\text{C}_6\text{H}_6} + \tilde{x}_{\text{CO}} + \tilde{x}_{\text{H}_2} + \tilde{x}_{\text{H}_2\text{O}} + \tilde{x}_{\text{N}_2} + \tilde{x}_{\text{NO}} + \tilde{x}_{\text{CO}_2} + \tilde{x}_{\text{O}_2} = 1 \quad (4.62)$$

An additional assumption is made, based on available exhaust gas composition data, that CO<sub>2</sub>, CO, H<sub>2</sub>O, and H<sub>2</sub> concentrations are related by

$$\frac{\tilde{x}_{\text{CO}} \tilde{x}_{\text{H}_2\text{O}}}{\tilde{x}_{\text{CO}_2} \tilde{x}_{\text{H}_2}} = K \quad (4.63)$$

where  $K$  is a constant.<sup>†</sup> Values of 3.8<sup>24, 25</sup> and 3.5<sup>27</sup> are commonly used for  $K$ . The difference between these values has little effect on the computed magnitude of  $\phi$ . To complete the analysis, various assumptions are made concerning the composition and relative importance of the unburned hydrocarbons. The most common approaches are summarized below.

<sup>†</sup> Equation (4.63) is often described as assuming a specific value for the water-gas reaction equilibrium constant. In fact  $K$  is an empirical constant determined from exhaust gas composition data.

**OXYGEN BALANCE AIR/FUEL AND EQUIVALENCE RATIOS.** For fuels comprised of carbon and hydrogen only, when all species are measured with the *same background moisture* (wet, dry, or partially dry), the following expression based on the ratio of measured and computed oxygen-containing species to measured carbon-containing species gives the air/fuel ratio. It has been assumed that the unburned hydrocarbons have the same C/H ratio as the fuel:<sup>32</sup>

$$\left(\frac{A}{F}\right) = 4.773 \left(\frac{M_{\text{air}}}{M_f}\right) \frac{(CO_2) + (CO)/2 + (H_2O)/2 + (NO)/2 + (NO_2) + (O_2)}{(HC) + (CO) + (CO_2)} \quad (4.64)$$

where ( ) are molar concentrations (all with the same background moisture) in percent,  $M_{\text{air}} = 28.96$ ,  $M_f = 12.01 + 1.008y$  where  $y$  is the H/C ratio of the fuel, (HC) is molar percent unburned hydrocarbons as C<sub>1</sub>, and

$$(H_2O) = 0.5y \frac{(CO_2) + (CO)}{(CO)/[K(CO_2)] + 1} \quad (4.65)$$

Since nitrogen oxides collectively comprise less than 0.5 percent of the exhaust mixture, their concentrations can be omitted with negligible error.

The fuel/air equivalence ratio  $\phi$  is obtained from the ratio of the stoichiometric air/fuel ratio [Eq. (3.6)] and Eq. (4.64) above.

**CARBON BALANCE AIR/FUEL AND EQUIVALENCE RATIOS.** When oxygen analysis is not available, for fuels comprised of carbon and hydrogen only, a carbon balance air/fuel ratio may be employed:<sup>25, 32</sup>

$$\frac{A}{F} = \frac{M_{\text{air}}}{M_f} \left[ \frac{100 + (HC) - (CO)/2 + 3(H_2O)/2 - (H_2O)_a - \frac{y}{2}}{(HC) + (CO) + (CO_2)} \right] \quad (4.66)$$

The symbols are as defined above. (H<sub>2</sub>O) is the molar percent water in the combustion products defined by Eq. (4.65) and (H<sub>2</sub>O)<sub>a</sub> is the molar percent water vapor at the analyzers.

This carbon balance ( $A/F$ ) is sensitive to moisture concentration at the analyzers. The use of ice bath exhaust sample chillers generally reduces the (H<sub>2</sub>O)<sub>a</sub> term to less than 1 percent and little accuracy is then lost by neglecting it. For completely "wet" analysis (uncondensed), (H<sub>2</sub>O)<sub>a</sub> = (H<sub>2</sub>O), and Eq. (4.66) is accurate. For partially dry exhaust gas analysis, knowledge of the dew point of the mixture will provide the (H<sub>2</sub>O)<sub>a</sub> term by reference to steam tables.

The fuel/air equivalence ratio  $\phi$  is obtained from the ratio of the stoichiometric air/fuel ratio [Eq. (3.6)] and Eq. (4.66) above.

**EQUIVALENCE RATIO BASED ON WET HC AND DRY INORGANIC GAS ANALYSIS.** Engine exhaust gas composition is often determined by analyzing a fully dried sample stream for CO<sub>2</sub>, CO, O<sub>2</sub>, and NO<sub>x</sub>, and a fully wet (uncondensed) stream with an FID for unburned hydrocarbons. Equations (4.64) and (4.66) are not applicable under these circumstances. The following equations

define the exhaust gas composition and equivalence ratio under these conditions. The notation  $\tilde{x}_i$  denotes the wet mole fraction of species  $i$  and  $\tilde{x}_i^*$  denotes the dry mole fraction of species  $i$ . Equations (4.57) to (4.62), with Eq. (4.63) to relate  $\text{CO}_2$ ,  $\text{CO}$ ,  $\text{H}_2\text{O}$ , and  $\text{H}_2$  concentrations and the assumption that  $b/a = m/n$ , were used to derive these results. The equations apply for a fuel of composition  $\text{C}_m\text{H}_n\text{O}_r$ .

The fuel/air equivalence ratio is given by

$$\phi = \frac{2\tilde{x}_{\text{O}_2}}{n_p \tilde{x}_{\text{H}_2\text{O}} + n_p(1 - \tilde{x}_{\text{H}_2\text{O}})(\tilde{x}_{\text{CO}}^* + 2\tilde{x}_{\text{CO}_2}^* + 2\tilde{x}_{\text{O}_2}^* + \tilde{x}_{\text{NO}}^* + 2\tilde{x}_{\text{NO}_2}^*) - r} \quad (4.67)$$

where the wet and dry mole fractions are related by

$$\tilde{x}_i = (1 - \tilde{x}_{\text{H}_2\text{O}})\tilde{x}_i^*$$

and

$$\begin{aligned} n_p &= \frac{n}{\tilde{x}_{\text{CH}_{b/a}} + (1 - \tilde{x}_{\text{H}_2\text{O}})(\tilde{x}_{\text{CO}}^* + \tilde{x}_{\text{CO}_2}^*)} \\ \tilde{x}_{\text{H}_2\text{O}} &= \frac{m}{2n} \frac{\tilde{x}_{\text{CO}}^* + \tilde{x}_{\text{CO}_2}^*}{[1 + \tilde{x}_{\text{CO}}^*/(K\tilde{x}_{\text{CO}_2}^*) + (m/2n)(\tilde{x}_{\text{CO}}^* + \tilde{x}_{\text{CO}_2}^*)]} \quad (4.68) \\ \tilde{x}_{\text{H}_2} &= \frac{\tilde{x}_{\text{H}_2\text{O}} \tilde{x}_{\text{CO}}^*}{K \tilde{x}_{\text{CO}_2}^*} \\ \tilde{x}_{\text{N}_2} &= \frac{3.773 n_{\text{O}_2}}{\phi n_p} - (1 - \tilde{x}_{\text{H}_2\text{O}}) \frac{(\tilde{x}_{\text{NO}}^* + \tilde{x}_{\text{NO}_2}^*)}{2} \end{aligned}$$

Note that  $\tilde{x}_{\text{CH}_{b/a}}$  is the measured (wet) HC concentration as a mole fraction  $C_1$  ( $\text{ppm } C_1 \times 10^{-6}$ ):  $\tilde{x}_{\text{CH}_{b/a}} = a\tilde{x}_{\text{C}_a\text{H}_b}$ . Figure 4-23 shows wet exhaust gas concentrations, based on the MIT measured dry concentrations of  $\text{CO}_2$ ,  $\text{CO}$ ,  $\text{O}_2$  shown in Fig. 4-20, and wet HC concentration, as well as Eqs. (4.68).

For lean mixtures, varying the value of  $K$  between 1.5 and 5.5 had a negligible effect on the value of  $\phi$  computed from Eq. (4.67). For stoichiometric mixtures, varying  $K$  from 2.5 to 4.5 varied the computed  $\phi$  by 2 to 3 percent. For  $\phi \approx 1.2$ , varying  $K$  from 2.5 to 4.5 varied the computed  $\phi$  by 3 to 4 percent. The error in  $\phi$  involved in omitting  $\text{NO}_x$  is 0.2 percent for an  $\text{NO}_x$  level of 1000 ppm, increasing to 1 percent for an  $\text{NO}_x$  level of 5000 ppm. The sensitivity of the computed  $\phi$  to errors in the measurements of  $\text{CO}_2$ ,  $\text{CO}$ , and  $\text{O}_2$  is modest within the normal range of  $\phi$  used. A 2 percent error in  $\text{CO}_2$  or  $\text{CO}$  or  $\text{O}_2$  at  $\phi \approx 1$  gives about a 0.1 percent error in computed  $\phi$ . For leaner and richer mixtures, the error in  $\phi$  increases for errors in measured  $\text{CO}_2$  concentration, and  $\text{CO}$  ( $\phi > 1$ ) and  $\text{O}_2$  ( $\phi < 1$ ) concentrations, but is still significantly less than the measurement error in fuel and air flow.

### 4.9.3 Effects of Fuel/Air Ratio

#### Nonuniformity

Neither the masses of air inducted into the different cylinders of a multicylinder engine per cycle nor the masses of fuel which enter the different cylinders per

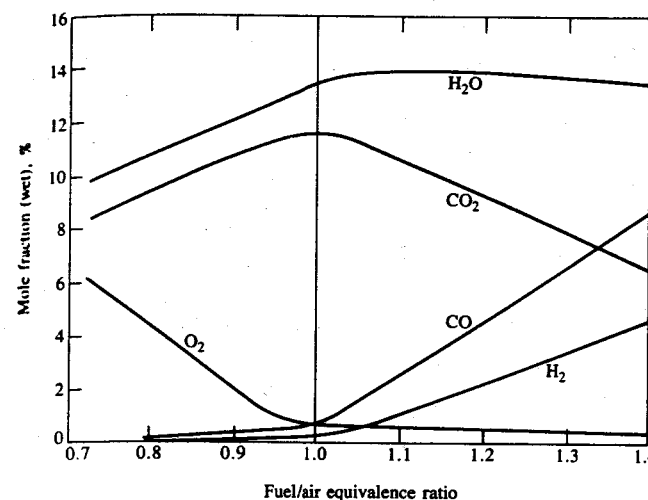


FIGURE 4-23

Wet exhaust gas species concentrations as a function of fuel/air equivalence ratio, based on the dry exhaust gas composition data in Fig. 4-20 and Eqs. (4.68).

cycle are exactly equal. In addition, mixing of fuel and air within each cylinder is not necessarily completely uniform. Thus the exhaust gas composition may correspond to a distribution in the fuel/air ratio in the unburned mixture about the mean value. For example, if the mean fuel/air ratio is stoichiometric, extra oxygen will be contributed by any cylinders operating lean of the average and extra carbon monoxide by any cylinders rich of the average, so that the exhaust gas will have higher levels of  $\text{O}_2$  and  $\text{CO}$  (and a lower level of  $\text{CO}_2$ ) relative to an engine operating with identical fuel/air ratios in each cylinder.

Eltinge has developed a method for defining this nonuniformity in the fuel/air ratio distribution for spark-ignition engines which operate close to stoichiometric.<sup>29</sup> A function  $f(x)$  for the fuel/air ratio distribution ( $x = F/A$ ) was assumed, with standard deviation  $S_x$ . For each value of  $x$  (i.e.,  $F/A$ ), complete utilization of the available oxygen was assumed (i.e., no exhaust HC) and the  $\text{CO}_2$ ,  $\text{H}_2\text{O}$ ,  $\text{CO}$ ,  $\text{H}_2$  concentrations were related by Eq. (4.63) (with  $K = 3.5$ ). The concentrations of each species for each ( $F/A$ ) were weighted by the distribution function  $f(x)$  and summed to produce the average exhaust concentration. (A correction to allow for the presence of unburned HC in the exhaust was also developed.) Figure 4-24 shows one set of results, for a fuel H/C ratio of 1.8 (typical of gasoline), for a normal distribution in the fuel/air ratio. For each mean ( $F/A$ ) and maldistribution parameter  $S_x$  (the standard deviation of the  $F/A$  distribution) the corresponding dry concentrations of  $\text{CO}_2$ ,  $\text{CO}$ , and  $\text{O}_2$  are shown. This type of information can be used to define the fuel-air mixture nonuniformities in spark-ignition engines operating relatively close to stoichiometric. For diesel engines the variations of major exhaust gas species concentrations with fuel/air equiva-

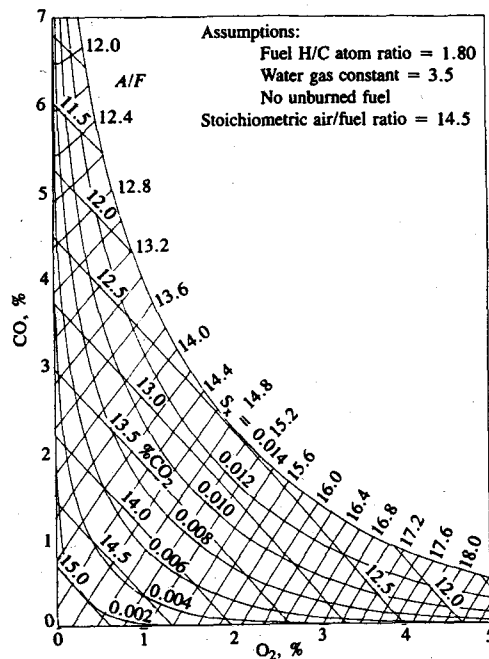


FIGURE 4-24

Computed relationship between dry exhaust gas composition ( $\text{CO}_2$ ,  $\text{CO}$ , and  $\text{O}_2$ ), air/fuel ratio, and maldistribution parameter  $S_x$ . Fuel:  $(\text{CH}_{1.8})_n$ . The correction to be added to the burned gas ( $F/A$ ) which allows for the measured unburned hydrocarbon concentration is  $4.7 \times 10^{-7} \times \text{HC}$  (ppm  $\text{C}_1$ ) (From Eltinge.<sup>29</sup>)

lence ratio are linear, so the effects of any nonuniformities are not apparent in this manner (see Fig. 4-22).

#### 4.9.4 Combustion Inefficiency

Internal combustion engine exhaust contains combustible species:  $\text{CO}$ ,  $\text{H}_2$ , unburned hydrocarbons, and particulates. When their concentrations are known, the combustion efficiency  $\eta_c$  given by Eq. (3.27) can be calculated. The chemical energy carried out of the engine in these combustibles represents the combustion inefficiency,  $1 - \eta_c$ :

$$1 - \eta_c = \frac{\sum_i x_i Q_{\text{HV},i}}{[\dot{m}_f / (\dot{m}_a + \dot{m}_f)] Q_{\text{HV},f}} \quad (4.69)$$

where the  $x_i$  are the mass fractions of  $\text{CO}$ ,  $\text{H}_2$ , HC, and particulates, respectively, the  $Q_{\text{HV},i}$  are the lower heating values of these species, and the subscripts  $f$  and  $a$  denote fuel and air. The heating values for  $\text{CO}$  (10.1 MJ/kg) and  $\text{H}_2$  (120 MJ/kg) are well defined. The composition of the unburned HC is not usually known. However, the heating values of hydrocarbons are closely comparable, so the fuel heating value (typically 42 to 44 MJ/kg) is used. The particulates (only present in diesels) are soot with some adsorbed hydrocarbons; usually the mass fraction is low enough for their contribution to be small, and a heating value for solid carbon (32.8 MJ/kg) can be used. Combustion efficiency data as a function of equivalence ratio have already been presented in Fig. 3-9.

## PROBLEMS

- 4.1. (a) Calculate the low-temperature burned gas composition resulting from the combustion of 7 g/s air with 0.48 g/s ethane ( $\text{C}_2\text{H}_6$ ). Assume  $K = 3.5$  in Eq. (4.6).  
(b) Calculate the low-temperature burned gas composition for the combustion of 7 g/s air with 0.48 g/s ethanol ( $\text{C}_2\text{H}_6\text{O}$ ). Assume  $K = 3.5$  in Eq. (4.6). (Note the large difference in burned gas composition due to this difference in fuel.)
- 4.2. To evaluate the accuracy of the simple analytic ideal gas model, use the results of Example 4.1 and Eqs. (4.23) (constant-volume adiabatic combustion) and (4.24) (constant-pressure adiabatic combustion) to calculate  $T_b$  for a stoichiometric isoctane-air mixture. Compare this result with that obtained using Figs. 4-3 and 4-8. Assume the following unburned mixture conditions:  $T = 700 \text{ K}$ ,  $v = 0.125 \text{ m}^3/\text{kg}$  air,  $p = 15 \text{ atm}$ , and  $x_b = 0.1$ .
- 4.3. (a) In Fig. 4-1, why does  $M_b$  decrease as  $x_b$  increases?  
(b) In Fig. 4-14, why does  $M_b$  decrease as  $T$  increases?  
(c) In Fig. 4-14, why does  $M_b$  decrease as  $\phi$  increases?
- 4.4. Show how, for an ideal gas with fixed composition, the molecular weight  $M$  is related to the specific heats  $c_p$  and  $c_v$ , and  $\tilde{R}$ . Use Figs. 4-15 and 4-16 to calculate  $M_b$  for  $T_b = 1750, 2250$ , and  $2750 \text{ K}$ , and  $\phi = 1.0$ . Compare these results with values of  $M_b$  obtained from Fig. 4-14 and explain any differences.
- 4.5. EGR, exhaust gas recirculation, is often used to reduce  $\text{NO}_x$  by acting as a diluent in the intake mixture.  
(a) For low-temperature isoctane-air combustion products at  $\phi = 1.0$ , determine the percentage of the burned gases' average specific heat at constant pressure which comes from each component in the burned gas mixture.  
(b) Compare the specific heat at constant pressure of isoctane-air combustion products at  $\phi = 1.0$  to that of air, both at  $1750 \text{ K}$ . This difference is one reason why EGR instead of leaner fuel-air mixture is used to control  $\text{NO}_x$  emissions.
- 4.6. Explain qualitatively the causes of the trends in the curves in Fig. 4-23 as  $\phi$  is increased from 1.0 and decreased from 1.0.
- 4.7. Compare the  $\text{O}_2$ ,  $\text{CO}_2$ , and  $\text{CO}$  data in Fig. 4-22 with the predictions of the elemental balance in Table 4.3. Explain any differences. Assume diesel fuel is a hydrocarbon with H/C ratio of 2.
- 4.8. The following exhaust data were obtained from a four-stroke cycle spark-ignition engine.  $\text{CO}_2$ ,  $\text{CO}_2$ , and  $\text{NO}_x$  molar concentrations are all measured fully dry; HC is measured fully wet as ppm  $\text{C}_1$ . Determine the fuel/air equivalence ratio  $\phi$  for the following three sets of data. Make the following assumptions: (1) the constant  $K$  in Eq. (4.63) equals 3.5; (2) the fuel composition is  $\text{C}_8\text{H}_{15.12}$ ; (3) the unburned hydrocarbon H/C ratio is the same as that of the fuel; and (4)  $\text{NO}_x$  is entirely NO.  
(a)  $\text{CO}_2$  14.0%,  $\text{CO}$  0.64%,  $\text{O}_2$  0.7%,  $\text{NO}_x$  3600 ppm, HC 3200 ppm.  
(b)  $\text{CO}_2$  13.8%,  $\text{CO}$  3.05%,  $\text{O}_2$  0%,  $\text{NO}_x$  1600 ppm, HC 3450 ppm.  
(c)  $\text{CO}_2$  12.5%,  $\text{CO}$  0.16%,  $\text{O}_2$  4.0%,  $\text{NO}_x$  4600 ppm, HC 2100 ppm.
- 4.9. The exhaust from a spark-ignition engine has the following composition (in mole fractions):  
$$\text{CO}_2 = 0.12; \text{H}_2\text{O} = 0.14; \text{CO} = 0.01; \text{H}_2 = 0.005;$$
  
$$\text{N}_2 = 0.7247; \text{C}_8\text{H}_{18} = 0.0003$$

The fuel is isoctane,  $\text{C}_8\text{H}_{18}$ ; as shown above, a small fraction of the fuel escapes

from the cylinder unburned. The lower heating value of iso-octane is 44.4 MJ/kg, of carbon monoxide is 10.1 MJ/kg, and of hydrogen is 120 MJ/kg. The atomic weights of the elements are: C = 12, O = 16, H = 1, N = 14.

(a) Calculate the combustion inefficiency in the engine; i.e., the percentage of the entering fuel enthalpy which is not fully released in the combustion process and leaves the engine in the exhaust gases (for this problem, the exhaust can be assumed to be at room temperature).

(b) What fraction of this inefficiency is due to the unburned fuel emissions?

- 4.10. A 2-liter displacement four-cylinder engine, operating at 2000 rev/min and 30 percent of its maximum power at that speed, has the following exhaust composition (in percent by volume or mole percent):

$\text{CO}_2$ , 11%;  $\text{H}_2\text{O}$ , 11.5%; CO, 0.5%;  $\text{H}_2$ , 0%;  $\text{O}_2$ , 2%; unburned hydrocarbons (expressed as  $\text{CH}_2$ , i.e., with a molecular weight of 14), 0.5%;  $\text{N}_2$ , 74.5%

The fuel is  $(\text{CH}_2)_n$  with a heating value of 44 MJ/kg. The atomic weights of the elements are C = 12, H = 1, O = 16, N = 14. The heating values of CO and HC are 10 and 44 MJ/kg, respectively.

- (a) Is the engine a diesel or spark-ignition engine? Is there enough oxygen in the exhaust to burn the fuel completely? Briefly explain.  
 (b) Calculate the fraction of the input fuel energy ( $m_f Q_{hv}$ ) which exits the engine unburned as (1) CO and (2) unburned HC.  
 (c) An inventor claims a combustion efficiency of 100 percent can be achieved. What percentage improvement in engine specific fuel consumption would result?

- 4.11. A gasoline engine operates steadily on a mixture of iso-octane and air. The air and fuel enter the engine at 25°C. The fuel consumption is 3.0 g/s. The output of the engine is 50 kW. The temperature of the combustion products in the exhaust manifold is 660 K. At this temperature, an analysis of the combustion products yields the following values (on a dry volumetric basis):

$\text{CO}_2$ , 11.4%;  $\text{O}_2$ , 1.6%; CO, 2.9%;  $\text{N}_2$ , 84.1%

- (a) Find the composition in moles (number of moles per mole of iso-octane) of the reactants and the reaction products.  
 (b) Determine the heat-transfer rate from the working fluid as the working fluid passes through the engine.

Constants for the calculations:

	Enthalpy of formation, kJ/kmol	Sensible enthalpy at 660 K, kJ/kmol
$\text{C}_8\text{H}_{18}$	-25920	—
$\text{CO}_2$	-393522	15823
CO	-110529	10789
$\text{H}_2\text{O}$	-241827	12710
$\text{O}_2$	—	11200
$\text{N}_2$	—	10749

- 4.12. A direct-injection four-stroke cycle diesel engine is used to provide power for pumping water. The engine operates at its maximum rated power at 2000 rev/min,

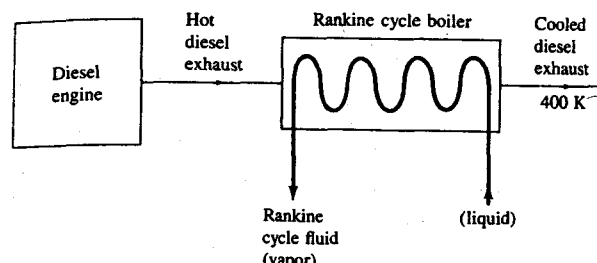


FIGURE P4-12

with an equivalence ratio of 0.8 and an air flow of 0.5 kg/s. The gross indicated fuel conversion efficiency is 45 percent, and the heat losses from the working fluid to the engine coolant and elsewhere within the engine are 280 kW. Diesel fuel has a heating value of 42 MJ/kg and stoichiometric fuel/air ratio of 0.067. Fuel and air enter the engine at ambient conditions. The mechanical efficiency of the diesel engine is 85 percent.

(a) Calculate the rated brake power of the engine, the average sensible enthalpy of the exhaust gases as they leave the engine, and the average exhaust gas temperature.

(b) Since the exhaust gas temperature is significantly above ambient, the advantages of using the diesel exhaust gas stream to heat the boiler of a Rankine cycle (see sketch) and generate additional power are to be explored. If the exhaust gases leave the Rankine-cycle system boiler at 400 K and 30 percent of the heat transferred from the exhaust gas stream in the boiler is converted to power at the Rankine-cycle power plant drive shaft, calculate the additional power obtained and the brake fuel conversion efficiency of the combined cycle system (diesel plus Rankine cycle).

- 4.13. A diesel engine has a compression ratio of 22 : 1. The conditions in the cylinder at the start of compression are  $p = 101.3 \text{ kPa}$  and  $T = 325 \text{ K}$ . Calculate the pressure and temperature at the end of compression, assuming the compression process is isentropic:

- (a) Assume the cylinder contains an ideal gas with  $\gamma = 1.4$  and  $R = 287 \text{ J/kg} \cdot \text{K}$ .  
 (b) Assume the cylinder contains air which may be regarded as a semiperfect gas (use the gas tables).  
 (c) Compare the work of compression in (a) and (b) above.

In practice, heat losses reduce the final compression temperature by 100 K. For a diesel engine operating at an equivalence ratio of 0.75 (full load):

- (d) Calculate the ratio of heat loss during compression to the fuel energy added per cycle.

- 4.14. While the geometric compression ratio of an engine is  $V_{\max}/V_{\min}$ , the actual compression process starts somewhere between bottom-center and when the inlet valve closes, and it is conditions at time of spark (for an SI engine) or fuel injection (for a CI engine) that determine ignition. At low engine speed, compression starts about the time when the inlet valve closes. With this assumption, for the diesel engine of Prob. 4.13, calculate the air pressure and temperature at the start of injection. The inlet valve closes at 30° after BC; injection commences 15° before TC. Use the gas tables. Compare your answers with those of Prob. 4.13(b).

- 4.15. Use an equilibrium computer code (which calculates the composition and properties of chemically reacting gas mixtures in equilibrium) to calculate the data you need for the following graphs:
- Values of  $c_p$ ,  $\gamma$ , molecular weight, and gas composition (mole fractions of N<sub>2</sub>, CO<sub>2</sub>, H<sub>2</sub>O, CO, H<sub>2</sub>, O<sub>2</sub>, OH, O, H, and NO) as a function of the equivalence ratio ( $\phi = 0.2$  to 1.4) for products of combustion of isoctane (C<sub>8</sub>H<sub>18</sub>) with air at  $p = 40$  atm and  $T = 2500$  K. Put all species concentrations on the same graph. Use a log scale for the composition axis.
  - Unburned mixture consisting of isoctane vapor and air at 700 K and 20 atm is burned first at constant pressure and then at constant volume.
    - Calculate the enthalpy and internal energy of isoctane vapor at 700 K in cal/gmol; also calculate the volume per unit mass of mixture (cm<sup>3</sup>/g) for  $\phi = 0.2, 0.4, 0.6, 0.8, 1.0, 1.2, 1.4$ .
    - Use these data and the equilibrium program to calculate the temperature attained after combustion at constant pressure, and temperature and pressure attained after combustion at constant volume. Plot these temperatures and pressures against the equivalence ratio  $\phi$ .

#### Thermodynamic data for isoctane vapor

$T, \text{K}$	$\bar{c}_p, \text{cal/mol} \cdot \text{K}$	$\bar{h} - \bar{h}_{298}, \text{kcal/mol}$	$\Delta\bar{h}_f^\circ, \text{kcal/mol}$
298	45.14	0.00	-53.57
700	85.66	27.02	-62.79

- 4.16. A heavy wall bomb with a volume of 1000 cm<sup>3</sup> contains a mixture of isoctane with the stoichiometric air requirement at  $p = 101.3$  kPa and  $T = 25^\circ\text{C}$ . The mixture is then ignited with a spark. Find the pressure and temperature of the equilibrium combustion products just after combustion is complete (i.e., before heat losses to the wall are significant). Assume the burned gases are uniform.
- 4.17. A gas engine, running on a gaseous mixture of butane, C<sub>4</sub>H<sub>10</sub>, and air has the following conditions in the cylinder prior to constant-volume adiabatic combustion: pressure,  $6.48 \times 10^5$  N/m<sup>2</sup>; temperature, 600 K. The charge composition is air plus 50 percent of the stoichiometric quantity of butane fuel. Calculate the pressure and temperature at the end of combustion using the data given below.

For air	$T, \text{K}$	$\bar{u}, \text{J/gmol}$
	298	6,161
	600	12,596

For butane	$T, \text{K}$	$\bar{u}, \text{J/gmol}$
	298	-77
	600	38,424

Internal energy of combustion of butane at 298 K is  $\Delta\bar{u} = -2.659$  MJ/gmol. Extract from gas tables for products of combustion for 50 percent stoichiometric fuel:

$T, \text{K}$	$\bar{u}, \text{J/gmol}$
298	6,293
2075	54,227
2080	54,380

#### REFERENCES

- Komiyama, K., and Heywood, J. B.: "Predicting NO<sub>x</sub> Emissions and the Effects of Exhaust Gas Recirculation in Spark-Ignition Engines," SAE paper 730475, *SAE Trans.*, vol. 82, 1973.
- Danieli, G., Ferguson, C., Heywood, J., and Keck, J. "Predicting the Emissions and Performance Characteristics of a Wankel Engine," SAE paper 740186, *SAE Trans.*, vol. 83, 1974.
- Hottel, H. C., Williams, G. C., and Satterfield, C. N.: *Thermodynamic Charts for Combustion Processes*, John Wiley, 1949. See also charts in C. F. Taylor, *The Internal Combustion Engine in Theory and Practice*, vol. 1, MIT Press, 1960.
- Newhall, H. K., and Starkman, E. S.: "Thermodynamic Properties of Octane and Air for Engine Performance Calculations," in *Digital Calculations of Engine Cycles, Progress in Technology*, vol. TP-7, pp. 38-48, SAE, 1964.
- Starkman, E. S., and Newhall, H. K.: "Thermodynamic Properties of Methane and Air, and Propane and Air for Engine Performance Calculations," SAE paper 670466, *SAE Trans.*, vol. 76, 1967.
- Keenan, J. H., Chao, J., and Kaye, J.: *Gas Tables*, 2d ed., John Wiley, 1983.
- Reynolds, W. C.: *Thermodynamic Properties in SI; Graphs, Tables, and Computational Equations for Forty Substances*, Department of Mechanical Engineering, Stanford University, 1979.
- JANAF Thermochemical Tables, 2d ed., NSRDS-NB537, U.S. National Bureau of Standards, June 1971.
- Gordon, S., and McBride, B. J.: "Computer Program for the Calculation of Complex Chemical Equilibrium Composition, Rocket Performance, Incident and Reflected Shocks, and Chapman-Jouguet Detonations," NASA publication SP-273, 1971 (NTIS number N71-37775).
- Svehla, R. A., and McBride, B. J.: "Fortran IV Computer Program for Calculation of Thermodynamic and Transport Properties of Complex Chemical Systems," NASA technical note TND-7056, 1973 (NTIS number N73-15954).
- Fremont, H. A., et al.: *Properties of Combustion Gases*, General Electric Company, Cincinnati, Ohio, 1955.
- Banes, B., McIntyre, R. W., and Sims, J. A.: *Properties of Air and Combustion Products with Kerosene and Hydrogen Fuels*, vols. I-XIII, Propulsion and Energetics Panel, Advisory Group for Aerospace Research and Development (AGARD), NATO, published by Bristol Siddeley Engines Ltd., Filton, Bristol, England, 1967.
- Hires, S. D., Ekchian, A., Heywood, J. B., Tabaczynski, R. J., and Wall, J. C.: "Performance and NO<sub>x</sub> Emissions Modelling of a Jet Ignition Prechamber Stratified Charge Engine," SAE paper 760161, *SAE Trans.*, vol. 85, 1976.
- LoRusso, J. A.: "Combustion and Emissions Characteristics of Methanol, Methanol-Water, and Gasoline-Methanol Blends in a Spark Ignition Engine," S. M. Thesis, Department of Mechanical Engineering, MIT, May 1976.
- By, A., Kempinski, B., and Rife, J. M.: "Knock in Spark-Ignition Engines," SAE paper 810147, 1981.

16. Rossini, F. D., Pitzer, K. S., Arnett, R. L., Braun, R. M., and Primentel, G. C.: *Selected Values of Physical and Thermodynamic Properties of Hydrocarbons and Related Compounds*, Carnegie Press, Pittsburgh, Pa., 1953.
17. Mansouri, S. H., and Heywood, J. B.: "Correlation for the Viscosity and Prandtl Number of Hydrocarbon-Air Combustion Products," *Combust. Sci. Technology*, vol. 23, pp. 251-256, 1980.
18. Olikara, C., and Borman, G. L.: "A Computer Program for Calculating Properties of Equilibrium Combustion Products with Some Applications to I.C. Engines," SAE paper 750468, 1975.
19. Krieger, R. B., and Borman, G. L.: "The Computation of Apparent Heat Release for Internal Combustion Engines," in *Proc. Diesel Gas Power*, ASME paper 66-WA/DGP-4, 1966.
20. Martin, M. K., and Heywood, J. B.: "Approximate Relationships for the Thermodynamic Properties of Hydrocarbon-Air Combustion Products," *Combust. Sci. Technology*, vol. 15, pp. 1-10, 1977.
21. Chapman, S., and Cowling, T. G.: *The Mathematical Theory of Non-Uniform Gases*, Cambridge University Press, Cambridge, 1955.
22. Hirschfelder, J. O., Curtiss, C. F., and Bird, R. B.: *Molecular Theory of Gases and Liquids*, John Wiley, 1954.
23. Patterson, D. J., and Henein, N. A.: *Emissions from Combustion Engines and Their Control*, Ann Arbor Science Publishers, 1972.
24. D'Alleva, B. A., and Lovell, W. G.: "Relation of Exhaust Gas Composition to Air-Fuel Ratio," *SAE J.*, vol. 38, no. 3, pp. 90-96, March 1936.
25. Stivender, D. L.: "Development of a Fuel-Based Mass Emission Measurement Procedure," SAE paper 710604, 1971.
26. Harrington, J. A., and Shishu, R. C.: "A Single-Cylinder Engine Study of the Effects of Fuel Type, Fuel Stoichiometry and Hydrogen-to-Carbon Ratio on CO, NO, and HC Exhaust Emissions," SAE paper 730476, 1973.
27. Spindt, R. S., "Air-Fuel Ratios from Exhaust Gas Analysis," SAE paper 650507, *SAE Trans.*, vol. 74, 1965.
28. Fleming, R. D., and Eccleston, D. B.: "The Effect of Fuel Composition, Equivalence Ratio, and Mixture Temperature on Exhaust Emissions," SAE paper 710012, 1971.
29. Eltinge, L.: "Fuel-Air Ratio and Distribution from Exhaust Gas Composition," SAE paper 680114, *SAE Trans.*, vol. 77, 1968.
30. Leonard, L. S.: "Fuel Distribution by Exhaust Gas Analysis," SAE paper 379A, 1961.
31. Bishop, R. P.: "Combustion Efficiency in Internal Combustion Engines," B.S. Thesis, Department of Mechanical Engineering, MIT, February 1985.
32. The Engine Test Code Subcommittee of the General Technical Committee, *General Motors Automotive Engine Test Code for Four Cycle Spark Ignition Engines*, 6th ed., 1975.

# CHAPTER

# 5

## IDEAL MODELS OF ENGINE CYCLES

### 5.1 INTRODUCTION

The operating cycle of an internal combustion engine can be broken down into a sequence of separate processes: intake, compression, combustion, expansion, and exhaust. With models for each of these processes, a simulation of a complete engine cycle can be built up which can be analysed to provide information on engine performance. Models of individual engine processes at various levels of approximation have been developed. In this chapter we consider the simplest set of models which provide useful insights into the performance and efficiency of engines. The cycles analysed are commonly called the constant-volume, constant-pressure, and limited-pressure cycles; each title describes the approximation made for the engine combustion process.<sup>†</sup> The description of more accurate simulations of engine processes is deferred until Chap. 14.

For each engine cycle, a choice of models for working fluid thermodynamic properties must be made. These models have been reviewed in Chap. 4. Ideal

<sup>†</sup> These cycles are also referred to by the titles Otto cycle, Diesel cycle, and dual cycle, respectively, for historical reasons. The more descriptive titles used above are preferred because they avoid the often-made assumption that the SI or Otto engine is best approximated by the constant-volume cycle, and the CI or diesel engine is best approximated by the constant-pressure cycle. These assumptions are not necessarily correct.

engine cycle models combined with a simple ideal gas model (specific heats constant throughout the engine cycle—model 1 in Table 4.2) provide analytic results and are useful for illustrative purposes; we will call these cycles *ideal gas standard cycles*. Ideal engine cycles combined with more realistic models of working fluid properties (a frozen mixture of ideal gases for the unburned mixture and an equilibrium mixture for the burned mixture—model 5 in Table 4.2) are called *fuel-air cycles* and provide more quantitative information on engine operation.

An internal combustion engine is not a heat engine in the thermodynamic definition of the term. It is not a closed system. The working fluid does not execute a thermodynamic cycle. The temperature changes which occur around minimum and maximum cylinder volumes are not primarily a result of heat-transfer interactions. An engine can best be analyzed as an open system which exchanges heat and work with its surrounding environment (the atmosphere). Reactants (fuel and air) flow into the system; products (exhaust gases) flow out. (An overall second law analysis of the engine from this point of view has already been presented in Sec. 3.6.) Thus, the cycles discussed in this chapter are not thermodynamic cycles. Rather, each is a consecutive sequence of processes through which we can follow the state of the working fluid as the engine executes a complete operating cycle.

## 5.2 IDEAL MODELS OF ENGINE PROCESSES

The sequence of processes which make up a typical SI and CI engine operating cycle has been described in Sec. 1.3. To illustrate these processes, cylinder pressure ( $p$ ) and volume ( $V$ ) data from a throttled four-stroke cycle SI engine are plotted as a  $p$ - $V$  diagram in Fig. 5-1. The cycle can be divided into compression,

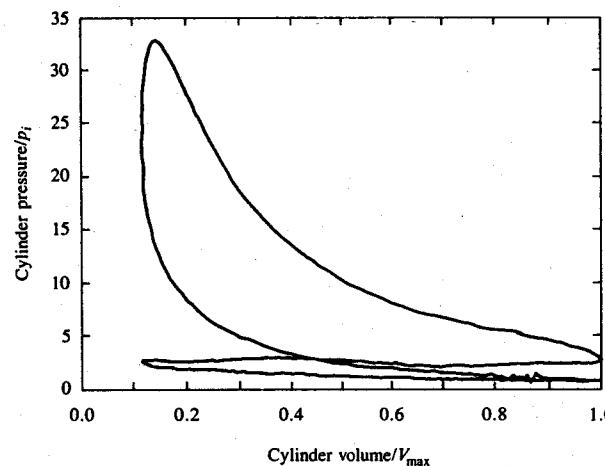


**FIGURE 5-1**  
Pressure-volume diagram of firing spark-ignition engine.  $r_c = 8.4$ , 3500 rev/min,  $p_i = 0.4$  atm,  $p_e = 1$  atm, imep<sub>n</sub> = 2.9 atm.

TABLE 5.1  
Ideal models of engine processes

Process	Assumptions
Compression (1-2)	1. Adiabatic and reversible (hence isentropic)
Combustion (2-3)	1. Adiabatic 2. Combustion occurs at (a) Constant volume (b) Constant pressure (c) Part at constant volume and part at constant pressure (called limited pressure)
Expansion (3-4)	3. Combustion is complete ( $\eta_c = 1$ )
Exhaust (4-5-6) and intake (6-7-1)	1. Adiabatic 2. Valve events occur at top- and bottom-center 3. No change in cylinder volume as pressure differences across open valves drop to zero 4. Inlet and exhaust pressures constant 5. Velocity effects negligible

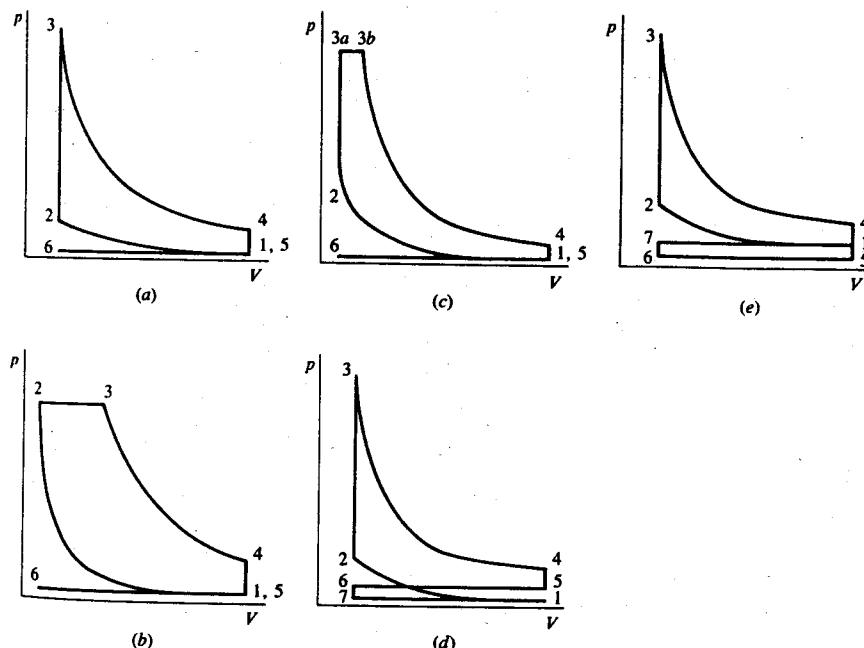


**FIGURE 5-2**  
Pressure-volume diagrams of ideal cycles. Unthrottled operation: (a) constant-volume combustion; (b) constant-pressure combustion; (c) limited-pressure combustion. (d) Throttled constant-volume cycle; (e) supercharged constant-volume cycle.

combustion, expansion, exhaust, and intake processes. Sets of assumptions which simplify each of these processes to a form convenient for analysis are given in Table 5.1.

Pressure-volume diagrams for the constant-volume, constant-pressure, and limited-pressure cycles for unthrottled engine operation ( $p_i < p_e$ ) and supercharged engine operation ( $p_i > p_e$ ) are illustrated in Fig. 5-2a to c. Throttled engine operation ( $p_i < p_e$ ) and supercharged engine operation ( $p_i > p_e$ ) are shown in Fig. 5-2d and e. In each cycle 1-2 is the compression process, 2-3 is the combustion process, 3-4 (or 2-4 in the constant-pressure cycle) is the expansion process, 4-5-6 is the exhaust process, and 6-7-1 is the intake process.

The most critical assumption in determining how useful these ideal cycles are as indicators of engine performance is the form assumed for the combustion process. The real engine combustion process occupies a finite crank angle period (between about 20 and 70 crank angle degrees), and the spark or fuel-injection timing may be retarded from its optimum advance to closer to TC. The constant-volume cycle is the limiting case of infinitely fast combustion at TC; the constant-pressure cycle would correspond to slow and late combustion; the limited-pressure cycle lies in between.

### 5.3 THERMODYNAMIC RELATIONS FOR ENGINE PROCESSES

The overall engine operating parameters of greatest interest which can be determined from a thermodynamic analysis of the engine operating cycle are:

The indicated fuel conversion efficiency  $\eta_{f,i}$ :

$$\eta_{f,i} = \frac{W_{c,i}}{m_f Q_{LHV}} \quad (5.1)$$

(which, since the combustion efficiency is unity, is equal to the indicated thermal conversion efficiency  $\eta_{t,i}$ ; see Sec. 3.6.2)

The indicated mean effective pressure (imep):

$$\text{imep} = \frac{W_{c,i}}{V_d} = \frac{m_f Q_{LHV} \eta_{f,i}}{V_d} \quad (5.2)$$

$W_{c,i}$ , the indicated work per cycle, is the sum of the compression stroke work and the expansion stroke work:

$$W_{c,i} = W_C + W_E \quad (5.3)$$

Using the notation of Fig. 5-2 to define the endpoints of each engine process, the following relationships are obtained by applying the first and second laws of thermodynamics to the cylinder contents:

*Compression stroke:*

$$\frac{v_1}{v_2} = r_c \quad (5.4)$$

Since the process is adiabatic and reversible

$$s_2 = s_1 \quad (5.5)$$

The compression work is

$$W_C = U_1 - U_2 = m(u_1 - u_2) \quad (5.6)$$

*Combustion process:*

For the constant-volume cycle,

$$v_3 = v_2 \quad u_3 - u_2 = 0 \quad (5.7a, b)$$

For the constant-pressure cycle,

$$p_3 = p_2 \quad h_3 - h_2 = 0 \quad (5.7c, d)$$

For the limited-pressure cycle,

$$v_{3a} = v_2 \quad p_{3b} = p_{3a} \quad (5.7e, f)$$

$$\text{and} \quad u_{3a} - u_2 = 0 \quad h_{3b} - h_{3a} = 0 \quad (5.7g, h)$$

*Expansion stroke:*

For the constant-volume cycle,

$$\frac{v_4}{v_3} = r_c \quad s_4 = s_3 \quad (5.8a, b)$$

and the expansion work is

$$W_E = U_3 - U_4 = m(u_3 - u_4) \quad (5.9)$$

For the constant-pressure cycle,

$$p_3 = p_2 \quad \frac{v_4}{v_2} = r_c \quad s_4 = s_3 \quad (5.10a, b, c)$$

and the expansion work is

$$\begin{aligned} W_E &= U_3 - U_4 + p_2(V_3 - V_2) \\ &= m[(u_3 - u_4) + p_2(v_3 - v_2)] \\ &= m[(h_3 - h_4) + p_2 v_3 - p_2 v_2] \end{aligned} \quad (5.11)$$

For the limited-pressure cycle,

$$v_4/v_{3a} = r_c \quad p_{3b} = p_{3a} \quad s_4 = s_{3b} \quad (5.12a, b, c)$$

and the expansion work is

$$\begin{aligned} W_E &= U_{3b} - U_4 + p_3(V_{3b} - V_4) \\ &= m[(u_{3b} - u_4) + p_3(v_{3b} - v_4)] \\ &= m[(h_{3b} - h_4) + p_4 v_4 - p_3 v_{3a}] \end{aligned} \quad (5.13)$$

The indicated fuel conversion efficiency is found by substitution into Eqs. (5.3) and (5.1):

For the constant-volume cycle:

$$\eta_{f,i} = \frac{m[(u_3 - u_4) - (u_2 - u_1)]}{m_f Q_{LHV}} \quad (5.14)$$

For the constant-pressure cycle:

$$\eta_{f,i} = \frac{m[(h_3 - h_4) - (u_2 - u_1) + p_4 v_4 - p_2 v_2]}{m_f Q_{LHV}} \quad (5.15)$$

For the limited-pressure cycle:

$$\eta_{f,i} = \frac{m[(h_{3b} - h_4) - (u_2 - u_1) + p_4 v_4 - p_3 v_{3a}]}{m_f Q_{LHV}} \quad (5.16)$$

The state of the mixture at point 1 in the cycle depends on the intake mixture properties and the residual gas properties at the end of the exhaust stroke.

When the exhaust valve opens at point 4, the cylinder pressure is above the exhaust manifold pressure and a *blowdown* process occurs. In the ideal exhaust process model, this blowdown occurs with the piston stationary at BC. During this blowdown process, the gas which remains inside the cylinder expands isentropically. The gases escaping from the cylinder undergo an unrestrained expansion or throttling process which is irreversible. It is assumed that the kinetic energy acquired by each gas element as it is accelerated through the exhaust valve is dissipated in a turbulent mixing process in the exhaust port into internal energy and flow work. Since it is also assumed that no heat transfer occurs, the enthalpy of each element of gas after it leaves the cylinder remains constant.

These processes are illustrated on an *h-s* diagram in Fig. 5-3. The gas remaining in the cylinder expands isentropically along the line 4-5. The first element of gas which leaves the cylinder at point 4 enters the exhaust manifold at state *a* on the pressure =  $p_e$  line. An element that leaves the cylinder at an intermediate state *b* on the expansion line 4-5 would enter the exhaust manifold at state *c*. At the end of the blowdown process the gas in the cylinder and the last

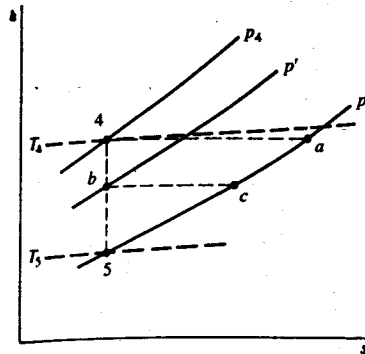


**FIGURE 5-3**  
Enthalpy-entropy diagram of gas state during exhaust process. See text for explanation.

gas to leave have the same state—5. There is, therefore, a gradient in temperature within the exhausted gas. The temperature of the first element exhausted,  $T_a$ , is slightly less than  $T_4$ ; the temperature of the last element exhausted is  $T_5$ .

A displacement of gas out of the cylinder follows the blowdown process as the piston moves from BC to TC. If heat-transfer and kinetic energy dissipation effects are neglected, no change in thermodynamic state of the gas occurs. In this *displacement* process, the mass of gas within the cylinder at the end of the blowdown process is further decreased by the ratio  $V_5/V_6$ .

The mass of residual gas  $m_r$  in the cylinder at point 6 in the cycle is obtained by first determining the state of the gas ( $T_5, v_5$ ) at the end of the blowdown process following an isentropic expansion from  $p_4$  to  $p_e$  and then by reducing the cylinder volume to the clearance volume  $V_6$ . The residual mass fraction is thus given by

$$\frac{m_r}{m} = x_r = \frac{v_4/v_5}{r_c} = \frac{v_2}{v_5} \quad (5.17)$$

The average state of the exhausted gas can be determined by considering the open system defined by the piston face, cylinder walls, and cylinder head, shown in Fig. 5-4. Applying the first law of thermodynamics for an open system gives

$$U_6 - U_4 = p_e(V_4 - V_6) - H_e \quad (5.18a)$$

where  $H_e$  is the enthalpy of the mass of gas exhausted from the cylinder. The average specific exhaust enthalpy is, therefore,

$$\bar{h}_e = \frac{m_4 u_4 - m_6 u_6 + p_e V_6}{m_4 - m_6} \quad (5.18b)$$

which, with  $p = p_e$ , defines the average exhausted-gas state.

The mixture temperature at the end of the intake stroke and at the start of the compression stroke (point 1 in Fig. 5-2) can now be determined, again using

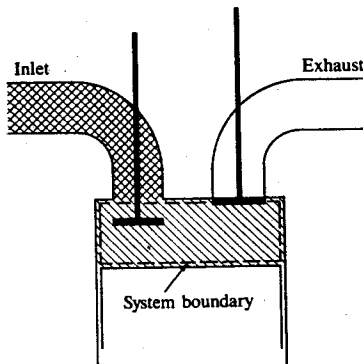


**FIGURE 5-4**  
Definition of system boundary for thermodynamic analysis of ideal cycle processes.

the open system in Fig. 5-4. Application of the first law between points 6 and 1 gives

$$U_1 - U_6 = -p_i(V_1 - V_6) + (m_1 - m_6)h_i \quad (5.19a)$$

or  $m_1 u_1 - m_6 u_6 = -p_i(V_1 - V_6) + (m_1 - m_6)h_i \quad (5.19b)$

or  $m_1 h_1 = m_6 h_6 + (m_1 - m_6)h_i + V_2(p_i - p_e) \quad (5.19c)$

where  $h_i$  is the specific enthalpy of the inlet mixture and  $p_1 = p_i$ .

Note that when  $p_i < p_e$ , part of the residual gas in the cylinder at the end of the exhaust stroke will flow into the intake system when the intake valve opens. This flow will cease when the cylinder pressure equals  $p_i$ . However, provided no heat transfer occurs, this backflow will not affect Eqs. (5.19) above, since the flow of residual through the intake valve is a constant enthalpy process.

In many engines, the closing of the exhaust valve and the opening of the intake valve overlap. Flow of exhausted gases from the exhaust system through the cylinder into the intake system can then occur. Equations (5.18) and (5.19) would have to be modified to account for valve overlap.

In the four-stroke engine cycle, work is done on the piston during the intake and the exhaust processes. The work done by the cylinder gases on the piston during exhaust is

$$W_e = p_e(V_2 - V_1) \quad (5.20)$$

The work done by the cylinder gases on the piston during intake is

$$W_i = p_i(V_1 - V_2) \quad (5.21)$$

The net work to the piston over the exhaust and intake strokes, the *pumping work*, is

$$W_p = (p_i - p_e)(V_1 - V_2) \quad (5.22)$$

which, for the cylinder gas system, is negative for  $p_i < p_e$  and positive for  $p_i > p_e$ .

The pumping mean effective pressure (pmep) is usually defined as a positive quantity. Thus:

$$\text{For } p_i < p_e: \quad \text{pmep} = p_e - p_i \quad (5.23a)$$

$$\text{For } p_i > p_e: \quad \text{pmep} = p_i - p_e \quad (5.23b)$$

The net and gross indicated mean effective pressures are related by

$$\text{imep}_n = \text{imep}_g - (p_e - p_i) \quad (5.24)$$

The net indicated fuel conversion efficiency is related to the gross indicated fuel conversion efficiency by

$$\eta_{f,in} = \eta_{f,ig} \left( 1 - \frac{p_e - p_i}{\text{imep}_g} \right) \quad (5.25)$$

## 5.4 CYCLE ANALYSIS WITH IDEAL GAS WORKING FLUID WITH $c_v$ AND $c_p$ CONSTANT

If the working fluid in these ideal cycles is assumed to be an ideal gas, with  $c_v$  and  $c_p$  constant throughout the engine operating cycle, the equations developed in the previous section which describe engine performance and efficiency can be further simplified. We will use the notation of Fig. 5-2.

### 5.4.1 Constant-Volume Cycle

The compression work (Eq. 5.6) becomes

$$W_C = mc_v(T_1 - T_2) \quad (5.26)$$

The expansion work (Eq. 5.9) becomes

$$W_E = mc_v(T_3 - T_4) \quad (5.27)$$

The denominator in Eq. (5.14),  $m_f Q_{LHV}$ , can be related to the temperature rise during combustion. For the working fluid model under consideration, the  $U(T)$  lines for the reactants and products on a  $U-T$  diagram such as Fig. 3-5 are parallel and have equal slopes, of magnitude  $c_v$ . Hence, for a constant-volume adiabatic combustion process

$$mc_v(T_3 - T_2) = m_f Q_{LHV} \quad (5.28)\dagger$$

<sup>\dagger</sup> Note that if insufficient air is available for complete combustion of the fuel, Eq. (5.28) must be modified. The right-hand side of the equation should then be  $\eta_c m_f Q_{LHV}$ , where  $\eta_c$  is the combustion efficiency given by Eq. (3.27).

Note that the heating values at constant volume and constant pressure are the same for this working fluid. For convenience we will define

$$Q^* = \frac{m_f Q_{LHV}}{m} \quad (5.29)$$

$Q^*$  is the specific internal energy (and enthalpy) decrease, during isothermal combustion, per unit mass of working fluid.

The relation for indicated fuel conversion efficiency (Eq. 5.14) becomes

$$\eta_{f,i} = \frac{(T_3 - T_4) - (T_2 - T_1)}{T_3 - T_2} = 1 - \frac{T_4 - T_1}{T_3 - T_2} \quad (5.30)$$

Since 1-2 and 3-4 are isentropic processes between the same volumes,  $V_1$  and  $V_2$ ,

$$\frac{T_2}{T_1} = \left( \frac{V_1}{V_2} \right)^{\gamma-1} = r_c^{\gamma-1} = \left( \frac{V_4}{V_3} \right)^{\gamma-1} = \frac{T_3}{T_4}$$

where  $\gamma = c_p/c_v$ . Hence:

$$\frac{T_4}{T_1} = \frac{T_3}{T_2}$$

and Eq. (5.30) can be rearranged as

$$\eta_{f,i} = 1 - \frac{1}{r_c^{\gamma-1}} \quad (5.31)$$

Values of  $\eta_{f,i}$  for different values of  $\gamma$  are shown in Fig. 5-5. The indicated fuel conversion efficiency increases with increasing compression ratio and decreases as  $\gamma$  decreases.

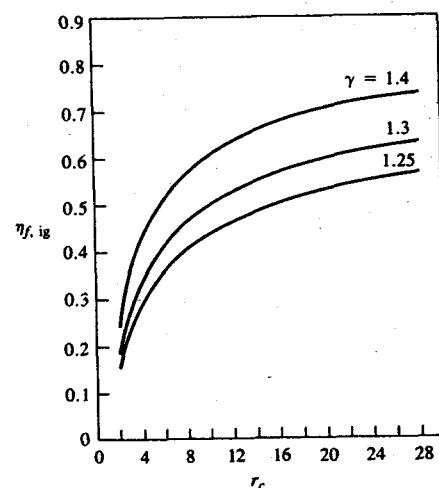


FIGURE 5-5  
Ideal gas constant-volume cycle fuel conversion efficiency as a function of compression ratio;  $\gamma = c_p/c_v$ .

The indicated mean effective pressure, using Eqs. (5.2) and (5.31), becomes

$$\text{imep} = \left( \frac{Q^*}{c_v T_1} \right) \left( \frac{1}{\gamma-1} \right) \left( \frac{r_c}{r_c-1} \right) \left( 1 - \frac{1}{r_c^{\gamma-1}} \right) \quad (5.32)$$

The dimensionless numbers  $r_c$ ,  $\gamma$ , and  $Q^*/(c_v T_1)$  are sufficient to describe the characteristics of the constant-volume ideal gas standard cycle, relative to its initial conditions  $p_1$ ,  $T_1$ .

It is useful to compare the imep—a measure of the effectiveness with which the displaced volume of the engine is used to produce work—and the maximum pressure in the cycle,  $p_3$ . The ratio  $p_3/p_1$  can be determined from the ideal gas law applied at points 2 and 3, and the relation

$$\frac{T_3}{T_2} = 1 + \frac{Q^*}{c_v T_1 r_c^{\gamma-1}} \quad (5.33)$$

obtained from Eq. (5.28). Equations (5.32) and (5.33) then give

$$\text{imep} = \frac{1}{(y-1)r_c^{\gamma}} \left( \frac{r_c}{r_c-1} \right) \frac{1 - 1/r_c^{\gamma-1}}{c_v T_1 / Q^* + 1/r_c^{\gamma-1}} \quad (5.34)$$

A high value of  $\text{imep}/p_3$  is desirable. Engine weight will increase with increasing  $p_3$  to withstand the increasing stresses in components.

The indicated fuel conversion efficiency and the ratios  $\text{imep}/p_1$  and  $\text{imep}/p_3$  for this ideal cycle model do not depend on whether the cycle is throttled or supercharged. However, the relationships between the working fluid properties at points 1 and 6 do depend on the degree of throttling or supercharging. For throttled engine operation, the residual gas mass fraction  $x_r$  can be determined as follows. From Eq. (5.17), since state 5 corresponds to an isentropic expansion from state 4 to  $p = p_e$ ,  $x_r$  is given by

$$x_r = \frac{(p_e/p_4)^{1/\gamma}}{r_c} = \frac{(p_e/p_i)^{1/\gamma}(p_1/p_4)^{1/\gamma}}{r_c}$$

Since

$$\frac{p_1}{p_4} = \frac{p_1}{p_2} \frac{p_2}{p_3} \frac{p_3}{p_4} = \frac{1}{r_c^{\gamma}} \frac{T_2}{T_3} r_c^{\gamma} = \left( 1 + \frac{Q^*}{c_v T_1 r_c^{\gamma-1}} \right)^{-1}$$

it follows that

$$x_r = \frac{1}{r_c} \frac{(p_e/p_i)^{1/\gamma}}{[1 + Q^*/(c_v T_1 r_c^{\gamma-1})]^{1/\gamma}} \quad (5.35)$$

The residual mass fraction increases as  $p_i$  decreases below  $p_e$ , decreases as  $r_c$  increases, and decreases as  $Q^*/(c_v T_1)$  increases.

Through a similar analysis, the temperature of the residual gas  $T_6$  can be determined:

$$\frac{T_6}{T_1} = \left( \frac{p_e}{p_i} \right)^{(\gamma-1)/\gamma} \left( 1 + \frac{Q^*}{c_v T_1 r_c^{\gamma-1}} \right)^{1/\gamma} \quad (5.36)$$

The mixture temperature at point 1 in the cycle can be related to the inlet mixture temperature,  $T_i$ , with Eq. (5.19). For a working fluid with  $c_v$  and  $c_p$  constant, this equation becomes

$$c_p T_1 = x_r c_p T_6 + (1 - x_r) c_p T_i - \frac{RT_1}{r_c} \left( \frac{p_e}{p_i} - 1 \right) \quad (5.37)$$

Use of Eqs. (5.36) and (5.37) leads to the relation

$$\frac{T_1}{T_i} = \frac{1 - x_r}{1 - 1/(r_c)[p_e/p_i + (\gamma - 1)]} \quad (5.38)$$

Extensive results for the constant-volume cycle with  $\gamma = 1.4$  can be found in Taylor.<sup>1</sup>

#### 5.4.2 Limited- and Constant-Pressure Cycles

The constant-pressure cycle is a limited-pressure cycle with  $p_3 = p_2$ . For the limited-pressure cycle, the compression work remains

$$W_C = mc_v(T_1 - T_2) \quad (5.39)$$

The expansion work, from Eq. (5.13), becomes

$$W_E = m[c_v(T_{3b} - T_4) + p_3(v_{3b} - v_{3a})] \quad (5.40)$$

For the combustion process, Eqs. (5.7g, h) give

$$m_{f2-3a} Q_{LHV} = mc_v(T_{3a} - T_2) \quad (5.41a)$$

$$m_{f3a-3b} Q_{LHV} = mc_p(T_{3b} - T_{3a}) \quad (5.41b)$$

or  $m_f Q_{LHV} = m[c_v(T_{3a} - T_2) + c_p(T_{3b} - T_{3a})]$  (5.41c)

for a working fluid with  $c_v$  and  $c_p$  constant throughout the cycle.

Combining Eqs. (5.1), (5.3), and (5.39) to (5.41) and simplifying gives

$$\eta_{f,i} = 1 - \frac{T_4 - T_1}{(T_{3a} - T_2) + \gamma(T_{3b} - T_{3a})}$$

Use of the isentropic relationships for the working fluid along 1-2 and 3b-4, with the substitutions

$$\alpha = \frac{p_3}{p_2} \quad \beta = \frac{V_{3b}}{V_{3a}} \quad (5.42a, b)$$

leads to the result

$$\eta_{f,i} = 1 - \frac{1}{r_c^{\gamma-1}} \left[ \frac{\alpha\beta^\gamma - 1}{\alpha\gamma(\beta - 1) + \alpha - 1} \right] \quad (5.43)$$

For  $\beta = 1$  this result becomes the constant-volume cycle efficiency (Eq. 5.31). For  $\alpha = 1$ , this result gives the constant-pressure cycle efficiency as a special case.

The mean effective pressure is related to  $p_1$  and  $p_3$  via

$$\frac{\text{imep}}{p_1} = \frac{Q^*}{c_v T_1(\gamma - 1)} \left( \frac{r_c}{r_c - 1} \right) \eta_{f,i} \quad (5.44)$$

$$\frac{\text{imep}}{p_3} = \frac{1}{\alpha r_c^\gamma} \left( \frac{Q^*}{c_v T_1} \right) \left( \frac{1}{\gamma - 1} \right) \left( \frac{r_c}{r_c - 1} \right) \eta_{f,i} \quad (5.45)$$

#### 5.4.3 Cycle Comparison

The above expressions are most useful if values for  $\gamma$  and  $Q^*/(c_v T_1)$  are chosen to match real working fluid properties. Figure 5-5 has already shown the sensitivity of  $\eta_{f,i}$  for the constant-volume cycle to the value of  $\gamma$  chosen. In Sec. 4.4, average values of  $\gamma_u$  and  $\gamma_b$  were determined which match real working fluid properties over the compression and expansion strokes, respectively. Values for a stoichiometric mixture appropriate to an SI engine are  $\gamma_u \approx 1.3$ ,  $\gamma_b \approx 1.2$ . However, analysis of pressure-volume data for real engine cycles indicates that  $pV^n$ , where  $n \approx 1.3$ , is a good fit to the expansion stroke  $p$ - $V$  data.<sup>2</sup> Heat transfer from the burned gases increases the exponent above the value corresponding to  $\gamma_b$ . A value of  $\gamma = 1.3$  for the entire cycle is thus a reasonable compromise.

$Q^*$ , defined by Eq. (5.29), is the enthalpy decrease during isothermal combustion per unit mass of working fluid. Hence

$$Q^* = \left( \frac{m_f}{m_a} \right) Q_{LHV} \left( \frac{m_a}{m} \right) \quad (5.46)$$

A simple approximation for  $(m_a/m)$  is  $(r_c - 1)/r_c$ ; i.e., fresh air fills the displaced volume and the residual gas fills the clearance volume at the same density. Then, for isoctane fuel, for a stoichiometric mixture,  $Q^*$  is given by  $2.92 \times 10^6 (r_c - 1)/r_c$  J/kg air. For  $\gamma = 1.3$  and an average molecular weight  $M = 29.3$ ,  $c_v = 946$  J/kg·K. For  $T_1 = 333$  K,  $Q^*/(c_v T_1)$  becomes  $9.3(r_c - 1)/r_c$ . For this value of  $Q^*/(c_v T_1)$  all cycles would be burning a stoichiometric mixture with an appropriate residual gas fraction.

Pressure-volume diagrams for the three ideal cycles for the same compression ratio and unburned mixture composition are shown in Fig. 5-6. For each cycle,  $\gamma = 1.3$ ,  $r_c = 12$ ,  $Q^*/(c_v T_1) = 9.3(r_c - 1)/r_c = 8.525$ . Overall performance characteristics for each of these cycles are summarized in Table 5.2. The constant-volume cycle has the highest efficiency, the constant-pressure cycle the lowest efficiency. This can be seen from Eq. (5.43) where the term in square brackets is equal to unity for the constant-volume cycle and greater than unity for the limited- and constant-pressure cycles. The imep values are proportional to  $\eta_{f,i}$  since the mass of fuel burned per cycle is the same in all three cases.

As the peak pressure  $p_3$  is decreased, the ratio of imep to  $p_3$  increases. This ratio is important because imep is a measure of the useful pressure on the piston, and the maximum pressure chiefly affects the strength required of the engine structure.

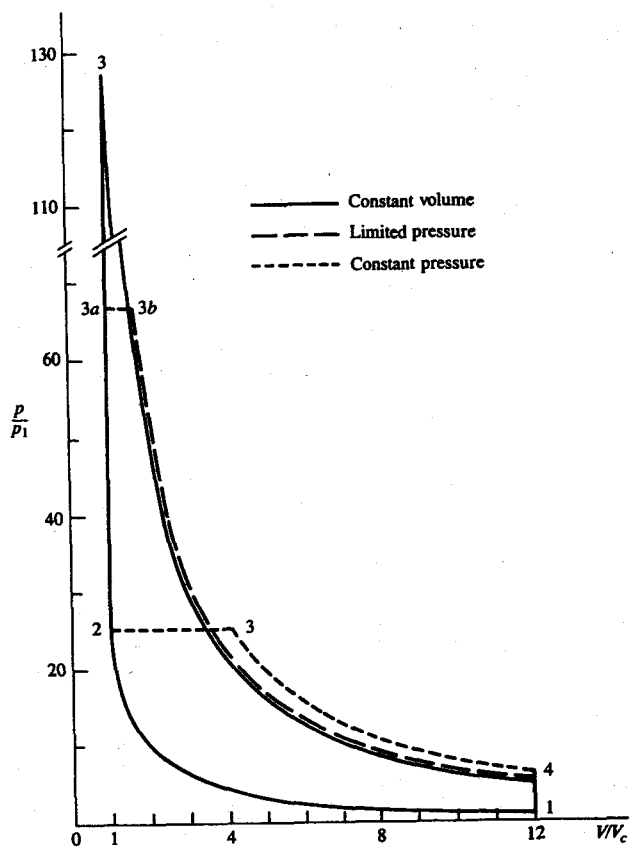


**FIGURE 5-6**  
Pressure-volume diagrams for constant-volume, limited-pressure, and constant-pressure ideal gas standard cycles.  $r_c = 12$ ,  $\gamma = 1.3$ ,  $Q^*/(c_v T_1) = 9.3(r_c - 1)/r_c = 8.525$ ,  $p_{3a}/p_1 = 67$ .

**TABLE 5.2**  
Comparison of ideal cycle results

	$\eta_{f,i}$	imep $p_1$	imep $p_3$	$p_{max}$ $p_1$
Constant volume	0.525	16.3	0.128	128
Limited pressure	0.500	15.5	0.231	67
Constant pressure	0.380	11.8	0.466	25.3

$$\gamma = 1.3; r_c = 12; Q^*/(c_v T_1) = 8.525.$$

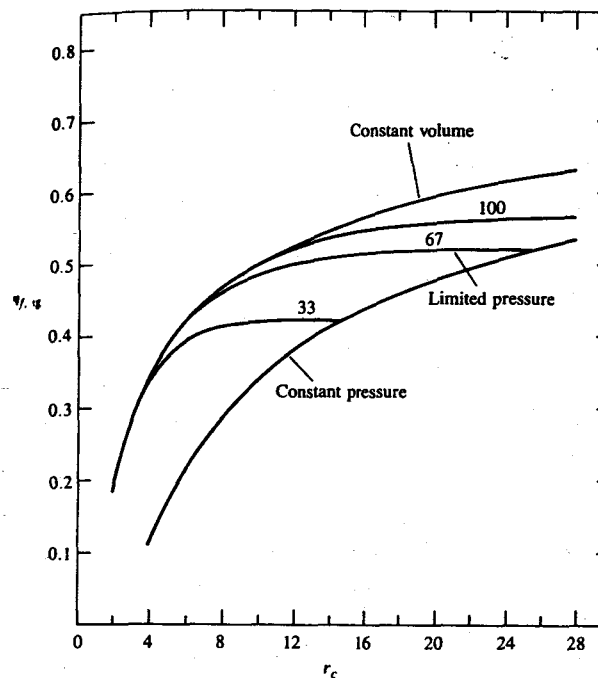


**FIGURE 5-7**  
Fuel conversion efficiency as a function of compression ratio, for constant-volume, constant-pressure, and limited-pressure ideal gas cycles.  $\gamma = 1.3$ ,  $Q^*/(c_v T_1) = 9.3(r_c - 1)/r_c$ . For limited-pressure cycle,  $p_3/p_1 = 33, 67, 100$ .

A more extensive comparison of the three cycles is given in Figs. 5-7 and 5-8, over a range of compression ratios. For all cases  $\gamma = 1.3$  and  $Q^*/(c_v T_1) = 9.3(r_c - 1)/r_c$ . At any given  $r_c$ , the constant-volume cycle has the highest efficiency and lowest imep/ $p_3$ . For a given maximum pressure  $p_3$ , the constant-pressure cycle has the highest efficiency (and the highest compression ratio). For the limited-pressure cycle, at constant  $p_3/p_1$ , there is little improvement in efficiency and imep above a compression ratio of about 8 to 10 as  $r_c$  is increased.

Example 5.1 shows how ideal cycle equations relate residual and intake conditions with the gas state at point 1 in the cycle. An iterative procedure is required if intake conditions are specified.

**Example 5.1.** For  $\gamma = 1.3$ , compression ratio  $r_c = 6$ , and a stoichiometric mixture with intake temperature 300 K, find the residual gas fraction, residual gas temperature, and mixture temperature at point 1 in the constant-volume cycle for  $p_e/p_i = 1$  (unthrottled operation) and 2 (throttled operation).

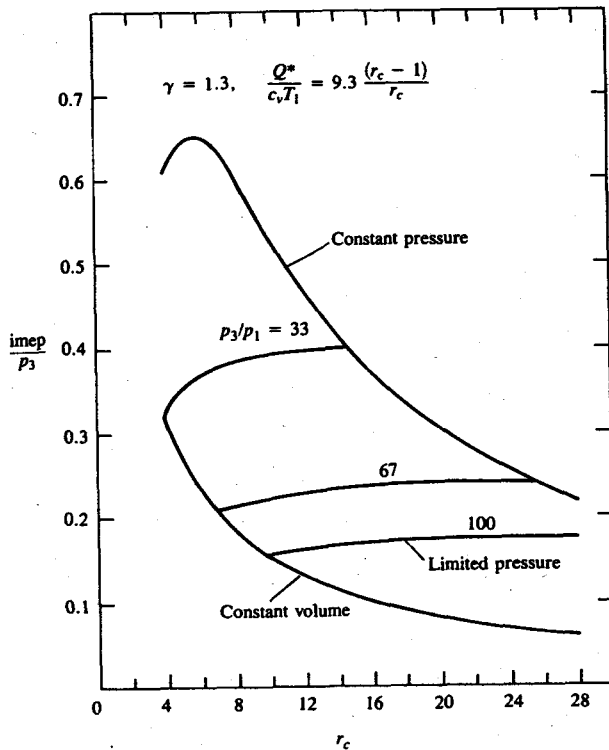


**FIGURE 5-8**  
Indicated mean effective pressure (imep) divided by maximum cycle pressure ( $p_3$ ) as a function of compression ratio for constant-volume, constant-pressure, and limited-pressure cycles. Details same as Fig. 5-7.

For a stoichiometric mixture, for isoctane,

$$Q^* = \frac{m_f}{m} Q_{LHV} = \left( \frac{m_f}{m_i} \right) \left( \frac{m_i}{m} \right) Q_{LHV} = \frac{44.38}{16.14} (1 - x_r) = 2.75(1 - x_r) \quad \text{MJ/kg}$$

For  $\gamma = 1.3$ ,  $c_v = 946 \text{ J/kg}\cdot\text{K}$  and

$$\frac{Q^*}{c_v T_1} = \frac{2.75 \times 10^6}{946 T_1} (1 - x_r) = \frac{2910}{T_1} (1 - x_r) \quad (a)$$

Equations (5.35), (5.36), and (5.38), for  $r_c = 6$  and  $\gamma = 1.3$ , become

$$x_r = \frac{1}{6} \frac{(p_e/p_i)^{0.769}}{[1 + Q^*/(c_v T_1 \times 6^{0.3})]^{0.769}} \quad (b)$$

$$\frac{T_r}{T_1} = \left( \frac{p_e}{p_i} \right)^{0.23} \left( 1 + \frac{Q^*}{c_v T_1 \times 6^{0.3}} \right)^{-0.769} \quad (c)$$

$$\frac{T_1}{300} = \frac{1 - x_r}{1 - [1/(1.3 \times 6)](p_e/p_i + 0.3)} \quad (d)$$

A trial-and-error solution of Eqs. (a) to (d) is required. It is easiest to estimate  $x_r$ , solve for  $T_1$  from (d), evaluate  $Q^*/(c_v T_1)$  from (a), and check the value of  $x_r$  assumed with that given by (b).

For  $(p_e/p_i) = 1$  (unthrottled operation) the following solution is obtained:

$$x_r = 0.044, \quad T_1 = 344 \text{ K}, \quad \frac{Q^*}{c_v T_1} = 8.1, \quad T_r = 1316 \text{ K}$$

For  $(p_e/p_i) = 2$  the following solution is obtained:

$$x_r = 0.082, \quad T_1 = 391 \text{ K}, \quad \frac{Q^*}{c_v T_1} = 6.8, \quad T_r = 1580 \text{ K}$$

## 5.5 FUEL-AIR CYCLE ANALYSIS

A more accurate representation of the properties of the working fluid inside the engine cylinder is to treat the unburned mixture as frozen in composition and the burned gas mixture as in equilibrium. Values for thermodynamic properties for these working fluid models can be obtained with the charts for unburned and burned gas mixtures described in Sec. 4.5, or the computer codes summarized in Sec. 4.7. When these working fluid models are combined with the ideal engine process models in Table 5.1, the resulting cycles are called fuel-air cycles.<sup>1</sup> The sequence of processes and assumptions are (with the notation of Fig. 5-2):

1-2 Reversible adiabatic compression of a mixture of air, fuel vapor, and residual gas without change in chemical composition.

2-3 Complete combustion (at constant volume or limited pressure or constant pressure), without heat loss, to burned gases in chemical equilibrium.

3-4 Reversible adiabatic expansion of the burned gases which remain in chemical equilibrium.

4-5-6 Ideal adiabatic exhaust blowdown and displacement processes with the burned gases fixed in chemical composition.

6-7-1 Ideal intake process with adiabatic mixing between residual gas and fresh mixture, both of which are fixed in chemical composition.

The basic equations for each of these processes have already been presented in Sec. 5.3. The use of the charts for a complete engine cycle calculation will now be illustrated.

### 5.5.1 SI Engine Cycle Simulation

The mixture conditions at point 1 must be known or must be estimated. The following approximate relationships can be used for this purpose:<sup>3</sup>

$$x_r = \left\{ 1 + \frac{T_r}{T_i} \left[ r_c \left( \frac{p_i}{p_e} \right) - \left( \frac{p_i}{p_e} \right)^{(y-1)/y} \right] \right\}^{-1} \quad (5.47)$$

$$T_1 = T_r r_c x_r \left( \frac{p_i}{p_e} \right) \quad (5.48)$$

where  $T_r = 1400$  K and  $(y-1)/y = 0.24$  are appropriate average values to use for initial estimates.

Given the equivalence ratio  $\phi$  and initial conditions  $T_1$  (K),  $p_1 = p_i$  (Pa), and  $v_1$  ( $\text{m}^3/\text{kg}$  air), the state at point 2 at the end of compression through a volume ratio  $v_1/v_2 = r_c$  is obtained from Eq. (4.25a) and the isentropic compression chart (Fig. 4-4). The compression work  $W_C$  (J/kg air) is found from Eq. (5.6) with the internal energy change determined from the unburned mixture chart (Fig. 4-3).

The use of charts to relate the state of the burned mixture to the state of the unburned mixture prior to combustion, for adiabatic constant-volume and constant-pressure combustion, has already been illustrated in Sec. 4.5.3.

For the *constant-volume cycle*,

$$u_3 = u_{s2} + \Delta u_{f,u}^o \quad \text{J/kg air} \quad (5.49)$$

where  $u_{s2}$  is the sensible internal energy of the unburned mixture at  $T_2$  from Fig. 4-3 and  $\Delta u_{f,u}^o$  is the internal energy of formation of the unburned mixture [given by Eq. (4.32)]. Since  $v_3 = v_2$ , the burned gas state at point 3 can be located on the appropriate burned gas chart (Figs. 4-5 to 4-9).

For the *constant-pressure cycle*,

$$h_3 = h_{s2} + \Delta h_{f,u}^o \quad \text{J/kg air} \quad (5.50)$$

Since  $p_3 = p_2$ , the burned gas state at point 3 can be located (by iteration) on the high-temperature burned gas charts, as illustrated by Example 4.5.

For the *limited-pressure cycle*, application of the first law to the mixture between states 2 and 3b gives

$$h_{3b} = u_{3b} + p_3 v_{3b} = u_2 + p_3 v_2 = u_{s2} + \Delta u_{f,u}^o + p_3 v_2 \quad \text{J/kg air} \quad (5.51)$$

Since  $p_3$  for a limited-pressure cycle is given, point 3b can be located on the appropriate burned gas chart.

The expansion process 3-4 follows an isentropic line from  $v_3$  to  $v_4$  ( $v_4 = v_1$ ) on the burned mixture charts. Equation (5.9) [or (5.11) or (5.13)] now gives the expansion work  $W_E$ . The state of the residual gas at points 5 and 6 in the cycle is obtained by continuing this isentropic expansion from state 4 to  $p = p_e$ . The residual gas temperature can be read from the equilibrium burned gas chart; the residual gas fraction is obtained from Eq. (5.17). If values of  $T_r$  and  $x_r$  were assumed at the start of the cycle calculation to determine  $T_1$ , the assumed values

can be checked against the calculated values and an additional cycle computation carried out with the new calculated values if required. The convergence is rapid.

The indicated fuel conversion efficiency is obtained from Eq. (5.1). The indicated mean effective pressure is obtained from Eq. (5.2). The volumetric efficiency (see Sec. 2.10) for a four-stroke cycle engine is given by

$$\eta_v = \frac{r_c(1-x_r)}{v_1 \rho_{a,i}(r_c - 1)} \quad (5.52)$$

where  $\rho_{a,i}$  is the inlet air density (in kilograms per cubic meter) and  $v_1$  is the chart mixture specific volume (in cubic meters per kilogram of air in the original mixture).

**Example 5.2.** Calculate the performance characteristics of the constant-volume fuel-air cycle defined by the initial conditions of Examples 4.2, 4.3, and 4.5. The compression ratio is 8; the fuel is isoctane and the mixture is stoichiometric; the pressure and temperature inside the cylinder at the start of compression are 1 atm and 350 K, respectively. Use the notation of Fig. 5-2a to define the states at the beginning and end of each process.

Example 4.2 analyzed the compression process:

$$T_1 = 350 \text{ K}, \quad p_1 = 101.3 \text{ kPa}, \quad v_1 = 1 \text{ m}^3/\text{kg air}, \quad u_{s1} = 40 \text{ kJ/kg air}$$

$$T_2 = 682 \text{ K}, \quad p_2 = 1.57 \text{ MPa}, \quad v_2 = 0.125 \text{ m}^3/\text{kg air}, \quad u_{s2} = 350 \text{ kJ/kg air}$$

$$W_{1-2} = W_C = -310 \text{ kJ/kg air}$$

Example 4.5 analyzed the constant-volume adiabatic combustion process (it was assumed that the residual gas fraction was 0.08):

$$u_{b3} = u_{s2} = u_{s,u2} + \Delta u_{f,u}^o = -5 \text{ kJ/kg air}, \quad s_3 = 9.33 \text{ kJ/kg air} \cdot \text{K}$$

$$v_3 = v_2 = 0.125 \text{ m}^3/\text{kg air}, \quad T_3 = 2825 \text{ K}, \quad p_3 = 7100 \text{ kPa}$$

Example 4.3 analyzed the expansion process, from these conditions after combustion at TC, to the volume  $v_4$  at BC of 1  $\text{m}^3/\text{kg}$  air:

$$T_4 = 1840 \text{ K}, \quad p_4 = 570 \text{ kPa}, \quad u_4 = -1540 \text{ kJ/kg air}$$

$$W_{3.4} = W_E = 1535 \text{ kJ/kg air}$$

To check the assumed residual gas fraction, the constant entropy expansion process on the chart in Fig. 4-8 is continued from state 4 to the exhaust pressure  $p_5$  of 1 atm = 101.3 kPa. This gives  $v_5 = 4.0 \text{ m}^3/\text{kg air}$  and  $T_5 = 1320 \text{ K}$ . The residual fraction from Eq. (5.17) is

$$x_r = \frac{v_2}{v_5} = \frac{0.125}{4.0} = 0.031$$

which is significantly different from the assumed value of 0.08. The combustion and expansion calculations are now repeated with the new residual fraction of 0.031 (the compression process will not be changed significantly and the initial temperature is

assumed fixed):

$$u_{b3} = 350 - 118.2 - 2956 \times 0.031 = 140 \text{ kJ/kg air}$$

With  $v_3 = 0.125 \text{ m}^3/\text{kg air}$ , Fig. 4-8 gives

$$p_3 = 7270 \text{ kPa}, \quad T_3 = 2890 \text{ K}$$

Expand at constant entropy to  $v_4 = 1 \text{ m}^3/\text{kg air}$ :

$$p_4 = 595 \text{ kPa}, \quad T_4 = 1920 \text{ K}, \quad u_4 = -1457 \text{ kJ/kg air}$$

$$W_{3.4} = W_E = 1597 \text{ kJ/kg air}$$

Continue expansion at constant entropy to the exhaust pressure,  $p_5 = 1 \text{ atm}$ :

$$v_5 = 4 \text{ m}^3/\text{kg air}, \quad T_5 = 1360 \text{ K}$$

Equation (5.17) now gives the residual fraction

$$x_r = \frac{v_2}{v_5} = \frac{0.125}{4} = 0.031$$

which agrees with the value assumed for the second iteration.

The fuel conversion efficiency can now be calculated:

$$\eta_{f,i} = \frac{W_E + W_C}{m_f Q_{LHV}}$$

where

$$m_f = \text{kg fuel/kg air at state 1} = \left(\frac{F}{A}\right)(1 - x_r)$$

Thus

$$\eta_{f,i} = \frac{1597 - 310}{0.0661 \times (1 - 0.031) \times 44.4 \times 10^3} = 0.45$$

The indicated mean effective pressure is

$$\text{imep} = \frac{W_E + W_C}{V_d} = \frac{1597 - 310}{1 - 0.125} = 1470 \text{ kPa}$$

or

$$\text{imep} = \frac{p_1}{p_1} = 14.6$$

## 5.5.2 CI Engine Cycle Simulation

With a diesel engine fuel-air cycle calculation, additional factors must be taken into account. The mixture during compression is air plus a small amount of residual gas. At point 2 liquid fuel is injected into the hot compressed air at temperature  $T_2$ ; as the fuel vaporizes and heats up, the air is cooled. For a constant-volume mixing process which is adiabatic overall, the mixture internal energy is unchanged, i.e.:

$$m_f [u_{fg} + c_{v,f}(T_2 - T_0)] + m_a c_{v,a}(T_2 - T_0) = 0 \quad (5.53)$$

where  $m_f$  is the mass of fuel injected,  $u_{fg}$  is the latent heat of vaporization of the fuel,  $c_{v,f}$  is the specific heat at constant volume of the fuel vapor,  $T_2$  is the mixture temperature (assumed uniform) after vaporization and mixing is complete,  $m_a$  is the mass of air used, and  $c_{v,a}$  is the specific heat at constant volume of air. Substitution of typical values for fuel and air properties gives  $(T_2 - T_0) \approx 70 \text{ K}$  at full load. Localized cooling in a real engine will be greater.

The limited-pressure cycle is a better approximation to the diesel engine than the constant-pressure or constant-volume cycles.

Note that because nonuniformities in the fuel/air ratio exist during and after combustion in the CI engine, the burned gas charts which assume uniform composition will not be as accurate an approximation to working fluid properties as they are for SI engines.

## 5.5.3 Results of Cycle Calculations

Extensive results of constant-volume fuel-air cycle calculations are available.<sup>1, 3, 4</sup> Efficiency is little affected by variables other than the compression ratio  $r_c$  and equivalence ratio  $\phi$ . Figures 5-9 and 5-10 show the effect of variations in these two parameters on indicated fuel conversion efficiency and mean effective pressure. From the available results, the following conclusions can be drawn:

1. The effect of increasing the compression ratio on efficiency at a constant equivalence ratio is similar to that demonstrated by the constant  $\gamma$  constant-volume cycle analysis (provided the appropriate value of  $\gamma$  is used; see Fig. 5-19).
2. As the equivalence ratio is decreased below unity (i.e., the fuel-air mixture is made progressively leaner than stoichiometric), the efficiency increases. This occurs because the burned gas temperatures after combustion decrease, decreasing the burned gas specific heats and thereby increasing the effective value of  $\gamma$  over the expansion stroke. The efficiency increases because, for a given volume-expansion ratio, the burned gases expand through a larger temperature ratio prior to exhaust; therefore, per unit mass of fuel, the expansion stroke work is increased.
3. As the equivalence ratio increases above unity (i.e., the mixture is made progressively richer than stoichiometric), the efficiency decreases because lack of sufficient air for complete oxidation of the fuel more than offsets the effect of decreasing burned gas temperatures which decrease the mixture's specific heats.
4. The mean effective pressure, from Eq. (5.2), is proportional to the product  $\phi \eta_{f,i}$ . This exhibits a maximum between  $\phi \approx 1.0$  and  $\phi \approx 1.1$ , i.e., slightly rich of stoichiometric. For  $\phi$  less than the value corresponding to this maximum, the decreasing fuel mass per unit displaced volume more than offsets the increasing fuel conversion efficiency. For  $\phi$  greater than this value, the decreasing fuel conversion efficiency (due to decreasing combustion efficiency) more than offsets the increasing fuel mass.

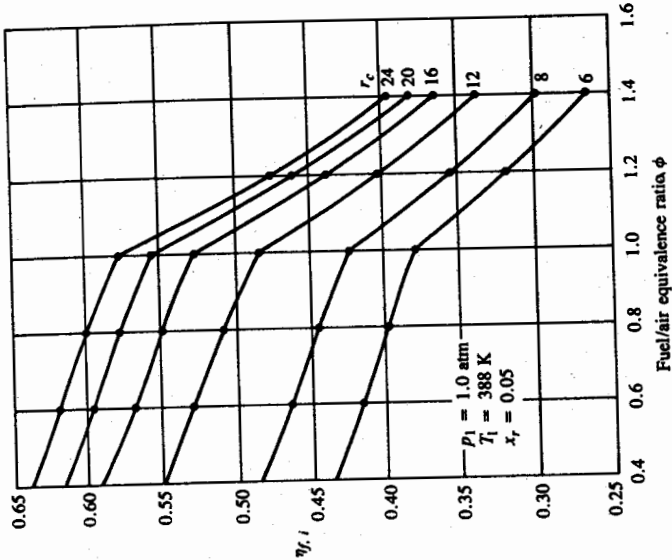


FIGURE 5-9  
Fuel-air cycle results for indicated fuel conversion efficiency as a function of compression ratio and equivalence ratio. Fuel: octene;  $p_1 = 1 \text{ atm}$ ,  $T_1 = 388 \text{ K}$ ,  $x_r = 0.05$ . (From Edson and Taylor.<sup>4</sup>)

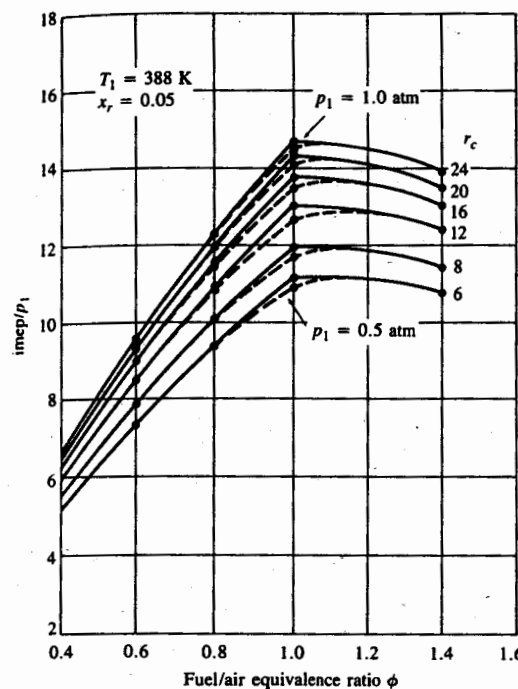
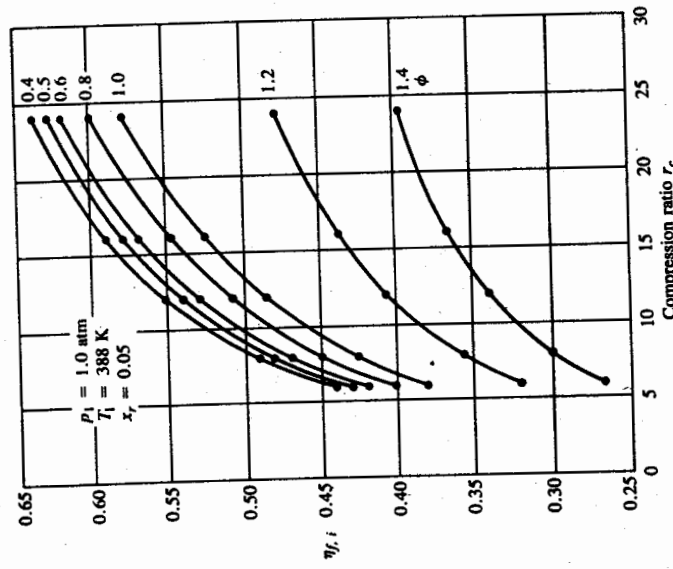


FIGURE 5-10  
Fuel-air cycle results for indicated mean effective pressure as a function of equivalence ratio and compression ratio. Fuel: octene;  $p_1 = 1 \text{ atm}$ ,  $T_1 = 388 \text{ K}$ ,  $x_r = 0.05$ . (From Edson and Taylor.<sup>4</sup>)

- Variations in initial pressure, inlet temperature, residual gas fraction, and atmospheric moisture fraction have only a modest effect on the fuel conversion efficiency. The effects of variations in these variables on imep are more substantial, however, because imep depends directly on the initial charge density.
- Comparison of results from limited-pressure and constant-volume fuel-air cycles<sup>1</sup> shows that placing a realistic limit on the maximum pressure reduces the advantages of increased compression ratio on both efficiency and imep.

## 5.6 OVEREXPANDED ENGINE CYCLES

The gas pressure within the cylinder of a conventional four-stroke engine at exhaust valve opening is greater than the exhaust pressure. The available energy of the cylinder gases at this point in the cycle is then dissipated in the exhaust blowdown process. Additional expansion within the engine cylinder would increase the indicated work per cycle, as shown in Fig. 5-11, where expansion continues beyond point 4' (the conventional ideal cycle exhaust valve opening point) at  $V_{4'} = r_e V_c$  to point 4 at  $V_4 = r_e V_c$ . The exhaust stroke in this overexpanded cycle is 4-5-6. The intake stroke is 6-1. The area 14'451 has been added

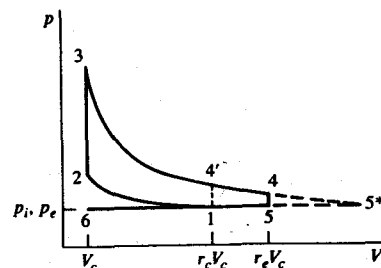


FIGURE 5-11

Pressure-volume diagram for overexpanded engine cycle (1234561) and Atkinson cycle (123561).  $r_c$  and  $r_e$  are volumetric compression and expansion ratios, respectively.

to the conventional cycle  $p$ - $V$  diagram area, for the same fuel input, thereby increasing the engine's efficiency.

Complete expansion within the cylinder to exhaust pressure  $p_e$  (point 5\*) is called the *Atkinson cycle*. Unthrottled operation is shown in Fig. 5-11; throttled operating cycles can also be generated. Many crank and valve mechanisms have been proposed to achieve this additional expansion. For example, it can be achieved in a conventional four-stroke cycle engine by suitable choice of exhaust valve opening and intake valve closing positions relative to BC. If the crank angle between exhaust valve opening and BC on the expansion stroke is less than the crank angle between BC and intake valve closing on the compression stroke, then the actual volumetric expansion ratio is greater than the actual volumetric compression ratio (these *actual* ratios are both less than the *nominal* compression ratio with normal valve timing).

The effect of overexpansion on efficiency can be estimated from an analysis of the ideal cycle shown in Fig. 5-11. An ideal gas working fluid with specific heats constant throughout the cycle will be assumed. The indicated work per cycle for the overexpanded cycle is

$$W_{c,i} = m[(u_3 - u_4) - (u_2 - u_1) - p_1(v_4 - v_1)] \quad (5.54)$$

The isentropic relations for 1-2 and 3-4 are

$$\frac{T_2}{T_1} = r_c^{\gamma-1} \quad \frac{T_3}{T_4} = r_e^{\gamma-1}$$

With Eq. (5.33) to relate  $T_3$  and  $T_2$ , the following expression for indicated fuel conversion efficiency can be derived from Eqs. (5.1), (5.29), and (5.54):

$$\eta_{f,i} = 1 - \frac{1}{(r r_c)^{\gamma-1}} \left\{ 1 + \frac{c_v T_1}{Q^*} r_c^{\gamma-1} [1 - \gamma r^{\gamma-1} + (\gamma - 1)r^\gamma] \right\} \quad (5.55)$$

where

$$r = \frac{r_e}{r_c}$$

Note that the efficiency given by Eq. (5.55) is a function of load (via  $Q^*$ ), and is a

maximum at maximum load. This contrasts with the ideal constant-volume cycle efficiency [Eq. (5.31)], which is independent of load. The ratio  $r_e/r_c$  for complete expansion is given by

$$r^\gamma = 1 + \frac{Q^*}{c_v T_1 r_c^{\gamma-1}} \quad (5.56)$$

The effect of overexpansion on fuel conversion efficiency is shown in Fig. 5-12 for  $r_c = 4, 8$ , and  $16$  with  $\gamma = 1.3$ . The ratio of overexpanded cycle efficiency to the standard cycle efficiency is plotted against  $r$ . The Atkinson cycle (complete expansion) values are indicated by the transition from a continuous line to a dashed line. Significant increases in efficiency can be achieved, especially at low compression ratios.

One major disadvantage of this cycle is that imep and power density decrease significantly because only part of the total displaced volume is filled with fresh charge. From Eqs. (5.2), (5.29), and the relations  $V_d = V_1(r_e - 1)/r_c$  and

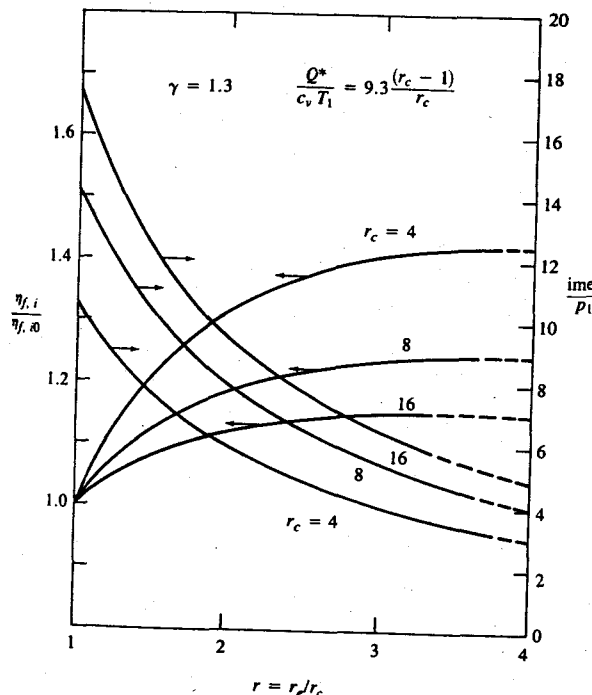


FIGURE 5-12

Indicated fuel conversion efficiency and mean effective pressure for overexpanded engine cycle as a function of  $r_e/r_c$ . Efficiencies given relative to  $r_e = r_c$  value,  $\eta_{f,10}$ ;  $\gamma = 1.3$ ,  $Q^*/(c_v T_1) = 9.3(r_c - 1)/r_c$ . Solid to dashed line transition marks the complete expansion point (Atkinson cycle).

$p_1 V_1 = mRT_1$  it follows that imep for the overexpanded cycle is given by

$$\frac{\text{imep}}{p_1} = \left( \frac{Q^*}{c_v T_1} \right) \left( \frac{1}{\gamma - 1} \right) \left( \frac{r_e}{r_c - 1} \right) \eta_{f,i} \quad (5.57)$$

Values of  $\text{imep}/p_1$  are plotted in Fig. 5-12 as a function of  $r (= r_e/r_c)$ . The substantial decrease from the standard constant-volume cycle values at  $r = 1$  is clear.

## 5.7 AVAILABILITY ANALYSIS OF ENGINE PROCESSES

### 5.7.1 Availability Relationships

Of interest in engine performance analysis is the amount of *useful work* that can be extracted from the gases within the cylinder at each point in the operating cycle. The problem is that of determining the maximum possible work output (or minimum work input) when a system (the charge within the cylinder) is taken from one specified state to another in the presence of a specified environment (the atmosphere). The first and second laws of thermodynamics together define this maximum or minimum work, which is best expressed in terms of the property of such a system-environment combination called *availability*<sup>5</sup> or sometimes *exergy*.<sup>6, 7</sup>

Consider the system-atmosphere combination shown in Fig. 5-13. In the absence of mass flow across the system boundary, as the system changes from state 1 to state 2, the first and second laws give

$$W_{1-2} = -(U_2 - U_1) + Q_{1-2}$$

$$Q_{1-2} \leq T_0(S_2 - S_1)$$

Combining these two equations gives the *total work transfer*:

$$W_{t,1-2} \leq -[(U_2 - U_1) - T_0(S_2 - S_1)] \quad (5.58)$$

The work done by the system against the atmosphere is not available for pro-

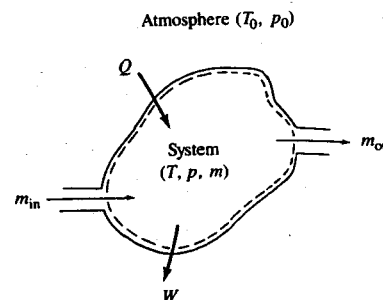


FIGURE 5-13  
System-atmosphere configuration for availability analysis.

ductive use. It must, therefore, be subtracted from the total work to obtain the *useful work transfer*:

$$W_{U,1-2} \leq -[(U_2 - U_1) + p_0(V_2 - V_1) - T_0(S_2 - S_1)] \quad (5.59)$$

The *maximum useful work* will be obtained when the final state of the system is in thermal and mechanical equilibrium with the atmosphere.<sup>†</sup> The *availability* of this system which is in communication with the atmosphere

$$A = U + p_0 V - T_0 S \quad (5.60)$$

is thus the property of the system-atmosphere combination which defines its capacity for useful work. The useful work such a system-atmosphere combination can provide, as the system changes from state 1 to state 2, is less than or equal to the change in availability:

$$W_{U,1-2} \leq -(A_2 - A_1) \quad (5.61)$$

When mass flow across the system boundary occurs, the availability associated with this mass flow is

$$B = H - T_0 S \quad (5.62)$$

*B* is usually called the *steady-flow availability function*.

With these relations, an availability balance for the gas working-fluid system around the engine cycle can be carried out. For any process between specified end states which this system undergoes (interacting only with the atmosphere), the change in availability  $\Delta A$  is given by

$$\Delta A = A_{in} - A_{out} - A_{destroyed} \quad (5.63)$$

The availability transfers in and out occur as a result of work transfers, heat transfers, and mass transfers across the system boundary. The availability transfer associated with a work transfer is equal to the work transfer. The availability transfer  $dA_Q$  associated with a heat transfer  $\delta Q$  occurring when the system temperature is  $T$  is given by

$$dA_Q = \delta Q \left( 1 - \frac{T_0}{T} \right) \quad (5.64)$$

since both an energy and entropy transfer occurs across the system boundary. The availability transfer associated with a mass transfer is given by Eq. (5.62).

<sup>†</sup> The issue of chemical equilibrium with the atmosphere must also be considered. Attainment of chemical equilibrium with the environment requires the capacity to extract work from the partial pressure differences between the various species in the working fluid and the partial pressures of those same species in the environment. This would require such devices as ideal semipermeable membranes and efficient low input pressure, high pressure ratio, expansion devices (which are not generally available for mobile power plant systems). Inclusion of these additional steps to achieve full equilibrium beyond equality of temperature and pressure is inappropriate.<sup>8</sup>

Availability is destroyed by the irreversibilities that occur in any real process. The availability destroyed is given by

$$A_{\text{destroyed}} = T_0 \Delta S_{\text{irrev}} \quad (5.65)$$

where  $\Delta S_{\text{irrev}}$  is the entropy increase associated with the irreversibilities occurring within the system boundary.<sup>7, 8</sup>

### 5.7.2 Entropy Changes in Ideal Cycles

The ideal models of engine processes examined earlier in this chapter provide useful illustrative examples for availability analysis. First, however, we will consider the variation in the entropy of the cylinder gases as they proceed through these ideal operating cycles.

For an adiabatic reversible compression process, the entropy is constant. For the combustion process in each of the ideal gas standard cycles, the entropy increase can be calculated from the relations of Eq. (4.14) (with constant specific heats):

$$s - s_0 = c_v \ln \left( \frac{T}{T_0} \right) + R \ln \left( \frac{v}{v_0} \right) = c_p \ln \left( \frac{T}{T_0} \right) - R \ln \left( \frac{p}{p_0} \right)$$

For the constant-volume cycle:

$$S_3 - S_2 = m(s_3 - s_2) = mc_v \ln \left( \frac{T_3}{T_2} \right) \quad (5.66a)$$

For the constant-pressure cycle:

$$S_3 - S_2 = m(s_3 - s_2) = mc_p \ln \left( \frac{T_3}{T_2} \right) \quad (5.66b)$$

For the limited-pressure cycle:

$$S_{3b} - S_2 = c_v \ln \left( \frac{T_{3a}}{T_2} \right) + c_p \ln \left( \frac{T_{3b}}{T_{3a}} \right) = c_v \ln \alpha + c_p \ln \beta \quad (5.66c)$$

with  $\alpha$  and  $\beta$  defined by Eq. (5.42).

Since the expansion process, after combustion is complete, is adiabatic and reversible, there is no further change in entropy, 3 to 4 (or 3b to 4). Figure 5-14 shows the entropy changes that occur during each process of these three ideal engine operating cycles, calculated from the above equations, on a  $T$ - $s$  diagram. The three cycles shown correspond to those of the  $p$ - $V$  diagrams of Fig. 5-6 with  $r_c = 12$ ,  $\gamma = 1.3$ , and  $Q^*/(c_v T_1) = 8.525$ . Since the combustion process was assumed to be adiabatic, the increase in entropy during combustion clearly demonstrates the irreversible nature of this process.

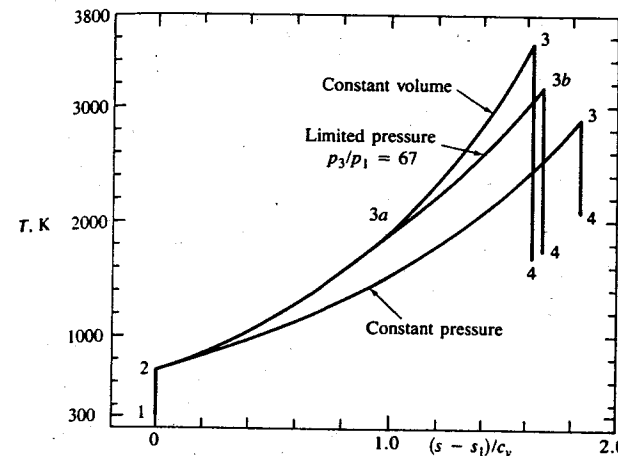


FIGURE 5-14

Temperature-entropy diagram for ideal gas constant-volume, constant-pressure, and limited-pressure cycles. Assumptions same as in Fig. 5-6.

### 5.7.3 Availability Analysis of Ideal Cycles

An availability analysis for each process in the ideal cycle illustrates the magnitude of the availability transfers and where the losses in availability occur.<sup>9</sup> In general, for the system of Fig. 5-4 in communication with an atmosphere at  $p_0$ ,  $T_0$  as indicated in Fig. 5-13, the change in availability between states  $i$  and  $j$  during the portion of the cycle when the valves are closed is given by

$$A_j - A_i = m(a_j - a_i) = m[(u_j - u_i) + p_0(v_j - v_i) - T_0(s_j - s_i)] \quad (5.67)$$

The appropriate normalizing quantity for these changes in availability is the thermomechanical availability of the fuel supplied to the engine cylinder each cycle,  $m_f(-\Delta g_{298})^\dagger$  (see Sec. 3.6.2). However, it is more convenient to use  $m_f(-\Delta h_{298})^\ddagger = m_f Q_{\text{LHV}}$  as the normalizing quantity since it can be related to the temperature rise during combustion via Eq. (5.28). As shown in Table 3.3, these two quantities differ by only a few percent for common hydrocarbon fuels. Equation (5.67), with Eq. (5.29), then becomes

$$\frac{A_j - A_i}{m_f Q_{\text{LHV}}} = \frac{m(a_j - a_i)}{m_f Q_{\text{LHV}}} = \frac{a_j - a_i}{Q^*} \quad (5.68)$$

<sup>†</sup>  $\Delta g_{298}$  is the Gibbs free energy change for the combustion reaction, per unit mass of fuel.

<sup>‡</sup>  $\Delta h_{298}$  is the enthalpy change for the combustion reaction, again per unit mass of fuel.

The compression process is isentropic, so:

$$\begin{aligned}\frac{A_2 - A_1}{m_f Q_{LHV}} &= \frac{a_2 - a_1}{Q^*} = \frac{(u_2 - u_1) + p_0(v_2 - v_1)}{Q^*} \\ &= \frac{c_v T_1}{Q^*} \left[ \left( \frac{T_2}{T_1} - 1 \right) - (\gamma - 1) \left( 1 - \frac{V_2}{V_1} \right) \right] \\ &= \frac{c_v T_1}{Q^*} \left[ (r_c^\gamma - 1) - (\gamma - 1) \left( 1 - \frac{1}{r_c} \right) \right] \quad (5.69)\end{aligned}$$

where we have assumed  $p_0 = p_1$ . The first term in the square brackets is the compression stroke work transfer. The second term is the work done by the atmosphere on the system, which is subtracted because it does not increase the useful work which the system-atmosphere combination can perform.

During combustion, for the constant-volume cycle, the volume and internal energy remain unchanged (Eqs. 5.7a, b). Thus

$$\begin{aligned}\frac{A_3 - A_2}{m_f Q_{LHV}} &= \frac{a_3 - a_2}{Q^*} = -\frac{T_0(s_3 - s_2)}{Q^*} \\ &= -\frac{c_v T_0}{Q^*} \ln \left( \frac{T_3}{T_2} \right) = -\frac{c_v T_0}{Q^*} \ln \left( 1 + \frac{Q^*}{c_v T_1 r_c^{\gamma-1}} \right) \quad (5.70)\end{aligned}$$

This loss in availability results from the increase in entropy associated with the irreversibilities of the combustion process. This lost or destroyed availability, as a fraction of the initial availability of the fuel-air mixture, decreases as the compression ratio increases (since  $T_2$  increases as the compression ratio increases,  $T_3/T_2$  decreases for fixed heat addition) and increases as  $Q^*$  decreases [e.g., when the mixture is made leaner; see Eq. (5.46)]. The changes in availability during combustion for the constant-pressure and limited-pressure cycles are more complex because there is a transfer of availability out of the system equal to the expansion work transfer which occurs.

For the constant-volume cycle expansion stroke:

$$\begin{aligned}\frac{A_4 - A_3}{m_f Q_{LHV}} &= \frac{a_4 - a_3}{Q^*} = \frac{(u_4 - u_3) + p_0(v_4 - v_3)}{Q^*} \\ &= \frac{c_v T_3}{Q^*} \left[ \left( \frac{T_4}{T_3} - 1 \right) + (\gamma - 1) \left( \frac{p_0}{p_3} \right) \left( \frac{V_4}{V_3} - 1 \right) \right] \\ &= - \left[ \left( 1 + \frac{c_v T_1 r_c^{\gamma-1}}{Q^*} \right) \left( 1 - \frac{1}{r_c^{\gamma-1}} \right) - (\gamma - 1) \frac{c_v T_1}{Q^*} \left( \frac{r_c - 1}{r_c} \right) \right] \quad (5.71)\end{aligned}$$

The availability of the exhaust gas at state 4 relative to its availability at  $(T_1, p_1)$  is given by

$$\frac{A_4 - A_1}{m_f Q_{LHV}} = \frac{c_v T_1}{Q^*} \left[ \left( \frac{T_4}{T_1} - 1 \right) - \frac{T_0}{T_1} \ln \left( \frac{T_4}{T_1} \right) \right] \quad (5.72)$$

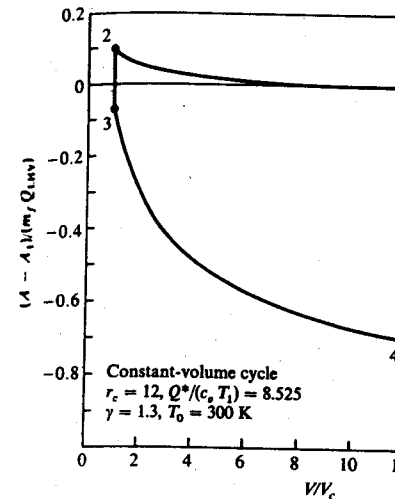


FIGURE 5-15

Availability of cylinder charge relative to availability at state 1 for constant-volume ideal gas cycle as a function of cylinder volume. Availability made dimensionless by  $m_f Q_{LHV}$ . Assumptions as in Fig. 5-6.

The availability of the gases inside the cylinder relative to their availability at  $(T_1, p_1)$  over the compression and expansion strokes of the constant-volume operating cycle example used in Figs. 5-6 and 5-14 is shown in Fig. 5-15. Equations (5.69) and (5.71), with  $T_2$  and  $T_4$  replaced by temperatures intermediate between  $T_1$  and  $T_2$  and  $T_3$  and  $T_4$ , respectively, were used to compute the variations during compression and expansion. Table 5.3 summarizes the changes in availability during each process and the availability of the cylinder gases, at the beginning and end of each process, relative to the datum for the atmosphere

TABLE 5.3  
Availability changes in constant-volume cycle

Process or state	$\frac{A_i - A_1}{m_f Q_{LHV}}$	$\frac{A_i}{m_f Q_{LHV}}$
1		1.0294
1-2	0.0976	
2		1.1270
2-3	-0.1710	
3		0.9560
3-4	-0.6237	
4		0.3323
Fuel conversion efficiency $\eta_{f,i}$		0.526
Availability conversion efficiency $\eta_{a,i}$		0.511

$r_c = 12, \gamma = 1.3, Q^*/(c_v T_1) = 8.525, T_0 = 300 \text{ K}, T_1 = 333 \text{ K}$

(1 atm, 300 K). The availability at state 1 of the fuel, air, residual-gas mixture is  $(1.0286 + 0.0008)m_f Q_{LHV}$ . 1.0286 is the ratio  $(-\Delta g_{298}^o)/(-\Delta h_{298}^o)$  for isoctane (see Table 3.3). The second number, 0.0008, allows for the difference between  $T_1$  and  $T_0$ . Because both work-transfer processes in this ideal cycle case are reversible, the fuel conversion efficiency  $\eta_{f,i}$  is given by  $(A_3 - A_4)/(m_f Q_{LHV}) - (A_2 - A_1)/(m_f Q_{LHV})$ . It is, of course, equal to the value obtained for  $r_c = 12$  and  $\gamma = 1.3$  from the formula for efficiency (Eq. 5.31), obtained previously. The availability conversion efficiency is  $\eta_{f,i}/1.0286$ . Note that it is the availability destroyed during combustion, plus the inability of this ideal constant-volume cycle to use the availability remaining in the gas at state 4, that decrease the availability conversion efficiency below unity. Both these loss mechanisms decrease in magnitude, relative to the fuel availability, as the compression ratio increases. This is the fundamental reason why engine indicated efficiency increases with an increasing compression ratio.

#### 5.7.4 Effect of Equivalence Ratio

The fuel-air cycle with its more accurate models for working fluid properties can be used to examine the effect of variations in the fuel/air equivalence ratio on the availability conversion efficiency. Figure 5-16 shows the temperature attained and the entropy rise that occurs in constant-volume combustion of a fuel-air mixture of different equivalence ratios, following isentropic compression from ambient temperature and pressure through different volumetric compression ratios.<sup>8</sup> The entropy increase is the result of irreversibilities in the combustion process and mixing of complete combustion products with excess air. The significance of these combustion-related losses—the destruction of availability that occurs in this process—is shown in Fig. 5-17 where the availability after constant-volume combustion divided by the availability of the initial fuel-air mixture is shown as a function of equivalence ratio for compression ratios of 12 and 36.<sup>8</sup> The loss of

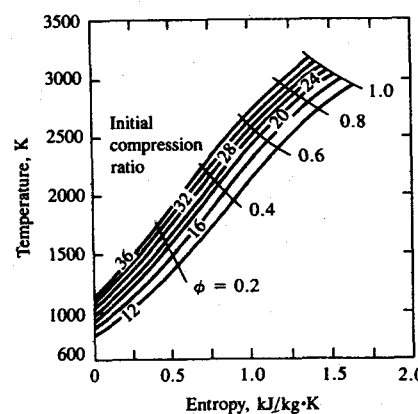


**FIGURE 5-16**  
Temperature and entropy of combustion products after constant-volume combustion following isentropic compression from ambient conditions through specified compression ratio as a function of compression ratio and equivalence ratio. (From Flynn et al.<sup>8</sup>)

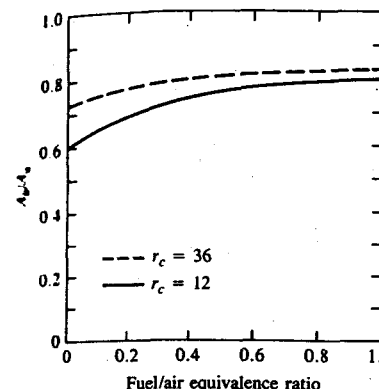


**FIGURE 5-17**

Availability of combustion products after constant-volume combustion relative to availability before combustion following isentropic compression from ambient through specified compression ratio as a function of equivalence ratio. (From Flynn et al.<sup>8</sup>)

availability increases as the equivalence ratio decreases.<sup>†</sup> The combustion loss is a stronger function of the rise in temperature and pressure which occurs than of the change in the specific heat ratio that occurs.

Why then does engine efficiency increase with a decreasing equivalence ratio as shown in Fig. 5-9? The reason is that the expansion stroke work transfer, as a fraction of the fuel availability, increases as the equivalence ratio decreases; hence, the availability lost in the exhaust process, again expressed as a fraction of the fuel availability, decreases. The increase in the expansion stroke work as the equivalence ratio decreases more than offsets the increase in the availability lost during combustion; so the availability conversion efficiency (or the fuel conversion efficiency which closely approximates it) increases.

#### 5.8 COMPARISON WITH REAL ENGINE CYCLES

To put these ideal models of engine processes in perspective, this chapter will conclude with a brief discussion of the additional effects which are important in real engine processes.

A comparison of a real engine *p-V* diagram over the compression and expansion strokes with an equivalent fuel-air cycle analysis is shown in Fig. 5-18.<sup>4</sup> The real engine and the fuel-air cycle have the same geometric compression ratio, fuel chemical composition and equivalence ratio, residual fraction and mixture density before compression. Midway through the compression stroke,

<sup>†</sup> This is consistent with the ideal gas standard cycle result (Eq. 5.70). As  $\phi$  decreases, so does  $Q^o/(c_v T_1)$ . The factor which multiplies the natural logarithm (which increases) has a greater impact than the logarithmic term (which decreases).

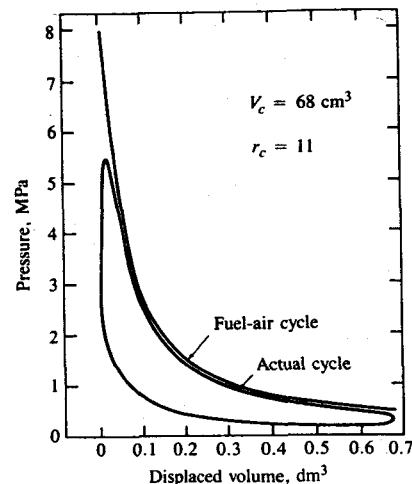


FIGURE 5-18

Pressure-volume diagram for actual spark-ignition engine compared with that for equivalent fuel-air cycle.  $r_e = 11$ . (From Edson and Taylor.<sup>4</sup>)

the pressure in the fuel-air cycle has been made equal to the real cycle pressure.<sup>†</sup> The compression stroke pressures for the two cycles essentially coincide. Modest differences in pressure during intake and the early part of the compression process result from the pressure drop across the intake valve during the intake process and the closing of the intake valve 40 to 60° after BC in the real engine. The expansion stroke pressures for the engine fall below the fuel-air cycle pressures for the following reasons: (1) heat transfer from the burned gases to the walls; (2) finite time required to burn the charge; (3) exhaust blowdown loss due to opening the exhaust valve before BC; (4) gas flow into crevice regions and leakage past the piston rings; (5) incomplete combustion of the charge.

These differences, in decreasing order of importance, are described below. Together, they contribute to the enclosed area on the  $p$ - $V$  diagram for a properly adjusted engine with optimum timing being about 80 percent of the enclosed area of an equivalent fuel-air cycle  $p$ - $V$  diagram. The indicated fuel conversion or availability conversion efficiency of the actual engine is therefore about 0.8 times the efficiency calculated for the fuel-air cycle.<sup>1</sup> Use is often made of this ratio to estimate the performance of actual engines from fuel-air cycle results.

1. *Heat transfer.* Heat transfer from the unburned mixture to the cylinder walls has a negligible effect on the  $p$ - $V$  line for the compression process. Heat transfer from the burned gases is much more important (see Chap. 12). Due to heat transfer during combustion, the pressure at the end of combustion in the real

cycle will be lower. During expansion, heat transfer will cause the gas pressure in the real cycle to fall below an isentropic expansion line as the volume increases. A decrease in efficiency results from this heat loss.

2. *Finite combustion time.* In an SI engine with spark-timing adjusted for optimum efficiency, combustion typically starts 10 to 40 crank angle degrees before TC, is half complete at about 10° after TC, and is essentially complete 30 to 40° after TC. Peak pressure occurs at about 15° after TC (see Fig. 1-8). In a diesel engine, the burning process starts shortly before TC. The pressure rises rapidly to a peak some 5 to 10° after TC since the initial rate of burning is fast. However, the final stages of burning are much slower, and combustion continues until 40 to 50° after TC (see Fig. 1-15). Thus, the peak pressure in the engine is substantially below the fuel-air cycle peak pressure value, because combustion continues until well after TC, when the cylinder volume is much greater than the clearance volume. After peak pressure, expansion stroke pressures in the engine are higher than fuel-air cycle values in the absence of other loss mechanisms, because less work has been extracted from the cylinder gases. A comparison of the constant-volume and limited-pressure cycles in Fig. 5-6 demonstrates this point.

For spark or fuel-injection timing which is retarded from the optimum for maximum efficiency, the peak pressure in the real cycle will be lower, and expansion stroke pressures after the peak pressure will be higher than in the optimum timing cycle.

3. *Exhaust blowdown loss.* In the real engine operating cycle, the exhaust valve is opened some 60° before BC to reduce the pressure during the first part of the exhaust stroke in four-stroke engines and to allow time for scavenging in two-stroke engines. The gas pressure at the end of the expansion stroke is therefore reduced below the isentropic line. A decrease in expansion-stroke work transfer results.

4. *Crevice effects and leakage.* As the cylinder pressure increases, gas flows into crevices such as the regions between the piston, piston rings, and cylinder wall. These crevice regions can comprise a few percent of the clearance volume. This flow reduces the mass in the volume above the piston crown, and this flow is cooled by heat transfer to the crevice walls. In premixed charge engines, some of this gas is unburned and some of it will not burn. Though much of this gas returns to the cylinder later in the expansion, a fraction, from behind and between the piston rings, flows into the crankcase. However, leakage in a well-designed and maintained engine is small (usually less than one percent of the charge). All these effects reduce the cylinder pressure during the latter stages of compression, during combustion, and during expansion below the value that would result if crevice and leakage effects were absent.

5. *Incomplete combustion.* Combustion of the cylinder charge is incomplete; the exhaust gases contain combustible species. For example, in spark-ignition engines the hydrocarbon emissions from a warmed-up engine (which come largely from the crevice regions) are 2 to 3 percent of the fuel mass under

<sup>†</sup> Note that in the fuel-air cycle with idealized valve timing, the compression process starts immediately after BC. In most engines, the charge compression starts later, close to the time that the inlet valve closes some 40 to 60° after BC. This matching process is approximate.

normal operating conditions; carbon monoxide and hydrogen in the exhaust contain an additional 1 to 2 percent or more of the fuel energy, even with excess air present (see Sec. 4.9). Hence, the chemical energy of the fuel which is released in the actual engine is about 5 percent less than the chemical energy of the fuel inducted (the combustion efficiency, see Sec. 3.5.5, is about 95 percent). The fuel-air cycle pressures after combustion will be higher because complete combustion is assumed. In diesel engines, the combustion inefficiency is usually less, about 1 to 2 percent, so this effect is smaller.

**SUMMARY.** The effect of all these loss mechanisms on engine efficiency is best defined by an availability balance for the real engine cycle. A limited number of such calculations have been published (e.g., Refs. 8, 10, and 11). Table 5.4 shows the magnitude of the loss in availability (as a fraction of the initial availability) that occurs due to real cycle effects in a typical naturally aspirated diesel engine.<sup>10</sup> The combustion and exhaust losses are present in the ideal cycle models also (they are smaller, however<sup>9</sup>). The loss in availability due to heat losses, flow or aerodynamic losses, and mechanical friction are real engine effects.

Figure 5-19 shows standard and fuel-air cycle efficiencies as a function of the compression ratio compared with engine indicated efficiency data. The top three sets of engine data are for the best efficiency air/fuel ratio. Differences in the data are in part due to different fuels [(12) isoctane; (13) gasoline; (14) propane] which affect efficiency slightly through their different composition and heating values (see Table D.4). They also result from different combustion chamber shapes which affect the combustion rate and heat transfer. The trends in the data with increasing compression ratio and the  $\phi = 0.8$  fuel-air cycle curve (which corresponds approximately to the actual air/fuel ratios used) are similar. The factor of 0.8 relating real engine and fuel-air cycle efficiencies holds roughly. At compression ratios above about 14, however, the data show that the indicated efficiency of actual engines is essentially constant. Increasing crevice and heat

TABLE 5.4  
Availability losses in naturally aspirated diesel

Loss mechanism	Loss, fraction of fuel availability
Combustion	0.225
Exhaust	0.144
Heat transfer	0.135
Aerodynamic	0.047
Mechanical friction	0.048
Total losses	0.599
Availability conversion efficiency (brake)	0.401

Source: Traupel.<sup>10</sup>

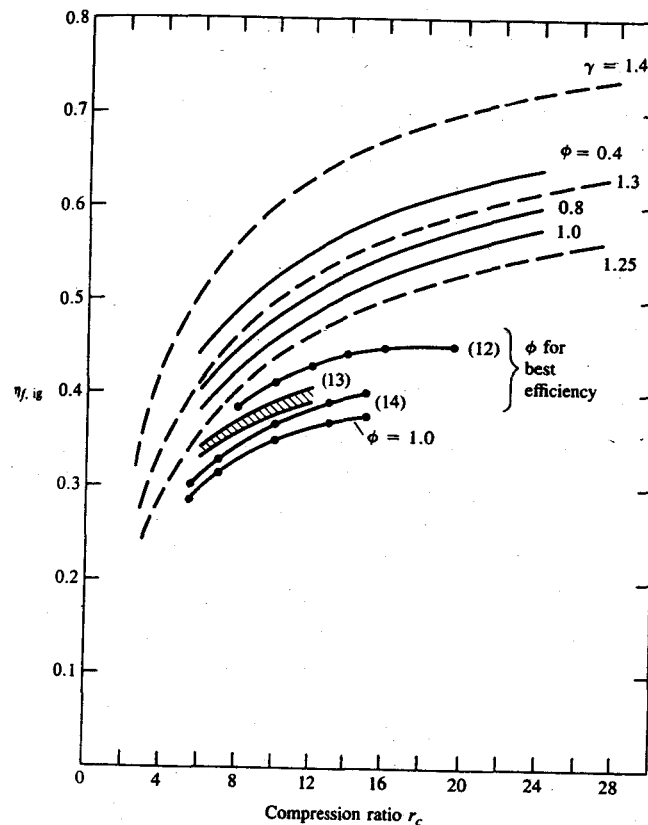


FIGURE 5-19  
Indicated fuel conversion efficiency as a function of compression ratio for ideal gas constant-volume cycle (dashed lines,  $\gamma = 1.25, 1.3, 1.4$ ) and fuel-air cycle (solid lines,  $\phi = 0.4, 0.8, 1.0$ ). Also shown are available engine data for equivalence ratios given: best efficiency  $\phi^{12-14}$ ,  $\phi = 1^{14}$ .

losses offset the calculated ideal cycle efficiency increase as the compression ratio is raised above this value. The standard ideal gas cycle analysis results, with an appropriate choice for the value of  $\gamma$  (1.25 to 1.3), correspond closely to the fuel-air cycle analysis results.

The ideal cycle provides a convenient but crude approximation to the real engine operating cycle. It is useful for illustrating the thermodynamic aspects of engine operation. It can also provide approximate estimates of trends as major engine parameters change. The weakest link in these ideal cycles is the modeling of the combustion processes in SI and CI engines. None of the models examined in this chapter are sufficiently close to reality to provide accurate predictions of engine performance. More sophisticated models of the spark-ignition and diesel engine operating cycles have been developed and are the subject of Chap. 14.

## PROBLEMS

- 5.1. Many diesel engines can be approximated by a limited-pressure cycle. In a limited-pressure cycle, a fraction of the fuel is burnt at constant volume and the remaining fuel is burnt at constant pressure. Use this cycle approximation with  $\gamma = c_p/c_v = 1.3$  to analyze the following problem:

Inlet conditions:	$p_1 = 1.0 \text{ bar}$ , $T_1 = 289 \text{ K}$
Compression ratio:	15 : 1
Heat added during combustion:	43,000 kJ/kg of fuel
Overall fuel/air ratio:	0.045 kg fuel/kg air

- (a) Half of the fuel is burnt at constant volume, then half at constant pressure. Draw a  $p$ - $V$  diagram and compute the fuel conversion efficiency of the cycle.
- (b) Compare the efficiency and peak pressure of the cycle with the efficiency and peak pressure that would be obtained if all of the fuel were burnt at constant pressure or at constant volume.
- 5.2. It is desired to increase the output of a spark-ignition engine by either (1) raising the compression ratio from 8 to 10 or (2) increasing the inlet pressure from 1.0 atm to 1.5 atm. Using the constant-volume cycle as a model for engine operation, which procedure will give:
- (a) The highest pressure of the cycle?
  - (b) The highest efficiency?
  - (c) The highest imep?
- Assume  $\gamma = 1.3$  and  $(m_f Q_{\text{HV}})/(mc_v T_1) = 9.3(r_c - 1)/r_c$ .
- 5.3. When a diesel engine, originally designed to be naturally aspirated, is turbocharged the fuel/air equivalence ratio  $\phi$  at full load must be reduced to maintain the maximum cylinder pressure essentially constant. If the naturally aspirated engine was designed for  $\phi = 0.75$  at full load, estimate the maximum permissible value of  $\phi$  for the turbocharged engine at full load if the air pressure at the engine inlet is 1.6 atm. Assume that the engine can be modeled with the limited-pressure cycle, with half the injected fuel burned at constant volume and half at constant pressure. The compression ratio is 16. The fuel heating value is 42.5 MJ/kg fuel. Assume  $\gamma = c_p/c_v = 1.35$ , that the air temperature at the start of compression is 325 K, and  $(F/A)_{\text{stoich}} = 0.0666$ .
- 5.4. A spark-ignition engine is throttled when operating at part load (the inlet pressure is reduced) while the fuel/air ratio is held essentially constant. Part-load operation of the engine is modeled by the cycle shown in Fig. 5-2d; the inlet air is at pressure  $p_i$ , the exhaust pressure is atmospheric  $p_a$ , and the ambient temperature is  $T_a$ . Derive an expression for the decrease in net indicated fuel conversion efficiency due to throttling from the ideal constant-volume cycle efficiency and show that it is proportional to  $(p_a/p_i - 1)$ . Assume mass fuel  $\ll$  mass air.
- 5.5. (a) Use the ideal gas cycle with constant-volume combustion to describe the operation of an SI engine with a compression ratio of 9. Find the pressure and temperature at points 2, 3, 4, and 5 on Fig. 5-2a. Assume a pressure of 100 kPa and a temperature of 320 K at point 1. Assume  $m_f/m = 0.06$ ,  $c_v = 946 \text{ J/kg} \cdot \text{K}$ ,  $\gamma = 1.3$ .  $Q_{\text{LHV}}$  for gasoline is 44 MJ/kg.
- (b) Find the indicated fuel conversion efficiency and imep for this engine under these operating conditions.

- 5.6. Use a limited-pressure cycle analysis to obtain a plot of indicated fuel conversion efficiency versus  $p_3/p_1$  for a compression ratio of 15 with light diesel oil as fuel. Assume  $m_f/m = 0.04$ ,  $T_1 = 45^\circ\text{C}$ . Use  $\gamma = 1.3$  and  $c_v = 946 \text{ J/kg} \cdot \text{K}$ .
- 5.7. Explain why constant-volume combustion gives a higher indicated fuel conversion efficiency than constant-pressure combustion for the same compression ratio.
- 5.8. Two engines are running at a bimep of 250 kPa. One is an SI engine with the throttle partially closed to maintain the correct load. The second engine is a naturally aspirated CI engine which requires no throttle. Mechanical friction mep for both engines is 100 kPa. If the intake manifold pressures for the SI and CI engines are 25 kPa and 100 kPa respectively, and both exhaust manifold pressures are 105 kPa, use an ideal cycle model to estimate and compare the gross imep of the two engines. You may neglect the pressure drop across the valves during the intake and exhaust processes.
- 5.9. (a) Plot net imep versus  $p_i$  for  $20 \text{ kPa} < p_i < 100 \text{ kPa}$  for a constant-volume cycle using the following conditions:  $m_f/m = 0.06$ ,  $T_1 = 40^\circ\text{C}$ ,  $c_v = 946 \text{ J/kg} \cdot \text{K}$ ,  $\gamma = 1.3$ ,  $r_c = 9.5$ ,  $Q_{\text{LHV}} = 44 \text{ MJ/kg}$  fuel. Assume  $p_e = 100 \text{ kPa}$ .
- (b) What additional information is necessary to draw a similar plot for the engine's indicated torque, and indicated power?
- 5.10. (a) Draw a diagram similar to those in Fig. 5-2 for a supercharged cycle with constant-pressure combustion.
- (b) Use the ideal gas cycle with constant-pressure combustion to model an engine with a compression ratio of 14 through such a supercharged cycle. Find the pressure and temperature at points corresponding to 2, 3, 4, and 5 in Fig. 5-2. Assume a pressure of 200 kPa and temperature of 325 K at point 1, and a pressure of 100 kPa at points 5 and 6.  $m_f/m = 0.03$  and the fuel is a light diesel oil.
- (c) Calculate the gross and net indicated fuel conversion efficiency and imep for this engine under these operating conditions.
- 5.11. Use the appropriate tables and charts to carry out a constant-pressure fuel-air cycle calculation for the supercharged engine described in Prob. 5.10. Assume the same initial conditions at point 1, with  $\phi = 0.4$  and a residual gas fraction of 0.025. A single cycle calculation is sufficient.
- (a) Determine the pressure and temperature at points 2, 3, 4, and 5. Calculate the compression stroke, expansion stroke, and pumping work per cycle per kg air.
  - (b) Find the gross and net indicated fuel conversion efficiency and imep.
  - (c) Compare the calculated residual gas fraction with the assumed value of 0.025.
- 5.12. One method proposed for reducing the pumping work in throttled spark-ignition engines is *early intake valve closing* (EIVC). The ideal cycle  $p$ - $V$  diagram shown illustrates the concept. The EIVC cycle is 1-2-3-4-5-6-7-8-1 (the conventional throttled cycle is 1-2-3-4-5-6-7\*-1). With EIVC, the inlet manifold is held at a pressure  $p_i$  (which is higher than the normal engine intake pressure,  $p_i^*$ ), and the inlet valve is closed *during* the inlet stroke at 8. The trapped fresh charge and residual is then *expanded* to the normal cycle (lower) intake pressure,  $p_i^*$ . You can assume that both cycles have the same mass of gas in the cylinder, temperature, and pressure at state 1 of the cycle.
- (a) On a sketch of the intake and exhaust process  $p$ - $V$  diagram, shade in the area that corresponds to the difference between the pumping work of the EIVC cycle and that of the normal cycle.
  - (b) What value of  $p_i$  and  $V_{\text{EIVC}}$  will give the maximum reduction in pumping work for the EIVC cycle?

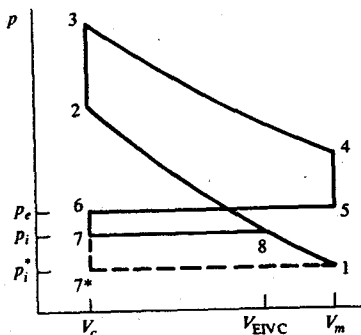


FIGURE PS-12

- (c) Derive an expression for this maximum difference in pumping work between the normal cycle and the EIVC cycle in terms of  $p_e$ ,  $p_i^*$ ,  $V_c$ , and  $V_m$ . You can make the appropriate ideal cycle assumptions.
- 5.13. Calculate the following parameters for a constant-volume fuel-air cycle (Fig. 5-2a):  
 (a) The pressures and temperatures at states 1, 2, 3, 4, 5, and 6  
 (b) The indicated fuel conversion efficiency  
 (c) The imep  
 (d) The residual fraction  
 (e) The volumetric efficiency  
 Inlet pressure = 1 atm, exhaust pressure = 1 atm, inlet temperature = 300 K, compression ratio = 8 : 1, equivalence ratio =  $\phi = 1$ .  
 Calculate the above parameters (points a-e) using the SI units charts. Use 44.4 MJ/kg for heating value of the fuel. Hint: Start the calculations using the residual mass fraction 0.03 and the residual gas temperature 1370 K.
- 5.14. The cycle 1-2-3-4-5-6-1 is a conventional constant-volume fuel-air cycle with a compression ratio of 8. The fuel is iso-octane,  $C_8H_{18}$ , with a lower heating value of 44.4 MJ/kg. The gas state at 1 is  $T_1 = 300$  K,  $p_1 = 1$  atmosphere with an equivalence ratio of 1.0 and zero residual fraction. The specific volume at state 1 is  $0.9 \text{ m}^3/\text{kg}$  air in the mixture. The temperature at the end of compression at state 2 is 600 K.  
 (a) Find the indicated fuel conversion efficiency and mean effective pressure of this fuel-air cycle model of a spark-ignition engine.  
 (b) The efficiency of the cycle can be increased by increasing the expansion ratio  $r_e$  while maintaining the same compression ratio  $r_c$  (cycle 1-2-3-4A-5A-6-1). (This

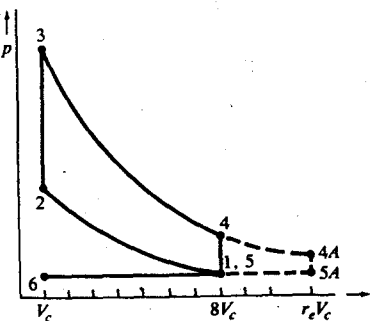


FIGURE PS-14

can be done with valve timing.) If the expansion ratio  $r_e$  is 12, while the compression ratio and other details of the cycle remain the same as in (a), what is the indicated efficiency and mean effective pressure (based on the new, larger, displaced volume) of this new engine cycle?

- 5.15. In spark-ignition engines, exhaust gas is recycled to the intake at part load to reduce the peak burned gas temperatures and lower emissions of nitrogen oxides.  
 (a) Calculate the reduction in burned gas temperature that occurs when, due to exhaust gas recycle, the burned gas fraction in the unburned gas mixture ( $x_b$ ) inside the cylinder is increased from 10 percent (the normal residual fraction) to 30 percent. Assume combustion occurs at top-center, at constant volume, and is adiabatic. Conditions at the end of compression for both cases are:  $T = 700$  K,  $p = 1000$  kPa,  $v = 0.2 \text{ m}^3/\text{kg}$  air in the original mixture; the equivalence ratio is 1.0. The fuel can be modeled as iso-octane.  
 (b) The compression ratio is 8. The compression stroke work is 300 kJ/kg air in the original mixture. Find the indicated work per cycle for the compression and expansion strokes, per kilogram of air in the original mixture, for these two cases.  
 (c) Briefly explain how you would increase the work per cycle with 30 percent burned gas fraction in the unburned mixture to the value obtained with 10 percent burned gas fraction, with fixed engine geometry. (A qualitative answer, only, is required here.)
- 5.16. The following cycle has been proposed for improving the operation of a four-stroke cycle engine. Its aim is to expand the postcombustion cylinder gases to a lower pressure and temperature by extending the expansion stroke, and hence extract more work per cycle.  
 The cycle consists of: (1) an intake stroke; (2) a compression stroke, where the inlet valve remains open (and the cylinder pressure is constant) for the first portion of the stroke; (3) a combustion process, which occurs rapidly close to top-center; (4) an expansion stroke, where the exhaust valve remains closed until the end of the stroke; (5) an exhaust stroke, where the cylinder pressure blows down to the exhaust pressure rapidly and most of the remaining combustion products are expelled as the piston moves from the BC to the TC position. Thus, for this engine concept, the compression ratio  $r_c$  (ratio of cylinder volume at inlet valve closing to clearance volume) is less than the expansion ratio  $r_e$  (ratio of cylinder volume at exhaust valve opening to clearance volume).  
 (a) Sketch a  $p$ - $V$  diagram for the cylinder gases for this cycle operating unthrottled.  
 (b) Using the charts in SI units developed for fuel-air cycle calculations, carry out an analysis of an appropriate ideal model for this cycle where the compression ratio  $r_c$  is 8 and the expansion ratio  $r_e$  is (1) 8; (2) 16. Assume the following:

Pressure in the cylinder at inlet valve close 1 atm

Mixture temperature at inlet valve close 300 K

Mixture equivalence ratio = 1.0

Fuel: iso-octane  $C_8H_{18}$

Lower heating value = 44.4 MJ/kg

Residual gas mass fraction at inlet valve close 0.05

Stoichiometric fuel/air ratio = 0.066

Calculate the indicated work per cycle per kg of air in the original mixture (the standard chart units) and the indicated mean effective pressure for these two expansion ratios. Base the mean effective pressure on the volume displaced by

the piston during the *expansion* stroke. Tabulate your answers. (Note: You are given the initial conditions for the cycle calculation; changing the value of  $r_e$  requires only modest changes in the cycle calculation.)

- (c) Comment briefly on the effect of increasing the ratio  $r_e/r_c$  above 1.0 with this concept on engine efficiency and specific power (power per unit engine weight). Additional calculations are not required.
- 5.17. In a direct-injection stratified-charge (DISC) engine fuel is injected into the engine cylinder just before top-center (like a diesel); a spark discharge is then used to initiate the combustion process. A four-stroke cycle version of this engine has a displaced volume of 2.5 liters and a compression ratio of 12. At high load, the inlet pressure is boosted by a compressor to above atmospheric pressure. The compressor is geared directly to the engine drive shaft. The exhaust pressure is 1 atm. This DISC engine is to replace an equal displacement conventional naturally aspirated spark-ignition (SI) engine, which has a compression ratio of 8.
- (a) Draw qualitative sketches of the appropriate constant-volume ideal cycle pressure-volume diagrams for the complete operating cycles for these two engines at maximum load.
- (b) Use available fuel-air results to estimate how much the DISC engine inlet pressure must be boosted above atmospheric pressure by the compressor to provide the same maximum gross indicated power as the naturally aspirated SI engine. The SI engine operates with an equivalence ratio of 1.2; the DISC engine is limited by smoke emissions to a maximum equivalence ratio of 0.7.
- (c) Under these conditions, will the brake powers of these engines be the same, given that the mechanical rubbing friction is the same? Briefly explain.
- (d) At part load, the SI engine operates at an equivalence ratio of 1.0 and inlet pressure of 0.5 atm. At part load the DISC engine has negligible boost and operates with an inlet pressure of 1.0 atm. Use fuel-air cycle results to determine the equivalence ratio at which the DISC engine must be operated to provide the same net indicated mean effective pressure as the SI engine. What is the ratio of DISC engine net indicated fuel conversion efficiency to SI engine efficiency at these conditions?

5.18. The earliest successful reciprocating internal combustion engine was an engine developed by Lenoir in the 1860s. The operating cycle of this engine consisted of two strokes (i.e., one crankshaft revolution). During the first half of the first stroke, as the piston moves away from its top-center position, fuel-air mixture is drawn into the cylinder through the inlet valve. When half the total cylinder volume is filled with fresh mixture, the inlet valve is closed. The mixture is then ignited and burns rapidly. During the second half of the first stroke, power is delivered from the high-pressure burned gases to the piston. With the piston in its bottom-center position, the exhaust valve is opened. The second stroke, the exhaust stroke, completes the cycle as the piston returns to top-center.

- (a) Sketch a cylinder pressure versus cylinder volume diagram for this engine.
- (b) Using the charts in SI units developed for fuel-air cycle calculations, carry out a cycle analysis and determine the indicated fuel conversion efficiency and mean effective pressure for the Lenoir engine. Assume the following:

$$\text{Inlet pressure} = 1 \text{ atm}$$

$$\text{Inlet mixture temperature} = 300 \text{ K}$$

$$\text{Mixture equivalence ratio} = 1.0$$

Fuel: isoctane C<sub>8</sub>H<sub>18</sub>  
Lower heating value = 44.4 MJ/kg  
Clearance volume negligible

- (c) Compare these values with typical values for the constant-volume fuel-air cycle. Explain (with thermodynamic arguments) why the two cycles have such different indicated mean effective pressures and efficiencies.
- (d) Explain briefly why the real Lenoir engine would have a lower efficiency than the value you calculated in (b) (the actual *brake* fuel conversion efficiency of the engine was about 5 percent).
- 5.19. Estimate from fuel-air cycle results the indicated fuel conversion efficiency, the indicated mean effective pressure, and the maximum indicated power (in kilowatts) at wide-open throttle of these two four-stroke cycle spark-ignition engines:

A six-cylinder engine with a 9.2-cm bore, 9-cm stroke, compression ratio of 7, operated at an equivalence ratio of 0.8

A six-cylinder engine with an 8.3-cm bore, 8-cm stroke, compression ratio of 10, operated at an equivalence ratio of 1.1

Assume that actual indicated engine efficiency is 0.8 times the appropriate fuel-air cycle efficiency. The inlet manifold pressure is close to 1 atmosphere. The maximum permitted value of the mean piston speed is 15 m/s. Briefly summarize the reasons why:

- (a) The efficiency of these two engines is approximately the same despite their different compression ratios.
- (b) The maximum power of the smaller displacement engine is approximately the same as that of the larger displacement engine.

5.20. The constant-volume combustion fuel-air cycle model can be used to estimate the effect of changes in internal combustion engine design and operating variables on engine efficiency. The following table gives the major differences between a diesel and a spark-ignition engine both operating at half maximum power.

	Diesel engine	Spark-ignition engine
Compression ratio	16 : 1	9 : 1
Fuel/air equivalence ratio	0.4	1.0
Inlet manifold pressure	1 atm	0.5 atm

- (a) Use the graphs of fuel-air cycle results (Figs. 5-9 and 5-10) to estimate the ratio of the diesel engine *brake* fuel conversion efficiency to the spark-ignition engine *brake* fuel conversion efficiency.
- (b) Estimate what percentage of the higher diesel *brake* fuel conversion efficiency comes from:
- The higher diesel compression ratio
  - The leaner diesel equivalence ratio
  - The lack of intake throttling in the diesel compared with the spark-ignition engine

The values of fuel conversion efficiency and mean effective pressure given in the graphs are *gross* indicated values (i.e., values obtained from  $\int p dV$  over the compression and expansion strokes only).

You may assume, if necessary, that for the real engines, the gross indicated efficiency and gross indicated mean effective pressure are 0.8 times the fuel-air cycle values. Also, the mechanical rubbing friction for each engine is 30 percent of the *net* indicated power or mep.

## REFERENCES

1. Taylor, C. F.: *The Internal Combustion Engine in Theory and Practice*, vol. 1: *Thermodynamics, Fluid Flow, Performance*, 2d ed., chaps. 2 and 4, 1966.
2. Lancaster, D. R., Krieger, R. B., and Lienesch, J. H.: "Measurement and Analysis of Engine Pressure Data," SAE paper 750026, *SAE Trans.*, vol. 84, 1975.
3. Edson, M. H.: "The Influence of Compression Ratio and Dissociation on Ideal Otto Cycle Engine Thermal Efficiency," *Digital Calculations of Engine Cycles*, SAE Prog. in Technology, vol. 7, pp. 49-64, 1964.
4. Edson, M. H., and Taylor, C. F.: "The Limits of Engine Performance—Comparison of Actual and Theoretical Cycles," *Digital Calculations of Engine Cycles*, SAE Prog. in Technology, vol. 7, pp. 65-81, 1964.
5. Keenan, J. H.: *Thermodynamics*, John Wiley, New York, 1941; MIT Press, Cambridge, Mass., 1970.
6. Haywood, R. W.: "A Critical Review of the Theorems of Thermodynamic Availability, with Concise Formulations; Part 1. Availability," *J. Mech. Engng Sci.*, vol. 16, no. 3, pp. 160-173, 1974.
7. Haywood, R. W.: "A Critical Review of the Theorems of Thermodynamic Availability, with Concise Formulations; Part 2. Irreversibility," *J. Mech. Engng Sci.*, vol. 16, no. 4, pp. 258-267, 1974.
8. Flynn, R. F., Hoag, K. L., Kamel, M. M., and Primus, R. J.: "A New Perspective on Diesel Engine Evaluation Based on Second Law Analysis," SAE paper 840032, *SAE Trans.*, vol. 93, 1984.
9. Clarke, J. M.: "The Thermodynamic Cycle Requirements for Very High Rational Efficiencies," paper C53/76, Institution of Mechanical Engineers, *J. Mech. Engng Sci.*, 1974.
10. Traupel, W.: "Reciprocating Engine and Turbine in Internal Combustion Engineering," in *Proc. CIMAC Int. Congr. on Combustion Engines*, Zurich, pp. 39-54, 1957.
11. Clarke, J. M.: "Letter: Heavy Duty Diesel Fuel Economy," *Mech. Engng.*, pp. 105-106, March 1983.
12. Caris, D. F., and Nelson, E. E.: "A New Look at High Compression Engines," *SAE Trans.*, vol. 67, pp. 112-124, 1959.
13. Kerley, R. V., and Thurston, K. W.: "The Indicated Performance of Otto-Cycle Engines," *SAE Trans.*, vol. 70, pp. 5-37, 1962.
14. Bolt, J. A., and Holkeboer, D. H.: "Lean Fuel-Air Mixtures for High-Compression Spark Ignition Engines," *SAE Trans.*, vol. 70, p. 195, 1962.

# CHAPTER 6

## GAS EXCHANGE PROCESSES

This chapter deals with the fundamentals of the gas exchange processes—intake and exhaust in four-stroke cycle engines and scavenging in two-stroke cycle engines. The purpose of the exhaust and inlet processes or of the scavenging process is to remove the burned gases at the end of the power stroke and admit the fresh charge for the next cycle. Equation (2.38) shows that the indicated power of an internal combustion engine at a given speed is proportional to the mass flow rate of air. Thus, inducing the maximum air mass at wide-open throttle or full load and retaining that mass within the cylinder is the primary goal of the gas exchange processes. Engine gas exchange processes are characterized by overall parameters such as volumetric efficiency (for four-stroke cycles), and scavenging efficiency and trapping efficiency (for two-stroke cycles). These overall parameters depend on the design of engine subsystems such as manifolds, valves, and ports, as well as engine operating conditions. Thus, the flow through individual components in the engine intake and exhaust system has been extensively studied also. Supercharging and turbocharging are used to increase air flow through engines, and hence power density. Obviously, whether the engine is naturally aspirated or supercharged (or turbocharged) significantly affects the gas exchange processes. The above topics are the subject of this chapter.

For spark-ignition engines, the fresh charge is fuel, air, and (if used for emission control) recycled exhaust, so mixture preparation is also an important

goal of the intake process. Mixture preparation includes both achieving the appropriate mixture composition and achieving equal distribution of air, fuel, and recycled exhaust amongst the different cylinders. In diesels, only air (or air plus recycled exhaust) is inducted. Mixture preparation and manifold flow phenomena are discussed in Chap. 7. A third goal of the gas exchange processes is to set up the flow field within the engine cylinders that will give a fast-enough combustion process for satisfactory engine operation. In-cylinder flows are the subject of Chap. 8.

### 6.1 INLET AND EXHAUST PROCESSES IN THE FOUR-STROKE CYCLE

In a spark-ignition engine, the intake system typically consists of an air filter, a carburetor and throttle or fuel injector and throttle or throttle with individual fuel injectors in each intake port, and intake manifold. During the induction process, pressure losses occur as the mixture passes through or by each of these components. There is an additional pressure drop across the intake port and valve. The exhaust system typically consists of an exhaust manifold, exhaust pipe, often a catalytic converter for emission control, and a muffler or silencer. Figure 6-1 illustrates the intake and exhaust gas flow processes in a conventional spark-ignition engine. These flows are pulsating. However, many aspects of these flows can be analysed on a quasi-steady basis, and the pressures indicated in the intake system in Fig. 6-1a represent time-averaged values for a multicylinder engine.

The drop in pressure along the intake system depends on engine speed, the flow resistance of the elements in the system, the cross-sectional area through which the fresh charge moves, and the charge density. Figure 6-1d shows the inlet and exhaust valve lifts versus crank angle. The usual practice is to extend the valve open phases beyond the intake and exhaust strokes to improve emptying and charging of the cylinders and make the best use of the inertia of the gases in the intake and exhaust systems. The exhaust process usually begins 40 to 60° before BC. Until about BC the burned cylinder gases are discharged due to the pressure difference between the cylinder and the exhaust system. After BC, the cylinder is scavenged by the piston as it moves toward TC. The terms *blowdown* and *displacement* are used to denote these two phases of the exhaust process. Typically, the exhaust valve closes 15 to 30° after TC and the inlet valve opens 10 to 20° before TC. Both valves are open during an *overlap period*, and when  $p_i/p_e < 1$ , backflow of exhausted gas into the cylinder and of cylinder gases into the intake will usually occur. The advantage of valve overlap occurs at high engine speeds when the longer valve-open periods improve volumetric efficiency. As the piston moves past TC and the cylinder pressure falls below the intake pressure, gas flows from the intake into the cylinder. The intake valve remains open until 50 to 70° after BC so that fresh charge may continue to flow into the cylinder after BC.

In a diesel engine intake system, the carburetor or EFI system and the throttle plate are absent. Diesel engines are more frequently turbocharged. A

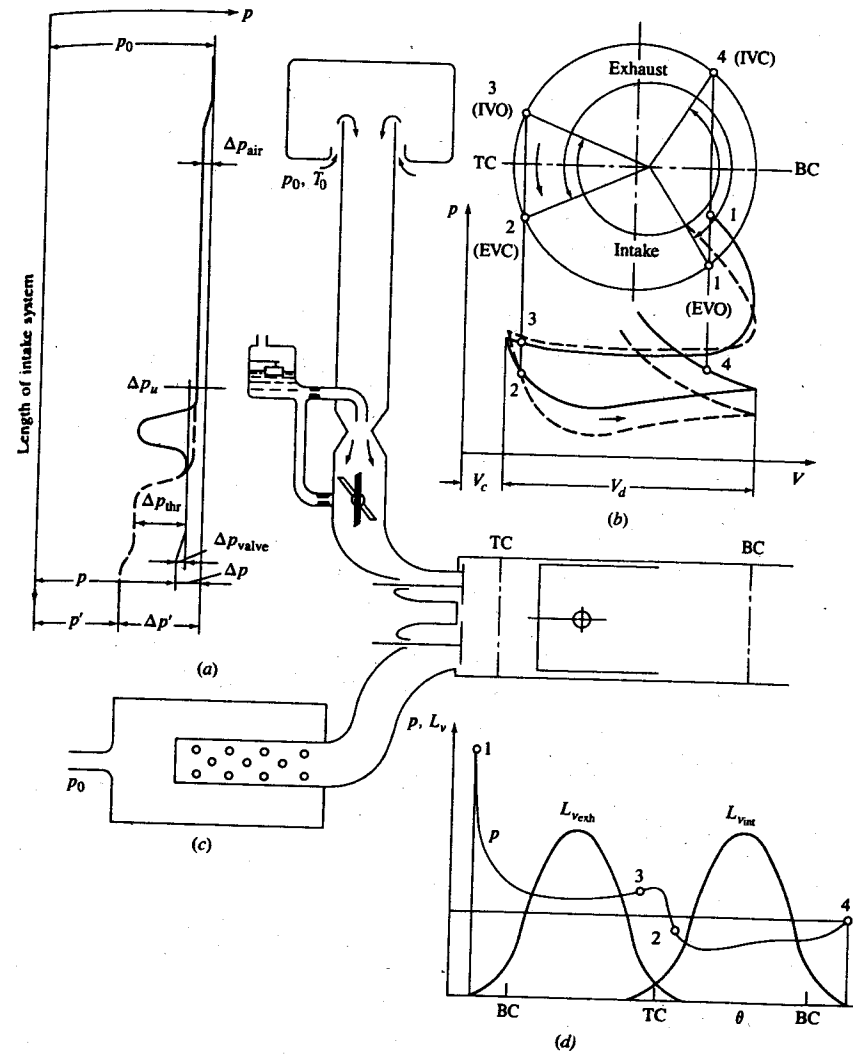
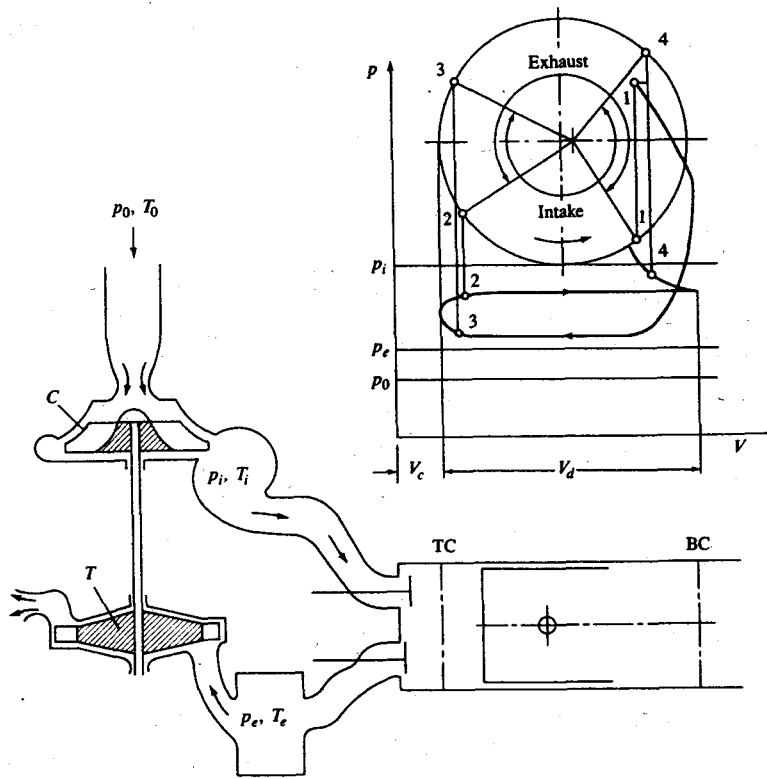


FIGURE 6-1

Intake and exhaust processes for four-stroke cycle spark-ignition engine: (a) intake system and average pressures within it; (b) valve timing and pressure-volume diagrams; (c) exhaust system; (d) cylinder pressure  $p$  and valve lift  $L_v$  versus crank angle  $\theta$ . Solid lines are for wide-open throttle, dashed lines for part throttle;  $p_0$ ,  $T_0$ , atmospheric conditions;  $\Delta p_{air}$  = pressure losses in air cleaner;  $\Delta p_u$  = intake losses upstream of throttle;  $\Delta p_{thr}$  = losses across throttle;  $\Delta p_{valve}$  = losses across the intake valve.<sup>1</sup>



**FIGURE 6-2**  
Intake and exhaust process for turbocharged four-stroke cycle engine. The turbocharger compressor C raises air pressure and temperature from ambient  $p_0$ ,  $T_0$  to  $p_i$ ,  $T_i$ . Cylinder pressure during intake is less than  $p_i$ . During exhaust, the cylinder gases flow through the exhaust manifold to the turbocharger turbine T. Manifold pressure  $p_e$  may vary during the exhaust process and lies between cylinder pressure and ambient.<sup>1</sup>

similar set of diagrams illustrating the intake and exhaust processes for a turbocharged four-stroke diesel is shown in Fig. 6-2. When the exhaust valve opens, the burned cylinder gases are fed to a turbine which drives a compressor which compresses the air prior to entry to the cylinder.

Due to the time-varying valve open area and cylinder volume, gas inertia effects, and wave propagation in the intake and exhaust systems, the pressures in the intake, the cylinder, and the exhaust during these gas exchange processes vary in a complicated way. Analytical calculation of these processes is difficult (see Secs. 7.6.2 and 14.3 for a review of available methods). In practice, these processes are often treated empirically using overall parameters such as volumetric efficiency to define intake and exhaust system performance.

## 6.2 VOLUMETRIC EFFICIENCY

Volumetric efficiency is used as an overall measure of the effectiveness of a four-stroke cycle engine and its intake and exhaust systems as an air pumping device. It is defined [see Sec. 2.10, Eq. (2.27)] as

$$\eta_v = \frac{2\dot{m}_a}{\rho_{a,0} V_d N} \quad (6.1)$$

The air density  $\rho_{a,0}$  can be evaluated at atmospheric conditions;  $\eta_v$  is then the overall volumetric efficiency. Or it can be evaluated at inlet manifold conditions;  $\eta_v$  then measures the pumping performance of the cylinder, inlet port, and valve alone. This discussion will cover unthrottled (wide-open throttle) engine operation only. It is the air flow under these conditions that constrains maximum engine power. Lesser air flows in SI engines are obtained by restricting the intake system flow area with the throttle valve.

Volumetric efficiency is affected by the following fuel, engine design, and engine operating variables:

1. Fuel type, fuel/air ratio, fraction of fuel vaporized in the intake system, and fuel heat of vaporization
2. Mixture temperature as influenced by heat transfer
3. Ratio of exhaust to inlet manifold pressures
4. Compression ratio
5. Engine speed
6. Intake and exhaust manifold and port design
7. Intake and exhaust valve geometry, size, lift, and timings

The effects of several of the above groups of variables are essentially quasi steady in nature; i.e., their impact is either independent of speed or can be described adequately in terms of mean engine speed. However, many of these variables have effects that depend on the unsteady flow and pressure wave phenomena that accompany the time-varying nature of the gas exchange processes.

### 6.2.1 Quasi-Static Effects

**VOLUMETRIC EFFICIENCY OF AN IDEAL CYCLE.** For the ideal cycles of Fig. 5-2d and e, an expression for volumetric efficiency can be derived which is a function of the following variables: intake mixture pressure  $p_i$ , temperature  $T_i$ , and fuel/air ratio ( $F/A$ ); compression ratio  $r_c$ ; exhaust pressure  $p_e$ ; and molecular weight  $M$  and  $\gamma$  for the cycle working fluid. The overall volumetric efficiency is

$$\eta_v = \frac{\dot{m}_a}{\rho_{a,0} V_d} = \frac{m(1 - x_r)}{\rho_{a,0}[1 + (F/A)]} \frac{r_c}{(r_c - 1)V_1}$$

where  $m$  is the mass in the cylinder at point 1 in the cycle. Since

$$p_i V_1 = m \frac{\tilde{R}}{M} T_1 \quad \text{and} \quad p_{a,0} = \rho_{a,0} \frac{\tilde{R}}{M_a} T_{a,0}$$

and Eq. (5.38) relates  $T_1$  to  $T_i$ , the above expression for  $\eta_v$  can be written

$$\eta_v = \left( \frac{M}{M_a} \right) \left( \frac{p_i}{p_{a,0}} \right) \left( \frac{T_{a,0}}{T_i} \right) \frac{1}{[1 + (F/A)]} \left\{ \frac{r_c}{r_c - 1} - \frac{1}{\gamma(r_c - 1)} \left[ \left( \frac{p_e}{p_i} \right) + (\gamma - 1) \right] \right\} \quad (6.2)$$

For  $(p_e/p_i) = 1$ , the term in {} is unity.

**EFFECT OF FUEL COMPOSITION, PHASE, AND FUEL/AIR RATIO.** In a spark-ignition engine, the presence of gaseous fuel (and water vapor) in the intake system reduces the air partial pressure below the mixture pressure. For mixtures of air, water vapor, and gaseous or evaporated fuel we can write the intake manifold pressure as the sum of each component's partial pressure:

$$p_i = p_{a,i} + p_{f,i} + p_{w,i}$$

which with the ideal gas law gives

$$\frac{p_{a,i}}{p_i} = \left[ 1 + \left( \frac{\dot{m}_f}{\dot{m}_a} \right) \left( \frac{M_a}{M_f} \right) + \left( \frac{\dot{m}_w}{\dot{m}_a} \right) \left( \frac{M_a}{M_w} \right) \right]^{-1} \quad (6.3)$$

The water vapor correction is usually small ( $\leq 0.03$ ). This ratio,  $p_{a,i}/p_i$ , for several common fuels as a function of  $(\dot{m}_f/\dot{m}_a)$  is shown in Fig. 6-3. Note that  $(\dot{m}_f/\dot{m}_a)$  only equals the engine operating fuel/air ratio if the fuel is fully vaporized.

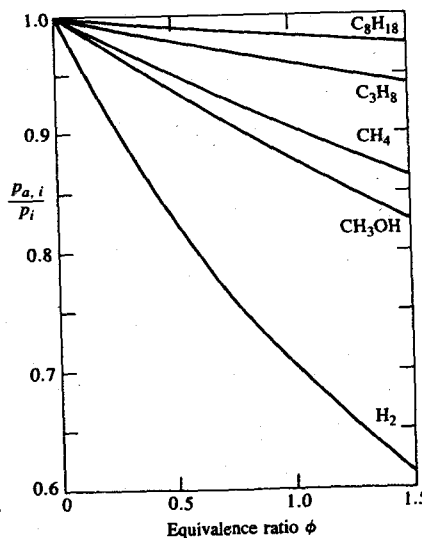


FIGURE 6-3  
Effect of fuel (vapor) on inlet air partial pressure.  
Ratio of air inlet pressure  $p_{a,i}$  to mixture inlet pressure  $p_i$  versus fuel/air equivalence ratio  $\phi$  for iso-octane vapor, propane, methane, methanol vapor, and hydrogen.

For conventional liquid fuels such as gasoline the effect of fuel vapor, and therefore fuel/air ratio, is small. For gaseous fuels and for methanol vapor, the volumetric efficiency is significantly reduced by the fuel vapor in the intake mixture.

**FRACTION FUEL VAPORIZED, HEAT OF VAPORIZATION, AND HEAT TRANSFER.** For a constant-pressure flow with liquid fuel evaporation and with heat transfer, the steady-flow energy equation is

$$[\dot{m}_a h_a + (1 - x_e) \dot{m}_f h_{f,L} + x_e \dot{m}_f h_{f,V}]_A = \dot{Q} + (\dot{m}_a h_a + \dot{m}_f h_{f,L})_B \quad (6.4)$$

where  $x_e$  is the mass fraction evaporated and the subscripts denote:  $a$ , air properties;  $f$ , fuel properties;  $L$ , liquid;  $V$ , vapor;  $B$  before evaporation;  $A$  after evaporation. Approximating the change in enthalpy per unit mass of each component of the mixture by  $c_p \Delta T$ , and with  $h_{f,V} - h_{f,L} = h_{f,LV}$  (the enthalpy of vaporization), Eq. (6-4) becomes

$$T_A - T_B = \frac{(\dot{Q}/\dot{m}_a) - x_e(F/A)h_{f,LV}}{c_{p,a} + (F/A)c_{f,L}} \quad (6.5)$$

Since  $c_{f,L} \approx 2c_{p,a}$  the last term in the denominator can often be neglected.

If no heat transfer to the inlet mixture occurs, the mixture temperature decreases as liquid fuel is vaporized. For complete evaporation of iso-octane, with  $\phi = 1.0$ ,  $T_A - T_B = -19^\circ\text{C}$ . For methanol under the same conditions,  $T_A - T_B$  would be  $-128^\circ\text{C}$ . In practice heating occurs; also, the fuel is not necessarily fully evaporated prior to entry to the cylinder. Experimental data show that the decrease in air temperature that accompanies liquid fuel evaporation more than offsets the reduction in air partial pressure due to the increased amount of fuel vapor: for the same heating rate, volumetric efficiency with fuel vaporization is higher by a few percent.<sup>2</sup>

The ideal cycle equation for volumetric efficiency [Eq. (6.2)] shows that the effect of gas temperature variations, measured at entry to the cylinder, is through the factor  $(T_{a,0}/T_i)$ . Engine test data indicate that a square root dependence of volumetric efficiency on temperature ratio is closer to real engine behavior. The square root dependence is a standard assumption in engine test data reduction (see Sec. 2.12).

**EFFECT OF INLET AND EXHAUST PRESSURE RATIO AND COMPRESSION RATIO.** As the pressure ratio ( $p_e/p_i$ ) and the compression ratio are varied, the fraction of the cylinder volume occupied by the residual gas at the intake pressure varies. As this volume increases so volumetric efficiency decreases. These effects on ideal-cycle volumetric efficiency are given by the {} term in Eq. (6.2). For  $\gamma = 1.3$  these effects are shown in Fig. 6-4.

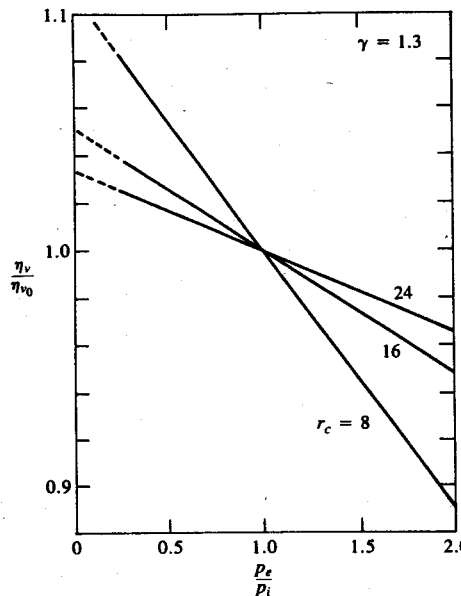


**FIGURE 6-4**  
Effect of exhaust to inlet pressure ratio on ideal-cycle volumetric efficiency.

### 6.2.2 Combined Quasi-Static and Dynamic Effects

When gas flows unsteadily through a system of pipes, chambers, ports, and valves, both friction, pressure, and inertial forces are present. The relative importance of these forces depends on gas velocity and the size and shape of these passages and their junctions. Both quasi-steady and dynamic effects are usually significant. While the effects of changes in engine speed, and intake and exhaust manifold, port and valve design are interrelated, several separate phenomena which affect volumetric efficiency can be identified.

**FRictional LOSSES.** During the intake stroke, due to friction in each part of the intake system, the pressure in the cylinder  $p_c$  is less than the atmospheric pressure  $p_{atm}$  by an amount dependent on the square of the speed. This total pressure drop is the sum of the pressure loss in each component of the intake system: air filter, carburetor and throttle, manifold, inlet port, and inlet valve. Each loss is a few percent, with the port and valve contributing the largest drop. As a result, the pressure in the cylinder during the period in the intake process when the piston is moving at close to its maximum speed can be 10 to 20 percent lower than atmospheric. For each component in the intake (and the exhaust) system, Bernoulli's equation gives

$$\Delta p_j = \xi_j \rho v_j^2$$

where  $\xi_j$  is the resistance coefficient for that component which depends on its

geometric details and  $v_j$  is the local velocity. Assuming the flow is quasi-steady,  $v_j$  is related to the mean piston speed  $\bar{S}_p$  by

$$v_j A_j = \bar{S}_p A_p$$

where  $A_j$  and  $A_p$  are the component minimum flow area and the piston area, respectively. Hence, the total quasi-steady pressure loss due to friction is

$$p_{atm} - p_c = \sum \Delta p_j = \sum \xi_j \rho v_j^2 = \rho \bar{S}_p^2 \sum \xi_j \left( \frac{A_p}{A_j} \right)^2 \quad (6.6)$$

Equation (6.6) indicates the importance of large component flow areas for reducing frictional losses, and the dependence of these losses on engine speed. Figure 6-5 shows an example of the pressure losses due to friction across the air cleaner, carburetor, throttle, and manifold plenum of a standard four-cylinder

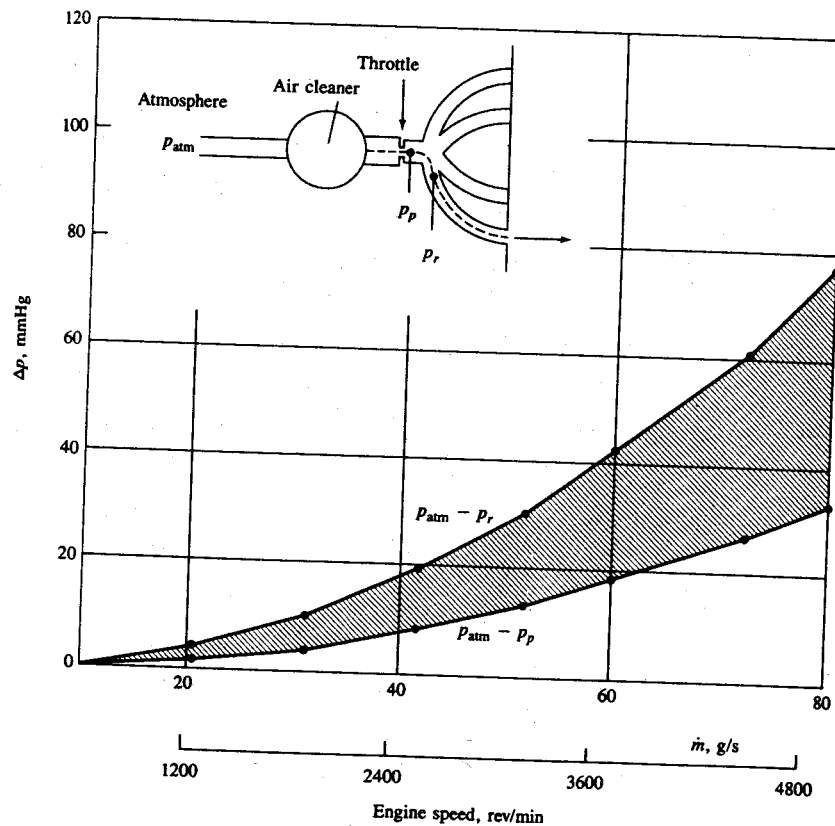


**FIGURE 6-5**  
Pressure losses in the intake system of a four-stroke cycle spark-ignition engine determined under steady flow conditions.<sup>3</sup> Stroke = 89 mm. Bore = 84 mm.

automobile engine intake system. These steady flow tests, conducted over the full engine speed range,<sup>3</sup> show that the pressure loss depends on speed squared.

Equivalent flow-dependent pressure losses in the exhaust system result in the exhaust port and manifold having average pressure levels that are higher than atmospheric. Figure 6-6 shows the time-averaged exhaust manifold gauge pressure as a function of inlet manifold vacuum (which varies inversely to load) and

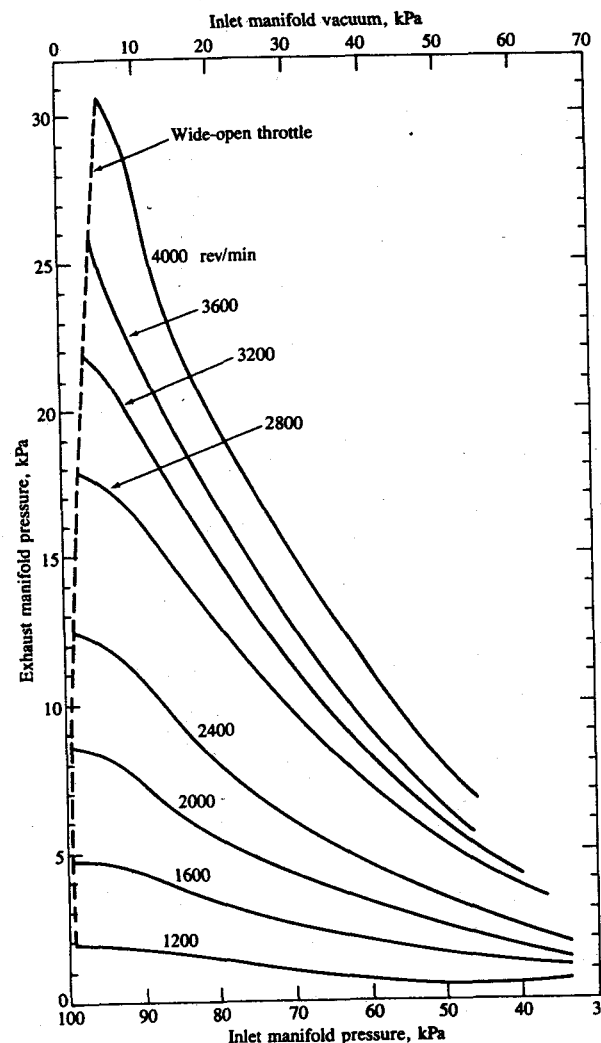


**FIGURE 6-6**  
Exhaust manifold pressure as a function of load (defined by inlet manifold vacuum) and speed, four-stroke cycle four-cylinder spark-ignition engine.<sup>4</sup>

speed for a four-cylinder automobile spark-ignition engine.<sup>4</sup> At high speeds and loads the exhaust manifold operates at pressures substantially above atmospheric.

**RAM EFFECT.** The pressure in the inlet manifold varies during each cylinder's intake process due to the piston velocity variation, valve open area variation, and the unsteady gas-flow effects that result from these geometric variations. The mass of air inducted into the cylinder, and hence the volumetric efficiency, is almost entirely determined by the pressure level in the inlet port during the short period before the inlet valve is closed.<sup>5</sup> At higher engine speeds, the inertia of the gas in the intake system as the intake valve is closing increases the pressure in the port and continues the charging process as the piston slows down around BC and starts the compression stroke. This effect becomes progressively greater as engine speed is increased. The inlet valve is closed some 40 to 60° after BC, in part to take advantage of this ram phenomenon.

**REVERSE FLOW INTO THE INTAKE.** Because the inlet valve closes after the start of the compression stroke, a reverse flow of fresh charge from the cylinder back into the intake can occur as the cylinder pressure rises due to piston motion toward TC. This reverse flow is largest at the lowest engine speeds. It is an inevitable consequence of the inlet valve closing time chosen to take advantage of the ram effect at high speeds.

**TUNING.** The pulsating flow from each cylinder's exhaust process sets up pressure waves in the exhaust system. These pressure waves propagate at the local sound speed relative to the moving exhaust gas. The pressure waves interact with the pipe junctions and ends in the exhaust manifold and pipe. These interactions cause pressure waves to be reflected back toward the engine cylinder. In multi-cylinder engines, the pressure waves set up by each cylinder, transmitted through the exhaust and reflected from the end, can interact with each other. These pressure waves may aid or inhibit the gas exchange processes. When they aid the process by reducing the pressure in the exhaust port toward the end of the exhaust process, the exhaust system is said to be *tuned*.<sup>6</sup>

The time-varying inlet flow to the cylinder causes expansion waves to be propagated back into the inlet manifold. These expansion waves can be reflected at the open end of the manifold (at the plenum) causing positive pressure waves to be propagated toward the cylinder. If the timing of these waves is appropriately arranged, the positive pressure wave will cause the pressure at the inlet valve at the end of the intake process to be raised above the nominal inlet pressure. This will increase the inducted air mass. Such an intake system is described as *tuned*.<sup>6</sup>

Methods which predict the unsteady flows in the intake and exhaust systems of internal combustion engines with good accuracy have been developed. These methods are complicated, however, so more detailed discussion is deferred to Chap. 14.

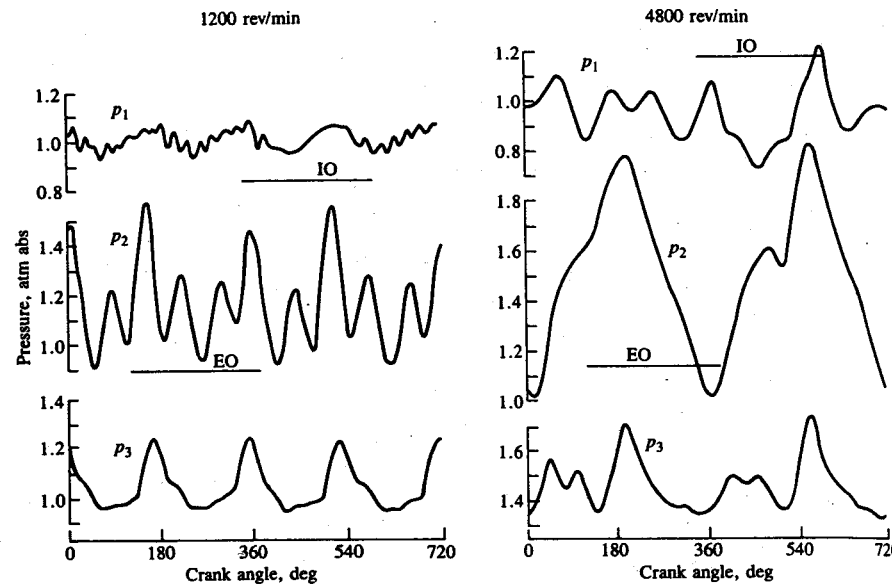


FIGURE 6-7

Instantaneous pressures in the intake and exhaust manifolds of a four-stroke cycle four-cylinder spark-ignition engine, at wide-open throttle. Locations:  $p_1$ , intake manifold runner 150 mm from cylinder 1;  $p_2$ , exhaust manifold runner 200 mm from cylinder 1;  $p_3$ , exhaust manifold runner 700 mm from cylinder 1. IO and EO, intake and exhaust valve open periods for that cylinder, respectively.<sup>3</sup> Stroke = 89 mm. Bore = 84 mm.

Examples of the pressure variations in the inlet and exhaust systems of a four-cylinder automobile spark-ignition engine at wide-open throttle are shown in Fig. 6-7. The complexity of the phenomena that occur is apparent. The amplitude of the pressure fluctuations increases substantially with increasing engine speed. The primary frequency in both the intake and exhaust corresponds to the frequency of the individual cylinder intake and exhaust processes. Higher harmonics that result from pressure waves in both the intake and exhaust are clearly important also.

### 6.2.3 Variation with Speed, and Valve Area, Lift, and Timing

Flow effects on volumetric efficiency depend on the velocity of the fresh mixture in the intake manifold, port, and valve. Local velocities for quasi-steady flow are equal to the volume flow rate divided by the local cross-sectional area. Since the intake system and valve dimensions scale approximately with the cylinder bore, mixture velocities in the intake system will scale with piston speed. Hence, volumetric efficiencies as a function of speed, for different engines, should be compared at the same mean piston speed.<sup>7</sup> Figure 6-8 shows typical curves of

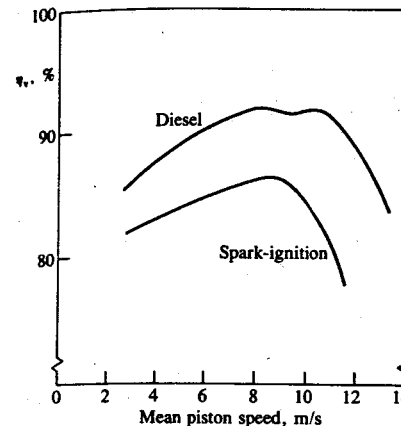


FIGURE 6-8

Volumetric efficiency versus mean piston speed for a four-cylinder automobile indirect-injection diesel<sup>8</sup> and a six-cylinder spark-ignition engine.<sup>9</sup>

volumetric efficiency versus mean piston speed for a four-cylinder automobile indirect-injection diesel engine<sup>8</sup> and a six-cylinder spark-ignition engine.<sup>9</sup> The volumetric efficiencies of spark-ignition engines are usually lower than diesel values due to flow losses in the carburetor and throttle, intake manifold heating, the presence of fuel vapor, and a higher residual gas fraction. The diesel curve with its double peak shows the effect of intake system tuning.

The shape of these volumetric efficiency versus mean piston speed curves can be explained with the aid of Fig. 6-9. This shows, in schematic form, how the

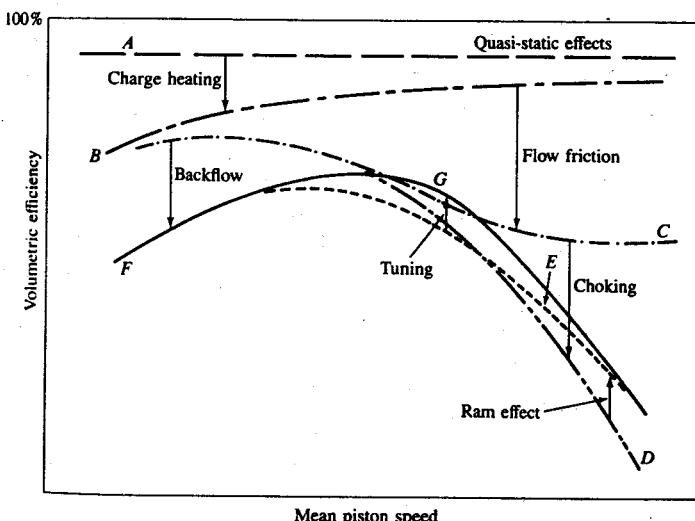


FIGURE 6-9

Effect on volumetric efficiency of different phenomena which affect the air flow rate as a function of speed. Solid line is final  $\eta_v$  versus speed curve.

effect on volumetric efficiency of each of the different phenomena described in this section varies with speed. Non-speed-dependent effects (such as fuel vapor pressure) drop  $\eta_v$  below 100 percent (curve A). Charge heating in the manifold and cylinder drops curve A to curve B. It has a greater effect at lower engine speeds due to longer gas residence times. Frictional flow losses increase as the square of engine speed, and drop curve B to curve C. At higher engine speeds, the flow into the engine during at least part of the intake process becomes choked (see Sec. 6.3.2). Once this occurs, further increases in speed do not increase the flow rate significantly so volumetric efficiency decreases sharply (curve C to D). The induction ram effect, at higher engine speeds, raises curve D to curve E. Late inlet valve closing, which allows advantage to be taken of increased charging at higher speeds, results in a decrease in  $\eta_v$  at low engine speeds due to backflow (curves C and D to F). Finally, intake and/or exhaust tuning can increase the volumetric efficiency (often by a substantial amount) over part of the engine speed range, curve F to G.

An example of the effect on volumetric efficiency of tuning the intake manifold runner is shown in Fig. 6-10. In an unsteady flow calculation of the gas exchange processes of a four-cylinder spark-ignition engine, the length of the intake manifold runners was increased successively by factors of 2. The 34-cm length produces a desirable "tuned" volumetric efficiency curve with increased low-speed air flow and flat mid-speed characteristics. While the longest runner further increases low-speed air flow, the loss in  $\eta_v$  at high speed would be unacceptable.<sup>10</sup> Further discussion of intake system tuning can be found in Sec. 7.6.2.

Figure 6-11 shows data from a four-cylinder spark-ignition engine<sup>3</sup> which illustrates the effect of varying valve timing and valve lift on the volumetric efficiency versus speed curve. Earlier-than-normal inlet valve closing reduces backflow losses at low speed and increases  $\eta_v$ . The penalty is reduced air flow at high speed. Later-than-normal inlet valve closing is only advantageous at very high

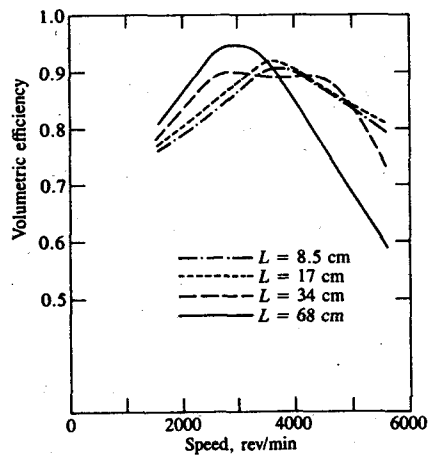


FIGURE 6-10  
Effect of intake runner length on volumetric efficiency versus speed for 2.3-dm<sup>3</sup> four-cylinder spark-ignition engine.<sup>10</sup>

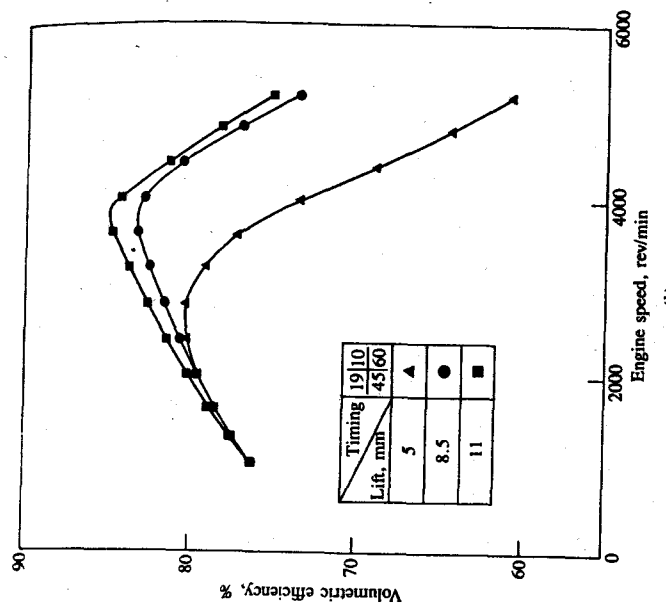


FIGURE 6-11  
Effect of (a) valve timing and (b) valve lift on volumetric efficiency versus speed curves.

Four-cylinder 1.6-dm<sup>3</sup> displacement spark-ignition engine at wide-open throttle, firing conditions, ( $A/F$ ) = 13, MBT ignition timing. Timing numbers are: inlet valve opens (before TC) top left, closes (after BC) bottom left; exhaust valve opens (before BC) top right, closes (after TC) bottom right. Stroke = 89 mm.

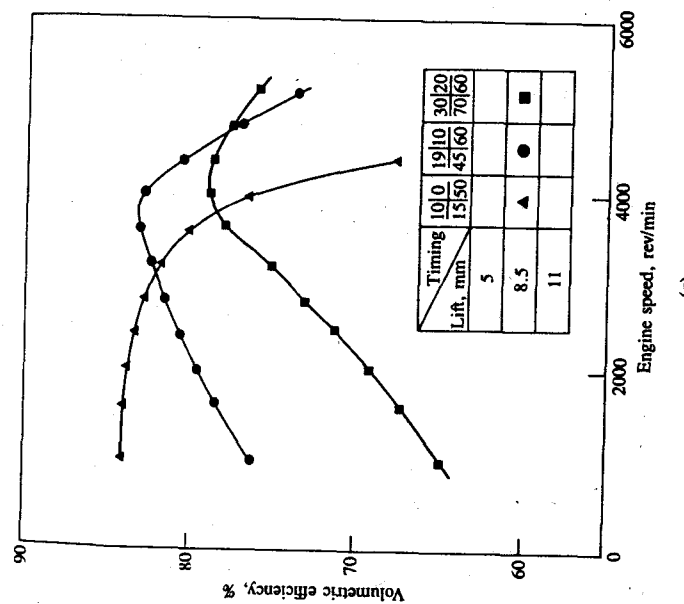


FIGURE 6-11  
Effect of (a) valve timing and (b) valve lift on volumetric efficiency versus speed curves.

Four-cylinder 1.6-dm<sup>3</sup> displacement spark-ignition engine at wide-open throttle, firing conditions, ( $A/F$ ) = 13, MBT ignition timing. Timing numbers are: inlet valve opens (before TC) top left, closes (after BC) bottom left; exhaust valve opens (before BC) top right, closes (after TC) bottom right. Stroke = 89 mm.

speeds. Low valve lifts significantly restrict engine breathing over the mid-speed and high-speed operating ranges. Above a critical valve lift, lift is no longer a major constraint on effective valve open area (see Sec. 6.3).

### 6.3 FLOW THROUGH VALVES

The valve, or valve and port together, is usually the most important flow restriction in the intake and the exhaust system of four-stroke cycle engines. The characteristics of flows through poppet valves will now be reviewed.

#### 6.3.1 Poppet Valve Geometry and Timing

Figure 6-12 shows the main geometric parameters of a poppet valve head and seat. Figure 6-13 shows the proportions of typical inlet and exhaust valves and ports, relative to the valve inner seat diameter  $D$ . The inlet port is generally circular, or nearly so, and the cross-sectional area is no larger than is required to achieve the desired power output. For the exhaust port, the importance of good valve seat and guide cooling, with the shortest length of exposed valve stem, leads to a different design. Although a circular cross section is still desirable, a rectangular or oval shape is often essential around the guide boss area. Typical valve head sizes for different shaped combustion chambers in terms of cylinder bore  $B$  are given in Table 6.1.<sup>11</sup> Each of these chamber shapes (see Secs. 10.2 and 15.4 for a discussion of spark-ignition and diesel combustion chamber design) imposes different constraints on valve size. Larger valve sizes (or four valves compared with two) allow higher maximum air flows for a given cylinder displacement.

Typical valve timing, valve-lift profiles, and valve open areas for a four-stroke cycle spark-ignition engine are shown in Fig. 6-14. There is no universally accepted criterion for defining valve timing points. Some are based upon a spe-

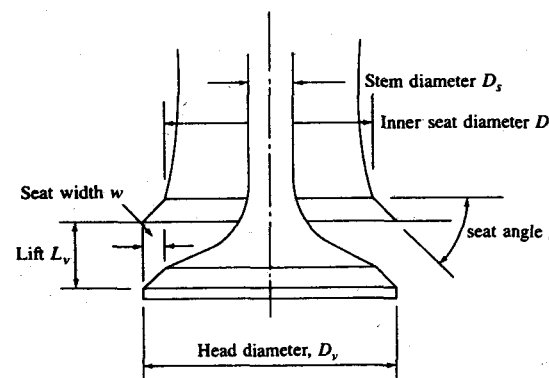
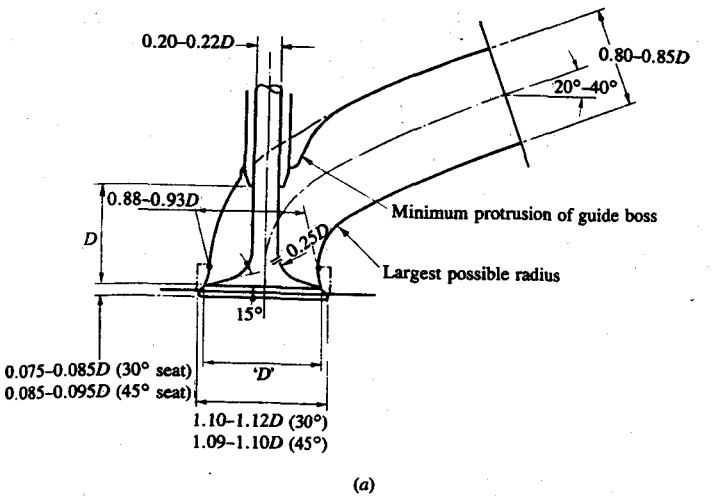
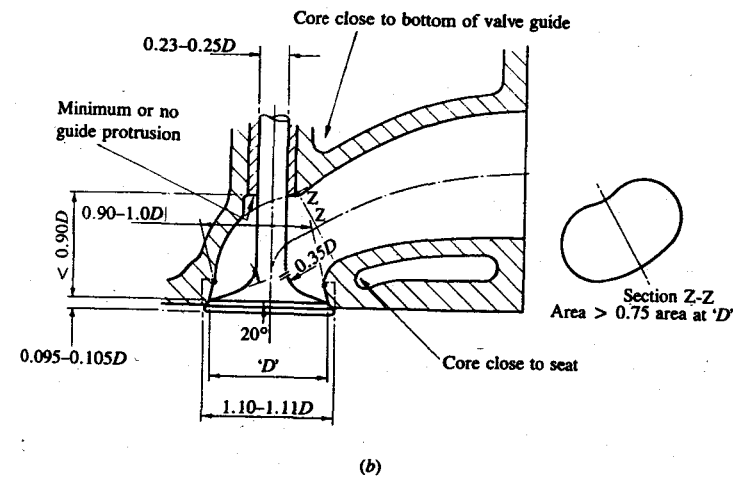


FIGURE 6-12  
Parameters defining poppet valve geometry.



(a)



(b)

FIGURE 6-13  
Shape, proportions, and critical design areas of typical inlet (top) and exhaust (bottom) valves and ports.<sup>11</sup>

cific lift criterion. For example, SAE defines valve timing events based on reference valve-lift points:<sup>13</sup>

1. Hydraulic lifters. Opening and closing positions are the 0.15-mm (0.006-in) valve-lift points.
2. Mechanical lifters. Valve opening and closing positions are the points of 0.15-mm (0.006-in) lift plus the specified lash.

TABLE 6.1  
Valve head diameter in terms of cylinder bore  $B^{11}$

Combustion chamber shape†	Inlet	Exhaust	Approximate mean piston speed, max power, m/s
Wedge or bathtub	0.43–0.46B	0.35–0.37B	15
Bowl-in-piston	0.42–0.44B	0.34–0.37B	14
Hemispherical	0.48–0.5B	0.41–0.43B	18
Four-valve pent-roof	0.35–0.37B	0.28–0.32B	20

† See Fig. 15-15.

Alternatively, valve events can be defined based on angular criteria along the lift curve.<sup>12</sup> What is important is when significant gas flow through the valve-open area either starts or ceases.

The instantaneous valve flow area depends on valve lift and the geometric details of the valve head, seat, and stem. There are three separate stages to the flow area development as valve lift increases,<sup>14</sup> as shown in Fig. 6-14b. For low valve lifts, the minimum flow area corresponds to a frustum of a right circular cone where the conical face between the valve and the seat, which is perpendicular to the seat, defines the flow area. For this stage:

$$\frac{w}{\sin \beta \cos \beta} > L_v > 0$$

and the minimum area is

$$A_m = \pi L_v \cos \beta \left( D_v - 2w + \frac{L_v}{2} \sin 2\beta \right) \quad (6.7)$$

where  $\beta$  is the valve seat angle,  $L_v$  is the valve lift,  $D_v$  is the valve head diameter (the outer diameter of the seat), and  $w$  is the seat width (difference between the inner and outer seat radii).

For the second stage, the minimum area is still the slant surface of a frustum of a right circular cone, but this surface is no longer perpendicular to the valve seat. The base angle of the cone increases from  $(90 - \beta)^\circ$  toward that of a cylinder,  $90^\circ$ . For this stage:

$$\left[ \left( \frac{D_p^2 - D_s^2}{4D_m} \right)^2 - w^2 \right]^{1/2} + w \tan \beta \geq L_v > \frac{w}{\sin \beta \cos \beta}$$

and

$$A_m = \pi D_m [(L_v - w \tan \beta)^2 + w^2]^{1/2} \quad (6.8)$$

where  $D_p$  is the port diameter,  $D_s$  is the valve stem diameter, and  $D_m$  is the mean seat diameter ( $D_v - w$ ).

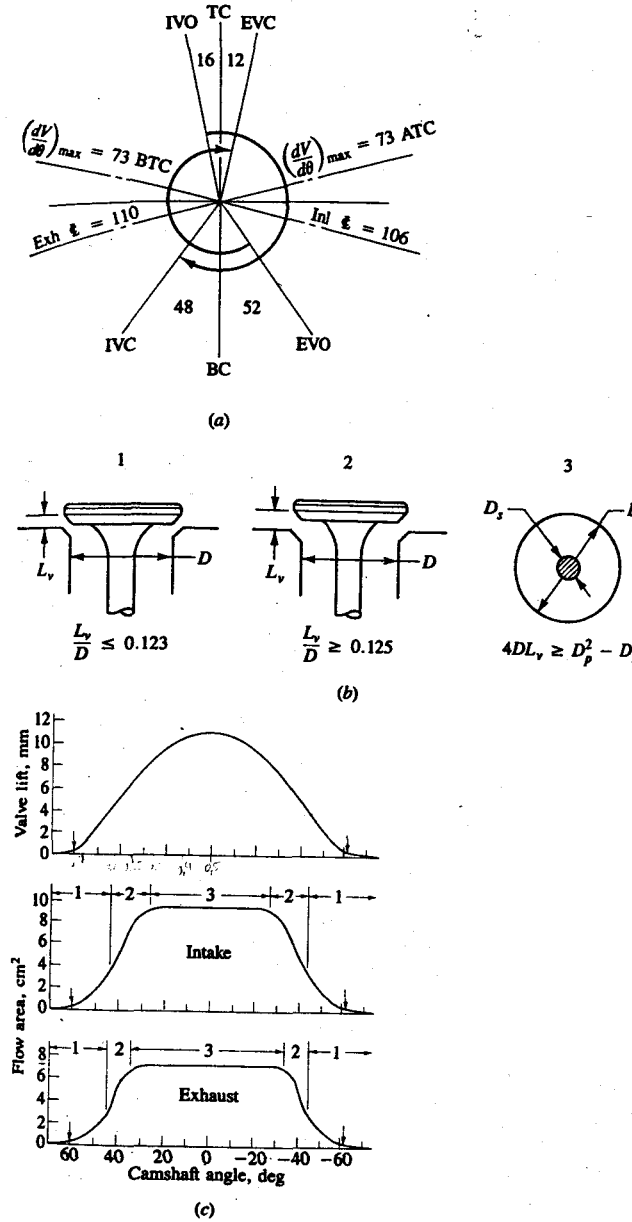


FIGURE 6-14

(a) Typical valve timing diagram for high-speed 2.2-dm<sup>3</sup> four-cylinder spark-ignition engine. (b) Schematic showing three stages of valve lift. (c) Valve-lift curve and corresponding minimum intake and exhaust valve open areas as a function of camshaft angle. Inlet and exhaust valve diameters are 3.6 and 3.1 cm, respectively.<sup>12</sup>

Finally, when the valve lift is sufficiently large, the minimum flow area is no longer between the valve head and seat; it is the port flow area minus the sectional area of the valve stem. Thus, for

$$L_v > \left[ \left( \frac{D_p^2 - D_s^2}{4D_m} \right)^2 - w^2 \right]^{1/2} + w \tan \beta$$

then

$$A_m = \frac{\pi}{4} (D_p^2 - D_s^2) \quad (6.9)$$

Intake and exhaust valve open areas corresponding to a typical valve-lift profile are plotted versus camshaft angle in Fig. 6-14c. These three different flow regimes are indicated. The maximum valve lift is normally about 12 percent of the cylinder bore.

Inlet valve opening (IVO) typically occurs 10 to 25° BTC. Engine performance is relatively insensitive to this timing point. It should occur sufficiently before TC so that cylinder pressure does not dip early in the intake stroke. Inlet valve closing (IVC) usually falls in the range 40 to 60° after BC, to provide more time for cylinder filling under conditions where cylinder pressure is below the intake manifold pressure at BC. IVC is one of the principal factors that determines high-speed volumetric efficiency; it also affects low-speed volumetric efficiency due to backflow into the intake (see Sec. 6.2.3). Exhaust valve opening (EVO) occurs 50 to 60° before BC, well before the end of the expansion stroke, so that blowdown can assist in expelling the exhaust gases. The goal here is to reduce cylinder pressure to close to the exhaust manifold pressure as soon as possible after BC over the full engine speed range. Note that the timing of EVO affects the cycle efficiency since it determines the effective expansion ratio. Exhaust valve closing (EVC) ends the exhaust process and determines the duration of the valve overlap period. EVC typically falls in the range 8 to 20° after TC. At idle and light load, in spark-ignition engines (which are throttled), it therefore regulates the quantity of exhaust gases that flow back into the combustion chamber through the exhaust valve under the influence of intake manifold vacuum. At high engine speeds and loads, it regulates how much of the cylinder burned gases are exhausted. EVC timing should occur sufficiently far after TC so that the cylinder pressure does not rise near the end of the exhaust stroke. Late EVC favors high power at the expense of low-speed torque and idle combustion quality. Note from the timing diagram (Fig. 6-14a) that the points of maximum valve lift and maximum piston velocity (Fig. 2-2) do not coincide.

The effect of valve geometry and timing on air flow can be illustrated conceptually by dividing the rate of change of cylinder volume by the instantaneous minimum valve flow area to obtain a *pseudo flow velocity* for each valve.<sup>12</sup>

$$v_{ps} = \frac{1}{A_m} \frac{dV}{d\theta} = \frac{\pi B^2}{4A_m} \frac{ds}{d\theta} \quad (6.10)$$

where  $V$  is the cylinder volume [Eq. (2.4)],  $B$  is the cylinder bore,  $s$  is the distance

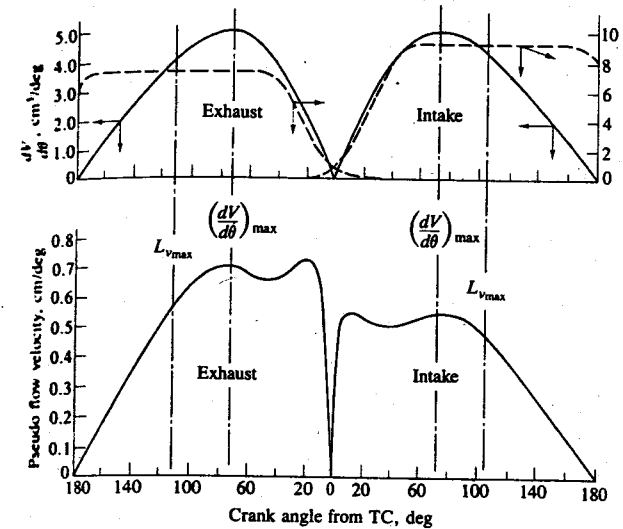


FIGURE 6-15  
Rate of change of cylinder volume  $dV/d\theta$ , valve minimum flow area  $A_m$ , and pseudo flow velocity as function of crank angle for exhaust and inlet valves of Fig. 6-14.<sup>12</sup>

between the wrist pin and crank axis [see Fig. 2-1 and Eq. (2.5)] and  $A_m$  is the valve area given by Eqs. (6.7), (6.8), or (6.9). Instantaneous pseudo flow velocity profiles for the exhaust and intake strokes of a four-stroke four-cylinder engine are shown in Fig. 6-15. Note the appearance of two peaks in the pseudo flow velocity for both the exhaust and intake strokes. The broad peaks occurring at maximum piston velocity reflect the fact that valve flow area is constant at this point. The peaks close to TC result from the exhaust valve closing and intake valve opening profiles. The peak at the end of the exhaust stroke is important since it indicates a high pressure drop across the valve at this point, which will result in higher trapped residual mass. The magnitude of this exhaust stroke pseudo velocity peak depends strongly on the timing of exhaust valve closing. The pseudo velocity peak at the start of the intake stroke is much less important. That the pseudo velocities early in the exhaust stroke and late in the intake stroke are low indicates that phenomena other than quasi-steady flow govern the flow rate. These are the periods when exhaust blowdown and ram and tuning effects in the intake are most important.

### 6.3.2 Flow Rate and Discharge Coefficients

The mass flow rate through a poppet valve is usually described by the equation for compressible flow through a flow restriction [Eqs. (C.8) or (C.9) in App. C]. This equation is derived from a one-dimensional isentropic flow analysis, and

real gas flow effects are included by means of an experimentally determined discharge coefficient  $C_D$ . The air flow rate is related to the upstream stagnation pressure  $p_0$  and stagnation temperature  $T_0$ , static pressure just downstream of the flow restriction (assumed equal to the pressure at the restriction,  $p_T$ ), and a reference area  $A_R$  characteristic of the valve design:

$$\dot{m} = \frac{C_D A_R p_0}{(RT_0)^{1/2}} \left( \frac{p_T}{p_0} \right)^{1/\gamma} \left\{ \frac{2\gamma}{\gamma-1} \left[ 1 - \left( \frac{p_T}{p_0} \right)^{(\gamma-1)/\gamma} \right] \right\}^{1/2} \quad (6.11)$$

When the flow is choked, i.e.,  $p_T/p_0 \leq [2/(\gamma+1)]^{\gamma/(\gamma-1)}$ , the appropriate equation is

$$\dot{m} = \frac{C_D A_R p_0}{(RT_0)^{1/2}} \gamma^{1/2} \left( \frac{2}{\gamma+1} \right)^{(\gamma+1)/2(\gamma-1)} \quad (6.12)$$

For flow into the cylinder through an intake valve,  $p_0$  is the intake system pressure  $p_i$  and  $p_T$  is the cylinder pressure. For flow out of the cylinder through an exhaust valve,  $p_0$  is the cylinder pressure and  $p_T$  is the exhaust system pressure.

The value of  $C_D$  and the choice of reference area are linked together: their product,  $C_D A_R$ , is the effective flow area of the valve assembly  $A_E$ . Several different reference areas have been used. These include the valve head area  $\pi D_v^2/4$ ,<sup>7</sup> the port area at the valve seat  $\pi D_p^2/4$ ,<sup>15</sup> the geometric minimum flow area [Eqs. (6.7), (6.8), and (6.9)], and the curtain area  $\pi D_v L_v$ ,<sup>16</sup> where  $L_v$  is the valve lift. The choice is arbitrary, though some of these choices allow easier interpretation than others. As has been shown above, the geometric minimum flow area is a complex function of valve and valve seat dimensions. The most convenient reference area in practice is the so-called valve curtain area:

$$A_C = \pi D_v L_v \quad (6.13)$$

since it varies linearly with valve lift and is simple to determine.

**INLET VALVES.** Figure 6-16 shows the results of steady flow tests on a typical inlet valve configuration with a sharp-cornered valve seat.<sup>16</sup> The discharge coefficient based on valve curtain area is a discontinuous function of the valve-lift/diameter ratio. The three segments shown correspond to different flow regimes as indicated. At very low lifts, the flow remains attached to the valve head and seat, giving high values for the discharge coefficient. At intermediate lifts, the flow separates from the valve head at the inner edge of the valve seat as shown. An abrupt decrease in discharge coefficient occurs at this point. The discharge coefficient then increases with increasing lift since the size of the separated region remains approximately constant while the minimum flow area is increasing. At high lifts, the flow separates from the inner edge of the valve seat as well.<sup>14, 17</sup> Typical maximum values of  $L_v/D_v$  are 0.25.

An important question is whether these steady flow data are representative of the dynamic flow behavior of the valve in an operating engine. There is some evidence that the "change points" between different flow regimes shown in Fig. 6-16 occur at slightly different valve lifts under dynamic operation than under

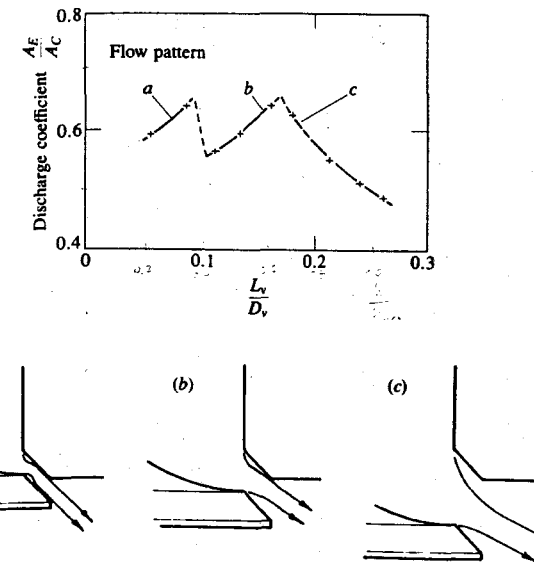


FIGURE 6-16  
Discharge coefficient of typical inlet poppet valve (effective flow area/valve curtain area) as a function of valve lift. Different segments correspond to flow regimes indicated.<sup>16</sup>

steady flow operation. Also, as has been discussed in Sec. 6.2.2, the pressure upstream of the valve varies significantly during the intake process. However, it has been shown that over the normal engine speed range, steady flow discharge-coefficient results can be used to predict dynamic performance with reasonable precision.<sup>14, 18</sup>

In addition to valve lift, the performance of the inlet valve assembly is influenced by the following factors: valve seat width, valve seat angle, rounding of the seat corners, port design, cylinder head shape. In many engine designs the port and valve assembly are used to generate a rotational motion (swirl) inside the engine cylinder during the induction process, or the cylinder head can be shaped to restrict the flow through one side of the valve open area to generate swirl. Swirl production is discussed later, in Section 8.3. Swirl generation significantly reduces the valve (and port) flow coefficient. Changes in seat width affect the  $L_v/D_v$  at which the shifts in flow regimes illustrated in Fig. 6-16 occur.  $C_D$  increases as seat width decreases. The seat angle  $\beta$  affects the discharge coefficient in the low-lift regime in Fig. 6-16. Rounding the upstream corner of the valve seat reduces the tendency of the flow to break away, thus increasing  $C_D$  at higher lifts. At low valve lifts, when the flow remains attached, increasing the Reynolds number decreases the discharge coefficient. Once the flow breaks away from the wall, there is no Reynolds number dependence of  $C_D$ .<sup>16</sup>

For well-designed ports (e.g., Fig. 6-13) the discharge coefficient of the port and valve assembly need be no lower than that of the isolated valve (except when

the port is used to generate swirl). However, if the cross-sectional area of the port is not sufficient or the radius of the surface at the inside of the bend is too small, a significant reduction in  $C_D$  for the assembly can result.<sup>16</sup>

At high engine speeds, unless the inlet valve is of sufficient size, the inlet flow during part of the induction process can become choked (i.e., reach sonic velocity at the minimum valve flow area). Choking substantially reduces volumetric efficiency. Various definitions of inlet Mach number have been used to identify the onset of choking. Taylor and coworkers<sup>7</sup> correlated volumetric efficiencies measured on a range of engine and inlet valve designs with an *inlet Mach index Z* formed from an average gas velocity through the inlet valve:

$$Z = \frac{A_p \bar{S}_p}{C_i A_i a} \quad (6.14)$$

where  $A_i$  is the nominal inlet valve area ( $\pi D_v^2/4$ ),  $C_i$  is a mean valve discharge coefficient based on the area  $A_i$ , and  $a$  is the sound speed. From the method used to determine  $C_i$ , it is apparent that  $C_i A_i$  is the average effective open area of the valve (it is the average value of  $C_D \pi D_v L_v$ ).  $Z$  corresponds closely, therefore, to the mean Mach number in the inlet valve throat. Taylor's correlations show that  $\eta_v$  decreases rapidly for  $Z \geq 0.5$ . An alternative equivalent approach to this problem has been developed, based on the average flow velocity through the valve during the period the valve is open.<sup>19</sup> A *mean inlet Mach number* was defined:

$$\bar{M}_i = \frac{\bar{v}_i}{a} \quad (6.15)$$

where  $\bar{v}_i$  is the mean inlet flow velocity during the valve open period.  $\bar{M}_i$  is related to  $Z$  via

$$\bar{M}_i = \frac{Z(\eta_v/100)180}{\theta_{IVC} - \theta_{IVO}} \quad (6.16)$$

This mean inlet Mach number correlates volumetric efficiency characteristics better than the Mach index. For a series of modern small four-cylinder engines, when  $\bar{M}_i$  approaches 0.5 the volumetric efficiency decreases rapidly. This is due to the flow becoming choked during part of the intake process. This relationship can be used to size the inlet valve for the desired volumetric efficiency at maximum engine speed. Also, if the inlet valve is closed too early, volumetric efficiency will decrease gradually with increasing  $\bar{M}_i$ , for  $\bar{M}_i < 0.5$ , even if the valve open area is sufficiently large.<sup>19</sup>

**EXHAUST VALVES.** In studies of the flow from the cylinder through an exhaust poppet valve, different flow regimes at low and high lift occur, as shown in Fig. 6-17. Values of  $C_D$  based on the valve curtain area, for several different exhaust valve and port combinations, are given in Fig. 6-18. A sharp-cornered isolated poppet valve (i.e., straight pipe downstream, no port) gives the best performance.

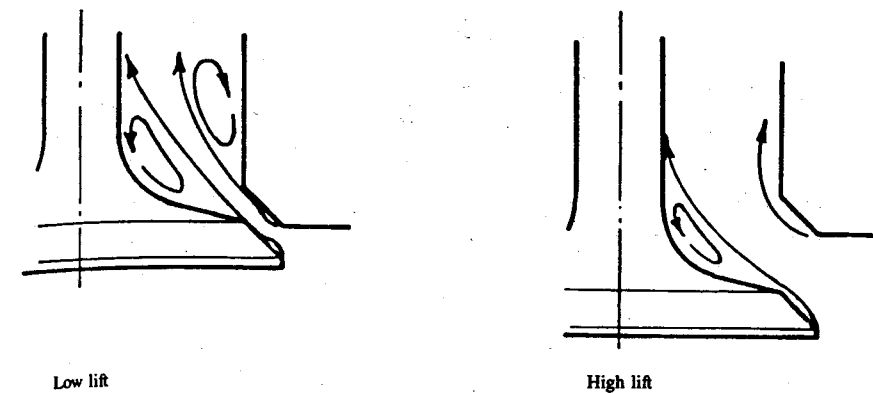


FIGURE 6-17  
Flow pattern through exhaust valve at low and high lift.<sup>16</sup>

At high lifts,  $L_v/D_v \geq 0.2$ , the breakaway of the flow reduces the discharge coefficient. (At  $L_v/D_v = 0.25$  the effective area is about 90 percent of the minimum geometric area. For  $L_v/D_v < 0.2$  it is about 95 percent.<sup>16</sup>) The port design significantly affects  $C_D$  at higher valve lifts, as indicated by the data from four port designs in Fig. 6-18. Good designs can approach the performance of isolated

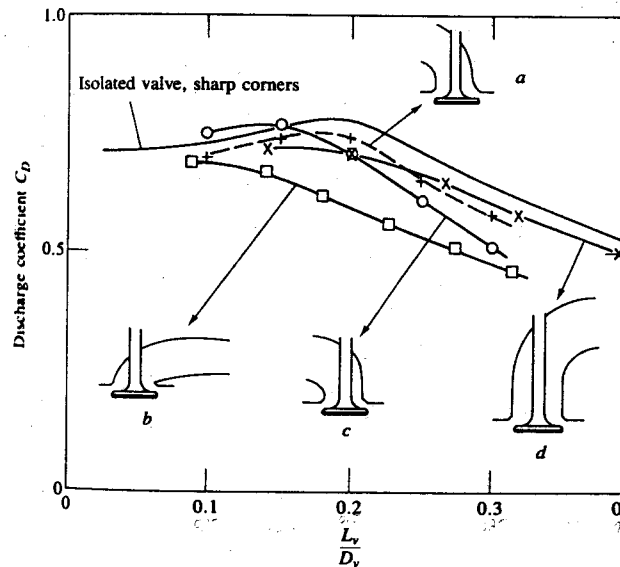
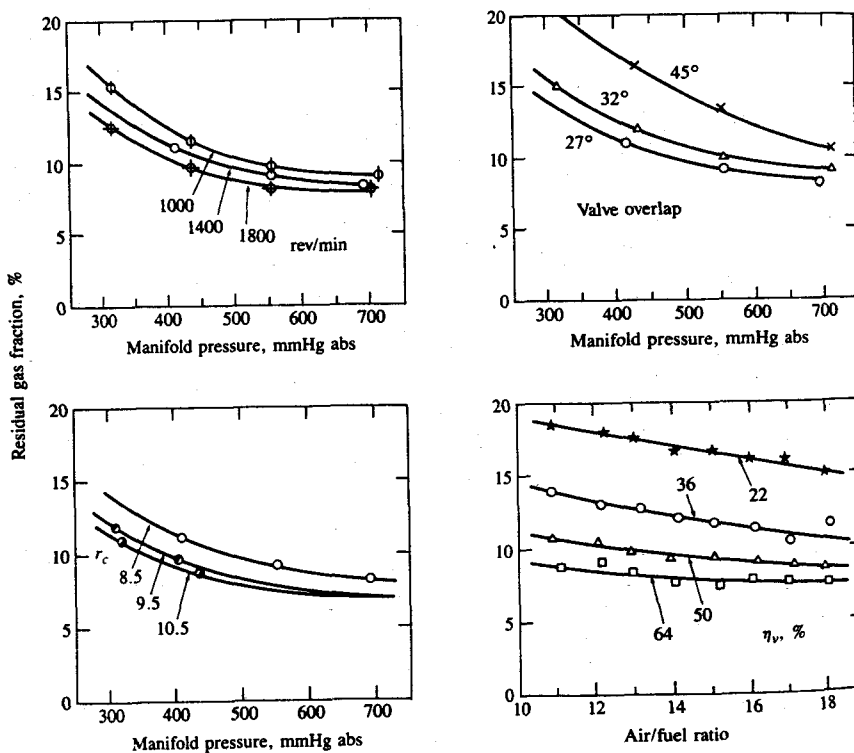


FIGURE 6-18  
Discharge coefficient as function of valve lift for several exhaust valve and port designs.<sup>16</sup> a,<sup>20</sup> b,<sup>15</sup> c,<sup>20</sup> d.<sup>21</sup>

valves, however. Exhaust valves operate over a wide range of pressure ratios (1 to 5). For pressure ratios greater than about 2 the flow will be choked, but the effect of pressure ratio on discharge coefficient is small and confined to higher lifts (e.g.,  $\pm 5$  percent at  $L_v/D_v = 0.3$ ).<sup>15</sup>

#### 6.4 RESIDUAL GAS FRACTION

The residual gas fraction in the cylinder during compression is determined by the exhaust and inlet processes. Its magnitude affects volumetric efficiency and engine performance directly, and efficiency and emissions through its effect on working-fluid thermodynamic properties. The residual gas fraction is primarily a function of inlet and exhaust pressures, speed, compression ratio, valve timing, and exhaust system dynamics.



**FIGURE 6-19**  
Residual gas fraction for 2-dm<sup>3</sup> four-cylinder spark-ignition engine as a function of intake manifold pressure for a range of speeds, compression ratios, and valve overlaps; also as a function of air/fuel ratio for a range of volumetric efficiencies. Operating conditions, unless noted: speed = 1400 rev/min, A/F = 14.5, spark timing set to 0.95 maximum torque, compression ratio = 8.5.<sup>22</sup>

The residual gas mass fraction  $x_r$  (or burned gas fraction if EGR is used) is usually determined by measuring the CO<sub>2</sub> concentration in a sample of gas extracted from the cylinder during the compression stroke. Then

$$x_r = \frac{(\tilde{x}_{CO_2})_C}{(\tilde{x}_{CO_2})_e} \quad (6.17)$$

where the subscripts C and e denote compression and exhaust, and  $\tilde{x}_{CO_2}$  are mole fractions in the wet gas. Usually CO<sub>2</sub> volume or mole fractions are measured in dry gas streams (see Sec. 4.9). A correction factor K,

$$K = \frac{(\tilde{x}_i)_{wet}}{(\tilde{x}_i)_{dry}} = \frac{1}{1 + 0.5[y(\tilde{x}_{CO_2}^* + x_{CO}^*) - 0.74\tilde{x}_{CO}^*]} \quad (6.18)$$

where y is the molar hydrogen/carbon ratio of the fuel and  $\tilde{x}_{CO_2}^*$ ,  $\tilde{x}_{CO}^*$  are dry mole fractions, can be used to convert the dry mole fraction measurements.

Residual gas measurements in a spark-ignition engine are given in Fig. 6-19, which shows the effect of changes in speed, valve overlap, compression ratio, and air/fuel ratio for a range of inlet manifold pressures for a 2-dm<sup>3</sup>, 88.5-mm bore, four-cylinder engine.<sup>22</sup> The effect of variations in spark timing was negligible. Inlet pressure, speed, and valve overlap are the most important variables, though the exhaust pressure also affects the residual fraction.<sup>23</sup> Normal settings for inlet valve opening (about 15° before TC) and exhaust valve closing (about 12° after TC) provide sufficient overlap for good scavenging, but avoid excessive backflow from the exhaust port into the cylinder.

Residual gas fractions in diesel engines are substantially lower than in SI engines because inlet and exhaust pressures are comparable in magnitude and the compression ratio is 2 to 3 times as large. Also, a substantial fraction of the residual gas is air.

#### 6.5 EXHAUST GAS FLOW RATE AND TEMPERATURE VARIATION

The exhaust gas mass flow rate and the properties of the exhaust gas vary significantly during the exhaust process. The origin of this variation for an ideal exhaust process is evident from Fig. 5-3. The thermodynamic state (pressure, temperature, etc.) of the gas in the cylinder varies continually during the exhaust blowdown phase, until the cylinder pressure closely approaches the exhaust manifold pressure. In the real exhaust process, the exhaust valve restricts the flow out of the cylinder, the valve lift varies with time, and the cylinder volume changes during the blowdown process, but the principles remain the same.

Measurements have been made of the variation in mass flow rate through the exhaust valve and gas temperature at the exhaust port exit during the exhaust process of a spark-ignition engine.<sup>24</sup> Figure 6-20 shows the instantaneous mass flow rate data at three different engine speeds. The blowdown and displacement

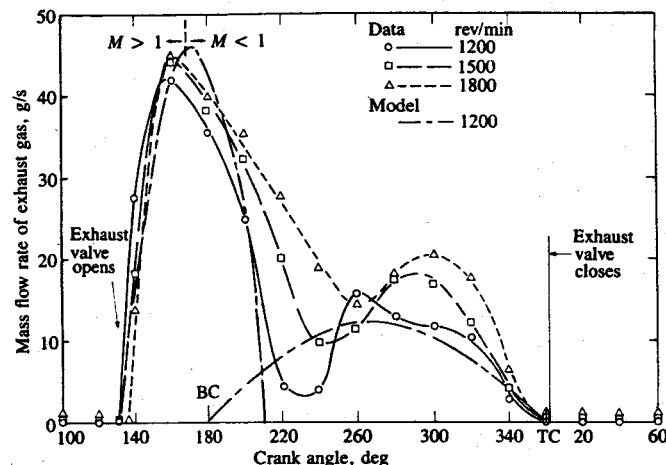


FIGURE 6-20

Instantaneous mass flow rate of exhaust gas through the valve versus crank angle: equivalence ratio = 1.2, wide-open throttle, compression ratio = 7. Dash-dot line is one-dimensional compressible flow model for blowdown and incompressible displacement model for exhaust stroke.<sup>24</sup>

phases of the exhaust process are evident. Simple quasi-steady models of these phases give good agreement with the data at lower engine speeds. The blowdown model shown applies orifice flow equations to the flow across the exhaust valve using the measured cylinder pressure and estimated gas temperature for upstream stagnation conditions. Equation (C.9) is used when the pressure ratio across the valve exceeds the critical value. Equation (C.8) is used when the pressure ratio is less than the critical value. The displacement model assumes the gas in the cylinder is incompressible as the piston moves through the exhaust stroke. As engine speed increases, the crank angle duration of the blowdown phase increases. There is evidence of dynamic effects occurring at the transition between the two phases. The peak mass flow rate during blowdown does not vary substantially with speed since the flow is choked. The mass flow rate at the time of maximum piston speed during displacement scales approximately with piston speed. As the inlet manifold pressure is reduced below the wide-open throttle value, the proportion of the charge which exits the cylinder during the blowdown phase decreases but the mass flow rate during displacement remains essentially constant.

The exhaust gas temperature varies substantially through the exhaust process, and decreases due to heat loss as the gas flows past the exhaust valve and through the exhaust system.

Figure 6-21 shows the measured cylinder pressure, calculated cylinder gas temperature and exhaust mass flow rate, and measured gas temperature at the exhaust port exit for a single-cylinder spark-ignition engine at mid-load and low speed.<sup>25</sup> The average cylinder-gas temperature falls rapidly during blowdown, and continues to fall during the exhaust stroke due to heat transfer to the cylinder walls.

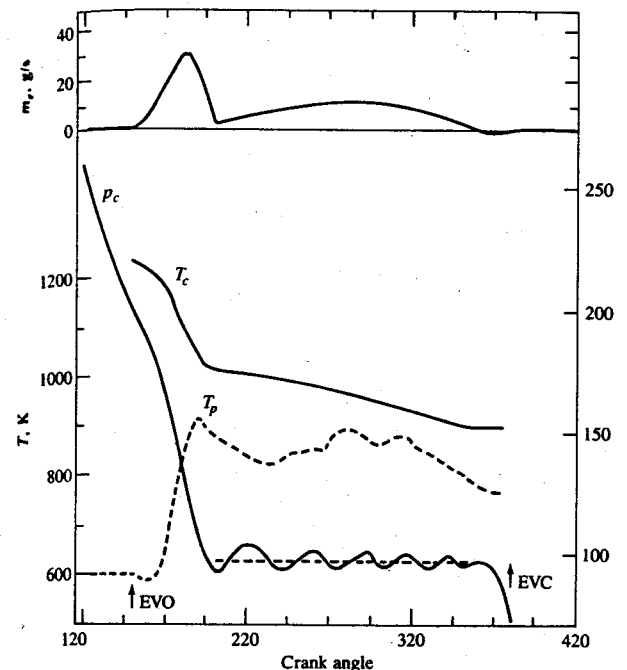


FIGURE 6-21

Measured cylinder pressure  $p_c$ , calculated cylinder-gas temperature  $T_c$ , exhaust mass flow rate  $m_e$ , and measured gas temperature at exhaust port exit  $T_p$ , for single-cylinder spark-ignition engine. Speed = 1000 rev/min, imep = 414 kPa, equivalence ratio = 1.2, spark timing = 10° BTC,  $r_t$  = 7.2.<sup>25</sup>

The gas temperature at the port exit at the start of the exhaust flow pulse is a mixture of hotter gas which has just left the cylinder and cooler gas which left the cylinder at the end of the previous exhaust process and has been stationary in the exhaust port while the valve has been closed. The port exit temperature has a minimum where the transition from blowdown flow to displacement occurs, and the gas comes momentarily to rest and loses a substantial fraction of its thermal energy to the exhaust port walls.

Figure 6-22 shows the effect of varying load and speed on exhaust port exit temperatures. Increasing load ( $A \rightarrow B \rightarrow C$ ) increases the mass and temperature in the blowdown pulse. Increasing speed ( $B \rightarrow D$ ) raises the gas temperature throughout the exhaust process. These effects are the result of variations in the relative importance of heat transfer in the cylinder and heat transfer to the exhaust valve and port. The time available for heat transfer, which depends on engine speed and exhaust gas flow rate, is the most critical factor. The exhaust temperature variation with equivalence ratio follows from the variation in expansion stroke temperatures, with maximum values at  $\phi = 1.0$  and lower values for leaner and richer mixtures.<sup>24</sup> Diesel engine exhaust temperatures are significantly

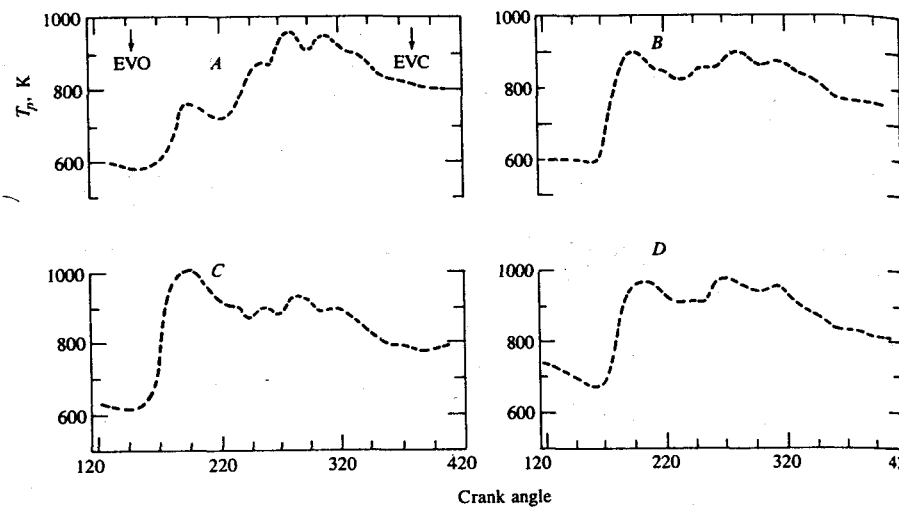


FIGURE 6-22

Measured gas temperature at exhaust port exit as a function of crank angle, single-cylinder spark-ignition engine, for different loads and speeds. Curve A: imep = 267 kPa, 1000 rev/min; curve B: imep = 414 kPa, 1000 rev/min; curve C: imep = 621 kPa, 1000 rev/min; curve D: imep = 414 kPa, 1600 rev/min. Equivalence ratio = 1.2, spark timing = 10° BTC, compression ratio = 7.2.<sup>25</sup>

lower than spark-ignition engine exhaust temperatures because of the lean operating equivalence ratio and their higher expansion ratio during the power stroke.

The average exhaust gas temperature is an important quantity for determining the performance of turbochargers, catalytic converters, and particulate traps. The time-averaged exhaust temperature does not correspond to the average energy of the exhaust gas because the flow rate varies substantially. An enthalpy-averaged temperature

$$\bar{T}_h = \left( \int_{\text{EVO}}^{\text{EVC}} \dot{m} c_p T_g d\theta \right) / \left( \int_{\text{EVO}}^{\text{EVC}} \dot{m} c_p d\theta \right) \quad (6.19)$$

is the best indicator of exhaust thermal energy. Average exhaust gas temperatures are usually measured with a thermocouple. Thermocouple-averaged temperatures are close to time-averaged temperatures. Mass-averaged exhaust temperatures (which are close to  $\bar{T}_h$  if  $c_p$  variations are small) for a spark-ignition engine at the exhaust port exit are about 100 K higher than time-averaged or thermocouple-determined temperatures. Mass-average temperatures in the cylinder during the exhaust process are about 200 to 300 K higher than mass-averaged port temperatures. All these temperatures increase with increasing speed, load, and spark retard, with speed being the variable with the largest impact.<sup>26</sup>

## 6.6 SCAVENGING IN TWO-STROKE CYCLE ENGINES

### 6.6.1 Two-Stroke Engine Configurations

In two-stroke cycle engines, each outward stroke of the piston is a power stroke. To achieve this operating cycle, the fresh charge must be supplied to the engine cylinder at a high-enough pressure to displace the burned gases from the previous cycle. Raising the pressure of the intake mixture is done in a separate pump or blower or compressor. The operation of clearing the cylinder of burned gases and filling it with fresh mixture (or air)—the combined intake and exhaust process—is called *scavenging*. However, air capacity is just as important as in the four-stroke cycle; usually, a greater air mass flow rate must be achieved to obtain the same output power. Figures 1-12, and 1-5 and 1-24 show sectioned drawings of a two-stroke spark-ignition engine and two two-stroke diesels.

The different categories of two-stroke cycle scavenging flows and the port (and valve) arrangements that produce them are illustrated in Figs. 6-23 and 6-24. Scavenging arrangements are classified into: (a) *cross-scavenged*, (b) *loop-scavenged*, and (c) *uniflow-scavenged configurations*. The location and orientation of the scavenging ports control the scavenging process, and the most common arrangements are indicated. Cross- and loop-scavenging systems use exhaust and inlet ports in the cylinder wall, uncovered by the piston as it approaches BC.<sup>27</sup> The uniflow system may use inlet ports with exhaust valves in the cylinder head,

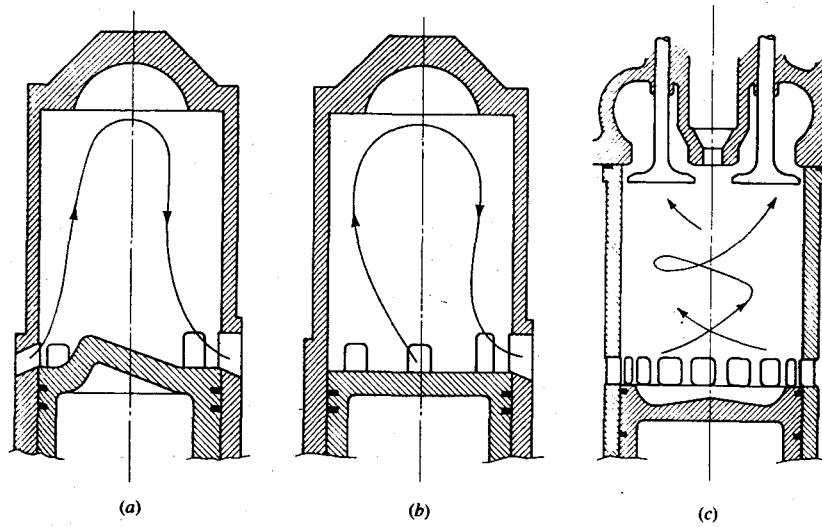


FIGURE 6-23

(a) Cross-scavenged, (b) loop-scavenged, and (c) uniflow-scavenged two-stroke cycle flow configurations.

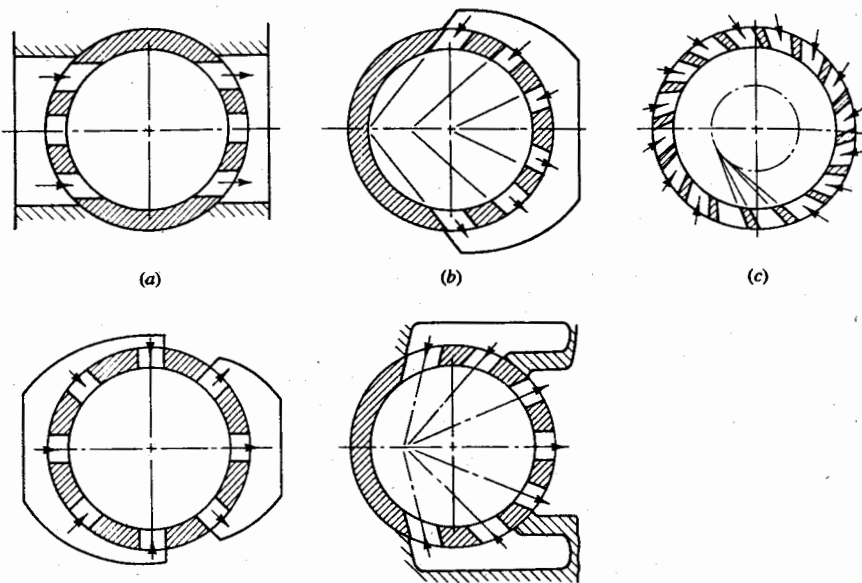


FIGURE 6-24

Common porting arrangements that go with (a) cross-scavenged, (b) loop-scavenged, and (c) uniflow-scavenged configurations.

or inlet and exhaust ports with opposed pistons. Despite the different flow patterns obtained with each cylinder geometry, the general operating principles are similar. Air in a diesel, or fuel-air mixture in a spark-ignition engine, must be supplied to the inlet ports at a pressure higher than the exhaust system pressure.

Figure 6-25 illustrates the principles of the scavenging process for a uniflow engine design. Between 100 and 110° after TC, the exhaust valve opens and a blowdown discharge process commences. Initially, the pressure ratio across the exhaust valve exceeds the critical value (see App. C) and the flow at the valve will be sonic: as the cylinder pressure decreases, the pressure ratio drops below the critical value. The discharge period up to the time of the scavenging port opening is called the blowdown (or free exhaust) period. The scavenging ports open between 60 and 40° before BC when the cylinder pressure slightly exceeds the scavenging pump pressure. Because the burned gas flow is toward the exhaust valves, which now have a large open area, the exhaust flow continues and no backflow occurs. When the cylinder pressure falls below the inlet pressure, air enters the cylinder and the scavenging process starts. This flow continues as long as the inlet ports are open and the inlet total pressure exceeds the pressure in the cylinder. As the cylinder pressure rises above the exhaust pressure, the fresh charge flowing into the cylinder displaces the burned gases: a part of the fresh charge mixes with the burned gases and is expelled with them. The exhaust valves usually close after the inlet ports close. Since the flow in the cylinder is toward the exhaust valve, additional scavenging is obtained. Figure 1-16 illustrates the

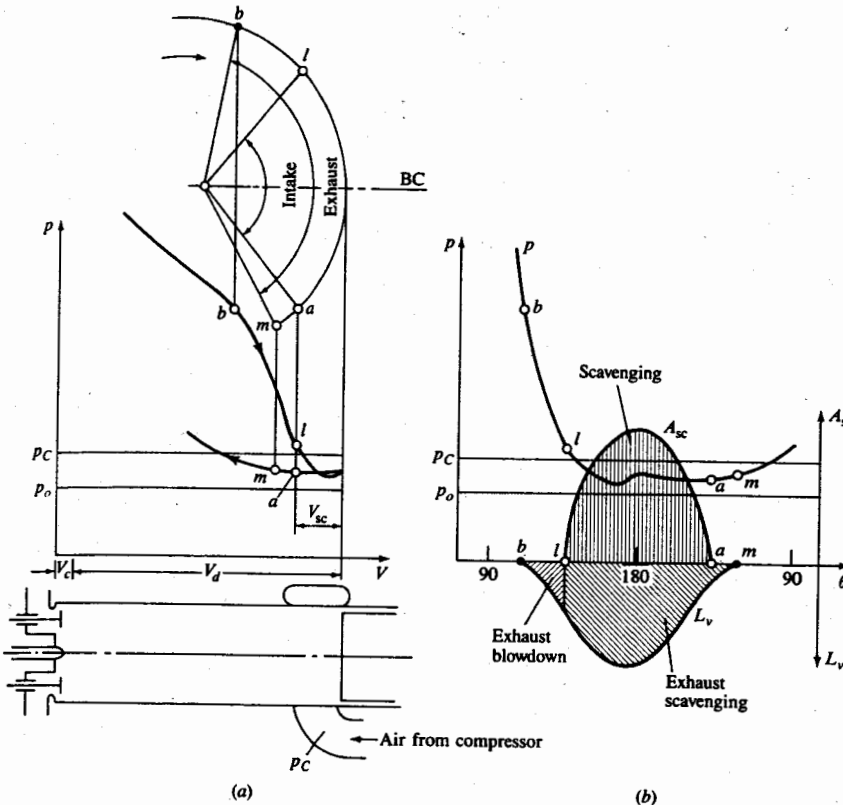


FIGURE 6-25

Gas exchange process in two-stroke cycle uniflow-scavenged diesel engine: (a) valve and port timing and pressure-volume diagram; (b) pressure, scavenging port open area  $A_{sc}$ , and exhaust valve lift  $L_v$  as functions of crank angle.<sup>13</sup>

similar sequence of events for a loop-scavenged engine. Proper flow patterns for the fresh charge are extremely important for good scavenging and charging of the cylinder.

Common methods for supercharging or pressurizing the fresh charge are shown in Fig. 6-26. In large two-stroke cycle engines, more complex combinations of these approaches are often used, as shown in Fig. 1-24.

## 6.6.2 Scavenging Parameters and Models

The following overall parameters are used to describe the scavenging process.<sup>13</sup>

The *delivery ratio*  $\Lambda$ :

$$\Lambda = \frac{\text{mass of delivered air (or mixture) per cycle}}{\text{reference mass}} \quad (6.20)$$

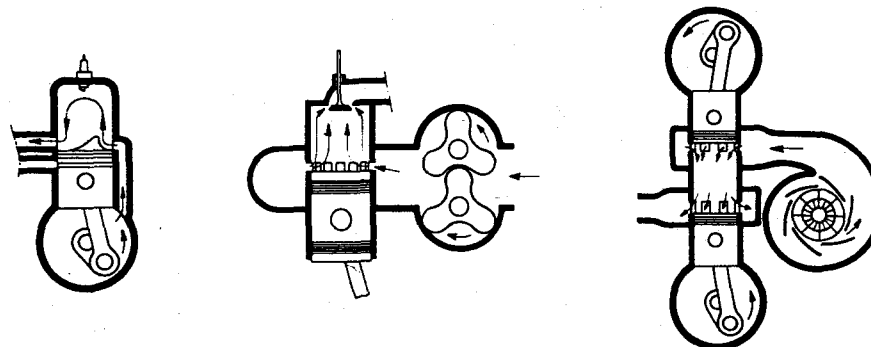


FIGURE 6-26

Common methods of pressurizing the fresh charge in two-stroke cycle engines: left, crankcase compression; center, roots blower; right, centrifugal compressor.<sup>7</sup>

compares the actual scavenging air mass (or mixture mass) to that required in an ideal charging process.<sup>†</sup> The reference mass is defined as displaced volume  $\times$  ambient air (or mixture) density. Ambient air (or mixture) density is determined at atmospheric conditions or at intake conditions. This definition is useful for experimental purposes. For analytical work, it is often convenient to use the trapped cylinder mass  $m_{tr}$  as the reference mass.

The *trapping efficiency*  $\eta_{tr}$ :

$$\eta_{tr} = \frac{\text{mass of delivered air (or mixture) retained}}{\text{mass of delivered air (or mixture)}} \quad (6.21)$$

indicates what fraction of the air (or mixture) supplied to the cylinder is retained in the cylinder.

The *scavenging efficiency*  $\eta_{sc}$ :

$$\eta_{sc} = \frac{\text{mass of delivered air (or mixture) retained}}{\text{mass of trapped cylinder charge}} \quad (6.22)$$

indicates to what extent the residual gases in the cylinder have been replaced with fresh air.

The *purity* of the charge:

$$\text{Purity} = \frac{\text{mass of air in trapped cylinder charge}}{\text{mass of trapped cylinder charge}} \quad (6.23)$$

indicates the degree of dilution, with burned gases, of the unburned mixture in the cylinder.

<sup>†</sup> If scavenging is done with fuel-air mixture, as in spark-ignition engines, then mixture mass is used instead of air mass.

The *charging efficiency*  $\eta_{ch}$ :

$$\eta_{ch} = \frac{\text{mass of delivered air (or mixture) retained}}{\text{displaced volume} \times \text{ambient density}} \quad (6.24)$$

indicates how effectively the cylinder volume has been filled with fresh air (or mixture). Charging efficiency, trapping efficiency, and delivery ratio are related by

$$\eta_{ch} = \Lambda \eta_{tr} \quad (6.25)$$

When the reference mass in the definition of delivery ratio is the trapped cylinder mass  $m_{tr}$  (or closely approximated by it) then

$$\eta_{sc} = \Lambda \eta_{tr} \quad (6.26)$$

In real scavenging processes, mixing occurs as the fresh charge displaces the burned gases and some of the fresh charge may be expelled. Two limiting ideal models of this process are: (1) perfect displacement and (2) complete mixing. Perfect displacement or scavenging would occur if the burned gases were pushed out by the fresh gases without any mixing. Complete mixing occurs if entering fresh mixture mixes instantaneously and uniformly with the cylinder contents.

For *perfect displacement* (with  $m_{tr}$  as the reference mass in the delivery ratio),

$$\begin{aligned} \eta_{sc} &= \Lambda & \text{and} & \eta_{tr} = 1 & \text{for } \Lambda \leq 1 \\ \eta_{sc} &= 1 & \text{and} & \eta_{tr} = \Lambda^{-1} & \text{for } \Lambda > 1 \end{aligned} \quad (6.27)$$

For the *complete mixing* limit, consider the scavenging process as a quasi-steady flow process. Between time  $t$  and  $t + dt$ , a mass element  $dm_{ad}$  of air is delivered to the cylinder and is uniformly mixed throughout the cylinder volume. An equal amount of fluid, with the same proportions of air and burned gas as the cylinder contents at time  $t$ , leaves the cylinder during this time interval. Thus the mass of air delivered between  $t$  and  $t + dt$  which is retained,  $dm_{ar}$ , is given by

$$dm_{ar} = dm_{ad} \left( 1 - \frac{m_{ar}}{m_{tr}} \right)$$

Assuming  $m_{tr}$  is constant, this integrates over the duration of the scavenging process to give

$$\frac{m_{ar}}{m_{tr}} = 1 - \exp \left( \frac{m_{ad}}{m_{tr}} \right) \quad (6.28)$$

Thus, for *complete mixing*, with the above definitions,

$$\begin{aligned} \eta_{sc} &= 1 - e^{-\Lambda} \\ \eta_{tr} &= \frac{1}{\Lambda} (1 - e^{-\Lambda}) \end{aligned} \quad (6.29)$$

Figure 6-27 shows  $\eta_{sc}$  and  $\eta_{tr}$  for the perfect displacement and complete mixing assumptions as a function of  $\Lambda$ , the delivery ratio.

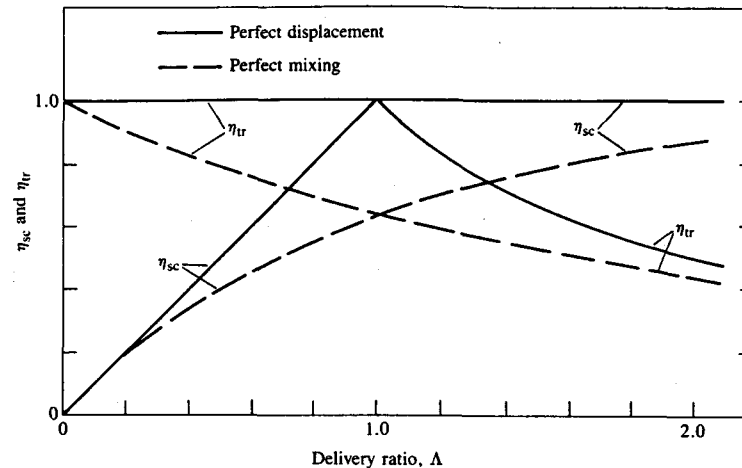


FIGURE 6-27

Scavenging efficiency  $\eta_{sc}$  and trapping efficiency  $\eta_{tr}$  versus delivery ratio  $\Lambda$  for perfect displacement and complete mixing models.

An additional possibility is the direct flow of fresh mixture through the cylinder into the exhaust without entraining burned gases. This is called *short-circuiting*; it is obviously undesirable since some fresh air or mixture is wasted. There is no simple model for this process. When short-circuiting occurs, lower scavenging efficiencies result even though the volume occupied by the short-circuiting flow through the cylinder does displace an equal volume of the burned gases. Another phenomenon which reduces scavenging efficiency is the formation of *pockets* or *dead zones* in the cylinder volume where burned gases can become trapped and escape displacement or entrainment by the fresh scavenging flow. These unscavenged zones are most likely to occur in regions of the cylinder that remain secluded from the main fresh mixture flow path.

### 6.6.3 Actual Scavenging Processes

Several methods have been developed for determining what occurs in actual cylinder scavenging processes.<sup>27</sup> Accurate measurement of scavenging efficiency is difficult due to the problem of measuring the trapped air mass. Estimation of  $\eta_{sc}$  from indicated mean effective pressure and from gas sampling are the most reliable methods.<sup>7</sup> Flow visualization experiments<sup>28-30</sup> in liquid analogs of the cylinder and flow velocity mapping techniques<sup>31</sup> have proved useful in providing a qualitative picture of the scavenging flow field and identifying problems such as short-circuiting and dead volumes.

Flow visualization studies indicate the key features of the scavenging process. Figure 6-28 shows a sequence of frames from a movie of one liquid scavenging another in a model of a large two-stroke cycle loop-scavenged

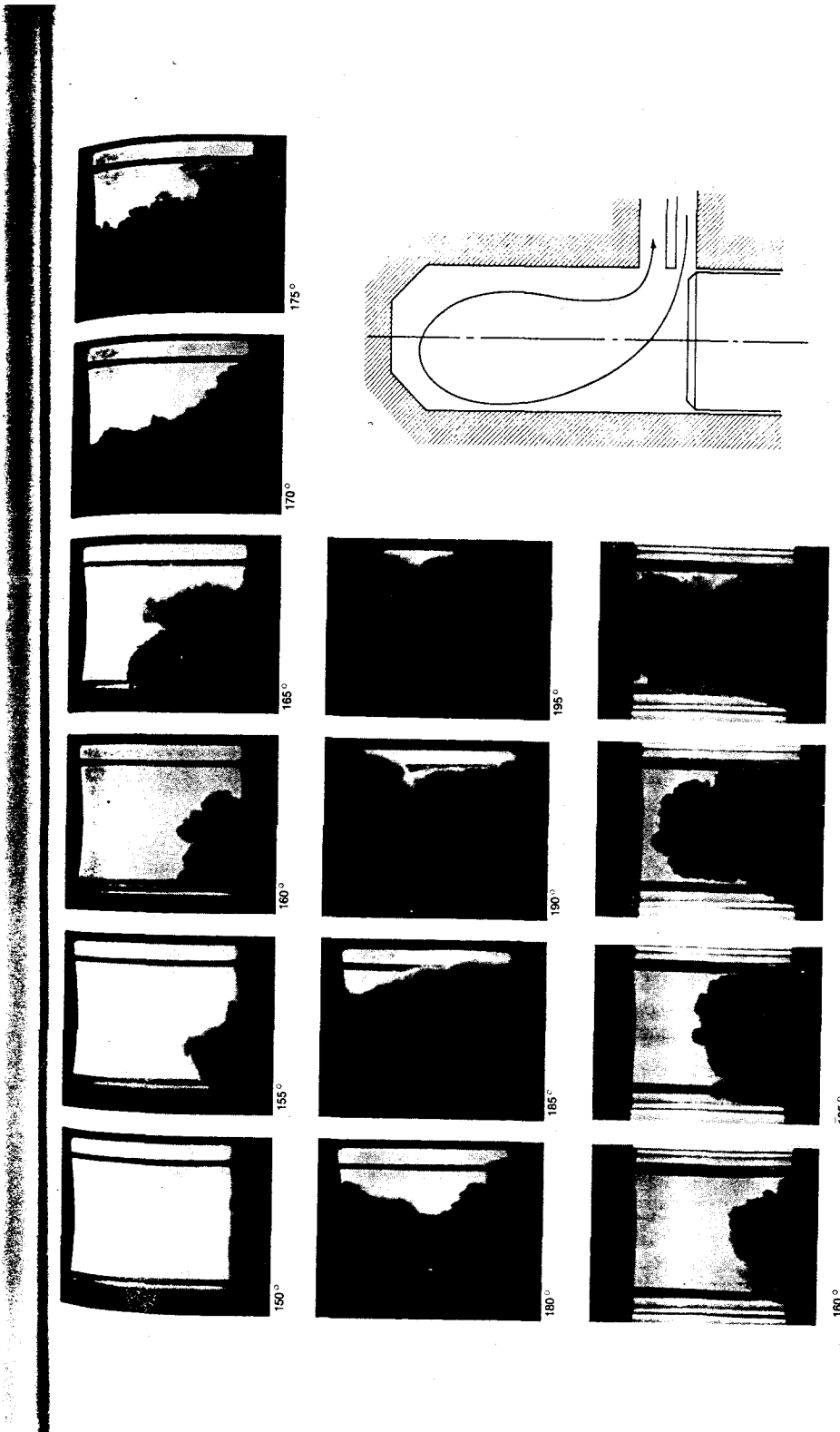


FIGURE 6-28

Photos of one fluid scavenging another in liquid analog experiments in model loop-scavenged engine cylinder. Top two rows: View perpendicular to scavenging loop. Bottom row: Orthogonal views. Dark denser fluid displacing light less dense fluid.<sup>29</sup>

diesel.<sup>29</sup> The physical variables were scaled to maintain the same values of the appropriate dimensionless numbers for the liquid analog flow and the real engine flow. The density of the liquid representing air (which is dark) was twice the density of the liquid representing burned gas (which is clear). Early in the scavenging process, the fresh air jets penetrate into the burned gas and displace it first toward the cylinder head and then toward the exhaust ports (the schematic gives the location of the ports). During this initial phase, the outflowing gas contains no air; pure displacement of the burned gas from the cylinder is being achieved. Then short-circuiting losses start to occur, due to the damming-up or buildup of fresh air on the cylinder wall opposite the exhaust ports. The short-circuiting fluid flows directly between the scavenge ports and the exhaust ports above them. Since this damming-up of the inflowing fresh air back toward the exhaust ports continues, short-circuiting losses will also continue. While the scavenging front remains distinct as it traverses the cylinder, its turbulent character indicates that mixing between burned gas and air across the front is taking place. For both these reasons (short-circuiting and short-range mixing), the outflowing gas, once the "displacement" phase is over, contains an increasing amount of fresh air.

Outflowing fluid composition measurements from this model study of a Sulzer two-stroke loop-scavenged diesel engine confirm this sequence of events. At 24 crank angle degrees after the onset of scavenging, fresh air due to short-circuiting was detected in the exhaust. At the time the displacement front reached the exhaust port (65° after the onset of scavenging), loss of fresh air due to scavenging amounted to 13 percent of the scavenge air flow. The actual plot of degree of purity (or  $\eta_{sc}$ ) versus delivery ratio ( $\Lambda$ ) closely followed the perfect displacement line for  $\Lambda < 0.4$ . For  $\Lambda > 0.4$ , the shape of the actual curve was similar in shape to the complete mixing curve.

Engine tests confirm these results from model studies. Initially, the exhausted gas contains no fresh air or mixture; only burned gas is being displaced from the cylinder. However, within the cylinder both displacement and mixing at the interface between burned gas and fresh gas are occurring. The departure from perfect scavenging behavior is evident when fresh mixture first appears in the exhaust. For loop-scavenged engines this is typically when  $\Lambda \approx 0.4$ . For uniflow scavenging this perfect scavenging phase lasts somewhat longer; for cross-scavenging it is over sooner (because the short-circuiting path is shorter).

The mixing that occurs is short-range mixing, not mixing throughout the cylinder volume. The jets of scavenging mixture, on entering the cylinder, mix readily with gases in the immediate neighborhood of the jet efflux. More efficient scavenging—i.e., less mixing—is obtained by reducing the size of the inlet ports while increasing their number.<sup>32</sup> It is important that the jets from the inlet ports slow down significantly once they enter the cylinder. Otherwise the scavenging front will reach the exhaust ports or valves too early. The jets are frequently directed to impinge on each other or against the cylinder wall. Swirl in uniflow-scavenged systems may be used to obtain an equivalent result.

The most desirable loop-scavenging flow is illustrated in Fig. 6-29. The

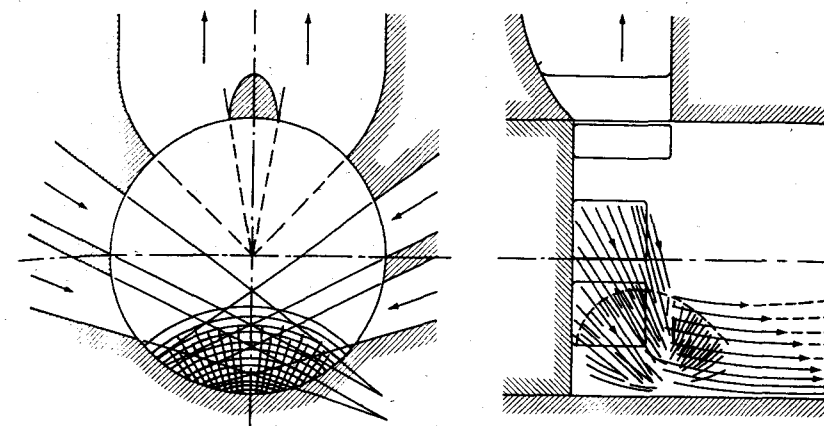


FIGURE 6-29

Desirable air flow in loop-scavenged engine: air from the entering jets impinges on far cylinder wall and flows toward the cylinder head.<sup>31</sup>

scavenging jets enter symmetrically with sufficient velocity to fill up about half the cylinder cross section, and thereafter flow at lower velocity along the cylinder wall toward the cylinder head. By proper direction of the scavenging jets it is possible to achieve almost no outflow in the direction of the exhaust from the cross-hatched stagnation zone on the opposite cylinder wall. In fact, measurement of the velocity profile in this region is a good indicator of the effectiveness of the scavenging flow. If the flow along the cylinder wall toward the head is stable, i.e., if its maximum velocity occurs near the wall and the velocity is near zero on the plane perpendicular to the axis of symmetry of the ports (which passes through the cylinder axis), the scavenging flow will follow the desired path. If there are "tongues" of scavenging flow toward the exhaust port, either in the center of the cylinder or along the walls, then significant short-circuiting will occur.<sup>31</sup>

In uniflow-scavenged configurations, the inlet ports are evenly spaced around the full circumference of the cylinder and are usually directed so that the scavenging jets create a swirling flow within the cylinder (see Fig. 6-24). Results of measurements of scavenging front location in rig flow tests of a valved uniflow two-stroke diesel cylinder, as the inlet port angle was varied to give a wide range of swirl, showed that inlet jets directed tangentially to a circle of half the cylinder radius gave the most stable scavenging front profile over a wide range of conditions.<sup>33</sup>

Though the scavenging processes in spark-ignition and diesel two-stroke engines are similar, these two types of engine operate with quite different delivery ratios. In mixture-scavenged spark-ignition engines, any significant expulsion of fresh fluid with the burned gas results in a significant loss of fuel and causes high hydrocarbon emissions as well as loss of the energy expended in pumping the

flow which passes straight through the cylinder. In diesels the scavenging medium is air, so only the pumping work is lost. One consequence of this is that two-stroke spark-ignition engines are usually crankcase pumped. This approach provides the maximum pressure and thus also the maximum velocity in the scavenging medium at the start of the scavenging process just after the cylinder pressure has blown down; as the crankcase pressure falls during the scavenging process, the motion of the scavenging front within the cylinder also slows down. Figure 6-30 shows the delivery ratio and trapping, charging, and scavenging efficiencies of two crankcase-scavenged spark-ignition engines as a function of engine speed. These quantities depend significantly on intake and exhaust port design and open period and the exhaust system configuration.<sup>34-36</sup> For two-stroke cycle spark-ignition engines, which use crankcase pumping, delivery ratios vary between about 0.5 and 0.8.

Figure 6-31 shows scavenging data typical of large two-stroke diesels.<sup>37</sup> The purity (mass of air in trapped cylinder charge/mass of trapped cylinder charge) is shown as a function of the delivery ratio. The different scavenging configurations have different degrees of effectiveness, with uniflow scavenging being the most efficient. These diesel engines normally operate with delivery ratios in the range 1.2 to 1.4.

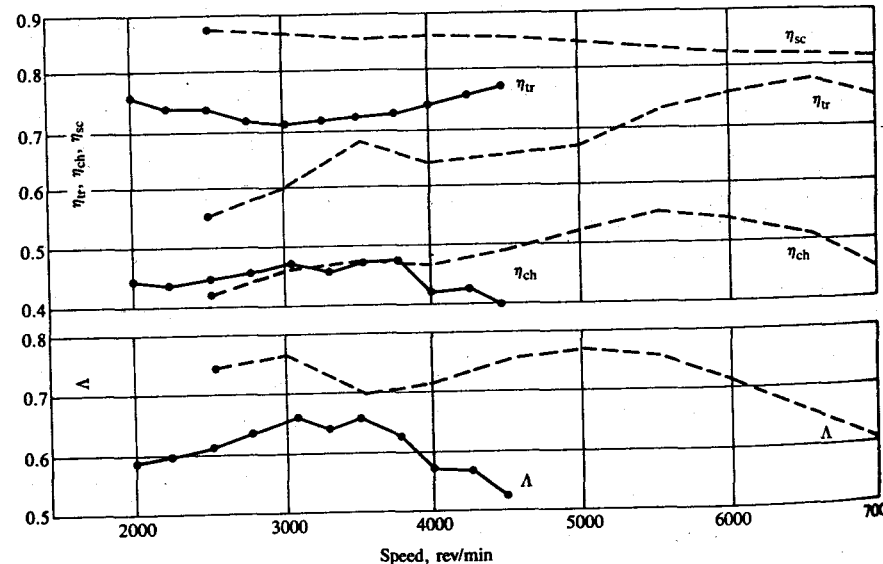


FIGURE 6-30  
Delivery ratio  $\Lambda$ , trapping efficiency  $\eta_{tr}$ , charging efficiency  $\eta_{ch}$ , and scavenging efficiency  $\eta_{sc}$ , at full load, as functions of speed for two single-cylinder two-stroke cycle spark-ignition engines. Solid line is 147 cm<sup>3</sup> displacement engine.<sup>34</sup> Dashed line is loop-scavenged 246 cm<sup>3</sup> displacement engine.<sup>35</sup>

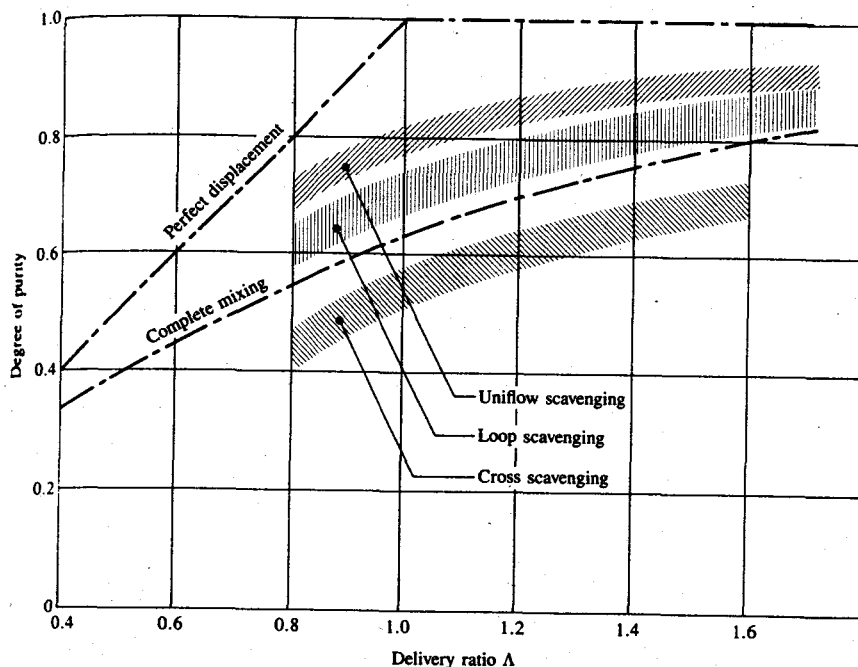
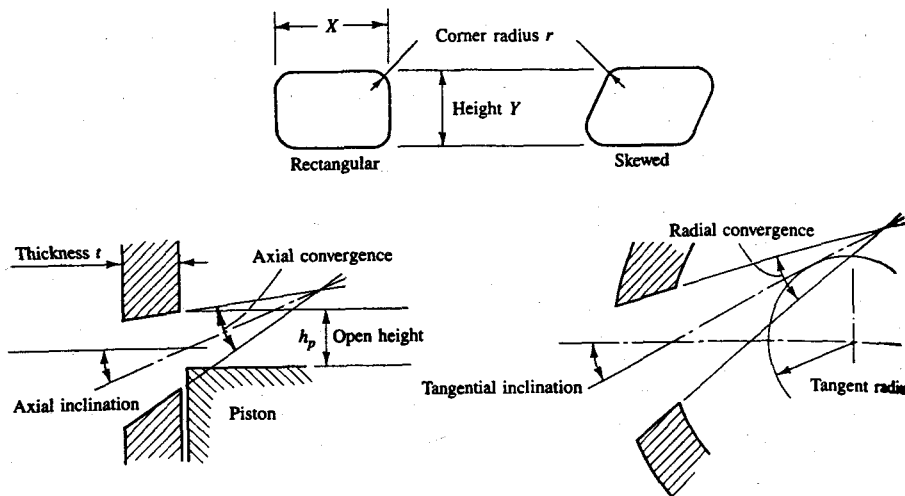


FIGURE 6-31  
Purity as a function of delivery ratio  $\Lambda$  for different types of large marine two-stroke diesel engines.<sup>37</sup>

## 6.7 FLOW THROUGH PORTS

The importance of the intake and exhaust ports to the proper functioning of the two-stroke cycle scavenging process is clear from the discussion in Sec. 6.6. The crank angle at which the ports open, the size, number, geometry, and location of the ports around the cylinder circumference, and the direction and velocity of the jets issuing from the ports into the cylinder all affect the scavenging flow. A summary of the information available on flow through piston-controlled ports can be found in Annand and Roe.<sup>16</sup> Both the flow resistance of the inlet and exhaust port configurations, as well as the details of the flow pattern produced by the port system inside the cylinder during scavenging, are important. Figure 6-32 defines the essential geometrical characteristics of inlet ports. Rectangular ports make best use of the cylinder wall area and give precise timing control. Ports can be tapered, and may have axial and tangential inclination as shown.

Figure 6-33 illustrates the flow patterns expected downstream of piston-controlled inlet ports. For small openings, the flow remains attached to the port walls. For fully open ports with sharp corners the flow detaches at the upstream corners. Both a rounded entry and converging taper to the port help prevent flow detachment within the port. Discharge coefficients for ports have been measured as a function of the open fraction of the port, the pressure ratio across the port,



**FIGURE 6-32**  
Parameters which define geometry of inlet ports.<sup>16</sup>

and port geometry and inclination (see Ref. 16 for a detailed summary). The most appropriate reference area for evaluating the discharge coefficient is the open area of the port (see Fig. 6-32). For the open height  $h_p$  less than  $(Y - r)$  but greater than  $r$  this is

$$A_R = Xh_p - 0.43r^2 \quad (6.30)$$

where  $Y$  is the port height,  $X$  the port width, and  $r$  the corner radius. For  $h_p = Y$ , the reference area is

$$A_R = XY - 0.86r^2 \quad (6.31)$$

The effect of variations in geometry and operating conditions on the discharge coefficient  $C_D$  can usually be interpreted by reference to the flow patterns illustrated in Fig. 6-33. The effects of inlet port open fraction and port geometry on  $C_D$  are shown in Fig. 6-34: geometry effects are most significant at small and large open fractions.<sup>20</sup>  $C_D$  varies with pressure ratio, increasing as the pressure

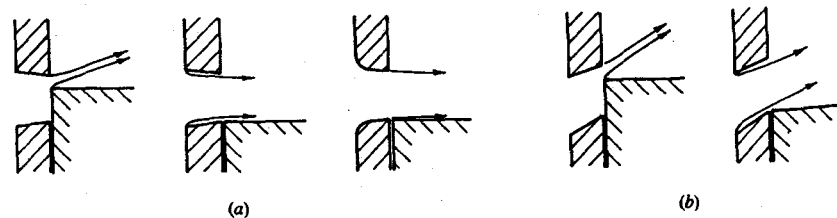


**FIGURE 6-33**  
Flow pattern through piston-controlled inlet ports: (a) port axis perpendicular to wall; small opening and large opening with sharp and rounded entry;<sup>16</sup> (b) port axis inclined.

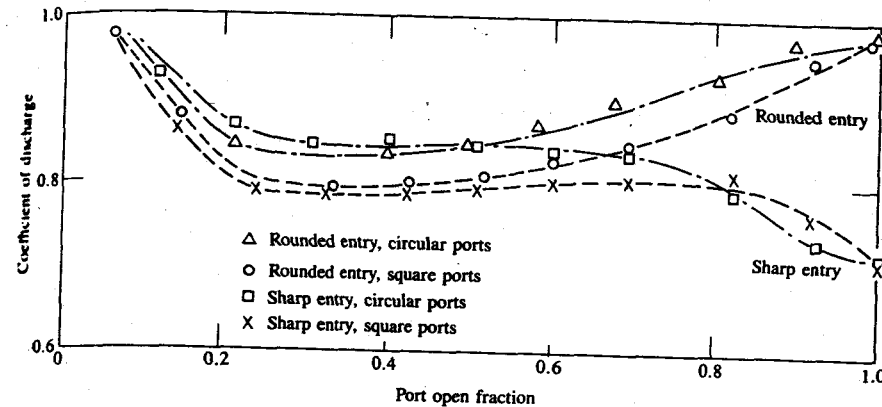


**FIGURE 6-34**  
Discharge coefficients as a function of port open fraction (uncovered height/port height) for different inlet port designs. Pressure ratio across port = 2.35.<sup>20</sup>

ratio increases. Empirical relations that predict this variation with pressure ratio have been developed.<sup>38</sup>

Tangentially inclined inlet ports are used when swirl is desired to improve scavenging or when jet focusing or impingement within the cylinder off the cylinder axis is required (see Sec. 6.6.3). The discharge coefficient decreases as the jet tangential inclination increases. The jet angle and the port angle can deviate significantly from each other depending on the details of the port design and the open fraction.<sup>31</sup>

In piston-controlled exhaust ports, the angle of the jet from a thin-walled exhaust port increases as indicated in Fig. 6-35.<sup>31</sup> In thick ports, the walls are

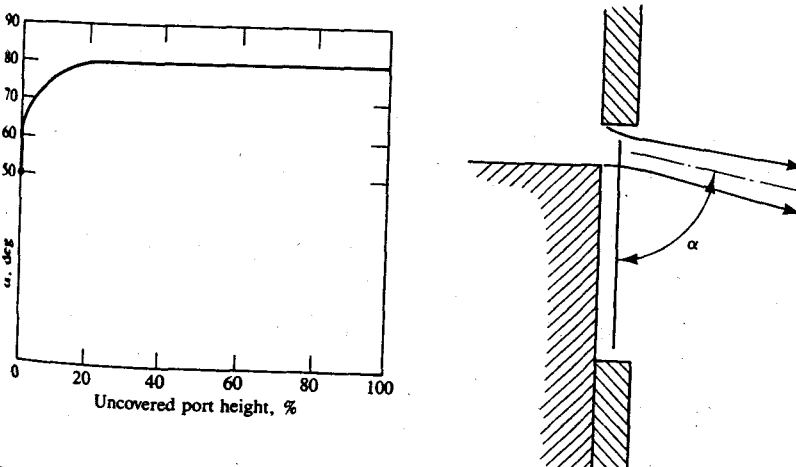


**FIGURE 6-35**  
Angle of jet exiting exhaust port as a function of open port height.<sup>31</sup>

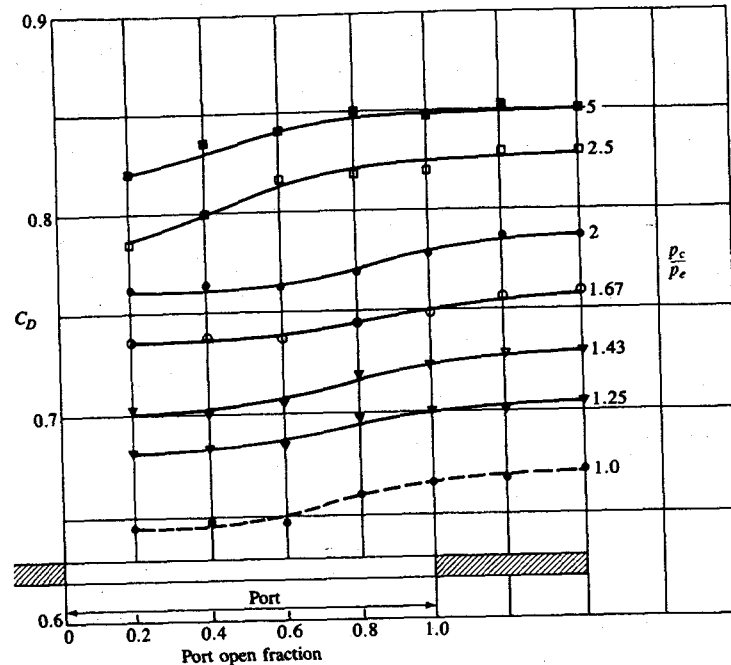


FIGURE 6-36  
Discharge coefficient of a single rectangular exhaust port (7.6 mm wide  $\times$  12.7 mm high) in the wall of a 51-mm bore cylinder as a function of open fraction and pressure ratio. Steady-flow rig tests at 21°C.  $p_c$  = cylinder pressure,  $p_e$  = exhaust system pressure.<sup>39</sup>

usually tapered to allow the outward flow to diffuse. The pressure ratio across the exhaust ports varies substantially during the exhaust process. The pressure ratio has a significant effect on the exhaust port discharge coefficient, as shown in Fig. 6-36. The changes in exit jet angle and separation point explain the effects of increasing open fraction and pressure ratio. The discharge coefficient also increases modestly with increasing gas temperature.<sup>39</sup>

## 6.8 SUPERCHARGING AND TURBOCHARGING

### 6.8.1 Methods of Power Boosting

The maximum power a given engine can deliver is limited by the amount of fuel that can be burned efficiently inside the engine cylinder. This is limited by the amount of air that is introduced into each cylinder each cycle. If the inducted air is compressed to a higher density than ambient, prior to entry into the cylinder, the maximum power an engine of fixed dimensions can deliver will be increased. This is the primary purpose of supercharging; Eqs. (2.39) to (2.41) show how power, torque, and mean effective pressure are proportional to inlet air density.

The term *supercharging* refers to increasing the air (or mixture) density by increasing its pressure prior to entering the engine cylinder. Three basic methods are used to accomplish this. The first is *mechanical supercharging* where a separate pump or blower or compressor, usually driven by power taken from the engine, provides the compressed air. The second method is *turbocharging*, where a turbocharger—a compressor and turbine on a single shaft—is used to boost the inlet air (or mixture) density. Energy available in the engine's exhaust stream is used to drive the turbocharger turbine which drives the turbocharger compressor which raises the inlet fluid density prior to entry to each engine cylinder. The third method—*pressure wave supercharging*—uses wave action in the intake and exhaust systems to compress the intake mixture. The use of intake and exhaust manifold tuning to increase volumetric efficiency (see Sec. 6.2.2) is one example of this method of increasing air density. An example of a pressure wave supercharging device is the Comprex, which uses the pressure available in the exhaust gas stream to compress the inlet mixture stream by direct contact of the fluids in narrow flow channels (see Sec. 6.8.5). Figure 6-37 shows typical arrangements of the different supercharging and turbocharging systems. The most common arrangements use a mechanical supercharger (Fig. 6-37a) or turbocharger (Fig. 6-37b). Combinations of an engine-driven compressor and a turbocharger (Fig. 6-37c) are used (e.g., in large marine engines; Fig. 1-24). Two-stage turbocharging (Fig. 6-37d) is one viable approach for providing very high boost pressures (4 to 7 atm) to obtain higher engine brake mean effective pressures. Turbocompounding, i.e., use of a second turbine in the exhaust directly geared to the engine drive shaft (Fig. 6-37e), is an alternative method of increasing engine power (and efficiency). Charge cooling with a heat exchanger (often called an aftercooler or intercooler) after compression, prior to entry to the cylinder, can be used to increase further the air or mixture density as shown in Fig. 6-37f.

Supercharging is used in four-stroke cycle engines to boost the power per unit displaced volume. Some form of supercharging is necessary in two-stroke cycle engines to raise the fresh air (or mixture) pressure above the exhaust pressure so that the cylinder can be scavenged effectively. With additional boost in two-stroke cycle engines, the power density is also raised. This section reviews the operating characteristics of the blowers, compressors, turbines, and wave-compression devices used to increase inlet air or mixture density or convert exhaust-gas availability to work. The operating characteristics of supercharged and turbocharged engine systems are discussed in Chap. 15.

### 6.8.2 Basic Relationships

Expressions for the work required to drive a blower or compressor and the work produced by a turbine are obtained from the first and second laws of thermodynamics. The first law, in the form of the steady flow energy equation, applied to a control volume around the turbomachinery component is

$$\dot{Q} - \dot{W} = \dot{m} \left[ \left( h + \frac{C^2}{2} + gz \right)_{\text{out}} - \left( h + \frac{C^2}{2} + gz \right)_{\text{in}} \right] \quad (6.32)$$

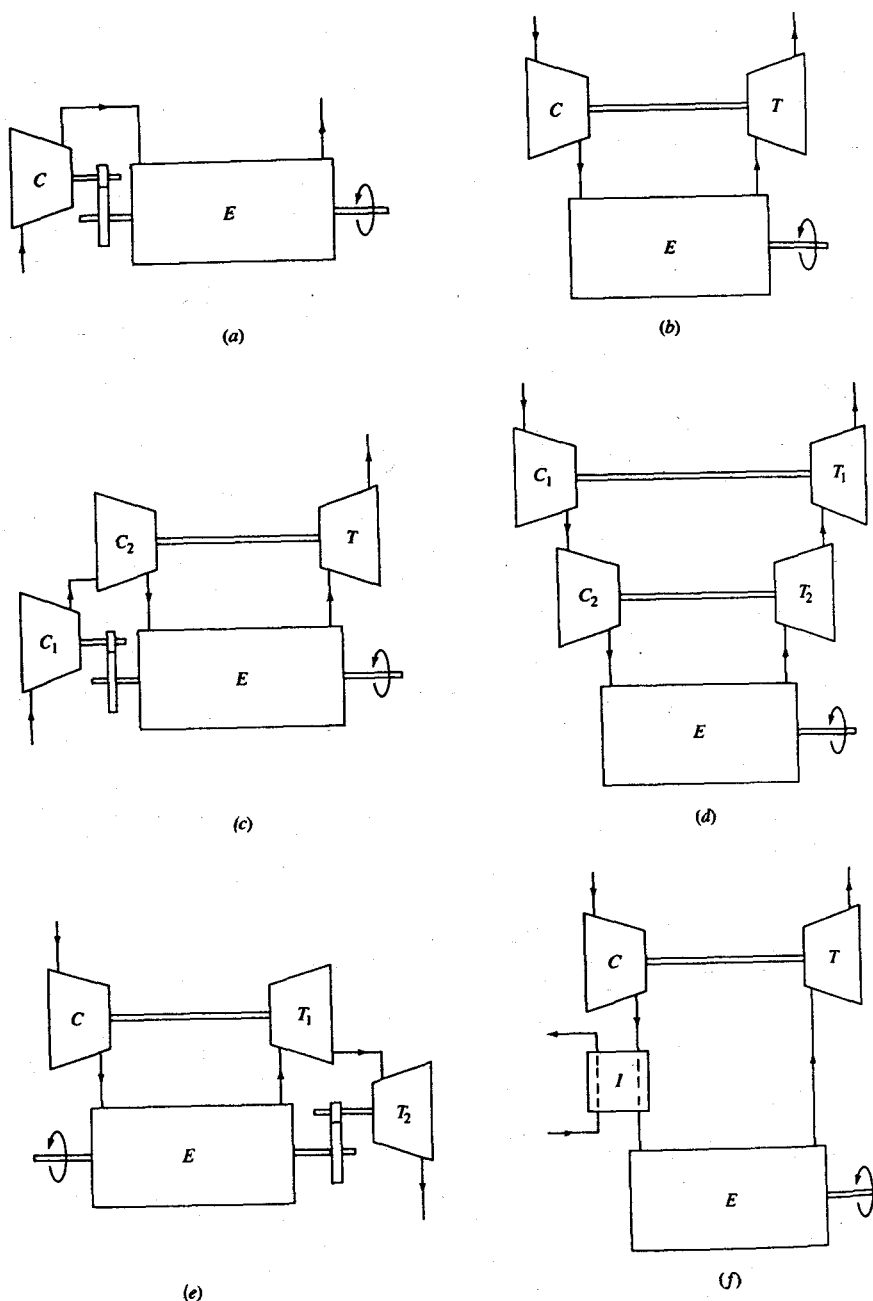


**FIGURE 6-37**  
Supercharging and turbocharging configurations: (a) mechanical supercharging; (b) turbocharging; (c) engine-driven compressor and turbocharger; (d) two-stage turbocharging; (e) turbocharging with turbocompounding; (f) turbocharger with intercooler. C Compressor, E Engine, I Inter-cooler, T Turbine.

where  $\dot{Q}$  is the heat-transfer rate into the control volume,  $\dot{W}$  is the shaft work-transfer rate out of the control volume,  $\dot{m}$  is the mass flow,  $h$  is the specific enthalpy,  $C^2/2$  is the specific kinetic energy, and  $gz$  is the specific potential energy (which is not important and can be omitted).

A stagnation or total enthalpy,  $h_0$ , can be defined as

$$h_0 = h + \frac{C^2}{2} \quad (6.33)$$

For an ideal gas, with constant specific heats, a stagnation or total temperature follows from Eq. (6.33):

$$T_0 = T + \frac{C^2}{2c_p} \quad (6.34)$$

A stagnation or total pressure is also defined: it is the pressure attained if the gas is isentropically brought to rest:

$$p_0 = p \left( \frac{T_0}{T} \right)^{\gamma/(\gamma-1)} \quad (6.35)$$

$\dot{Q}$  in Eq. (6.32) for pumps, blowers, compressors, and turbines is usually small enough to be neglected. Equation (6.32) then gives the work-transfer rate as

$$-\dot{W} = \dot{m}(h_{0,\text{out}} - h_{0,\text{in}}) \quad (6.36)$$

A component efficiency is used to relate the actual work-transfer rate to the work-transfer rate required (or produced) by an equivalent reversible adiabatic device operating between the same pressures. The second law is then used to determine this reversible adiabatic work-transfer rate, which is that occurring in an isentropic process.

For a compressor, the *compressor isentropic efficiency*  $\eta_C$  is

$$\eta_C = \frac{\text{reversible power requirement}}{\text{actual power requirement}} \quad (6.37)$$

Figure 6-38 shows the end states of the gas passing through a compressor on an *h-s* diagram. Both static ( $p_1, p_2$ ) and stagnation ( $p_{01}, p_{02}$ ) constant-pressure lines are shown. The total-to-total isentropic efficiency is, from Eq. (6.37),

$$\eta_{CTT} = \frac{h_{02s} - h_{01}}{h_{02} - h_{01}} \quad (6.38)$$

which, since  $c_p$  is essentially constant for air, or fuel-air mixture, becomes

$$\eta_{CTT} = \frac{T_{02s} - T_{01}}{T_{02} - T_{01}} \quad (6.39)$$

Since the process 01 to 02s is isentropic,

$$T_{02s} = T_{01} \left( \frac{p_{02}}{p_{01}} \right)^{(\gamma-1)/\gamma}$$

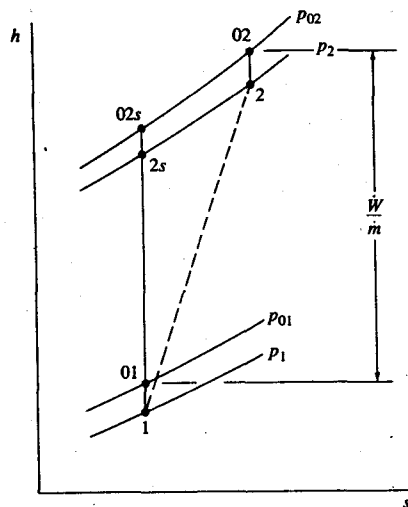


FIGURE 6-38  
Enthalpy-entropy diagram for compressor. Inlet state 01, exit state 2; equivalent isentropic compressor exit state 2s.

Equation (6.39) becomes

$$\eta_{CTT} = \frac{(p_{02}/p_{01})^{(\gamma-1)/\gamma} - 1}{(T_{02}/T_{01}) - 1} \quad (6.40)$$

In deriving Eq. (6.40) it has been tacitly assumed that the kinetic energy pressure head ( $p_{02} - p_2$ ) can be recovered. In internal combustion engine applications the compressor feeds the engine via a large manifold, and much of this kinetic energy will be dissipated. The blower or compressor should be designed for effective recovery of this kinetic energy before the exit duct. Since the kinetic energy of the gas leaving the compressor is not usually recovered, a more realistic definition of efficiency is based on exit static conditions:<sup>40</sup>

$$\eta_{CTS} = \frac{T_{2s} - T_{01}}{T_{02} - T_{01}} = \frac{(p_2/p_{01})^{(\gamma-1)/\gamma} - 1}{(T_{02}/T_{01}) - 1} \quad (6.41)$$

This is termed the total-to-static efficiency. The basis on which the efficiency is calculated should always be clearly stated.

The work-transfer rate or power required to drive the compressor is obtained by combining Eq. (6.36), the ideal gas model, and Eq. (6.40):

$$-\dot{W}_C = \dot{m}_i c_{p,i} (T_{02} - T_{01}) = \frac{\dot{m}_i c_{p,i} T_{01}}{\eta_{CTT}} \left[ \left( \frac{p_{02}}{p_{01}} \right)^{(\gamma-1)/\gamma} - 1 \right] \quad (6.42)$$

where the subscript *i* denotes inlet mixture properties. If  $\eta_{CTS}$  is used to define the compressor performance, then  $p_2$  replaces  $p_{02}$  in Eq. (6.42). Equation (6.42) gives the thermodynamic power requirement. There will also be mechanical losses in

the blower or compressor. Thus the power required to drive the device,  $-\dot{W}_{C,D}$ , will be

$$-\dot{W}_{C,D} = -\frac{\dot{W}_C}{\eta_m} \quad (6.43)$$

where  $\eta_m$  is the blower or compressor mechanical efficiency.

Figure 6-39 shows the gas states at inlet and exit to a turbine on an *h-s* diagram. State 03 is the inlet stagnation state; 4 and 04 are the exit static and stagnation states, respectively. States 4s and 04s define the static and stagnation exit states of the equivalent reversible adiabatic turbine. The *turbine isentropic efficiency* is defined as

$$\eta_T = \frac{\text{actual power output}}{\text{reversible power output}} \quad (6.44)$$

Thus, the total-to-total turbine efficiency is

$$\eta_{TTT} = \frac{h_{03} - h_{04}}{h_{03} - h_{04s}} \quad (6.45)$$

If the exhaust gas is modeled as an ideal gas with constant specific heats, then Eq. (6.45) can be written

$$\eta_{TTT} = \frac{T_{03} - T_{04}}{T_{03} - T_{04s}} = \frac{1 - (T_{04}/T_{03})}{1 - (p_{04}/p_{03})^{(\gamma-1)/\gamma}} \quad (6.46)$$

Note that for exhaust gas over the temperature range of interest,  $c_p$  may vary significantly with temperature (see Figs. 4-10 and 4-17).

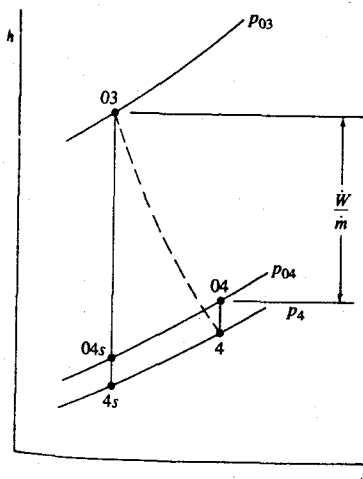


FIGURE 6-39  
Enthalpy-entropy diagram for a turbine. Inlet state 03, exit state 4; equivalent isentropic turbine exit state 4s.

Since the kinetic energy at the exit of a turbocharger turbine is usually wasted, a total-to-static turbine isentropic efficiency, where the reversible adiabatic power output is that obtained between inlet stagnation conditions and the exit static pressure, is more realistic.<sup>40</sup>

$$\eta_{TTS} = \frac{h_{03} - h_{04}}{h_{03} - h_{4s}} = \frac{T_{03} - T_{04}}{T_{03} - T_{4s}} = \frac{1 - (T_{04}/T_{03})}{1 - (p_4/p_{03})^{(\gamma-1)/\gamma}} \quad (6.47)$$

The power delivered by the turbine is given by [Eqs. (6.36) and (6.46)]

$$\dot{W}_T = \dot{m}_e(h_{03} - h_{04}) = \dot{m}_e c_{p,e}(T_{03} - T_{04}) = \dot{m}_e c_{p,e} \eta_{TTS} T_{03} \left[ 1 - \left( \frac{p_{04}}{p_{03}} \right)^{(\gamma_e-1)/\gamma_e} \right] \quad (6.48)$$

where the subscript *e* denotes exhaust gas properties. If the total-to-static turbine efficiency ( $\eta_{TTS}$ ) is used in the relation for  $\dot{W}_T$ , then  $p_4$  replaces  $p_{04}$  in Eq. (6.48). With a turbocharger, the turbine is mechanically linked to the compressor. Hence, at constant turbocharger speed,

$$-\dot{W}_C = \eta_m \dot{W}_T \quad (6.49)$$

where  $\eta_m$  is the mechanical efficiency of the turbocharger. The mechanical losses are mainly bearing friction losses. The mechanical efficiency is usually combined with the turbine efficiency since these losses are difficult to separate out.

It is advantageous if the operating characteristics of blowers, compressors, and turbines can be expressed in a manner that allows easy comparison between different designs and sizes of devices. This can be done by describing the performance characteristics in terms of dimensionless numbers.<sup>40</sup> The most important dependent variables are: mass flow rate  $\dot{m}$ , component isentropic efficiency  $\eta$ , and temperature difference across the device  $\Delta T_0$ . Each of these are a function of the independent variables:  $p_{0,in}$ ,  $p_{0,out}$  (or  $p_{out}$ ),  $T_{0,in}$ ,  $N$ (speed),  $D$ (characteristic dimension),  $R$ (gas constant),  $\gamma$  ( $c_p/c_v$ ), and  $\mu$ (viscosity); i.e.,

$$\dot{m}, \eta, \Delta T_0 = f(p_{0,in}, p_{0,out}, T_{0,in}, N, D, R, \gamma, \mu) \quad (6.50)$$

By dimensional analysis, these eight independent variables can be reduced to four dimensionless groups:

$$\frac{\dot{m}\sqrt{RT_{0,in}}}{p_{0,in}D^2}, \eta, \frac{\Delta T_0}{T_{0,in}} = f\left(\frac{ND}{\sqrt{RT_{0,in}}}, \frac{p_{0,out}}{p_{0,in}}, \frac{\dot{m}}{\mu D}, \gamma\right) \quad (6.51)$$

The Reynolds number,  $\dot{m}/(\mu D)$ , has little effect on performance and  $\gamma$  is fixed by the gas. Therefore these variables can be omitted and Eq. (6.51) becomes

$$\frac{\dot{m}\sqrt{RT_{0,in}}}{p_{0,in}D^2}, \eta, \frac{\Delta T_0}{T_{0,in}} = f\left(\frac{ND}{\sqrt{RT_{0,in}}}, \frac{p_{0,out}}{p_{0,in}}\right) \quad (6.52)$$

For a particular device, the dimensions are fixed and the value of  $R$  is fixed. So it has become the convention to plot

$$\frac{\dot{m}\sqrt{T_{0,in}}}{p_{0,in}}, \eta, \frac{\Delta T_0}{T_{0,in}} = f\left(\frac{N}{\sqrt{T_{0,in}}}, \frac{p_{0,out}}{p_{0,in}}\right) \quad (6.53)$$

$\dot{m}\sqrt{T_{0,in}}/p_{0,in}$  is referred to as the corrected mass flow;  $N/\sqrt{T_{0,in}}$  is referred to as the corrected speed. The disadvantage of this convention of removing  $D$  and  $R$  is that the groups of variables are no longer dimensionless, and performance plots or maps relate to a specific machine.

Compressor characteristics are usually plotted in terms of the pressure ratio ( $p_{02}/p_{01}$ ) or ( $p_2/p_{01}$ ) against the corrected mass flow ( $\dot{m}\sqrt{T_{01}}/p_{01}$ ) along lines of constant corrected speed ( $N/\sqrt{T_{01}}$ ). Contours of constant efficiency are superposed. Similar plots are used for turbines:  $p_{03}/p_4$  against  $\dot{m}\sqrt{T_{03}}/p_{03}$  along lines of constant  $N/\sqrt{T_{03}}$ . Since these occupy a narrow region of the turbine performance map, other plots are often used (see Sec. 6.8.4).

### 6.8.3 Compressors

Practical mechanical supercharging devices can be classified into: (1) sliding vane compressors, (2) rotary compressors, and (3) centrifugal compressors. The first two types are positive displacement compressors; the last type is an aerodynamic compressor. Four different types of positive displacement compressors are illustrated in Fig. 6-40.

In the sliding vane compressor (Fig. 6-40a), deep slots are cut into the rotor to accommodate thin vanes which are free to move radially. The rotor is mounted eccentrically in the housing. As the rotor rotates, the centrifugal forces acting on the vanes force them outward against the housing, thereby dividing the crescent-shaped space into several compartments. Ambient air is drawn through the intake port into each compartment as its volume increases to a maximum. The trapped air is compressed as the compartment volume decreases, and is then discharged through the outlet port. The flow capacity of the sliding vane compressor depends on the maximum induction volume which is determined by the housing cylinder bore, rotor diameter and length, eccentricity, number of vanes, dimensions of the inlet and outlet ports. The actual flow rate and pressure rise at constant speed will be reduced by leakage. Also, heat transfer from the moving vanes and rotor and stator surfaces will reduce compression efficiency unless cooling is used to remove the thermal energy generated by friction between the vanes, and the rotor and stator. The volumetric efficiency can vary between 0.6 and 0.9 depending on the size of the machine, the quality of the design, and the method of lubrication and cooling employed. The displaced volume  $V_D$  is given by

$$V_D = \pi \varepsilon l(2r + \varepsilon) \quad (6.54)$$

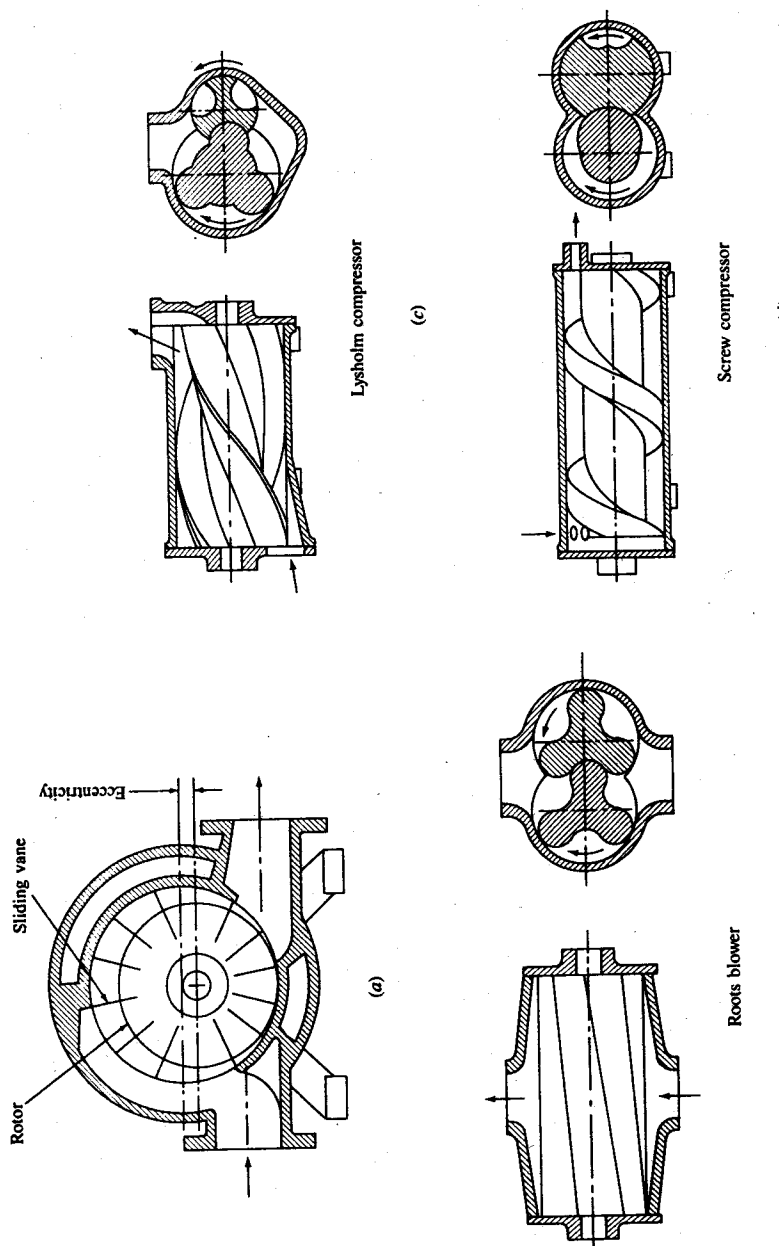


FIGURE 6-40  
Positive displacement compressors: (a) sliding vane compressor; (b) roots blower; (c) Lysholm compressor; (d) screw compressor.<sup>41</sup>

where  $r$  is the rotor radius,  $\varepsilon$  the eccentricity, and  $l$  the axial length of the compressor. The mass flow rate parameter is

$$\frac{\dot{m}\sqrt{T_0/T_{std}}}{p_0/p_{std}} = \text{constant} \times \rho_i \eta_c N e l (2r + \varepsilon) \quad (6.55)$$

where  $\eta_c$  is the device volumetric efficiency,  $N$  its speed, and the subscripts  $i$ , 0 and std refer to inlet, inlet stagnation, and standard atmospheric conditions, respectively. Figure 6-41 shows the performance characteristics of a typical sliding vane compressor. The mass flow rate at constant speed depends on the pressure ratio only through its (weak) effect on volumetric efficiency. The isentropic efficiency is relatively low.<sup>41</sup>

An alternative positive displacement supercharger is the roots blower (Fig. 6-40b). The two rotors are connected by gears. The working principles are as follows. Air trapped in the recesses between the rotor lobes and the housing is carried toward the delivery port without significant change in volume. As these recesses open to the delivery line, since the suction side is closed, the trapped air is suddenly compressed by the backflow from the higher-pressure delivery line. This intermittent delivery produces nonuniform torque on the rotor and pressure pulses in the delivery line. Roots blowers are most suitable for small pressure ratios (about 1.2). The volumetric efficiency depends on the running clearances, rotor length, rotational speed, and pressure ratio. In the three-lobe machines shown (two lobes are sometimes used) the volume of each recess  $V_R$  is

$$V_R = 0.546R^2 l$$

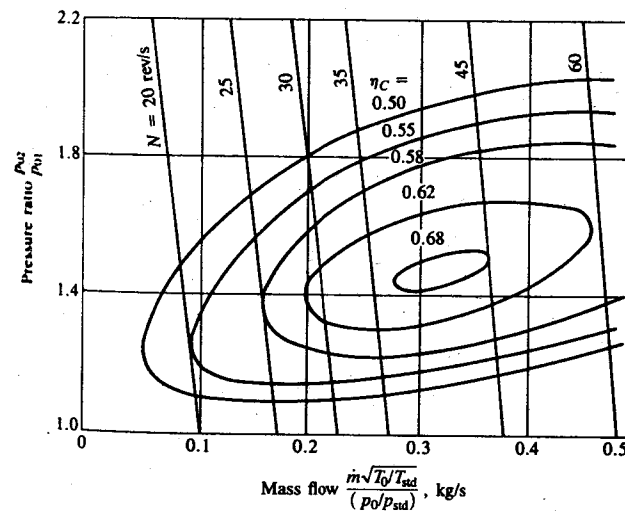


FIGURE 6-41  
Performance map for sliding vane compressor.<sup>41</sup>

where  $R$  is the rotor radius and  $l$  the blower length. The mass flow parameter is

$$\frac{\dot{m}\sqrt{T_0/T_{std}}}{p_0/p_{std}} = \text{constant} \times \rho_i \eta_v NR^2 l \quad (6.56)$$

A performance map of a typical small roots blower is shown in Fig. 6-42. It is similar in character to that of the sliding vane compressor. At constant speed, the flow rate depends on increasing pressure ratio only through the resulting decrease in volumetric efficiency (Eq. 6.56).<sup>41</sup> The advantage of the roots blower is that its performance range is not limited by surge and choking as is the centrifugal compressor (see below). Its disadvantages are its high noise level, poor efficiency, and large size.<sup>42</sup>

Screw compressors (Fig. 6-40c and d) must be precision machined to achieve close tolerances between rotating and stationary elements for satisfactory operation. They run at speeds between 3000 and 30,000 rev/min. It is usually necessary to cool the rotors internally. High values of volumetric and isentropic efficiency are claimed.<sup>43</sup>

A *centrifugal compressor* is primarily used to boost inlet air or mixture density coupled with an exhaust-driven turbine in a turbocharger. It is a single-stage radial flow device, well suited to the high mass flow rates at the relatively low pressure ratios (up to about 3.5) required by the engine. To operate efficiently it must rotate at high angular speed. It is therefore much better suited to direct coupling with the exhaust-driven turbine of the turbocharger than to mechanical coupling through a gearbox to the engine for mechanical supercharging.

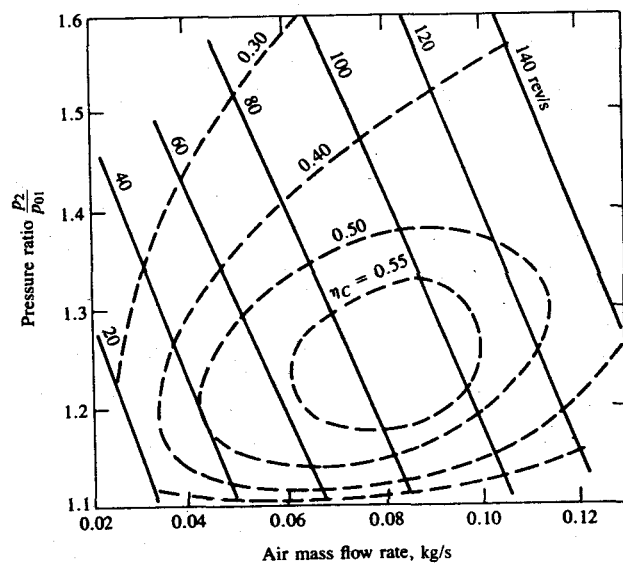


FIGURE 6-42  
Performance map at standard inlet conditions for roots blower.<sup>42</sup>

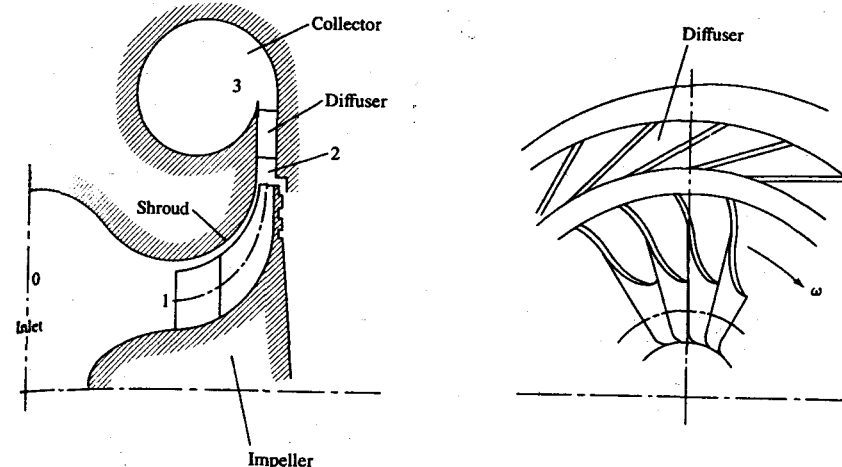


FIGURE 6-43  
Schematic of centrifugal compressor.<sup>40</sup>

The centrifugal compressor consists of a stationary inlet casing, a rotating bladed impellor, a stationary diffuser (with or without vanes), and a collector or volute to bring the compressed air leaving the diffuser to the engine intake system (see Fig. 6-43). Figure 6-44 indicates, on an  $h-s$  diagram, how each component contributes to the overall pressure rise across the compressor. Air at stagnation

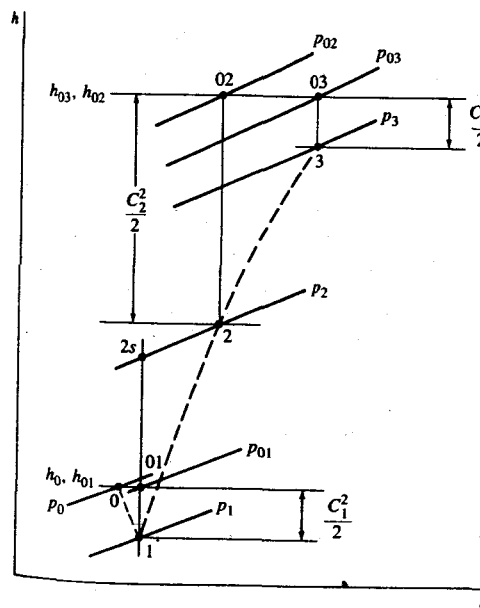


FIGURE 6-44  
Enthalpy-entropy diagram for flow through centrifugal compressor.

state 0 is accelerated in the inlet to pressure  $p_1$  and velocity  $C_1$ . The enthalpy change 01 to 1 is  $C_1^2/2$ . Compression in the impeller flow passages increases the pressure to  $p_2$  and velocity to  $C_2$ , corresponding to a stagnation state 02 if all the exit kinetic energy were recovered. The isentropic equivalent compression process has an exit static state 2s. The diffuser, 2 to 3, converts as much as practical of the air kinetic energy at exit to the impeller ( $C_2^2/2$ ) to a pressure rise ( $p_3 - p_2$ ) by slowing down the gas in carefully shaped expanding passages. The final state, in the collector, has static pressure  $p_3$ , low kinetic energy  $C_3^2/2$ , and a stagnation pressure  $p_{03}$  which is less than  $p_{02}$  since the diffusion process is incomplete as well as irreversible.<sup>40</sup>

The work transfer to the gas occurs in the impeller. It can be related to the change in gas angular momentum via the velocity components at the impeller entry and exit, which are shown in Fig. 6-45. Here  $C_1$  and  $C_2$  are the absolute gas velocities,  $U_1$  and  $U_2$  are the tangential blade velocities, and  $w_1$  and  $w_2$  are the gas velocities relative to the impeller all at inlet (1) and exit (2), respectively. The torque  $T$  exerted on the gas by the impeller equals the rate of change of angular momentum:

$$T = \dot{m}(r_2 C_{\theta_2} - r_1 C_{\theta_1}) \quad (6.57)$$

The rate of work transfer to the gas is given by

$$-\dot{W}_C = T\omega = \dot{m}\omega(r_2 C_{\theta_2} - r_1 C_{\theta_1}) = \dot{m}(U_2 C_{\theta_2} - U_1 C_{\theta_1}) \quad (6.58)$$

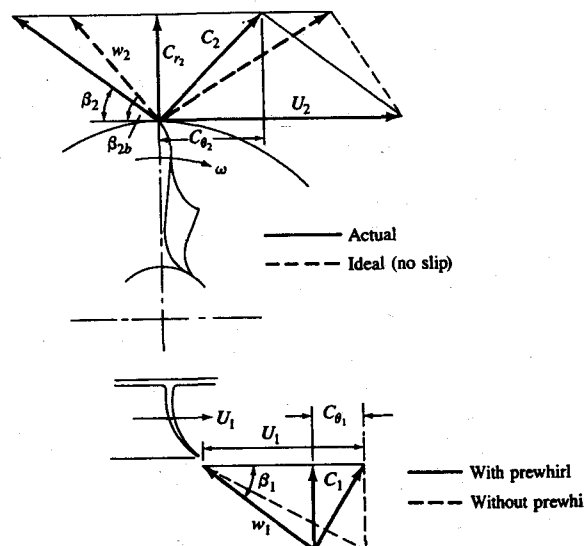


FIGURE 6-45  
Velocity diagrams at inlet (1) and exit (2) to centrifugal compressor rotor or impeller.<sup>40</sup>

This is often called the Euler equation. Normally in compressors the inlet flow is axial so  $C_{\theta_1} = 0$ . Thus Eq. (6.58) can be written:

$$-\frac{\dot{W}_C}{\dot{m}} = U_2 C_{\theta_2} = U_2 \left( 1 - \frac{C_{r2}}{U_2} \cot \beta_2 \right) \quad (6.59)$$

where  $\beta_2$  is the backsweep angle. In the ideal case with no slip,  $\beta_2$  is the blade angle,  $\beta_{2b}$ . In practice, there is slip and  $\beta_2$  is less than  $\beta_{2b}$ . Many compressors have radial vanes (i.e.,  $\beta_{2b} = 90^\circ$ ). A recent trend is backswept vanes ( $\beta_{2b} < 90^\circ$ ) which give higher efficiency. Since work transfer to the gas occurs only in the impeller, the work-transfer rate given by Eq. (6.59) equals the change in stagnation enthalpy ( $h_{03} - h_{01}$ ) in Fig. 6-44 [see Eq. (6.36)].

The operating characteristics of the centrifugal compressor are usually described by a *performance map*. This shows lines of constant compressor efficiency  $\eta_C$ , and constant corrected speed  $N/\sqrt{T_{0,in}}$ , on a plot of pressure ratio  $p_{0,out}/p_{0,in}$  against corrected mass flow  $\dot{m}\sqrt{T_{0,in}/p_{0,in}}$  [see Eq. (6.53)]. Figure 6-46 indicates the form of such a map. The stable operating range in the center of the map is separated from an unstable region on the left by the *surge line*. When the mass flow is reduced at a constant pressure ratio, local flow reversal eventually occurs in the boundary layer. Further reductions in mass flow cause the flow to reverse completely, causing a drop in pressure. This relieves the adverse pressure gradient. The flow reestablishes itself, builds up again, and the process repeats. Compressors should not be operated in this unstable regime. The

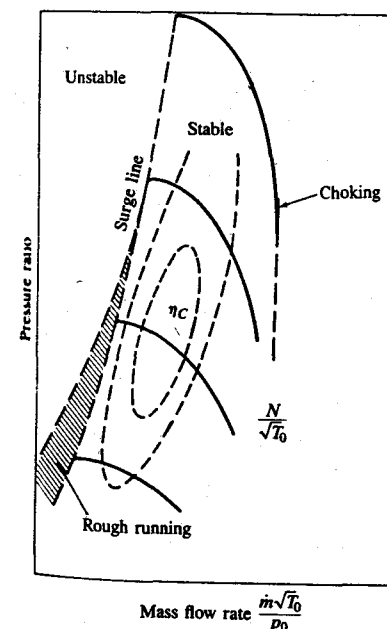
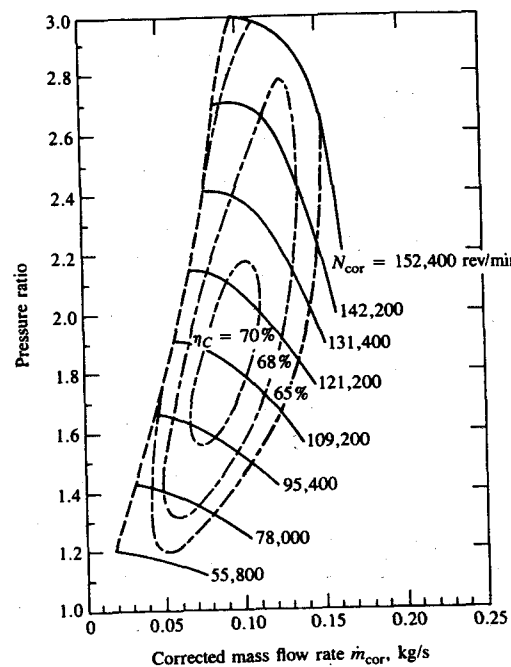


FIGURE 6-46  
Schematic of compressor operating map showing stable operating range.<sup>40</sup>



**FIGURE 6-47**  
Centrifugal compressor operating map. Lines of constant corrected speed and compressor efficiency are plotted on a graph of pressure ratio against corrected mass flow.<sup>43</sup>

stable operating regime is limited on the right by choking. The velocities increase as  $\dot{m}$  increases, and eventually the flow becomes sonic in the limiting area of the machine. Extra mass flow through the compressor can only be obtained by higher speed. When the diffuser is choked, compressor speed may rise substantially with only a limited increase in the mass flow rate.<sup>40</sup>

Figure 6-47 shows an actual turbocharger compressor performance map. In practice, the map variables corrected speed and mass flow rate are usually defined as<sup>44</sup>

$$\begin{aligned} N_{\text{cor}} &= N \left( \frac{T_{\text{ref}}}{T_{0,\text{in}}} \right)^{1/2} \\ \dot{m}_{\text{cor}} &= \dot{m} \left( \frac{T_{0,\text{in}}}{T_{\text{ref}}} \right)^{1/2} \left( \frac{p_{\text{ref}}}{p_{0,\text{in}}} \right) \end{aligned} \quad (6.60)$$

where  $T_{\text{ref}}$  and  $p_{\text{ref}}$  are standard atmospheric temperature and pressure, respectively. Though the details of different compressor maps vary, their general characteristics are similar. The high efficiency region runs parallel to the surge line (and close to it for vaneless diffusers). A wide flow range for the compressor (see Fig. 6-46) is important in turbochargers used for transportation applications.

#### 6.8.4 Turbines

The turbocharger turbine is driven by the energy available in the engine exhaust. The ideal energy available is shown in Fig. 6-48. It consists of the blowdown work transfer produced by expanding the gas in the cylinder at exhaust valve opening to atmospheric pressure (area  $abc$ ) and (for the four-stroke cycle engine) the work done by the piston displacing the gases remaining in the cylinder after blowdown (area  $cdef$ ).

The reciprocating internal combustion engine is inherently an unsteady pulsating flow device. Turbines can be designed to accept such an unsteady flow, but they operate more efficiently under steady flow conditions. In practice, two approaches for recovering a fraction of the available exhaust energy are commonly used: constant-pressure turbocharging and pulse turbocharging. In constant-pressure turbocharging, an exhaust manifold of sufficiently large volume to damp out the mass flow and pressure pulses is used so that the flow to the turbine is essentially steady. The disadvantage of this approach is that it does not make full use of the high kinetic energy of the gases leaving the exhaust port; the losses inherent in the mixing of this high-velocity gas with a large volume of low-velocity gas cannot be recovered. With pulse turbocharging, short small-cross-section pipes connect each exhaust port to the turbine so that much of the kinetic energy associated with the exhaust blowdown can be utilized. By suitably grouping the different cylinder exhaust ports so that the exhaust pulses are sequential and have minimum overlap, the flow unsteadiness can be held to an acceptable level. The turbine must be specifically designed for this pulsating flow to achieve adequate efficiencies. The combination of increased energy available at the turbine, with reasonable turbine efficiencies, results in the pulse system being more commonly used for larger diesels.<sup>40</sup> For automotive engines, constant-pressure turbocharging is used.

Two types of turbines are used in turbochargers: radial and axial flow turbines. The radial flow turbine is similar in appearance to the centrifugal compressor; however, the flow is radially inward not outward. Radial flow turbines are

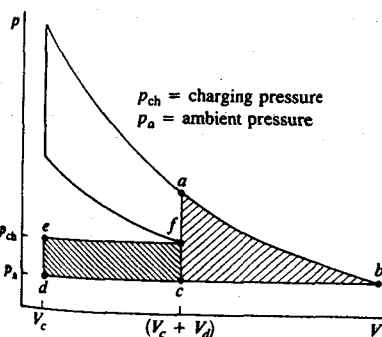


**FIGURE 6-48**  
Constant-volume cycle  $p$ - $V$  diagram showing available exhaust energy.

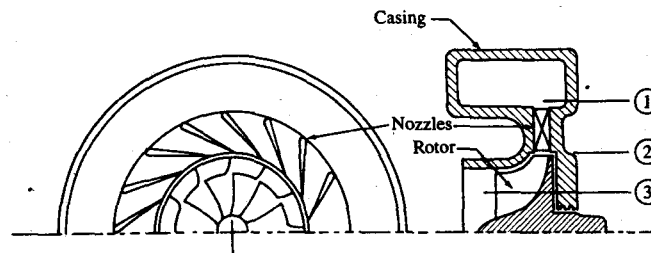


FIGURE 6-49

Schematic of radial flow turbine.

normally used in automotive or truck applications. Larger engines—locomotive, stationary, or marine—use axial flow turbines.

A drawing of a radial flow turbine is shown in Fig. 6-49. It consists of an inlet casing or scroll, a set of inlet nozzles (often omitted with small turbines), and the turbine rotor or wheel. The function of each component is evident from the *h-s* diagram and velocity triangles in Fig. 6-50. The nozzles (01-2) accelerate the flow, with modest loss in stagnation pressure. The drop in stagnation enthalpy, and hence the work transfer, occurs solely in the rotor passages, 2-3; hence, the rotor is designed for minimum kinetic energy  $C_3^2/2$  at exit. The velocity triangles at inlet and exit relate the work transfer to the change in angular momentum via the Euler equation:

$$\dot{W}_T = T\omega = \dot{m}\omega(r_2 C_{\theta_2} - r_3 C_{\theta_3}) = \dot{m}(U_2 C_{\theta_2} - U_3 C_{\theta_3}) \quad (6.61)$$

where  $T$  is the torque and  $\omega$  the rotor angular speed. For maximum work transfer the exit velocity should be axial. The work-transfer rate relates to the change in stagnation enthalpy via

$$\dot{W}_T = \dot{m}(h_{02} - h_{03}) = \dot{m}(h_{01} - h_{03}) \quad (6.62)$$

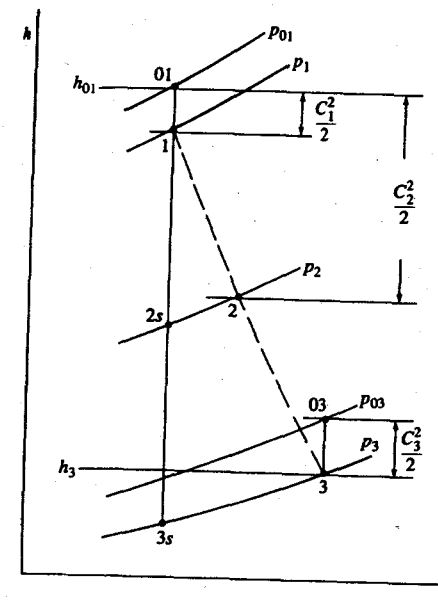
The turbine isentropic efficiency is given by Eqs. (6.44) to (6.47).

Many different types of plots have been used to define radial flow turbine characteristics. Figure 6-51 shows lines of constant corrected speed and efficiency on a plot of pressure ratio versus corrected mass flow rate. As flow rate increases at a given speed, it asymptotically approaches a limit corresponding to the flow becoming choked in the stator nozzle blades or the rotor. For turbines, efficiency is usually presented on a different diagram because the operating regime in Fig. 6-51 is narrow. Figure 6-52 shows an alternative plot for a radial turbine: corrected mass flow rate against corrected rotor speed. On this map, the operating regime appears broader.

A schematic of a turbocharger axial flow turbine is shown in Fig. 6-53. Usually a single stage is sufficient to expand the exhaust gas efficiently through the pressure ratios associated with engine turbocharging. This turbine consists of an annular flow passage, a single row of nozzles or stator blades, and a rotating blade ring. The changes in gas state across each component are similar to those

of the radial turbine shown in the *h-s* diagram of Fig. 6-50. The velocity triangles at entry and exit to the rotor, shown in Fig. 6-54, relate the work transfer from the gas to the rotor to the change in angular momentum:

$$\dot{W}_T = \omega T = \dot{m}\omega(r_2 C_{\theta_2} + r_3 C_{\theta_3})$$



(a)

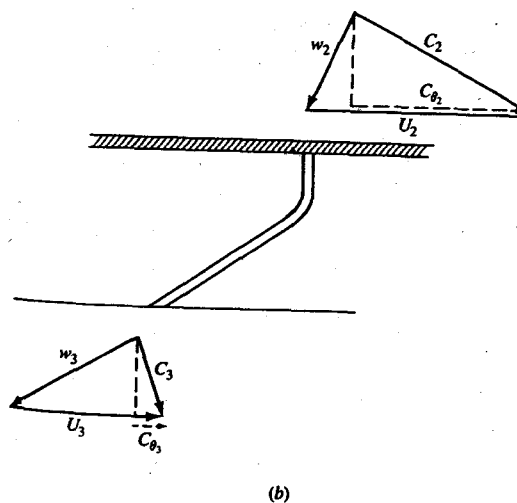


FIGURE 6-50

(a) Enthalpy-entropy diagram for radial turbine. (b) Velocity diagrams at turbine rotor inlet (2) and exit (3).

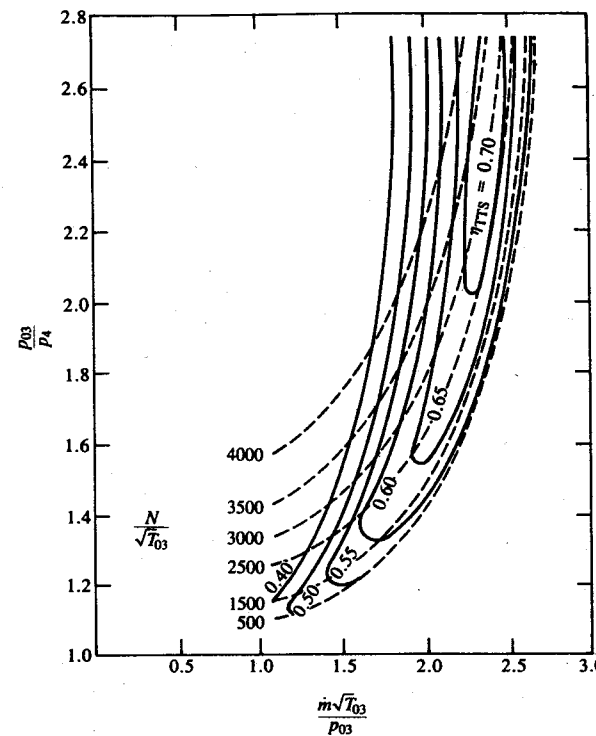


FIGURE 6-51

Radial turbine performance map showing lines of constant corrected speed and efficiency on a plot of pressure ratio versus corrected mass flow rate.  $T_{03}$  = turbine inlet temperature (K),  $p_{03}$  = turbine inlet pressure (bar),  $p_4$  = turbine exit pressure (bar),  $\dot{m}$  = mass flow rate (kg/s),  $N$  = speed (rev/min).<sup>40</sup>

Since the mid-radius  $r_2$  usually equals the mid-radius  $r_3$ ,

$$\begin{aligned} \dot{W}_T &= \dot{m}U(C_{\theta_2} + C_{\theta_3}) = \dot{m}U(C_2 \sin \alpha_2 + C_3 \sin \alpha_3) \\ &= \dot{m}U(C_{z_2} \tan \beta_2 + C_{z_3} \tan \beta_3) \end{aligned} \quad (6.63)$$

Equation (6.62) relates the work-transfer rate to the stagnation enthalpy change as in the radial turbine.

Figure 6-55 shows axial turbine performance characteristics on the standard dimensionless plot of pressure ratio versus corrected mass flow rate. Here the constant speed lines converge to a single choked flow limit as the mass flow is increased. In the radial turbine, the variation in centrifugal effects with speed cause a noticeable spread in the constant speed lines (Fig. 6-51).

An alternative performance plot for turbines is efficiency versus *blade speed ratio*. This ratio is the blade speed  $U$  (at its mean height) for an axial flow turbine

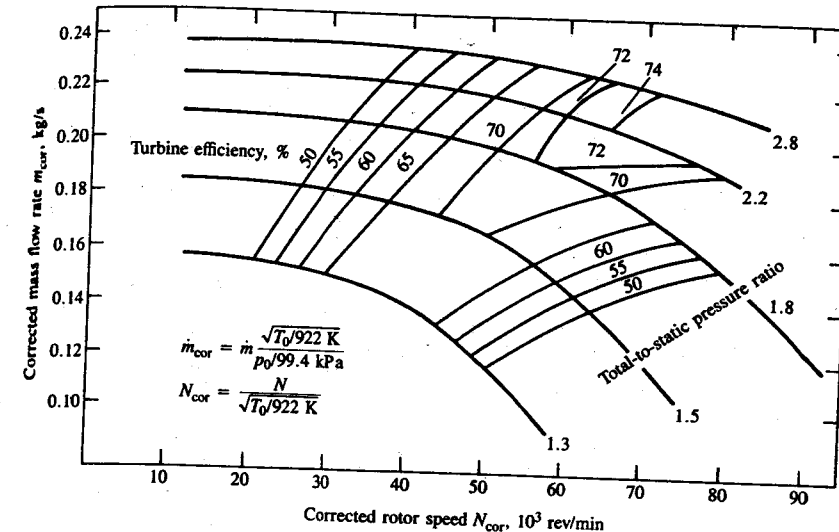


FIGURE 6-52

Alternative radial turbine performance map: corrected mass flow rate is plotted against corrected rotor speed.<sup>45</sup>

or the wheel tip speed for a radial flow turbine, divided by the velocity equivalent of the isentropic enthalpy drop across the turbine stage,  $C_s$ ; i.e.,

$$\text{Blade speed ratio} = \frac{U}{C_s}$$

where

$$C_s = [2(h_{03} - h_{4s})]^{1/2} \quad (6.64)$$

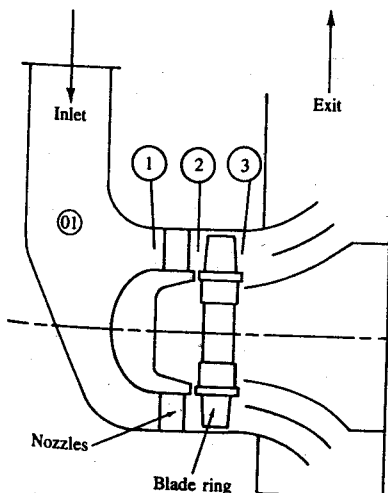


FIGURE 6-53  
Schematic of single-stage axial flow turbine.

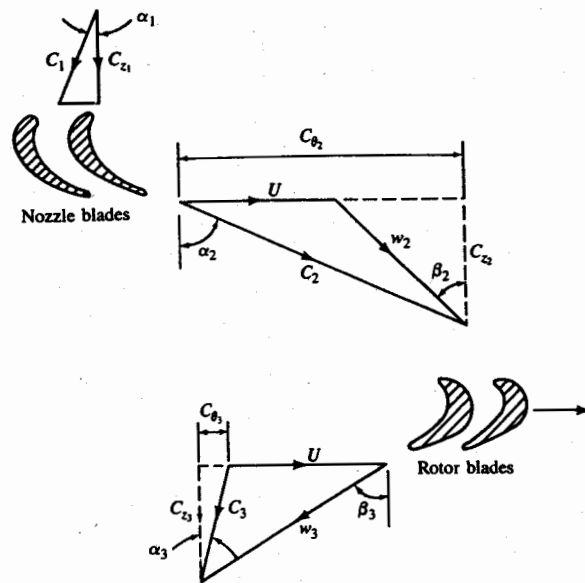


FIGURE 6-54  
Velocity diagrams at entry (2) and exit (3) to axial flow turbine blade ring.<sup>40</sup>

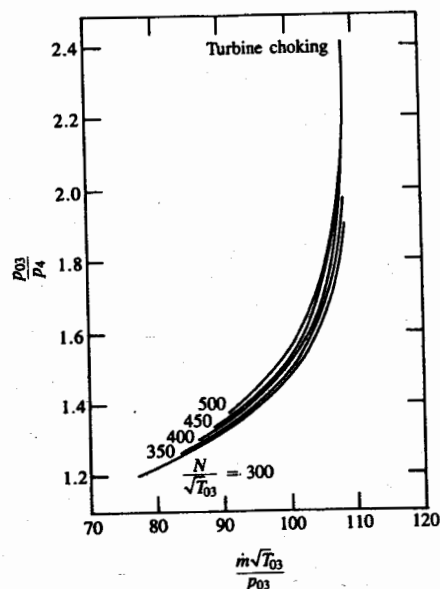


FIGURE 6-55  
Axial flow turbine performance map: pressure ratio is plotted against corrected mass flow rate.  $T_{03}$  = turbine inlet temperature (K),  $p_{03}$  = turbine inlet pressure (bar),  $p_4$  = turbine exit pressure (bar),  $\dot{m}$  = mass flow rate ( $\text{kg/s}$ ),  $N$  = speed (rev/min).<sup>40</sup>

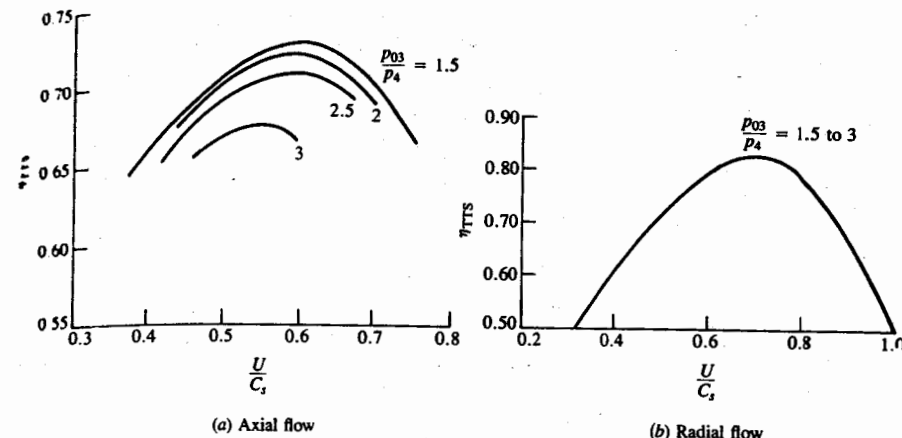


FIGURE 6-56  
Plot of turbine total-to-static efficiency versus blade speed ratio  $U/C_s$  for (a) axial flow and (b) radial flow turbines.<sup>40</sup>

This method of displaying performance is useful for matching compressor and turbine wheel size for operation of the turbine at optimum efficiency. Figure 6-56 shows such plots for an axial and radial flow turbine. The peak efficiency can occur for  $0.4 < U/C_s < 0.8$ , depending on turbine design and application.<sup>40</sup>

For a given turbocharger, the compressor and turbine characteristics are linked. Since the compressor and turbine are on a common shaft with speed  $N$ :

$$\frac{N}{\sqrt{T_{01}}} = \frac{N}{\sqrt{T_{03}}} \left( \frac{T_{03}}{T_{01}} \right)^{1/2} \quad (6.65)$$

For  $\dot{m}_C = \dot{m}_T = \dot{m}$  (if  $\dot{m}_C[1 + (F/A)] = \dot{m}_T$ , the equation is easily modified):

$$\frac{\dot{m}\sqrt{T_{01}}}{p_{01}} = \frac{\dot{m}\sqrt{T_{03}}}{p_{03}} \left( \frac{p_{03}}{p_{01}} \right) \left( \frac{T_{01}}{T_{03}} \right)^{1/2} \quad (6.66)$$

Since the compressor and turbine powers are equal in magnitude:

$$h_{02} - h_{01} = \eta_m (h_{03} - h_{04}) \quad (6.67)$$

or, with an ideal gas model,

$$c_p c(T_{02} - T_{01}) = \eta_m c_{p,T} (T_{03} - T_{04}) \quad (6.68)$$

Equation (6.68), with Eqs. (6.40) and (6.46), gives

$$\left( \frac{p_{02}}{p_{01}} \right)^{(y_C - 1)/y_C} - 1 = \eta_C \eta_T \eta_m \frac{c_{p,T}}{c_{p,C}} \left[ 1 - \left( \frac{p_4}{p_{03}} \right)^{(y_T - 1)/y_T} \right] \frac{T_{03}}{T_{01}} \quad (6.69)$$

Assuming that the turbine exit pressure  $p_4$  equals atmospheric pressure  $p_{01}$ , the equilibrium or steady-state running lines for constant values of  $T_{03}/T_{01}$  can be

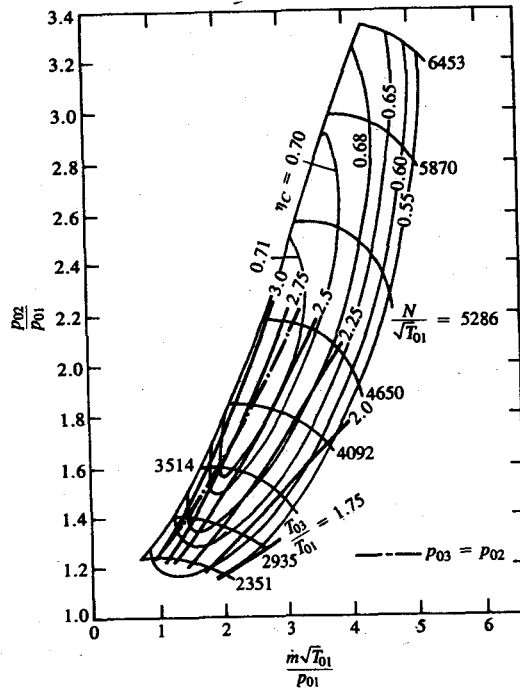


FIGURE 6-57

Steady-state turbocharger operating lines plotted as constant  $T_{03}/T_{01}$  lines on compressor map. Turbine characteristics defined by Fig. 6-51.  $p_{01}$  = compressor inlet pressure (bar),  $p_{02}$  = compressor exit pressure (bar),  $T_{01}$  = compressor inlet temperature (K),  $T_{03}$  = turbine inlet temperature (K),  $\dot{m}$  = mass flow rate (kg/s),  $N$  = speed (rev/min).<sup>40</sup>

determined. Figure 6-57 shows an example of such a set of turbocharger characteristics, plotted on a turbocharger compressor map for a radial turbine with characteristics similar to Fig. 6-51. The dash-dot-dash line is for  $p_{02} = p_{03}$ . To the right of this line,  $p_{03} > p_{02}$ ; to the left of this line  $p_{02} > p_{03}$ .<sup>40</sup>

The problem of overspeeding the turbocharger and generating very high cylinder pressures often requires that some of the exhaust be bypassed around the turbine. The bypass valve or *wastegate* is usually built into the turbocharger casing. It consists of a spring-loaded valve acting in response to the inlet manifold pressure on a controlling diaphragm. When the wastegate is open, only a portion of the exhaust gases will flow through the turbine and generate power; the remainder passes directly into the exhaust system downstream of the turbine.

### 6.8.5 Wave-Compression Devices

Pressure wave superchargers make use of the fact that if two fluids having different pressures are brought into direct contact in long narrow channels, equalization of pressure occurs faster than mixing. One such device, the Comprex, has been developed for internal combustion engine supercharging which operates using this principle.<sup>46</sup> It is shown schematically in Fig. 6-58. The working channels of the Comprex are arranged on a rotor or cell wheel (b) which is rotated

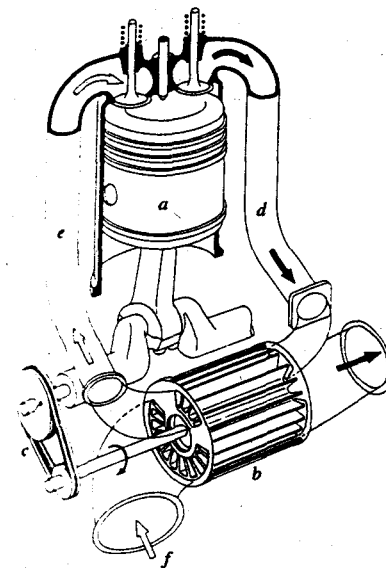


FIGURE 6-58

Schematic of Comprex supercharger.<sup>47</sup> a Engine, b Cell wheel or rotor, c Belt drive, d High-pressure exhaust gas (G-HP), e High-pressure air (A-HP), f Low-pressure air (A-LP), g Low-pressure exhaust gas (G-LP)

between two castings by a belt driven from the crankshaft (c). There is no contact between the rotor and the casing, but the gaps are kept small to minimize leakage. The belt drive merely overcomes friction and maintains the rotor at a speed proportional to engine speed (usually 4 or 5 times faster); it provides no compression work. One casing (the air casing) contains the passage which brings low-pressure air (f) to one set of ports and high-pressure air (e) from another set of ports in the rotor-side inner casing. The other casing (the gas casing) connects the high-pressure engine exhaust gas (d) to one set of ports at the other end of the rotor, and connects a second set of ports to the exhaust system (g). Fluid can flow into and out of the rotor channels through these ports. The exhaust gas inlet port is made small enough to cause a significant pressure rise in the exhaust manifold (e.g., 2 atm) when the engine is operated at its rated power. The pressure wave process does not depend on the pressure and flow fluctuations within the manifold caused by individual cylinder exhaust events: its operation can be explained assuming constant pressure at each set of ports. As the rotor makes one revolution, the ends of each channel are alternatively closed, or are open to a flow passage. By appropriate arrangement of these passages and selection of the geometry and location of the ports, an efficient energy transfer between the engine exhaust gases and the fresh charge can be realized.<sup>46</sup>

The wave-compression process in the Comprex can be explained in more detail with the aid of Fig. 6-59, where the rotational motion of the channels has been unrolled. Consider the channel starting at the top; it is closed at both ends and contains air at atmospheric pressure. As it opens at the upper edge of the high-pressure gas (G-HP) duct, a compression or shock wave (1) propagates from

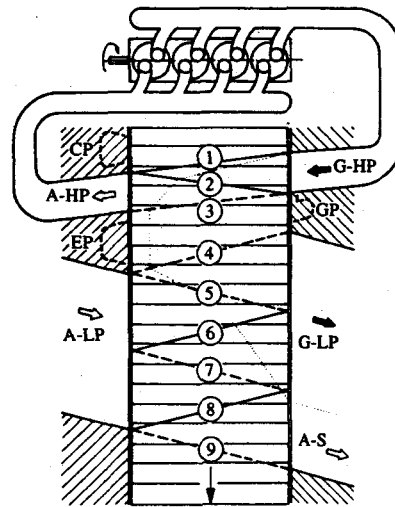


FIGURE 6-59

Unrolled view of the Comprex pressure-wave process.<sup>47</sup> A Air, G Gas, S Scavenging, HP High pressure, LP Low pressure; CP, EP, GP are pockets.

the right end of the channel toward the left, compressing the air through which it passes. The compressed air behind the wave occupies less space so the high-pressure exhaust gas moves into the channel as indicated by the dotted line. This line is the boundary between the two fluids. As this wave (1) reaches the left end, the channel is opened and compressed air flows into the engine inlet duct (A-HP). The inlet duct is shaped to provide the same mass flow at lower velocity: this deceleration of the air produces a second compression wave (2) which propagates back into the channel. As a result the compressed air leaving the cell on the left has a higher pressure than the driving gas on the right. As this wave (2) arrives at the right-hand side, the high-pressure gas (G-HP) channel closes. An expansion wave (3) then propagates back to the left, separating the now motionless and partly expanded fluid on the right from still-moving fluid on the left. When this wave (3) reaches the left-hand end, A-HP is closed and all the gases in the channel are at rest. Note that the first gas particles (dotted line) have not quite reached the air end of the channel: a cushion of air remains to prevent breakthrough.

The cell's contents are still at a higher pressure than the low pressure in the exhaust gas duct. When the right-hand end of the cell reaches this duct, the cell's contents expand into the exhaust. This motion is transferred through the channel by an expansion wave (4) which propagates to the left at sonic speed. When this wave reaches the left-hand end, the cell opens to the low-pressure air duct (A-LP) and fresh air is drawn into the cell. The flow to the right continues, but with decreasing speed due to wave action (5, 6, 7, 8) and pressure losses at each end of the cell. When the dotted line—the interface between air and the exhaust gas—reaches the right end of the cell, all the driving gas has left. The cell is then

purged by the scavenging air flow (A-S) and filled with fresh air at atmospheric pressure. At wave (9), the cell is closed at both ends, restoring it to its initial state.<sup>47</sup>

The speed of these pressure waves is the local sound speed and is a function of local gas temperature only. Thus, the above process will only work properly for a given exhaust gas temperature at a particular cell speed. The operating range is extended by the use of "pockets" as shown in Fig. 6-59. The pockets prevent the reflection of sound waves from a closed channel end which would cause a substantial change in flow velocity in the channel. These pockets, marked CP and EP on the air side and GP on the exhaust gas side, allow flow from one channel to adjacent channels via the pocket if the wave action requires it. Thus the device can be tuned for full-load medium-speed operation and still give acceptable performance at other loads and speeds because the pockets allow the particle paths to change without major losses.<sup>46</sup>

Figure 6-60 shows the apparent compressor performance map of a Comprex when connected to a small three-cylinder diesel engine. Note that the map depends on the engine to which the device is coupled because the exhaust gas expansion process and fresh air compression process occur within the same rotor. The volume flow rate is the net air: it is the total air flow into the device less the scavenging air flow. The values of isentropic efficiency [defined by Eq. (6.39)] are comparable to those of mechanical and aerodynamic compressors.

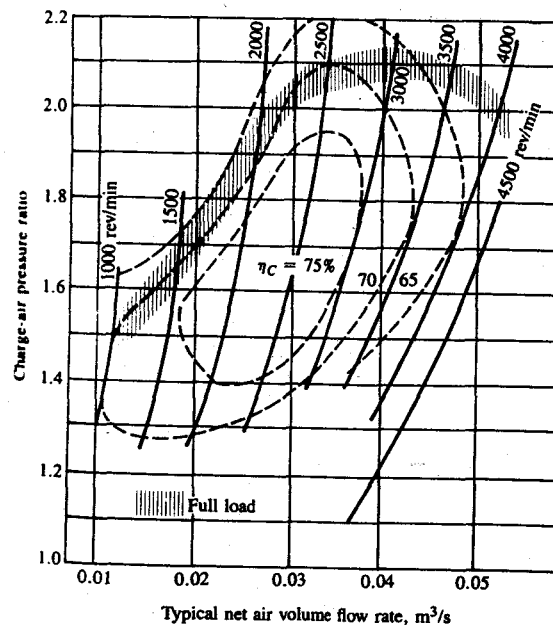


FIGURE 6-60  
Apparent compressor map of Comprex connected to a 1.2-dm<sup>3</sup> diesel engine: charge-air pressure ratio plotted versus net air volume flow rate (total air flow less scavenging air flow).<sup>46</sup>

## PROBLEMS

6.1. A conventional spark-ignition engine operating with gasoline will not run smoothly (due to incomplete combustion) with an equivalence ratio leaner than about  $\phi = 0.8$ . It is desirable to extend the smooth operating limit of the engine to leaner equivalence ratios so that at part-throttle operation (with intake pressure less than 1 atmosphere) the pumping work is reduced. Leaner than normal operation can be achieved by adding hydrogen gas ( $H_2$ ) to the mixture in the intake system. The addition of  $H_2$  makes the fuel-air mixture easier to burn.

- (a) The fuel composition with "mixed" fuel operation is  $H_2 + C_8H_{18}$ —one mole of hydrogen to every mole of gasoline, which is assumed the same as isoctane. What is the stoichiometric air/fuel ratio for the "mixed" fuel?
- (b) The lower heating value of  $H_2$  is 120 MJ/kg and for isoctane is 44.4 MJ/kg. What is the heating value per kilogram of fuel mixture?
- (c) Engine operation with isoctane and the mixed ( $H_2 + C_8H_{18}$ ) fuel is compared in a particular engine at a part-load condition (brake mean effective pressure of 275 kPa and 1400 rev/min). You are given the following information about the engine operation:

Fuel	$C_8H_{18}$	$H_2 + C_8H_{18}$
Equivalence ratio	0.8	0.5
Gross indicated fuel conversion efficiency	0.35	0.4
Mechanical rubbing friction mep	138 kPa	138 kPa
Inlet manifold pressure	46 kPa	?
Pumping mep	55 kPa	?

Estimate approximately the inlet manifold pressure and the pumping mean effective pressure with ( $H_2 + C_8H_{18}$ ) fuel. Explain your method and assumptions clearly. Note that mechanical efficiency  $\eta_m$  is defined as

$$\eta_m = \frac{b\text{mep}}{im\text{ep}_s} = \frac{b\text{mep}}{b\text{mep} + r\text{fmeep} + p\text{mep}}$$

- 6.2. Hydrogen is a possible future fuel for spark-ignition engines. The lower heating value of hydrogen is 120 MJ/kg and for gasoline ( $C_8H_{18}$ ) is 44 MJ/kg. The stoichiometric air/fuel ratio for hydrogen is 34.3 and for gasoline is 14.4. A disadvantage of hydrogen fuel in the SI engine is that the partial pressure of hydrogen in the  $H_2$ -air mixture reduces the engine's volumetric efficiency, which is proportional to the partial pressure of air. Find the partial pressure of air in the intake manifold downstream of the hydrogen fuel-injection location at wide-open throttle when the total intake manifold pressure is 1 atmosphere; the equivalence ratio is 1.0. Then estimate the ratio of the fuel energy per unit time entering a hydrogen-fueled engine operating with a stoichiometric mixture to the fuel energy per unit time entering an identical gasoline-fueled engine operating at the same speed with a stoichiometric mixture. (Note that the "fuel energy" per unit mass of fuel is the fuel's heating value.)
- 6.3. Sketch (a) shows an ideal cycle  $p$ - $V$  diagram for a conventional throttled spark-ignition engine, 1-2-3-4-5-6-7-1. The gas properties  $c_v$ ,  $c_p$ ,  $\gamma$ ,  $R$  throughout the cycle are constant. The mass of gas in the cylinder is  $m$ . The exhaust pressure is  $p_e$ .

Sketch (b) shows an ideal cycle  $p$ - $V$  diagram 1-2-3-4-5-6-8-1 for a spark-ignition engine with novel inlet valve timing. The inlet manifold is unthrottled; it has essentially the same pressure as the exhaust. To reduce the mass inducted at part

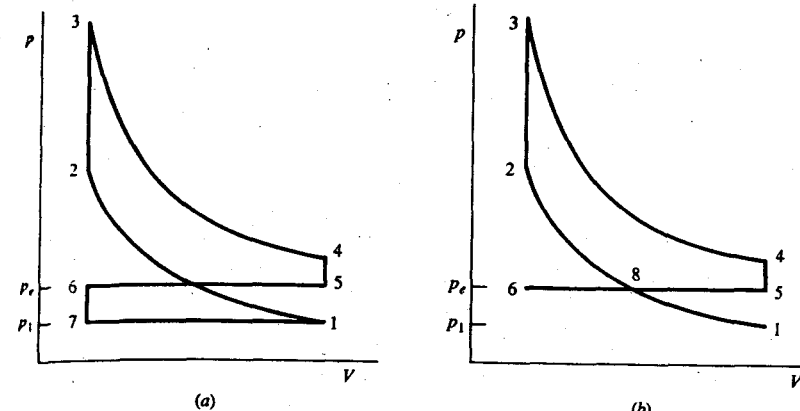


FIGURE P6-3

load, the inlet valve is closed rapidly *partway* through the intake stroke at point 8. The gas in the cylinder at inlet valve closing at 8 is then expanded isentropically to 1 with the inlet valve closed. The pressure  $p_1$  at the start of compression is the same for both cycles.

- (a) Indicate on  $p$ - $V$  diagrams the area that corresponds to the pumping work per cycle for cycles (a) and (b). Which area is greater?
- (b) Derive expressions for the pumping work per cycle  $W_p$  in terms of  $m$ ,  $c_v$ ,  $\gamma$ ,  $T_1$ ,  $(p_e/p_1)$ , and the compression ratio  $r_c$  for cycles (a) and (b). Be consistent about the signs of the work transfers to and from the gas.
- (c) For  $\gamma = 1.3$ ,  $r_c = 8$ , and  $(p_e/p_1) = 2$  find the ratio  $W_p(b)/W_p(a)$ , assuming the values of  $T_1$  and  $m$  are the same in both cases.
- 6.4. For four-stroke cycle engines, the inlet and exhaust valve opening and closing crank angles are typically: IVO 15° BTC; IVC 50° ABC; EVO 55° BBC; EVC 10° ATC. Explain why these valve timings improve engine breathing relative to valve opening and closing at the beginnings and ends of the intake and exhaust strokes. Are there additional design issues that are important?
- 6.5. Estimate approximately the pressure drop across the inlet valve about halfway through the intake stroke and across the exhaust valve halfway through the exhaust stroke, when the piston speed is at its maximum for a typical four-stroke cycle spark-ignition engine with  $B = L = 85$  mm at 2500 and 5000 rev/min at WOT. Assume appropriate values for any valve and port geometric details required, and for the gas composition and state.
- 6.6. Using the data in Fig. 6-21, estimate the fraction of the original mass left in the cylinder: (a) at the end of the blowdown process and (b) at the end of the exhaust stroke.
- 6.7. Compare the engine residual gas fraction data in Fig. 6-19 with ideal cycle estimates of residual gas fraction as follows. Using Eq. (5.47) plot the fuel-air cycle residual mass fraction  $x_r$  against  $p/p_e$  for  $r_c = 8.5$  on the same graph as the engine data in Fig. 6-19 at 1400 rev/min and 27° valve overlap. Assume  $T_1 = 1400$  K and  $(\gamma - 1)/\gamma = 0.24$  in Eq. (5.47). Suggest an explanation for any significant difference.

- 6.8. One concept that would increase SI engine efficiency is early intake valve closing (EIVC) where the intake valve closes *before* the piston reaches BC on the intake stroke, thus limiting the amount of charge inducted into the cylinder.  
 (a) Explain why EIVC improves engine efficiency at part load. (*Hint:* consider what must happen to the inlet manifold pressure in order to maintain constant mass in the cylinder as the intake valve is closed sooner.)  
 (b) This part load reduction in charge could be achieved by using late intake valve closing where the intake valve is not closed until the compression stroke has pushed some of the cylinder gases back out into the intake manifold. Based on a comparison of *p-V* diagrams, is this method inferior to EIVC?
- 6.9. An eight-cylinder turbocharged aftercooled four-stroke cycle diesel engine operates with an inlet pressure of 1.8 atmospheres at its maximum rated power at 2000 rev/min.  $B = 128$  mm,  $L = 140$  mm,  $\eta_c$  (based on inlet manifold conditions of 1.8 atm and 325 K after the aftercooler) = 0.9. The compressor isentropic efficiency is 0.7.  
 (a) Calculate the power required to drive the turbocharger compressor.  
 (b) If the exhaust gas temperature is 650°C and the turbocharger isentropic efficiency is 0.65, estimate the pressure at turbine inlet. The turbine exhausts to the atmosphere.
- 6.10. The charging efficiency of two-stroke cycle diesel engines can be estimated from measurement of the concentration of O<sub>2</sub> and CO<sub>2</sub> in the burned gases within the cylinder, or in the exhaust blowdown pulse prior to any mixing with fresh air. The engine bore = 125 mm, stroke = 150 mm, compression ratio = 15. The fuel flow rate at 1800 rev/min is 1.6 g/s per cylinder. The conditions used to evaluate the air density for the reference mass are 300 K and 1 atm. The molar concentrations (dry) of CO<sub>2</sub> and O<sub>2</sub> in the in-cylinder burned gases are 7.2 and 10.4 percent (see Fig. 4-22). The scavenging air flow rate is 80 g/s. Evaluate (a) the charging efficiency, (b) the delivery ratio, and (c) the trapping efficiency (assuming the trapped mass equals the reference mass).

## REFERENCES

- Khovakh, M.: *Motor Vehicle Engines*, English Translation, Mir Publishers, Moscow, 1976.
- Matsuoka, S., Tasaka, H., and Tsuruta, J.: "The Evaporation of Fuel and Its Effect on Volumetric Efficiency," JARI technical memorandum no. 2, pp. 17-22, 1971.
- Takizawa, M., Uno, T., Oue, T., and Yura, T.: "A Study of Gas Exchange Process Simulation of an Automotive Multi-Cylinder Internal Combustion Engine," SAE paper 820410, *SAE Trans.*, vol. 91, 1982.
- Kay, I. W.: "Manifold Fuel Film Effects in an SI Engine," SAE paper 780944, 1978.
- Ohata, A., and Ishida, Y.: "Dynamic Inlet Pressure and Volumetric Efficiency of Four Cycle Four Cylinder Engine," SAE paper 820407, *SAE Trans.*, vol. 91, 1982.
- Benson, R. S., and Whitehouse, N. D.: *Internal Combustion Engines*, vol. 2, Pergamon Press, 1979.
- Taylor, C. F.: *The Internal-Combustion Engine in Theory and Practice*, vol. 1, 2d ed., revised, MIT Press, Cambridge, Mass., 1985.
- Hofbauer, P., and Sator, K.: "Advanced Automotive Power Systems, Part 2: A Diesel for a Subcompact Car," SAE paper 770113, *SAE Trans.*, vol. 86, 1977.
- Armstrong, D. L., and Stirrat, G. F.: "Ford's 1982 3.8L V6 Engine," SAE paper 820112, *SAE Trans.*, vol. 91, 1982.
- Chapman, M., Novak, J. M., and Stein, R. A.: "Numerical Modeling of Inlet and Exhaust Flows in Multi-Cylinder Internal Combustion Engines," in *Flows in Internal Combustion Engines*, Winter Annual Meeting, ASME, New York, 1982.
- Barnes-Moss, H. W.: "A Designers Viewpoint," in *Passenger Car Engines, Conference Proceedings*, pp. 133-147, Institution of Mechanical Engineers, London, 1975.
- Asmus, T. W.: "Valve Events and Engine Operation," SAE paper 820749, *SAE Trans.*, Vol. 91, 1982.
- SAE Recommended Practice, "Engine Terminology and Nomenclature—General," in *SAE Handbook*, J604d.
- Kastner, L. J., Williams, T. J., and White, J. B.: "Poppet Inlet Valve Characteristics and Their Influence on the Induction Process," *Proc. Instn Mech. Engrs.*, vol. 178, pt. 1, no. 36, pp. 955-978, 1963-1964.
- Woods, W. A., and Khan, S. R.: "An Experimental Study of Flow through Poppet Valves," *Proc. Instn Mech. Engrs.*, vol. 180, pt. 3N, pp. 32-41, 1965-1966.
- Annand, W. J. D., and Roe, G. E.: *Gas Flow in the Internal Combustion Engine*, Haessner Publishing, Newfoundland, N.J., 1974.
- Tanaka, K.: "Air Flow through Exhaust Valve of Conical Seat," *Int. Congr. Appl. Mech.*, vol. 1, pp. 287-295, 1931.
- Bicen, A. F., and Whitelaw, J. H.: "Steady and Unsteady Air Flow through an Intake Valve of a Reciprocating Engine," in *Flows in Internal Combustion Engines—II*, FED-vol. 20, Winter Annual Meeting, ASME, 1984.
- Fukutani, I., and Watanabe, E.: "An Analysis of the Volumetric Efficiency Characteristics of 4-Stroke Cycle Engines Using the Mean Inlet Mach Number Mim," SAE paper 790484, *SAE Trans.*, vol. 88, 1979.
- Wallace, W. B.: "High-Output Medium-Speed Diesel Engine Air and Exhaust System Flow Losses," *Proc. Instn Mech. Engrs.*, vol. 182, pt. 3D, pp. 134-144, 1967-1968.
- Cole, B. N., and Mills, B.: "The Theory of Sudden Enlargements Applied to Poppet Exhaust-Valve, with Special Reference to Exhaust-Pulse Scavenging," *Proc. Instn Mech. Engrs.*, pt. 1B, pp. 364-378, 1953.
- Toda, T., Nohira, H., and Kobashi, K.: "Evaluation of Burned Gas Ratio (BGR) as a Predominant Factor to NO<sub>x</sub>," SAE paper 760763, *SAE Trans.*, vol. 85, 1976.
- Benson, J. D., and Stebar, R. F.: "Effects of Charge Dilution on Nitric Oxide Emission from a Single-Cylinder Engine," SAE paper 710008, *SAE Trans.*, vol. 80, 1971.
- Tabaczynski, R. J., Heywood, J. B., and Keck, J. C.: "Time-Resolved Measurements of Hydrocarbon Mass Flow Rate in the Exhaust of a Spark-Ignition Engine," SAE paper 720112, *SAE Trans.*, vol. 81, 1972.
- Caton, J. A., and Heywood, J. B.: "An Experimental and Analytical Study of Heat Transfer in an Engine Exhaust Port," *Int. J. Heat Mass Transfer*, vol. 24, no. 4, pp. 581-595, 1981.
- Caton, J. A.: "Comparisons of Thermocouple, Time-Averaged and Mass-Averaged Exhaust Gas Temperatures for a Spark-Ignited Engine," SAE paper 820050, 1982.
- Phatak, R. G.: "A New Method of Analyzing Two-Stroke Cycle Engine Gas Flow Patterns," SAE paper 790487, *SAE Trans.*, vol. 88, 1979.
- Rizk, W.: "Experimental Studies of the Mixing Processes and Flow Configurations in Two-Cycle Engine Scavenging," *Proc. Instn Mech. Engrs.*, vol. 172, pp. 417-437, 1958.
- Dedeoglu, N.: "Scavenging Model Solves Problems in Gas Burning Engine," SAE paper 710579, *SAE Trans.*, vol. 80, 1971.
- Sher, E.: "Investigating the Gas Exchange Process of a Two-Stroke Cycle Engine with a Flow Visualization Rig," *Israel J. Technol.*, vol. 20, pp. 127-136, 1982.
- Jante, A.: "Scavenging and Other Problems of Two-Stroke Cycle Spark-Ignition Engines," SAE paper 680468, *SAE Trans.*, vol. 77, 1968.
- Kannappan, A.: "Cumulative Sampling Technique for Investigating the Scavenging Process in Two-Stroke Engine," ASME paper 74-DGP-11, 1974.
- Ohigashi, S., Kashiwada, Y., and Achiwa, J.: "Scavenging the 2-Stroke Diesel Engine," *Bull. JSME*, vol. 3, no. 9, pp. 130-136, 1960.
- Huber, E. W.: "Measuring the Trapping Efficiency of Internal Combustion Engines through Continuous Exhaust Gas Analysis," SAE paper 710144, *SAE Trans.*, vol. 80, 1971.
- Blair, G. P., and Kenny, R. G.: "Further Developments in Scavenging Analysis for Two-Cycle Engines," SAE paper 800038, *SAE Trans.*, vol. 89, 1980.

36. Baudequin, F., and Rochelle, P.: "Some Scavenging Models for Two-Stroke Engines," *Proc. Instn Mech. Engrs, Automobile Division*, vol. 194, no. 22, pp. 203-210, 1980.
37. Gyssler, G.: "Problems Associated with Turbocharging Large Two-Stroke Diesel Engines," *Proc. CIMAC*, paper B.16, 1965.
38. Annand, W. J. D.: "Compressible Flow through Square-Edged Orifices: An Empirical Approximation for Computer Calculations," *J. Mech. Engng Sci.*, vol. 8, p. 448, 1966.
39. Benson, R. S.: "Experiments on a Piston Controlled Port," *The Engineer*, vol. 210, pp. 875-880, 1960.
40. Watson, N., and Janota, M. S.: *Turbocharging the Internal Combustion Engine*, Wiley-Interscience Publications, John Wiley, New York, 1982.
41. Bhinder, F. S.: "Supercharging Compressors—Problems and Potential of the Various Alternatives," SAE paper 840243, 1984.
42. Bhinder, F. S.: "Some Fundamental Considerations Concerning the Pressure Charging of Small Diesel Engines," SAE paper 830145, 1983.
43. Brandstetter, W., and Dziggel, R.: "The 4- and 5-Cylinder Turbocharged Diesel Engines for Volkswagen and Audi," SAE paper 820441, *SAE Trans.*, vol. 91, 1982.
44. SAE Recommended Practice, "Turbocharger Nomenclature and Terminology," in *SAE Handbook*, J922.
45. Flynn, P. F.: "Turbocharging Four-Cycle Diesel Engines," SAE paper 790314, *SAE Trans.*, vol. 88, 1979.
46. Gyarmathy, G.: "How Does the Comprex Pressure-Wave Supercharger Work?" SAE paper 830234, 1983.
47. Kollbrunner, T. A.: "Comprex Supercharging for Passenger Diesel Car Engines," SAE paper 800884, *SAE Trans.*, vol. 89, 1980.

# CHAPTER

---

# 7

---

## SI ENGINE FUEL METERING AND MANIFOLD PHENOMENA

### 7.1 SPARK-IGNITION ENGINE MIXTURE REQUIREMENTS

The task of the engine induction and fuel systems is to prepare from ambient air and fuel in the tank an air-fuel mixture that satisfies the requirements of the engine over its entire operating regime. In principle, the optimum air/fuel ratio for a spark-ignition engine is that which gives the required power output with the lowest fuel consumption, consistent with smooth and reliable operation. In practice, the constraints of emissions control may dictate a different air/fuel ratio, and may also require the recycling of a fraction of the exhaust gases (EGR) into the intake system. The relative proportions of fuel and air that provide the lowest fuel consumption, smooth reliable operation, and satisfy the emissions requirements, at the required power level, depend on engine speed and load. Mixture requirements and preparation are usually discussed in terms of the air/fuel ratio or fuel/air ratio (see Sec. 2.9) and percent EGR [see Eq. (4.2)]. While the fuel metering system is designed to provide the appropriate fuel flow for the *actual* air flow at each speed and load, the relative proportions of fuel and air can be stated more generally in terms of the fuel/air equivalence ratio  $\phi$ , which is the actual fuel/air ratio normalized by dividing by the stoichiometric fuel/air ratio [Eq.

(3.8)]. The combustion characteristics of fuel-air mixtures and the properties of combustion products, which govern engine performance, efficiency, and emissions, correlate best for a wide range of fuels relative to the stoichiometric mixture proportions. Where appropriate, therefore, the equivalence ratio will be used as the defining parameter. A typical value for the stoichiometric air/fuel ratio of gasoline is 14.6.<sup>†</sup> Thus, for gasoline,

$$\phi \approx \frac{14.6}{A/F} \quad (7.1)$$

The effects of equivalence ratio variations on engine combustion, emissions, and performance are discussed more fully in Chaps. 9, 11, and 15. A brief summary is sufficient here. Mixture requirements are different for full-load (wide-open throttle) and for part-load operation. At the former operating condition, complete utilization of the *inducted air* to obtain maximum power for a given displaced volume is the critical issue. Where less than the maximum power at a given speed is required, efficient utilization of the *fuel* is the critical issue. At wide-open throttle, maximum power for a given volumetric efficiency is obtained with rich-of-stoichiometric mixtures,  $\phi \approx 1.1$  (see the discussion of the fuel-air cycle results in Sec. 5.5.3). Mixtures that are richer still are sometimes used to increase volumetric efficiency by increasing the amount of charge cooling that accompanies fuel vaporization [see Eq. (6.5)], thereby increasing the inducted air density.

At part-load (or part-throttle) operating conditions, it is advantageous to dilute the fuel-air mixture, either with excess air or with recycled exhaust gas. This dilution improves the fuel conversion efficiency for three reasons:<sup>‡</sup> (1) the expansion stroke work for a given expansion ratio is increased as a result of the change in thermodynamic properties of the burned gases—see Secs. 5.5.3 and 5.7.4; (2) for a given mean effective pressure, the intake pressure increases with increasing dilution, so pumping work decreases—see Fig. 5-10; (3) the heat losses to the walls are reduced because the burned gas temperatures are lower. In the absence of strict engine NO<sub>x</sub> emission requirements, excess air is the obvious diluent, and at part throttle engines have traditionally operated lean. When tight control of NO<sub>x</sub>, HC, and CO emissions is required, operation of the engine with a stoichiometric mixture is advantageous so that a three-way catalyst<sup>‡</sup> can be used to clean up the exhaust. The appropriate diluent is then recycled exhaust gases which significantly reduces NO<sub>x</sub> emissions from the engine itself. The amount of diluent that the engine will tolerate at any given speed and load depends on the details of the engine's combustion process. Increasing excess air

or the amount of recycled exhaust slows down the combustion process and increases its variability from cycle to cycle. A certain minimum combustion repeatability or stability level is required to maintain smooth engine operation. Deterioration in combustion stability therefore limits the amount of dilution an engine can tolerate. As load decreases, less dilution of the *fresh* mixture can be tolerated because the internal dilution of the mixture with residual gas increases (see Sec. 6.4). At idle conditions, the fresh mixture will not usually tolerate any EGR and may need to be stoichiometric or fuel-rich to obtain adequate combustion stability.

Mixture composition requirements over the engine load and speed range are illustrated schematically for the two approaches outlined above in Fig. 7-1. If stoichiometric operation and EGR are not required for emissions control, as load increases the mixture is leaned out from a fuel-rich or close-to-stoichiometric composition at very light load. As wide-open throttle operation is approached at each engine speed, the mixture is steadily enriched to rich-of-stoichiometric at the maximum bmeep point. With the stoichiometric operating conditions required for three-way-catalyst-equipped engines, when EGR is used, the percentage of recycled exhaust increases from zero at light load to a maximum at mid-load, and then decreases to zero as wide-open throttle conditions are approached so maximum bmeep can be obtained. Combinations of these strategies are possible. For example, lean operation at light load can be used for best efficiency, and

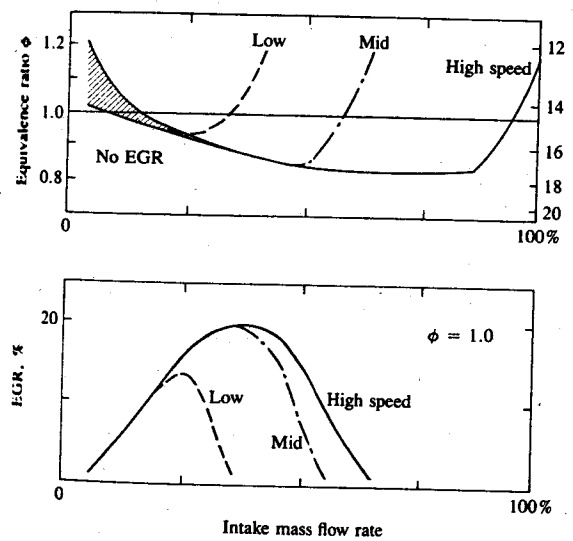


**FIGURE 7-1**  
Typical mixture requirements for two common operating strategies. Top diagram shows equivalence ratio variation with intake mass flow rate (percent of maximum flow at rated speed) at constant low, mid, and high engine speeds. Bottom diagram shows recycled exhaust (EGR) schedule as a function of intake flow rate, for low, mid, and high speeds for stoichiometric operation.

<sup>†</sup> Typical value only. Most gasolines have (A/F), in the range 14.4 to 14.7. (A/F), could lie between 14.1 and 15.2.

<sup>‡</sup> A three-way catalyst system, when operated with a close-to-stoichiometric mixture, achieves substantial reductions in NO<sub>x</sub>, CO, and HC emissions simultaneously; see Sec. 11.6.2.

stoichiometric mixtures (with a three-way catalyst) and/or EGR can be used at mid loads to control NO<sub>x</sub> emissions.

In practical spark-ignition engine induction systems, the fuel and air distribution between engine cylinders is not uniform (and also varies in each individual cylinder on a cycle-by-cycle basis). A spread of one or more air/fuel ratios between the leanest and richest cylinders over the engine's load and speed range is not uncommon in engines with conventional carburetors. The average mixture composition must be chosen to avoid excessive combustion variability in the leanest operating cylinder. Thus, as the spread in mixture nonuniformity increases, the mean equivalence ratio must be moved toward stoichiometric and away from the equivalence ratio which gives minimum fuel consumption.

## 7.2 CARBURETORS

### 7.2.1 Carburetor Fundamentals

A carburetor has been the most common device used to control the fuel flow into the intake manifold and distribute the fuel across the air stream. In a carburetor, the air flows through a converging-diverging nozzle called a venturi. The pressure difference set up between the carburetor inlet and the throat of the nozzle (which depends on the air flow rate) is used to meter the appropriate fuel flow for that air flow. The fuel enters the air stream through the fuel discharge tube or ports in the carburetor body and is atomized and convected by the air stream past the throttle plate and into the intake manifold. Fuel evaporation starts within the carburetor and continues in the manifold as fuel droplets move with the air flow and as liquid fuel flows over the throttle and along the manifold walls. A modern carburetor which meters the appropriate fuel flow into the air stream over the complete engine operating range is a highly developed and complex device. There are many types of carburetors; they share the same basic concepts which we will now examine.

Figure 7-2 shows the essential components of an elementary carburetor. The air enters the intake section of the carburetor (1) from the air cleaner which removes suspended dust particles. The air then flows into the carburetor venturi (a converging-diverging nozzle) (2) where the air velocity increases and the pressure decreases. The fuel level is maintained at a constant height in the float chamber (3) which is connected via an air duct (4) to the carburetor intake section (1). The fuel flows through the main jet (a calibrated orifice) (5) as a result of the pressure difference between the float chamber and the venturi throat and through the fuel discharge nozzle (6) into the venturi throat where the air stream atomizes the liquid fuel. The fuel-air mixture flows through the diverging section of the venturi where the flow decelerates and some pressure recovery occurs. The flow then passes the throttle valve (7) and enters the intake manifold.

Note that the flow may be unsteady even when engine load and speed are constant, due to the periodic filling of each of the engine cylinders which draws air through the carburetor venturi. The induction time,  $1/(2N)$  (20 ms at 1500

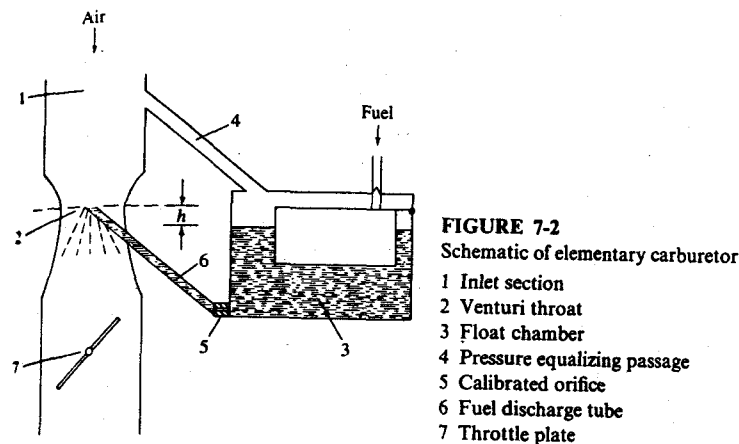


FIGURE 7-2  
Schematic of elementary carburetor.

- 1 Inlet section
- 2 Venturi throat
- 3 Float chamber
- 4 Pressure equalizing passage
- 5 Calibrated orifice
- 6 Fuel discharge tube
- 7 Throttle plate

rev/min), is the characteristic time of this periodic cylinder filling process. Generally, the characteristic times of changes in throttle setting are longer; it takes several engine operating cycles to reestablish steady-state engine operation after a sudden change in throttle position.<sup>2</sup> It is usually assumed that the flow processes in the carburetor can be modeled as quasi steady.

**FLOW THROUGH THE VENTURI.** Equation (C.8) in App. C relates the mass flow rate of a gas through a flow restriction to the upstream stagnation pressure and temperature, and the pressure at the throat. For the carburetor venturi:

$$\dot{m}_a = \frac{C_{D_T} A_T p_0}{\sqrt{RT_0}} \left( \frac{p_T}{p_0} \right)^{1/2} \left\{ \frac{2\gamma}{\gamma - 1} \left[ 1 - \left( \frac{p_T}{p_0} \right)^{(\gamma-1)/\gamma} \right] \right\}^{1/2} \quad (7.2)$$

where  $C_{D_T}$  and  $A_T$  are the discharge coefficient and area of the venturi throat, respectively. If we assume the velocity at the carburetor inlet can be neglected, Eq. (7.2) can be rearranged in terms of the pressure drop from upstream conditions to the venturi throat for the air stream,  $\Delta p_a = p_0 - p_T$ , as

$$\dot{m}_a = C_{D_T} A_T (2\rho_{ao} \Delta p_a)^{1/2} \Phi \quad (7.3)$$

where

$$\Phi = \left[ \left( \frac{\gamma}{\gamma - 1} \right) \frac{(p_T/p_0)^{2/\gamma} - (p_T/p_0)^{(\gamma+1)/\gamma}}{1 - (p_T/p_0)} \right]^{1/2} \quad (7.4)$$

and accounts for the effects of compressibility. Figure C-3 shows the value of  $\Phi$  as a function of pressure drop. For the normal carburetor operating range, where  $\Delta p_a/p_0 \leq 0.1$ , the effects of compressibility which reduce  $\Phi$  below 1.0 are small.

**FLOW THROUGH THE FUEL ORIFICE.** Since the fuel is a liquid and therefore essentially incompressible, the fuel flow rate through the main fuel jet is given by

Eq. (C.2) in App. C as

$$\dot{m}_f = C_{D_o} A_o (2\rho_f \Delta p_f)^{1/2} \quad (7.5)$$

where  $C_{D_o}$  and  $A_o$  are the discharge coefficient and area of the orifice, respectively,  $\Delta p_f$  is the pressure difference across the orifice, and the orifice area is assumed much less than the passage area. Usually, the fuel level in the float chamber is held below the fuel discharge nozzle, as shown in Fig. 7-2, to prevent fuel spillage when the engine is inclined to the horizontal (e.g., in a vehicle on a slope). Thus,

$$\Delta p_f = \Delta p_a - \rho_f gh$$

where  $h$  is typically of order 10 mm.

The discharge coefficient  $C_{D_o}$  in Eq. (7.5) represents the effect of all deviations from the ideal one-dimensional isentropic flow. It is influenced by many factors of which the most important are the following: (1) fluid mass flow rate; (2) orifice length/diameter ratio; (3) orifice/approach-area ratio; (4) orifice surface area; (5) orifice surface roughness; (6) orifice inlet and exit chamfers; (7) fluid specific gravity; (8) fluid viscosity; and (9) fluid surface tension. The use of the orifice Reynolds number,  $Re_o = \rho V D_o / \mu$ , as a correlating parameter for the discharge coefficient accounts for effects of mass flow rate, fluid density and viscosity, and length scale to a good first approximation. The discharge coefficient of a typical carburetor main fuel-metering system orifice increases smoothly with increasing  $Re_o$ .<sup>3</sup>

**CARBURETOR PERFORMANCE.** The air/fuel ratio delivered by this carburetor is given by

$$\left(\frac{A}{F}\right) = \frac{\dot{m}_a}{\dot{m}_f} = \left(\frac{C_{D_T}}{C_{D_o}}\right) \left(\frac{A_T}{A_o}\right) \left(\frac{\rho_{a0}}{\rho_f}\right)^{1/2} \left(\frac{\Delta p_a}{\Delta p_a - \rho_f gh}\right)^{1/2} \Phi \quad (7.6)$$

and the equivalence ratio  $\phi [= (A/F)_s / (A/F)]$  by

$$\phi = \frac{(A/F)_s}{\Phi} \left(\frac{C_{D_o}}{C_{D_T}}\right) \left(\frac{A_o}{A_T}\right) \left(\frac{\rho_f}{\rho_{a0}}\right)^{1/2} \left(1 - \frac{\rho_f gh}{\Delta p_a}\right)^{1/2} \quad (7.7)$$

where  $(A/F)_s$  is the stoichiometric air/fuel ratio. The terms  $A_o$ ,  $A_T$ ,  $\rho_f$ , and  $\rho_{a0}$  are all constant for a given carburetor, fuel, and ambient conditions. Also, except for very low flows,  $\rho_f gh \ll \Delta p_a$ . The discharge coefficients,  $C_{D_o}$  and  $C_{D_T}$ , and  $\Phi$  vary with flow rates, however. Hence, the equivalence ratio of the mixture delivered by an elementary carburetor is not constant.

Figure 7-3 illustrates the performance of the elementary carburetor. The top set of curves shows how  $\Phi$ ,  $C_{D_T}$ , and  $C_{D_o}$  typically vary with the venturi pressure drop.<sup>4</sup> Note that for  $\Delta p_a \leq \rho_f gh$  there is no fuel flow. Once fuel starts to flow, as a consequence of these variations the fuel flow rate increases more rapidly than the air flow rate. The carburetor delivers a mixture of increasing fuel/air equivalence ratio as the flow rate increases. Suppose the venturi and orifice are sized to

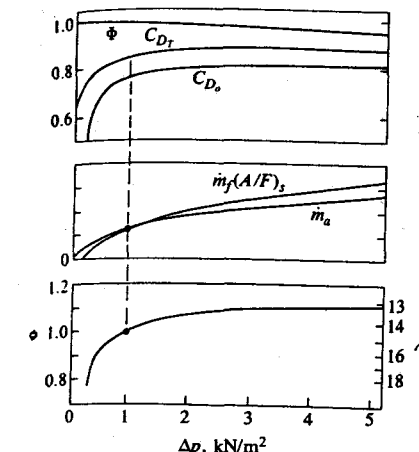


FIGURE 7-3

Performance of elementary carburetor: variation of  $C_{D_T}$ ,  $C_{D_o}$ ,  $\Phi$ ,  $\dot{m}_f (A/F)_s$ ,  $\dot{m}_a$ , and equivalence ratio  $\phi$  with venturi pressure drop.

give a stoichiometric mixture at an air flow rate corresponding to  $1 \text{ kN/m}^2$  venturi pressure drop (middle graph in Fig. 7-3). At higher air flow rates, the carburetor will deliver a fuel-rich mixture; at very high flow rates it will eventually deliver an essentially constant equivalence ratio. At lower air flow rates, the mixture delivered leans out rapidly. Thus, the elementary carburetor cannot provide the variation in mixture ratio which the engine requires over the complete load range at any given speed (see Fig. 7-1).

The deficiencies of the elementary carburetor can be summarized as follows:

- At low loads the mixture becomes leaner; the engine requires the mixture to be enriched at low loads.
- At intermediate loads, the mixture equivalence ratio increases slightly as the air flow increases. The engine requires an almost constant equivalence ratio.
- As the air flow approaches the maximum wide-open throttle value, the equivalence ratio remains essentially constant. However, the mixture equivalence ratio should increase to 1.1 or greater to provide maximum engine power.
- The elementary carburetor cannot compensate for transient phenomena in the intake manifold. Nor can it enrich the mixture during engine starting and warm-up.
- The elementary carburetor cannot adjust to changes in ambient air density (due primarily to changes in altitude).

## 7.2.2 Modern Carburetor Design

The changes required in the elementary carburetor so that it provides the equivalence ratio versus air flow distribution shown in Fig. 7-1 are:

1. The *main metering system* must be compensated to provide essentially constant lean or stoichiometric mixtures over the 20 to 80 percent air flow range.
2. An *idle system* must be added to meter the fuel flow at idle and light loads.
3. An *enrichment system* must be added so the engine can provide its maximum power as wide-open throttle is approached.
4. An *accelerator pump* which injects additional fuel when the throttle is opened rapidly is required to maintain constant the equivalence ratio delivered to the engine cylinder.
5. A *choke* must be added to enrich the mixture during engine starting and warm-up to ensure a combustible mixture within each cylinder at the time of ignition.
6. *Altitude compensation* is required to adjust the fuel flow to changes in air density.

In addition, it is necessary to increase the magnitude of the pressure drop available for controlling the fuel flow. Two common methods used to achieve this are the following.

**BOOST VENTURIS.** The carburetor venturi should give as large a vacuum at the throat as possible at maximum air flow, within the constraints of a low pressure loss across the complete venturi and diffuser. In a single venturi, as the diameter of the throat is decreased at a given air flow to increase the flow velocity and hence the metering signal at the throat, the pressure loss increases. A higher vacuum signal at the venturi throat and higher velocities for improved atomization can be obtained without increasing the overall pressure loss through the use of multiple venturis. Figure 7-4 shows the geometry and the pressure distribution in a typical double-venturi system. A boost venturi is positioned upstream of the throat of the larger main venturi, with its discharge at the location of maximum velocity in the main venturi. Only a fraction of the air flows through the boost venturi. Since the pressure at the boost venturi exit equals the pressure

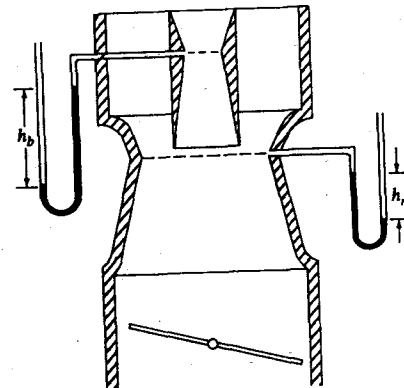


FIGURE 7-4  
Schematic of carburetor double-venturi system.

at the main venturi *throat*, a higher vacuum  $\Delta p_b = \rho_m gh_b$  is obtained at the boost venturi throat which can be used to obtain more precise metering of the fuel ( $\rho_m$  is the manometer fluid density). Best results are obtained with the boost venturi exit slightly upstream ( $\approx 5$  mm) of the main venturi throat. Because only a fraction of the total air flow goes through the boost venturi, the use of multiple venturis makes it possible to obtain a high velocity air stream (up to 200 m/s) where the fuel is introduced at the boost venturi throat, and adequate vacuum, and to reduce the pressure loss across the total venturi system, without increasing the height of the carburetor. The fuel is better atomized in the smaller boost venturi with its higher air velocity, and since this air and fuel mixture is discharged centrally into the surrounding venturi, a more homogeneous mixture results. The vacuum developed at the venturi throat of a typical double-venturi system is about twice the theoretical vacuum of a single venturi of the same flow area.<sup>5</sup> A triple-venturi system can be used to give further increases in metering signal. The overall discharge coefficient of a multiple-venturi carburetor is lower than a single-venturi carburetor of equal cross-sectional area. The throat area of the main venturi in a multiple-venturi system is usually increased, therefore, above the single-venturi size to compensate for this. Some decrease in air stream velocity is tolerated to maintain a high discharge coefficient (and hence a high volumetric efficiency).<sup>6</sup>

**MULTIPLE-BARREL CARBURETORS.** Use of carburetors with venturi systems in parallel is a common way of maintaining an adequate part-load metering signal, high volumetric efficiency at wide-open throttle, and minimum carburetor height as engine size and maximum air flow increases. As venturi size in a single-barrel carburetor is increased to provide a higher engine air flow at maximum power, the venturi length increases and the metering signal generated at low flows decreases. Maximum wide-open throttle air flow is some 30 to 70 times the idle air flow (the value depending on engine displacement). Two-barrel carburetors usually consist of two single-barrel carburetors mounted in parallel. Four-barrel carburetors consist of a pair of two-barrel carburetors in parallel, with throttle plates compounded on two shafts. Air flows through the primary barrel(s) at low and intermediate engine loads. At higher loads, the throttle plate(s) on the secondary barrel(s) (usually of larger cross-sectional area) start to open when the air flow exceeds about 50 percent of the maximum engine air flow.

There are many different designs of complete carburetors. The operating principles of the methods most commonly used to achieve the above listed modifications will now be reviewed. Figure 7-5 shows a schematic of a conventional modern carburetor and the names of the various components and fuel passages.

**COMPENSATION OF MAIN METERING SYSTEM.** Figure 7-6 shows a main fuel-metering system with air-bleed compensation. As the pressure at the venturi throat decreases, air is bled through an orifice (or series of orifices) into the main fuel well. This flow reduces the pressure difference across the main fuel-metering orifice which no longer experiences the full venturi vacuum. The mixing of bleed

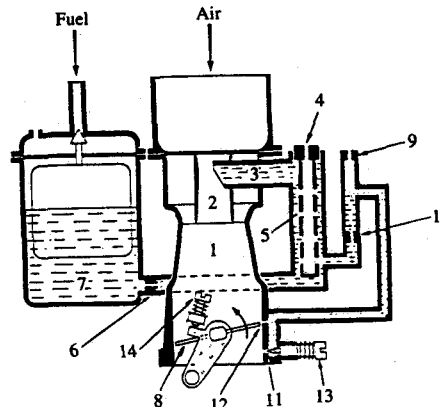


FIGURE 7-5  
Schematic of modern carburetor.

- 1 Main venturi
- 2 Boost venturi
- 3 Main metering spray tube or nozzle
- 4 Air-bleed orifice
- 5 Emulsion tube or well
- 6 Main fuel-metering orifice
- 7 Float chamber
- 8 Throttle plate
- 9 Idle air-bleed orifice
- 10 Idle fuel orifice
- 11 Idle mixture orifice
- 12 Transition orifice
- 13 Idle mixture adjusting screw
- 14 Idle throttle setting adjusting screw

Fuel enters the air stream from the main metering system through (3). At idle, fuel enters air at (11). During transition, fuel enters at (11), (12), and (3). (Courtesy S.p.A.E. Weber.)

air with the fuel forms an emulsion which atomizes more uniformly to smaller drop sizes on injection at the venturi throat. The schematic in Fig. 7-6 illustrates the operating principle. When the engine is not running, the fuel is at the same level in the float bowl and in the main well. With the engine running, as the throttle plate is opened, the air flow and the vacuum in the venturi throat increase. For  $\Delta p_v (= p_0 - p_v) < \rho_f g h_1$ , there is no fuel flow from the main metering system. For  $\rho_f g h_1 < \Delta p_v < \rho_f g h_2$ , only fuel flows through the main well and nozzle, and the system operates just like an elementary carburetor. For  $\Delta p_v > \rho_f g h_2$ , air enters the main well together with fuel. The amount of air entering the well is controlled by the size of the main air-bleed orifice. The amount of air is

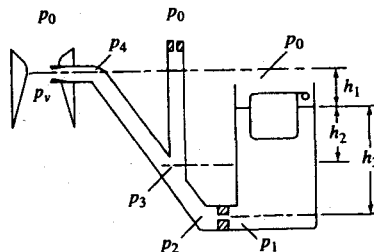


FIGURE 7-6  
Schematic of main metering system with air-bleed compensation.

small and does not significantly affect the composition of the mixture. The air-bleed mass flow rate is given by

$$\dot{m}_{ab} = C_{D_b} A_b [2(p_0 - p_3)\rho_a]^{1/2} \quad (7.8)$$

where  $C_{D_b}$  and  $A_b$  are the discharge coefficient and the area of the air-bleed orifice. The fuel mass flow rate through the fuel orifice is given by

$$\dot{m}_f = C_{D_o} A_o [2(p_1 - p_2)\rho_f]^{1/2} \quad (7.9)$$

where

$$p_1 = p_0 + \rho_f g h_3 \quad \text{and} \quad p_2 = p_3 + \rho_f g(h_3 - h_2)$$

The density of the emulsion  $\rho_{em}$  in the main well and nozzle is usually approximated by

$$\rho_{em} = \frac{\dot{m}_{ab} + \dot{m}_f}{\dot{m}_{ab}/\rho_a + \dot{m}_f/\rho_f} \quad (7.10)$$

Since typical values are  $\rho_f = 730 \text{ kg/m}^3$  and  $\rho_a = 1.14 \text{ kg/m}^3$ , usually  $\rho_f \gg \rho_{em} \gg \rho_a$ . Thus, as the air-bleed flow rate increases, the height of the column of emulsion becomes less significant. However, the decrease in emulsion density due to increasing air bleed increases the flow velocity, which results in a significant pressure drop across the main nozzle. This pressure drop depends on nozzle length and diameter, fuel flow rate, bleed air flow rate, relative velocity between fuel and bleed air, and fuel properties. It is determined empirically, and has been found to correlate with  $\rho_{em}$  [as defined by Eq. (7.10)].<sup>2,6</sup> The pressure loss at the main discharge nozzle with two-phase flow can be several times the pressure loss with single-phase flow.

Figure 7-7 illustrates the behavior of the system shown in Fig. 7-6:  $\dot{m}_a$ ,  $\dot{m}_f$ , and the fuel/air equivalence ratio  $\phi$  are plotted against  $\Delta p_v$ . Once the bleed system is operating ( $\Delta p_v > \rho_f g h_2$ ) the fuel flow rate is reduced below its equivalent elementary carburetor value (the  $A_b = 0$  line). As the bleed orifice area is increased, in the limit of large  $A_b$  and neglecting the pressure losses in the main nozzle, the fuel flow rate remains constant ( $A_b \rightarrow \infty$ ). An appropriate choice of bleed orifice area  $A_b$  will provide the desired equivalence ratio versus pressure drop or air flow characteristic.

Additional control flexibility is obtained in practice through use of a second orifice, or of a series of holes in the main well or emulsion tube as shown in Fig. 7-5. Main metering systems with controlled air bleed provide reliable and stable control of mixture composition at part throttle engine operation. They are simple, have considerable design flexibility, and atomize the fuel effectively. In some carburetor designs, an additional compensation system consisting of a tapered rod or needle in the main metering orifice is used. The effective open area of the main metering orifice, and hence the fuel flow rate, can thus be directly related to throttle position (and manifold vacuum).

A wide range of two-phase flow patterns can be generated by bleeding an air flow into a liquid flow. Fundamental studies of the generation and flow of

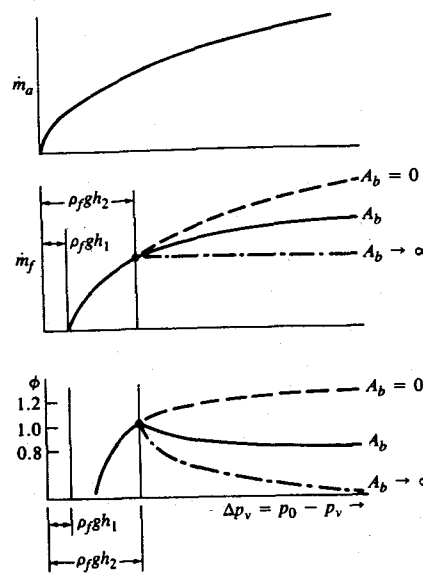


**FIGURE 7-7**  
Metering characteristics of system with air-bleed compensation: mass flow rate of air  $\dot{m}_a$ , mass flow rate of fuel  $\dot{m}_f$ , and equivalence ratio  $\phi$  as functions of venturi pressure drop for different air-bleed orifice areas  $A_b$ .

two-phase mixtures in small diameter tubes with bleed holes similar to those used in carburetors have been carried out.<sup>7</sup> For a given pipe and bleed hole size, the type of flow pattern set up depends on the flow rates of the two phases.

**IDLE SYSTEM.** The idle system is required because at low air flows through the carburetor insufficient vacuum is created at the venturi throat to draw fuel into the air stream. However, at idle and light loads, the manifold vacuum is high, with the pressure drop occurring across the almost-closed throttle plate. This low manifold pressure at idle is exploited for the idle fuel system by connecting the main fuel well to an orifice in the throttle body downstream of the throttle plate. Figure 7-5 shows the essential features of an idle system. The main well (5) is connected through one or more orifices (10), past one or more idle air-bleed orifices (or holes) (9), past an idle mixture adjusting screw (13), to the idle discharge port (11) in the throttle body. Emulsifying air is admitted into the idle system [at (9) and (12)] to reduce the pressure drop across the idle port and permit larger-sized ports (which are easier to manufacture) to be used. Satisfactory engine operation at idle is obtained empirically by means of the idle throttle position stop adjustment (14) and the idle mixture adjustment (13). As the throttle is opened from its idle position, the idle metering system performs a transitional function. One or more holes (12) located above the idle discharge port (11) assist as air bleeds when the throttle is at or near its idle position. As the throttle plate opens and the air flow increases, these additional discharge holes are exposed to the manifold vacuum. Additional fuel is forced out of these holes into the air stream to provide the appropriate mixture ratio. As the throttle plate is opened further, the main fuel metering system starts to supply fuel also. Because the two

systems are coupled, they interact and the main system behavior in this *transition region* is modified by the fuel flow through the idle system. The total combined fuel flow provides a rich (or close-to-stoichiometric) mixture at idle, a progressive leaning of the mixture as air flow increases, and eventually (as the main system takes over full control of the fuel flow rate) an approximately constant mixture composition.

**POWER ENRICHMENT SYSTEM.** This system delivers additional fuel to enrich the mixture as wide-open throttle is approached so the engine can deliver its maximum power. The additional fuel is normally introduced via a submerged valve which communicates directly with the main discharge nozzle, bypassing the metering orifice. The valve, which is spring loaded, is operated either mechanically through a linkage with the throttle plate (opening as the throttle approaches its wide-open position) or pneumatically (using manifold vacuum).

**ACCELERATOR PUMP.** When the throttle plate is opened rapidly, the fuel-air mixture flowing into the engine cylinder leans out temporarily. The primary reason for this is the time lag between fuel flow into the air stream at the carburetor and the fuel flow past the inlet valve (see Sec. 7.6.3). While much of the fuel flow into the cylinder is fuel vapor or small fuel droplets carried by the air stream, a fraction of the fuel flows onto the manifold and port walls and forms a liquid film. The fuel which impacts on the walls evaporates more slowly than fuel carried by the air stream and introduces a lag between the air/fuel ratio produced at the carburetor and the air/fuel ratio delivered to the cylinder. An accelerator pump is used as the throttle plate is opened rapidly to supply additional fuel into the air stream at the carburetor to compensate for this leaning effect. Typically, fuel is supplied to the accelerator pump chamber from the float chamber via a small hole in the bottom of the fuel bowl, past a check valve. A pump diaphragm and stem is actuated by a rod attached to the throttle plate lever. When the throttle is opened to increase air flow, the rod-driven diaphragm will increase the fuel pressure which shuts the valve and discharges fuel past a discharge check valve or weight in the discharge passage, through the accelerator pump discharge nozzle(s), and into the air stream. A calibrated orifice controls the fuel flow. A spring connects the rod and diaphragm to extend the fuel discharge over the appropriate time period and to reduce the mechanical strain on the linkage.

**CHOKE.** When a cold engine is started, especially at low ambient temperatures, the following factors introduce additional special requirements for the complete carburetor:

1. Because the starter-cracked engine turns slowly (70 to 150 rev/min) the intake manifold vacuum developed during engine start-up is low.
2. This low manifold vacuum draws a lower-than-normal fuel flow from the carburetor idle system.

3. Because of the low manifold temperature and vacuum, fuel evaporation in the carburetor, manifold, and inlet port is much reduced.

Thus, during cranking, the mixture which reaches the engine cylinder would be too lean to ignite. Until normal manifold conditions are established, fuel distribution is also impaired. To overcome these deficiencies and ensure prompt starts and smooth operation during engine warm-up, the carburetor must supply a fuel-rich mixture. This is obtained with a choke. Once normal manifold conditions are established, the choke must be excluded. The primary element of a typical choke system is a plate, upstream of the carburetor, which can close off the intake system. At engine start-up, the choke plate is closed to restrict the air flow into the carburetor barrel. This causes almost full manifold vacuum within the venturi which draws a large fuel flow through the main orifice. When the engine starts, the choke is partly opened to admit the necessary air flow and reduce the vacuum in the venturi to avoid flooding the intake with fuel. As the engine warms up, the choke is opened either manually or automatically with a thermostatic control. For normal engine operation the choke plate is fully open and does not influence carburetor performance. A manifold vacuum control is often used to close the choke plate partially if the engine is accelerated during warm-up. During engine warm-up the idle speed is increased to prevent engine stalling. A fast idle cam is rotated into position by the automatic choke lever.

**ALTITUDE COMPENSATION.** An inherent characteristic of the conventional float type carburetor is that it meters fuel flow in proportion to the air volume flow rate. Air density changes with ambient pressure and temperature, with changes due to changes in pressure with altitude being most significant. For example, at 1500 m above sea level, mean atmospheric pressure is 634 mmHg or 83.4 percent of the mean sea-level value. While ambient temperature variations, winter to summer, can produce changes of comparable magnitude, the temperature of the air entering the carburetor for warmed-up engine operation is controlled to within much closer tolerances by drawing an appropriate fraction of the air from around the exhaust manifold.

Equation (7.6) shows how the air/fuel ratio delivered by the main metering system will vary with inlet air conditions. The primary dependence is through the  $\sqrt{\rho_{a_0}}$  term; depending on what is held constant (e.g., throttle setting or air mass flow rate) there may be an additional, much smaller dependence through  $\Phi$  and  $\Delta p_a$  (see Ref. 5). To a good approximation, the enrichment  $E$  with increasing altitude  $z$  is given by

$$1 + E = \frac{(F/A)_z}{(F/A)_0} = \left( \frac{\rho_{a_0}}{\rho_{a_z}} \right)^{1/2} \quad (7.11)$$

For  $z = 1500$  m,  $E = 9.5$  percent; thus, a cruise equivalence ratio of 0.9 or  $(A/F) = 16.2$  would be enriched to close to stoichiometric.

The effects of increase in altitude on the carburetor flow curve shown in Fig. 7-1 are: (1) to enrich the entire part-throttle portion of the curve and (2) to

bring in the power-enrichment system at a lower air flow rate due to decreased manifold vacuum. To reduce the impact to changes in altitude on engine emissions of CO and HC, modern carburetors are altitude compensated. A number of methods can be used to compensate for changes in ambient pressure with altitude:

1. *Venturi bypass method.* To keep the air volume flow rate through the venturi equal to what it was at sea-level atmospheric pressure (calibration condition), a bypass circuit around the venturi for the additional volume flow is provided.
2. *Auxiliary jet method.* An auxiliary fuel metering orifice with a pressure-controlled tapered metering rod connects the fuel bowl to the main well in parallel with the main metering orifice.
3. *Fuel bowl back-suction method.* As altitude increases, an aneroid bellows moves a tapered rod from an orifice near the venturi throat, admitting to the bowl an increasing amount of the vacuum signal developed at the throat.
4. *Compensated air-bleed method.* The orifices in the bleed circuits to each carburetor system are fitted with tapered metering pins actuated by a single aneroid bellows.<sup>8</sup>

**TRANSIENT EFFECTS.** The pulsating and transient nature of the flow through a carburetor during actual engine operation is illustrated by the data shown in Fig. 7-8.<sup>2</sup> The changes in pressure with time in the intake manifold and at the boost venturi throat of a standard two-barrel carburetor installed on a production V-8 engine are shown as the throttle is opened from light load (22°) to wide-open throttle at 1000 rev/min. Note the rapid increase in boost venturi suction as the throttle is suddenly opened. This results from the sudden large increase in the air flow rate and corresponding increase in air velocity within the boost venturi. Note also that the pressure fluctuations decay rapidly, and within a few engine revolutions have stabilized at the periodic values associated with the new throttle angle. At wide-open throttle, the pulsating nature of the flow as each

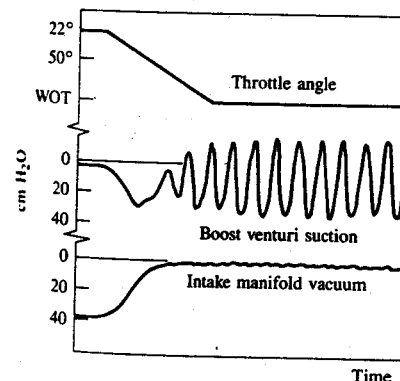


FIGURE 7-8

Throttle angle, boost venturi suction, and intake manifold vacuum variation with time as throttle is opened from light load (22°) to wide-open throttle at 1000 rev/min. Standard two-barrel carburetor and production V-8 engine.<sup>2</sup>

cylinder draws in its charge is evident. The pressure drop across the main metering jet also fluctuates. The pulsations in the venturi air flow (and hence fuel flow) due to the filling of each cylinder in turn are negligibly small at small throttle angles and increase to a maximum at wide-open throttle. At small throttle openings, the choked flow at the throttle plate prevents the manifold pressure fluctuations from propagating upstream into the venturi. The effective time-averaged boost venturi suction is greater for the pulsating flow case than for the steady flow case. If the ratio of the effective metering signal for a pulse cycle to that for steady air flow at the same average mass flow is denoted as  $1 + \Omega$ , where  $\Omega$  is the pulsation factor, then  $\Omega$  is related to the amplitude and frequency of pressure waves within the intake manifold as well as the damping effect of the throttle plate. An empirical equation for  $\Omega$  is

$$\Omega = \frac{\text{constant} \times (1 - M)p_m n_R}{Nn_{c/b}} \quad (7.12)$$

where  $M$  is the throttle plate Mach number,  $p_m$  the manifold pressure,  $n_R$  the number of revolutions per power stroke,  $N$  the crank speed, and  $n_{c/b}$  the number of cylinders per barrel. The value of the constant depends on carburetor and engine geometry. For  $p_m$  in kilonewtons per square meter and  $N$  in revolutions per minute a typical value for the constant is 7.3.<sup>2</sup> Thus, at wide-open throttle at 1500 rev/min,  $\Omega$  has a value of about 0.2. The transient behavior of the air and fuel flows in the manifold are discussed more fully in Sec. 7.6.

### 7.3 FUEL-INJECTION SYSTEMS

#### 7.3.1 Multipoint Port Injection

The fuel-injection systems for conventional spark-ignition engines inject the fuel into the engine intake system. This section reviews systems where the fuel is injected into the intake port of each engine cylinder. Thus these systems require one injector per cylinder (plus, in some systems, one or more injectors to supplement the fuel flow during starting and warm-up). There are both mechanical injection systems and electronically controlled injection systems. The advantages of port fuel injection are increased power and torque through improved volumetric efficiency and more uniform fuel distribution, more rapid engine response to changes in throttle position, and more precise control of the equivalence ratio during cold-start and engine warm-up. Fuel injection allows the amount of fuel injected per cycle, for each cylinder, to be varied in response to inputs derived from sensors which define actual engine operating conditions. Two basic approaches have been developed; the major difference between the two is the method used to determine the air flow rate.

Figure 7-9 shows a schematic of a *speed-density* system, where engine speed and manifold pressure and air temperature are used to calculate the engine air flow. The electrically driven fuel pump delivers the fuel through a filter to the fuel line. A pressure regulator maintains the pressure in the line at a fixed value (e.g.,

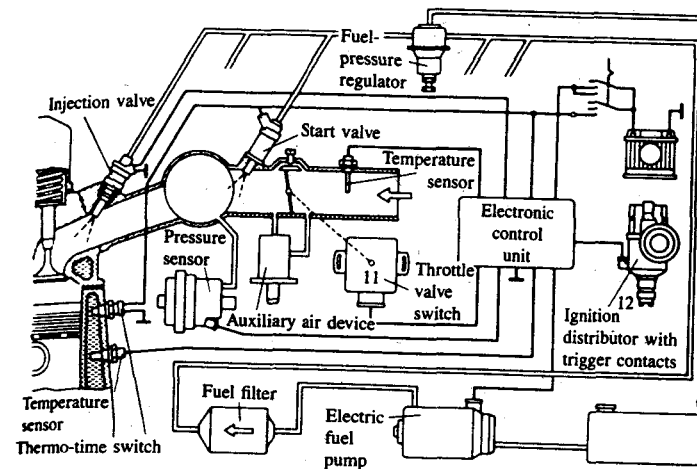


FIGURE 7-9  
Speed-density electronic multipoint port fuel-injection system: Bosch D-Jetronic System.<sup>9</sup> (Courtesy Robert Bosch GmbH and SAE.)

270 kN/m<sup>2</sup>, 39 lb/in<sup>2</sup>, usually relative to manifold pressure to maintain a constant fuel pressure drop across the injectors). Branch lines lead to each injector; the excess fuel returns to the tank via a second line. The induced air flows through the air filter, past the throttle plate to the intake manifold. Separate runners and branches lead to each inlet port and engine cylinder. An electromagnetically actuated fuel-injection valve (see Fig. 7-10) is located either in the intake manifold tube or the intake port of each cylinder. The major components of the injector are the valve housing, the injector spindle, the magnetic plunger to which the spindle is connected, the helical spring, and the solenoid coil. When the solenoid is not excited, the solenoid plunger of the magnetic circuit is forced, with its seal, against the valve seat by the helical spring and closes the fuel passage. When the solenoid coil is excited, the plunger is attracted and lifts the spindle about

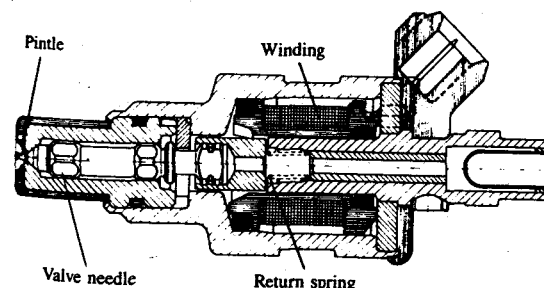


FIGURE 7-10  
Cross section of fuel injector.<sup>10</sup>

0.15 mm so that fuel can flow through the calibrated annular passage around the valve stem. The front end of the injector spindle is shaped as an atomizing pintle with a ground top to atomize the injected fuel. The relatively narrow spray cone of the injector, shown in the photo in Fig. 7-11, minimizes the intake manifold wall wetting with liquid fuel. The mass of fuel injected per injection is controlled by varying the duration of the current pulse that excites the solenoid coil. Typical injection times for automobile applications range from about 1.5 to 10 ms.<sup>11</sup>

The appropriate coil excitation pulse duration or width is set by the electronic control unit (ECU). In the speed-density system, the primary inputs to the ECU are the outputs from the manifold pressure sensor, the engine speed sensor (usually integral with the distributor), and the temperature sensors installed in the intake manifold to monitor air temperature and engine block to monitor the water-jacket temperature—the latter being used to indicate fuel-enrichment requirements during cold-start and warm-up. For warm-engine operation, the mass of air per cylinder per cycle  $m_a$  is given by

$$m_a = \eta_v(N) \rho_a(T_i, p_i) V_d = \frac{\eta_v V_d p_i}{R_a T_i} \quad (7.13)$$

where  $\eta_v$  is the volumetric efficiency,  $N$  is engine speed,  $\rho_a$  is the inlet air density, and  $V_d$  is the displaced volume per cylinder. The electronic control unit forms the pulse which excites the injector solenoids. The pulse width depends primarily on the manifold pressure; it also depends on the variation in volumetric efficiency  $\eta_v$  with speed  $N$  and variations in air density due to variations in air temperature. The control unit also initiates mixture enrichment during cold-engine operation and during accelerations that are detected by the throttle sensor.



FIGURE 7-11  
Short time-exposure photograph of liquid fuel spray from Bosch-type injector. (Courtesy Robert Bosch GmbH.)

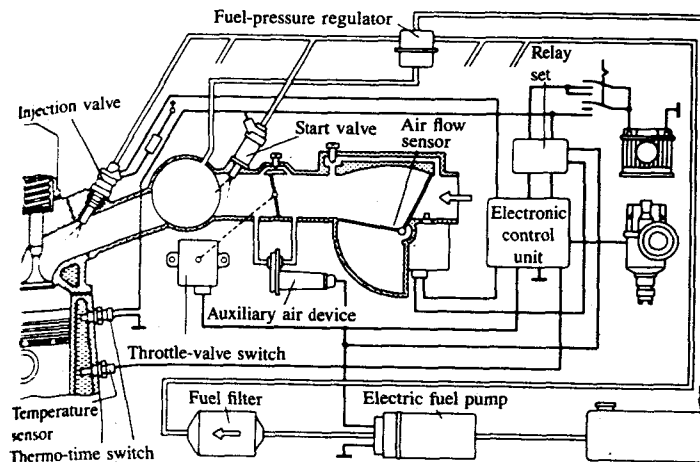


FIGURE 7-12

Electronic multipoint port fuel-injection system with air-flow meter: Bosch L-Jetronic system.<sup>9</sup> (Courtesy Robert Bosch GmbH and SAE.)

Figure 7-12 shows an alternative EFI system (the Bosch L-Jetronic) which uses an air-flow meter to measure air flow directly. The air-flow meter is placed upstream of the throttle. The meter shown measures the force exerted on a plate as it is displaced by the flowing air stream; it provides a voltage proportional to the air flow rate. An alternative air-flow measuring approach is to use a hot-wire air mass flow meter.<sup>10</sup> The advantages of direct air-flow measurement are:<sup>12</sup> (1) automatic compensation for tolerances, combustion chamber deposit buildup, wear and changes in valve adjustments; (2) the dependence of volumetric efficiency on speed and exhaust backpressure is automatically accounted for; (3) less acceleration enrichment is required because the air-flow signal precedes the filling of the cylinders; (4) improved idling stability; and (5) lack of sensitivity of the system to EGR since only the fresh air flow is measured.

The mass of air inducted per cycle to each cylinder,  $m_a$ , varies as

$$m_a \propto \frac{\dot{m}_a}{N} \quad (7.14)$$

Thus the primary signals for the electronic control unit are air flow and engine speed. The pulse width is inversely proportional to speed and directly proportional to air flow. The engine block temperature sensor, starter switch, and throttle valve switch provide input signals for the necessary adjustments for cold-start, warm-up, idling, and wide-open throttle enrichment.

For cold-start enrichment, one (or more) cold-start injector valve is used to inject additional fuel into the intake manifold (see Figs. 7-9 and 7-12). Since short opening and closing times are not important, this valve can be designed to

provide extremely fine atomization of the fuel to minimize the enrichment required.

Mechanical, air-flow-based metering, continuous injection systems are also used. Figure 7-13 shows a schematic of the Bosch K-Jetronic system.<sup>9,10</sup> Air is drawn through the air filter, flows past the air-flow sensor, past the throttle valve, into the intake manifold, and into the individual cylinders. The fuel is sucked out of the tank by a roller-cell pump and fed through the fuel accumulator and filter to the fuel distributor. A primary pressure regulator in the fuel distributor maintains the fuel pressure constant. Excess fuel not required by the engine flows back to the tank. The mixture-control unit consists of the air-flow sensor and fuel distributor. It is the most important part of the system, and provides the desired metering of fuel to the individual cylinders by controlling the cross section of the metering slits in the fuel distributor. Downstream of each of these metering slits is a differential pressure valve which for different flow rates maintains the pressure drop at the slits constant.

Fuel-injection systems offer several options regarding the timing and location of each injection relative to the intake event.<sup>10</sup> The K-Jetronic mechanical injection system injects fuel continuously in front of the intake valves with the spray directed toward the valves. Thus about three-quarters of the fuel required for any engine cycle is stored temporarily in front of the intake valve, and one-quarter enters the cylinder directly during the intake process.

With electronically controlled injection systems, the fuel is injected intermittently toward the intake valves. The fuel-injection pulse width to provide the appropriate mass of fuel for each cylinder air charge varies from about 1.5 to 10 ms over the engine load and speed range. In crank angle degrees this varies

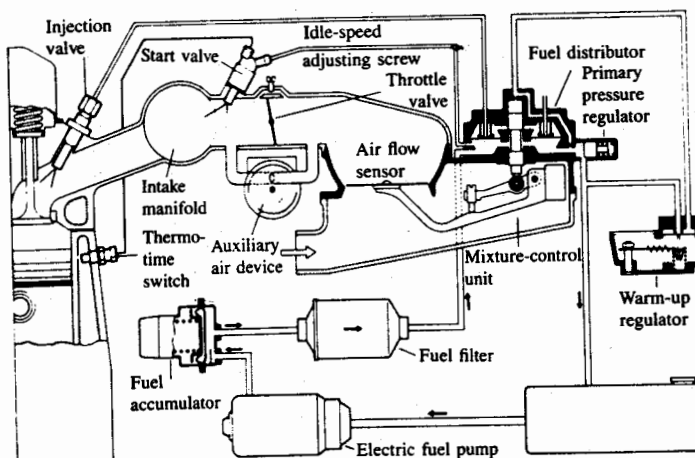


FIGURE 7-13  
Mechanical multipoint port fuel-injection system: Bosch K-Jetronic system.<sup>9</sup> (Courtesy Robert Bosch GmbH and SAE.)

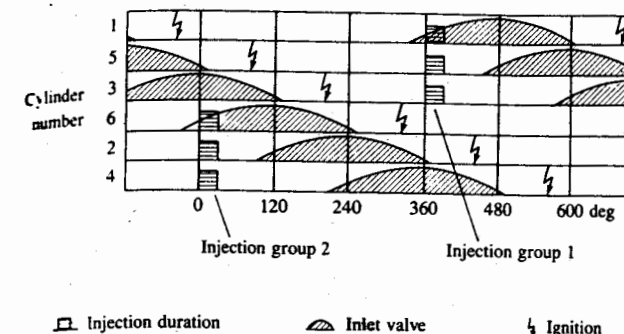
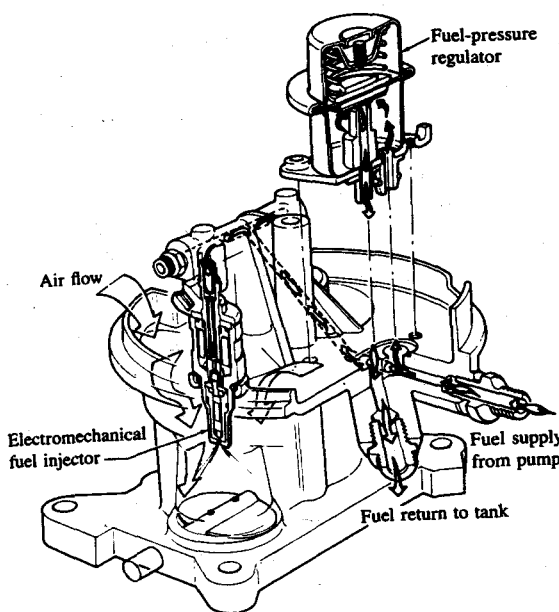


FIGURE 7-14  
Injection pulse diagram for D-Jetronic system in six-cylinder engine.<sup>10</sup>

from about 10° at light load and low speed to about 300° at maximum speed and load. Thus the pulse width varies from being much less than to greater than the duration of the intake stroke. To reduce the complexity of the electronic control unit, groups of injectors are often operated simultaneously. In the Bosch L-Jetronic system, all injectors are operated simultaneously. To achieve adequate mixture uniformity, given the short pulse width relative to the intake process over much of the engine load-speed range, fuel is injected twice per cycle; each injection contributes half the fuel quantity required by each cylinder per cycle. (This approach is called simultaneous double-firing.) In the speed-density system, the injectors are usually divided into groups, each group being pulsed simultaneously. For example, for a six-cylinder engine, two groups of three injectors may be used. Injection for each group is timed to occur while the inlet valves are closed or just starting to open, as shown in Fig. 7-14. The other group of injectors inject one crank revolution later. Sequential injection timing, where the phasing of each injection pulse relative to its intake valve lift profile is the same, is another option. Engine performance and emissions do change as the timing of the start of injection relative to inlet valve opening is varied. Injection with valve lift at its maximum, or decreasing, is least desirable.<sup>10</sup>

### 7.3.2 Single-Point Throttle-Body Injection

Single-point fuel-injection systems, where one or two electronically controlled injectors meter the fuel into the air flow directly above the throttle body, are also used. They provide straightforward electronic control of fuel metering at lower cost than multipoint port injection systems. However, as with carburetor systems, the problems associated with slower transport of fuel than the air from upstream of the throttle plate to the cylinder must now be overcome (see Sec. 7.6). Figure 7-15 shows a cutaway of one such system.<sup>13</sup> Two injectors, each in a separate air-flow passage with its own throttle plate, meter the fuel in response to calibrations of air flow based on intake manifold pressure, air temperature, and



**FIGURE 7-15**  
Cutaway drawing of a two-injector throttle-body electronic fuel-injection system.<sup>13</sup>

engine speed using the speed-density EFI logic described in the previous section. Injectors are fired alternatively or simultaneously, depending on load and speed and control logic used. Under alternative firing, each injection pulse corresponds to one cylinder filling. Smoothing of the fuel-injection pulses over time is achieved by proper placement of the fuel injector assembly above the throttle bore and plate. The walls and plate accumulate liquid fuel which flows in a sheet toward the annular throttle opening (see Sec. 7.6.3). The high air velocity created

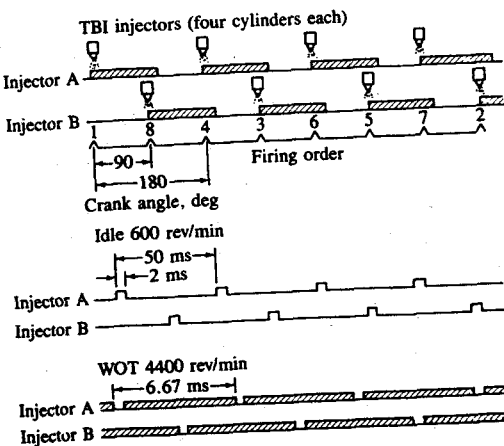


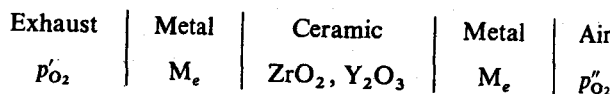
**FIGURE 7-16**  
Injector fuel delivery schedule for two-injector throttle-body injection system for eight-cylinder engine with dual plane intake manifold. Each injection nozzle feeds one plane of the manifold and its four cylinders.<sup>14</sup>

by the pressure drop across the throttle shears and atomizes the liquid sheet. Vigorous mixing of fuel and air then occurs, especially at part throttle, and provides good mixture uniformity and distribution between cylinders. Injector fuel delivery scheduling is illustrated in Fig. 7-16 for an eight-cylinder engine for a throttle-body fuel-injection system.<sup>14</sup>

#### 7.4 FEEDBACK SYSTEMS

It is possible to reduce engine emissions of the three pollutants—unburned hydrocarbons, carbon monoxide, and oxides of nitrogen—with a single catalyst in the exhaust system if the engine is operated very close to the stoichiometric air/fuel ratio. Such systems (called three-way catalyst systems) are described in more detail in Sec. 11.6.2. The engine operating air/fuel ratio is maintained close to stoichiometric through the use of a sensor in the exhaust system, which provides a voltage signal dependent on the oxygen concentration in the exhaust gas stream. This signal is the input to a feedback system which controls the fuel feed to the intake.

The sensor [called an oxygen sensor or lambda sensor— $\lambda$  being the symbol used for the relative air/fuel ratio, Eq. (3.9)] is an oxygen concentration cell with a solid electrolyte through which the current is carried by oxygen ions. The electrolyte is yttria ( $\text{Y}_2\text{O}_3$ )-stabilized zirconia ( $\text{ZrO}_2$ ) ceramic which separates two gas chambers (the exhaust manifold and the atmosphere) which have different oxygen partial pressures. The cell can be represented as a series of interfaces as follows:



$p''_\text{O}_2$  is the oxygen partial pressure of the air ( $\approx 20 \text{ kN/m}^2$ ) and  $p'_\text{O}_2$  is the equilibrium oxygen partial pressure in the exhaust gases. An electrochemical reaction takes place at the metal electrodes:



and the oxygen ions transport the current across the cell. The open-circuit output voltage of the cell  $V_o$  can be related to the oxygen partial pressures  $p'_\text{O}_2$  and  $p''_\text{O}_2$  through the Nernst equation:

$$V_o = \frac{RT}{4F} \ln \left( \frac{p''_\text{O}_2}{p'_\text{O}_2} \right) \quad (7.15)$$

where  $F$  is the Faraday constant. Equilibrium is established in the exhaust gases by the catalytic activity of the platinum metal electrodes. The oxygen partial pressure in equilibrated exhaust gases decreases by many orders of magnitude as the equivalence ratio changes from 0.99 to 1.01, as shown in Fig. 7-17a. Thus the sensor output voltage increases rapidly in this transition from a lean to a rich

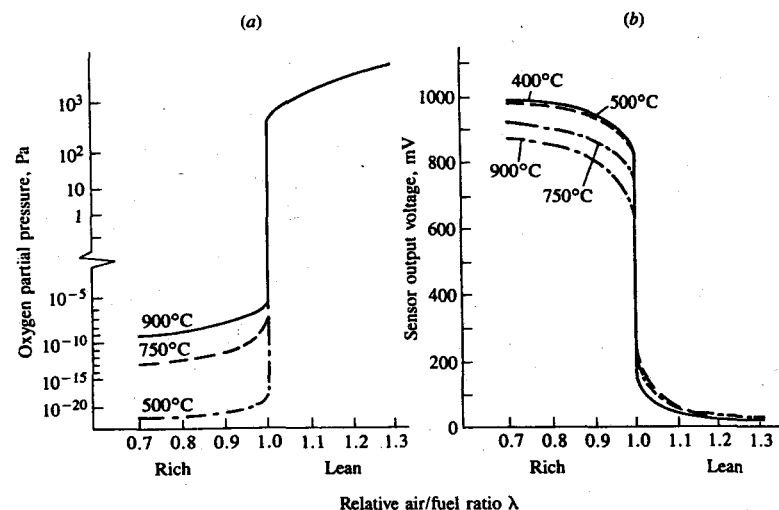


**FIGURE 7-17**  
Oxygen-sensor characteristics. Variation as a function of relative air/fuel ratio and temperature of: (a) oxygen partial pressure in equilibrated combustion products; (b) sensor output voltage.<sup>15</sup>

mixture at the stoichiometric point, as shown in Fig. 7-17b. Since this transition is not temperature dependent, it is well suited as a sensor signal for a feedback system.<sup>15</sup>

Figure 7-18 shows a cross-section drawing of a lambda sensor, screwed into the wall of the exhaust manifold. This location provides rapid warm-up of the sensor following engine start-up. It also gives the shortest flow time from the fuel injector or carburetor location to the sensor—a delay time which is important in the operation of the feedback system. The sensor body is made of  $ZrO_2$  ceramic stabilized with  $Y_2O_3$  to give adequate low-temperature electrical conductivity. The inner and outer electrodes are 10-\$\mu m\$ thick porous platinum layers to provide the required catalytic equilibration. The outer electrode which is exposed to the exhaust gases is protected against corrosion and erosion by a 100-\$\mu m\$ spinal coat and a slotted shield. Air passes to the inner electrode through holes in the protective sleeve. The shield, protective sleeve, and housing are made from heat- and corrosion-resistant steel alloys. Such sensors were first developed for air/fuel ratio control at close to the stoichiometric value. Use of a similar sensor to control air/fuel ratios at lean-of-stoichiometric values during part-throttle engine operation is also feasible.

For closed-loop feedback control at close-to-stoichiometric, use is made of the sensor's low-voltage output for lean mixtures and a high-voltage output for rich mixtures. A control voltage reference level is chosen at about the mid-point of the steep transition in Fig. 7-17b. In the electronic control unit the sensor signal is compared to the reference voltage in the comparator as shown in Fig. 7-19a. The comparator output is then integrated in the integral controller whose

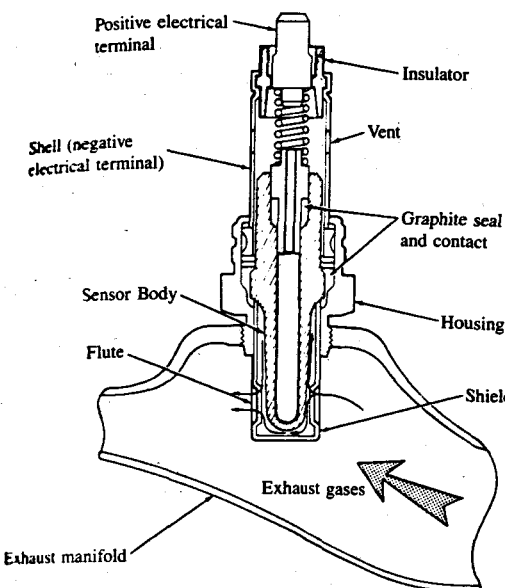


**FIGURE 7-18**  
Cross-section drawing of exhaust oxygen sensor.<sup>16</sup>

output varies the fuel quantity linearly in the opposite direction to the sign of the comparator signal. There is a time lag  $\tau_L$  in the loop composed of the transport time of fuel-air mixture from the point of fuel admission in the intake system to the sensor location in the exhaust, and the sensor and control system time delay. Because of this time lag, the controller continues to influence the fuel flow rate in the same direction, although the reference point  $\phi = 1.0$  has been passed, as shown in Fig. 7-19b. Thus, oscillations in the equivalence ratio delivered to the engine exist even under steady-state conditions of closed-loop control. This behavior of the control system is called the *limit cycle*. The frequency  $f$  of this limit cycle is given by

$$f_{LC} = \frac{1}{4\tau_L} \quad (7.16)$$

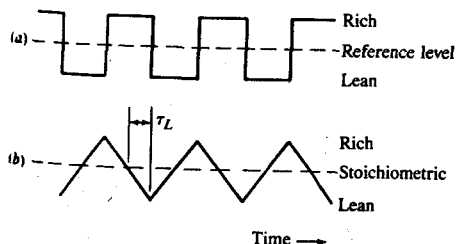


**FIGURE 7-19**  
Operation of electronic control unit for closed-loop feedback: (a) sensor signal compared with reference level; (b) controller output voltage—the integrated comparator output.<sup>12</sup>

and the change in equivalence ratio peak-to-peak is

$$\Delta\phi = 2K\tau_L \quad (7.17)$$

where  $K$  is the integrator gain (in equivalence ratio units per unit time).

Depending on the details of the three-way catalyst used for cleanup of all three pollutants (CO, HC, and NO<sub>x</sub>) in the exhaust, the optimum average equivalence ratio may not be precisely the stoichiometric value. Furthermore, the reference voltage for maximum sensor durability may not correspond exactly to the stoichiometric point or the desired catalyst mean operating point. While a small shift ( $\sim \pm 1$  percent) in operating point from the stoichiometric can be obtained by varying the reference voltage level, larger shifts are obtained by modifying the control loop to provide a steady-state bias. One method of providing a bias—asymmetrical gain rate biasing<sup>17</sup>—uses two separate integrator circuits with different gain rates  $K^+$  and  $K^-$  to integrate the comparator output, depending on whether the comparator output is positive (rich) or negative (lean). An alternative biasing technique incorporates an additional delay time  $\tau_D$  so that the controller output continues decreasing (or increasing) even though the sensor signal has switched from the high to the low level (or vice versa). By introducing this additional delay only on the negative slope of the sensor signal, a net lean bias is produced. Introducing the additional delay on the positive slope of the sensor signal produces a net rich bias.<sup>12</sup>

Note that the sensor only operates at elevated temperatures. During engine start-up and warm-up, the feedback system does not operate and conventional controls are required to obtain the appropriate fuel-air mixture for satisfactory engine operation.

## 7.5 FLOW PAST THROTTLE PLATE

Except at or close to wide-open throttle, the throttle provides the minimum flow area in the entire intake system. Under typical road-load conditions, more than 90 percent of the total pressure loss occurs across the throttle plate. The minimum-to-maximum flow area ratio is large—typically of order 100. Throttle

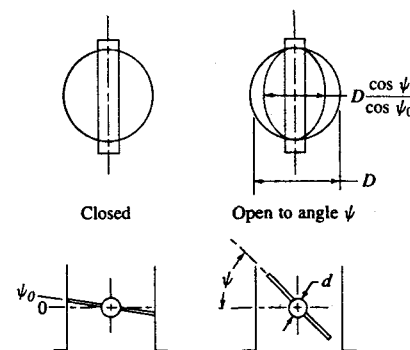


FIGURE 7-20  
Throttle plate geometry.<sup>2</sup>

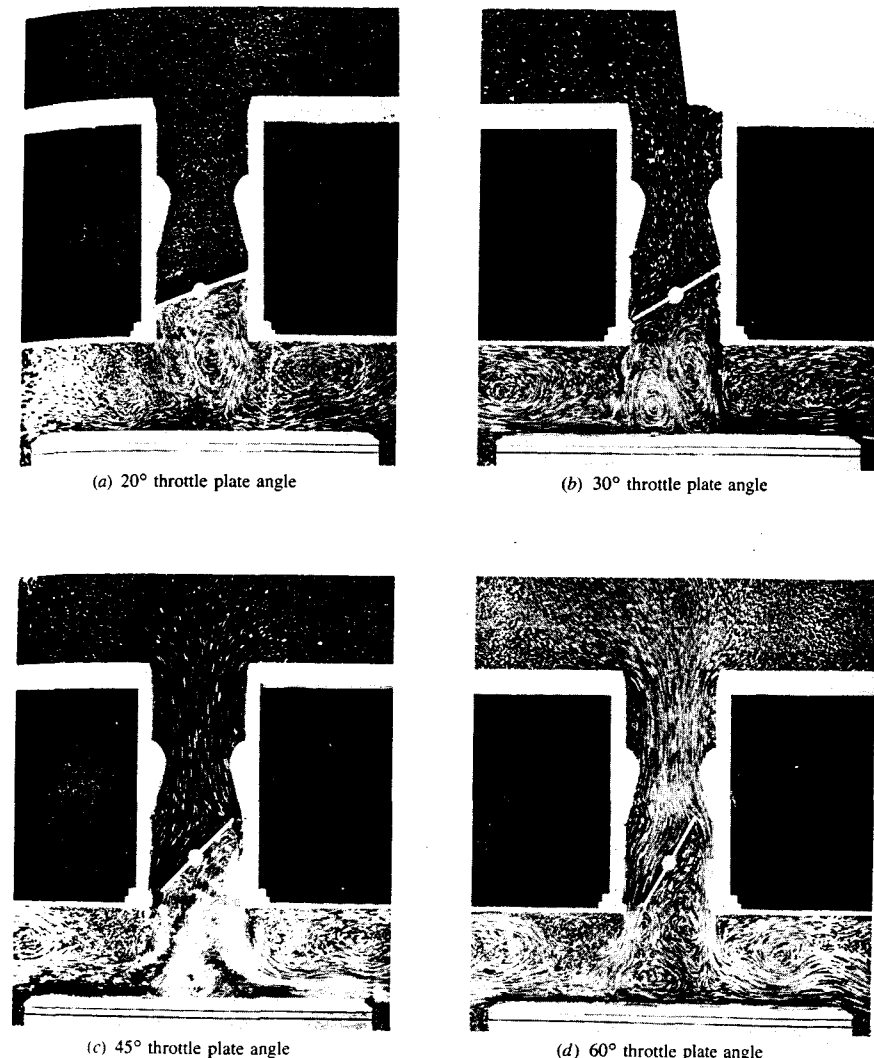


FIGURE 7-21

Photographs of flow in two-dimensional hydraulic analog of carburetor venturi, throttle plate, and manifold plenum floor at different throttle plate angles.<sup>18</sup>

plate geometry and parameters are illustrated in Fig. 7-20. A throttle plate of conventional design such as Fig. 7-20 creates a three-dimensional flow field. At part-throttle operating conditions the throttle plate angle is in the 20 to 45° range and jets issue from the “crescent moon”-shaped open areas on either side of the throttle plate. The jets are primarily two dimensional. Figure 7-21 shows photographs taken of a two-dimensional hydraulic analog of a typical carburetor

venturi and throttle plate in steady flow at different throttle angles. The path lines traced by the particles in the flow indicate the relative magnitude of the flow velocity.<sup>18</sup> The flow accelerates through the carburetor venturi (separation occurs at the corners of the entrance section); it then divides on either side of the throttle plate. There is a stagnation point on the upstream side of the throttle plate. The wake of the throttle plate contains two vortices which rotate in opposite directions. The jets on either side of the wake (at part throttle) are at or near sonic velocity. There is little or no mixing between the two jets. Thus, if maldistribution of the fuel-air mixture occurs above the throttle plate, it is not corrected immediately below the throttle plate.

In analyzing the flow through the throttle plate, the following factors should be considered:<sup>2, 19, 20</sup>

1. The throttle plate shaft is usually of sufficient size to affect the throttle open area.
2. To prevent binding in the throttle bore, the throttle plate is usually completely closed at some nonzero angle (5, 10, or 15°).
3. The discharge coefficient of the throttle plate is less than that of a smooth converging-diverging nozzle, and varies with throttle angle, pressure ratio, and throttle plate Reynolds number.
4. Due to the manufacturing tolerances involved, there is usually some minimum leakage area even when the throttle plate is closed against the throttle bore. This leakage area can be significant at small throttle openings.
5. The measured pressure drop across the throttle depends ( $\pm 10$  percent) on the circumferential location of the downstream pressure tap.
6. The pressure loss across the throttle plate under the actual flow conditions (which are unsteady even when the engine speed and load are constant, see Fig. 7-8) may be less than under steady flow conditions.

The throttle plate open area  $A_{th}$ , as a function of angle  $\psi$  for the geometry in Fig. 7-20, is given by<sup>2</sup>

$$\frac{4A_{th}}{\pi D^2} = \left(1 - \frac{\cos \psi}{\cos \psi_0}\right) + \frac{2}{\pi} \left[ \frac{a}{\cos \psi} (\cos^2 \psi - a^2 \cos^2 \psi_0)^{1/2} \right. \\ \left. - \frac{\cos \psi}{\cos \psi_0} \sin^{-1} \left( \frac{a \cos \psi_0}{\cos \psi} \right) - a(1 - a^2)^{1/2} + \sin^{-1} a \right] \quad (7.18)$$

where  $a = d/D$ ,  $d$  is the throttle shaft diameter,  $D$  is the throttle bore diameter, and  $\psi_0$  is the throttle plate angle when tightly closed against the throttle bore. When  $\psi = \cos^{-1}(a \cos \psi_0)$ , the throttle open area reaches its maximum value ( $\approx \pi D^2/4 - dD$ ). The throttle plate discharge coefficient (which varies with  $A_{th}$ ) and minimum leakage area, must be determined experimentally.

The mass flow rate through the throttle valve can be calculated from standard orifice equations for compressible fluid flow [see App. C, Eqs. (C-8) and

(C-9)]. For pressure ratios across the throttle less than the critical value ( $p_T/p_0 = 0.528$ ), the mass flow rate is given by

$$\dot{m}_{th} = \frac{C_D A_{th} p_0}{\sqrt{RT_0}} \left( \frac{p_T}{p_0} \right)^{1/2} \left\{ \frac{2\gamma}{\gamma - 1} \left[ 1 - \left( \frac{p_T}{p_0} \right)^{(\gamma-1)/\gamma} \right] \right\}^{1/2} \quad (7.19)$$

where  $A_{th}$  is the throttle plate open area [Eq. (7.18)],  $p_0$  and  $T_0$  are the upstream pressure and temperature,  $p_T$  is the pressure downstream of the throttle plate (assumed equal to the pressure at the minimum area; i.e., no pressure recovery occurs), and  $C_D$  is the discharge coefficient (determined experimentally). For pressure ratios greater than the critical ratio, when the flow at the throttle plate is choked,

$$\dot{m}_{th} = \frac{C_D A_{th} p_0}{\sqrt{RT_0}} \gamma^{1/2} \left( \frac{2}{\gamma + 1} \right)^{(y+1)/2(y-1)} \quad (7.20)$$

The relation between air flow rate, throttle angle, intake manifold pressure, and engine speed for a two-barrel carburetor and a 4.7-dm<sup>3</sup> (288-in<sup>3</sup>) displacement eight-cylinder production engine is shown in Fig. 7-22. While the lines are predictions from a quasi-steady computer simulation, the agreement with data is excellent. The figure shows that for an intake manifold pressure below the critical

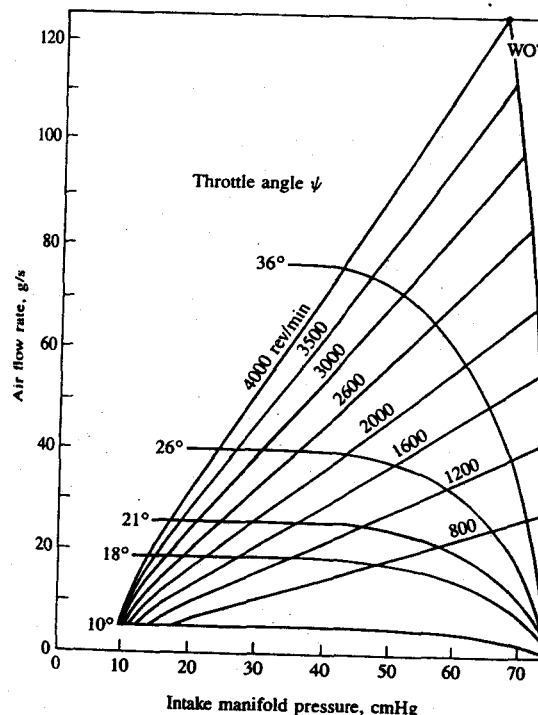


**FIGURE 7-22**  
Variation in air flow rate past a throttle, with inlet manifold pressure, throttle angle, and engine speed. 4.7-dm<sup>3</sup> displacement eight-cylinder engine.<sup>2</sup>

value ( $0.528 \times p_{atm} = 53.5 \text{ kN/m}^2 = 40.1 \text{ cmHg}$ ) the air flow rate at a given throttle position is independent of manifold pressure and engine speed because the flow at the throttle plate is choked.<sup>2</sup>

## 7.6 FLOW IN INTAKE MANIFOLDS

### 7.6.1 Design Requirements

The details of the air and fuel flow in intake manifolds are extremely complex. The combination of pulsating flow into each cylinder, different geometry flow paths from the plenum beneath the throttle through each runner and branch of the manifold to each inlet port, liquid fuel atomization, vaporization and transport phenomena, and the mixing of EGR with the fresh mixture under steady-state engine operating conditions are difficult enough areas to untangle. During engine transients, when the throttle position is changed, the fact that the processes which govern the air and the fuel flow to the cylinder are substantially different introduces additional problems. This section reviews our current understanding of these phenomena.

Intake manifolds consist typically of a plenum, to the inlet of which bolts the throttle body, with individual runners feeding branches which lead to each cylinder (or the plenum can feed the branches directly). Important design criteria are: low air flow resistance; good distribution of air and fuel between cylinders; runner and branch lengths that take advantage of ram and tuning effects; sufficient (but not excessive) heating to ensure adequate fuel vaporization with carbureted or throttle-body injected engines. Some compromises are necessary; e.g., runner and branch sizes must be large enough to permit adequate flow without allowing the air velocity to become too low to transport the fuel droplets. Some of these design choices are illustrated in Fig. 7-23 which shows an inlet manifold and carburetor arrangement for a modern four-cylinder 1.8-dm<sup>3</sup> engine. In this design the four branches that link the plenum beneath the carburetor and throttle with the inlet ports are similar in length and geometry, to provide closely comparable flow paths. This manifold is heated by engine coolant as shown and uses an electrically heated grid beneath the carburetor to promote rapid fuel evaporation.<sup>21</sup> Exhaust gas heated stoves at the floor of the plenum are also used in some intake manifolds to achieve adequate fuel vaporization and distribution. Note that with EGR, the intake manifold may contain passages to bring the exhaust gas to the plenum or throttle body.

With port fuel-injection systems, the task of the inlet manifold is to control the air (and EGR) flow. Fuel does not have to be transported from the throttle body through the entire manifold. Larger and longer runners and branches, with larger angle bends, can be used to provide equal runner lengths and take greater advantage of ram and tuning effects. With port fuel injection it is not normally necessary to heat the manifold.

A large number of different manifold arrangements are used in practice. Different cylinder arrangements (e.g., four, V-six, in-line-six, etc.) provide quite different air and fuel distribution problems. Air-flow phenomena in manifolds can

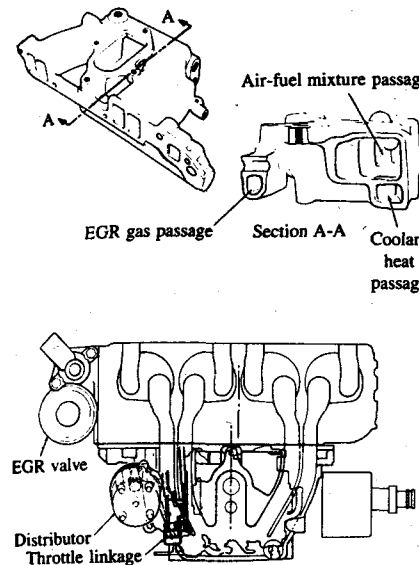


FIGURE 7-23  
Inlet manifold for four-cylinder 1.8-dm<sup>3</sup> displacement spark-ignition engine.<sup>21</sup>

be considered as unaffected by the fuel flow. The reverse is definitely not the case: the fuel flow—liquid and vapor—depends strongly on the air flow. These two topics will therefore be reviewed in sequence.

### 7.6.2 Air-Flow Phenomena

The air flow out of the manifold occurs in a series of pulses, one going to each cylinder. Each pulse is approximately sinusoidal in shape. For four- and eight-cylinder engines, these flow pulses sequence such that the outflow is essentially zero between pulses. For six-cylinder arrangements the pulses will overlap. When the engine is throttled, backflow from the cylinder into the intake manifold occurs during the early part of the intake process until the cylinder pressure falls below the manifold pressure. Backflow can also occur early in the compression stroke before the inlet valve closes, due to rising cylinder pressure. The flow at the throttle will fluctuate as a consequence of the pulsed flow out of the manifold into the cylinders. At high intake vacuum, the flow will be continuously inward at the throttle and flow pulsations will be small. When the outflow to the cylinder which is undergoing its intake stroke is greater than the flow through the throttle, the cylinder will draw mixture from the rest of the intake manifold. During the portion of the intake stroke when the flow into the cylinder is lower than the flow through the throttle, mixture will flow back into the rest of the manifold. At wide-open throttle when the flow restriction at the throttle is a minimum, flow pulsations at the throttle location will be much more pronounced.<sup>19</sup>

The air flows to each cylinder of a multicylinder engine, even under steady operating conditions, are not identical. This is due to differences in runner and

branch length and other geometric details of the flow path to each cylinder. Also, as each cylinder's intake flow commences, air is drawn from the branch and runner leading to the cylinder, the plenum, and the other runners and branches feeding the plenum, as well as past the throttle. This "drawing down" of other parts of the intake manifold depends on the arrangement of the plenum, runners, and branches, and the firing order of the cylinders. Thus the air flow to each individual cylinder is affected by the details of its own branch, how that branch connects to the rest of the intake manifold, and the cylinder firing order.<sup>22</sup> The differences between the air flows to individual cylinders have been measured. Variations in the average air mass flow rate to each individual cylinder of up to about 5 percent above and below the average are quite common. Larger peak-to-peak variations ( $\pm 15$  percent) have been measured. The extent of each cylinder's difference from the average flow varied significantly as engine speed and load were varied.<sup>23, 24</sup>

Typical quantities that characterize manifold air flow are given in Table 7.1 for a four- and an eight-cylinder spark-ignition engine. The volume of mixture pulled into each cylinder per cycle is about the same as the volume of one direct flow path between the throttle plate and inlet valve. Thus, one stroke loads the manifold, the next one pulls the charge into the cylinder.

An additional phenomenon becomes important when engine load is changed by opening or closing the throttle: the mass of air in the induction system volume takes a finite time to adjust to the new engine operating conditions. For example, as the throttle is opened the air flow into the manifold increases as the throttle open area increases. However, due to the finite volume of

TABLE 7.1  
Parameters that characterize manifold air flow

Engine geometry	I-4†	V-8‡
Typical flow-path distance between throttle bore and intake valve, cm	33	30
Average intake-passage flow area, $\text{cm}^2$	9.4	16
Volume of one direct flow path from throttle bore to intake valve, $\text{cm}^3$	300	500
Range of speeds, etc.	Maximum	Minimum
Crankshaft, rev/min	5000	650
Peak air velocity in manifold branch, m/s	130†, 100‡	15
Peak Reynolds number in manifold branch	$4 \times 10^5$	$5 \times 10^4$
Duration of individual cylinder intake process, ms	6	46

† 1.8- $\text{dm}^3$  four-cylinder in-line SI engine.<sup>21</sup>

‡ 5.6- $\text{dm}^3$  V eight-cylinder SI engine.<sup>23</sup>

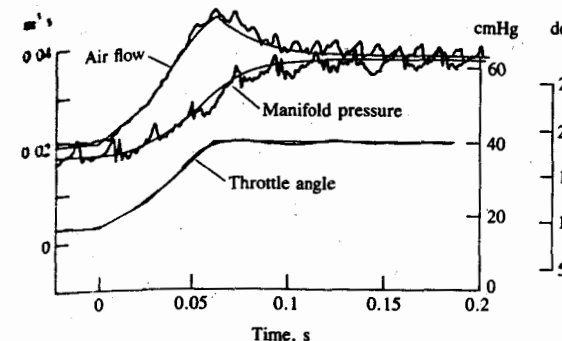


FIGURE 7-24

Throttle angle, intake manifold pressure, and air flow rate past the throttle versus time for 10° part-load throttle opening. 5- $\text{dm}^3$  V-8 engine.<sup>25</sup>

the manifold, the pressure level in the manifold increases more slowly than would be the case if steady-state conditions prevailed at each throttle position. Thus, the pressure difference across the throttle is larger than it would be under steady flow conditions and the throttle air flow overshoots its steady-state value. The air flow into each cylinder depends on the pressure in the manifold, so this lags the throttle air flow. This transient air-flow phenomenon affects fuel metering. For throttle-body injection or a carburetor, fuel flow should be related to throttle air flow. For port fuel injection, fuel flow should be related to cylinder air flow. Actual results for the air flow rate and manifold pressure in response to an opening of the throttle (increase in throttle angle) are shown in Fig. 7-24. The overshoot in throttle air flow and lag in manifold pressure as the throttle angle is increased are evident. Opposite effects will occur for a decrease in throttle angle.

**AIR-FLOW MODELS.** Several models of the flow in an intake manifold have been proposed.<sup>26, 27</sup> One simple manifold model that describes many of the above phenomena is the *plenum* or *filling and emptying* model. It is based on the assumption that at any given time the manifold pressure is uniform. The continuity equation for air flow into and out of the intake manifold is

$$\frac{dm_{a,m}}{dt} = \dot{m}_{a,\text{th}} - \sum \dot{m}_{a,\text{cyl}} \quad (7.21)$$

where  $m_{a,m}$  is the mass of air in the manifold, and  $\dot{m}_{a,\text{th}}$  and  $\dot{m}_{a,\text{cyl}}$  are the air mass flow rates past the throttle and into each cylinder, respectively. The flow rate past the throttle is given by Eq. (7.19) or (7.20). For manifold pressures sufficiently low to choke the flow past the throttle plate, the flow rate is independent of manifold pressure. The mass flow rate to the engine cylinders can be modeled at several levels of accuracy. The air flow through the valve to each cylinder can be computed from the valve area, discharge coefficient, and pressure

difference across the valve; or a sine wave function can be assumed. In the general case, Eq. (7.21) must be combined with the first law for an open system (see Sec. 14.2.2). For calculating the manifold response to a change in load or throttle setting, simplifying assumptions can be made. A quasi-steady approximation for the cylinder air flow:

$$\sum \dot{m}_{a, cyl} = \frac{\eta_v \rho_{a, m} V_d N}{2}$$

is usually adequate, and the air temperature can be assumed constant.<sup>25</sup> Then, using the ideal gas law for the manifold,  $p_m V_m = m_{a, m} R_a T_m$ , Eq. (7.21) can be written as

$$\frac{dp_m}{dt} + \frac{\eta_v V_d N}{2V_m} p_m = \dot{m}_{a, th} \frac{RT_m}{V_m} \quad (7.22)$$

Both  $\eta_v$  and  $\dot{m}_{a, th}$  have some dependence on  $p_m$  [e.g., see Eq. (6.2)]. In the absence of this weak dependence, Eq. (7.22) would be a first-order equation for  $p_m$  with a time constant  $\tau = 2V_m/(\eta_v V_d N) \approx V_m/\dot{V}_{cyl}$ , which is 2 to 4 times the intake stroke duration. The smooth curves in Fig. 7-24 are predictions made with Eq. (7.22) and show good agreement with the data. The plenum model is useful for investigating manifold pressure variations that result from load changes. It provides no information concerning pressure variations associated with momentum effects.

**Helmholtz resonator models** for the intake system have been proposed. This type of model can predict the resonant frequencies of the combined intake and engine cylinder system, and hence the engine speeds at which increases in air flow due to intake tuning occur. It does not predict the magnitude of the increase in volumetric efficiency. The Helmholtz resonator theory analyzes what happens during one inlet stroke, as the air in the manifold pipe is acted on by a forcing function produced by the piston motion. As the piston moves downward during the intake stroke, a reduced pressure occurs at the inlet valve relative to the pressure at the open end of the inlet pipe. A rarefaction wave travels down the intake pipe to the open end and is reflected as a compression wave. A positive tuning effect occurs when the compression wave arrives at the inlet valve as the valve is closing.<sup>27</sup> A single-cylinder engine modeled as a Helmholtz resonator is shown in Fig. 7-25a. The effective resonator volume  $V_{eff}$  is chosen to be one-half of the displaced volume plus the clearance volume; the piston velocity is then close to its maximum and the pressure in the inlet system close to its minimum. The tuning peak occurs when the natural frequency of the cylinder volume coupled to the pipe is about twice the piston frequency. For a single-cylinder, fed by a single pipe open to the atmosphere, the resonant tuning speed  $N_r$  is given by

$$N_r (\text{rev/min}) = \frac{955}{K} a \left( \frac{A}{lV_{eff}} \right)^{1/2} \quad (7.23)$$

where  $a$  is the sound speed (m/s),  $A$  the effective cross-sectional area of the inlet system ( $\text{cm}^2$ ),  $l$  the effective length of the inlet system (cm),  $K$  a constant equal to about 2 for most engines, and  $V_{eff} = V_d(r_c + 1)/[2(r_c - 1)] (\text{cm}^3)$ .<sup>28</sup>

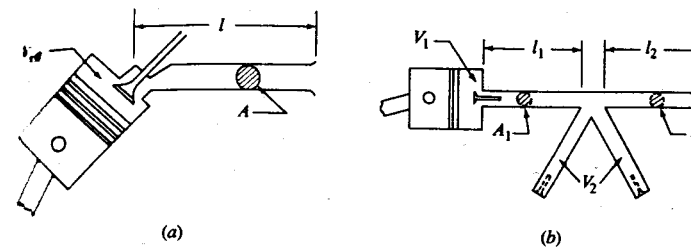


FIGURE 7-25  
Helmholtz resonator models for (a) single-cylinder engine and (b) multicylinder engine.<sup>27</sup>

The Helmholtz theory for multicylinder engines treats the pipes of cylinders not undergoing induction as an additional volume. The two pipes,  $(l_1, A_1)$  and  $(l_2, A_2)$ , and two volumes,  $V_1$  and  $V_2$ , in Fig. 7-25b form a vibrating system with two degrees of freedom and two resonant frequencies. The following equation, based on an electrical analog (in which capacitors represent volumes and inductors pipes), gives the two frequencies at which the manifold shown in Fig. 7-25b would be tuned:<sup>28</sup>

$$f_{\pm} = \frac{1}{2\pi} \left\{ \frac{(\alpha\beta + \alpha + 1) \mp [( \alpha\beta + \alpha + 1)^2 - 4\alpha\beta]^{1/2}}{2\alpha\beta L_1 C_1} \right\}^{1/2} \quad (7.24)$$

where  $\alpha = L_2/L_1$ ,  $\beta = C_2/C_1$ ,  $C_1 = V_1$ ,  $C_2 = V_2$ ,  $L_1 = (l/A)_1$ ,  $L_2 = (l/A)_2$ , and  $V_{eff} = V_1$ . The Helmholtz theory predicts the engine speeds at which positive tuning resonances occur with reasonable accuracy.<sup>27</sup>

The dynamics of the flow in multicylinder intake (and exhaust) systems can be modeled most completely using one-dimensional unsteady compressible flow equations. The standard method of solution of the governing equations has been the method of characteristics (see Benson<sup>29</sup>). Recently, finite difference techniques which are more efficient have been used.<sup>30</sup> The assumptions usually made in this type of analysis are:

1. The intake (or exhaust) system can be modeled as a combination of pipes, junctions, and plenums.
2. Flow in the pipes is one dimensional and no axial heat conduction occurs.
3. States in the engine cylinders and plenums are uniform in space.
4. Boundary conditions are considered quasi steady.
5. Coefficients of discharge, heat transfer, pipe friction, and bend losses for steady flow are valid for unsteady flow.
6. The gases can be modeled as ideal gases.

This approach to intake and exhaust flow analysis is discussed more fully in Sec. 14.3.4.

### 7.6.3 Fuel-Flow Phenomena

**TRANSPORT PROCESSES.** With conventional spark-ignition engine liquid-fuel metering systems, the fuel enters the air stream as a liquid jet. The liquid jet atomizes into droplets. These mix with the air and also deposit on the walls of the intake system components. The droplets vaporize; vaporization of the liquid fuel on the walls occurs. The flow of liquid fuel along the walls can be significant. The transport of fuel as vapor, droplets, and liquid streams or films can all be important. The fuel transport processes in the intake system are obviously extremely complex.

The details of the fuel transport process are different for multipoint fuel-injection systems than for carburetor and throttle-body injection systems. For the latter systems, fuel must be transported past the throttle plate and through the complete intake manifold. For the former systems, the liquid fuel is injected in the inlet port, toward the back of the intake valve. For all these practical fuel metering systems, the quality of the mixture entering the engine is imperfect. The fuel, air, recycled exhaust, mixture is not homogeneous; the fuel may not be fully vaporized as it enters the engine. The charge going to each cylinder is not usually uniform in fuel/air ratio throughout its volume, and the distribution of fuel between the different engine cylinders is not exactly equal. During engine transients, when engine fuel and air requirements and manifold conditions change, it is obvious that the above fuel transport processes will not all vary with time in the same way. Thus, in addition to the transient non-quasi-steady air-flow phenomena described above, there are transient fuel-flow phenomena. These have to be compensated for in the fuel metering strategy.

Since gasoline, the standard spark-ignition engine fuel, is a mixture of a large number of individual hydrocarbons it has a boiling temperature range rather than a single boiling point. Typically, this range is 30 to 200°C. Individual hydrocarbons have the saturation pressure-temperature relationships of a pure substance. The lower the molecular weight, the higher will be the saturated vapor pressure at a given temperature. The boiling point of hydrocarbons depends primarily on their molecular weight; the vapor pressure also depends on molecular structure. The equilibrium state of a hydrocarbon-air mixture depends therefore on the vapor pressure of the hydrocarbon at the given temperature, the relative amounts of the hydrocarbon and air, and the total pressure of the mixture. The equilibrium fraction of fuel evaporated at a given temperature and pressure can be calculated from Bridgeman charts<sup>31</sup> and the distillation characteristics of the fuel (defined by the ASTM distillation curve<sup>32</sup>). Figure 7-26a shows the effect of mixture temperature on percent of indolene fuel (a specific gasoline) evaporated at equilibrium at atmospheric pressure. Figure 7-26b shows the effect of reduced manifold pressure on the amount evaporated.<sup>18</sup> While insufficient time is usually available in the manifold to establish equilibrium, the trends shown are indicative of what happens in practice: lower pressures increase the relative amount of fuel vaporized and charge heating is usually required to vaporize a substantial fraction of the fuel.

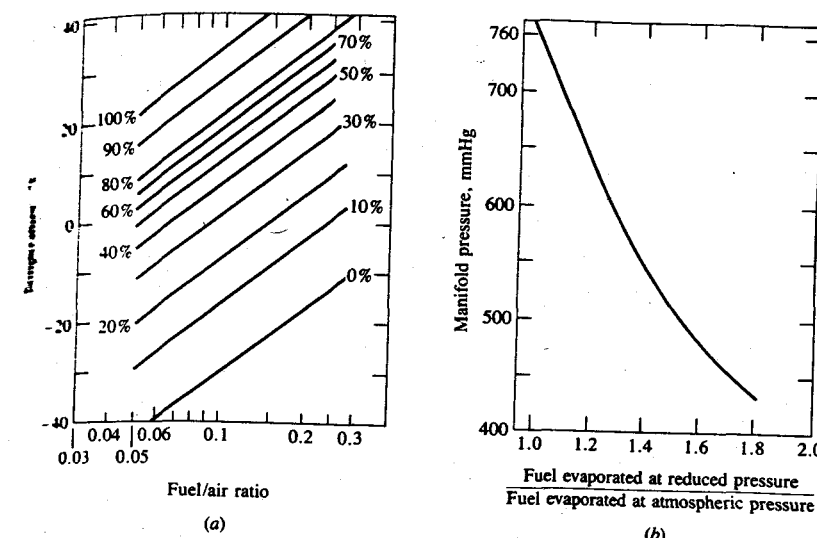


FIGURE 7-26  
(a) Percentage of indolene fuel evaporated at equilibrium at 1 atmosphere pressure. (b) Effect of pressure on amount of indolene fuel evaporated.<sup>18</sup>

For carbureted and throttle-body injection systems, the fuel path is the following. Until the throttle plate is close to fully opened, most of the fuel metered into the air stream impacts on the throttle plate and throttle-body walls. Only a modest fraction of the fuel vaporizes upstream of the throttle. The liquid is reentrained as the air flows at high velocity past the throttle plate. The fuel does not usually divide equally on either side of the throttle plate axis. The air undergoes a 90° bend in the plenum beneath the throttle; much of the fuel which has not evaporated is impacted on the manifold floor. Observations of fuel behavior in intake manifolds with viewing ports or transparent sections show that there is substantial liquid fuel on the walls with carburetor fuel metering systems. Figure 7-27 shows the engine conditions under which liquid fuel was observed on the floor of the manifold plenum beneath the throttle plate and in the manifold runners, in a standard four-cylinder production engine.<sup>23</sup> This manifold was heated by engine coolant at 90°C. The greatest amount of liquid was present at high engine loads and low speeds. Heating the manifold to a higher temperature with steam at 115°C resulted in a substantial reduction in the amount of liquid: there was no extensive puddling on the plenum floor, liquid films or rivulets were observed in a zone bounded by 120 mmHg vacuum and 2500 rev/min, and there were no films or rivulets in the manifold runner. Depending on engine operating conditions, transport of fuel as a liquid film or rivulet in the manifold and vaporization from these liquid fuel films and rivulets and subsequent transport as vapor may occur.

Vaporized fuel and liquid droplets which remain suspended in the air

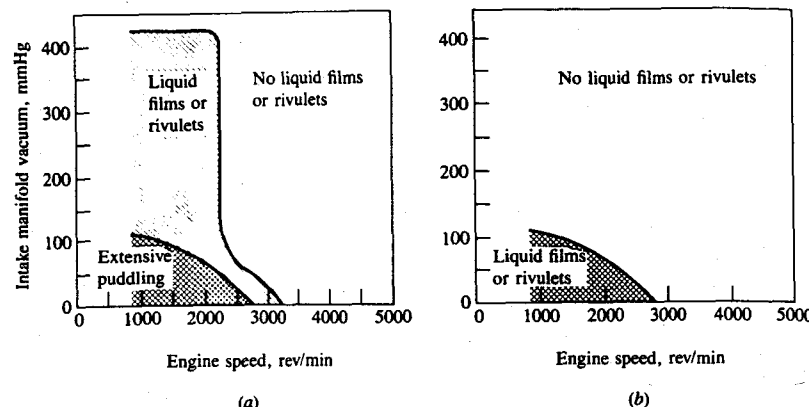


FIGURE 7-27

Regions of engine load and speed range where extensive pools or puddles, liquid films, or rivulets were observed: (a) on manifold plenum floor and (b) in manifold runner. Four-cylinder automobile engine. Manifold heated by coolant at 90°C.<sup>23</sup>

stream will be transported with the air stream. However, droplet deposition on the manifold walls may occur due to gravitational settling and to inertial effects as the flow goes round bends in the manifold.

The fuel transport processes for port fuel-injection systems are different and will depend significantly on the timing and duration of the injection pulse. Fuel is injected onto the back of the inlet valve (and surrounding port wall), usually while the valve is closed or only partly open. Vaporization of liquid fuel off the valve and walls occurs, enhanced by the backflow of hot residual gases from the cylinder (especially at part load). There is evidence that, even under fully warmed-up engine conditions, some fuel is carried as liquid drops into the cylinder.<sup>33</sup>

**FUEL DROPLET BEHAVIOR.** With carburetor and throttle-body injection systems, the liquid fuel atomizes as it enters the air stream. In the carburetor venturi this occurs as the fuel-air emulsion from the fuel jet(s) enters the high-velocity (> 100 m/s) air stream. With an injector, the velocity of the liquid jet as it exits the nozzle is high enough to shatter the flowing liquid, and its interaction with the coaxial air flow further atomizes the fuel. Typical droplet-size distributions are not well defined; size would vary over the load and speed range. Droplet diameters in the 25 to 100 μm range are usually assumed to be representative: larger drops are also produced. The liquid fuel drops are accelerated by the surrounding air stream and start to vaporize. Vaporization rates have been calculated using established formulas for heat and mass transfer between a droplet and a surrounding flowing gas stream (see Ref. 34 for a review of methods of calculating droplet vaporization rates). Calculations of fuel vaporization in a carburetor venturi and upstream of the throttle plate show that the temperature

of the liquid fuel droplets decreases rapidly (by up to about 30°C<sup>35</sup>), and the fraction of the fuel vaporized is small (in the 2 to 15 percent range<sup>35,36</sup>).

Liquid fuel drops, due to their density being many times that of the air, will not exactly follow the air flow. Droplet impaction on the walls may occur as the flow changes direction, and the greater inertia of the droplets causes them to move across the streamlines to the outer wall. Deposition on the manifold floor due to gravity may also occur. The equation of motion for an individual droplet in a flowing gas stream is

$$\left(\frac{1}{6}\pi D_d^3 \rho_f\right)a = m_d g - \frac{1}{2}(\rho_d - \rho_g)|v_d - v_g| \rho_g C_D \frac{\pi D_d^2}{4} \quad (7.25)$$

where  $D_d$  is the droplet diameter,  $\rho_f$  and  $\rho_g$  are liquid and gas densities,  $v_d$  and  $v_g$  are the droplet and gas velocities,  $a$  is the droplet acceleration,  $g$  acceleration due to gravity, and  $C_D$  is the drag coefficient. For  $6 < Re < 500$  the drag coefficient of an evaporating droplet is a strong function of the Reynolds number,  $Re$ : e.g.,

$$C_D = 27 Re^{-0.84} \quad (7.26)$$

where  $Re = (\rho_g D_d |v_d - v_g| / \mu_g)$ .

Studies of droplet impaction and evaporation using the above equations and typical manifold conditions and geometries indicate the following.<sup>26, 35, 37</sup> For 90° bends, drops of less than 10 μm diameter are essentially carried by the gas stream (< 10 percent impaction); almost all droplets larger than 25 μm impact on the walls. Droplet sizes produced first in the carburetor venturi or fuel injector spray and then by secondary atomization as liquid fuel is entrained from the throttle plate and throttle-body walls depend on the local gas velocity: higher local relative velocities between the gas and liquid produce smaller drop sizes. Approximate estimates which combine the two phenomena outlined above show that at low engine air flow rates, almost all of the fuel will impact first on the throttle plate and then on the manifold floor as the flow turns 90° into the manifold runners. At high air flows, because the drops are smaller, a substantial fraction of the drops may stay entrained in the air flow. Secondary atomization at the throttle at part-load operating conditions is important to the fuel transport process: the very high air velocities at the edge of the throttle plate produce droplets of order or less than 10 μm diameter. However, coalescence and deposition on the walls and subsequent reentrainment probably increase the mean droplet size. In the manifold, gravitational settling of large (> 100 μm) droplets would occur at low air flow rates,<sup>38</sup> but these drops are also likely to impact the walls due to their inertia as the flow is turned.

Estimates of droplet evaporation rates in the manifold indicate the following. With a representative residence time in the manifold of about one crank revolution (10 ms at 6000 rev/min, 100 ms at 600 rev/min), only drops of size less than about 10 μm will evaporate at the maximum speed; 100 μm droplets will not vaporize fully at any speed. Most of these large droplets impact on the walls, anyway. Drops small enough to be carried by the air stream are likely to vaporize in the manifold.<sup>26</sup>

**FUEL-FILM BEHAVIOR.** The fuel which impacts on the wall will also vaporize and, depending on where in the manifold deposition occurs and the local manifold geometry, may be transported along the manifold as a liquid film or rivulet. If the vaporization rate off the wall is sufficiently high, then a liquid film will not build up. Any liquid film or pool on the manifold floor or walls is important because it introduces additional fuel transport processes—deposition, liquid transport, and evaporation—which together have a much longer time constant than the air transport process. Thus changes in the air and the fuel flow into each engine cylinder, during a change in engine load, will not occur in phase with each other unless compensation is made for the slower fuel transport.

Several models of the behavior of liquid-fuel wall-films have been developed. One approach analyzes a liquid puddle on the floor of the manifold plenum.<sup>38</sup> Metered fuel enters the puddle; fuel leaves primarily through vaporization. The equation for rate of change of mass of fuel in the puddle is

$$\dot{m}_{f,p} = \dot{m}_{f,in} - \dot{m}_{f,out} = x\dot{m}_{f,m} - \frac{m_{f,p}}{\tau} \quad (7.27)$$

where  $m_{f,p}$  is the mass of fuel in the puddle,  $\dot{m}_{f,m}$  is the metered fuel flow rate, and  $x$  is the fraction of the metered flow that enters the puddle. It is assumed that the reentrainment/evaporation rate is proportional to the mass of fuel in the puddle divided by the characteristic time  $\tau$  of the reentrainment/evaporation process. The puddle behavior predicted by this model in response to a step increase in engine load is shown in Fig. 7-28a. Because only part  $(1-x)$  of the fuel flows directly with the air, as the throttle is opened rapidly a lean air/fuel ratio excursion is predicted. Figure 7-28b shows that this behavior (without any metering compensation) is observed in practice. Estimates of the volume of fuel in the puddle (for a 5-liter V-8 engine) are of order 1000 mm<sup>3</sup>, and increase with

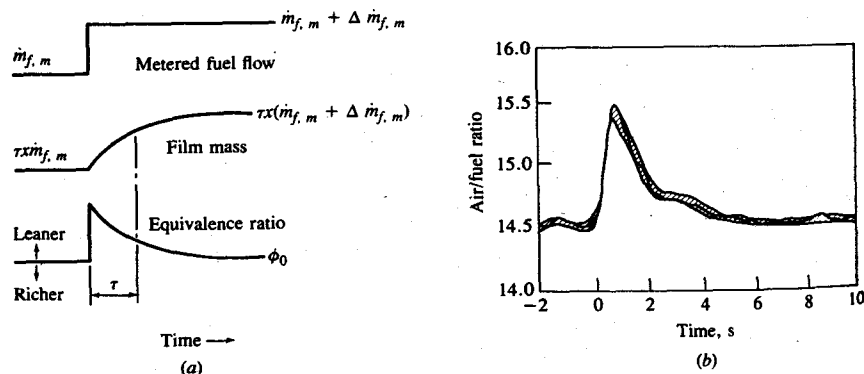
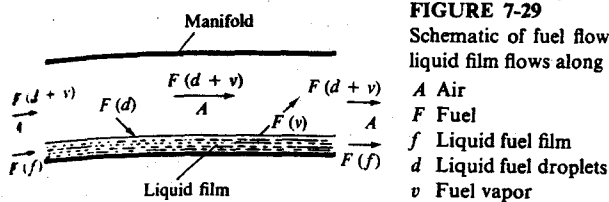


FIGURE 7-28  
(a) Predicted behavior of the fuel film for an uncompensated step change in engine operating conditions. (b) Observed variation in air/fuel ratio for uncompensated throttle opening at 1600 rev/min which increased manifold pressure from 48 to 61 cmHg.<sup>38</sup>



increasing load and speed. The time constant is of order 2 seconds for a fully warmed-up engine; it varies with engine operating conditions and is especially sensitive to intake manifold temperature. Such models have been used primarily to develop fuel metering strategies which compensate for the fuel transport lag.<sup>38</sup>

An alternative model, for liquid film flow in the manifold runner and branch, has been developed.<sup>37</sup> Fuel is deposited on the manifold walls and forms a film which flows toward the cylinder due to the shear force at the gas/liquid interface as shown in Fig. 7-29. Vaporization from the film also occurs. An analysis of the dynamics of the fuel film leads to expressions for steady-state film velocity and thickness. As air and metered fuel flows change due to a throttle position change, the characteristic time for reestablishing steady state is  $l/(2u_f)$ , where  $l$  is the manifold length and  $u_f$  the average film velocity. This characteristic response time is of order 1 second for typical manifold conditions, in approximate agreement with values obtained from transient engine experiments.

A more extensive analysis of both fuel droplet and film evaporation in a complete carburetor, throttle, manifold system,<sup>35</sup> with a multicomponent model for gasoline based on its distillation curve, indicates the following phenomena are important. Secondary atomization of the liquid fuel at the throttle, which produces the smallest droplet sizes when the throttle open angle is small, significantly increases the fraction of fuel evaporation in the manifold. Increasing inlet air temperature increases the fraction of fuel vaporized; this effect is larger at lower loads since secondary atomization under these conditions increases the liquid fuel surface area significantly. Heating the wall, which heats the liquid film on the wall directly, provides a greater increase in fraction evaporated than does equivalent heating of the air flow upstream of the carburetor. Due to the multi-component nature of the fuel, the residual liquid fuel composition changes significantly as fuel is transported from the carburetor to the manifold exit. Of the full boiling range liquid composition at entry, all the light ends, most of the mid-range components, but only a modest amount of the high boiling point fraction have evaporated at the manifold exit. The predicted fuel fraction evaporated ranged from 40 to 60 percent for the conditions examined. One set of measurements of the fraction of fuel vaporized in the manifold of a warmed-up four-cylinder engine showed that 70 to 80 percent of the fuel had vaporized, confirming that under these operating conditions "most" but not necessarily "all" the fuel enters the cylinder in vapor form.<sup>39</sup>

The engine operating range where fuel puddling, fuel films, and rivulets are observed (see Fig. 7-27) can now be explained. At light load, secondary atom-

ization at the throttle and the lower manifold pressure would reduce the amount of liquid fuel impinging on the manifold plenum floor. Also, typical manifold heating at light load substantially exceeds the heat required to vaporize the fuel completely,<sup>40</sup> and manifold floor temperatures are of order 15°C higher than at full load. All the above is consistent with less liquid on the floor and none in the runners at light load, compared to what occurs at full load. At high speed, drop sizes produced in the carburetor are much smaller, so impingement on the walls is much reduced.

The fuel flow to each cylinder per cycle is not exactly the same. There is a *geometric variation* where fuel is not divided equally among individual cylinders. There is also a *time variation* under steady-state engine conditions where the air/fuel ratio in a given cylinder varies cycle-by-cycle.<sup>41</sup> Data on time-averaged air/fuel ratios in each cylinder of multicylinder engines show that the extent of the maldistribution varies from engine to engine, and for a particular engine varies over the load and speed range. Spreads in the equivalence ratio (maximum to minimum) of about 5 percent of the mean value are typical at light load for carbureted engines. Largest variations between cylinders usually occur at wide-open throttle. WOT spreads in the equivalence ratio of about 15 percent of the mean appear to be typical, again for carbureted engines, while spreads as high as 20 to 30 percent are not uncommon at particular speeds for some engines.<sup>23,40</sup> Time variations are less well defined; the limited data available suggest they could be of comparable magnitude.<sup>41</sup>

With multipoint port fuel-injection systems, the fuel transport processes are substantially different and are not well understood. Air-flow phenomena are comparable to those with carbureted or throttle-body injection systems. However, manifold design can be optimized for air flow alone since fuel transport from the throttle through the manifold is no longer a design constraint. Because the manufacture and operation of individual fuel injectors are not identical, there is still some variation in fuel mass injected cylinder-to-cylinder and cycle-to-cycle. Since individual cylinder air flows depend on the design of the manifold, whereas the amount of fuel injected does not, uniform air distribution is especially important with port injection systems. The fuel vaporization and transport processes will depend on the duration of injection and the timing of injection pulse(s) relative to the intake valve-lift profile. Some of the injected fuel will impinge on the port walls, valve stem, and backside of the valve, especially when injection toward a closed valve occurs. Backflow of hot residual gases at part-load operation will have a substantial effect on fuel vaporization. Compensation for fuel lag during transient engine operation is still required; sudden throttle openings are accompanied by a "lean spike" in the mixture delivered to the engine, comparable to though smaller than that shown in Fig. 7-28 for a throttle-body fuel-injection system. Thus wall wetting, evaporation off the wall, and liquid flow along the wall are all likely to be important with port fuel-injection systems also.

With port fuel-injection systems, liquid fuel enters the cylinder and droplets are present during intake and compression. Limited measurements have been made of the distribution, size, and number density of these fuel droplets. During

intake, the droplet number density in the clearance volume increased to a maximum at the end of injection (the injection lasted from 45 to 153° ATC) and then decreased due to evaporation during compression to a very small value at the time of ignition. Average droplet size during intake was 10 to 20  $\mu\text{m}$  in diameter; it increased during compression as the smaller drops in the distribution evaporated. At the conditions tested, some 10 to 20 percent of the fuel was in droplet form at the end of injection. At ignition, the surviving droplets contained a negligible fraction of the fuel. During injection, the distribution of droplets across the clearance volume was nonuniform. It became much more uniform with time, after injection ended.<sup>33</sup>

## PROBLEMS

- 7.1. The equivalence ratio in a conventional spark-ignition engine varies from no load (idle) to full load, at a fixed engine speed, as shown at the top of Fig. P7-1. (By load is meant the percentage of the maximum brake torque at that speed.) Also shown is the variation in total friction (pumping plus mechanical rubbing plus accessory friction). Using formats similar to those shown, draw *carefully proportioned qualitative* graphs of the following parameters versus load (0 to 100 percent):

Combustion efficiency,  $\eta_c$   
 Gross indicated fuel conversion efficiency,  $\eta_{f,i}$   
 Gross indicated mean effective pressure,  $\text{imep}_g$   
 Brake mean effective pressure,  $\text{bmeep}$   
 Mechanical efficiency,  $\eta_m$

Indicate clearly where the maximum occurs if there is one, and where the value is zero or unity or some other obvious value, if appropriate. Provide a *brief justification* for the shape of the curves you draw.

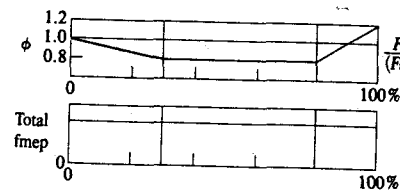


FIGURE P7-1

- 7.2. The four-cylinder spark-ignition engine shown in the figure uses an oxygen sensor in the exhaust system to determine whether the exhaust gas composition is lean or rich of the stoichiometric point, and a throttle-body injection system with feedback to maintain engine operation close to stoichiometric. However, since there is a time delay between a change in the fuel/air ratio at the injector location and the detection of that change by the sensor (corresponding to the flow time between the injector and the sensor), the control system shown results in oscillations in fuel/air ratio about the stoichiometric point.

(a) Estimate the average flow time between the injector and the sensor at an engine speed of 2000 rev/min.

- (b) The sensor and control unit provide a voltage  $V$  of  $+V_s$  volts when the fuel/air equivalence ratio  $\phi$  is less than one and a voltage of  $-V_s$  volts when  $\phi$  is greater than one. The feedback injection system provides a fuel/air ratio ( $F/A$ ) given by

$$\left(\frac{F}{A}\right) = \left(\frac{F}{A}\right)_{t=0} (1 + CVt)$$

where  $t$  is the time (in seconds) after the voltage signal last changed sign,  $(F/A)_{t=0}$  is the fuel/air ratio at the injector at  $t = 0$ , and  $C$  is a constant. Develop carefully proportioned quantitative sketches of the variation in the fuel/air ratio at the injector and at the exhaust sensor, with time, showing the phase relation between the two curves. Explain briefly how you developed these graphs.

- (c) Find the value of the constant  $C$ , in  $\text{volts}^{-1}\text{-seconds}^{-1}$  (the feedback system gain), such that  $(F/A)$  variations about the stoichiometric value do not exceed  $\pm 10$  percent for  $V_s = 1$  V.

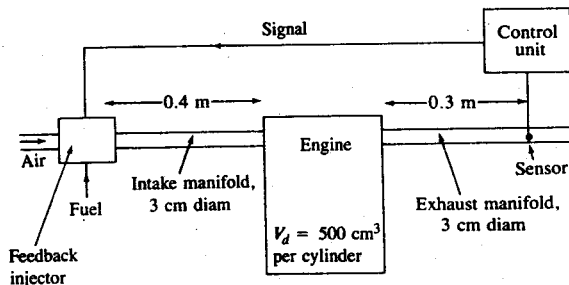


FIGURE P7-2

- 7.3. In many spark-ignition engines, liquid fuel is added to the inlet air upstream of the inlet manifold above the throttle. The inlet manifold is heated to ensure that under steady-state conditions the fuel is vaporized before the mixture enters the cylinder.
- (a) At normal wide-open throttle operating conditions, in a four-stroke cycle 1.6-dm<sup>3</sup> displacement four-cylinder engine, at 2500 rev/min, the temperature of the air entering the carburetor is 40°C. The heat of vaporization of the fuel is 350 kJ/kg and the rate of heat transfer to the intake mixture is 1.4 kW. Estimate the temperature of the inlet mixture as it passes through the inlet valve, assuming that the fuel is fully vaporized. The volumetric efficiency is 0.85. The air density is 1.06 kg/m<sup>3</sup> and  $c_p$  for air is 1 kJ/kg · K. You may neglect the effects of the heat capacity of the liquid and vapor fuel.
- (b) With port electronic fuel-injection systems, the fuel is injected directly into the intake port. The intake manifold is no longer heated. However, the fuel is only partly vaporized prior to entering the cylinder. Estimate the mixture temperature as it passes through the inlet valve with the EFI system, assuming that the air temperature entering the intake manifold is still 40°C and 50 percent of the fuel is vaporized.
- (c) Estimate the ratio of the maximum indicated power obtained at these conditions with this engine with a carburetor, to the maximum power obtained with port fuel injection. Assume that the inlet valve is the dominant restriction in the flow into the engine and that the pressure ratio across the inlet valve is the same for both carbureted and port-injection fueled engines. The intake mixture pressure and equivalence ratio remain the same in both these cases.

- 7.4. Port fuel-injection systems are replacing carburetors in automobile spark-ignition engines. List the major advantages and any disadvantages of fuel metering with port fuel injection relative to carburetion.
- 7.5. With multipoint port fuel injection and single-point injection systems, the fuel flow rate is controlled by the injection pulse duration. If each injector operates continuously at the maximum rated power point (wide-open throttle,  $A/F = 12$ , 5500 rev/min) of an automobile spark-ignition engine, estimate approximately the injection pulse duration (in crank angle degrees) for the same engine at idle. Idle conditions are: 700 rev/min, 0.3 atm inlet manifold pressure, stoichiometric-mixture.
- 7.6. The fuel-air cycle results indicate that the maximum imep is obtained with gasoline-air mixtures at equivalence ratios of about 1.0. In practice, the maximum wide-open throttle power of a spark-ignition engine at a given speed is obtained with an air/fuel ratio of about 12. The vaporization of the additional gasoline lowers the temperature of the inlet air and the richer mixture has a lower ratio of specific heats  $\gamma_u$  during compression. Estimate approximately the change in mixture temperature due to vaporization of the additional fuel used to decrease  $A/F$  from 14.6 (an equivalence ratio of 1.0) to 12.2 in the intake system, and the combined effect of vaporization and lower  $\gamma_u$  on the unburned mixture temperature at WOT when the cylinder pressure is at its peak of 40 atm. (The principal effect of the richer mixture is its impact on knock.)
- 7.7. (a) Plot dimensionless throttle plate open area  $4A_{th}/(\pi D^2)$  as a function of throttle plate angle  $\psi$ . Assume  $\psi_0 = 10^\circ$ ,  $D$  (throttle bore diameter) = 57 mm,  $d$  (throttle shaft diameter) = 10.4 mm. What is the *throttle plate area*?
- (b) Estimate the average velocity of the air flowing through the throttle plate open area for  $\psi = 26^\circ$  at 3000 rev/min and  $\psi = 36^\circ$  at 2000 rev/min. Use the relationship between  $\psi$ , engine speed, and inlet manifold pressure given in Fig. 7-22. Assume a discharge coefficient  $C_D = 0.8$ .
- (c) For the throttle of part (a), estimate and plot the total force on the throttle plate and shaft, and the force parallel and perpendicular to the throttle bore axis (i.e., in the mean flow direction and normal to that direction) as a function of throttle angle at 2000 rev/min. Again use Fig. 7-22 for the relationship between  $\psi$  and inlet manifold pressure.
- 7.8. For the engine and intake manifold shown in Fig. 7-23, estimate the ratio of the intake manifold runner cross-sectional area to  $(\pi B^2/4)$ , the ratio of the length of the flow path from the intake manifold entrance to the inlet valve seat to the bore, the ratio of the volume of each inlet port to each cylinder's displaced volume, and the ratio of the volume of each intake manifold runner to each cylinder's displaced volume. The cylinder bore is 89 mm.

## REFERENCES

- Nakajima, Y., Sugihara, K., Takagi, Y., and Muranaka, S.: "Effects of Exhaust Gas Recirculation on Fuel Consumption," in *Proceedings of Institution of Mechanical Engineers, Automobile Division*, vol. 195, no. 30, pp. 369-376, 1981.
- Harrington, D. L., and Bolt, J. A.: "Analysis and Digital Simulation of Carburetor Metering," SAE paper 700082, *SAE Trans.*, vol. 79, 1970.
- Bolt, J. A., Derezninski, S. J., and Harrington, D. L.: "Influence of Fuel Properties on Metering in Carburetors," SAE paper 710207, *SAE Trans.*, vol. 80, 1971.

4. Khovakh, M.: *Motor Vehicle Engines* (English translation), Mir Publishers, Moscow, 1976.
5. Bolt, J. A., and Boerma, M. J.: "Influence of Air Pressure and Temperature on Carburetor Metering," SAE paper 660119, 1966.
6. Shinoda, K., Koide, H., and Yui, A.: "Analysis and Experiments on Carburetor Metering at the Transition Region to the Main System," SAE paper 710206, *SAE Trans.*, vol. 80, 1971.
7. Oya, T.: "Upward Liquid Flow in a Small Tube into which Air Streams," *Bull. JSME*, vol. 14, no. 78, pp. 1320-1329, 1971.
8. Wrausmann, R. C., and Smith, R. J.: "An Approach to Altitude Compensation of the Carburetor," SAE paper 760286, 1976.
9. Bosch, *Automotive Handbook*, 1st English ed., Robert Bosch GmbH, Stuttgart, 1978.
10. Glöckler, O., Knapp, H., and Manger, H.: "Present Status and Future Development of Gasoline Fuel Injection Systems for Passenger Cars," SAE paper 800467, 1980.
11. Greiner, M., Romann, P., and Steinbrenner, U.: "BOSCH Fuel Injectors—New Developments," SAE paper 870124, 1987.
12. Gorille, I., Rittmannsberger, N., and Werner, P.: "Bosch Electronic Fuel Injection with Closed Loop Control," SAE paper 750368, *SAE Trans.*, vol. 84, 1975.
13. Czadreck, G. H.: "Ford's 1980 Central Fuel Injection System," SAE paper 790742, 1979.
14. Bowler, L. L.: "Throttle Body Fuel Injection (TBI)—An Integrated Engine Control System," SAE paper 800164, *SAE Trans.*, vol. 89, 1980.
15. Hamann, E., Manger, H., and Steinke, L.: "Lambda-Sensor with  $\text{Y}_2\text{O}_3$ -Stabilized  $\text{ZrO}_2$ -Ceramic for Application in Automotive Emission Control Systems," SAE paper 770401, *SAE Trans.*, vol. 86, 1977.
16. Seiter, R. E., and Clark, R. J.: "Ford Three-Way Catalyst and Feedback Fuel Control System," SAE paper 780203, *SAE Trans.*, vol. 87, 1978.
17. Camp, J., and Rachel, T.: "Closed-Loop Electronic Fuel and Air Control of Internal Combustion Engines," SAE paper 750369, 1975.
18. Liimatta, D. R., Hurt, R. F., Deller, R. W., and Hull, W. L.: "Effects of Mixture Distribution on Exhaust Emissions as Indicated by Engine Data and the Hydraulic Analogy," SAE paper 710618, *SAE Trans.*, vol. 80, 1971.
19. Benson, R. S., Baruah, P. C., and Sierens, I. R.: "Steady and Non-steady Flow in a Simple Carburetor," in *Proceedings of Institution of Mechanical Engineers*, vol. 188, no. 53/74, pp. 537-548, 1974.
20. Woods, W. A., and Goh, G. K.: "Compressible Flow through a Butterfly Throttle Valve in a Pipe," in *Proceedings of Institution of Mechanical Engineers*, vol. 193, no. 10, pp. 237-244, 1979.
21. Walker, J. W.: "The GM 1.8 Liter L-4 Gasoline Engine Designed by Chevrolet," SAE paper 820111, *SAE Trans.*, vol. 91, 1982.
22. Chapman, M.: "Two Dimensional Numerical Simulation of Inlet Manifold Flow in a Four Cylinder Internal Combustion Engine," SAE paper 790244, 1979.
23. Kay, I. W.: "Manifold Fuel Film Effects in an SI Engine," SAE paper 780944, 1978.
24. Brandstetter, W. R., and Carr, M. J.: "Measurement of Air Distribution in a Multicylinder Engine by Means of a Mass Flow Probe," SAE paper 730494, 1973.
25. Aquino, C. F.: "Transient A/F Control Characteristics of the 5 Liter Central Fuel Injection Engine," SAE 810494, *SAE Trans.*, vol. 90, 1981.
26. Trayser, D. A., Creswick, F. A., Giesike, J. A., Hazard, H. R., Weller, A. E., and Locklin, D. W.: "A Study of the Influence of Fuel Atomization, Vaporization, and Mixing Processes on Pollutant Emissions from Motor-Vehicle Powerplants," Battelle Memorial Institute, Columbus, Ohio, 1969.
27. Tabaczynski, R. J.: "Effects of Inlet and Exhaust System Design on Engine Performance," SAE paper 821577, 1982.
28. Engelman, H. W.: "Design of a Tuned Intake Manifold," ASME paper 73-WA/DGP-2, 1973.
29. Benson, R. S.: in J. H. Horlock and D. E. Winterbone (eds.), *The Thermodynamics and Gas Dynamics of Internal Combustion Engines*, vol. 1, Clarendon Press, Oxford, 1982.
30. Chapman, M., Novak, J. M., and Stein, R. A.: "Numerical Modeling of Inlet and Exhaust Flows in Multi-cylinder Internal Combustion Engines," in *Flows in Internal Combustion Engines*, ASME Winter Annual Meeting, Nov. 14-19, 1982, ASME, New York.
31. Bridgeman, O. C.: "Equilibrium Volatility of Motor Fuels from the Standpoint of Their Use in Internal Combustion Engines," National Bureau of Standards research paper 694, 1934.
32. ASTM Standard Method: "Distillation of Petroleum Products," ANSI/ASTM D86 (IP 123/68).
33. Peters, B. D.: "Laser-Video Imaging and Measurement of Fuel Droplets in a Spark-Ignition Engine," in *Proceedings of Conference on Combustion in Engineering*, Oxford, Apr. 11-14, 1983, Institution of Mechanical Engineers, 1983.
34. Sirignano, W. A.: "Fuel Droplet Vaporization and Spray Combustion Theory," *Prog. Energy and Combust. Sci.*, vol. 9, pp. 291-322, 1983.
35. Boam, D. J., and Finlay, I. C.: "A Computer Model of Fuel Evaporation in the Intake System of a Carbureted Petrol Engine," *Conference on Fuel Economy and Emissions of Lean Burn Engines*, London, June 12-14, 1979, paper C89/79, Institution of Mechanical Engineers, 1979.
36. Yun, H. J., and Lo, R. S.: "Theoretical Studies of Fuel Droplet Evaporation and Transportation in a Carburetor Venturi," SAE paper 760289, 1976.
37. Servati, H. B., and Yuen, W. W.: "Deposition of Fuel Droplets in Horizontal Intake Manifolds and the Behavior of Fuel Film Flow on Its Walls," SAE paper 840239, *SAE Trans.*, vol. 93, 1984.
38. Hires, S. D., and Overington, M. T.: "Transient Mixture Strength Excursions—An Investigation of Their Causes and the Development of a Constant Mixture Strength Fueling Strategy," SAE paper 810495, *SAE Trans.*, vol. 90, 1981.
39. Collins, M. H.: "A Technique to Characterize Quantitatively the Air/Fuel Mixture in the Inlet Manifold of a Gasoline Engine," SAE paper 690515, *SAE Trans.*, vol. 78, 1969.
40. Blackmore, D. R., and Thomas, A.: *Fuel Economy of the Gasoline Engine*, John Wiley, 1977.
41. Yu, H. T. C.: "Fuel Distribution Studies—A New Look at an Old Problem," *SAE Trans.*, vol. 71, pp. 596-613, 1963.

# CHAPTER 8

## CHARGE MOTION WITHIN THE CYLINDER

Gas motion within the engine cylinder is one of the major factors that controls the combustion process in spark-ignition engines and the fuel-air mixing and combustion processes in diesel engines. It also has a significant impact on heat transfer. Both the bulk gas motion and the turbulence characteristics of the flow are important. The initial in-cylinder flow pattern is set up by the intake process. It may then be substantially modified during compression. This chapter reviews the important features of gas motion within the cylinder set up by flows into and out of the cylinder through valves or ports, and by the motion of the piston.

### 8.1 INTAKE JET FLOW

The engine intake process governs many important aspects of the flow within the cylinder. In four-stroke cycle engines, the inlet valve is the minimum area for the flow (see Sec. 6.3) so gas velocities at the valve are the highest velocities set up during the intake process. The gas issues from the valve opening into the cylinder as a conical jet and the radial and axial velocities in the jet are about 10 times the mean piston speed. Figure 8-1 shows the radial and axial velocity components close to the valve exit, measured during the intake process, in a motored model engine with transparent walls and single valve located on the cylinder axis, using laser doppler anemometry (see next section).<sup>1</sup> The jet separates from the valve

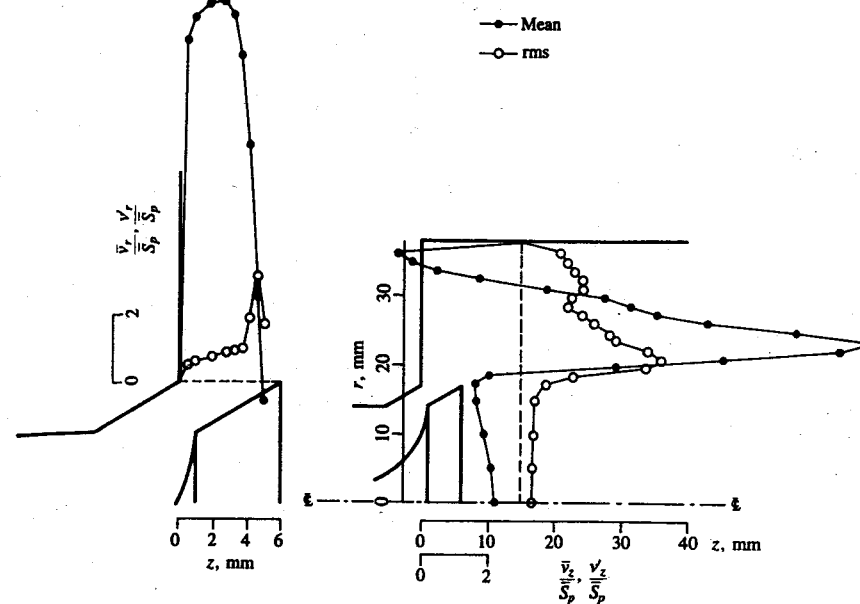


FIGURE 8-1

Radial mean velocity  $\bar{v}_r$  and root mean square (rms) velocity fluctuations  $v'_r$  at the valve exit plane, and axial mean velocity  $\bar{v}_z$  and rms velocity fluctuation  $v'_z$  15 mm below the cylinder head, at 36° ATC in model engine operated at 200 rev/min. Valve lift = 6 mm. Velocities normalized by mean piston speed.<sup>1</sup>

seat and lip, producing shear layers with large velocity gradients which generate turbulence. This separation of the jet sets up recirculation regions beneath the valve head and in the corner between the cylinder wall and cylinder head.

The motion of the intake jet within the cylinder is shown in the schlieren photographs in Fig. 8-2 taken in a transparent engine. This engine had a square cross-section cylinder made up of two quartz walls and two steel walls, to permit easy optical access. The schlieren technique makes regions with density gradients in the flow show up as lighter or darker regions on the film.<sup>2</sup> The engine was throttled to one-half an atmosphere intake pressure, so the jet starts after the intake stroke has commenced, at 35° ATC, following backflow of residual into the intake manifold. The front of the intake jet can be seen propagating from the valve to the cylinder wall at several times the mean piston speed. Once the jet reaches the wall ( $\theta > 41^\circ$  ATC), the wall deflects the major portion of the jet downward toward the piston; however, a substantial fraction flows upward toward the cylinder head. The highly turbulent nature of the jet is evident.

The interaction of the intake jet with the wall produces large-scale rotating flow patterns within the cylinder volume. These are easiest to visualize where the engine geometry has been simplified so the flow is axisymmetric. The photograph

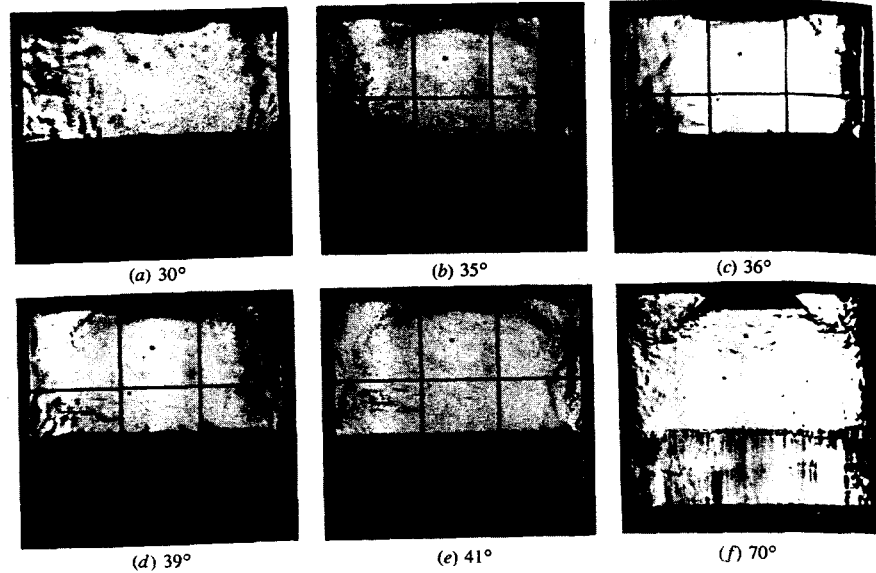


**FIGURE 8-2**  
Sequence of schlieren photographs of intake jet as it develops during intake stroke. Numbers are crank angle degrees after TC.<sup>2</sup>

In Fig. 8-3 of a water analog of an engine intake flow was taken in a transparent model of an engine cylinder and piston. The valve is located in the center of the cylinder head, and the flow into the valve is along the cylinder axis. The experimental parameters have been scaled so that the appropriate dimensionless numbers which govern the flow, the Reynolds and Strouhal numbers, were maintained equal to typical engine values. The photograph shows the major features



**FIGURE 8-3**  
Large-scale rotating flow patterns set up within the cylinder by the intake jet. Photograph of streak lines in water flow into model engine with axisymmetric valve.<sup>3</sup>

of the intake generated flow in a thin illuminated plane through the cylinder axis. The streaks are records of the paths of tracer particles in the flow during the period the camera shutter is open. The bulk of the cylinder as the piston moves down is filled with a large ring vortex, whose center moves downward and remains about halfway between the piston and the head. The upper corner of the cylinder contains a smaller vortex, rotating in the opposite direction. These vortices persist until about the end of the intake stroke, when they became unstable and break up.<sup>3</sup>

With inlet valve location and inlet port geometry more typical of normal engine practice, the intake generated flow is more complex. However, the presence of large-scale rotating flow patterns can still be discerned. Figure 8-4a shows the effect of off-axis valve location (with the flow into the valve still parallel to the cylinder and valve axis). During the first half of the inlet stroke, at least, a flow pattern similar in character to that in Fig. 8-3 is evident. The vortices are now displaced to one side, however, and the planes of their axes of rotation are no longer perpendicular to the cylinder axis but are tipped at an angle to it. The vortices become unstable and break up earlier in the intake stroke than was the case with the axisymmetric flow.<sup>3</sup> With an offset valve and a normal inlet port configuration which turns the flow through 50 to 70° (see Fig. 6-13), photographs

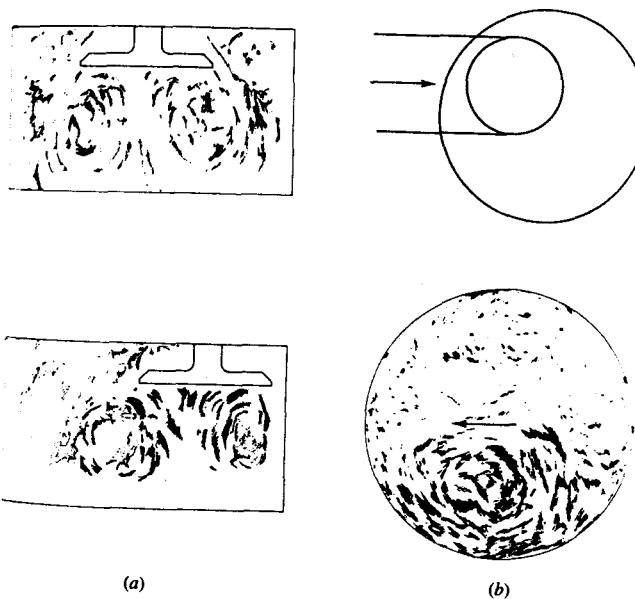


**FIGURE 8-4**  
Sketches from: (a) streak photographs of in-cylinder intake generated flow in water analog of intake process in model engine with offset inlet valve, at 90° ATC;<sup>3</sup> (b) streak photographs of flow in diametral plane; 30 mm below cylinder head, with intake port and valve geometry shown, with steady water flow into cylinder. Valve lift = 4 mm.<sup>4</sup>

of the flow pattern in a diametral plane show an additional large-scale rotation. Figure 8-4b shows the flow pattern observed in a water-flow model of the cylinder in a plane 30 mm (one-third of the bore) from the cylinder head, with a standard inlet port design. The direction of flow with this vortex pair is toward the left across the center of the cylinder. This flow pattern occurs because the cylinder wall closest to the valve impedes the flow out of the valve and forces the flow on either side of the plane passing through the valve and cylinder axes to circulate around the cylinder in opposite directions. The upper vortex follows the flow direction of the port and becomes larger still as the valve lift increases. The details of this aspect of the intake flow depend on the port design, valve stem orientation, and the valve lift.<sup>4</sup> With suitable port and/or cylinder head design, it is possible to develop a single vortex flow within the bulk of the cylinder. The production and characteristics of such "swirling" flows are reviewed in Sec. 8.3.

In summary, the jet-like character of the intake flow, interacting with the cylinder walls and moving piston, creates large-scale rotating flow patterns within the cylinder. The details of these flows are strongly dependent on the inlet port, valve, and cylinder head geometry. These flows appear to become unstable, either during the intake or the compression process, and break down into three-dimensional turbulent motions. Recirculating flows of this type are usually sensitive to small variations in the flow; hence there are probably substantial cycle-by-cycle flow variations.<sup>5</sup>

## 8.2 MEAN VELOCITY AND TURBULENCE CHARACTERISTICS

### 8.2.1 Definitions

The flow processes in the engine cylinder are turbulent. In turbulent flows, the rates of transfer and mixing are several times greater than the rates due to molecular diffusion. This turbulent "diffusion" results from the local fluctuations in the flow field. It leads to increased rates of momentum and heat and mass transfer, and is essential to the satisfactory operation of spark-ignition and diesel engines. Turbulent flows are always dissipative. Viscous shear stresses perform deformation work on the fluid which increases its internal energy at the expense of its turbulence kinetic energy. So energy is required to generate turbulence: if no energy is supplied, turbulence decays. A common source of energy for turbulent velocity fluctuations is shear in the mean flow. Turbulence is rotational and is characterized by high fluctuating vorticity: these vorticity fluctuations can only persist if the velocity fluctuations are three dimensional.<sup>6</sup>

The character of a turbulent flow depends on its environment. In the engine cylinder, the flow involves a complicated combination of turbulent shear layers, recirculating regions, and boundary layers. The flow is unsteady and may exhibit substantial cycle-to-cycle fluctuations. Both large-scale and small-scale turbulent motions are important factors governing the overall behavior of the flow.<sup>5</sup>

An important characteristic of a turbulent flow is its irregularity or ran-

domness. Statistical methods are therefore used to define such a flow field. The quantities normally used are: the mean velocity, the fluctuating velocity about the mean, and several length and time scales. In a steady turbulent flow situation, the instantaneous local fluid velocity  $U$  (in a specific direction) is written:

$$U(t) = \bar{U} + u(t) \quad (8.1)$$

For steady flow, the mean velocity  $\bar{U}$  is the time average of  $U(t)$ :

$$\bar{U} = \lim_{\tau \rightarrow \infty} \frac{1}{\tau} \int_{t_0}^{t_0 + \tau} U(t) dt \quad (8.2)$$

The fluctuating velocity component  $u$  is defined by its root mean square value, the turbulence intensity,  $u'$ :

$$u' = \lim_{\tau \rightarrow \infty} \left( \frac{1}{\tau} \int_{t_0}^{t_0 + \tau} u^2 dt \right)^{1/2} \quad (8.3a)$$

Alternatively,

$$u' = \lim_{\tau \rightarrow \infty} \left[ \frac{1}{\tau} \int_{t_0}^{t_0 + \tau} (U^2 - \bar{U}^2) dt \right]^{1/2} \quad (8.3b)$$

since the time average of  $(u\bar{U})$  is zero.

In engines, the application of these turbulence concepts is complicated by the fact that the flow pattern changes during the engine cycle. Also, while the overall features of the flow repeat each cycle, the details do not because the mean flow can vary significantly from one engine cycle to the next. There are both cycle-to-cycle variations in the mean or bulk flow at any point in the cycle, as well as turbulent fluctuations about that specific cycle's mean flow.

One approach used in quasi-periodic flows such as that which occurs in the engine cylinder is *ensemble-averaging* or *phase-averaging*. Usually, velocity measurements are made over many engine cycles, and over a range of crank angles. The instantaneous velocity at a specific crank angle position  $\theta$  in a particular cycle  $i$  can be written as

$$U(\theta, i) = \bar{U}(\theta, i) + u(\theta, i) \quad (8.4)$$

The ensemble- or phase-averaged velocity,  $\bar{U}(\theta)$ , is defined as the average of values at a specific phase or crank angle in the basic cycle. Figure 8-5 shows this approach applied schematically to the velocity variation during a two-stroke engine cycle, with small and large cycle-to-cycle variations. The ensemble-averaged velocity is the average over a large number of measurements taken at the same crank angle (two such points are indicated by dots):

$$\bar{U}_{EA}(\theta) = \frac{1}{N_c} \sum_{i=1}^{N_c} U(\theta, i) \quad (8.5)$$

where  $N_c$  is the number of cycles for which data are available. By repeating this

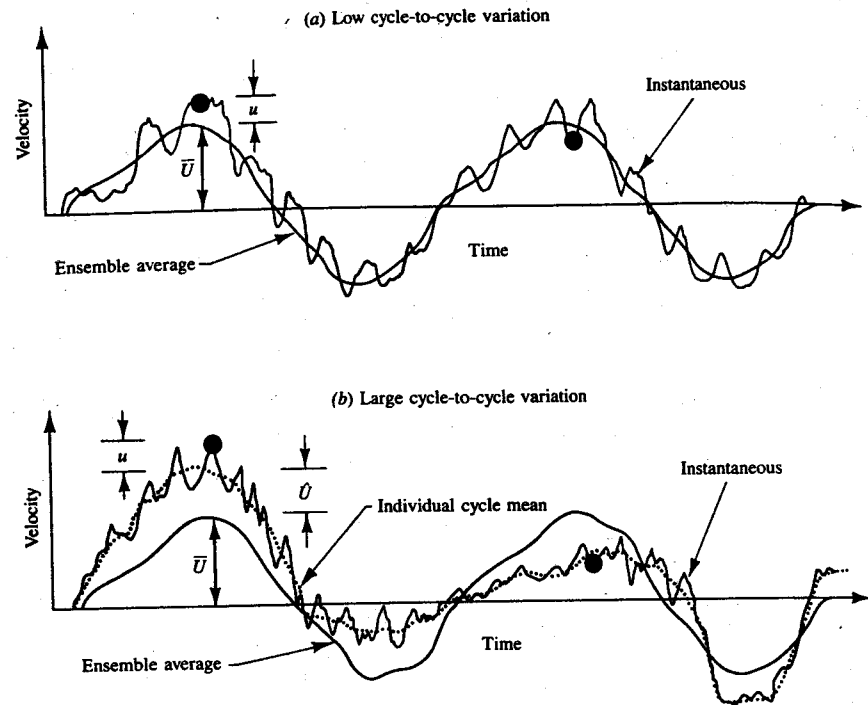


FIGURE 8-5

Schematic of velocity variation with crank angle at a fixed location in the cylinder during two consecutive cycles of an engine. Dots indicate measurements of instantaneous velocity at the same crank angle. Ensemble- or phase-averaged velocity obtained by averaging over a large number of such measurements shown as solid smooth line. Top graph: low cycle-to-cycle flow variations. Here the individual-cycle mean velocity and ensemble-averaged velocity are closely comparable. Bottom graph: large cycle-to-cycle variations. Here the individual-cycle mean velocity (dotted line) is different from the ensemble-averaged mean by  $\bar{U}$ . The turbulent fluctuation  $u$  is then defined in relation to the individual-cycle mean.<sup>5</sup>

process at many crank angle locations, the ensemble-averaged velocity profile over the complete cycle is obtained.

The ensemble-averaged mean velocity is only a function of crank angle since the cyclic variation has been averaged out. The difference between the mean velocity in a particular cycle and the ensemble-averaged mean velocity over many cycles is defined as the cycle-by-cycle variation in mean velocity:

$$\hat{U}(\theta, i) = \bar{U}(\theta, i) - \bar{U}_{EA}(\theta) \quad (8.6)$$

Thus the instantaneous velocity, given by Eq. (8.4), can be split into three components:<sup>7</sup>

$$U(\theta, i) = \bar{U}_{EA}(\theta) + \hat{U}(\theta, i) + u(\theta, i) \quad (8.7)$$

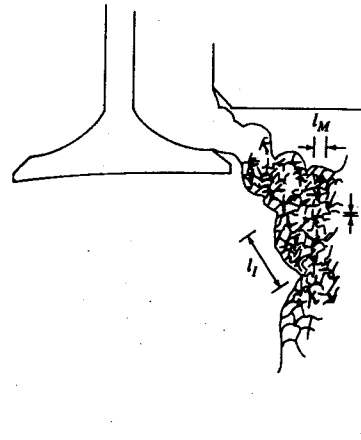


FIGURE 8-6

Schematic of jet created by flow through the intake valve indicating its turbulent structure.<sup>5,6</sup>

Figure 8-5 illustrates this breakdown of the instantaneous velocity into an ensemble-averaged component, an individual-cycle mean velocity, and a component which randomly fluctuates in time at a particular point in space in a single cycle. This last component is the conventional definition of the turbulent velocity fluctuation. Whether this differs significantly from the fluctuations about the ensemble-averaged velocity depends on whether the cycle-to-cycle fluctuations are small or large. The figure indicates these two extremes.<sup>†</sup>

In turbulent flows, a number of length scales exist that characterize different aspects of the flow behavior. The largest eddies in the flow are limited in size by the system boundaries. The smallest scales of the turbulent motion are limited by molecular diffusion. The important length scales are illustrated by the schematic of the jet issuing into the cylinder from the intake valve in Fig. 8-6. The eddies responsible for most of the turbulence production during intake are the large eddies in the conical inlet jet flow. These are roughly equal in size to the local jet thickness. This scale is called the *integral scale*,  $l_I$ : it is a measure of the largest scale structure of the flow field. Velocity measurements made at two points separated by a distance  $x$  significantly less than  $l_I$  will correlate with each other; with  $x \gg l_I$ , no correlation will exist. The integral length scale is, therefore, defined as the integral of the autocorrelation coefficient of the fluctuating velocity at two adjacent points in the flow with respect to the variable distance between

<sup>†</sup> There is considerable debate as to whether the fluctuating components of the velocity  $U(\theta, i)$  defined by Eq. (8.7) (cycle fluctuations in the mean velocity and fluctuations in time about the individual cycle mean) are physically distinct phenomena. The high-frequency fluctuations in velocity are often defined as "turbulence." The low-frequency fluctuations are generally attributed to the variations in the mean flow between individual cycles, a phenomenon that is well established. Whether this distinction is valid has yet to be resolved.

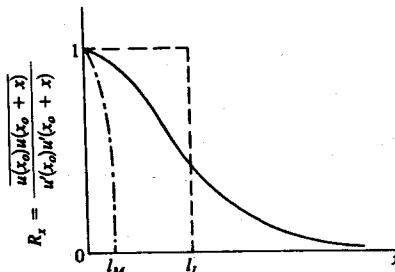


FIGURE 8-7

Spatial velocity autocorrelation  $R_x$  as a function of  $x$ , defining the integral length scale  $l_I$  and the micro length scale  $l_M$ .

the points, as shown in Fig. 8-7; i.e.,

$$l_I = \int_0^\infty R_x dx \quad (8.8a)$$

where

$$R_x = \frac{1}{N_m - 1} \sum_{i=1}^{N_m} \frac{u(x_0)u(x_0 + x)}{u'(x_0)u'(x_0 + x)} \quad (8.8b)$$

This technique for determining the integral scale requires simultaneous measurements at two points. Due to the difficulty of applying such a technique in engines, most efforts to determine length scales have first employed correlations to determine the *integral time scale*,  $\tau_I$ . The integral time scale of turbulence is defined as a correlation between two velocities at a fixed point in space, but separated in time:

$$\tau_I = \int_0^\infty R_t dt \quad (8.9a)$$

where

$$R_t = \frac{1}{N_m - 1} \sum_{i=1}^{N_m} \frac{u(t_0)u(t_0 + t)}{u'(t_0)u'(t_0 + t)} \quad (8.9b)$$

and  $N_m$  is the number of measurements. Under conditions where the turbulence pattern is convected past the observation point without significant distortion and the turbulence is relatively weak, the integral length and time scales are related by

$$l_I = \bar{U}\tau_I \quad (8.10)$$

In flows where the large-scale structures are convected,  $\tau_I$  is a measure of the time it takes a large eddy to pass a point. In flows without mean motion, the integral time scale is an indication of the lifetime of an eddy.<sup>5,8</sup>

Superposed on this large-scale flow is a range of eddies of smaller and smaller size, fed by the continual breakdown of larger eddies. Since the smaller eddies respond more rapidly to changes in local flow pattern, they are more likely

to be isotropic (have no preferred direction) than are the large eddies, and have a structure like that of other turbulent flows. The dissipation of turbulence energy takes place in the smallest structures. At this smallest scale of the turbulent motion, called the *Kolmogorov scale*, molecular viscosity acts to dissipate small-scale kinetic energy into heat. If  $\varepsilon$  is the energy dissipation rate per unit mass and  $v$  the kinematic viscosity, Kolmogorov length and time scales are defined by

$$l_K = \left( \frac{v^3}{\varepsilon} \right)^{1/4} \quad \tau_K = \left( \frac{v}{\varepsilon} \right)^{1/2} \quad (8.11)$$

The Kolmogorov length scale indicates the size of the smallest eddies. The Kolmogorov time scale characterizes the momentum-diffusion of these smallest structures.

A third scale is useful in characterizing a turbulent flow. It is called the *microscale* (or Taylor microscale). The micro length scale  $l_M$  is defined by relating the fluctuating strain rate of the turbulent flow field to the turbulence intensity:

$$\frac{\partial u}{\partial x} \approx \frac{u'}{l_M} \quad (8.12)$$

It can be determined from the curvature of the spatial correlation curve at the origin, as shown in Fig. 8-7.<sup>5,6</sup> More commonly, the micro time scale  $\tau_M$  is determined from the temporal autocorrelation function of Eq. (8.9):

$$\tau_M^2 = - \frac{2}{(\partial^2 R_t / \partial t^2)_{t_0}}$$

For turbulence which is homogeneous (has no spatial gradients) and is isotropic (has no preferred direction), the microscales  $l_M$  and  $\tau_M$  are related by

$$l_M = \bar{U}\tau_M \quad (8.13)$$

These different scales are related as follows. The turbulent kinetic energy per unit mass in the large-scale eddies is proportional to  $u'^2$ . Large eddies lose a substantial fraction of this energy in one "turnover" time  $l_I/u'$ . In an equilibrium situation the rate of energy supply equals the rate of dissipation:

$$\varepsilon \approx \frac{u'^3}{l_I}$$

Thus,

$$\frac{l_K}{l_I} \approx \left( \frac{u' l_I}{v} \right)^{-3/4} = Re_T^{-3/4} \quad (8.14)$$

where  $Re_T$  is the turbulent Reynolds number,  $u' l_I/v$ .

Within the restrictions of homogeneous and isotropic turbulence, an energy budget can be used to relate  $l_I$  and  $l_M$ .<sup>6</sup>

$$\varepsilon = \frac{A u'^3}{l_I} = \frac{15 v u'^2}{l_M^2}$$

where  $A$  is a constant of order 1. Thus,

$$\frac{l_M}{l_I} = \left( \frac{15}{A} \right)^{1/2} \text{Re}_T^{-1/2} \quad (8.15)$$

These restrictions are not usually satisfied within the engine cylinder during intake. They are approximately satisfied at the end of compression.

### 8.2.2 Application to Engine Velocity Data

As has been explained above, it is necessary to analyze velocity data on an individual cycle basis as well as using ensemble-averaging techniques. The basic definitions for obtaining velocities which characterize the flow will now be developed. The ensemble-averaged velocity  $\bar{U}_{EA}$  has already been defined by Eq. (8.5). The ensemble-averaged fluctuation intensity  $u'_{F, EA}$  is given by

$$u'_{F, EA}(\bar{\theta}) = \left\{ \frac{1}{N_c} \sum_{i=1}^{N_c} [u(\bar{\theta}, i)]^2 \right\}^{1/2} = \left\{ \frac{1}{N_c} \sum_{i=1}^{N_c} [U(\bar{\theta}, i)^2 - \bar{U}_{EA}(\bar{\theta})^2] \right\}^{1/2} \quad (8.16)$$

It includes all fluctuations about the ensemble-averaged mean velocity.

Use of Eqs. (8.5) and (8.16) requires values for  $U$  and  $u$  at each specific crank angle under consideration. While some measurement techniques (e.g., hot-wire anemometry) provide this, the preferred velocity measurement method (laser doppler anemometry) provides an intermittent signal. With laser doppler anemometry (LDA), interference fringes are produced within the small volume created by the intersection of two laser beams within the flow field. When a small particle passes through this volume, it scatters light at a frequency proportional to the particle velocity. By seeding the flow with particles small enough to be carried without slip by the flow and collecting this scattered light, the flow velocity is determined.<sup>9</sup> A signal is only produced when a particle moves through the measurement volume; thus one collects data as velocity crank angle pairs. It is necessary, therefore, to perform the ensemble-averaging over a finite crank angle window  $\Delta\theta$  around the specific crank angle of interest,  $\bar{\theta}$ . The ensemble-averaged velocity equation becomes

$$\bar{U}_{EA}(\bar{\theta}) = \frac{1}{N_t} \sum_{i=1}^{N_t} \sum_{j=1}^{N_i} U_{i,j} \left( \bar{\theta} \pm \frac{\Delta\theta}{2} \right) \quad (8.17)$$

where  $N_i$  is the number of velocity measurements recorded in the window during the  $i$ th cycle,  $N_t$  is the number of cycles, and  $N_t$  is the total number of measurements.<sup>†</sup> The corresponding equation for the ensemble-averaged root mean square

<sup>†</sup> This need to ensemble-average over a finite crank angle window introduces an error called crank angle broadening, due to change in the mean velocity across the window. This error depends on the velocity gradient, and can be made negligibly small by suitable choice of window size.<sup>9-11</sup>

velocity fluctuation is

$$u'_{F, EA}(\bar{\theta}) = \left\{ \frac{1}{N_t} \sum_{i=1}^{N_t} \sum_{j=1}^{N_i} \left[ u_{i,j} \left( \bar{\theta} \pm \frac{\Delta\theta}{2} \right) \right]^2 \right\}^{1/2} \quad (8.18)$$

where

$$u_{i,j} = U_{i,j} - \bar{U}_{EA} \quad (8.19)$$

As has already been explained, this definition of fluctuation intensity [the ensemble-averaged rms velocity fluctuation, Eq. (8.18)] includes cyclic variations in the mean flow as well as the turbulent fluctuations about each cycle's mean flow.<sup>7</sup> It is necessary to determine the mean and fluctuating velocities on an individual-cycle basis to characterize the flow field more completely. The critical part of this process is defining the mean velocity at a specific crank angle (or within a small window centered about that crank angle) in each cycle. Several methods have been used to determine this individual-cycle mean velocity (e.g., moving window, low-pass filtering, data smoothing, conditional sampling; see Ref. 7 for a summary). A high data rate is required.

In this individual-cycle velocity analysis the individual-cycle time-averaged or mean velocity  $\bar{U}(\bar{\theta}, i)$  is first determined.<sup>7,12</sup> The ensemble average of this mean velocity

$$\bar{U}_{EA}(\bar{\theta}) = \frac{1}{N_c} \sum_{i=1}^{N_c} \bar{U}\left(\bar{\theta} \pm \frac{\Delta\theta}{2}, i\right) \quad (8.20)$$

is identical to the ensemble-averaged value given by Eq. (8.17). The root mean square fluctuation in individual-cycle mean velocity can then be determined from

$$U_{RMS}(\bar{\theta}) = \left\{ \frac{1}{N_c} \sum_{i=1}^{N_c} \left[ \bar{U}\left(\bar{\theta} \pm \frac{\Delta\theta}{2}, i\right) - \bar{U}_{EA}(\bar{\theta}) \right]^2 \right\}^{1/2} \quad (8.21)$$

This indicates the magnitude of the cyclic fluctuations in the mean motion. The instantaneous velocity fluctuation from the mean velocity, within a specified window  $\Delta\theta$  at a particular crank angle  $\bar{\theta}$ , is obtained from Eq. (8.4). This instantaneous velocity fluctuation is ensemble-averaged, because it varies substantially cycle-by-cycle and because the amount of data is usually insufficient to give reliable individual-cycle results:

$$u'_{T, EA}(\bar{\theta}) = \left\{ \frac{1}{N_c} \sum_{i=1}^{N_c} \left[ U\left(\bar{\theta} \pm \frac{\Delta\theta}{2}, i\right) - \bar{U}\left(\bar{\theta} \pm \frac{\Delta\theta}{2}, i\right) \right]^2 \right\}^{1/2} \quad (8.22)$$

This quantity is the ensemble-averaged turbulence intensity.

Several different techniques have been used to measure gas velocities within the engine cylinder (see Refs. 13 and 14 for brief reviews and references). The technique which provides most complete and accurate data is laser doppler anemometry.<sup>9</sup> Sample results obtained with this technique will now be reviewed to

illustrate the major features of the in-cylinder gas motion. The available results must be interpreted with caution since they have been obtained in special engines where the geometry and flow have been modified to make the experiments and their interpretation easier. Also, the flow within the cylinder is three dimensional in nature. It takes measurements at many points within the flow field and the use of a flow visualization technique to characterize the flow adequately.

Figure 8-8 shows ensemble-averaged velocities throughout the engine cycle at two measurement locations in a special L-head engine designed to generate a swirling flow within the cylinder. The engine was motored at 300 rev/min, giving a mean piston speed of 0.76 m/s. Figure 8-8b shows the mean velocity in the path of the swirling intake flow within the clearance volume, in the swirl direction. High velocities are generated during the intake process, rising to a maximum and then decreasing in response to the piston motion (see Fig. 2-2). During the compression stroke, the velocity continues to decrease but at a much slower rate. This is a motored engine cycle. A comparison of intake and compression velocities with an equivalent firing cycle showed close agreement.<sup>15</sup> The expansion and

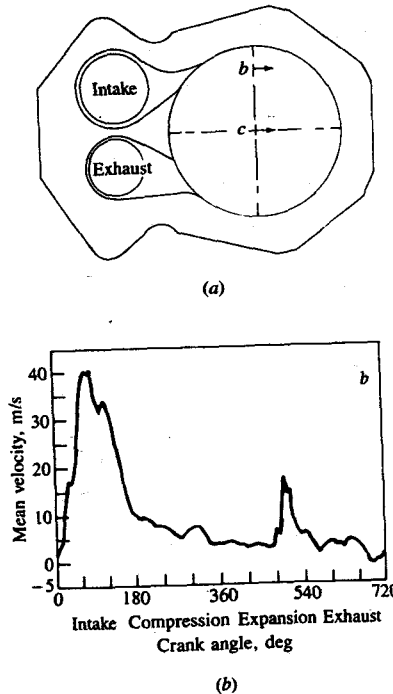


**FIGURE 8-8**  
Ensemble-averaged velocities throughout the engine cycle in motored four-stroke L-head engine:  
rev/min, mean piston speed 0.76 m/s. (a) Engine schematic showing measurement locations and velocity directions; (b) velocity at b in intake flow path; (c) velocity at c on cylinder axis.<sup>11</sup>

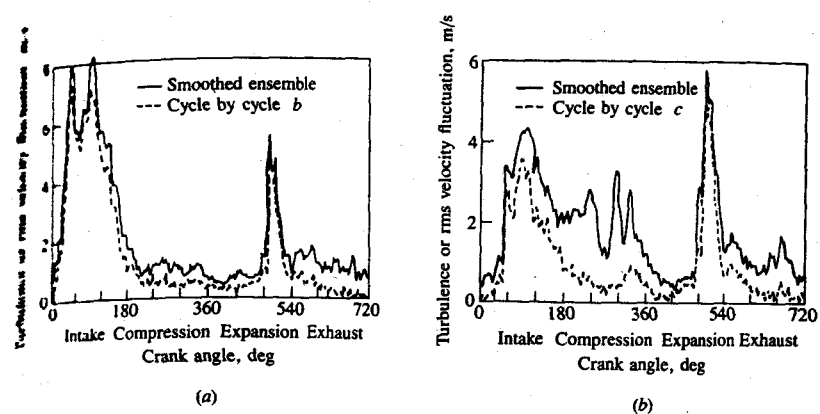


**FIGURE 8-9**  
Ensemble-averaged rms velocity fluctuation and ensemble-averaged individual-cycle turbulence intensity as a function of crank angle: (a) at location b in Fig. 8-8a; (b) at location c in Fig. 8-8a.<sup>11</sup>

exhaust stroke velocities are not typical of firing engine behavior, however.<sup>†</sup> Figure 8-8c shows the mean velocity in the clearance volume in the same direction but on the cylinder axis. At this location, positive and negative flow velocities were measured. Since this location is out of the path of the intake generated flow, velocities during the intake stroke are much lower. The nonhomogeneous character of this particular ensemble-mean flow is evident.

Figure 8-9 shows the ensemble-averaged rms velocity fluctuation (which includes contributions from cycle-by-cycle variations in the mean flow and turbulence) and the ensemble-averaged individual-cycle turbulence intensity at these same two locations and directions. The difference between the two curves in each graph is an indication of the cycle-by-cycle variation in the mean flow [see Eq. (8.7)]. During the intake process, within the directed intake flow pattern, the cycle-by-cycle variation in the mean flow is small in comparison to the high turbulence levels created by the intake flow. Outside this directed flow region, again during intake, this cycle-by-cycle contribution is more significant relative to the turbulence. During compression, the cycle-by-cycle mean flow variation is comparable in magnitude to the ensemble-averaged turbulence intensity. It is therefore highly significant.

Two important questions regarding the turbulence in the engine cylinder are whether it is homogeneous (i.e., uniform) and whether it is isotropic (i.e., independent of direction). The data already presented in Figs. 8-8 and 8-9 show that during intake the flow is far from homogeneous. Nor is it isotropic.<sup>11</sup>

\* The increase in velocity when the exhaust valve opens is due to the flow of gas into the cylinder because, due primarily to heat losses, the cylinder pressure is then below 1 atm.

However, it is the character of the turbulence at the end of the compression process that is most important: that is what controls the fuel-air mixing and burning rates. Only limited data are available which relate to these questions. With open disc-shaped combustion chambers, measurements at different locations in the clearance volume around TC at the end of compression show the turbulence intensity to be relatively homogeneous. In the absence of an intake generated swirling flow, the turbulence intensity was also essentially isotropic near TC.<sup>16</sup> These specific results support the more general conclusion that the inlet boundary conditions play the dominant role in the generation of the mean flow and turbulence fields during the intake stroke. However, in the absence of swirl, this intake generated flow structure has almost disappeared by the time the compression process commences. The turbulence levels follow this trend in the mean flow, with the rapid decay process lasting until intake valve closing. Later in the compression process the turbulence becomes essentially homogeneous.<sup>17</sup>

When a swirling flow is generated during intake, an almost solid-body rotating flow develops which remains stable for much longer than the inlet jet generated rotating flows illustrated in Fig. 8-3. With simple disc-shaped chambers, the turbulence still appears to become almost homogeneous at the end of compression. With swirl and bowl-in-piston geometry chambers, however, the flow is more complex (see Sec. 8.3).

The flow through the intake valve or port is responsible for many features of the in-cylinder motion. The flow velocity through the valve is proportional to the piston speed [see Eq. (6.10) for pseudo valve flow velocity, and Eq. 2.10]. It would be expected therefore that in-cylinder flow velocities at different engine speeds would scale with mean piston speed [Eq. (2.11)]. Figure 8-10 shows ensemble-averaged mean and rms velocity fluctuations, normalized by the mean piston speed through the cycle at three different engine speeds. The measurement location is in the path of the intake generated swirling flow (point *b* in Fig. 8-8a). All the curves have approximately the same shape and magnitude, indicating the

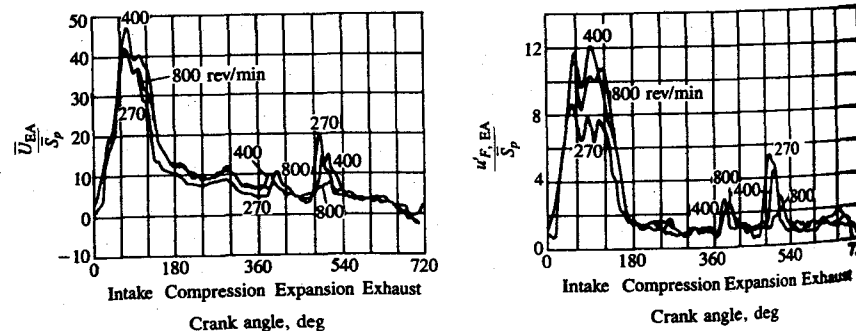


FIGURE 8-10  
Ensemble-averaged mean and rms velocity fluctuations, normalized by mean piston speed, throughout the engine cycle for three engine speeds. Location *b* in Fig. 8-8a.<sup>11</sup>

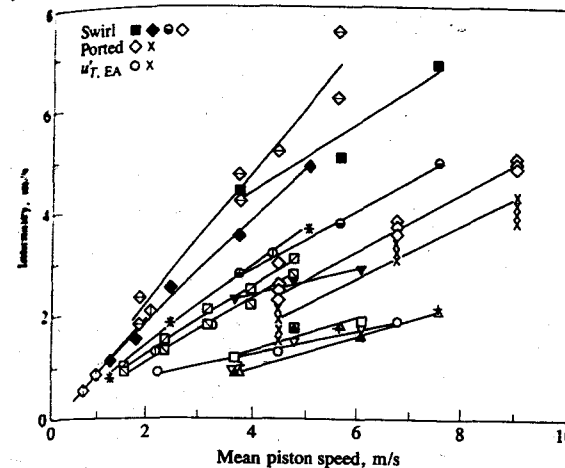


FIGURE 8-11

Individual-cycle turbulence intensity  $u'_T, EA$  (OX) and ensemble-averaged rms fluctuation velocity (remaining symbols) at TC at the end of compression, for a number of different flow configurations and chamber geometries as a function of mean piston speed.<sup>16</sup> Two data sets for two-stroke ported engines. Four data sets with intake generated swirl.

appropriateness of this velocity scaling.<sup>†</sup> Other results support this conclusion, though in the absence of an ordered mean motion such as swirl when the ensemble-averaged mean velocities at the end of compression are low, this scaling for the mean velocity does not always hold.<sup>16</sup> Figure 8-11 shows a compilation of ensemble-averaged rms fluctuation velocity or ensemble-averaged individual-cycle turbulence intensity results at TC at the end of compression, from 13 different flow configurations and combustion chamber geometries. Two of these sets of results are from two-stroke cycle ported configurations. The measured fluctuating velocities or turbulence intensities are plotted against mean piston speed. The linear relationship holds well. There is a substantial variation in the proportionality constant, in part because in most of these studies (identified in the figure) the ensemble-averaged rms fluctuation velocity was the quantity measured. Since this includes the cycle-by-cycle fluctuation in the mean velocity, it is larger (by up to a factor of 2) than the average turbulence intensity  $u'_T, EA$ .

A consensus conclusion is emerging from these studies that the turbulence intensity at top-center, with open combustion chambers in the absence of swirl, has a maximum value equal to about half the mean piston speed.<sup>16, 18</sup>

$$u'_T, EA(TC) \approx 0.5 \bar{S}_p \quad (8.23)$$

<sup>†</sup> Note that because of the valve and combustion chamber of this particular engine, the ratio of  $\bar{U}$  to  $\bar{s}$  is higher than is typical of normal engine geometries.

The available data show that the turbulence intensity at TC with swirl is usually higher than without swirl<sup>16</sup> (see the four data sets with swirl in Fig. 8-11). Some data, however, indicate that the rms fluctuation intensity with swirl may be lower.<sup>18</sup> The ensemble-averaged cyclic variation in individual-cycle mean velocity at the end of compression also scales with mean piston speed. This quantity can be comparable in magnitude to the turbulence intensity. It usually decreases when a swirling flow is generated within the cylinder during the intake process.<sup>11, 16</sup>

During the compression stroke, and also during combustion while the cylinder pressure continues to rise, the unburned mixture is compressed. Turbulent flow properties are changed significantly by the large and rapidly imposed distortions that result from this compression. Such distortions, in the absence of dissipation, would conserve the angular momentum of the flow: rapid compression would lead to an increase in vorticity and turbulence intensity. There is evidence that, with certain types of in-cylinder flow pattern, an increase in turbulence intensity resulting from piston motion and combustion does occur toward the end of the compression process. The compression of large-scale rotating flows can cause this increase due to the increasing angular velocity required to conserve angular momentum resulting in a growth in turbulence generation by shear.<sup>19</sup>

Limited results are available which characterize the turbulence time and length scales in automobile engine flows. During the intake process, the integral length scale is of the order of the intake jet diameter, which is of the order of the valve lift ( $\lesssim 10$  mm in automobile-size engines). During compression the flow relaxes to the shape of the combustion chamber. The integral time scale at the end of compression decreases with increasing engine speed. It is of order 1 ms at engine speeds of about 1000 rev/min. The integral length scale at the end of compression is believed to scale with the clearance height and varies little with engine speed. It decreases as the piston approaches TC to about 2 mm ( $0.2 \times$  clearance height). The micro time scale at the end of compression is of order 0.1 ms at 1000 rev/min, and decreases as engine speed increases (again in automobile-size engine cylinders). Micro length scales are of order 1 mm at the end of compression and vary little with engine speed. Kolmogorov length scales at the end of compression are of order  $10^{-2}$  mm.<sup>8, 20, 21</sup>

### 8.3 SWIRL

*Swirl* is usually defined as organized rotation of the charge about the cylinder axis. Swirl is created by bringing the intake flow into the cylinder with an initial angular momentum. While some decay in swirl due to friction occurs during the engine cycle, intake generated swirl usually persists through the compression, combustion, and expansion processes. In engine designs with bowl-in-piston combustion chambers, the rotational motion set up during intake is substantially modified during compression. Swirl is used in diesels and some stratified-charge engine concepts to promote more rapid mixing between the inducted air charge

and the injected fuel. Swirl is also used to speed up the combustion process in spark-ignition engines. In two-stroke engines it is used to improve scavenging. In some designs of prechamber engines, organized rotation about the prechamber axis is also called swirl. In prechamber engines where swirl within the precombustion chamber is important, the flow into the prechamber during the compression process creates the rotating flow. Prechamber flows are discussed in Sec. 8.5.

#### 8.3.1 Swirl Measurement

The nature of the swirling flow in an actual operating engine is extremely difficult to determine. Accordingly, steady flow tests are often used to characterize the swirl. Air is blown steadily through the inlet port and valve assembly in the cylinder head into an appropriately located equivalent of the cylinder. A common technique for characterizing the swirl within the cylinder has been to use a light paddle wheel, pivoted on the cylinder centerline (with low friction bearings), mounted between 1 and 1.5 bore diameters down the cylinder. The paddle wheel diameter is close to the cylinder bore. The rotation rate of the paddle wheel is used as a measure of the air swirl. Since this rotation rate depends on the location of the wheel and its design, and the details of the swirling flow, this technique is being superseded by the impulse swirl meter shown in Fig. 8-12. A honeycomb flow straightener replaces the paddle wheel: it measures the total torque exerted by the swirling flow. This torque equals the flux of angular

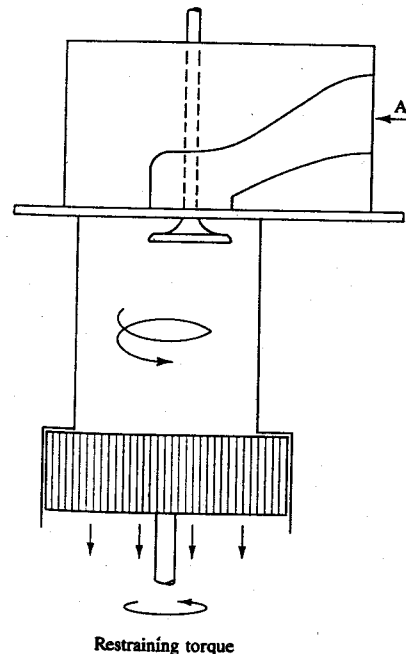


FIGURE 8-12  
Schematic of steady-flow impulse torque swirl meter.<sup>22</sup>

momentum through the plane coinciding with the flow-straightener upstream face.

For each of these approaches, a *swirl coefficient* is defined which essentially compares the flow's angular momentum with its axial momentum. For the paddle wheel, the swirl coefficient  $C_s$  is defined by

$$C_s = \frac{\omega_p B}{v_0} \quad (8.24)$$

where  $\omega_p$  is the paddle wheel angular velocity ( $= 2\pi N_p$ , where  $N_p$  is the rotational speed) and the bore  $B$  has been used as the characteristic dimension. The characteristic velocity,  $v_0$ , is derived from the pressure drop across the valve using an incompressible flow equation:

$$v_0 = \left[ \frac{2(p_0 - p_c)}{\rho} \right]^{1/2} \quad (8.25)$$

or a compressible flow equation:

$$v_0 = \left\{ \frac{2\gamma}{(\gamma - 1)} \frac{p_0}{\rho_0} \left[ 1 - \left( \frac{p_c}{p_0} \right)^{(\gamma-1)/\gamma} \right] \right\}^{1/2} \quad (8.26)$$

where the subscripts 0 and  $c$  refer to upstream stagnation and cylinder values, respectively. The difference between Eqs. (8.25) and (8.26) is usually small. With the impulse torque meter, characteristic velocity and length scales must also be introduced. Several swirl parameters have been defined.<sup>22, 23</sup> The simplest is

$$C_s = \frac{8T}{\dot{m}v_0 B} \quad (8.27)$$

where  $T$  is the torque and  $\dot{m}$  the air mass flow rate. The velocity  $v_0$ , defined by Eq. (8.25) or Eq. (8.26), and the bore have again been used to obtain a dimensionless coefficient. Note that for solid-body rotation of the fluid within the cylinder at the paddle wheel speed  $\omega_p$ , Eqs. (8.24) and (8.27) give identical swirl coefficients. In practice, because the swirling flow is not solid-body rotation and because the paddle wheel usually lags the flow due to slip, the impulse torque meter gives higher swirl coefficients.<sup>23</sup> When swirl measurements are made in an operating engine, a *swirl ratio* is normally used to define the swirl. It is defined as the angular velocity of a solid-body rotating flow  $\omega_s$ , which has equal angular momentum to the actual flow, divided by the crankshaft angular rotational speed:

$$R_s = \frac{\omega_s}{2\pi N} \quad (8.28)$$

During the induction stroke in an engine the flow and the valve open area, and consequently the angular momentum flux into the cylinder, vary with crank angle. Whereas in rig tests the flow and valve open area are fixed and the angular momentum passes down the cylinder continuously, in the engine intake process

the momentum produced under corresponding conditions of flow and valve lift remains in the cylinder. Steady-state impulse torque-meter flow rig data can be used to estimate engine swirl in the following manner.<sup>23</sup> Assuming that the port and valve retain the same characteristics under the transient conditions of the engine as on the steady-flow rig, the equivalent solid-body angular velocity  $\omega_s$  at the end of the intake process is given by

$$\omega_s = \frac{8}{B^2} \left( \int_{\theta_1}^{\theta_2} T d\theta \right) / \left( \int_{\theta_1}^{\theta_2} \dot{m} d\theta \right)$$

where  $\theta_1$  and  $\theta_2$  are crank angles at the start and end of the intake process and the torque  $T$  and mass flow rate  $\dot{m}$  are evaluated at the valve lift corresponding to the local crank angle. Using Eq. (8.27) for  $T$ , Eq. (6.11) for  $\dot{m}$ , assuming  $v_0$  and  $\rho$  are constant throughout the intake process, and introducing volumetric efficiency  $\eta_v$  based on intake manifold conditions via Eq. (2.27), it can be shown that

$$R_s = \frac{\omega_s}{2\pi N} = \pi \eta_v B L \left[ \int_{\theta_1}^{\theta_2} (A_v C_D) C_s d\theta \right] / \left[ \int_{\theta_1}^{\theta_2} (A_v C_D) d\theta \right]^2 \quad (8.29)$$

where  $A_v C_D$  is the effective valve open area at each crank angle. Note that the crank angle in Eq. (8.29) should be in radians. Except for its (weak) dependence on  $\eta_v$ , Eq. (8.29) gives  $R_s$  independent of operating conditions directly from rig test results and engine geometry.

The relationship between steady-flow rig tests (which are extensively used because of their simplicity) and actual engine swirl patterns is not fully understood. Steady-flow tests adequately describe the swirl generating characteristics of the intake port and valve (at fixed valve lift) and are used extensively for this purpose. However, the swirling flow set up in the cylinder during intake can change significantly during compression.

### 8.3.2 Swirl Generation during Induction

Two general approaches are used to create swirl during the induction process. In one, the flow is discharged into the cylinder tangentially toward the cylinder wall, where it is deflected sideways and downward in a swirling motion. In the other, the swirl is largely generated within the inlet port: the flow is forced to rotate about the valve axis *before* it enters the cylinder. The former type of motion is achieved by forcing the flow distribution around the circumference of the inlet valve to be nonuniform, so that the inlet flow has a substantial net angular momentum about the cylinder axis. The directed port and deflector wall port in Fig. 8-13 are two common ways of achieving this result. The directed port brings the flow toward the valve opening in the desired tangential direction. Its passage is straight, which due to other cylinder head requirements restricts the flow area and results in a relatively low discharge coefficient. The deflector wall port uses the port inner side wall to force the flow preferentially through the outer periphery of the valve opening, in a tangential direction. Since only one wall is used to obtain a directional effect, the port areas are less restrictive.

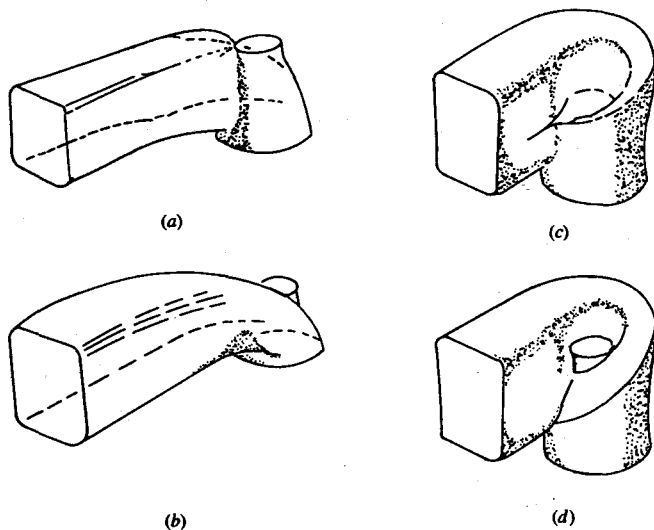


FIGURE 8-13

Different types of swirl-generating inlet ports: (a) deflector wall; (b) directed; (c) shallow ramp helical; (d) steep ramp helical.<sup>24</sup>

Flow rotation about the cylinder axis can also be generated by masking off or shrouding part of the peripheral inlet valve open area, as shown in Fig. 8-14. Use is often made of a mask or shroud on the valve in research engines because changes can readily be made. In production engines, the added cost and weight, problems of distortion, the need to prevent valve rotation, and reduced volumetric efficiency make masking the valve an unattractive approach. The more practical alternative of building a mask on the cylinder head around part of the inlet valve periphery is used in production spark-ignition engines to generate swirl. It can easily be incorporated in the cylinder head casting process.

The second broad approach is to generate swirl within the port, about the valve axis, prior to the flow entering the cylinder. Two examples of such *helical ports* are shown in Fig. 8-13. Usually, with helical ports, a higher flow discharge coefficient at equivalent levels of swirl is obtained, since the whole periphery of the valve open area can be fully utilized. A higher volumetric efficiency results. Also, helical ports are less sensitive to position displacements, such as can occur in casting, since the swirl generated depends mainly on the port geometry above the valve and not the position of the port relative to the cylinder axis.

Figure 8-15 compares steady-state swirl-rig measurements of examples of the ports in Fig. 8-13. The rig swirl number increases with increasing valve lift, reflecting the increasing impact of the port shape and decreasing impact of the flow restriction between the valve head and seat. Helical ports normally impart more angular momentum at medium lifts than do directed ports.<sup>23, 25</sup> The swirl

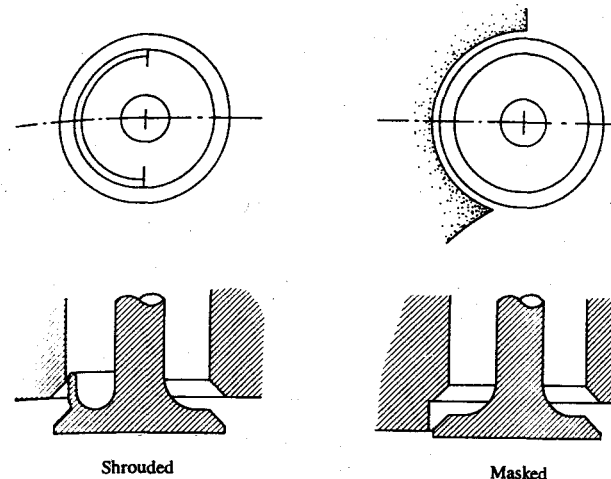


FIGURE 8-14

Shrouded inlet valve and masked cylinder head approaches for producing net in-cylinder angular momentum.

ratios for these ports calculated from this rig data using Eqs. (8.27) and (8.29) are: 2.5 for the directed port, 2.9 for the shallow ramp helical, and 2.6 for the steep ramp helical. Vane swirl-meter swirl ratios were about 30 percent less. These impulse-swirl-meter derived engine swirl ratios are within about 20 percent of the solid-body rotation rate which has equal angular momentum to that of the cylinder charge determined from tangential velocity measurements made within the cylinder of an operating engine with the same port, at the end of the induction process.<sup>23</sup>

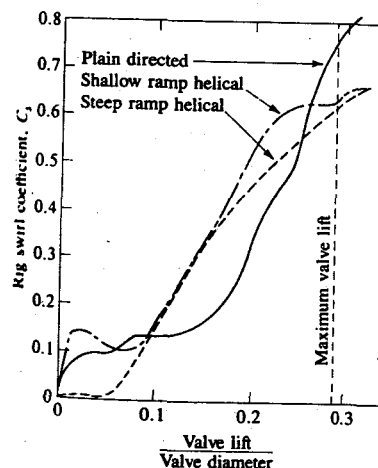


FIGURE 8-15

Steady-state torque meter swirl measurements of directed, shallow ramp, and steep ramp helical ports as a function of inlet valve lift/diameter ratio.<sup>23</sup>

Directed and deflector wall ports, and masked valve or head designs produce a tangential flow into the cylinder by increasing the flow resistance through that part of the valve open area where flow is not desired. A highly nonuniform flow through the valve periphery results and the flow into the cylinder has a substantial  $v_\theta$  velocity component in the same direction about the cylinder axis. In contrast, helical ports produce the swirl in the port upstream of the valve, and the velocity components  $v_r$ , and  $v_z$  through the valve opening, and  $v_\theta$  about the valve axis are approximately uniform around the valve open area. Figure 8-16 shows velocity data measured at the valve exit plane in steady-flow rig tests with examples of these two types of port. The valve and cylinder wall locations are shown. In Fig. 8-16a, the deflector wall of the tangentially oriented port effectively prevents any significant flow around half the valve periphery. In contrast, in Fig. 8-16b with the helical port, the air flows into the cylinder around

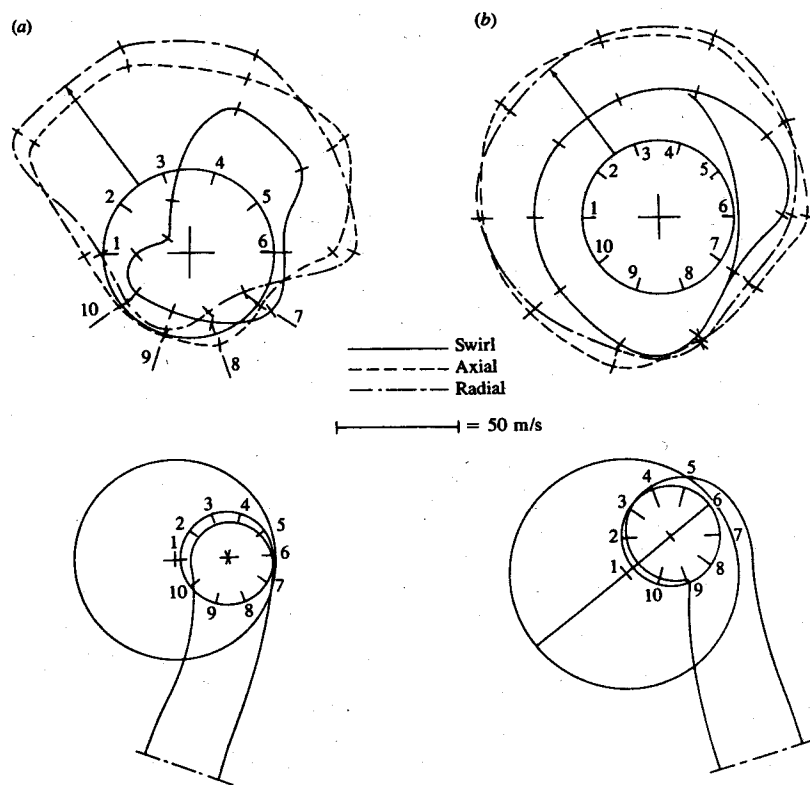


FIGURE 8-16

Swirl, axial, and radial velocities measured 2 mm from cylinder head around the valve circumference for (a) tangential deflector-wall port and (b) helical port; magnitude of velocity is given by the distance along a radial line (from valve axis), from valve outline to the respective curve scaled by the reference length (examples of radial velocity indicated by two arrows); valve lift = 12.8 mm.<sup>26, 27</sup>

the full valve open area. The radial and axial velocities are essentially uniform around the valve periphery. The swirl velocity about the valve axis (anticlockwise when viewed from above) for this helical port is relatively uniform and is about half the magnitude of the radial and axial velocities.

The swirling air flow within the cylinder of an operating engine is not uniform. The velocities generated at the valve at each point in the induction process depend on the valve open area and piston velocity. The velocities are highest during the first half of the intake process as indicated in Fig. 6-15. Thus, the swirl velocities generated during this portion of the induction stroke are higher than the swirl generated during the latter half of the stroke: there is swirl stratification. Also, the flow pattern close to the cylinder head during induction is comparatively disorganized, and not usually close to a solid-body rotation. It consists of a system of vortices, created by the high-velocity tangential or spiraling intake jet. Further down the cylinder, the flow pattern is closer to solid-body rotation with the swirl velocity increasing with increasing radius.<sup>23, 24</sup> This more ordered flow directly above the piston produces higher swirl velocities in that region of the cylinder. As the piston velocity decreases during intake, the swirl pattern redistributes, with swirl speeds close to the piston decreasing and swirl speeds in the center of the cylinder increasing.<sup>27</sup> Note that the axis of rotation of the in-cylinder gases may not exactly coincide with the cylinder axis.

### 8.3.3 Swirl Modification within the Cylinder

The angular momentum of the air which enters the cylinder at each crank angle during induction decays throughout the rest of the intake process and during the compression process due to friction at the walls and turbulent dissipation within the fluid. Typically one-quarter to one-third of the initial moment of momentum about the cylinder axis will be lost by top-center at the end of compression. However, swirl velocities in the charge can be substantially increased during compression by suitable design of the combustion chamber. In many designs of direct-injection diesel, air swirl is used to obtain much more rapid mixing between the fuel injected into the cylinder and the air than would occur in the absence of swirl. The tangential velocity of the swirling air flow set up inside the cylinder during induction is substantially increased by forcing most of the air into a compact bowl-in-piston combustion chamber, usually centered on the cylinder axis, as the piston approaches its top-center position. Neglecting the effects of friction, angular momentum is conserved, and as the moment of inertia of the air is decreased its angular velocity must increase.

However, the total angular momentum of the charge within the cylinder does decay due to friction at the chamber walls. The angular momentum of the cylinder charge  $\Gamma_c$  changes with time according to the moment of momentum conservation equation:

$$\frac{d\Gamma_c}{dt} = J_i - T_f \quad (8.30)$$

where  $J_i$  is the flux of angular momentum into the cylinder and  $T_f$  is the torque due to wall friction. At each point in the intake process  $J_i$  is given by

$$J_i = \int_{A_v} \rho r v_\theta \cdot dA_v \quad (8.31)$$

where  $dA_v$  is an element of the valve open area, as defined in Fig. 8-17. While the angular momentum entering the cylinder during the intake process is

$$\Gamma_{c,i} = \int_{t_{i,vo}}^{t_{i,vc}} \int_{A_v} \rho r v_\theta \cdot dA_v dt$$

the actual angular momentum within the cylinder at the end of induction will be less, due to wall friction during the intake process. Friction continues through the compression process so the total charge angular momentum at the end of compression is further reduced.

There is friction on the cylinder wall, cylinder head, and piston crown (including any combustion chamber within the crown). This friction can be estimated with sufficient accuracy using friction formulas developed for flow over a flat plate, with suitable definition of characteristic length and velocity scales. Friction on the cylinder wall can be estimated from the wall shear stress:

$$\tau = \frac{1}{2} \rho \left( \frac{\omega_s B}{2} \right)^2 C_F \quad (8.32)$$

where  $\omega_s$  is the equivalent solid-body swirl. The friction factor  $C_F$  is given by the flat plate formula:

$$C_F = 0.037 \lambda (\text{Re}_B)^{-0.2} \quad (8.33)$$

where  $\lambda$  is an empirical constant introduced to allow for differences between the flat plate and cylinder wall ( $\lambda \approx 1.5$ )<sup>28</sup> and  $\text{Re}_B$  is the equivalent of the flat plate Reynolds number [ $\text{Re}_B = \rho(B\omega_s/2)(\pi B)/\mu$ ]. Friction on the cylindrical walls of a piston cup or bowl can be obtained from the above expressions with  $D_B$ , the bowl diameter, replacing the bore.

Friction on the cylinder head, piston crown, and piston bowl floor can be estimated from expressions similar to Eqs. (8.32) and (8.33). However, since the

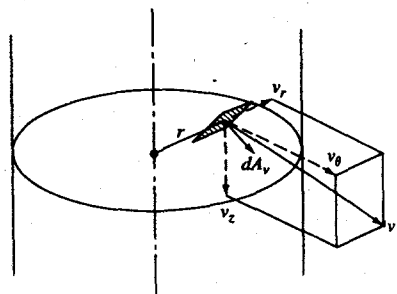


FIGURE 8-17  
Definition of symbols in equation for angular momentum flux into the cylinder [Eq. (8.31)].

tangential velocity  $v_\theta$  at the wall varies with radius, the shear stress should be evaluated at each radius and integrated over the surface: e.g.,<sup>29</sup>

$$\tau(r) = C_1 \frac{1}{2} \rho [v_\theta(r)]^2 \text{Re}^{-0.2} \quad (8.34)$$

with

$$\text{Re} = \frac{\rho v_\theta(r)r}{\mu}$$

where  $C_1$  is an empirical constant ( $\approx 0.055$ ). An alternative approximate approach is to evaluate these components of the wall shear stress at the mean radius.<sup>28</sup>

Next, consider the effects on swirl of radially inward displacement of the air charge during compression. The most common example of this phenomenon occurs with the bowl-in-piston combustion chamber design of medium- and high-speed direct-injection diesels (see Sec. 10.2.1). However, in spark-ignition engines where swirl is used to increase the burning rate, the shape of the combustion chamber close to top-center can also force radially inward motion of the charge. For a given swirling in-cylinder flow at the end of induction and neglecting the effects of friction, as the moment of inertia of the air about the cylinder axis is decreased the air's angular velocity must increase to conserve angular momentum. For example, for solid-body rotation of the cylinder air charge of mass  $m_c$ , the initial angular momentum  $\Gamma_{c,i}$  and solid-body rotation  $\omega_{s,i}$  are related at bottom-center by

$$\Gamma_{c,i} = I_c \omega_{s,i}$$

where  $I_c$  is the moment of inertia of the charge about the cylinder axis. For a disc-shaped combustion chamber,  $I_c = m_c B^2/8$  and is constant. For a bowl-in-piston combustion chamber,

$$I_c = \frac{m_c B^2}{8} \frac{[(z/h_B) + (D_B/B)^2]}{[(z/h_B) + (D_B/B)^4]} \quad (8.35)$$

where  $D_B$  and  $h_B$  are the diameter and depth of the bowl, respectively, and  $z$  is the distance of the piston crown from the cylinder head. At TC crank position,  $z \approx 0$  and  $I_c \approx m_c D_B^2/8$ . At the end of induction,  $I_c \approx m_c B^2/8$ . Thus, in the absence of friction  $\omega_s$  would increase by  $(B/D_B)^2$ , usually a factor of about 4.

In an operating engine with this bowl-in-piston chamber design, the observed increase in swirl in the bowl is less; it is usually about a factor of 2 to 3.<sup>23, 25</sup> This is because of wall friction, dissipation in the fluid due to turbulence and velocity gradients, and the fact that a fraction of the fluid remains in the clearance height above the piston crown. The loss in angular momentum due to these effects will vary with geometric details, initial swirl flow pattern, and engine speed.

Swirl velocity distributions in the cylinder at the end of induction show the tangential velocity increasing with radius, except close to the cylinder wall where friction causes the velocity to decrease. While the velocity distribution is not that of a solid-body rotation, depending on port design and operating conditions it is

often close to solid-body rotation.<sup>23, 25</sup> Departures from the solid-body velocity distribution are greater at higher engine speeds, suggesting that the flow pattern in the cylinder at this point in the cycle is still developing with time.<sup>23, 30</sup> In the absence of radially inward gas displacement during compression, the flow pattern continues to develop toward a solid-body distribution throughout the compression stroke.<sup>25</sup> Swirl ratios of 3 to 5 at top-center can be achieved with the ports shown in Fig. 8-13, with flat-topped pistons (i.e., in the absence of any swirl amplification during compression).<sup>23, 25</sup>

With combustion chambers where the chamber radius is less than the cylinder bore, such as the bowl-in-piston, the tangential velocity distribution with radius will change during compression. Even if the solid-body rotation assumption is reasonable at the end of induction, the profile will distort as gas moves into the piston bowl. Neglecting the effects of friction, the angular momentum of each fluid element will remain constant as it moves radially inward. Thus the increase in tangential velocity of each fluid element as it moves radially inward is proportional to the change in the reciprocal of its radius. Measurements of the swirl velocity distribution within the cylinder of bowl-in-piston engine designs support this description. The rate of displacement of gas into the bowl depends on the bowl volume  $V_B$ , cylinder volume  $V$ , and piston speed  $S_p$ , at that particular piston position:

$$\frac{dm_B}{dt} = \frac{m_c}{L} \left( \frac{V_B}{V} \right) \left( \frac{V_d}{V} \right) S_p$$

The gas velocity into the bowl will therefore increase rapidly toward the end of the compression stroke and reach a maximum just before TC (see Sec. 8.4 where this radial "squish" motion is discussed more fully). Thus, there is a rapid increase in  $v_\theta$  in the bowl as the crank angle approaches TC. The lower layers of the bowl rotate slower than the upper layers because that gas entered the bowl earlier in the compression process.<sup>23, 25</sup>

Velocity measurements illustrating the development of this radial distribution in tangential velocity are shown in Fig. 8-18. These measurements were made by analysing the motion of burning carbon particles in the cylinder of an operating diesel engine from movies of the combustion process. The figure shows the engine geometry and the data compared with a model based on gas displacement and conservation of angular momentum in each element of the charge as it is displaced inward. Different swirl velocity profiles exist within and outside the bowl as the piston approaches TC. Swirl velocities within the bowl increase as TC is approached, roughly as predicted by the ideal model. Outside the bowl, the swirl velocity decreases with increasing radius due to the combined effects of friction and inward gas displacement as the clearance height decreases.

Swirl ratios in bowl-in-piston engine designs of up to about 15 can be achieved with  $D_B \approx 0.5B$ , at top-center. Amplification factors relative to flat-topped piston swirl are typically about 2.5 to 3, some 30 percent lower than the ideal factor of  $(B/D_B)^2$  given by Eq. (8.35) as  $z \rightarrow 0$ . This difference is due to the mass remaining within the clearance height which does not enter the bowl, and

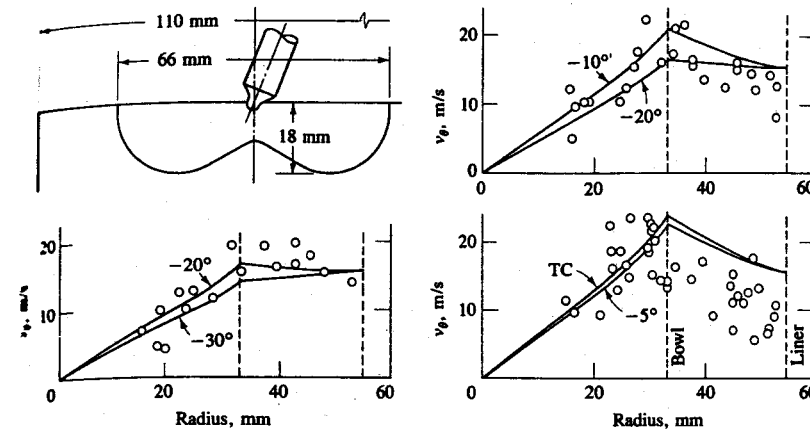


FIGURE 8-18

Velocity measurements as a function of radius across the combustion chamber of a firing, bowl-in-piston, direct-injection diesel engine. Schematic shows the chamber geometry. Solid lines are calculations based on the assumption of constant angular momentum for fluid elements as they move radially inward.<sup>31</sup>

the effects of wall friction (enhanced by the higher gas velocities in the bowl). Sometimes the bowl axis is offset from the cylinder axis and some additional loss in swirl amplification results.<sup>25</sup>

The effect of swirl generation during induction on velocity fluctuations in the combustion chamber at the end of compression has been examined.<sup>32</sup> The turbulence intensity with swirl was higher than without swirl (with the same chamber geometry). Integral scales of the turbulence were smaller with swirl than without. Cyclic fluctuations in the mean velocity are, apparently, reduced by swirl. Also, some studies show that the ensemble-averaged fluctuation intensity goes down when swirl is introduced.<sup>18</sup> There is evidence that swirl makes the turbulence intensity more homogeneous.<sup>30</sup>

#### 8.4 SQUISH

Squish is the name given to the radially inward or transverse gas motion that occurs toward the end of the compression stroke when a portion of the piston face and cylinder head approach each other closely. Figure 8-19 shows how gas is thereby displaced into the combustion chamber. Figure 8-19a shows a typical wedge-shaped SI engine combustion chamber and Fig. 8-19b shows a bowl-in-piston diesel combustion chamber. The amount of squish is often defined by the percentage squish area: i.e., the percentage of the piston area,  $\pi B^2/4$ , which closely approaches the cylinder head (the shaded areas in Fig. 8-19). Squish-generated gas motion results from using a compact combustion chamber geometry.

A theoretical squish velocity can be calculated from the instantaneous dis-

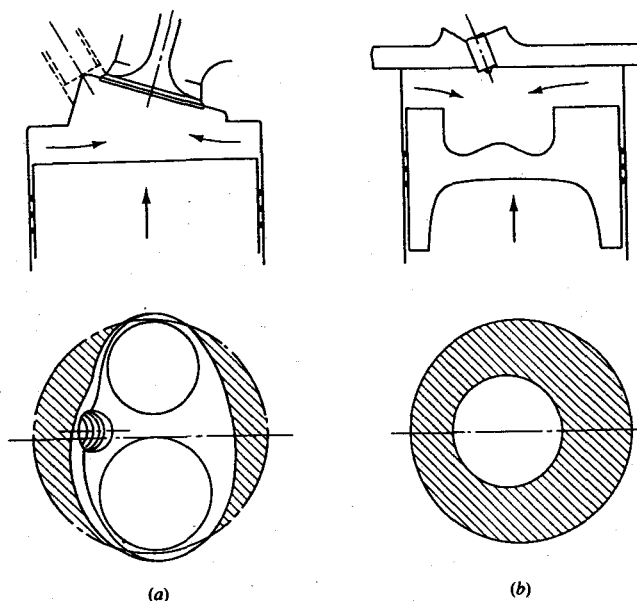


**FIGURE 8-19**  
Schematics of how piston motion generates squish: (a) wedge-shaped SI engine combustion chamber; (b) bowl-in-piston direct-injection diesel combustion chamber.

placement of gas across the inner edge of the squish region (across the dashed lines in the drawings in Fig. 8-20a and b), required to satisfy mass conservation. Ignoring the effects of gas dynamics (nonuniform pressure), friction, leakage past the piston rings, and heat transfer, expressions for the squish velocity are:

1. *Bowl-in-piston chamber* (Fig. 8-20a):<sup>33</sup>

$$\frac{v_{sq}}{S_p} = \frac{D_B}{4z} \left[ \left( \frac{B}{D_B} \right)^2 - 1 \right] \frac{V_B}{A_c z + V_B} \quad (8.36)$$

where  $V_B$  is the volume of the piston bowl,  $A_c$  is the cross-sectional area of the cylinder ( $\pi B^2/4$ ),  $S_p$  is the instantaneous piston speed [Eq. (2.11)], and  $z$  is the distance between the piston crown top and the cylinder head ( $z = c + Z$ , where  $Z = l + a - s$ ; see Fig. 2-1).

2. *Simple wedge chamber* (Fig. 8-20b):<sup>34</sup>

$$\frac{v_{sq}}{S_p} = \frac{A_s}{b(Z + c)} \left( 1 - \frac{Z + c}{C + Z} \right) \quad (8.37)$$

where  $A_s$  is the squish area,  $b$  is the width of the squish region, and  $C$  is  $Z/(r_c - 1)$  evaluated at the end of induction.

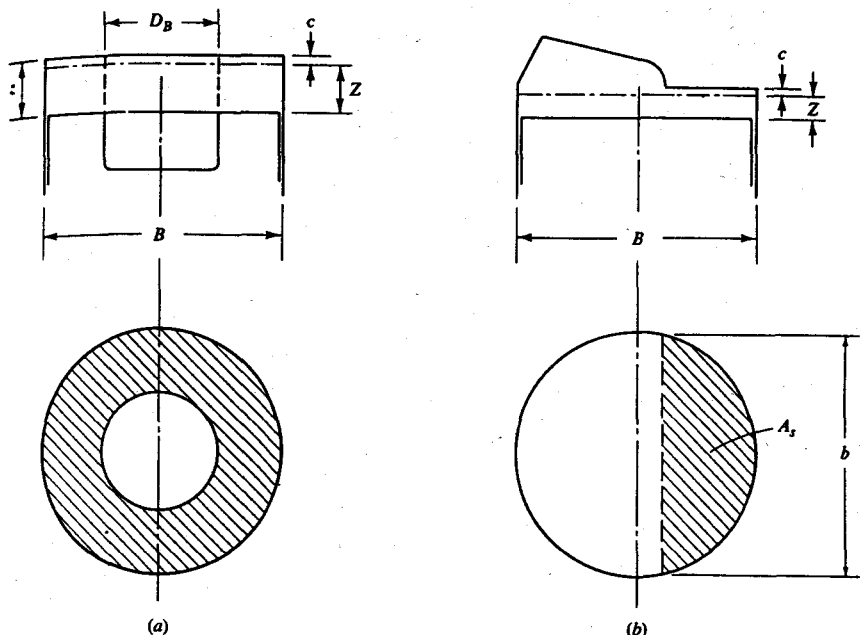


**FIGURE 8-20**  
(a) Schematic of axisymmetric bowl-in-piston chamber for Eq. (8.36). (b) Schematic of wedge chamber with transverse squish for Eq. (8.37).

The theoretical squish velocity for a bowl-in-piston engine normalized by the mean piston speed  $\bar{S}_p$  is shown in Fig. 8-21 for different ratios of  $D_B/B$  and clearance heights  $c$ . The maximum squish velocity occurs at about 10° before TC. After TC,  $v_{sq}$  is negative; a reverse squish motion occurs as gas flows out of the bowl into the clearance height region. Under motored conditions this is equal to the forward motion.

These models omit the effects of gas inertia, friction, gas leakage past the piston rings, and heat transfer. Gas inertia and friction effects have been shown to be small. The effects of gas leakage past the piston rings and of heat transfer are more significant. The squish velocity decrement  $\Delta v_L$  due to leakage is proportional to the mean piston speed and a dimensionless leakage number:

$$N_L = A_{E,L} \frac{\sqrt{\gamma R T_{IVC}}}{N V_d} \quad (8.38)$$

where  $A_{E,L}$  is the effective leakage area and  $T_{IVC}$  is the temperature of the cylinder gases at inlet valve closing. Leakage was modeled as a choked flow through the effective leakage area. Values of  $\Delta v_L/v_{sq}$  are shown in Fig. 8-22. The effect of leakage on  $v_{sq}$  is small for normal gas leakage rates. A decrement on squish

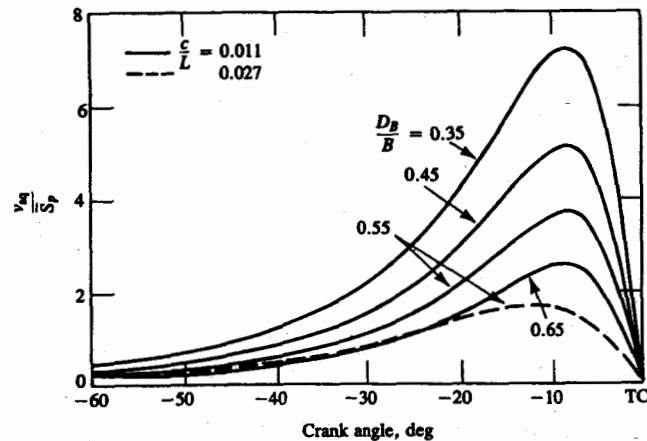


**FIGURE 8-21**  
Theoretical squish velocity divided by mean piston speed for bowl-in-piston chambers, for different  $D_B/B$  and  $c/L$  (clearance height/stroke).  $B/L = 0.914$ ,  $V_B/V_A = 0.056$ , connecting rod length/crank radius = 3.76.<sup>35</sup>

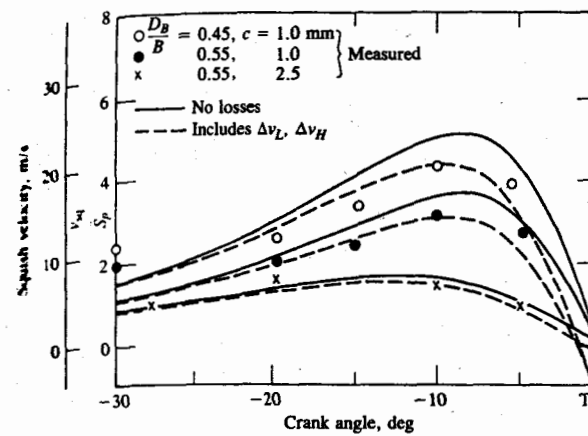
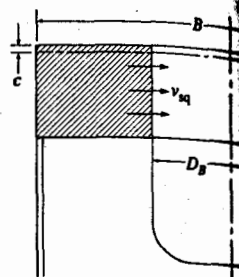


**FIGURE 8-23**  
Comparison of measured squish velocities in bowl-in-piston combustion chambers, with different bowl diameter/bore ratios and clearance heights, to calculated ideal squish velocity (solid lines) and calculations corrected for leakage and heat transfer (dashed lines). Bore = 85 mm, stroke = 93 mm, 1500 rev/min.<sup>35</sup>

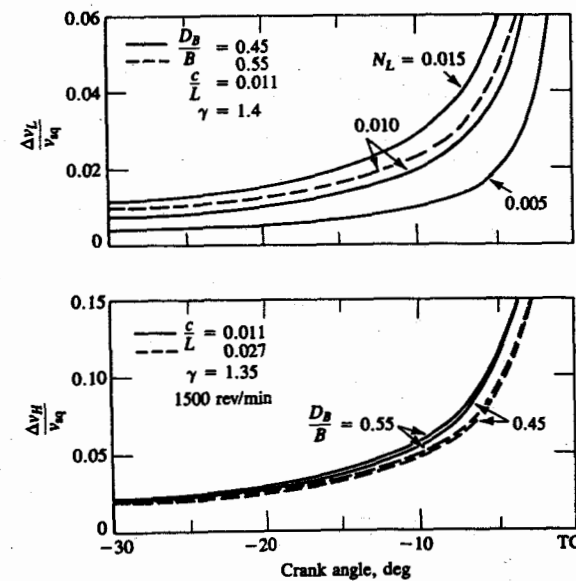


**FIGURE 8-22**  
Values of squish velocity decrement due to leakage  $\Delta v_L$  and heat transfer  $\Delta v_H$ , normalized by the ideal squish velocity, as a function of crank angle.<sup>35</sup>

velocity due to heat transfer,  $\Delta v_H$ , has also been derived, using standard engine heat-transfer correlations (see Sec. 12.4). Values of  $\Delta v_H/v_{sq}$  are also shown in Fig. 8-22. Again the effects are small in the region of maximum squish, though they become more important as the squish velocity decreases from its maximum value as the piston approaches TC.

Velocity measurements in engines provide good support for the above theory. The ideal theory adequately predicts the dependence on engine speed.<sup>36</sup> With appropriate corrections for leakage and heat-transfer effects, the above theory predicts the effects of the bowl diameter/bore ratio and clearance height on squish velocity (see Fig. 8-23). The change in direction of the radial motion as the piston moves through TC has been demonstrated under motored engine conditions. Under firing conditions, the combustion generated gas expansion in the open portion of the combustion chamber substantially increases the magnitude of the reverse squish motion after TC.<sup>37</sup>

## 8.5 PRECHAMBER ENGINE FLOWS

Small high-speed diesel engines use an auxiliary combustion chamber, or prechamber, to achieve adequate fuel-air mixing rates. The prechamber is connected to the main combustion chamber above the piston via a nozzle, passageway, or one or more orifices. Flow of air through this restriction into the prechamber during the compression process sets up high velocities in the prechamber at the time the fuel-injection process commences. This results in the required high fuel-air mixing rates. Figures 1-21 and 10-2 show examples of these prechamber or

indirect-injection diesels. The two most common designs of auxiliary chamber are: the swirl chamber (Fig. 10-2a), where the flow through the passageway enters the chamber tangentially producing rapid rotation within the chamber, and the prechamber (Fig. 10-2b) with one or more connecting orifices designed to produce a highly turbulent flow but no ordered motion within the chamber. Auxiliary chambers are sometimes used in spark-ignition engines. The torch-ignition three-valve stratified-charge engine (Fig. 1-27) is one such concept. The prechamber is used to create a rich mixture in the vicinity of the spark plug to promote rapid flame development. An alternative concept uses the prechamber around the spark plug to generate turbulence to enhance the early stages of combustion, but has no mixture stratification.

The most critical phase of flow into the prechamber occurs towards the end of compression. While this flow is driven by a pressure difference between the main chamber above the piston and the auxiliary chamber, this pressure difference is small, and the mass flow rate and velocity at the nozzle, orifice, or passageway can be estimated using a simple gas displacement model. Assuming that the gas density throughout the cylinder is uniform (an adequate assumption toward the end of compression—the most critical period), the mass in the prechamber  $m_p$  is given by  $m_c(V_p/V)$ , where  $m_c$  is the cylinder mass,  $V$  the cylinder volume, and  $V_p$  the prechamber volume. The mass flow rate through the throat of the restriction is, therefore,

$$\dot{m} = \frac{dm_p}{dt} = -\frac{m_c V_p}{V^2} \frac{dV}{dt} \quad (8.39)$$

Using the relations  $dV/dt = -(\pi B^2/4)S_p$ , where  $S_p$  is the instantaneous piston speed,  $V_d = \pi B^2 L/4$ , and  $\bar{S}_p = 2NL$ , Eq. (8.39) can be written as

$$\frac{\dot{m}}{m_c N} = 2(r_c - 1) \left( \frac{V_p}{V_c} \right) \left( \frac{S_p}{\bar{S}_p} \right) \left( \frac{V_c}{V} \right)^2 \quad (8.40)$$

where  $V_c$  is the clearance volume,  $S_p/\bar{S}_p$  is given by Eq. (2.11), and  $V/V_c$  is given by Eq. (2.6). The gas velocity at the throat  $v_T$  can be obtained from  $\dot{m}$  via the relation  $\rho v_T A_T = \dot{m}$ , the density  $\rho = m_c/V$ , and Eq. (8.40):

$$\frac{v_T}{\bar{S}_p} = \left( \frac{V_p}{V_c} \right) \left( \frac{\pi B^2/4}{A_T} \right) \left( \frac{S_p}{\bar{S}_p} \right) \left( \frac{V_c}{V} \right) \quad (8.41)$$

where  $A_T$  is the effective cross-sectional area of the throat. The variation of  $\dot{m}/(m_c N)$  and  $v_T/\bar{S}_p$  with crank angle during the compression process for values of  $r_c$ ,  $V_p/V_c$ , and  $A_T/(\pi B^2/4)$  typical of a swirl prechamber diesel are shown in Fig. 8-24. The velocity reaches its peak value about 20° before TC: very high gas velocities, an order of magnitude or more larger than the mean piston speed, can be achieved depending on the relative effective throat area. Note that as the piston approaches TC, first the nozzle velocity and then the mass flow rate decrease to zero. After TC, in the absence of combustion, an equivalent flow in the reverse direction out of prechamber would occur. Combustion in the pre-

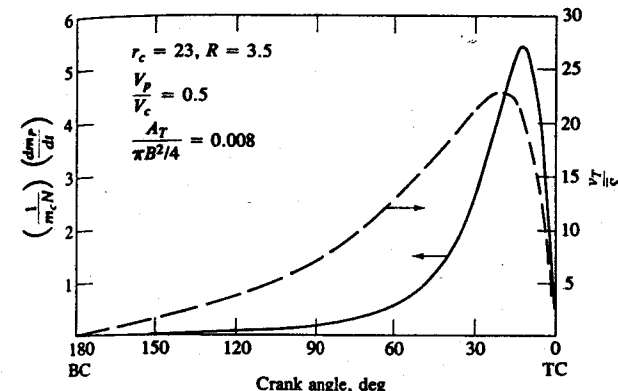


FIGURE 8-24  
Velocity and mass flow rate at the prechamber nozzle throat, during compression, for a typical small swirl-prechamber automotive diesel.

chamber diesel usually starts just before TC, and the pressure in the prechamber then rises significantly above the main chamber pressure. The outflow from the prechamber is then governed by the development of the combustion process, and the above simple gas displacement model no longer describes the flow. This combustion generated prechamber gas motion is discussed in Sec. 14.4.4.

In prechamber stratified-charge engines, the flow of gas into the prechamber during compression is critical to the creation of an appropriate mixture in the prechamber at the crank angle when the mixture is ignited. In the concept shown in Fig. 1-27, a very rich fuel-air mixture is fed directly to the prechamber during intake via the prechamber intake valve, while a lean mixture is fed to the main chamber via the main intake valve. During compression, the flow into the prechamber reduces the prechamber equivalence ratio to a close-to-stoichiometric value at the time of ignition. Figure 8-25 shows a gas displacement calculation of this process and relevant data; the prechamber equivalence ratio, initially greater

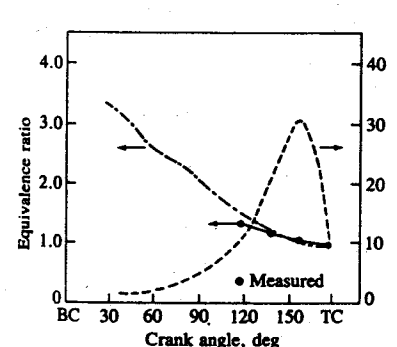


FIGURE 8-25  
Effect of gas flow into the prechamber during compression on the prechamber equivalence ratio in a three-valve prechamber stratified-charge engine. Calculations based on gas displacement model.<sup>38</sup>

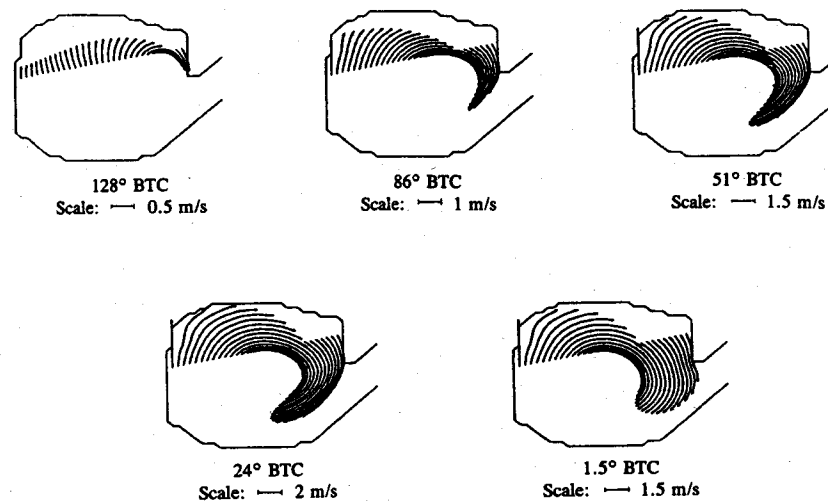


FIGURE 8-26

Calculations of developing flow field in (two-dimensional) swirl prechamber during compression process. Lines are instantaneous flow streamlines, analogous to streak photographs of flow field.<sup>41</sup>

than 3, is leaned out to unity as mass flows through the orifice into the prechamber (whose volume is 8.75 percent of the clearance volume).<sup>38</sup> Charts for estimating the final equivalence ratio, based on gas displacement, for this prechamber concept are available.<sup>39</sup>

The velocity field set up inside the prechamber during compression is strongly dependent on the details of the nozzle and prechamber geometry. Velocities vary linearly with mean piston speed.<sup>40</sup> In swirl prechambers, the nozzle flow sets up a vortex within the chamber. Figure 8-26 shows calculations of this developing flow field; instantaneous flow streamlines have been drawn in, with the length of the streamlines indicating how the particles of fluid move relative to each other.<sup>41</sup> The velocities increase with increasing crank angle as the compression process proceeds, and reach a maximum at about 20° before TC. Then, as the piston approaches TC and the flow through the passageway decreases to zero, the vortex in the swirl chamber expands to fill the entire chamber and mean velocities decay. Very high swirl rates can be achieved just before TC: local swirl ratios of up to 60 at intermediate radii and up to 20 at the outer radius have been measured. These high swirl rates produce large centrifugal accelerations.

## 8.6 CREVICE FLOWS AND BLOWBY

The engine combustion chamber is connected to several small volumes usually called *crevices* because of their narrow entrances. Gas flows into and out of these volumes during the engine operating cycle as the cylinder pressure changes.

The largest crevices are the volumes between the piston, piston rings, and cylinder wall. Some gas flows out of these regions into the crankcase; it is called *blowby*. Other crevice volumes in production engines are the threads around the spark plug, the space around the plug center electrode, the gap around the fuel injector, crevices between the intake and exhaust valve heads and cylinder head, and the head gasket cutout. Table 8.1 shows the size and relative importance of these crevice regions in one cylinder of a production V-6 spark-ignition engine determined from measurements of cold-engine components. Total crevice volume is a few percent of the clearance volume, and the piston and ring crevices are the dominant contributors. When the engine is warmed up, dimensions and crevice volumes will change.

The important crevice processes occurring during the engine cycle are the following. As the cylinder pressure rises during compression, unburned mixture or air is forced into each crevice region. Since these volumes are thin they have a large surface/volume ratio; the gas flowing into the crevice cools by heat transfer to close to the wall temperature. During combustion while the pressure continues to rise, unburned mixture or air, depending on engine type, continues to flow into these crevice volumes. After flame arrival at the crevice entrance, burned gases will flow into each crevice until the cylinder pressure starts to decrease. Once the crevice gas pressure is higher than the cylinder pressure, gas flows back from each crevice into the cylinder.

The volumes between the piston, piston rings, and cylinder wall are shown schematically in Fig. 8-27. These crevices consist of a series of volumes (numbered 1 to 5) connected by flow restrictions such as the ring side clearance and ring gap. The geometry changes as each ring moves up and down in its ring groove, sealing either at the top or bottom ring surface. The gas flow, pressure distribution, and ring motion are therefore coupled. Figure 8-28 illustrates this behavior: pressure distributions, ring motion, and mass flow of gas into and out

TABLE 8.1  
V-6 engine crevice data†<sup>42</sup>

	cm <sup>3</sup>	%
Displaced volume per cylinder	632	
Clearance volume per cylinder	89	100
Volume above first ring	0.93	1.05
Volume behind first ring	0.47	0.52
Volume between rings	0.68	0.77
Volume behind second ring	0.47	0.52
Total ring crevice volume	2.55	2.9
Spark plug thread crevice	0.25	0.28
Head gasket crevice	0.3	0.34
Total crevice volume	3.1	3.5

† Determined for cold engine.

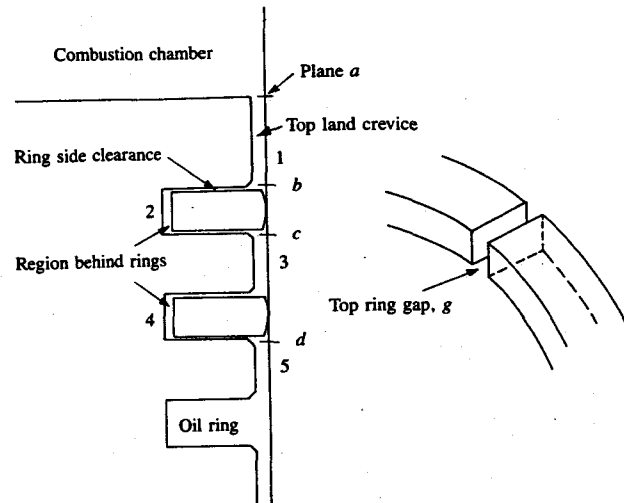


**FIGURE 8-27**  
Schematic of piston and ring assembly in automotive spark-ignition engine.

of the regions defined by planes *a*, *b*, *c*, *d*, and through the ring gap *g* are plotted versus crank angle through compression and expansion. These results come from an analysis of these regions as volumes connected by passageways, with a prescribed cylinder pressure versus crank angle profile coupled with a dynamic model for ring motion, and assuming that the gas temperature equals the wall temperature.<sup>42</sup> During compression and combustion, the rings are forced to the groove lower surfaces and mass flows into all the volumes in this total crevice region. The pressure above and behind the first ring is essentially the same as the cylinder pressure; there is a substantial pressure drop across each ring, however. Once the cylinder pressure starts to decrease (after 15° ATC) gas flows out of regions 1 and 2 in Fig. 8-27 into the cylinder, but continues to flow into regions 3, 4, and 5 until the pressure in the cylinder falls below the pressure beneath the top ring. The top ring then shifts to seal with the upper groove surface and gas flows out of regions 2, 3, and 4 (which now have the same pressure), both into the cylinder and as blowby into the crankcase. Some 5 to 10 percent of the total cylinder charge is trapped in these regions at the time of peak cylinder pressure. Most of this gas returns to the cylinder; about 1 percent goes to the crankcase as blowby. The gas flow back into the cylinder continues throughout the expansion process. In spark-ignition engines this phenomenon is a major contributor to unburned hydrocarbon emissions (see Sec. 11.4.3). In all engines it results in a loss of power and efficiency.

There is substantial experimental evidence to support the above description of flow in the piston ring crevice region. In a special square-cross-section flow visualization engine, both the low-velocity gas expansion out of the volume above the first ring after the time of peak pressure and the jet-like flows through

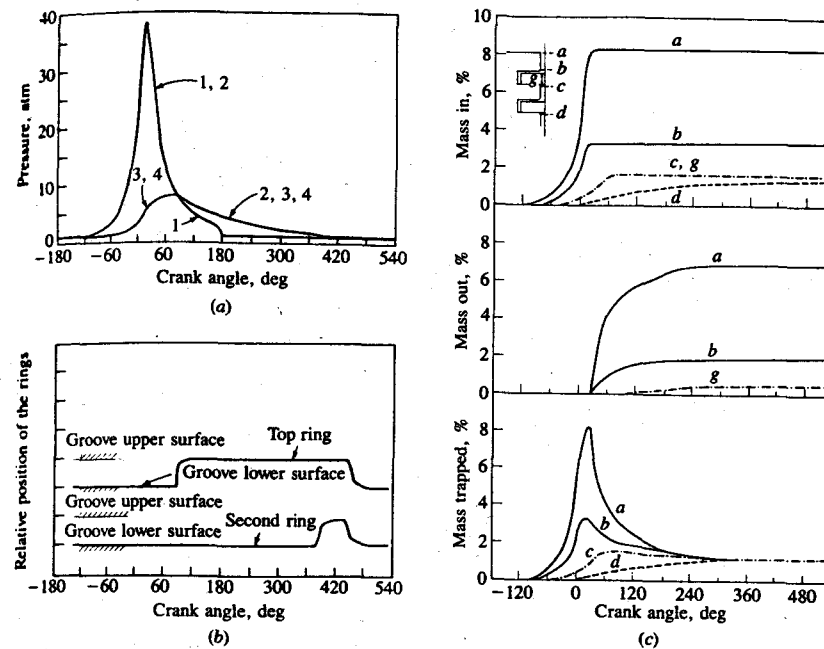


**FIGURE 8-28**  
(a) Pressures in the combustion chamber (1), in region behind top ring (2), in region between rings (3), and behind second ring (4); (b) relative position of top and second rings; (c) percentage of total cylinder mass that flows into and out of the different crevice regions across planes *a*, *b*, *c*, and *d* and through the ring gap *g* in Fig. 8-27, and the percentage of mass trapped beneath these planes, as a function of crank angle. Automotive spark-ignition engine at wide-open throttle and 2000 rev/min.<sup>42</sup>

the top ring gap later in the expansion process when the pressure difference across the ring changes sign have been observed. Figure 8-29 shows these flows with explanatory schematics.

Blowby is defined as the gas that flows from the combustion chamber past the piston rings and into the crankcase. It is forced through any leakage paths afforded by the piston-bore-ring assembly in response to combustion chamber pressuré. If there is good contact between the compression rings and the bore, and the rings and the bottom of the grooves, then the only leakage path of consequence is the ring gap. Blowby of gases from the cylinder to the crankcase removes gas from these crevice regions and thereby prevents some of the crevice gases from returning to the cylinder. Crankcase blowby gases used to be vented directly to the atmosphere and constituted a significant source of HC emissions. The crankcase is now vented to the engine intake system and the blowby gases are recycled. Blowby at a given speed and load is controlled primarily by the greatest flow resistance in the flow path between the cylinder and the crankcase. This is the smallest of the compression ring ring-gap areas. Figure 8-30 shows how measured blowby flow rates increase linearly with the smallest gap area.<sup>43</sup>

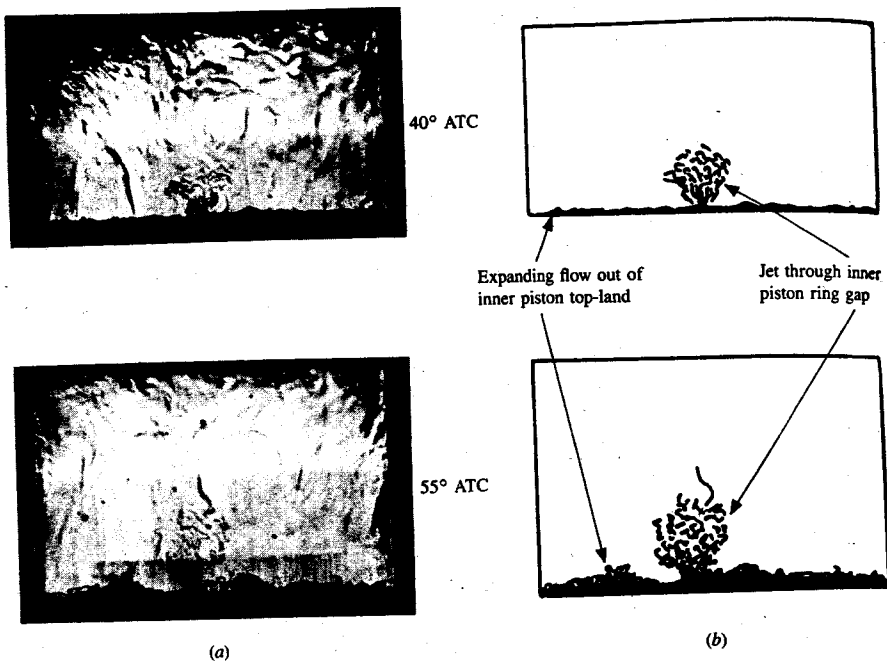


**FIGURE 8-29**  
Schlieren photographs of the flow out of the piston-cylinder wall crevices during the expansion stroke. A production piston was inserted into the square cross-section piston of the visualization engine. Gas flows at low velocity out of the crevice entrance all around the production piston circumference once the cylinder pressure starts decreasing early in the expansion stroke. Gas flows out of the ring gap as a jet once the pressure above the ring falls below the pressure beneath the ring.<sup>42</sup>

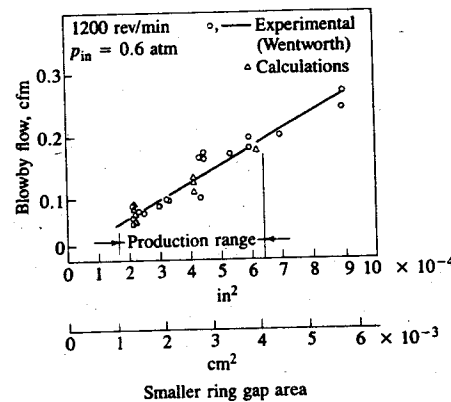


**FIGURE 8-30**  
Measured blowby for one cylinder of an automobile spark-ignition engine as a function of the smallest ring gap area, compared with blowby calculations based on flow model described in text.<sup>42, 43</sup>

Calculations of blowby based on the model described earlier are in good agreement.<sup>42</sup> Extrapolation back to the zero gap area gives nearly zero blowby. Note, however, that if the bore finish is rough, or if the rings do not contact the bore all around, or if the compression rings lift off the bottom of the groove, this linear relationship may no longer hold.

## 8.7 FLOWS GENERATED BY PISTON-CYLINDER WALL INTERACTION

Because a boundary layer exists on the cylinder wall, the motion of the piston generates unusual flow patterns in the corner formed by the cylinder wall and the piston face. When the piston is moving away from top-center a sink-type flow occurs. When the piston moves toward top-center a vortex flow is generated. Figure 8-31 shows schematics of these flows (in a coordinate frame with the piston face at rest). The vortex flow has been studied because of its effect on gas motion at the time of ignition and because it has been suggested as a mechanism for removing hydrocarbons off the cylinder wall during the exhaust stroke (see Sec. 11.4.3).

The vortex flow has been studied in cylinders with water as the fluid over the range of Reynolds numbers typical of engine operation.<sup>44, 45</sup> Laminar, transition, and turbulent flow regimes have been identified. It has been shown that a quasi-steady flow assumption is valid and that

$$\frac{A_V}{L^2} = f\left(\frac{v_w L}{v}\right)$$

where  $A_V$  is the vortex area (area inside the dashed line in Fig. 8-31),  $L$  is the stroke,  $v_w$  is the wall velocity in piston stationary coordinates ( $v_w = S_p$  in the engine),  $v$  is the kinematic viscosity, and  $(v_w L/v)$  is a Reynolds number.

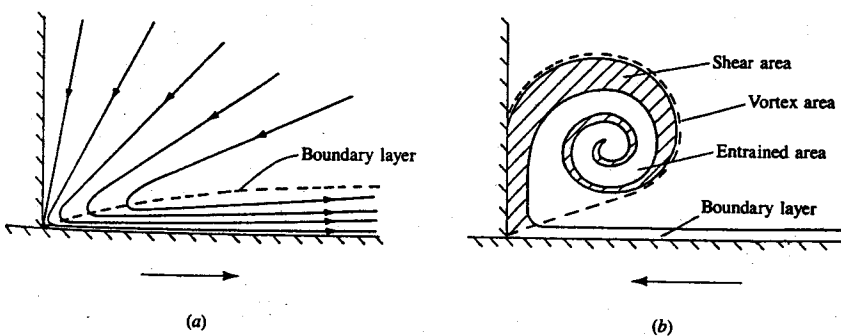


**FIGURE 8-31**  
Schematics of the flow pattern set up in the piston face-cylinder wall corner, in piston-stationary coordinates, due to the boundary layer on the cylinder wall. Piston crown on left; cylinder wall at bottom. (a) Sink flow set up during intake and expansion; (b) vortex flow set up during compression and exhaust.<sup>44</sup> Arrow shows cylinder wall velocity relative to piston.

For the laminar flow regime, a good assumption is that  $A_V$  is proportional to the shear area in the vortex (shown cross-hatched), which equals the boundary-layer area; this can be estimated from boundary-layer theory. In the turbulent flow regime, an entrainment theory was used, which assumed that the rate of change of vortex area was proportional to the product of the exposed perimeter of the vortex and the velocity difference between the vortex and the stationary fluid ( $\approx v_w$ ). The relevant relationships are:

$$\text{For } (v_w L/v) \leq 2 \times 10^4: \quad \frac{A_V}{L^2} = \left( \frac{v_w L}{v} \right)^{-1/2} \quad (8.42a)$$

$$\text{For } (v_w L/v) \geq 2 \times 10^4: \quad \frac{A_V}{L^2} = 0.006 \quad (8.42b)$$

Figure 8-32 shows these two theories correlated against hydraulic analog data.

These theories are for constant values of  $v$ . During compression,  $v$  decreases substantially as the gas temperature and pressure increase ( $v$  decreases by a factor of 4 for a compression ratio of 8). This will decrease the size of the vortex until the turbulent regime is reached. During the exhaust stroke following blowdown,  $v$  will remain approximately constant as the pressure and temperature do not change significantly. Typical parameter values at 1500 rev/min are:  $\bar{S}_p = 5 \text{ m/s}$ ,  $L = 0.1 \text{ m}$ ; average values of  $v$  are  $1.2 \times 10^{-5}$  and  $1.4 \times 10^{-4} \text{ m}^2/\text{s}$  for compression and exhaust stroke, respectively. Hence a Reynolds number for the compression stroke is  $4 \times 10^4$ ,  $A_V/L^2 \approx 0.006$ , and the vortex diameter  $d_V \approx 0.09L$ . For the exhaust stroke, the Reynolds number is  $4 \times 10^3$ ,  $A_V/L^2 \approx 0.015$ , and  $d_V \approx 0.14L$ . Thus the vortex dimensions at the end of the upward stroke of the piston are comparable to the engine clearance height.

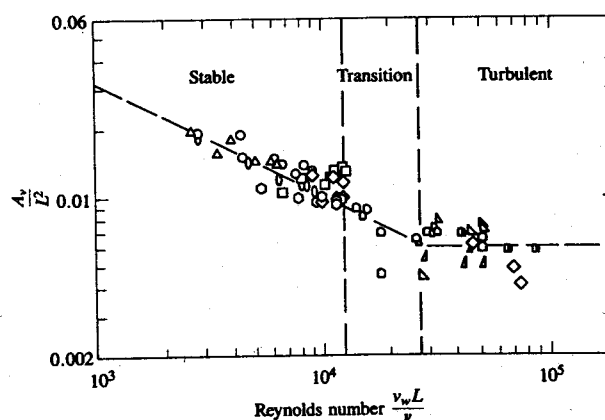
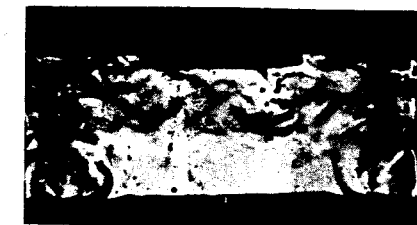


FIGURE 8-32  
Ratio of area of vortex in piston face-cylinder wall corner to square of stroke, as a function of Reynolds number based on piston velocity, for piston moving toward the cylinder head.<sup>44</sup>



60° BTC



20° BTC

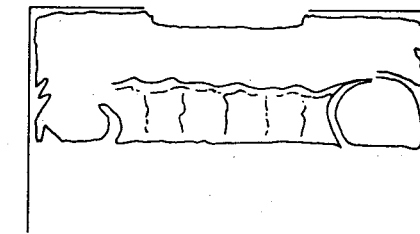


FIGURE 8-33

Schlieren photographs of in-cylinder flow during later stages of exhaust stroke. Growing vortex in the piston face-cylinder wall corner and turbulent outflow toward the valve are apparent at 60° BTC. At 20° BTC, the vortex has grown to of order 0.2B diameter.<sup>42</sup>

This vortex flow has been observed in an operating engine. Figure 8-33 shows schlieren photographs taken during the exhaust stroke in a special square-cross-section flow visualization spark-ignition engine. The accompanying schematic identifies the vortex structure which is visible in the photo because the cool boundary-layer gas is being scraped off the cylinder wall by the upward-moving piston and "rolled up." The vortex diameter as the piston approaches TC is about 20 percent of the bore.

## PROBLEMS

- 8.1. (a) Estimate the ratio of the maximum gas velocity in the center of the hollow cone inlet jet to the mean piston speed from the data in Fig. 8-1.  
 (b) Compare this ratio with the ratio of inlet valve pseudo flow velocity determined from Fig. 6-15 to the mean piston speed at the same crank angle. The engine is that of Fig. 1-4.  
 (c) Are the engine velocity data in (a) consistent with the velocity calculated from the simple piston displacement model of (b)? Explain.
- 8.2. Given the relationship between turbulence intensity and mean piston speed [Eq. (8.23)] and that the turbulence integral scale is  $\approx 0.2 \times$  clearance height, use Eqs. (8.14) and (8.15) to estimate the following quantities for a spark-ignition engine with bore = stroke = 86 mm,  $r_c = 9$ , at 1000 and 5000 rev/min and wide-open throttle:  
 (a) Mean and maximum piston speed, maximum gas velocity through the inlet valve (see Prob. 8.1)  
 (b) Turbulence intensity, integral length scale, micro length scale, and Kolmogorov length scale, all at TC

- 8.3. The swirl ratio at the end of induction at 2000 rev/min in a direct-injection diesel engine of bore = stroke = 100 mm is 4.0. What is the average tangential velocity (evaluated at the inlet valve-axis radial location) required to give this swirl ratio? What is the ratio of this velocity to the mean piston speed and to the mean flow velocity through the inlet valve estimated from the average valve open area and open time?
- 8.4. (a) Derive a relationship for the depth (or height)  $h_B$  of a disc-shaped bowl-in-piston direct-injection diesel engine combustion chamber in terms of compression ratio  $r_c$ , bore  $B$ , stroke  $L$ , bowl diameter  $D_B$ , and top-center cylinder-head to piston-crown clearance  $c$ . For  $B = L = 100$  mm,  $r_c = 16$ ,  $D_B = 0.5B$ ,  $c = 1$  mm find the fraction of the air charge within the bowl at TC.
- (b) If the swirl ratio at the end of induction at 2500 rev/min is 3 find the swirl ratio and average angular velocity in the bowl-in-piston chamber of dimensions given above. Assume the swirling flow is always a solid-body rotation. Compare the tangential velocity at the bowl edge with the mean piston speed. Neglect any friction effects.
- (c) What would the swirl ratio be if the top-center clearance height was zero?
- 8.5. Using Eq. (8.37) and Fig. 8-20b plot the squish velocity divided by the mean piston speed at 10° BTC (the approximate location of the maximum) as a function of squish area expressed as a percentage of the cylinder cross section,  $A_s/(nB^2/4) \times 100$ , from 50 to 0 percent.  $r_c = 10$ ,  $c/B = 0.01$ ,  $B/L = 1$ ,  $R = l/a = 3.5$ .
- 8.6. Figure 8-24 shows the velocity at the prechamber nozzle throat during compression for dimensions typical of a small swirl chamber indirect-injection diesel. Assuming that the swirl chamber shape is a disc of height equal to the diameter, that the nozzle throat is at  $0.8 \times$  prechamber radius, and that the flow enters the prechamber tangentially, estimate the swirl ratio based on the total angular momentum about the swirl chamber axis in the prechamber at top-center. Assume  $B = L$ ; neglect friction.
- 8.7. The total crevice volume in an automobile spark-ignition engine is about 3 percent of the clearance volume. If the gas in these crevice regions is close to the wall temperature (450 K) and at the cylinder pressure, estimate the fraction of the cylinder mass within these crevice regions at these crank angles: inlet valve closing (50° ABC), spark discharge (30° BTC), maximum cylinder pressure (15° ATC), exhaust valve opening (60° BBC), TC of the exhaust stroke. Use the information in Fig. 1-8 for your input data, and assume the inlet pressure is 0.67 atm.

## REFERENCES

1. Bicén, A. F., Vafidis, C., and Whitelaw, J. H.: "Steady and Unsteady Airflow through the Intake Valve of a Reciprocating Engine," *ASME Trans., J. Fluids Engng.*, vol. 107, pp. 413–420, 1985.
2. Namazian, M., Hansen, S. P., Lyford-Pike, E. J., Sanchez-Barsse, J., Heywood, J. B., and Rife, J.: "Schlieren Visualization of the Flow and Density Fields in the Cylinder of a Spark-Ignition Engine," *SAE paper 800044, SAE Trans.*, vol. 89, 1980.
3. Ekchian, A., and Hoult, D. P.: "Flow Visualization Study of the Intake Process of an Internal Combustion Engine," *SAE paper 790095, SAE Trans.*, vol. 88, 1979.
4. Hirotomi, T., Nagayama, I., Kobayashi, S., and Yamamasu, M.: "Study of Induction Swirl in a Spark Ignition Engine," *SAE paper 810496, SAE Trans.*, vol. 90, 1981.
5. Reynolds, W. C.: "Modeling of Fluid Motions in Engines—An Introductory Overview," in J. N. Mattavi and C. A. Amann (eds.), *Combustion Modelling in Reciprocating Engines*, pp. 69–124, Plenum Press, 1980.
6. Tennekes, H., and Lumley, J. L.: *A First Course in Turbulence*, MIT Press, 1972.

7. Rask, R. B.: "Laser Doppler Anemometer Measurements of Mean Velocity and Turbulence in Internal Combustion Engines," *ICALEO '84 Conference Proceedings*, vols. 45 and 47, *Inspection, Measurement and Control and Laser Diagnostics and Photochemistry*, Laser Institute of America, Boston, November 1984.
8. Tabaczynski, R. J.: "Turbulence and Turbulent Combustion in Spark-Ignition Engines," *Prog. Energy Combust. Sci.*, vol. 2, pp. 143–165, 1976.
9. Witze, P. O.: "A Critical Comparison of Hot-Wire Anemometry and Laser Doppler Velocimetry for I.C. Engine Applications," *SAE paper 800132, SAE Trans.*, vol. 89, 1980.
10. Witze, P. O., Martin, J. K., and Borgnakke, C.: "Conditionally-Sampled Velocity and Turbulence Measurements in a Spark Ignition Engine," *Combust. Sci. Technol.*, vol. 36, pp. 301–317, 1984.
11. Rask, R. B.: "Comparison of Window, Smoothed-Ensemble, and Cycle-by-Cycle Data Reduction Techniques for Laser Doppler Anemometer Measurements of In-Cylinder Velocity," in T. Morel, R. P. Lohmann, and J. M. Rackley (eds.), *Fluid Mechanics of Combustion Systems*, pp. 11–20, ASME, New York, 1981.
12. Liou, T.-M., and Santavicca, D. A.: "Cycle Resolved LDV Measurements in a Motored IC Engine," *ASME Trans., J. Fluids Engng.*, vol. 107, pp. 232–240, 1985.
13. Amann, C. A.: "Classical Combustion Diagnostics for Engine Research," *SAE paper 850395, in Engine Combustion Analysis: New Approaches*, P-156, SAE, 1985.
14. Dyer, T. M.: "New Experimental Techniques for In-Cylinder Engine Studies," *SAE paper 850396, in Engine Combustion Analysis: New Approaches*, P-156, SAE, 1985.
15. Rask, R. B.: "Laser Doppler Anemometer Measurements in an Internal Combustion Engine," *SAE paper 790094, SAE Trans.*, vol. 88, 1979.
16. Liou, T.-M., Hall, M., Santavicca, D. A., and Bracco, F. V.: "Laser Doppler Velocimetry Measurements in Valved and Ported Engines," *SAE paper 840375, SAE Trans.*, vol. 93, 1984.
17. Arcoumanis, C., and Whitelaw, J. H.: "Fluid Mechanics of Internal Combustion Engines: A Review," *Proc. Instn Mech. Engrs.*, vol. 201, pp. 57–74, 1987.
18. Bopp, S., Vafidis, C., and Whitelaw, J. H.: "The Effect of Engine Speed on the TDC Flowfield in a Motored Reciprocating Engine," *SAE paper 860023*, 1986.
19. Wong, V. W., and Hoult, D. P.: "Rapid Distortion Theory Applied to Turbulent Combustion," *SAE paper 790357, SAE Trans.*, vol. 88, 1979.
20. Fraser, R. A., Felton, P. G., and Bracco, F. V.: "Preliminary Turbulence Length Scale Measurements in a Motored IC Engine," *SAE paper 860021*, 1986.
21. Ikegami, M., Shioji, M., and Nishimoto, K.: "Turbulence Intensity and Spatial Integral Scale during Compression and Expansion Strokes in a Four-cycle Reciprocating Engine," *SAE paper 870372*, 1987.
22. Uzkan, T., Borgnakke, C., and Morel, T.: "Characterization of Flow Produced by a High-Swirl Inlet Port," *SAE paper 830266*, 1983.
23. Monaghan, M. L., and Pettifer, H. F.: "Air Motion and Its Effects on Diesel Performance and Emissions," *SAE paper 810255, in Diesel Combustion and Emissions*, pt. 2, SP-484, *SAE Trans.*, vol. 90, 1981.
24. Tindal, M. J., Williams, T. J., and Aldoory, M.: "The Effect of Inlet Port Design on Cylinder Gas Motion in Direct Injection Diesel Engines," in *Flows in Internal Combustion Engines*, pp. 101–111, ASME, New York, 1982.
25. Brandl, F., Reverencic, I., Cartellieri, W., and Dent, J. C.: "Turbulent Air Flow in the Combustion Bowl of a D.I. Diesel Engine and Its Effect on Engine Performance," *SAE paper 790040, SAE Trans.*, vol. 88, 1979.
26. Brandstätter, W., Johns, R. J. R., and Wigley, G.: "Calculation of Flow Produced by a Tangential Inlet Port," in *International Symposium on Flows in Internal Combustion Engines—III*, FED vol. 28, pp. 135–148, ASME, New York, 1985.
27. Brandstätter, W., Johns, R. J. R., and Wigley, G.: "The Effect of Inlet Port Geometry on In-Cylinder Flow Structure," *SAE paper 850499*, 1985.
28. Davis, G. C., and Kent, J. C.: "Comparison of Model Calculations and Experimental Measurements of the Bulk Cylinder Flow Processes in a Motored PROCO Engine," *SAE paper 790290*, 1979.

29. Borgnakke, C., Davis, G. C., and Tabaczynski, R. J.: "Predictions of In-Cylinder Swirl Velocity and Turbulence Intensity for an Open Chamber Cup in Piston Engine," SAE paper 810224, *SAE Trans.*, vol. 90, 1981.
30. Arcoumanis, C., Bicen, A. F., and Whitelaw, J. H.: "Squish and Swirl-Squish Interaction in Motored Model Engines," *Trans. ASME, J. Fluids Engng.*, vol. 105, pp. 105-112, 1983.
31. Ikegami, M., Mitsuda, T., Kawachi, K., and Fujikawa, T.: "Air Motion and Combustion in Direct Injection Diesel Engines," JARI technical memorandum no. 2, pp. 231-245, 1971.
32. Liou, T.-M., and Santavicca, D. A.: "Cycle Resolved Turbulence Measurements in a Ported Engine With and Without Swirl," SAE paper 830419, *SAE Trans.*, vol. 92, 1983.
33. Fitzgeorge, D., and Allison, J. L.: "Air Swirl in a Road-Vehicle Diesel Engine," *Proc. Instn Mech Engrs (A.D.)*, no. 4, pp. 151-168, 1962-1963.
34. Lichty, L. C.: *Combustion Engine Processes*, McGraw-Hill, 1967.
35. Shimamoto, Y., and Akiyama, K.: "A Study of Squish in Open Combustion Chambers of a Diesel Engine," *Bull. JSME*, vol. 13, no. 63, pp. 1096-1103, 1970.
36. Dent, J. C., and Derham, J. A.: "Air Motion in a Four-Stroke Direct Injection Diesel Engine," *Proc. Instn Mech. Engrs.* vol. 188, 21/74, pp. 269-280, 1974.
37. Asanuma, T., and Obokata, T.: "Gas Velocity Measurements of a Motored and Firing Engine by Laser Anemometry," SAE paper 790096, *SAE Trans.*, vol. 88, 1979.
38. Asanuma, T., Babu, M. K. G., and Yagi, S.: "Simulation of Thermodynamic Cycle of Three-Valve Stratified Charge Engine," SAE paper 780319, *SAE Trans.*, vol. 87, 1978.
39. Hires, S. D., Ekchian, A., Heywood, J. B., Tabaczynski, R. J., and Wall, J. C.: "Performance and NO<sub>x</sub> Emissions Modelling of a Jet Ignition Prechamber Stratified Charge Engine," SAE paper 760161, *SAE Trans.*, vol. 85, 1976.
40. Zimmerman, D. R.: "Laser Anemometer Measurements of the Air Motion in the Prechamber of an Automotive Diesel Engine," SAE paper 830452, 1983.
41. Meintjes, K., and Alkidas, A. C.: "An Experimental and Computational Investigation of the Flow in Diesel Prechambers," SAE paper 820275, *SAE Trans.*, vol. 91, in *Diesel Engine Combustion, Emissions, and Particulates*, P-107, SAE, 1982.
42. Namazian, M., and Heywood, J. B.: "Flow in the Piston-Cylinder-Ring Crevices of a Spark-Ignition Engine: Effect on Hydrocarbon Emissions, Efficiency and Power," SAE paper 820088, *SAE Trans.*, vol. 91, 1982.
43. Wentworth, J. T.: "Piston and Ring Variables Affect Exhaust Hydrocarbon Emissions," SAE paper 680109, *SAE Trans.*, vol. 77, 1968.
44. Tabaczynski, R. J., Hoult, D. P., and Keck, J. C.: "High Reynolds Number Flow in a Moving Corner," *J. Fluid Mech.*, vol. 42, pp. 249-255, 1970.
45. Daneshyar, H. F., Fuller, D. E., and Deckker, B. E. L.: "Vortex Motion Induced by the Piston of an Internal Combustion Engine," *Int. J. Mech. Sci.*, vol. 15, pp. 381-390, 1973.

# CHAPTER

# 9

## COMBUSTION IN SPARK-IGNITION ENGINES

### 9.1 ESSENTIAL FEATURES OF PROCESS

In a conventional spark-ignition engine the fuel and air are mixed together in the intake system, inducted through the intake valve into the cylinder, where mixing with residual gas takes place, and then compressed. Under normal operating conditions, combustion is initiated towards the end of the compression stroke at the spark plug by an electric discharge. Following inflammation, a turbulent flame develops, propagates through this essentially premixed fuel, air, burned gas mixture until it reaches the combustion chamber walls, and then extinguishes. Photographs of this process taken in operating engines illustrate its essential features. Figure 9-1 (color plate) shows a sequence of frames from a high-speed color movie of the combustion process in a special single-cylinder engine with a glass piston crown.<sup>1</sup> The spark discharge is at  $-30^\circ$ . The flame first becomes visible in the photos at about  $-24^\circ$ . The flame, approximately circular in outline in this

FIGURE 9-1 (On color plate opposite p. 498)

Color photographs from high-speed movie of spark-ignition engine combustion process, taken through glass piston crown. Ignition timing  $30^\circ$  BTC, light load, 1430 rev/min,  $(A/F) = 19$ .<sup>1</sup>

view through the piston, then propagates outward from the spark plug location. The blue light from the flame is emitted most strongly from the front. The irregular shape of the turbulent flame front is apparent. At TC the flame diameter is about two-thirds of the cylinder bore. The flame reaches the cylinder wall farthest from the spark plug about  $15^\circ$  ATC, but combustion continues around parts of the chamber periphery for another  $10^\circ$ . At about  $10^\circ$  ATC, additional radiation—initially white, turning to pinky-orange—centered at the spark plug location is evident. This afterglow comes from the gases behind the flame which burned earlier in the combustion process, as these are compressed to the highest temperatures attained within the cylinder (at about  $15^\circ$  ATC) while the rest of the charge burns.<sup>2,3</sup>

Additional features of the combustion process are evident from the data in Fig. 9-2, taken from several consecutive cycles of an operating spark-ignition engine. The cylinder pressure, fraction of the charge mass which has burned (determined from the pressure data, see Sec. 9.2), and fraction of the cylinder volume enflamed by the front (determined from photographs like Fig. 9-1) are shown, all as a function of crank angle.<sup>4</sup> Following spark discharge, there is a period during which the energy release from the developing flame is too small for the pressure rise due to combustion to be discerned. As the flame continues to grow and propagate across the combustion chamber, the pressure then steadily rises above the value it would have in the absence of combustion. The pressure reaches a maximum after TC but before the cylinder charge is fully burned, and then decreases as the cylinder volume continues to increase during the remainder of the expansion stroke.

The flame development and subsequent propagation obviously vary, cycle-by-cycle, since the shape of the pressure, volume fraction enflamed, and mass fraction burned curves for each cycle differ significantly. This is because flame growth depends on local mixture motion and composition. These quantities vary in successive cycles in any given cylinder and may vary cylinder-to-cylinder. Especially significant are mixture motion and composition in the vicinity of the spark plug at the time of spark discharge since these govern the early stages of flame development. Cycle-by-cycle and cylinder-to-cylinder variations in combustion are important because the extreme cycles limit the operating regime of the engine (see Sec. 9.4.1).

Note that the volume fraction enflamed curves rise more steeply than the mass fraction burned curves. In large part, this is because the density of the unburned mixture ahead of the flame is about four times the density of the burned gases behind the flame. Also, there is some unburned mixture behind the visible front to the flame: even when the entire combustion chamber is fully enflamed, some 25 percent of the mass has still to burn. From this description it is plausible to divide the combustion process into four distinct phases: (1) spark ignition; (2) early flame development; (3) flame propagation; and (4) flame termination. Our understanding of each of these phases will be developed in the remainder of this chapter.

The combustion event must be properly located relative to top-center to

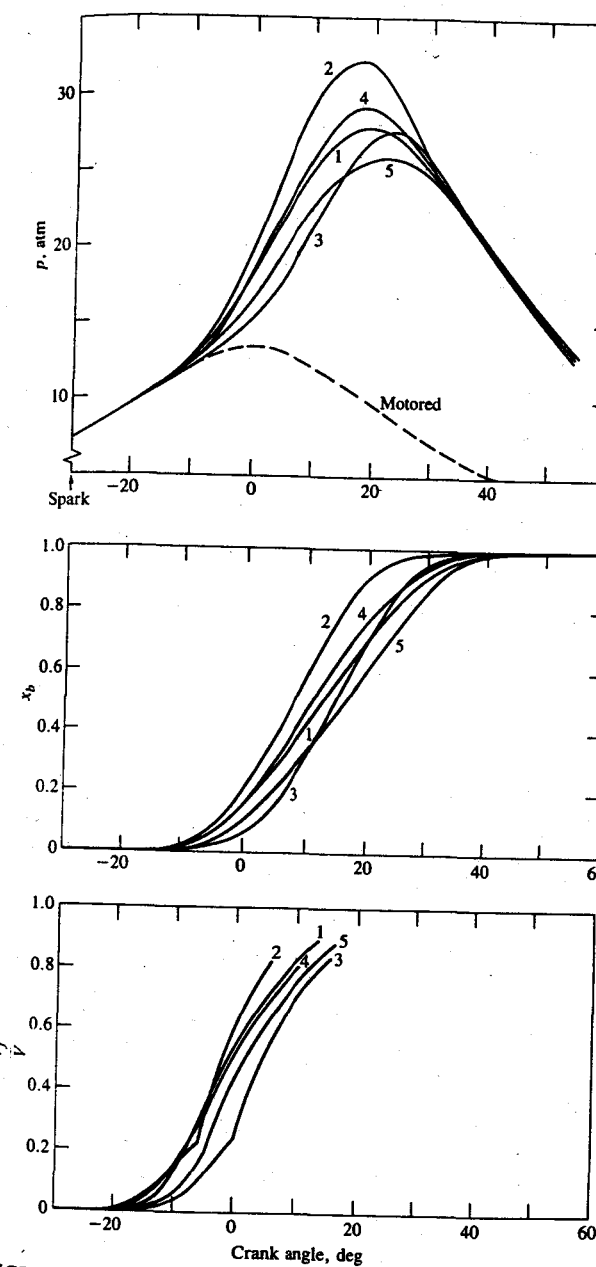


FIGURE 9-2

Cylinder pressure, mass fraction burned, and volume fraction enflamed for five consecutive cycles in a spark-ignition engine as a function of crank angle. Ignition timing  $30^\circ$  BTC, wide-open throttle, 1044 rev/min,  $\phi = 0.98$ .<sup>4</sup>

obtain the maximum power or torque. The combined duration of the flame development and propagation process is typically between 30 and 90 crank angle degrees. Combustion starts before the end of the compression stroke, continues through the early part of the expansion stroke, and ends after the point in the cycle at which the peak cylinder pressure occurs. The pressure versus crank angle curves shown in Fig. 9-3a allow us to understand why engine torque (at given engine speed and intake manifold conditions) varies as spark timing is varied relative to TC. If the start of the combustion process is progressively advanced before TC, the compression stroke work transfer (which is *from* the piston *to* the cylinder gases) increases. If the end of the combustion process is progressively delayed by retarding the spark timing, the peak cylinder pressure occurs later in the expansion stroke and is reduced in magnitude. These changes reduce the expansion stroke work transfer *from* the cylinder gases *to* the piston. The optimum timing which gives the maximum brake torque—called *maximum brake torque, or MBT, timing*—occurs when the magnitudes of these two opposing trends just offset each other. Timing which is advanced or retarded from this optimum gives lower torque. The optimum spark setting will depend on the rate of flame development and propagation, the length of the flame travel path across the combustion chamber, and the details of the flame termination process after it reaches the wall. These depend on engine design and operating conditions, and the properties of the fuel, air, burned gas mixture. Figure 9-3b shows the effect of variations in spark timing on brake torque for a typical spark-ignition engine. The maximum is quite flat.

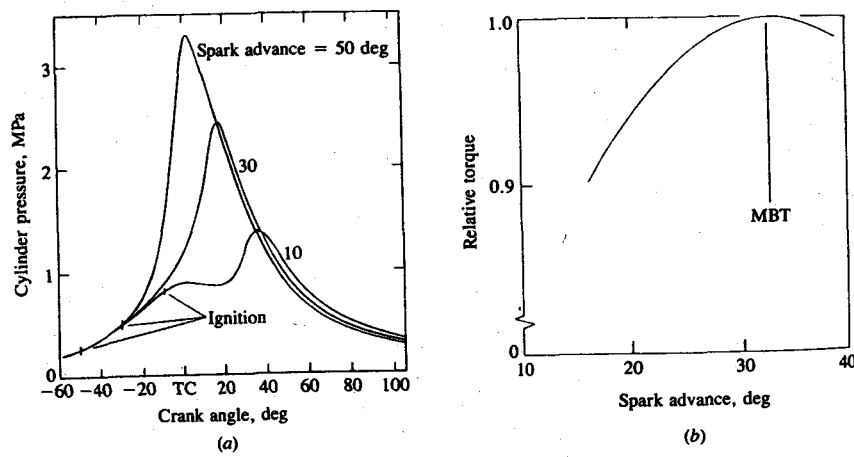


FIGURE 9-3  
(a) Cylinder pressure versus crank angle for overadvanced spark timing (50°), MBT timing (30°), and retarded timing (10°). (b) Effect of spark advance on brake torque at constant speed and (A/F), at wide-open throttle. MBT is maximum brake torque timing.<sup>3</sup>

Empirical rules for relating the mass burning profile and maximum cylinder pressure to crank angle at MBT timing are often used. For example, with optimum spark timing: (1) the maximum pressure occurs at about 16° after TC; (2) half the charge is burned at about 10° after TC. In practice, the spark is often retarded to give a 1 or 2 percent reduction in brake torque from the maximum value, to permit a more precise definition of timing relative to the optimum.

So far we have described normal combustion in which the spark-ignited flame moves *steadily* across the combustion chamber until the charge is fully consumed. However, several factors—e.g., fuel composition, certain engine design and operating parameters, and combustion chamber deposits—may prevent this normal combustion process from occurring. Two types of abnormal combustion have been identified: knock and surface ignition.

*Knock* is the most important abnormal combustion phenomenon. Its name comes from the noise that results from the autoignition of a portion of the fuel, air, residual gas mixture ahead of the advancing flame. As the flame propagates across the combustion chamber, the unburned mixture ahead of the flame—called the *end gas*—is compressed, causing its pressure, temperature, and density to increase. Some of the end-gas fuel-air mixture may undergo chemical reactions prior to normal combustion. The products of these reactions may then autoignite: i.e., spontaneously and rapidly release a large part or all of their chemical energy. When this happens, the end gas burns very rapidly, releasing its energy at a rate 5 to 25 times that characteristic of normal combustion. This causes high-frequency pressure oscillations inside the cylinder that produce the sharp metallic noise called knock.

The presence or absence of knock reflects the outcome of a race between the advancing flame front and the precombustion reactions in the unburned end gas. Knock will not occur if the flame front consumes the end gas before these reactions have time to cause the fuel-air mixture to autoignite. Knock will occur if the precombustion reactions produce autoignition before the flame front arrives.

The other important abnormal combustion phenomenon is *surface ignition*. Surface ignition is ignition of the fuel-air charge by overheated valves or spark plugs, by glowing combustion-chamber deposits, or by any other hot spot in the engine combustion chamber: it is ignition by any source other than normal spark ignition. It may occur before the spark plug ignites the charge (preignition) or after normal ignition (postignition). It may produce a single flame or many flames. Uncontrolled combustion is most evident and its effects most severe when it results from preignition. However, even when surface ignition occurs after the spark plug fires (postignition), the spark discharge no longer has complete control of the combustion process.

Surface ignition may result in knock. Knock which occurs following normal spark ignition is called *spark knock* to distinguish it from knock which has been preceded by surface ignition. Abnormal combustion phenomena are reviewed in more detail in Sec. 9.6.

## 9.2 THERMODYNAMIC ANALYSIS OF SI ENGINE COMBUSTION

### 9.2.1 Burned and Unburned Mixture States

Because combustion occurs through a flame propagation process, the changes in state and the motion of the unburned and burned gas are much more complex than the ideal cycle analysis in Chapter 5 suggests. The gas pressure, temperature, and density change as a result of changes in volume due to piston motion. During combustion, the cylinder pressure increases due to the release of the fuel's chemical energy. As each element of fuel-air mixture burns, its density decreases by about a factor of four. This combustion-produced gas expansion compresses the unburned mixture ahead of the flame and displaces it toward the combustion chamber walls. The combustion-produced gas expansion also compresses those parts of the charge which have already burned, and displaces them back toward the spark plug. During the combustion process, the unburned gas elements move away from the spark plug; following combustion, individual gas elements move back toward the spark plug. Further, elements of the unburned mixture which burn at different times have different pressures and temperatures just prior to combustion, and therefore end up at different states after combustion. The thermodynamic state and composition of the burned gas is, therefore, non-uniform. A first law analysis of the spark-ignition engine combustion process enables us to quantify these gas states.

Consider the schematic of the engine cylinder while combustion is in progress, shown in Fig. 9-4. Work transfer occurs between the cylinder gases and the piston (to the gas before TC; to the piston after TC). Heat transfer occurs to the chamber walls, primarily from the burned gases. At the temperatures and pressures typical of spark-ignition engines it is a reasonable approximation to assume that the volume of the reaction zone where combustion is actually occurring is a negligible fraction of the chamber volume even though the thickness of the turbulent flame may not be negligible compared with the chamber dimensions (see Sec. 9.3.2). With normal engine operation, at any point in time or crank angle, the pressure throughout the cylinder is close to uniform. The condi-

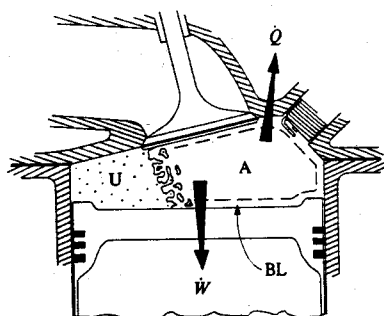


FIGURE 9-4

Schematic of flame in the engine cylinder during combustion: unburned gas (U) to left of flame, burned gas to right. A denotes adiabatic burned-gas core, BL denotes thermal boundary layer in burned gas,  $W$  is work-transfer rate to piston,  $Q$  is heat transfer rate to chamber walls.

tions in the burned and unburned gas are then determined by conservation of mass:

$$\frac{V}{m} = \int_0^{x_b} v_b dx + \int_{x_b}^1 v_u dx \quad (9.1)$$

and conservation of energy:

$$\frac{U_0 - W - Q}{m} = \int_0^{x_b} u_b dx + \int_{x_b}^1 u_u dx \quad (9.2)$$

where  $V$  is the cylinder volume,  $m$  is the mass of the cylinder contents,  $v$  is the specific volume,  $x_b$  is the mass fraction burned,  $U_0$  is the internal energy of the cylinder contents at some reference point  $\theta_0$ ,  $u$  is the specific internal energy,  $W$  is the work done on the piston, and  $Q$  is the heat transfer to the walls. The subscripts  $u$  and  $b$  denote unburned and burned gas properties, respectively. The work and heat transfers are

$$W = \int_{V_0}^V p dV' \quad Q = \int_{\theta_0}^{\theta} \left( \frac{Q}{360N} \right) d\theta \quad (9.3)$$

where  $Q$  is the instantaneous heat-transfer rate to the chamber walls.

To proceed further, models for the thermodynamic properties of the burned and unburned gases are required. Several categories of models are described in Chap. 4. Accurate calculations of the state of the cylinder gases require an equilibrium model (or good approximation to it) for the burned gas and an ideal gas mixture model (of frozen composition) for the unburned gas (see Table 4.2). However, useful illustrative results can be obtained by assuming that the burned and unburned gases are different ideal gases, each with constant specific heats,<sup>6</sup> i.e.,

$$pv_b = R_b T_b \quad u_b = c_{v,b} T_b + h_{f,b} \quad (9.4)$$

$$pv_u = R_u T_u \quad u_u = c_{v,u} T_u + h_{f,u} \quad (9.5)$$

Combining Eqs. (9.1) to (9.5) gives

$$\frac{pV}{m} = x_b R_b \bar{T}_b + (1 - x_b) R_u \bar{T}_u \quad (9.6)$$

and

$$\frac{U_0 - W - Q}{m} = x_b (c_{v,b} \bar{T}_b + h_{f,b}) + (1 - x_b) (c_{v,u} \bar{T}_u + h_{f,u}) \quad (9.7)$$

where

$$\bar{T}_b = \frac{1}{x_b} \int_0^{x_b} T_b dx \quad \bar{T}_u = \frac{1}{1 - x_b} \int_{x_b}^1 T_u dx$$

are the mean temperatures of the burned and unburned gases. Equations (9.6) and (9.7) may now be solved to obtain

$$x_b = \frac{pV - p_0 V_0 + (\gamma_b - 1)(W + Q) + (\gamma_b - \gamma_u)mc_{p,u}(\bar{T}_u - T_0)}{m[(\gamma_b - 1)(h_{f,u} - h_{f,b}) + (\gamma_b - \gamma_u)c_{p,u}\bar{T}_u]} \quad (9.8)$$

and  $\bar{T}_b = \frac{R_u}{R_b} \bar{T}_u + \frac{pV - mR_u \bar{T}_u}{mR_b x_b}$  (9.9)

If we now assume the unburned gas is initially uniform and undergoes isentropic compression, then

$$\frac{\bar{T}_u}{T_0} = \left( \frac{p}{p_0} \right)^{(\gamma_u - 1)/\gamma_u} \quad (9.10)$$

This equation, with Eqs. (9.8) and (9.9) enables determination of both  $x_b$  and  $\bar{T}_b$  from the thermodynamic properties of the burned and unburned gases, and known values of  $p$ ,  $V$ ,  $m$ , and  $Q$ . Alternatively, if  $x_b$  is known then  $p$  can be determined. Mass fraction burned and cylinder gas pressure are uniquely related.

While Eq. (9.9) defines a mean burned gas temperature, the burned gas is not uniform. Mixture which burns early in the combustion process is further compressed after combustion as the remainder of the charge is burned. Mixture which burns late in the combustion process is compressed prior to combustion and, therefore, ends up at a different final state. A temperature gradient exists across the burned gas with the earlier burning portions at the higher temperature.<sup>7,8</sup> Two limiting models bracket what occurs in practice: (1) a *fully mixed* model, where it is assumed that each element of mixture which burns mixes instantaneously with the already burned gases (which therefore have a uniform temperature), and (2) an *unmixed* model, where it is assumed that no mixing occurs between gas elements which burn at different times.

In the fully mixed model the burned gas is uniform,  $T_b = \bar{T}_b$ , and the equations given above fully define the state of the cylinder contents. In the unmixed model, the assumption is made that no mixing occurs between gas elements that burn at different times, and each burned gas element is therefore isentropically compressed (and eventually expanded) after combustion.<sup>†</sup> Thus:

$$\frac{T_b(x'_b, x_b)}{T_b(x'_b)} = \left[ \frac{p(x_b)}{p(x'_b)} \right]^{(\gamma_b - 1)/\gamma_b} \quad (9.11)$$

<sup>†</sup> This model applies to burned gas regions of the chamber away from the walls. Heat transfer to the walls results in a thermal boundary layer on the walls which grows with time. The gas in the boundary layer is not isentropically compressed and expanded.

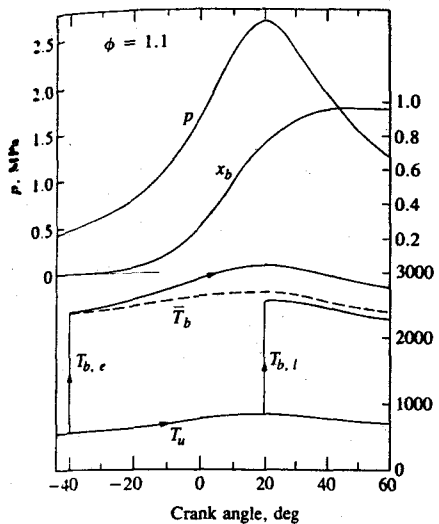


FIGURE 9-5

Cylinder pressure, mass fraction burned, and gas temperatures as functions of crank angle during combustion.  $T_u$  is unburned gas temperature,  $T_b$  is burned gas temperature, the subscripts *e* and *l* denote early and late burning gas elements, and  $\bar{T}_b$  is the mean burned gas temperature.<sup>9</sup> (Reprinted with permission. Copyright 1973, American Chemical Society.)

where  $T_b(x'_b, x_b)$  is the temperature of the element which burned at the pressure  $p(x'_b)$  when the pressure is  $p(x_b)$ , and

$$T_b(x'_b) = \frac{h_{f,u} - h_{f,b} + c_{p,u} T_u(x'_b)}{c_{p,b}} \quad (9.12)$$

is the temperature resulting from isenthalpic combustion of the unburned gas at  $T_u(x'_b)$ ,  $p(x'_b)$ . An example of the temperature distribution computed with this model is shown in Fig. 9-5. A mixture element that burns right at the start of the combustion process reaches, in the absence of mixing, a peak temperature after combustion about 400 K higher than an element that burns toward the end of the combustion process. The mean burned gas temperature is closer to the lower of these temperatures. These two models approximate respectively to situations where the time scale that characterizes the turbulent mixing process in the burned gases is (1) much less than the overall burning time (for the fully mixed model) or (2) much longer than the overall burning time (for the unmixed model). The real situation lies in between.

Measurements of burned gas temperatures have been made in engines using spectroscopic techniques through quartz windows in the cylinder head. Examples of measured temperatures are shown in Fig. 9-6. The solid lines marked *A*, *B*, and *C* are the burned gas temperatures measured by Rassweiler and Withrow<sup>7</sup> using the sodium line reversal technique in an L-head engine, for the spark plug end (*A*), the middle (*B*), and the opposite end (*C*) of the chamber, respectively. Curves labeled *W*<sub>2</sub> and *W*<sub>3</sub> were measured by Lavoie<sup>8</sup> through two different windows, *W*<sub>2</sub> and *W*<sub>3</sub> (with *W*<sub>2</sub> closer to the spark), again in an L-head engine. Each set of experimental temperatures shows a temperature gradient across the burned gas comparable to that predicted, and the two sets have similar shapes.

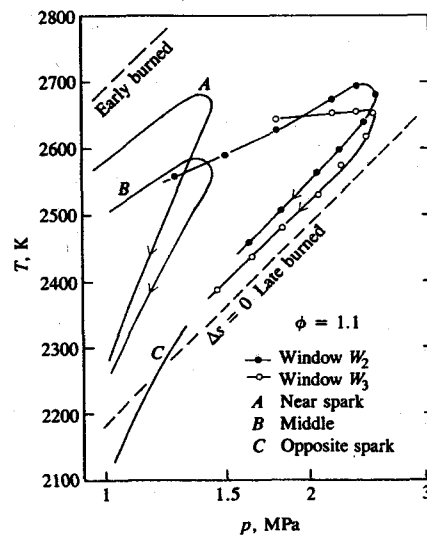


FIGURE 9-6

Burned gas temperatures measured using spectroscopic techniques through windows in the cylinder head, as a function of cylinder pressure. Temperatures measured closer to spark plug have higher values. Dashed lines show isentropic behavior.<sup>7,8</sup>

In the unmixed model, the temperature of each burned gas element follows a different isentropic line as it is first compressed as  $p$  increases to  $p_{\max}$  and then expanded as the pressure falls after  $p_{\max}$ . The measured temperature curves in Fig. 9-6 do not follow the calculated isentropes because of gas motion past the observation ports. As has already been mentioned, the expansion of a gas element which occurs during combustion compresses the gas ahead of the flame and moves it away from the spark plug. At the same time, previously burned gas is compressed and moved back toward the spark plug. Defining this motion in an engine requires sophisticated flow models, because the combustion chamber shape is rarely symmetrical, the spark plug is not usually centrally located, and often there is a bulk gas motion at the time combustion is initiated. However, the gas motion in a spherical or cylindrical combustion bomb with central ignition which can readily be computed illustrates the features of the combustion-induced motion in an engine. Figure 9-7 shows calculated particle trajectories for a stoichiometric methane-air mixture, initially at ambient conditions, as a laminar

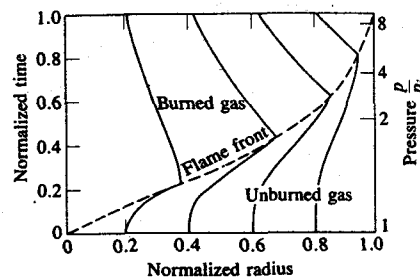


FIGURE 9-7

Particle trajectories in unburned and burned gas as flame propagates outward at constant velocity from the center of a spherical combustion bomb. Stoichiometric methane-air mixture initially at 1 atm and 300 K.

flame with a constant burning velocity propagates outward from the center of a spherical container. Applying this gas motion model to an engine, it can be concluded that a window in the cylinder head initially views earlier burned gas (of higher temperature and entropy) and that as more of the charge burns, the window views later burned gas of progressively lower entropy. The experimental curves fit this description: they cross the constant entropy lines toward lower entropy. Note that the gradient in temperature persists well into the expansion stroke, indicating that the "unmixed" model is closer to reality than the "fully mixed" model.

More accurate calculations relating the mass fraction burned, gas pressure, and gas temperature distribution are often required. Note that the accuracy of such calculations depends on the accuracy with which the time-varying heat loss to the chamber walls can be estimated (see Sec. 12.4.3) and whether flows into and out of crevice regions are significant (see Sec. 8.6), as well as the accuracy of the models used to describe the thermodynamic properties of the gases. Appropriate more accurate models for the thermodynamic properties are: an equilibrium model for the burned gas, and specific heat models which vary with temperature for each of the components of the unburned mixture (see Secs. 4.1 and 4.7). In the absence of significant crevice effects, Eqs. (9.1) and (9.2) can be written as

$$\frac{V}{m} = \bar{v}_b x_b + \bar{v}_u (1 - x_b) \quad (9.13)$$

$$\frac{U_0 - W - Q}{m} = \bar{u}_b x_b + \bar{u}_u (1 - x_b) \quad (9.14)$$

where

$$\bar{v}_b = \frac{1}{x_b} \int_0^{x_b} v_b dx \quad \text{and} \quad \bar{v}_u = \frac{1}{1 - x_b} \int_{x_b}^1 v_u dx$$

and similar definitions hold for  $\bar{u}_b$  and  $\bar{u}_u$ . For a given equivalence ratio, fuel and burned gas fraction:

$$h_u = h_u(T_u) \quad h_b = h_b(T_b, p) \quad (9.15a, b)$$

$$pv_u = \left( \frac{\bar{R}}{M_u} \right) T_u \quad pv_b = \left( \frac{\bar{R}}{M_b} \right) T_b \quad (9.16a, b)$$

and

$$\bar{u}_u = \bar{h}_u - p\bar{v}_u \quad \bar{u}_b = \bar{h}_b - p\bar{v}_b \quad (9.17a, b)$$

To simplify the calculations, it is convenient to assume that, for the burned gas,  $\bar{u}_b = u_b(\bar{T}_b, p)$  and  $\bar{v}_b = v_b(\bar{T}_b, p)$ . This corresponds to the fully mixed assumption described above. The effect of neglecting the temperature distribution in the calculation of mass fraction burned is small. In addition, the heat losses from the unburned gas can usually be neglected; the unburned gas is then compressed isentropically.  $\bar{T}_u$  is specified for some initial state of the unburned gas (where

$x_b = 0$ ) by  $p_0$ ,  $V_0$ ,  $M_u$ , and the mass of charge  $m$ . Then, since for any isentropic process

$$\left(\frac{\partial T}{\partial p}\right)_s = \frac{v - (\partial h/\partial p)_T}{(\partial h/\partial T)_p} \quad (9.18)$$

$\bar{T}_u$  can be determined.

Equations (9.13) to (9.18) constitute a set of nine equations for the nine unknowns  $\bar{v}_u$ ,  $\bar{v}_b$ ,  $\bar{u}_u$ ,  $\bar{u}_b$ ,  $\bar{h}_u$ ,  $\bar{h}_b$ ,  $\bar{T}_u$ ,  $T_b$ , and  $x_b$  or  $p$ . One convenient solution method is to eliminate  $x_b$  from Eqs. (9.13) and (9.14) to obtain

$$\frac{(V/m) - \bar{v}_u}{\bar{v}_b - \bar{v}_u} - \frac{(U/m) - \bar{u}_u}{\bar{u}_b - \bar{u}_u} = f(\bar{T}_b, \bar{T}_u) = 0 \quad (9.19)$$

where  $U = U_0 - W - Q$ .  $\bar{T}_u$  can be determined from Eq. (9.18). Equation (9.19) can then be solved using an appropriate iterative technique for  $\bar{T}_b$ , and  $x_b$  can be obtained from Eq. (9.13). An alternative formulation based on the rate of change of pressure  $dp/d\theta$  and equations for  $d\bar{T}_u/d\theta$ ,  $d\bar{T}_b/d\theta$ ,  $dm_b/d\theta$ , and  $dV_b/d\theta$  can be found in Ref. 10. Some examples of mass fraction burned curves obtained from measured pressure data, with gasoline and methanol fuels, are shown in Fig. 9-8. With accurate pressure versus crank angle records, values of final mass fraction burned should be close to but lower than unity, usually in the range 0.93 to 0.96; the difference from unity is the combustion inefficiency for lean mixtures (see Fig. 3-9) and incomplete oxygen utilization for rich mixtures (see Fig. 4-20).

More accurate burned gas temperature calculations need to account for the presence of a thermal boundary layer (of order 1 mm thick) around the combustion chamber walls (see Sec. 12.6.5). The burned gas region in Fig. 9-4 can be

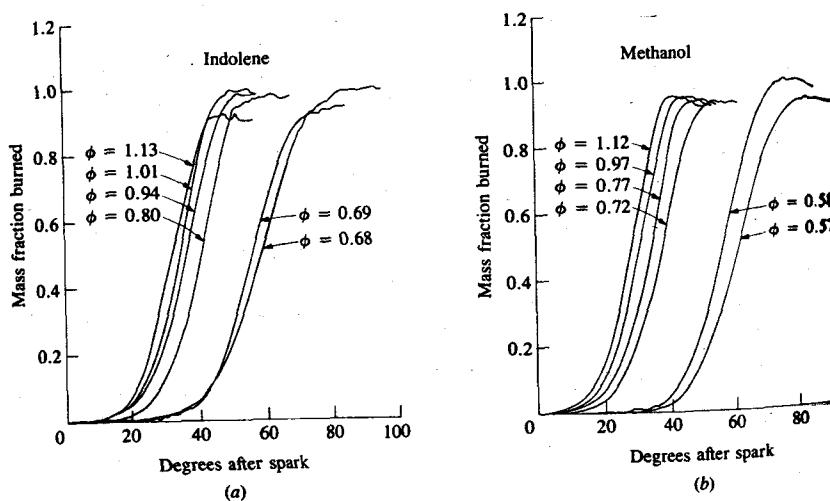


FIGURE 9-8  
Mass fraction burned curves determined from measured cylinder pressure data using two-zone combustion model: (a) gasoline; (b) methanol.  $\phi$  = fuel/air equivalence ratio.<sup>11</sup>

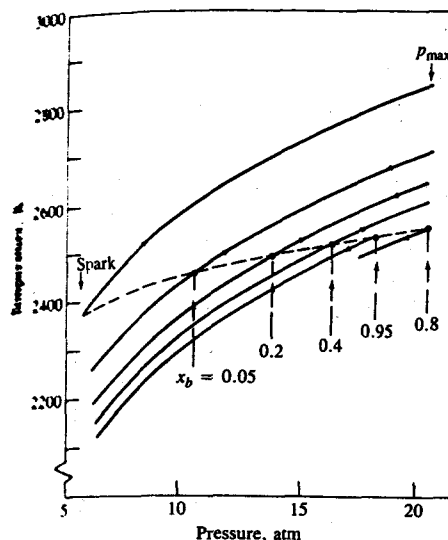


FIGURE 9-9  
Calculated temperature distribution in the adiabatic core of the burned gas zone for the unmixed model assuming thermodynamic equilibrium.  $\phi = 1.0$ . Dashed line is temperature of each element just after it burns.

divided into an adiabatic core and a boundary layer that grows in thickness with time. In the adiabatic core, in the absence of mixing between gas elements that burn at different times, burned gas is compressed and then expanded isentropically. The burned gas temperature distribution can be calculated as follows. Given the pressure versus crank angle data, the unburned mixture state can be determined using Eq. (9.18) above. Each small element of unburned mixture burns in a constant-enthalpy constant-pressure process. So the burned state of an element of unburned charge, which burns at  $p = p_i$ , can be obtained from the relation

$$h_b(T_{b,i}, p_i) = h_u(T_{u,i}, p_i)$$

After combustion, this element which burned at  $p = p_i$  is compressed and expanded along the isentropic:

$$s_b(T_b, p) = s_b(T_{b,i}, p_i)$$

An example of the temperature distribution computed in this manner for this unmixed model in the burned gas adiabatic core is shown in Fig. 9-9. The element ignited by the spark is compressed to the highest peak temperature at  $P_{max}$ . The temperature difference across the bulk of the charge ( $0.05 < x_b < 0.95$ ) is about 200 K.

## 9.22 Analysis of Cylinder Pressure Data

Cylinder pressure changes with crank angle as a result of cylinder volume change, combustion, heat transfer to the chamber walls, flow into and out of crevice regions, and leakage. The first two of these effects are the largest. The effect of

volume change on the pressure can readily be accounted for; thus, combustion rate information can be obtained from accurate pressure data provided models for the remaining phenomena can be developed at an appropriate level of approximation. The previous section has developed the fundamental basis for such calculations.

Cylinder pressure is usually measured with piezoelectric pressure transducers. This type of transducer contains a quartz crystal. One end of the crystal is exposed through a diaphragm to the cylinder pressure; as the cylinder pressure increases, the crystal is compressed and generates an electric charge which is proportional to the pressure. A charge amplifier is then used to produce an output voltage proportional to this charge. Accurate cylinder pressure versus crank angle data can be obtained with these systems provided the following steps are carried out: (1) the correct reference pressure is used to convert the measured pressure signals to absolute pressures; (2) the pressure versus crank angle (or volume) phasing is accurate to within about  $0.2^\circ$ ; (3) the clearance volume is estimated with sufficient accuracy; (4) transducer temperature variations (which can change the transducer calibration factor) due to the variation in wall heat flux during the engine cycle are held to a minimum. Log  $p$  versus log  $V$  plots can be used to check the quality of cylinder pressure data. The first three of the above requirements can be validated using log  $p$ -log  $V$  diagrams for a motored engine. If the effects of thermal cycling are significant, the expansion stroke on the log  $p$ -log  $V$  plot for a firing engine shows excessive curvature.<sup>12</sup>

Figure 9-10 shows pressure-volume data from a firing spark-ignition engine on both a linear  $p$ - $V$  and a log  $p$ -log  $V$  diagram. On the log  $p$ -log  $V$  diagram the compression process is a straight line of slope 1.3. The start of combustion can be identified by the departure of the curve from the straight line. The end of com-

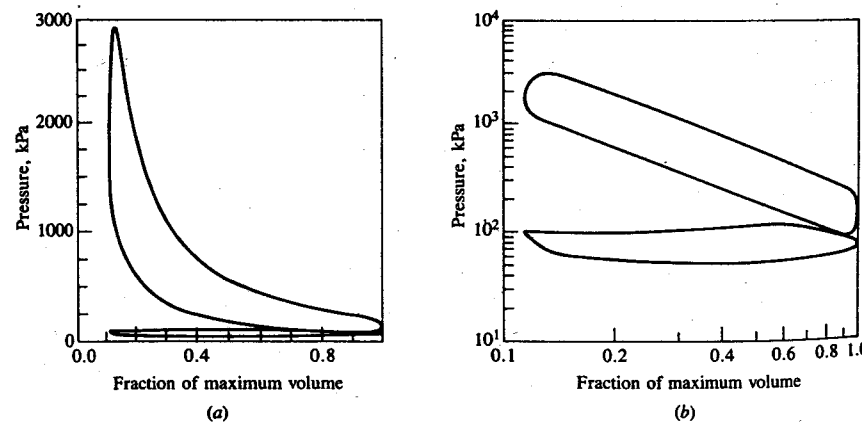


FIGURE 9-10  
(a) Pressure-volume diagram; (b) log  $p$ -log ( $V/V_{\max}$ ) plot. 1500 rev/min, MBT timing, imep = 513 kPa,  $\phi = 0.8$ ,  $r_c = 8.72$ , propane fuel.<sup>12</sup>

bustion can be located approximately in similar fashion; the expansion stroke following combustion is essentially linear with slope 1.33. Since both the compression of the unburned mixture prior to combustion and the expansion of the burned gases following the end of combustion are close to adiabatic isentropic processes (for which  $pV^\gamma = \text{constant}$ ;  $\gamma = c_p/c_v$ ), the observed behavior is as expected. More extensive studies<sup>12, 13</sup> show that the compression and expansion processes are well fitted by a polytropic relation:

$$pV^n = \text{constant} \quad (9.20)$$

The exponent  $n$  for the compression and expansion processes is 1.3 ( $\pm 0.05$ ) for conventional fuels. It is comparable to the average value of  $\gamma_u$  for the unburned mixture over the compression process, but is larger than  $\gamma_b$  for the burned gas mixture during expansion due to heat loss to the combustion chamber walls (see Figs. 4-13 and 4-16).

Log  $p$ -log  $V$  plots such as Fig. 9-10 approximately define the start and end of combustion, but do not provide a mass fraction burned profile. One well-established technique for estimating the mass fraction burned profile from the pressure and volume data is that developed by Rassweiler and Withrow.<sup>2</sup> They correlated cylinder pressure data with flame photographs, and showed how Eq. (9.20) could be used to account for the effect of cylinder volume change on the pressure during combustion. Assuming that the unburned gas filling the volume  $V_u$  ahead of the flame at any crank angle during combustion has been compressed polytropically by the advancing flame front, then the volume  $V_{u,0}$  it occupied at time of spark is

$$V_{u,0} = V_u \left( \frac{p}{p_0} \right)^{1/n} \quad (9.21)$$

Similarly, the burned gas behind the flame filling the volume  $V_b$  would, at the end of combustion, fill a volume  $V_{b,f}$  given by

$$V_{b,f} = V_b \left( \frac{p}{p_f} \right)^{1/n} \quad (9.22)$$

The mass fraction burned  $x_b$  is equal to  $1 - (V_{u,0}/V_0)$  and to  $V_{b,f}/V_f$ , where  $V_0$  and  $V_f$  are the total cylinder volumes at time of spark and at the end of combustion, respectively. Since  $V = V_u + V_b$ , Eqs. (9.21) and (9.22) then give:

$$x_b = \frac{p^{1/n}V - p_0^{1/n}V_0}{p_f^{1/n}V_f - p_0^{1/n}V_0} \quad (9.23)$$

This method is widely used, though it contains several approximations. Heat-transfer effects are included only to the extent that the polytropic exponent  $n$  in Eq. (9.22) differs appropriately from  $\gamma$ . The pressure rise due to combustion is proportional to the amount of fuel chemical energy released rather than the mass of mixture burned. Also, the polytropic exponent  $n$  is not constant during combustion. Selecting an appropriate value for  $n$  (whether  $n$  is assumed to be con-

stant or to vary through the combustion process) is the major difficulty in applying this pressure data analysis procedure.

The effects of heat transfer, crevices, and leakage can be explicitly incorporated into cylinder pressure data analysis by using a "heat release" approach based on the first law of thermodynamics. A major advantage of such an approach is that the pressure changes can be related directly to the amount of fuel chemical energy released by combustion, while retaining the simplicity of treating the combustion chamber contents as a single zone. Figure 9-11 shows the appropriate open-system boundary for the combustion chamber.<sup>14</sup> The first law for this open system is

$$\delta Q_{ch} = dU_s + \delta Q_{ht} + \delta W + \sum h_i dm_i \quad (9.24)$$

The change in sensible energy of the charge  $dU_s$  is separated from that due to change in composition: the term  $\delta Q_{ch}$  represents the "chemical energy" released by combustion. The work is piston work and equal to  $p dV$ .  $\delta Q_{ht}$  is heat transfer to the chamber walls. The mass flux term represents flow across the system boundary. In the absence of fuel injection, it represents flow into and out of crevice regions (see Sec. 8.6).

The accuracy with which this energy balance can be made depends on how adequately each term in the above equation can be quantified. Assuming that  $U_s$  is given by  $m u(T)$ , where  $T$  is the mean charge temperature and  $m$  is the mass within the system boundary, then

$$dU_s = mc_v(T) dT + u(T) dm$$

Note that this mean temperature determined from the ideal gas law is close to the mass-averaged cylinder temperature during combustion since the molecular weights of the burned and unburned gases are essentially identical. Crevice effects can usually be modeled adequately by flow into and out of a single volume at the cylinder pressure, with the gas in the crevice at a substantially lower temperature. Leakage to the crankcase can usually be neglected. Then Eq. (9.24), on substituting for  $dU_s$  and  $dm_i$  ( $= dm_{cr} = -dm$ ), becomes

$$\delta Q_{ch} = mc_v dT + (h' - u)dm_{cr} + p dV + \delta Q_{ht} \quad (9.25)$$

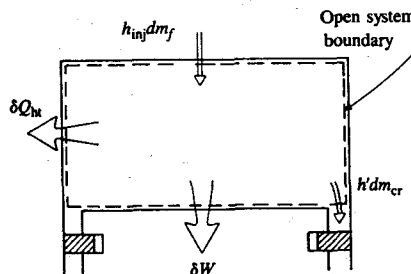


FIGURE 9-11  
Open system boundary for combustion chamber for heat-release analysis.

where

- $dm_{cr} > 0$  when flow is out of the cylinder into the crevice
- $dm_{cr} < 0$  when flow is from the crevice to the cylinder
- $h'$  is evaluated at cylinder conditions when  $dm_{cr} > 0$  and at crevice conditions when  $dm_{cr} < 0$

Use of the ideal gas law (neglecting the change in gas constant  $R$ ) with Eq. (9.25) then gives

$$\delta Q_{ch} = \left(\frac{c_v}{R}\right)V dp + \left(\frac{c_v}{R} + 1\right)p dV + (h' - u + c_v T) dm_{cr} + \delta Q_{ht} \quad (9.26)$$

This equation can be used in several ways. When the heat or energy release term,  $\delta Q_{ch}$ , is combined with the heat-transfer and crevice terms, the combination is termed *net heat release*—the combustion energy release less heat lost to the walls. It is equal to the first two terms on the right-hand side of Eq. (9.26) which, together, represent the sensible energy change and work transfer to the piston. While heat losses during combustion are a small fraction of the fuel energy (10 to 15 percent), the distributions of heat release and heat transfer with crank angle are different; heat transfer becomes more important as the combustion process ends and average gas temperatures peak. The net heat-release profile obtained from integrating the first two terms on the right-hand side of Eq. (9.26), normalized to give unity at its maximum value, is often interpreted as the burned mass fraction (or, more correctly, the energy-release fraction) versus crank angle profile.

Use of Eq. (9.26) requires a value for  $c_v/R$  [ $= 1/(\gamma - 1)$ ]. The ratio of specific heats  $\gamma$  for both unburned and burned gases decreases with increasing temperature and varies with composition (see Figs. 4-13, 4-16, and 4-18). As the mean charge temperature increases during compression and combustion and then decreases during expansion,  $\gamma$  should vary. An approximate approach, modeling  $\gamma(T)$  with a linear function of temperature fitted to the appropriate curves in Figs. 4-13, 4-16, and 4-18 and with  $\gamma$  constant during combustion, has been shown to give adequate results.<sup>15</sup>

The convective heat-transfer rate to the combustion chamber walls can be calculated from the relation

$$\frac{dQ_{ht}}{dt} = Ah_c(T - T_w)$$

where  $A$  is the chamber surface area,  $T$  is the mean gas temperature,  $T_w$  is the mean wall temperature, and  $h_c$  is the heat-transfer coefficient (averaged over the chamber surface area).  $h_c$  can be estimated from engine heat-transfer correlations (see Sec. 12.4.3). Since crevice effects are usually small, a sufficiently accurate model for their overall effect is to consider a single aggregate crevice volume where the gas is at the same pressure as the combustion chamber, but at a different temperature. Since these crevice regions are narrow, an appropriate assumption is that the crevice gas is at the wall temperature. Inserting this crevice model

into Eq. (9.26), with  $\gamma(T) = a + bT$ , gives the chemical energy- or gross heat-release rate:

$$\begin{aligned} \frac{dQ_{ch}}{d\theta} &= \frac{\gamma}{\gamma - 1} p \frac{dV}{d\theta} + \frac{1}{\gamma - 1} V \frac{dp}{d\theta} \\ &\quad + V_{cr} \left[ \frac{T'}{T_w} + \frac{T}{T_w(\gamma - 1)} + \frac{1}{bT_w} \ln \left( \frac{\gamma - 1}{\gamma' - 1} \right) \right] \frac{dp}{d\theta} + \frac{dQ_{ht}}{d\theta} \quad (9.27) \end{aligned}$$

An example of the use of Eq. (9.27) to analyze an experimental pressure versus crank angle curve for a conventional spark-ignition engine is shown in Fig. 9-12. The integrated heat release is plotted against crank angle. The lowest curve shown is the net heat release. The addition of heat transfer and crevice models gives the chemical energy release. The curve at the top of the figure is the mass of fuel within the combustion chamber times its lower heating value. It decreases slightly as  $p_{max}$  is approached due to flow into crevices. The difference between the final value of  $Q_{ch}$  and  $(m_f Q_{LHV})$  should equal the combustion inefficiency (which is a few percent of  $m_f Q_{LHV}$ ). The combustion inefficiency can be determined from the exhaust gas composition (see Sec. 4.9.4). Inaccuracies in the cylinder pressure data and the heat-release calculation will also contribute to this difference. An important advantage of a heat-release analysis that relates the pressure changes to the amount of fuel chemical energy within the cylinder is that this error can be determined. In the example in Fig. 9-12, the measured combustion inefficiency was close to the amount shown.

Two-zone models (one zone representing the unburned mixture ahead of the flame and one the burned mixture behind the flame) are used to calculate the mass fraction burned profile from measured cylinder pressure data.<sup>10</sup> Figure 9-8 shows results from such an analysis, using the methodology described in Sec. 9.2.1. The advantage of a two-zone analysis is that the thermodynamic properties of the cylinder contents can be quantified more accurately. The disadvantages are that the unburned and the burned zone heat-transfer areas must both now be estimated, and a model for the composition of the gas flowing into the crevice

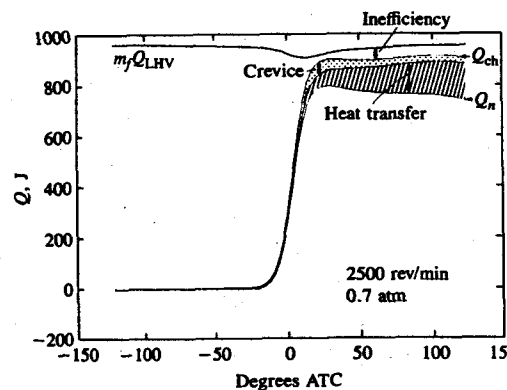


FIGURE 9-12  
Results of heat-release analysis showing the effects of heat transfer, crevices, and combustion inefficiency.<sup>14</sup>

region must be developed. Due to this complexity, crevice models are usually omitted despite the fact that their impact can be significant.

### 9.2.3 Combustion Process Characterization

The mass fraction burned profiles as a function of crank angle in each individual cycle shown in Fig. 9-2 and the chemical energy- or gross heat-release curve in Fig. 9-12 have a characteristic S-shape. The rate at which fuel-air mixture burns increases from a low value immediately following the spark discharge to a maximum about halfway through the burning process and then decreases to close to zero as the combustion process ends. It proves convenient to use these mass fraction burned or energy-release fraction curves to characterize different stages of the spark-ignition engine combustion process by their duration in crank angles, thereby defining the fraction of the engine cycle that they occupy. The flame development process, from the spark discharge which initiates the combustion process to the point where a small but measurable fraction of the charge has burned, is one such stage. It is influenced primarily by the mixture state, composition, and motion in the vicinity of the spark plug (see Sec. 9.3). The stage during which the major portion of the charge burns as the flame propagates to the chamber walls is next. This stage is obviously influenced by conditions throughout the combustion chamber. The final stage, where the remainder of the charge burns to completion, cannot as easily be quantified because energy-release rates are comparable to other energy-transfer processes that are occurring.

The following definitions are most commonly used to characterize the energy-release aspects of combustion:

**Flame-development angle  $\Delta\theta_d$ .** The crank angle interval between the spark discharge and the time when a small but significant fraction of the cylinder mass has burned or fuel chemical energy has been released. Usually this fraction is 10 percent, though other fractions such as 1 and 5 percent have been used.<sup>†</sup>

**Rapid-burning angle  $\Delta\theta_b$ .** The crank angle interval required to burn the bulk of the charge. It is defined as the interval between the end of the flame-development stage (usually mass fraction burned or energy-release fraction of 10 percent) and the end of the flame-propagation process (usually mass fraction burned or energy-release fraction of 90 percent).<sup>‡</sup>

**Overall burning angle  $\Delta\theta_o$ .** The duration of the overall burning process. It is the sum of  $\Delta\theta_d$  and  $\Delta\theta_b$ .

<sup>†</sup> This angle is sometimes called the *ignition delay*. Since the flame starts to propagate outward immediately following the spark discharge there is no delay, and the terminology used here is preferred (see Sec. 9.3).

<sup>‡</sup> An alternative definition for  $\Delta\theta_b$  uses the maximum burning rate to define an angle or time characteristic of the bulk charge burning process<sup>14</sup> (see Fig. 9-13).  $\Delta\theta_b$  and  $\Delta\theta^*$  are usually closely comparable.

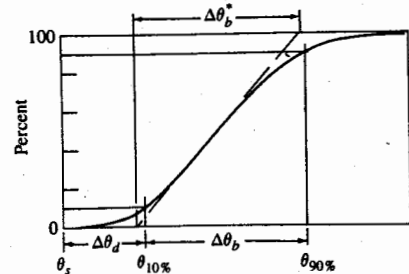


FIGURE 9-13  
Definition of flame-development angle,  $\Delta\theta_d$ , and rapid-burning angle,  $\Delta\theta_b$ , on mass fraction burned versus crank angle curve.

Figure 9-13 illustrates these definitions on a mass fraction burned, or fraction of fuel energy released, versus crank angle plot. While the selection of the 10 and 90 percent points is arbitrary, such a choice avoids the difficulties involved in determining accurately the shape of the curve at the start and end of combustion. These angles can be converted to times (in seconds) by dividing by  $6N$  (with  $N$  in revolutions per minute).

A functional form often used to represent the mass fraction burned versus crank angle curve is the Wiebe function:

$$x_b = 1 - \exp \left[ -a \left( \frac{\theta - \theta_0}{\Delta\theta} \right)^{m+1} \right] \quad (9.28)$$

where  $\theta$  is the crank angle,  $\theta_0$  is the start of combustion,  $\Delta\theta$  is the total combustion duration ( $x_b = 0$  to  $x_b = 1$ ), and  $a$  and  $m$  are adjustable parameters. Varying  $a$  and  $m$  changes the shape of the curve significantly. Actual mass fraction burned curves have been fitted with  $a = 5$  and  $m = 2$ .<sup>16</sup>

### 9.3 FLAME STRUCTURE AND SPEED

#### 9.3.1 Experimental Observations

The combustion process in the spark-ignition engine takes place in a turbulent flow field. This flow field is produced by the high shear flows set up during the intake process and modified during compression, as described in Chap. 8. The importance of the turbulence to the engine combustion process was recognized long ago through experiments where the intake event, and the turbulence it generates, was eliminated and the rate of flame propagation decreased substantially. Understanding the structure of this engine flame as it develops from the spark discharge and the speed at which it propagates across the combustion chamber, and how that structure and speed depend on charge motion, charge composition, and chamber geometry, are critical to engine optimization. This section reviews experimental evidence that describes the essential features of the flame development and propagation processes.

Direct flame photographs such as those in Fig. 9-1 indicate the location and shape of the actual reaction zone which radiates in the blue region of the visible spectrum. An irregular front is apparent. Further insight into the structure of the

flame can be obtained from photographs taken with techniques that are sensitive to density changes in the flow field, such as schlieren and shadowgraph. With these techniques, a parallel light beam is passed through the combustion chamber. Portions of the beam which pass through regions where density gradients normal to the beam exist are deflected, due to the refractive index gradients that result from the density gradients. In the schlieren technique, the beam is focused on a knife edge; the deflected parts of the beam are displaced relative to the knife edge and produce lighter or darker regions when subsequently refocused onto film. With the shadowgraph technique, the parallel beam emerging from the combustion chamber is photographed directly; deflected parts of the beam produce lighter and darker regions on the film. With these techniques, details of flame structure can be discerned.

Figure 9-14 shows a set of photographs from one engine cycle, from a high-speed schlieren movie taken in a special visualization spark-ignition engine operating at 1400 rev/min and 0.5 atm inlet pressure. Also shown are the cylinder pressure versus crank angle data, and the mass fraction burned profile calculated from the pressure data using the method of Rassweiler and Withrow<sup>2</sup> (see Sec. 9.2.2). This engine had a square-cross-section cylinder with two quartz walls to permit easy optical access, but otherwise operated normally.<sup>17</sup> Visualization of

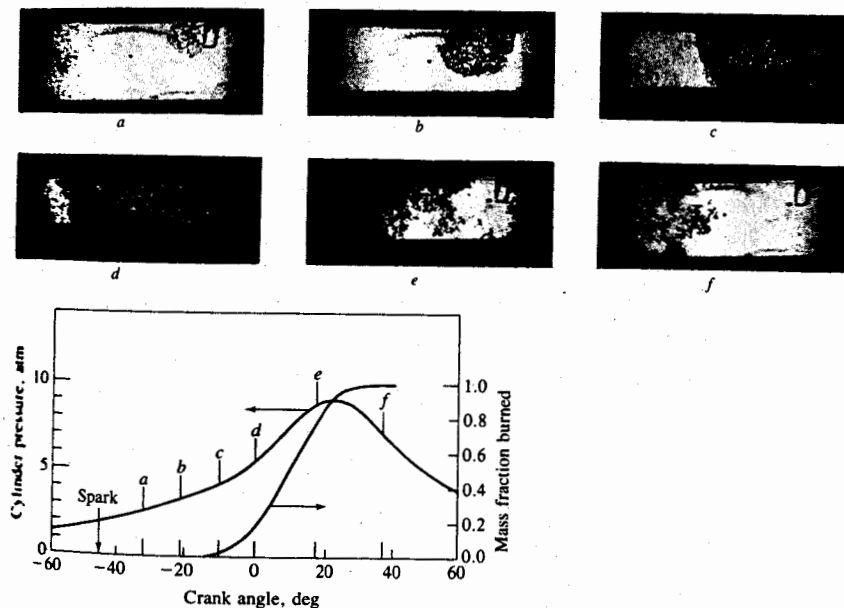


FIGURE 9-14  
Sequence of movie frames from one engine cycle in a square-cross-section cylinder, single-cylinder, engine with two glass walls, and corresponding pressure and mass fraction burned curves. 1400 rev/min, 0.5 atm inlet pressure.

the flame is especially important during the early stages of flame development when the pressure rise due to combustion is too small to be detected.

These photographs show how the flame "ball," roughly spherical in shape, grows steadily from the time of spark discharge. The effect of turbulence is already visible in the convoluted flame surface in Fig. 9-14a. The volume enflamed behind the front continues to grow in a roughly spherical manner, except where intersected by the chamber walls, as seen in Fig. 9-14b and c. The mass fraction burned and the associated pressure rise due to combustion become significant by the time the flame front has traversed two-thirds to three-quarters of the field of view. Note that the fraction of the cylinder filled with enflamed charge is less than is suggested by the photos because the front of the flame is approximately spherical and the cylinder has a square cross section. Maximum cylinder pressure occurs close to the time the flame makes contact with the far wall, as seen in Fig. 9-14e. Finally, the unburned mixture ahead of and within the front burns out and the density gradients associated with the flame reaction zone disappear, clearing the field of view as shown in Fig. 9-14e and f.

A useful relationship between the mass fraction burned,  $x_b (= m_b/m)$ , and the volume fraction occupied by the burned gas,  $y_b (= V_b/V)$ , can be obtained from the identities

$$m = m_u + m_b \quad V = V_u + V_b$$

and the ideal gas law:

$$x_b = \left[ 1 + \frac{\rho_u}{\rho_b} \left( \frac{1}{y_b} - 1 \right) \right]^{-1} \quad (9.29)$$

While the density ratio ( $\rho_u/\rho_b$ ) does depend on the equivalence ratio, burned gas fraction in the unburned mixture, gas temperature, and pressure, its value is close to 4 for most spark-ignition engine operating conditions. Thus, the plot of  $x_b$  against  $y_b$  has a universal form,<sup>10</sup> as shown in Fig. 9-15. This curve is an important aid in interpreting flame geometry information.

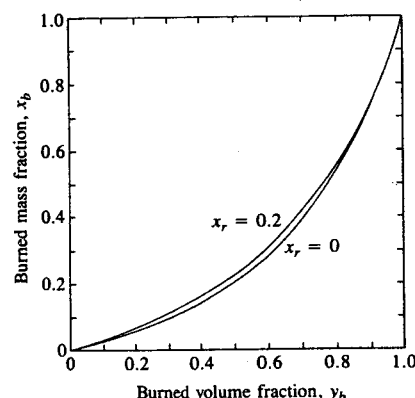


FIGURE 9-15  
Relation between mass fraction burned  $x_b$  and volume fraction burned  $y_b$ .  $x_r$  is residual mass fraction.<sup>4</sup>

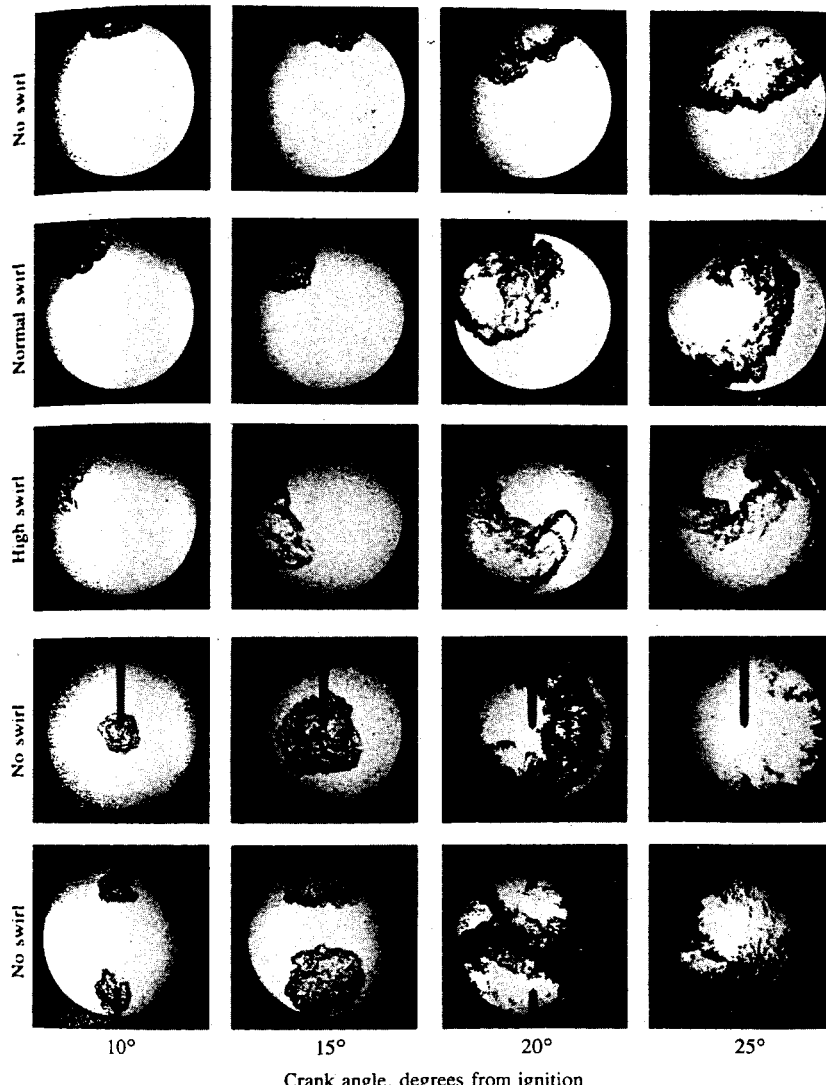


FIGURE 9-16  
Crank angle, degrees from ignition

Laser shadowgraph photographs of engine combustion process taken in single-cylinder engine with transparent cylinder head. From top to bottom: side plug without swirl; side plug with normal swirl; side plug with high swirl; central plug without swirl; two plugs without swirl.<sup>18</sup>

The above-described features of the developing and propagating flame are common to almost all engine geometries and operating conditions. Figure 9-16 shows shadowgraph photographs of the flame at fixed crank angle intervals after ignition, taken through a transparent cylinder head with different geometric and flow configurations.<sup>18</sup> The approximately spherical development of the flame

from the vicinity of the spark plug, except where it intercepts the chamber walls, is evident for side and center ignition with one plug, and for ignition with two plugs in the absence of any intake generated swirl. With normal levels of swirl, the flame center is convected with the swirling flow, but the flame front as it grows is still approximately spherical in shape. Only with unusually high levels of swirl and aerodynamic stabilization of the flame at the spark plug location does the flame become stretched out and distorted by the flow in a major way.<sup>18</sup>

At any given flame radius, the geometry of the combustion chamber and the spark plug location govern the flame front surface area—the area of the approximately spherical surface corresponding to the leading edge of the flame contained by the piston, cylinder head, and cylinder wall. The larger this surface area, the greater the mass of fresh charge that can cross this surface and enter the flame zone. The photos in Fig. 9-16 illustrate the importance of flame area. The center plug location gives approximately twice the flame area of the side plug geometry at a given flame radius, and burns about twice as fast (the fraction of the cylinder volume enflamed is about twice the size, at a fixed crank angle interval after spark). The arrangement with two spark plugs at opposite sides of the chamber is not significantly different in enflamed volume from the single center plug because, once the flame fronts are intersected by the cylinder wall, the flame front areas are comparable.

Mixture burning rate is strongly influenced by engine speed. It is well established that the duration of combustion in crank angle degrees only increases slowly with increasing engine speed.<sup>19</sup> Figure 9-17 shows how the interval between the spark discharge and 10 percent mass fraction burned, the flame development angle  $\Delta\theta_d$ , and the interval between the spark and 90 percent mass fraction burned, the overall burning angle  $\Delta\theta_d + \Delta\theta_b$  (see Sec. 9.2.3), vary with engine speed.<sup>20</sup> Both intervals increase by a factor of about 1.6 for a factor of 4 increase in engine speed; i.e., the burning rate throughout the combustion process increases almost, though not quite, as rapidly as engine speed. Additionally, at a given engine speed, increasing in-cylinder gas velocities (e.g., with intake generated swirl) increases the burning rate: the flame size for the swirling flows in Fig. 9-16 is larger than for the quiescent case with the same plug location at the crank angle intervals after spark shown. Increasing engine speed and introducing swirl both increase the levels of turbulence in the engine cylinder at the time of combustion (see Sec. 8.2.2). Increased turbulence increases the rate of development and propagation of the turbulent premixed engine flame.

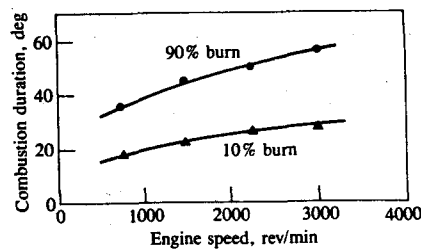


FIGURE 9-17  
Effect of engine speed on flame-development angle (0 to 10 percent burned) and overall burning angle (0 to 90 percent burned).  $\phi = 1.0$ , intake pressure 0.54 atm, spark 30° BTC.<sup>20</sup>

It is also well established that unburned mixture composition and state affect the burning rate. Reducing the inlet pressure (and maintaining the ratio of exhaust to inlet pressure fixed to hold the residual gas fraction constant) increases both the flame development and rapid burning angles.<sup>19</sup> The fuel/air equivalence ratio affects the burning rate. Both flame development and burning angles show a minimum for slightly rich mixtures ( $\phi \approx 1.2$ ) and increase significantly as the mixture becomes substantially leaner than stoichiometric.<sup>19, 20</sup> The burned gas fraction in the unburned mixture, due to the residual gas fraction and any recycled exhaust gases, affects the burning rate: increasing the burned gas fraction slows down both flame development and propagation.<sup>20</sup> Fuel composition changes can be significant also. While mixtures of isoctane or conventional gasolines with air and burned gases (at identical conditions) have closely comparable burning rates, propane, methane, methanol, and ethanol mixtures exhibit modest differences in burning rate and hydrogen-air mixtures substantial differences. The basic combustion chemistry of the fuel, air, burned gas mixture influences the combustion process. However, the relative importance of combustion chemistry effects depends on combustion chamber design and burn rate. Faster burning engines (which have higher turbulence) are less sensitive to changes in mixture composition, pressure, and temperature than are slower burning engines (which have lower turbulence). The effects of chamber geometry, gas motion, and gas composition and state are interrelated.<sup>21</sup>

### 9.3.2 Flame Structure

Laminar flames in premixed fuel, air, residual gas mixtures are characterized by a laminar flame speed  $S_L$  and a laminar flame thickness  $\delta_L$  (see Sec. 9.3.3). The laminar flame speed is the velocity at which the flame propagates into quiescent premixed unburned mixture ahead of the flame. There are several ways to define the thickness of a laminar flame.<sup>22</sup> Given the molecular diffusivity  $D_L$  (see Sec. 4.8), dimensional arguments give the most commonly used definition:  $\delta_L = D_L/S_L$ . Turbulent flames are also characterized by the root mean square velocity fluctuation, the turbulence intensity  $u'$  [Eq. (8.3)], and the various length scales of the turbulent flow ahead of the flame. The integral length scale  $l_I$  [Eq. (8.8)] is a measure of the size of the large energy-containing structures of the flow. The Kolmogorov scale  $l_K$  [Eq. (8.11)] defines the smallest structures of the flow where small-scale kinetic energy is dissipated via molecular viscosity.

Several dimensionless parameters are used to characterize turbulent premixed flames. The dimensionless parameter used to define the turbulence is the turbulent Reynolds number,  $Re_T = u'l_I/v$ . For homogeneous and isotropic (no preferred direction) turbulence, the integral and Kolmogorov scales are related by Eq. (8.14):  $l_K/l_I = Re_T^{-3/4}$ . A characteristic turbulent eddy turnover time  $\tau_T$  can be defined as

$$\tau_T = \frac{l_I}{u'}$$

A characteristic chemical reaction time is the residence time in a laminar flame:

$$\tau_L = \frac{\delta_L}{S_L}$$

The ratio of the characteristic eddy turnover time to the laminar burning time is called the *Damköhler number*:

$$Da = \frac{\tau_T}{\tau_L} = \left( \frac{l_I}{\delta_L} \right) \left( \frac{S_L}{u'} \right) \quad (9.30)$$

It is an inverse measure of the influence of the turbulent flow on the chemical processes occurring in the flame. Other ratios are of interest. The ratio  $\delta_L/l_K$  is a measure of the stretch or local distortion to which a laminar flame is subjected by the turbulent flow. Unless  $l_I/\delta_L \gg 1$  the concept of a localized flame region has little significance. The ratio  $u'/S_L$  is a measure of the relative strength of the turbulence.<sup>22</sup>

Different regimes of turbulent flames are apparent in the plot of Damköhler number versus turbulent Reynolds number in Fig. 9-18.<sup>22</sup> It has been assumed that  $D_L \approx v$  and that the relationships for homogeneous isotropic turbulence are valid. Two regimes—distributed reactions and reaction sheets—are normally identified. In the distributed reaction regime, chemical reactions proceed in distributed reaction zones and thin-sheet flames do not occur. A sufficient condition for this regime is  $l_I \ll \delta_L$ . In the reaction sheet regime, propagating reaction fronts are wrinkled and convoluted by the turbulence. A sufficient condition for the existence of reaction sheets is  $l_K \gg \delta_L$ . For  $Re_T > 1$ , there is a region in Fig. 9-18 where  $l_I > \delta_L > l_K$ : the characteristics of flames in this regime are unclear.

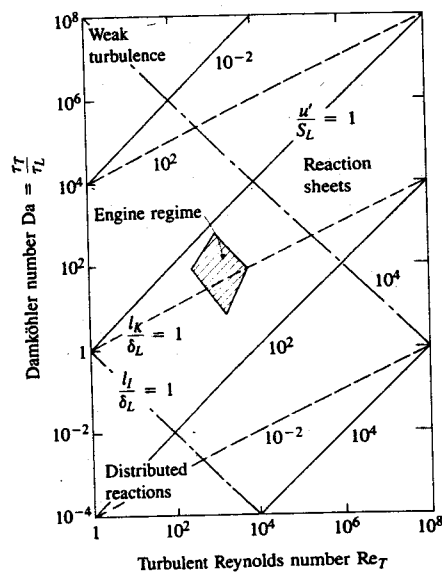


FIGURE 9-18  
Different turbulent flame regimes on plot of Damköhler number versus turbulence Reynolds number,  $u'$  is turbulence intensity;  $S_L$  is laminar flame speed;  $l_I$ ,  $l_K$ , and  $\delta_L$  are integral scale, Kolmogorov scale, and laminar flame thickness. (From Abraham et al.<sup>22</sup>)

Values of  $Da$  and  $Re_T$  for a typical spark-ignition engine (the cross-hatched region in Fig. 9-18) lie predominantly in the reaction sheet flame regime. Engine operation at high speed (the lower right boundary) and low load (the lower left boundary) gives values of  $Da$  and  $Re_T$  which fall below the  $l_K/\delta_L = 1$  line. This is largely due to the low values of laminar flame speed that result from the high amounts of residual gas and EGR under these conditions (see Sec. 9.3.4 and Fig. 6-19). Whether the flame structure under these conditions is significantly different is not known. Observations of engine flames to date, described below, lie above the  $l_K/\delta_L = 1$  line, within the reaction sheet regime. One would expect, then, the structure of the flame in a spark-ignition engine, once developed, to be that of a thin reaction sheet wrinkled and convoluted by the turbulent flow.

Detailed observations have been made of flame structure from ignition to flame extinguishing at the far cylinder wall. A flame develops from the spark discharge which causes ignition as follows. In the initial breakdown phase of ignition, a cylindrical discharge between the spark plug electrodes is established.<sup>23</sup> As electrical energy is fed into the discharge, the arc expands and exothermic chemical reactions capable of sustaining a propagating flame develop. Figure 9-19 shows how this development of a flame kernel occurs, with a set of shadowgraph photographs taken at 40- $\mu s$  intervals of the spark plug electrode gap in one cylinder of a 2-liter conventional engine. The first photograph is between 20 and 50  $\mu s$  after the spark breakdown occurred. The complete sequence ( $\sim 200 \mu s$ ) corresponds to 1.3 crank angle degrees. The outer boundary of this developing flame kernel is approximately spherical and is smooth with modest irregularities, corresponding to a thin reaction zone with high-temperature gases inside. As this developing sheetlike flame grows it interacts with the turbulent flow field in the vicinity of the spark plug: the flame outer surface becomes increasingly convoluted and the flame center can be convected away from the plug in a direction and with a velocity that can vary substantially cycle-by-cycle, as seen in Fig. 9-20.<sup>4,17</sup>

The structure of the flame continues to develop as it propagates across the chamber. Evidence, largely from schlieren photographs and studies of flame structure with laser diagnostics, shows that early in the burning process the flame

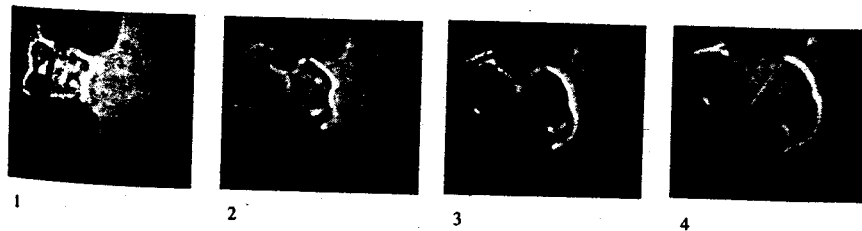


FIGURE 9-19  
Shadowgraph photographs of spark-generated kernel between the spark plug electrodes. First photograph on left, 20 to 50  $\mu s$  after breakdown; 40  $\mu s$  between photos. Stoichiometric mixture, 1100 rev/min. (Courtesy A. Douad, Institut Francais du Petrole.)

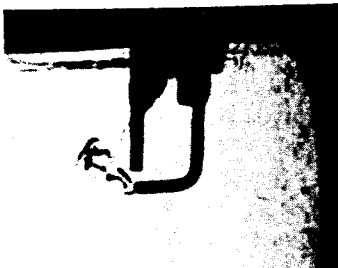


FIGURE 9-20

Schlieren photographs of developing flame, 5° after spark discharge, showing different convection processes in two different cycles. Spark plug wires 0.8 mm diameter, 1400 rev/min; 0.5 atm inlet pressure; propane fuel;  $\phi = 0.9$ ; spark advance 45° BTC.<sup>17</sup>

is a thin, moderately wrinkled but simply connected, front or reaction sheet between unburned and burned gas. The thickness of the front is about 0.1 mm which is comparable to the thickness of a laminar flame under the prevailing conditions. The scale of the wrinkles is typically about 2 mm at engine speeds of 1000 to 2000 rev/min. As the flame propagates across the chamber, the thickness of the reaction sheet front remains roughly constant, the flame front becomes more convoluted, and the scale of the wrinkles tends to decrease with time.<sup>24</sup>

Further evidence that the thin reaction sheet front becomes highly wrinkled and convoluted by the turbulent flow field into a thick turbulent flame "brush" is provided by the schlieren photographs in Fig. 9-21. These show a flame propagating across the combustion chamber of a square-cross-section single-cylinder engine with a special transparent piston crown containing a 13-mm wide channel to isolate a small section of the flame.<sup>25</sup> The flame on the left is for a propane-air mixture; that on the right is hydrogen-air. The energy density per unit volume of mixture and the flow field are comparable for each fuel. The effective thickness of this turbulent flame—the average distance between the region ahead of the flame, where only unburned mixture exists, and the region behind the flame, where only



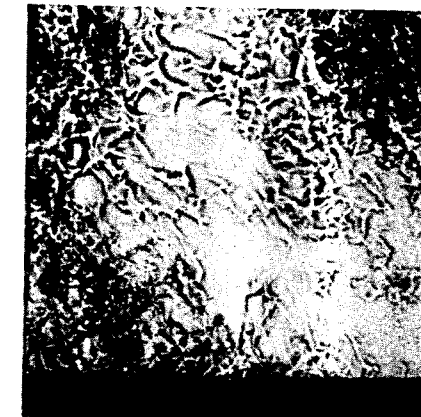
(a)



(b)

FIGURE 9-21

Schlieren photographs of flame in square-cross-section cylinder engine, with narrow channel in piston crown (at bottom of pictures) which permits observation of 13-mm wide section of flame. (a) Propane fuel, spark timing 36° BTC, photograph at 14° ATC, flame thickness  $\approx 4.6$  mm. (b) Hydrogen fuel, spark timing 3° BTC, photograph at 10° ATC, flame thickness  $\approx 1.5$  mm. Stoichiometric mixture, 1380 rev/min, 0.5 atm inlet pressure.<sup>25</sup>



(a)



(b)

FIGURE 9-22

Enlarged schlieren photographs of (a) flame front and (b) flame back in square-cross-section cylinder engine with two glass side walls. 1400 rev/min, 0.5 atm inlet pressure, propane fuel,  $\phi = 0.9$ .<sup>17</sup>

burned mixture exists—is apparent.<sup>†</sup> It was 4 to 5 mm for propane and 1.5 mm for hydrogen. The difference is due to the substantially higher laminar flame speed for the hydrogen, air, burned gas mixture (see Sec. 9.3.4) which increases the Damköhler number and shifts the flame toward the weak-turbulence (i.e., less wrinkled) flame regime in Fig. 9-18.

Additional insight into the structure of the developed engine flame can be obtained by enlarging photographs of the leading and trailing edges of the flame, obtained with the schlieren or shadowgraph technique. Figure 9-22a shows the front of the flame 40° after the spark, when it has propagated about halfway across the chamber. It shows the irregular but smoothly curved surfaces which comprise the leading edge of the flame. Figure 9-22b shows the back of the flame 70° after the spark, when the front of the flame has just reached the wall of the combustion chamber farthest from the spark plug. It shows large clear regions of burned gas behind the flame and smaller clear regions connected by a lacelike

<sup>†</sup> These photographs were selected from a large number to give the minimum flame thickness corresponding to the flame front perpendicular to the channel length.

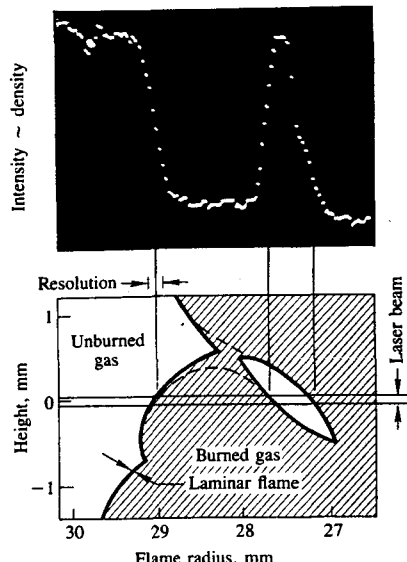


FIGURE 9-23

Upper picture: oscillogram of output of optical multichannel analyzer showing the intensity of light scattered from a narrow laser beam as a function of distance through the flame. Intensity is a measure of gas density. Lower picture: schematic of flame structure corresponding to this signal. 600 rev/min, 1 atm inlet pressure, propane fuel,  $\phi = 1.0^{24}$

structure within which the remaining regions of unburned mixture are being consumed.<sup>17</sup> The analogy with a crumpled sheet of paper is appropriate.

Laser scattering experiments, where "snapshots" of the density profile along a laser beam passed through the flame were obtained using Rayleigh scattered light from the gas molecules, provide explicit evidence of this structure.<sup>26</sup> Figure 9-23 shows an oscillogram of the output of the optical analyzer. Each dot represents the intensity of the scattered light which is a measure of the gas density. The signal on the left corresponds to unburned gas. The flame is propagating from right to left. The oscillogram shows a thin transition zone of width 0.25 mm between unburned and burned gas, followed at a distance of 1.5 mm by an "island" of unburned gas. The fraction of oscillograms showing such "islands" varied from 0 at 300 rev/min to 20 percent at 1800 rev/min. An interpretation of this signal consistent with the available photographic evidence is shown underneath.<sup>24</sup>

The above results suggest that increasing engine speed, which increases turbulence levels in the unburned charge, increasingly convolutes and probably multiply-connects the thin reaction sheet flame front. Enlarged schlieren photographs of a 9-mm diameter section of the developed engine flame, viewed normal to the flame surface, indicate that increasing turbulence intensity and decreasing turbulence scales result in increasingly finely wrinkled flame structures. Figure 9-24 shows a set of such photographs, arranged in order of increasing turbulent Reynolds number. Increases in turbulence intensity, which was measured, were achieved by increases in engine speed and by modifying the inlet valve. Relevant parameters for each photograph are given in Table 9.1.

The above theoretical discussion and experimental evidence indicates that

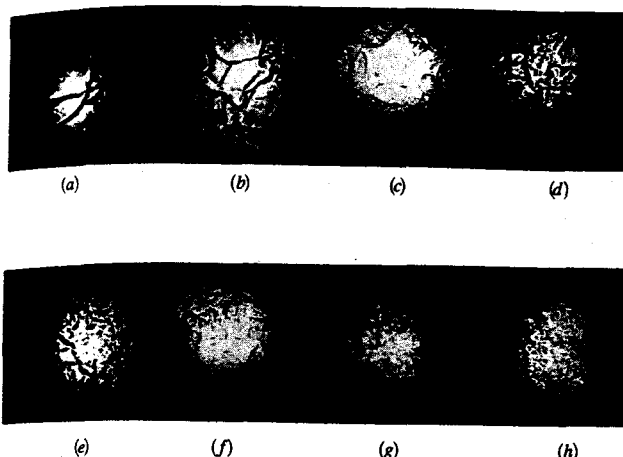


FIGURE 9-24

Shadowgraph photographs, with light beam normal to flame front, of 10-mm diameter section of flame. Photographs, arranged in order of increasing turbulent Reynolds number, suggest this is an appropriate scaling parameter (see Table 9.1).<sup>27</sup>

developed turbulent flames in spark-ignition engines, under normal operating conditions, are highly wrinkled and probably multiply-connected thin reaction sheets. The overall thickness of the turbulent flame "brush," front to back, is of order 1 cm. The thickness of the thin reaction sheet is comparable to estimates of the laminar flame thickness under the prevailing unburned mixture conditions which are of order 0.1 mm. The scale of the wrinkles is of order 1 mm.<sup>24</sup> Direct evidence to date is limited to the low to mid engine speed and low to high engine

TABLE 9.1  
Parameters for shadowgraph photographs in Fig. 9-24

Photograph	Engine speed, rev/min	Turbulence intensity, m/s	Valve	$Re_M$	$Re_T$
a	300	0.44	S	106	229
b	600	0.88	S	157	503
c	300	1.07	US	173	611
d	900	1.33	S	193	760
e	1200	1.80	S	224	1024
f	600	1.95	US	234	1117
g	900	2.90	US	285	1658
h	1200	4.0	US	333	2263

Note: Valve: S, shrouded; US, unshrouded (produced higher turbulence due to less ordered flow).  $Re_M = l_M u'/v$ ;  $Re_T = l_T u'/v$  (see Sec. 8.2.1).<sup>27</sup>

load ranges. Whether the structure becomes significantly different at high engine speed is not known. Models of this turbulent flame development and propagation process are reviewed in Chap. 14.

### 9.3.3 Laminar Burning Speeds

An important intrinsic property of a combustible fuel, air, burned gas mixture is its laminar burning velocity. This burning velocity is defined as the velocity, relative to and normal to the flame front, with which unburned gas moves into the front and is transformed to products under laminar flow conditions. Some details of flame structure help explain the significance of this quantity. A flame is the result of a self-sustaining chemical reaction occurring within a region of space called the flame front where unburned mixture is heated and converted into products. The flame front consists of two regions: a preheat zone and a reaction zone. In the preheat zone, the temperature of the unburned mixture is raised mainly by heat conduction from the reaction zone: no significant reaction or energy release occurs and the temperature gradient is concave upward ( $\partial^2 T / \partial x^2 > 0$ ). Upon reaching a critical temperature, exothermic chemical reaction begins. The release of chemical energy as heat results in a zone where the temperature gradient is concave downward ( $\partial^2 T / \partial x^2 < 0$ ). The region between the temperature where exothermic chemical reaction begins and the hot boundary at the downstream equilibrium burned gas temperature is called the reaction zone. The thicknesses of the preheat and reaction zones can be calculated for one-dimensional flames from conservation equations of mass and energy. The thickness of the preheat zone  $\delta_{L, ph}$  is

$$\delta_{L, ph} = \frac{4.6\bar{k}}{\bar{c}_p \rho_u S_L} \quad (9.31)$$

where  $\bar{k}$  and  $\bar{c}_p$  are the mean thermal conductivity and specific heat at constant pressure in the preheat zone and  $S_L$  is the laminar burning velocity.<sup>28</sup> Thus, the factors which govern the laminar burning velocity of a specific unburned mixture—the velocity at which this flame structure propagates relative to the unburned gas ahead of it—are the temperature and species concentration gradients within the flame and the mixture transport and thermodynamic properties.

Laminar burning velocities at pressures and temperatures typical of unburned mixture in engines are usually measured in spherical closed vessels by propagating a laminar flame radially outward from the vessel center. The laminar burning velocity is then given by

$$S_L = \frac{dm_b/dt}{A_f \rho_u} \quad (9.32)$$

where the mass burning rate is determined from the rate of pressure rise in the vessel and  $A_f$  is the flame area. Because the laminar flame thickness [e.g., given by Eq. (9.31)] under engine conditions is of order 0.2 mm<sup>26</sup> and is therefore much less than characteristic vessel dimensions, in applying Eq. (9.32) the flame can be

treated as negligibly thin. Laminar burning velocities for methane, propane, iso-octane, methanol, gasoline, and hydrogen—premixed with air—at pressures, temperatures, and equivalence ratios which occur in engines have been measured using this technique.<sup>29-33</sup> Also, the effect of a burned gas diluent on laminar burning velocity with gasoline-air mixtures has been determined.<sup>32</sup> Correlations derived from these data are the most accurate means available for estimating laminar burning velocities for mixtures and conditions relevant to spark-ignition engines.

The effect of the mixture fuel/air equivalence ratio on laminar burning velocity for several hydrocarbon fuels and methanol is shown in Fig. 9-25. The burning velocity peaks slightly rich of stoichiometric for all the fuels shown. The values for iso-octane and gasoline are closely comparable. Data at higher pressures and temperatures have been fitted to a power law of the form:

$$S_L = S_{L, 0} \left( \frac{T_u}{T_0} \right)^\alpha \left( \frac{p}{p_0} \right)^\beta \quad (9.33)$$

where  $T_0 = 298$  K and  $p_0 = 1$  atm are the reference temperature and pressure, and  $S_{L, 0}$ ,  $\alpha$ , and  $\beta$  are constants for a given fuel, equivalence ratio, and burned gas diluent fraction. For propane, iso-octane, and methanol, these constants can be represented by

$$\alpha = 2.18 - 0.8(\phi - 1) \quad (9.34a)$$

$$\beta = -0.16 + 0.22(\phi - 1) \quad (9.34b)$$

$$S_{L, 0} = B_m + B_\phi (\phi - \phi_m)^2 \quad (9.35)$$

where  $\phi_m$  is the equivalence ratio at which  $S_{L, 0}$  is a maximum with value  $B_m$ .

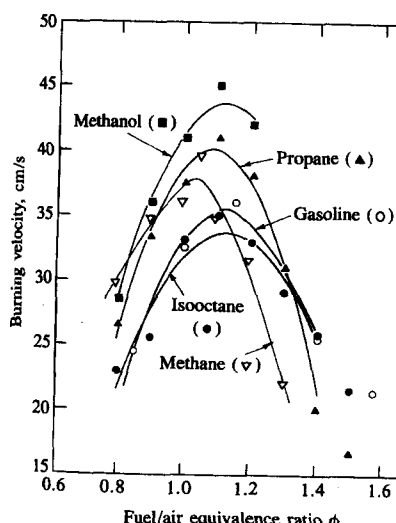


FIGURE 9-25

Laminar burning velocity for several fuels as function of equivalence ratio, at 1 atm and 300 K. Lines are least-squares polynomial fits to data.<sup>29, 30</sup>

TABLE 9.2  
Parameters  $\phi_m$ ,  $B_m$ , and  $B_\phi$  for Eq.  
(9.35)

Fuel	$\phi_m$	$B_m$ , cm/s	$B_\phi$ , cm/s	Ref.
Methanol	1.11	36.9	-140.5	30
Propane	1.08	34.2	-138.7	30
Isooctane	1.13	26.3	-84.7	30
Gasoline	1.21	30.5	-54.9	32

Note: Values of  $S_{L,0}$  given by Eq. (9.35) are obtained from least-squares fits of Eq. (9.33) to data over the range  $p = 1\text{-}8 \text{ atm}$ ,  $T_u = 300\text{-}700 \text{ K}$ . They do not correspond exactly to the laminar flame speed data at 1 atm and 298 K in Fig. 9-25.

Values of  $\phi_m$ ,  $B_m$ , and  $B_\phi$  are given in Table 9.2.<sup>30</sup> For gasoline (a reference gasoline with average molecular weight of 107 and an H/C ratio of 1.69) additional data were available and were correlated by<sup>32</sup>

$$\alpha_g = 2.4 - 0.271\phi^{3.51} \quad (9.36a)$$

$$\beta_g = -0.357 + 0.14\phi^{2.77} \quad (9.36b)$$

For methane, simple equations such as (9.34a, b) do not adequately correlate the data over the range of  $p$  and  $T_u$  relevant to engines. However, laminar burning velocity data from a spherical constant-volume bomb experiment have been obtained along an unburned gas isentropic path, as the pressure in the bomb rises during combustion. Variation in laminar burning velocity along such unburned gas isentropes does correlate with a power law:

$$S_{L,s} = S_{L,0} \left( \frac{\rho_u}{\rho_{u0}} \right)^z \quad (9.37)$$

Values for  $S_{L,0}$  and  $z$  from the literature are summarized in Table 9.3.

TABLE 9.3  
Parameters for methane-air laminar  
burning velocity correlation [Eq. (9.37)]

$\phi$	$p_i$ , atm	$S_{L,0}, \dagger$ , cm/s	$z$	Ref.
1.0	0.5	49	0.51	31
1.0	1.0	35	0.2	31
0.8-1.2	1-8	‡	0.17-0.19	33

† At 298 K initial temperature.

‡ See Fig. 9-25.

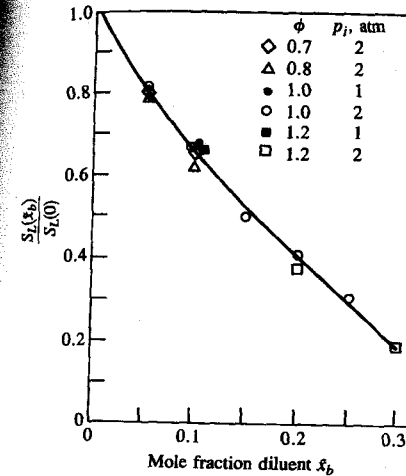


FIGURE 9-26  
Effect of burned gas mole fraction  $\tilde{x}_b$  in unburned mixture on laminar burning velocity. Fuel: gasoline.<sup>32</sup>

The presence of burned gas in the unburned cylinder charge due to residual gases and any recycled exhaust gases causes a substantial reduction in the laminar burning velocity. Any burned gas in the unburned mixture reduces the heating value per unit mass of mixture and, thus, reduces the adiabatic flame temperature. It acts as a diluent. The effect of increasing burned gas or diluent fraction on laminar flame speed is shown in Fig. 9-26. The diluent used was a mixture of  $\text{CO}_2$  and  $\text{N}_2$ , chosen to match the heat capacity of actual gasoline-air combustion products.<sup>†</sup> The proportional reduction in laminar burning velocity is essentially independent of the unburned mixture equivalence ratio, pressure, and temperature over the range of interest in engines. The data in Fig. 9-26 are correlated by the relation:

$$S_L(\tilde{x}_b) = S_L(\tilde{x}_b = 0)(1 - 2.06\tilde{x}_b^{0.77}) \quad (9.38)$$

where  $\tilde{x}_b$  is the mole fraction of burned gas diluent. Other studies corroborate the magnitude of this burned gas effect.<sup>32</sup>

Note that for equal heat capacity added to the unburned mixture, burned gases have a much larger effect on laminar burning velocity than does excess air. For example, the laminar burning velocity of a stoichiometric mixture as it is leaned to  $\phi = 0.8$  is reduced by 23 percent. The excess air required has a heat capacity of about 0.2 times that of the combustion products of the undiluted mixture. Adding the same heat capacity by adding stoichiometric burned gases (which requires a burned gas mole fraction of 0.175) reduces the laminar burning

† The water in actual residual and exhaust gas was omitted. A mixture of 80 percent  $\text{N}_2$  and 20 percent  $\text{CO}_2$ , by volume, was used.

velocity by 55 percent.<sup>32</sup> Proper allowance for the burned gas fraction in estimating laminar burning velocities for spark-ignition engines is most important.

The above correlations define the laminar burning velocity as a function of unburned mixture thermodynamic properties and composition, only. It has been assumed that flame thickness and curvature effects are negligible.<sup>28</sup> Our interest in laminar burning velocity is twofold: first, it is used to define the characteristic chemical reaction time of the mixture in Eq. (9.30); second, a presumed consequence of the wrinkled thin-reaction-sheet turbulent-flame structure is that, locally, the sheet propagates at the laminar burning velocity. The above correlations adequately characterize a quiescent burning process. However, laminar flame propagation can be influenced by the local flow field in the unburned gas. If the flame thickness is less than the Kolmogorov scale, the primary effect is one of straining which affects both the flame area (usually referred to as flame stretching for an area increase) and the local (laminar) burning velocity. While this problem is not yet well understood, it is known that straining can affect the laminar burning velocity and can cause flame extinction. The laminar burning velocity decreases with increasing strain rate, and the Lewis number of the unburned mixture has a significant influence on this rate of decrease. The Lewis number is the ratio of diffusivities of heat and mass. For stoichiometric mixtures it is close to one; it increases above about unity as the unburned fuel-air mixture is leaned out. Thus the local flow field may have a discernable effect on the local burning velocity of the thin laminarlike reaction-sheet flame, especially for lean or dilute mixtures.<sup>34</sup>

### 9.3.4 Flame Propagation Relations

If the heat-release or mass burning rate analysis of Sec. 9.2.2 is coupled with an analysis of flame geometry data, substantial additional insight into the behavior of spark-ignition engine flames is obtained. Flame photographs (such as those in Figs. 9-1, 9-14, and 9-16 and Refs. 4 and 35) effectively define the position of the front or leading edge of the turbulent engine flame. The "shadow" of the enflamed zone, under normal engine conditions, is close to circle: only in the presence of very high swirl does substantial distortion of the flame shape occur.<sup>18</sup> Thus, to a good approximation, the surface which defines the leading edge of the turbulent flame (ahead of which only unburned mixture exists) is a portion of the surface of a sphere. Figure 9-27 indicates the geometrical parameters which define this flame surface:  $r_c$ ,  $\alpha_c$ ,  $z_c$ , the coordinates of the flame center;  $r_f$ , the radius of the best-fit circle to the flame front silhouette; and the geometry of the combustion chamber walls. The flame is initiated at the spark plug; however, it may move away from the plug during the early stages of its development as shown. We define the *flame front area*  $A_f$  as the spherical surface of radius  $r_f$  coinciding with the leading edge of the flame contained within the combustion chamber, and the *enflamed volume*  $V_f$  as the volume within the chamber behind this flame front.

The thermodynamic analysis of cylinder pressure data allows us to define additional geometrical parameters. The *burned gas radius*  $r_b$  is the radius of the

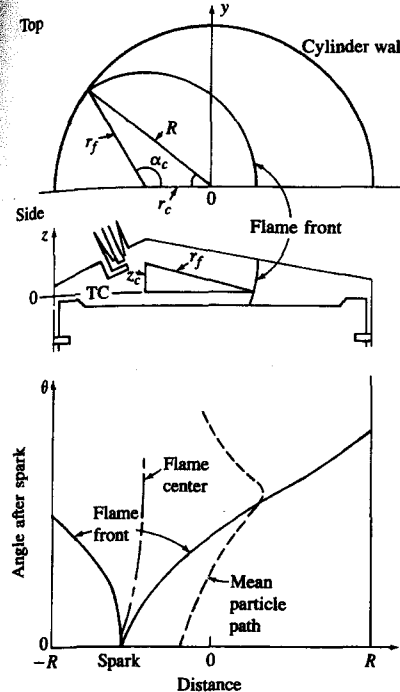


**FIGURE 9-27**  
Schematic of spherical flame front in engine combustion chamber identifying parameters which define flame geometry. (From Beretta et al.<sup>4</sup>)

spherical surface within the combustion chamber which would contain all the burned gas behind it; i.e.,

$$V_b(r_b, r_c, \alpha_c, z_c) = V_b(p, \theta) \quad (9.39)$$

The *spherical burning area*  $A_b$  is the area of this spherical surface; i.e.,

$$A_b = \frac{\partial V_b(r_b, r_c, \alpha_c, z_c)}{\partial r_b} \quad (9.40)$$

The *laminar burning area*  $A_L$  is the surface area the flame would have if it burned at the laminar flame speed, i.e.,

$$A_L = \frac{dm_b/dt}{\rho_u S_L} \quad (9.41)$$

where  $S_L$  is the laminar flame speed in the unburned mixture ahead of the flame (see Sec. 9.3.3).

Several velocities can be defined. The *mean expansion speed* of the front  $u_f$  is given by

$$u_f = \frac{dA_S/dt}{L_s} \quad (9.42)$$

where  $A_s$  is the "shadow" area enclosed by the "best-fit" circle through the leading edge of the flame and

$$L_s = \frac{\partial A_s}{\partial r_f}$$

is the arc length within the chamber of this "best-fit" circle. The *mean expansion speed* of the *burned gas*  $u_b$  is

$$u_b = \frac{\partial V_b / \partial t}{A_b} \quad (9.43)$$

This derivative is taken with the piston position fixed since only burned volume changes due to combustion are of interest. The *burning speed*  $S_b$  is defined by

$$S_b = \frac{dm_b / dt}{\rho_u A_b} \quad (9.44)$$

The *mean gas speed* just ahead of the flame front  $u_g$  is

$$u_g = u_b - S_b \quad (9.45)$$

Note that combining Eqs. (9.41) and (9.44) gives the relation

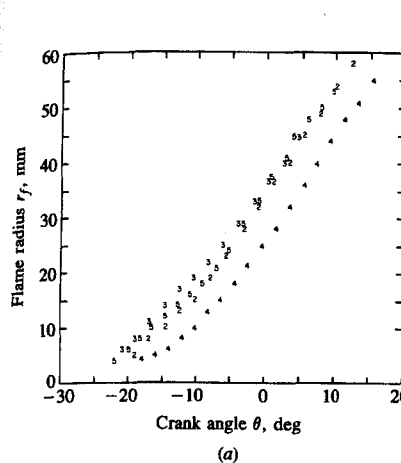
$$S_b A_b = S_L A_L \quad (9.46)$$

Also, it follows from Eqs. (9.29), (9.43), and (9.44) that

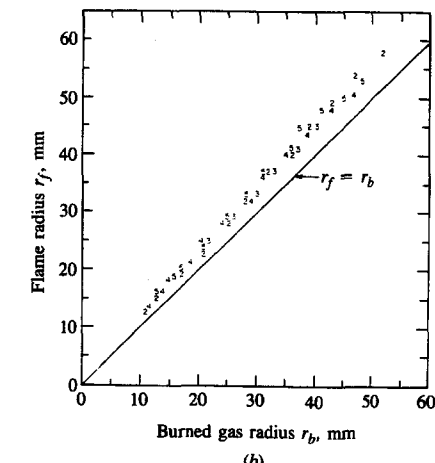
$$\frac{u_b}{S_b} = \frac{\rho_u}{\rho_b} (1 - y_b) + y_b = \frac{\rho_u / \rho_b}{[(\rho_u / \rho_b) - 1]x_b + 1} \quad (9.47)$$

As  $x_b$  and  $y_b \rightarrow 0$ ,  $u_b/S_b$  approaches the expansion ratio  $\rho_u/\rho_b$ . As  $x_b$  and  $y_b \rightarrow 1$ ,  $u_b/S_b$  approaches unity.

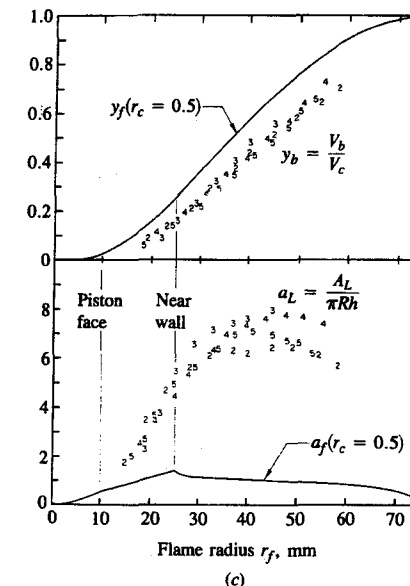
The variation of the above quantities during the engine combustion process, coupled with the photographs and discussion in Sec. 9.3.2, provide substantial insight into the flame development and propagation process. Figure 9-28 shows results from an analysis of cylinder pressure data and the corresponding flame front location information (determined from high-speed movies through a window in the piston) of several individual engine operating cycles. The combustion chamber was a typical wedge design with a bore of 102 mm and a compression ratio of 7.86. The flame radius initially grows at a rate that increases with time and exhibits substantial cycle-by-cycle variation in its early development (Fig. 9-28a). Later ( $r_f \gtrsim 30$  mm) the growth rate, which approximates the expansion speed  $u_b$ , reaches an essentially constant value. The flame radius  $r_f$  is initially equal to the burned gas radius  $r_b$ ; it increases above  $r_b$  as the flame grows and becomes increasingly distorted by the turbulent flow field (Fig. 9-28b). Eventually  $r_f - r_b$  goes to an essentially constant value of about 6 mm for  $r_b \gtrsim 30$  mm. This difference,  $r_f - r_b$ , is approximately half the thickness of the turbulent flame brush.



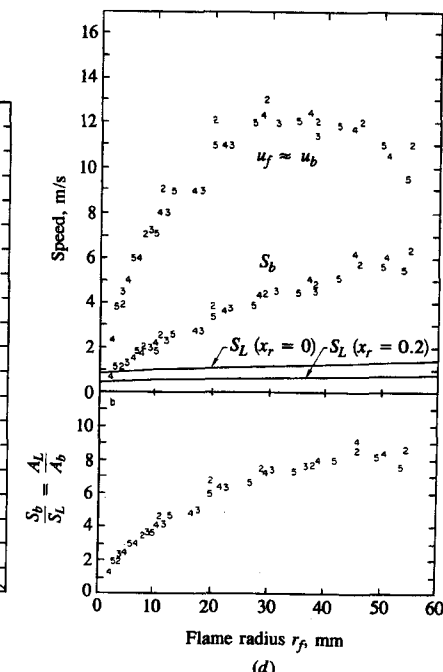
(a)



(b)



(c)



(d)

**FIGURE 9-28**  
Variation of flame geometry and velocity parameters during four individual combustion cycles at 1044 rev/min,  $\phi = 0.98$ , 1 atm inlet pressure: (a) flame radius  $r_f$  versus crank angle; (b) flame radius  $r_f$  versus burned gas radius  $r_b$ ; (c) normalized enflamed volume  $y_f$ , burned volume  $y_b$ , normalized flame front area  $a_f$ , and laminar area  $a_L$  versus flame radius; (d) front expansion speed  $u_b$ , burning speed  $S_b$ , and laminar flame speed  $S_L$  versus flame radius. (From Beretta et al.<sup>4</sup>)

Normalized enflamed and burned volumes, and flame front area and laminar burning area, are shown in Fig. 9-28c. Volumes are normalized by the cylinder volume, and areas by  $\pi Rh$ , where  $h$  is the average clearance height and  $R$  the cylinder radius. Discontinuities occur in the flame area  $A_f$  at the points where the flame front contacts first the piston face and then the near cylinder wall. The laminar area  $A_L$  is initially close to the flame area  $A_f$  and then increases rapidly as the flame grows beyond 10 mm in radius. During the rapid burning combustion phase ( $y_f \gtrsim 0.2$ ) the value of  $y_f$  is significantly greater than  $y_b$ . During this phase, the laminar area exceeds the flame area by almost an order of magnitude. These observations indicate the existence of substantial pockets of unburned mixture behind the leading edge of the flame.<sup>4</sup>

The ratio of the volume of the unburned mixture within the turbulent flame zone ( $V_f - V_b$ ) to the reaction-sheet area within the flame zone ( $A_L - A_f$ ) defines a characteristic length

$$l_T = \frac{V_f - V_b}{A_L - A_f} \quad (9.48)$$

which can be thought of as the scale of the pockets of unburned mixture within the flame. For the data set of Fig. 9-28,  $l_T$  is approximately constant and of order 1 mm.<sup>24</sup>

These flame geometry results would be expected from the previous photographic observations of how the flame grows from a small approximately spherical smooth-surfaced kernel shortly after ignition to a highly wrinkled reaction-sheet turbulent flame of substantial overall thickness. Initially, the amount of unburned gas within the enflamed volume is small. During the rapid burning phase of the combustion process, however, a significant fraction (some 25 percent; see Fig. 9-2) of the gas entrained into the flame zone is unburned.

The front expansion speed  $u_f$ , burning speed  $S_b$ , and laminar flame speed  $S_L$  are shown in Fig. 9-28d. The expansion speed increases as the flame develops to a maximum value that is several times the mean piston speed of 3.1 m/s and is comparable to the mean flow velocity through the inlet valve of 18 m/s.<sup>24</sup> The burning speed increases steadily from a value close to the laminar flame speed at early times to almost an order of magnitude greater than  $S_L$  during the rapid burning phase. During this rapid burning phase, since  $(r_f - r_b)$  is approximately constant, the flame front expansion speed and the mean burned gas expansion speed are essentially equal. The difference between  $u_b \approx u_f$  and  $S_b$  is the unburned gas speed  $u_g$  just ahead of the flame front. Note that the ratio  $u_f/S_b$  ( $\approx u_b/S_b$ ) decreases monotonically from a value equal to the expansion ratio ( $\rho_u/\rho_b$ ) at spark to unity as the flame approaches the far wall, as required by Eq. (9.47).

The effect of flame propagation on the flow field in the unburned mixture ahead of the flame is important because it is the turbulence just ahead of the flame that determines the local burning velocity. Measurements of mean velocities, rms fluctuation velocities, and turbulence intensities have been made using laser doppler anemometry (see Sec. 8.2.2) at different locations within engine combustion chambers (e.g., Refs. 36 and 37). Such data are difficult to interpret

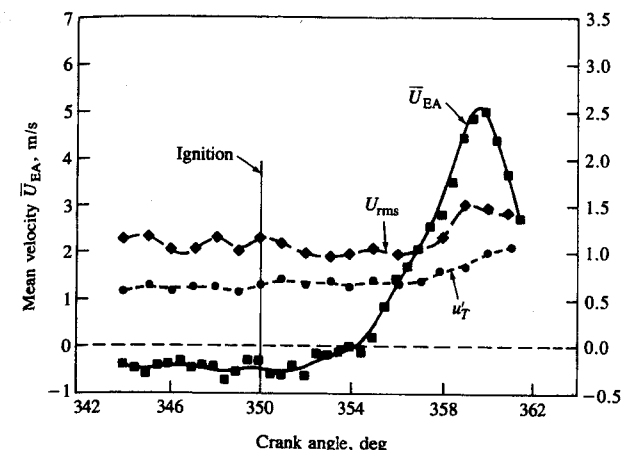


FIGURE 9-29

Laser doppler anemometer measurements of ensemble-averaged mean velocity  $\bar{U}_{EA}$  [Eq. (8.20)], rms fluctuation in individual-cycle mean velocity  $U_{rms}$  [Eq. (8.21)] and turbulence intensity  $u'_T$  [Eq. (8.22)], close to the cylinder axis, from before ignition to after flame arrival. Disc-shaped chamber, spark plug in cylinder wall, measurement at  $x/B = 0.57$ ,  $B = 76$  mm, 300 rev/min.  $\bar{S}_p = 0.83$  m/s.<sup>36</sup>

because the mean flow varies cycle-by-cycle, the turbulence is not homogeneous, and the flame motion and shape show substantial cyclic variations. The results in Fig. 9-29 were taken in a special single-cylinder engine with a disc-shaped combustion chamber where the spark plug was located in the cylinder liner. Shown are the ensemble-averaged mean velocity, cyclic variation in mean velocity, and the turbulence intensity, normal to the front, during the major portion of the combustion process, close to the chamber center.

The mean velocity normal to the front increases steadily from shortly after ignition, as the combustion-produced gas expansion displaces unburned mixture toward the wall. It peaks as the flame arrives at the measurement location. The cyclic variation in mean velocity and the turbulence intensity normal to the front remain essentially constant until a few degrees before the flame arrival. These two quantities are comparable in magnitude; thus the turbulence intensity is lower than the rms fluctuation velocity (in this case by about a factor of 2) (see Sec. 8.2.2). Whether the increase in turbulence as the flame approaches is due to rapid distortion resulting from the compression of the unburned mixture which occurs during combustion or is the result of inadequate resolution of cycle-to-cycle flow variations is unclear. Rapidly imposed distortions of a turbulent flow field, such as those imposed by combustion-produced gas expansion, would lead to an increase in vorticity and turbulence intensity. Other studies, e.g., Ref. 37, indicate there is little or no increase in turbulence intensity ahead of the flame.

The variation of burning speed with engine speed has also been carefully examined in a study where flame position was determined from high-speed movies, mass burning rates from cylinder pressure, and turbulence information

from experiments at equivalent motored conditions.<sup>35</sup> The turbulence quantity obtained during motoring experiments was the ensemble-averaged root mean square velocity fluctuation defined by Eq. (8.18). Values of  $S_b/S_L$  and  $u'_F/S_L$  were determined at two points in the combustion process: at a flame radius of 30 mm (the end of the flame development process) and at mass fraction burned equal to 0.5 (halfway through the rapid burning phase). To correct the motored turbulence data for the higher pressure levels corresponding to engine firing conditions, a simple rapid distortion model (see Sec. 14.4.2) based on conservation of angular momentum in turbulent eddies was used. A linear correlation between  $S_b$  and  $u'_F$  results, as shown in Fig. 9-30, for the rapid burning combustion phase. Note that as  $u'_F/S_L$  goes to zero,  $S_b/S_L$  approaches a value close to unity.

Once the flame front reaches the far cylinder wall (see Fig. 9-27) the front can no longer propagate; however, combustion continues behind the front until all the unburned mixture entrained into the enflamed region is consumed. This final burning or termination phase of the combustion process can be approximated by an exponential decay in the mass burning rate with a characteristic time constant  $\tau_b$  of order 1 ms. Since these "islands" or "pockets" of unburned mixture behind the leading edge of the flame have a characteristic scale  $l_T$  based on the laminar flame area [Eqs. (9.41) and (9.48)], it follows that

$$l_T = \tau_b S_L \quad (9.49)$$

In summary, the above flame data analysis procedures show that the relationships between  $r_f$  and  $r_b$ ,  $V_f$  and  $V_b$ ,  $A_f$  and  $A_L$ ,  $u'_F$ ,  $S_b$  and  $S_L$  are distinctly different in the three phases of combustion: (1) the development phase, where a highly wrinkled reaction-sheet "thick"-overall turbulent flame evolves from the essentially spherical flame kernel established by the spark discharge; (2) the rapid-burning phase, where this thick "developed" turbulent flame propagates across the combustion chamber to the far wall, during which most of the mass is burned; and (3) the termination phase after the flame front has reached the far wall and propagation of the front is no longer possible, when the remaining unburned mixture within the flame burns up. The burning velocity, in the rapid-burning phase of the combustion process, scales with turbulence intensity, which in turn scales with engine speed.

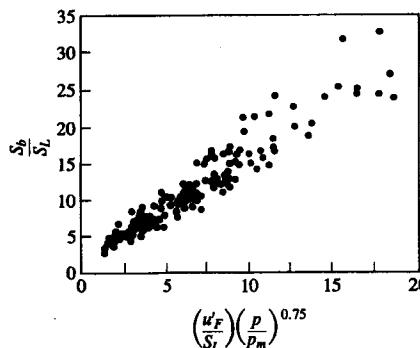


FIGURE 9-30

Variation of burning speed with turbulence intensity. The ensemble-averaged rms velocity fluctuation was measured during motoring engine operation. The ratio  $p/p_m$  (firing pressure/motoring pressure) corrects for the effect of additional compression on the turbulence intensity. Range of engine speeds and spark timings.<sup>35</sup>

## 9.4 CYCLIC VARIATIONS IN COMBUSTION, PARTIAL BURNING, AND MISFIRE

### 9.4.1 Observations and Definitions

Observation of cylinder pressure versus time measurements from a spark-ignition engine, for successive operating cycles, shows that substantial variations on a cycle-by-cycle basis exist. Since the pressure development is uniquely related to the combustion process, substantial variations in the combustion process on a cycle-by-cycle basis are occurring. In addition to these variations in each individual cylinder, there can be significant differences in the combustion process and pressure development between the cylinders in a multicylinder engine. Cyclic variations in the combustion process are caused by variations in mixture motion within the cylinder at the time of spark cycle-by-cycle, variations in the amounts of air and fuel fed to the cylinder each cycle, and variations in the mixing of fresh mixture and residual gases within the cylinder each cycle, especially in the vicinity of the spark plug. Variations between cylinders are caused by differences in these same phenomena, cylinder-to-cylinder.

Cycle-by-cycle variations in the combustion process are important for two reasons. First, since the optimum spark timing is set for the "average" cycle, faster-than-average cycles have effectively overadvanced spark-timing and slower-than-average cycles have retarded timing, so losses in power and efficiency result. Second, it is the extremes of the cyclic variations that limit engine operation. The fastest burning cycles with their overadvanced spark timing are most likely to knock. Thus, the fastest burning cycles determine the engine's fuel octane requirement and limit its compression ratio (see Sec. 9.6.3). The slowest burning cycles, which are retarded relative to optimum timing, are most likely to burn incompletely. Thus these cycles set the practical lean operating limit of the engine or limit the amount of exhaust gas recycle (used for NO emissions control) which the engine will tolerate. Due to cycle-by-cycle variations, the spark timing and average air/fuel ratio must always be compromises, which are not necessarily the optimum for the average cylinder combustion process. Variations in cylinder pressure have been shown to correlate with variations in brake torque which directly relate to vehicle driveability.

An example of the cycle-by-cycle variations in cylinder pressure and the variations in mixture burning rate that cause them are shown in Fig. 9-31. Pressure and gross heat-release rate [calculated from the cylinder pressure using Eq. (9.27)] for several successive cycles at a mid-load, mid-speed point are shown as a function of crank angle. The maximum heat-release rate and the duration of the heat release or burning process vary by a factor of two from the slowest to the fastest burning cycle shown. The peak cylinder pressure varies accordingly. The faster burning cycles have substantially higher values of maximum pressure than do the slower burning cycles; with the faster burning cycles peak pressure occurs closer to TC.

The heat-release rate data in Fig. 9-31 show that there are cycle-by-cycle variations in the early stages of flame development (from zero to a few percent of

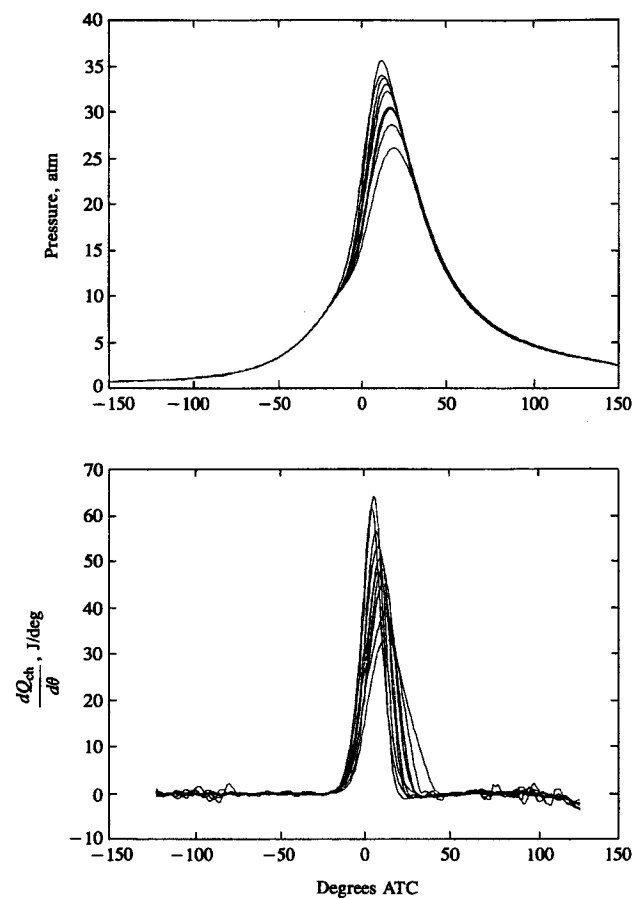


**FIGURE 9-31**  
Measured cylinder pressure and calculated gross heat-release rate for ten cycles in single-cylinder spark-ignition engine operating at 1500 rev/min,  $\phi = 1.0$ ,  $p_{inlet} = 0.7$  atm, MBT timing 25° BTC.<sup>14</sup>

the total heat release) and in the major portion of the combustion process—the rapid-burning phase—indicated by the variations in the maximum burning rate.

As the mixture becomes leaner with excess air or more dilute with a higher burned gas fraction from residual gases or exhaust gas recycle, the magnitude of cycle-by-cycle combustion variations increases. Eventually, some cycles become sufficiently slow burning that combustion is not completed by the time the exhaust opens: a regime where *partial burning* occurs in a fraction of the cycles is encountered. For even leaner or more dilute mixtures, the *misfire* limit is reached. At this point, the mixture in a fraction of the cycles fails to ignite. While spark-ignition engines will continue to operate with a small percentage of the cycles in the partial-burn or misfire regimes, such operation is obviously undesirable from

the point of efficiency, hydrocarbon emissions, torque variations, and roughness. The partial-burn and misfire regimes are discussed in Sec. 9.4.3.

Various measures of cycle-by-cycle combustion variability are used. It can be defined in terms of variations in the cylinder pressure between different cycles, or in terms of variations in the details of the burning process which cause the differences in pressure. The following quantities have been used:

1. *Pressure-related parameters.* The maximum cylinder pressure  $p_{max}$ ; the crank angle at which this maximum pressure occurs  $\theta_{p_{max}}$ ; the maximum rate of pressure rise  $(dp/d\theta)_{max}$ ; the crank angle at which  $(dp/d\theta)_{max}$  occurs; the indicated mean effective pressure [which equals  $\int p dV/V_d$ , see Eqs. (2.14), (2.15), and (2.19)].
2. *Burn-rate-related parameters.* The maximum heat-release rate (net or gross, see Sec. 9.2.2); the maximum mass burning rate; the flame development angle  $\Delta\theta_f$  and the rapid burning angle,  $\Delta\theta_b$  (see Sec. 9.2.3).
3. *Flame front position parameters.* Flame radius, flame front area, enflamed or burned volume, all at given times; flame arrival time at given locations.

Pressure-related quantities are easiest to determine; however, the relation between variations in combustion rate and variations in cylinder pressure is complex.<sup>38</sup> Equation (9.26) defines the factors that govern this relationship. Because the rate of change of pressure is substantially affected by the rate of change of cylinder volume as well as rate of burning, changes in the phasing of the combustion process relative to TC (e.g., which result from changes in flame development angle) as well as changes in the shape and magnitude of the heat-release rate profile affect the pressure. Figure 9-32 illustrates how the magnitude of the maximum cylinder pressure  $p_{max}$  and the crank angle at which it occurs  $\theta_{p_{max}}$  vary as the crank angle at which combustion effectively starts (e.g.,  $\theta$  at which 1 percent of the cylinder mass has burned) and the burning rate are varied. Curve *CABE* shows how  $p_{max}$  and  $\theta_{p_{max}}$  vary for a fixed fast-burning heat-release profile (the duration of the heat-release process and its maximum value are held

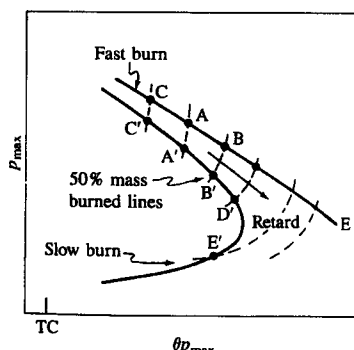


**FIGURE 9-32**  
Schematic of variation in maximum cylinder pressure and crank angle at which it occurs, in individual cycles. *CABE* typical of fast heat-release process; *C'A'B'D'E'* typical of slow heat-release process. (From Matekunas.<sup>38</sup>)

constant), as the phasing of this combustion process relative to TC is varied. A corresponds to MBT timing where the start of combustion is phased to give maximum brake torque, B corresponds to retarded timing, and C to over-advanced timing. C'A'B'D'E' is a similar curve for a slow-burning heat-release profile. A' corresponds to MBT timing, and B' and D' to increasingly retarded timing. Note that with a sufficiently slow-burning heat-release profile, beyond D',  $\theta_{p_{max}}$  decreases as the burn process is increasingly retarded. This occurs when the rate of increase of pressure due to combustion becomes so low that it is more than offset by the pressure decrease due to volume increase: eventually for extremely slow and late burning, the maximum pressure approaches the motored pressure at TC. The dashed lines show the constant start-of-combustion timing relative to MBT for each burn rate curve. Note that  $\theta_{p_{max}}$  for constant relative timing varies little as the heat-release profile or burn rate varies.<sup>38</sup>

We can now explain the effects of variations in the heat-release profile (both in the development stage of the burning process, which effectively changes the location of the start of combustion, and in the rate of burning throughout the process) on  $p_{max}$  and  $\theta_{p_{max}}$ , when the spark timing occurs at a fixed crank angle. For a fixed burning rate profile (duration of burn and maximum burning rate) as the start of combustion is delayed to be closer to TC,  $p_{max}$  decreases and  $\theta_{p_{max}}$  initially increases (A to B or A' to B'). This is the effect of a change in relative timing or phase of the burning process due to a slower initial rate of flame development with fixed spark timing. If, in addition to the flame development being slower, the heat-release rate throughout the burning process is lower, then that combustion process is even more retarded from the optimum and  $p_{max}$  decreases and  $\theta_{p_{max}}$  increases further, to their values at D'. The effect of a faster initial flame development and faster burning rate, with fixed spark time, is the opposite. The magnitudes of the changes in  $p_{max}$  and  $\theta_{p_{max}}$  depend, obviously, on the extent of the cyclic variations; they also depend on whether the average burn process is fast or slow. For fast-burning engines, a larger fraction of the heat release occurs near TC when the chamber volume is changing relatively slowly. Thus pressure variations are mainly due to combustion variations. With slow-burning engines, where a significant fraction of the energy release occurs well after TC, the effect of volume change also becomes significant and augments the effect of combustion variations. For large variations and a slow average burning process,  $p_{max}$  can fall below E', and  $\theta_{p_{max}}$  then decreases. A fast-burning combustion process significantly reduces the impact of cyclic combustion variations on engine performance.<sup>39</sup>

We can now evaluate the various measures of combustion variability. The maximum pressure variation has been shown to depend on both changes in phasing and burning rate. The magnitude of this variation depends on whether the combustion chamber is faster or slower burning, on average. It also depends on whether the burning process is substantially retarded relative to MBT. It depends, too, on cyclic cylinder fuel and air charging variations. Thus the interpretation of variations in  $p_{max}$  [or in the maximum rate of pressure rise ( $dp/d\theta$ )<sub>max</sub>] in terms of variations in the rate and phasing of the burning process

must be done with care. The location of maximum pressure  $\theta_{p_{max}}$  also depends on relative phasing of combustion and on the burn rate profile. In addition, for slow-burning chambers and retarded timing (around E') variations produce little change in  $\theta_{p_{max}}$ . However, for fast-burning chambers, with MBT or only slightly retarded timing, the location of peak pressure depends essentially on the phasing of each combustion process relative to its MBT phasing, and is independent of charging variations. For these reasons,  $\theta_{p_{max}}$  is a useful measure of variability in combustion event phasing.<sup>38</sup>

One important measure of cyclic variability, derived from pressure data, is the coefficient of variation in indicated mean effective pressure. It is the standard deviation in imep divided by the mean imep, and is usually expressed in percent:

$$\text{COV}_{\text{imep}} = \frac{\sigma_{\text{imep}}}{\text{imep}} \times 100 \quad (9.50)$$

It defines the cyclic variability in indicated work per cycle, and it has been found that vehicle driveability problems usually result when  $\text{COV}_{\text{imep}}$  exceeds about 10 percent.

Figure 9-33 illustrates the relationships between  $p_{max}$ ,  $\theta_{p_{max}}$ , and imep for 120 cycles of an engine cylinder at fixed operating conditions and three different spark timings.<sup>38</sup> The MBT timing data show a spread in imep at a fixed value of  $\theta_{p_{max}}$ . This imep data band is relatively flat and is centered around  $\theta_{p_{max}} \approx 16^\circ$ ; only at later values of  $\theta_{p_{max}}$  does imep fall off significantly. The vertical spread in imep around  $\theta_{p_{max}} = 16^\circ$  is due to variations in the amount of fuel entering the cylinder each cycle; normal variations in the burn profile under these conditions, which effectively change the phasing of the combustion process, produce only modest reductions in imep. For early  $\theta_{p_{max}}$  (the extreme upper left of Fig. 9-33a), the variations in  $p_{max}$  are also due mainly to these fuel-charging variations, cycle-by-cycle; these are the fastest burning cycles with the most advanced phasing. As

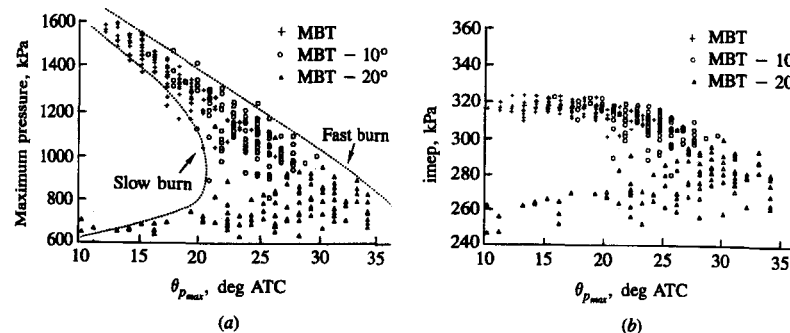


FIGURE 9-33  
(a) Individual-cycle maximum pressure versus crank angle at which  $p_{max}$  occurs. (b) Individual-cycle indicated mean effective pressure versus  $\theta_{p_{max}}$ .<sup>38</sup>

$\theta_{p\max}$  increases, the dispersion increases as cyclic variations in phasing and burning rate have increasing impact.

An important issue is whether variations in the early stages of flame development and variations in subsequent portions of the burning process are independent of each other or are correlated. Plots of early flame development angle (spark to 1 percent mass burned) against the burning angle (1 to 90 percent burned) from individual cycles for several different combustion chambers indicate the following. There is a trend with increasing flame development angle for the burning angle to increase (or the burning rate to decrease); however, there is much scatter about this trend (for a given value of flame development angle different cycles show a substantial range in burning angle), and the quantitative aspects of the trend depend on operating conditions and on combustion chamber design. In addition, as the mean rapid burning angle increases (due to changing operating conditions or a slower-burning chamber design) the mean flame development angle, the cyclic variation in the flame development angle, and the cyclic variation in the rapid burning angle all increase.<sup>40</sup> This topic is discussed more fully in the following section.

The shapes of the frequency distributions in individual-cycle pressure data (e.g., in  $p_{\max}$ ,  $(dp/d\theta)_{\max}$ ,  $\theta_{p\max}$ ) and in burn rate data such as  $\Delta\theta_d$ ,  $\Delta\theta_b$ ,  $(dQ/d\theta)_{\max}$  depend on whether the combustion process is fast and "robust" (e.g., with close-to-stoichiometric mixtures at higher loads at optimum timing—well away from the lean operating limit of the engine) or slower and less repeatable, closer to the lean or dilute-mixture operating limit. Under robust combustion conditions these distributions are close to normal distributions.<sup>41-43</sup> When the combustion process is much slower, the cyclic variability becomes large and the distribution becomes skewed toward the slower burning cycles which have low imep (due to the substantial retard of these slower cycles). When partial burning and then misfire occur, the low-pressure tail of the distribution approaches the motored pressure value at TC.<sup>44</sup> Examples of the frequency distributions of imep in these two combustion variability regimes are shown later in Fig. 9-36.

Cylinder pressure data are often averaged over many cycles to obtain the mean cylinder pressure at each crank angle. The primary use of this average pressure versus crank angle data is in calculating the average indicated mean effective pressure (which is a linear function of  $p$ ). Since combustion parameters are not linearly related to the cylinder pressure [see Eq. (9-27)], analysis of the average pressure data will not necessarily yield accurate values of average combustion parameters. The error will be most significant when the combustion variability is largest. It is best to determine mean combustion parameters by averaging their values obtained from a substantial number of individual cycle analysis results. The number of cycles which must be averaged to obtain the desired accuracy depends on the extent of the combustion variability. For example, while 40 to 100 cycles may define imep to within a few percent when combustion is highly repeatable, several hundred cycles of data may be required when cyclic combustion variations are large.<sup>12</sup>

#### 9.4.2 Causes of Cycle-by-Cycle and Cylinder-to-Cylinder Variations

Cycle-by-cycle combustion variations are evident from the beginning of the combustion process. Analysis of flame photographs from many engine cycles taken in special research engines with windows in the combustion chamber has shown that dispersion in the fraction of the combustion chamber volume inflamed is present from the start of combustion (e.g., see Refs. 3 and 23). Dispersion in burning rate is also evident throughout the combustion process (see Figs. 9-2 and 9-31). Three factors have been found to influence this dispersion:<sup>45</sup>

1. The variation in gas motion in the cylinder during combustion, cycle-by-cycle
2. The variation in the amounts of fuel, air, and recycled exhaust gas supplied to a given cylinder each cycle
3. Variations in mixture composition within the cylinder each cycle—especially near the spark plug—due to variations in mixing between air, fuel, recycled exhaust gas, and residual gas

The relative importance of these factors is not yet fully defined, and depends on engine design and operating variables. The variation in the velocity field within the engine cylinder throughout the cycle, and from one cycle to the next, has been reviewed in Sec. 8.2.2. Toward the end of the compression stroke, the ensemble-averaged rms velocity fluctuation is of comparable magnitude to the mean piston speed, and may be larger than the mean flow velocity if there is no strongly directed local mean flow pattern (see Figs. 8-8 and 8-9). This ensemble-averaged velocity fluctuation combines both cycle-by-cycle variation in the mean flow and the turbulent velocity fluctuations. During compression, these two components are of comparable magnitude (see Figs. 8-9 and 9-29). While this data base is limited, it indicates that substantial variations in the mean flow exist, cycle-by-cycle, both in the vicinity of the spark plug and throughout the combustion chamber. Velocity variations contribute in a major way to variations in the initial motion of the flame center as it grows from the kernel established by the spark, and in the initial rate of growth of the flame; they can also affect the burning rate once the flame has developed to fill a substantial fraction of the combustion chamber. Variations in gas motion near the spark plug convect the flame in its early stages in different directions and at different velocities, cycle-by-cycle. This affects the flame's interaction with the cylinder walls, changing the flame area development with time. Variations in the turbulent velocity fluctuations near the spark plug will result in variations in the rate at which the small initially laminarlike flame kernel develops into a turbulent flame. Variations in the mean flow throughout the chamber will produce differences in flame front shape; also, they may produce differences in turbulence which affect the propagation velocity of the front (see Fig. 9-30 for the relation between mean burning speed and turbulence intensity).

It is well known that, on a time-averaged basis, the fuel, air, and recycled exhaust gas flows into each cylinder of a multicylinder engine are not identical. These flow rate differences are typically a few percent (see Secs. 7.6.2 and 7.6.3). It is also known that the flow patterns within the different cylinders are not necessarily identical due to differences between the individual intake manifold runner and port geometries in many production engines. All these factors contribute to cylinder-to-cylinder variations in the combustion process: there can be significant differences in the mean burn rate parameters as well as in the cyclic variations in these parameters.<sup>41</sup> Also, the limited data available on the variation in mixture composition within each cylinder for each cycle indicates that cyclic charging variations in individual cylinders are comparable in magnitude to cylinder-to-cylinder differences (i.e., of order  $\pm 5$  percent<sup>46</sup>). Whether the amount of residual gas left in the cylinder varies significantly, cycle-by-cycle, is not known. At higher loads, where the combustion process is more repeatable (and always completed relatively early in the expansion stroke) and the residual gas fraction smaller (see Sec. 6.4), variations in the total amount of residual are not expected to be significant. At light loads (particularly at idle), where combustion variability is much higher and partial-burning cycles may occur, and especially with high valve overlap engine designs, variations in the residual gas mass and its composition may become important.

In addition, mixing of fuel, air, recycled exhaust, and residual is not complete: nonuniformities in composition exist within the cylinder at the start of combustion. Composition variations, cycle-by-cycle, in the vicinity of the spark plug electrode gap will affect the early stages of flame development, especially as the flame grows through the laminarlike burning phase following the creation of a small flame kernel by the spark discharge (see Sec. 9.5.1). Figure 9-34 indicates the extent of these composition nonuniformities. The available data comes from experiments where a small rapid-acting sampling valve located in the spark plug center electrode was used to extract gas from the vicinity of the electrode gap, close to the start of combustion, for individual cycle composition analysis. Figure 9-34a shows the cycle-by-cycle air/fuel ratio fluctuations in the burned gases sampled from one cylinder of a four-cylinder gasoline-fueled carbureted engine just after combustion has started. The standard deviation was typically 2 to 6 percent of the mean ( $A/F$ ).<sup>46-48</sup> Figure 9-34b shows the relationship between total hydrocarbon and  $\text{CO}_2$  concentrations in unburned mixture, sampled just before spark discharge. The  $\text{CO}_2$  concentration is a measure of the burned gas fraction in the sampled unburned mixture; hence on average it correlates inversely with the total hydrocarbon concentration. However, there is substantial fluctuation in  $\text{CO}_2$  concentration about the mean value, at a given fuel fraction, indicating significant fluctuations, cycle-by-cycle, in the mixing of fresh mixture with residual gas. Nonuniformities in EGR distribution between cylinders and EGR mixing within the cylinder would also increase the variations in burned gas fraction locally at the spark gap, cycle-by-cycle.<sup>48</sup>

Experiments in a multicylinder production SI engine, where the fuel/air ratio nonuniformities and the nonuniform mixing of fresh mixture with residual

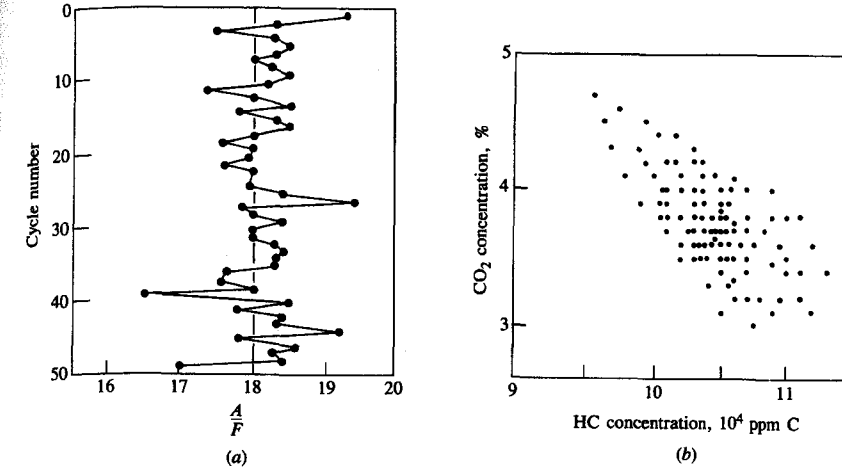


FIGURE 9-34

(a) Air/fuel ratio in 50 consecutive cycles, in vicinity of spark plug, measured just after ignition with a rapid-acting sampling valve located in the plug center electrode. Engine operated at 1400 rev/min, MBT timing,  $\text{imep} = 314 \text{ kPa}$ .<sup>47</sup> (b)  $\text{CO}_2$  and unburned HC concentrations in gas sampled in individual cycles from the vicinity of the spark plug just prior to ignition. Engine operated at 1200 rev/min,  $\phi = 0.98$ ,  $p_{\text{inlet}} = 0.5 \text{ atm}$ , gasoline fuel.<sup>48</sup>

gas were removed in turn as contributors to cycle-by-cycle variations (by comparing premixed propane operation with conventional carbureted operation with gasoline, and by removing residual gas by purging with nonfiring cycles), showed that the three contributing factors to cyclic combustion variations—velocity variations, fuel/air ratio variations, and residual gas mixing variations—are of comparable importance at road-load conditions.<sup>45</sup>

An explanation for cycle-by-cycle variations can be developed from the description of the turbulent flame propagation process in Sec. 9.3. Conditions in the vicinity of the spark plug will influence the initial stages of the flame propagation process—establishing a stable kernel and its development into a turbulent flame. During the developed flame propagation phase, the *average* conditions in the bulk gas within the combustion chamber will be the determining factors since the flame front spans the chamber, effectively averaging out local non-uniformities. By conditions are meant the turbulent velocity fluctuations and length scales in the flow, proportions of fuel, air, and burned gas in the mixture, and the mixture state.

Using the turbulent combustion model described in Sec. 14.4.2 (which is based on the description of the flame development and propagation process in Sec. 9.3), the flame development angle  $\Delta\theta_d$  (the time to burn a few large eddies and establish a developed turbulent flame) can be expressed as<sup>20</sup>

$$\Delta\theta_d = C \left( \frac{l_I}{u'} \right)^{1/3} \left( \frac{l_M}{S_L} \right)^{2/3} \quad (9.51)$$

The turbulent flow field influences  $\Delta\theta_d$  through  $l_I$ ,  $u'$ , and  $l_M$ , the integral scale, the turbulence intensity, and the microscale, respectively. The mixture composition influences  $\Delta\theta_d$  through the laminar flame speed  $S_L$ . There is therefore a variability in the flame development period, since all of these quantities can vary in the vicinity of the spark plug on a cycle-by-cycle basis.

The pressure development during the rapid-burning developed turbulent flame propagation phase, when the flame spans the combustion chamber, depends on the average rate of burning in the flame. Thus, variations in the turbulent flow field and mixture composition across the gas entering the flame front are averaged out and are not important. However, variation in chamber-average quantities are significant. The combustion model in Sec. 14.4.2 leads to the following expression for the maximum burning rate:

$$\left(\frac{dm_b}{dt}\right)_{\max} = \frac{Cm_f(h^*/B)(\rho_u^*/\rho_i)^{10/9}[(\bar{u}'^*S_L^*)/h_i]^{2/3}}{v^{*1/3}} \quad (9.52)$$

Here,  $m_f$  is the mass of fuel in the chamber,  $h$  is the instantaneous (mean) clearance height,  $B$  is the bore,  $\rho$  the density,  $\bar{u}'$  the average turbulence intensity across the flame front, and  $v$  the kinematic viscosity; the \* denotes the value at the time of the maximum burning rate and the subscript  $i$  the value at spark;  $C$  is a constant depending on engine design. It can be seen from Eq. (9.52) that cycle-by-cycle variations in the maximum burning rate can result from variations in the overall flow pattern within the combustion chamber (which vary  $\bar{u}'^*$ ) and from variations in the amount of fuel ( $m_f$ ) that enters the cylinder each cycle.<sup>†</sup> Also, it can be seen that variations in the flame development process will result in variations in the maximum burning rate because the crank angle at which the maximum burning rate occurs is shifted, and all the starred parameters in Eq. (9.52) will have different values.

From the discussion of flame development and structure in Sec. 9.3, and Eqs. (9.51) and (9.52) above, we would expect that mixture conditions and motion leading to slower flame development rates (longer flame development angles,  $\Delta\theta_d$ )—lower turbulence intensities and more dilute mixtures—would also give lower burning rates (longer rapid burning angles,  $\Delta\theta_b$ ). Data from many different engines and a wide range of operating cases show that this is the case, on average, though there is substantial variation about the mean trend. Figure 9-35 shows these trends; it also shows that the standard deviation of  $\Delta\theta_d$  and the standard deviation of  $\Delta\theta_b$  for a given chamber and operating condition generally increase as the average burning process becomes slower.<sup>40</sup>

One final factor of importance is how variations in flame development and burning rate affect engine torque. With fixed spark timing, such variations in the combustion process cycle-by-cycle result in slower developing and/or burning

<sup>†</sup> Variations in the total amount of air, recycled exhaust gas, and residual in the chamber could also, for some operating regimes, be significant.

cycles being retarded and faster developing and/or burning cycles being over-advanced. The curve of torque versus combustion timing (relative to optimum timing), Fig. 9-3b, is almost independent of the burning rate; i.e., a given magnitude retard (of say 10°) relative to optimum timing gives almost the same reduction in torque for a very fast burn as it does for a very slow burn. This is because the burning process, for optimum timing, is centered at about 10° ATC independent of the burn rate, and retard or advance shifts this "center" by equal amounts for all burn rates.<sup>16</sup> One of the major advantages of fast-burn engines is now apparent. The magnitude of the variations in the flame development process and subsequent flame propagation rate are decreased as the burning rate is increased (see Fig. 9-35): the ratio of standard deviation in  $\Delta\theta_d$  and  $\Delta\theta_b$  to the mean values remains approximately constant. Thus, these smaller combustion variations in fast-burn engines, which correspond to modest retard and over-advance in nonaverage burn rate cycles, have little effect on torque. In contrast, the larger combustion variations of slow-burning engines result in significant cyclic torque variations.

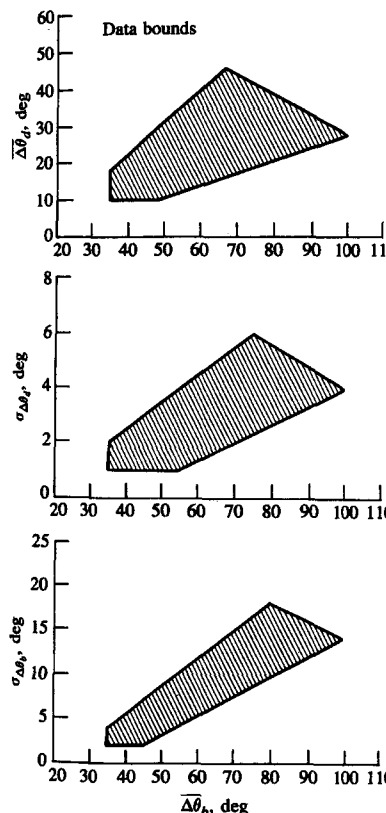


**FIGURE 9-35**  
Variation in mean value of flame development angle  $\overline{\Delta\theta_d}$  (spark to 1 percent mass burned) and standard deviations of flame development angle and rapid burning angle  $\Delta\theta_b$  (1 to 90 percent mass burned) with mean rapid burning angle  $\overline{\Delta\theta_b}$ . Range of combustion chamber geometries and engine operating conditions.<sup>40</sup>

### 9.4.3 Partial Burning, Misfire, and Engine Stability

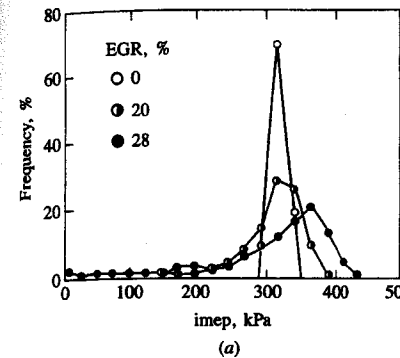
As the unburned mixture in a spark-ignition engine is leaned out with excess air or is diluted with increasing amounts of burned residual gas and exhaust gas recycle, the flame development period, the duration of the rapid burning phase, and the cycle-by-cycle fluctuations in the combustion process all increase. Eventually a point is reached where engine operation becomes rough and unstable, and hydrocarbon emissions increase rapidly. The point at which these phenomena occur effectively defines the engine's *stable operating limit*.<sup>†</sup> These phenomena result from the lengthening of all stages of the combustion process as the unburned mixture is diluted. With increasing dilution, first a fraction of the cycles burns so slowly that combustion is only just completed prior to exhaust valve opening. Then as burning lengthens further, in some cycles there is insufficient time to complete combustion within the cylinder; also, flame extinguishment before the exhaust valve opens and before the flame has propagated across the chamber may start to occur in some cycles. Finally, misfiring cycles where the mixture never ignites may start to occur. The proportion of partial burning or nonburning cycles increases rapidly if the mixture is made even more lean or dilute, and the point is soon reached where the engine will not run at all.

The impact on engine stability of increasing combustion variability, due to increased exhaust gas recycle at part-load, is shown in Fig. 9-36. Figure 9-36a shows the distributions of individual-cycle indicated mean effective pressure values for 0, 20, and 28 percent EGR. Without EGR at these conditions, the spread in imep is narrow. Increasing EGR widens the distribution significantly and cycles with low imep, and eventually zero imep, occur. Figure 9-36b shows how the coefficient of variation of imep and hydrocarbon emissions increase as EGR is increased. Slow burn, then partial burn, and then misfire cycles occur with increasing frequency. In the slow-burn cycles, combustion is complete but ends after 80° ATC and the indicated mean effective pressure is low (between 85 and 46 percent of the mean value). Imep in partial-burn cycles was less than 46 percent of the mean. In misfiring cycles, imep < 0. Empirically, it has been found that  $\text{COV}_{\text{imep}}$  [see Eq. (9.50)] is about 10 percent at the engine's stable operating limit, which here occurs just before the onset of partial-burning cycles.<sup>49</sup>

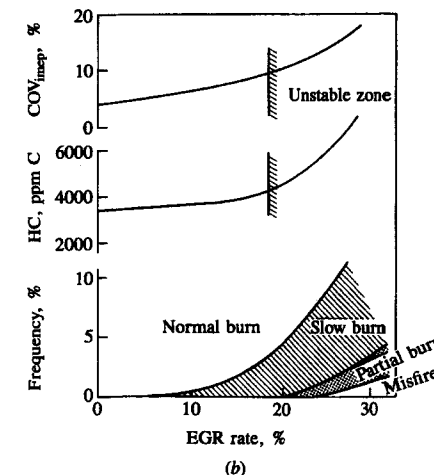
An explanation of combustion phenomenon at the engine stable operating limit has been developed by Quader.<sup>50</sup> It involves the following terms:

**Ignition-limited spark timing or the ignition limit.** The spark timing [advanced from maximum brake torque (MBT) timing] at which *misfire* (i.e., failure of flame initiation) first occurs at a given mixture composition, in a given small but arbitrary fraction of cycles (e.g., 0.5 to 1 percent).

<sup>†</sup> This limit has often been called the *lean operating limit*. Since what limits engine operation in practice is excessive torque fluctuations, cycle-by-cycle, and high hydrocarbon emissions, resulting from the use of mixtures made overly dilute with either air or burned gases (or with both), *stable operating limit* is a more appropriate term.



(a)



(b)

FIGURE 9-36

(a) Frequency distributions in indicated mean effective pressure at different EGR rates; 0 percent gave excellent engine stability, 20 percent acceptable stability, and 28 percent poor stability. (b) Coefficient of variation in imep, HC emissions, and percentage of normal, slow, partial-burn, and misfire cycles. Engine conditions: 1400 rev/min,  $\phi = 1.0$ , MBT timing, imep = 324 kPa.<sup>49</sup>

**Partial-burn-limited spark timing or the partial-burn limit.** The spark timing (retarded from MBT) at which incomplete flame propagation occurs at a given mixture composition in a given small percent of the cycles (again, this frequency is selected arbitrarily for experimental convenience).

**Lean misfire limit at MBT spark.** The leanest mixture stoichiometry at which the engine could be stabilized to operate at MBT spark timing with a misfire frequency below a specified value (again, this frequency, usually a percent or less of the cycles, is selected arbitrarily for convenience). A *dilute misfire limit*, the maximum amount of exhaust gas recycle that can be absorbed at a given stoichiometry for stable engine operation, can be similarly defined.

Engine experiments have defined the locations of the ignition limit line and the partial-burn limit line; they are shown qualitatively in Fig. 9-37. At a given spark timing, on this spark timing versus equivalence ratio plot, progressive leaning of the mixture fed to the engine will lead to the onset of misfire or to the onset of partial burning, depending on the location of the lines and the spark timing selected. The individual figures show the possible interactions of the maximum brake torque (MBT) timing line—leaner mixtures require greater advance—with the ignition limit and partial-burn limit lines. At MBT timing, the partial-burn limit may or may not be reached prior to misfire or the ignition limit. It will depend on the engine and ignition system design and operating conditions. For spark timings retarded relative to MBT, partial burning and not failure of flame initiation is the primary cause of unstable engine operation.

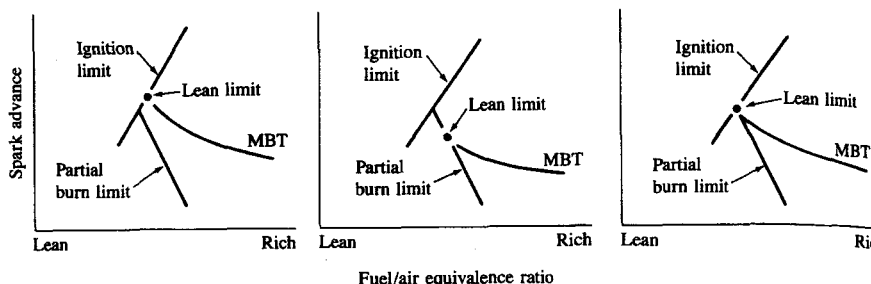


FIGURE 9-37

Schematics of three possible combinations of ignition limit, partial-burn limit, and MBT timing curves as function of fuel/air equivalence ratio. (From Quader.<sup>50</sup>)

An example of these limiting combustion regimes for lean engine operation is shown in Fig. 9-38. With MBT timing, as the mixture is leaned out (at constant air flow rate), complete combustion in all cycles changes to partial burning in some cycles which changes to no ignition in some cycles at the ignition limit. In the partial-burning regime, the most common type of incomplete-combustion cycle was a slow-burning cycle which required more time to complete burning than was available: flame extinguishment during expansion was much less common. Engine performance measurements showed that the engine stability limit—evidenced by minimum fuel consumption and onset of rapid increase in HC emissions—occurred at  $\phi = 0.65$ , just before the partial-burn limit line where some slow-burning cycles occur but combustion is still complete in all cycles.<sup>44</sup>

From the above it is clear that flame initiation is a necessary but not sufficient condition for complete combustion. Too-slow flame development and prop-

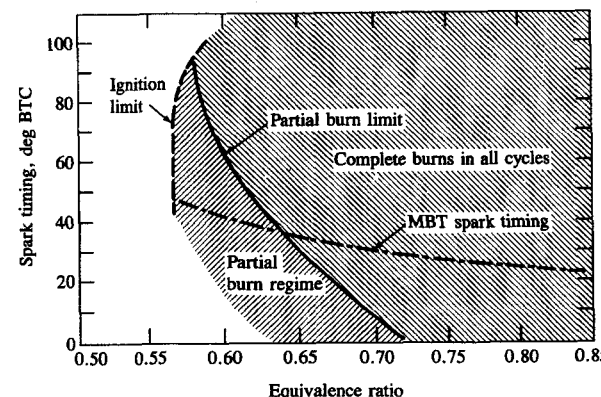


FIGURE 9-38

Actual limiting combustion regimes for lean-operating engine. 1200 rev/min, volumetric efficiency  $\approx 60$  percent, methane fuel, 40 mJ spark energy, 2.5 ms spark duration.<sup>44</sup>

agation following successful ignition is usually the factor which limits engine operation with dilute mixtures. Experiments have shown that a limited interval, of order 80 crank angle degrees (depending on engine geometry and spark plug location), is available during the engine cycle when conditions are favorable for complete flame propagation.<sup>49, 51</sup> Outside of this interval, the mixture pressure and temperature are too low, and the turbulence intensity is too low to sustain a sufficiently rapid rate of combustion. Thus, it is factors which increase the flame development and propagation rates which primarily extend the partial-burn limit.

## 9.5 SPARK IGNITION

In spark-ignition engines, the electrical discharge produced between the spark plug electrodes by the ignition system starts the combustion process close to the end of the compression stroke. The high-temperature plasma kernel created by the spark develops into a self-sustaining and propagating flame front—a thin reaction sheet where the exothermic combustion chemical reactions occur. The function of the ignition system is to initiate this flame propagation process, in a repeatable manner cycle-by-cycle, over the full load and speed range of the engine at the appropriate point in the engine cycle. Shadowgraph and schlieren photographs of the kernel created by the discharge between the plug electrodes, the growth of that kernel, and its transition to a propagating flame have already been presented in Figs. 9-19 and 9-20, and described in the accompanying text. A spark can arc from one electrode to another when a sufficiently high voltage is applied. Ignition systems commonly used to provide this spark are: battery ignition systems where the high voltage is obtained with an ignition coil (coil ignition systems); battery systems where the spark energy is stored in a capacitor and transferred as a high-voltage pulse to the spark plug by means of a special transformer (capacitive-discharge ignition systems); and magneto ignition systems where the magneto—a rotating magnet or armature—generates the current used to produce a high-voltage pulse.

This section reviews our basic understanding of electrical discharges in inflammable gas mixtures relevant to engine ignition (Sec. 9.5.1), the major design and operating characteristics of conventional engine ignition systems (Sec. 9.5.2), and, briefly, some alternative approaches to generating a propagating flame (Sec. 9.5.3).

### 9.5.1 Ignition Fundamentals

A spark can arc from one plug electrode to the other only if a sufficiently high voltage is applied. In a typical spark discharge, the electrical potential across the electrode gap is increased until breakdown of the intervening mixture occurs. Ionizing streamers then propagate from one electrode to the other. The impedance of the gap decreases drastically when a streamer reaches the opposite electrode, and the current through the gap increases rapidly. This stage of the

discharge is called the *breakdown phase*. It is followed by the *arc phase*, where the thin cylindrical plasma expands largely due to heat conduction and diffusion and, with inflammable mixtures, the exothermic reactions which lead to a propagating flame develop. This may be followed by a *glow discharge phase* where, depending on the details of the ignition system, the energy storage device (e.g., the ignition coil) will dump its energy into the discharge circuit.<sup>52, 53</sup>

Figure 9-39 shows the behavior of the discharge voltage and current as a function of time for a conventional coil ignition system. Typical values are shown; actual values depend on the details of the electrical components. The breakdown phase is characterized by a high-voltage (~10 kV), high-peak current (~200 A), and an extremely short duration (~10 ns). A narrow (~40 μm diameter) cylindrical ionized gas channel is established very early. The energy supplied is transferred almost without loss to this plasma column. The temperature and pressure in the column rise very rapidly to values up to about 60,000 K and a few hundred atmospheres, respectively. A strong shock or blast wave propagates outward, the channel expands, and, as a result, the plasma temperature and pressure fall. Some 30 percent of the plasma energy is carried away by the shock wave; however, most of this is regained since spherical blast waves transfer most of their energy to the gas within a small (~2 mm diameter) sphere into which the breakdown plasma soon expands.<sup>52, 53</sup>

A breakdown phase always precedes arc and glow discharges: it creates the electrically conductive path between the electrodes. The arc phase voltage is low

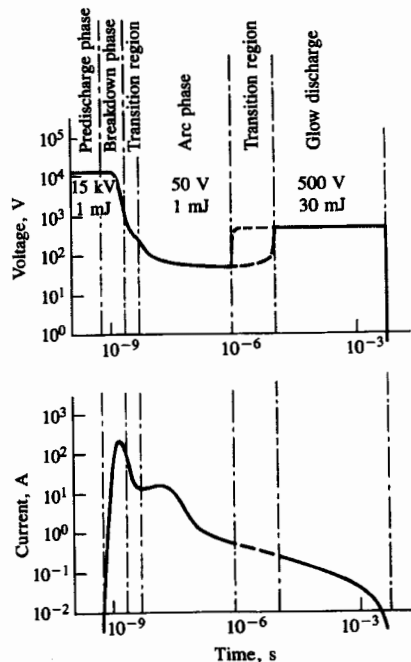


**FIGURE 9-39**  
Schematic of voltage and current variation with time for conventional coil spark-ignition system. Typical values for energy and voltage in the three phases—breakdown, arc, and glow discharge—are given.<sup>52</sup>

(<100 V), though the current can be as high as the external circuit permits. In contrast to the breakdown phase where the gas in the channel is fully dissociated and ionized, in the arc phase the degree of dissociation may still be high at the center of the discharge, but the degree of ionization is much lower (about 1 percent). Voltage drops at the cathode and anode electrodes are a significant fraction of the arc voltage, and the energy deposited in these electrode sheath regions, which is conducted away by the metal electrodes, is a substantial fraction of the total arc energy (see Table 9.4 below). The arc requires a hot cathode spot, so evaporation of the cathode material occurs. The arc increases in size due primarily to heat conduction and mass diffusion. Due to these energy transfers the gas temperature in the arc is limited to about 6000 K: the temperature and degree of dissociation decrease rapidly with increasing distance from the arc axis. Currents less than 200 mA, a large electrode voltage drop at the cathode (300 to 500 V), a cold cathode, and less than 0.01 percent ionization are typical for the glow discharge. Energy losses are higher than in the arc phase, and peak equilibrium gas temperatures are about 3000 K.<sup>52</sup>

About 0.2 mJ of energy is required to ignite a quiescent stoichiometric fuel-air mixture at normal engine conditions by means of a spark. For substantially leaner and richer mixtures, and where the mixture flows past the electrodes, an order of magnitude greater energy (~3 mJ) may be required.<sup>54</sup> Conventional ignition systems deliver 30 to 50 mJ of electrical energy to the spark. Due to the physical characteristics of the discharge modes discussed above, only a fraction of the energy supplied to the spark gap is transmitted to the gas mixture. The energy balance for the breakdown, arc, and glow phases of the discharge is given in Table 9.4. Radiation losses are small throughout. The end of the breakdown phase occurs when a hot cathode spot develops, turning the discharge into an arc; heat losses to the electrodes then become substantial. The breakdown phase reaches the highest power level (~1 MW), but the energy supplied is small (0.3 to 1 mJ). The glow discharge has the lowest power level (~10 W) but the highest energy (30 to 100 mJ), due to its long discharge time. The arc phase lies between.

The proportions of the electrical energy supplied, which can be transferred to the plasma in these three phases of the discharge, are shown in Fig. 9-40.<sup>53, 55</sup> The different transfer capabilities for breakdown, arc, and glow discharges arise

**TABLE 9.4**  
Energy distribution for breakdown, arc, and glow discharges†

	Breakdown, %	Arc, %	Glow, %
Radiation loss	<1	5	<1
Heat loss to electrodes	5	45	70
Total losses	6	50	70
Plasma energy	94	50	30

† Typical values, under idealized conditions with small electrodes.  
Source: Maly and Vogel.<sup>52</sup>

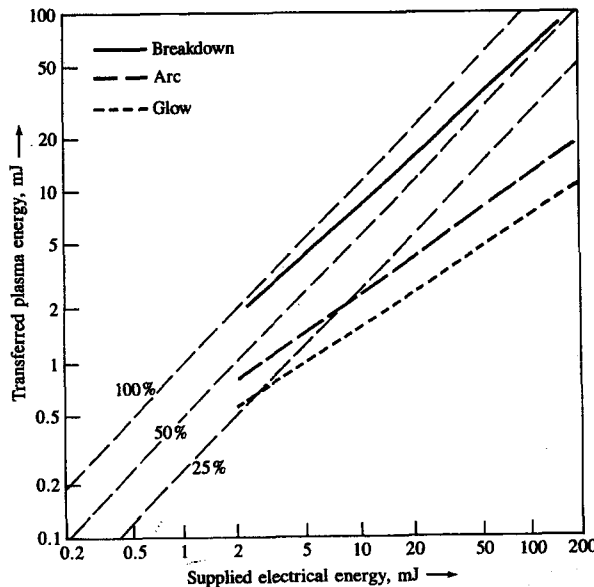


FIGURE 9-40

Energy transferred to the spark kernel as a function of supplied electrical energy for breakdown, arc, and glow discharges.<sup>55</sup>

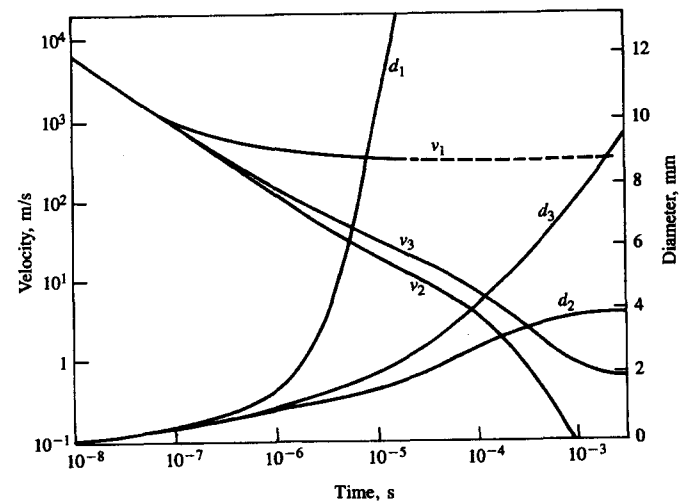


FIGURE 9-41

Diameters ( $d$ ) and expansion velocities ( $v$ ) of volumes activated by a capacitive-discharge ignition system: 3 mJ electrical energy, 100  $\mu$ s duration. Subscripts denote: 1, shock in air at 1 atm; 2, plasma in air at 1 atm; 3, electrical and chemical plasma in stoichiometric methane-air mixture at 1 atm.<sup>52</sup>

primarily from the differences in heat losses to the electrodes, as explained above. These losses increase with increasing supplied energy. In arc and glow discharges, increases in either discharge time or discharge current (or in both) always lead to substantial decreases in energy-transfer efficiency. If the glow discharge current is increased above about 100 mA, the discharge changes to the arc mode and heavy electrode erosion will result. Thus there are practical limits to the arc and glow discharge currents; also, the time available for ignition in the engine limits increases in discharge time.

The initial expansion velocities in the discharge are much higher than those in self-propagating flames. Figure 9-41 shows the expansion velocities and diameters of the volumes activated by a 3-mJ, 100- $\mu$ s discharge from a capacitor-discharge ignition system as a function of time after spark onset.<sup>52</sup> The curves shown are (1) for the shock wave following a discharge in air at 1 atm; (2) the plasma in air at 1 atm; (3) the electrical and chemical plasma following a discharge in a stoichiometric methane-air mixture at 1 atm. The initially strong shock wave attenuates rapidly to the local sound speed. Up to times of order microseconds, the effects of fuel combustion chemistry are small. The change in slope of the velocity curves for the plasmas at about 100  $\mu$ s indicates the transition from an expansion caused by the initial high pressure in the breakdown discharge to expansion resulting from heat conduction and diffusion.

The temperature distributions within the three different types of discharge provide additional insight. During the breakdown discharge, on a time scale of nanoseconds, the temperature rises to 60,000 K. Increasing the breakdown energy does not produce *higher* kernel temperatures; instead the channel diameter increases, producing a larger plasma volume. The kernel temperatures then decrease to the order of 10,000 K on a microsecond time scale as the plasma expands behind the shock wave. Arc and glow discharges, because their power inputs are much lower, do not increase the kernel temperatures; rather, they extend the cooling period on a microsecond and millisecond time scale, respectively.<sup>52</sup>

The characters of the temperature profiles that each of these three types of discharge create in air, with essentially the same total electrical energy input (30 to 33 mJ), are indicated in Fig. 9-42. The radial profiles in the undisturbed mid-plane of the arc are shown. The expansion-wave-induced expansion of the plasma behind the shock with the breakdown discharge produces a larger plasma, earlier, with a steep temperature front. Thus it creates favorable conditions for transferring heat and radicals to the surrounding unburned mixture. In addition cold gas flows into the central region of the plasma, due to the boundary layers which the rapidly expanding flow sets up on the electrodes, effectively insulating the hottest plasma region from the cold electrode surfaces.<sup>53</sup> The arc and glow discharges, each preceded by a much lower energy initial breakdown process, show a much slower expansion rate and the more gradual temperature profile produced by heat conduction and diffusion.

Chemical reactions can be observed spectroscopically a few nanoseconds after spark onset. They are initiated by the very high radical density in the break-

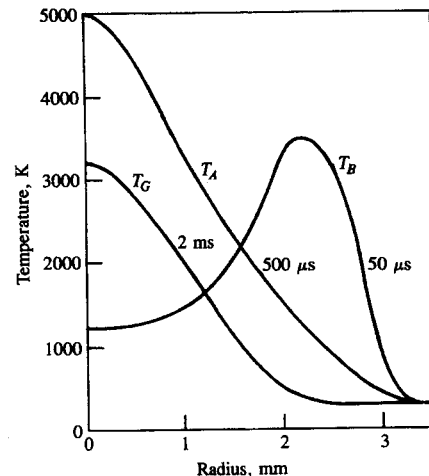


FIGURE 9-42

Radial temperature profiles at selected times after spark onset for ignition systems with different electrical energies and discharge times in air at 1 atm.  $T_B$ , breakdown discharge, 30 mJ energy, 60 ns duration;  $T_A$ , capacitive discharge, 3 mJ energy, 100  $\mu$ s duration with superimposed current arc of 2 A, 30 mJ energy, for 230  $\mu$ s;  $T_G$ , capacitive-discharge system, 3 mJ energy, 100  $\mu$ s duration with superimposed constant-current glow discharge of 60 mA, 30 mJ energy, 770  $\mu$ s duration.<sup>52</sup>

down plasma where all the heavy particles are present as highly excited atoms and ions. Since the kernel temperatures are much too high to allow the species present in normal combustion products to exist, combustion reactions take place at the outer plasma surface where the conditions are ideal for rapid chemical activity (temperatures of one thousand to a few thousand kelvins). The chemical energy released is added to the plasma energy and becomes evident when the plasma velocity falls below about 100 m/s (see Fig. 9-41). At this point, the inte-

TABLE 9.5  
Equilibrium composition of stoichiometric isoctane-air combustion products

Species	Temperature, K†			
	2000	3000	4000	5000
CO	2.4(-3)	6.1(-2)	9.4(-2)	9.0(-2)
CO <sub>2</sub>	1.2(-1)	5.7(-2)	5.0(-3)	3.5(-4)
H	2(-5)	9.7(-3)	1.2(-1)	1.9(-1)
H <sub>2</sub>	6.1(-4)	1.5(-2)	2.4(-2)	3.5(-3)
H <sub>2</sub> O	1.4(-1)	1.0(-1)	1.1(-2)	1.2(-4)
N	n	1(-5)	6.6(-4)	1.2(-2)
NH	n	2(-5)	6(-5)	
NO	5.7(-4)	1.5(-2)	2.9(-2)	1.7(-2)
N <sub>2</sub>	7.3(-1)	6.9(-1)	5.7(-1)	5.1(-1)
O	1(-5)	8.6(-3)	9.8(-2)	1.6(-1)
OH	4.5(-4)	2.2(-2)	3.3(-2)	5.6(-3)
O <sub>2</sub>	1.1(-3)	2.3(-2)	1.7(-2)	2.2(-3)

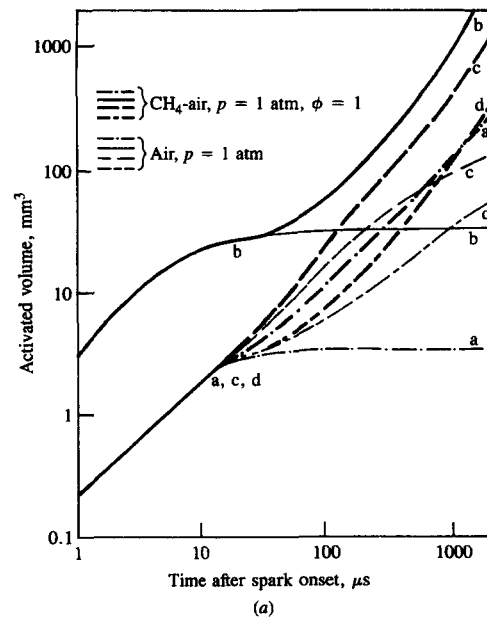
† At 4 atm pressure: mole fractions,  $9.0(-2) = 9.0 \times 10^{-2}$ .  
 $n = < 5 \times 10^{-6}$

rior of the plasma still consists of a fully dissociated reacted gas mixture with most of its energy stored in radicals. An indication of the gas composition across the steep temperature profile at the plasma interface can be obtained from Table 9.5, which shows the equilibrium composition of C<sub>8</sub>H<sub>18</sub>-air combustion products over the relevant temperature range. Note, however, that the gas will not be in equilibrium. The different radicals have different diffusivities, with the hydrogen atom some five times that of other species. Thus the H radical will diffuse furthest into the as-yet unreacted mixture. On the high-temperature side of the inflammation zone, the large number of radical particles transfer their energy to the mixture molecules within a few collisions. On the low-temperature side of the zone, above-equilibrium concentrations of combustion-initiating radicals (O and H) build up. In addition, a high heat flux into the region occurs, from the plasma core, by conduction down the steep temperature gradient. As a consequence of these conditions, reactions will occur and energy will be released more rapidly than in a normal flame.<sup>53</sup>

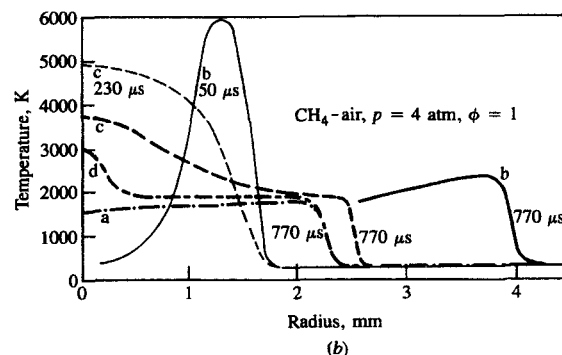
Figure 9-43a shows the size of the activated volume as a function of time for several types of discharge, both in a stoichiometric mixture and in air. It can be seen from the air curves for the capacitive discharge (CDI) and breakdown discharge that, after about 10  $\mu$ s, the plasma ceases to be the energy source for continued growth of the activated volume. At this time, the plasma temperature at the interface has fallen to a value comparable to flame temperatures. With combustible mixtures, molecules such as OH, CH, C<sub>2</sub>, CO, etc., appear, indicating that combustion reactions are now occurring. Figure 9-43a shows that for  $t \geq 20 \mu$ s, the volume activated by the discharge with the combustible mixture grows much faster than the volume activated in air. Continuing the supply of electrical energy in the arc and glow discharge does produce a higher expansion rate in both the combustible mixture and in air, due to additional heat conduction and diffusion to the interface, but the onset of inflammation is not significantly affected. The radial temperature profiles across the discharge at selected times, shown in Fig. 9-43b, illustrate these points. This, therefore, is the critical point in the inflammation process: at some 20  $\mu$ s after onset of the discharge the flame reactions must be proceeding sufficiently rapidly to be self-sustaining; i.e., chemical energy release must more than offset heat losses across the front to the surrounding unburned mixture via diffusion and conduction.<sup>53</sup>

Thus the characteristics of the breakdown phase of the discharge have the greatest impact on inflammation. The size of the activated volume a given time interval after spark initiation, the temperature difference across the kernel interface, and the velocity of the interface are all substantially increased by increasing the breakdown phase energy (see Fig. 9-43). Additional energy input during the arc and glow discharge phases has a more modest effect on these critical kernel properties. This is graphically illustrated by Fig. 9-44 where the same energy input into breakdown, arc, and glow discharge modes produces substantially different ignition limits.

Several models of the plasma-unburned mixture interface have been developed in attempts to quantify the complex phenomena described above (e.g., Refs.



(a)



(b)

FIGURE 9-43

(a) Size of discharge-activated volume as function of time for several types of discharge in air and in stoichiometric methane-air mixture at 1 atm. a: CDI, 3 mJ energy, 100  $\mu$ s duration; b: breakdown discharge, 30 mJ energy, 20 ns duration; c: CDI plus arc discharge, 1.5 A, 40 V, 500  $\mu$ s duration; d: CDI + glow discharge, 30 mA, 500 V, 2 ms duration. (b) Temperature profiles for different discharge modes at different times in stoichiometric methane-air mixture at 300 K, 4 atm. a: CDI, 3 mJ energy, 100  $\mu$ s duration; b: breakdown discharge, 20 mJ energy, 80 ns duration; c: CDI, 3 mJ energy, 100  $\mu$ s duration, plus 2 A, 30 mJ energy, 230  $\mu$ s duration arc; d: CDI, 3 mJ energy, 100  $\mu$ s duration, plus 60 mA, 30 mJ energy, 770  $\mu$ s duration glow discharge.<sup>53</sup>

56 and 57). They are based on the requirement that the energy release due to chemical reaction in the plasma front (and production of radical species) exceed the losses due to conduction and diffusion to the unburned gas ahead of the front. While these models are incomplete, they do provide a theoretical basis for the well-known fact that the minimum energy required to ignite a premixed fuel-air mixture depends strongly on mixture composition. Figure 9-45 shows a typical set of results on the minimum ignition energy as a function of the equivalence ratio under quiescent conditions.<sup>58</sup> The curve shows a minimum for slightly rich-of-stoichiometric mixtures; the minimum energy required for successful ignition increases rapidly as the mixture is leaned out. While the initial plasma kernel

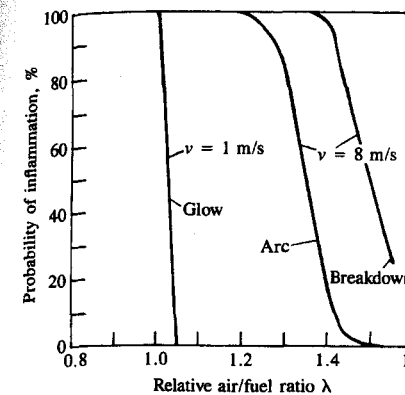


FIGURE 9-44

Probability of inflammation of stoichiometric methane-air mixture, at 300 K, 4 atm, as function of relative air/fuel ratio  $\lambda$  ( $= 1/\phi$ ) for different ignition discharges with equal total electrical energy (30–33 mJ). Breakdown: 30 mJ, 60 ns duration. Arc: CDI, 3 mJ, 100  $\mu$ s duration; plus 2 A, 30 mJ, 230  $\mu$ s duration arc. Glow: CDI, 3 mJ, 100  $\mu$ s duration; plus 60 mA, 30 mJ, 770  $\mu$ s duration glow discharge.  $v$  = mixture velocity.<sup>52</sup>

growth (up to 10 to 100  $\mu$ s) is not greatly affected by the mixture equivalence ratio, the inflammation process and the thickness and rate of propagation of the resulting flame are strongly affected. The lean side of the minimum is of more practical interest than the rich side. Because the chemical energy density of the mixture and flame temperature decrease as the mixture is leaned out, the flame speed decreases and the flame becomes thicker. Thus more time is available for heat losses from the inflammation zone, less energy is available to offset these losses, and the rate of energy transfer into the zone decreases. The consequence is that, as the mixture is leaned out, the approximately spherical discharge-created plasma must grow to a larger size before inflammation will occur. Substantially, more energy must therefore be supplied to the discharge.<sup>53</sup>

In engines, the mixture is not quiescent: mean and fluctuating velocities in the range 1 to 10 m/s exist in the clearance volume at TC (see Sec. 8.2.2). On the time scale of the breakdown discharge phase (10 ns), this fluid motion is not important. In the arc and glow discharge phases, however, the arc is convected

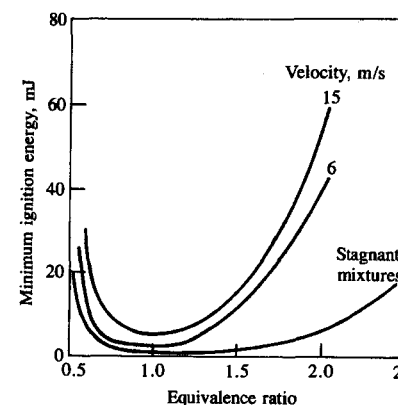


FIGURE 9-45

Effect of mixture equivalence ratio and flow velocity on minimum ignition energy for propane-air mixtures at 0.17 atm.<sup>58</sup>

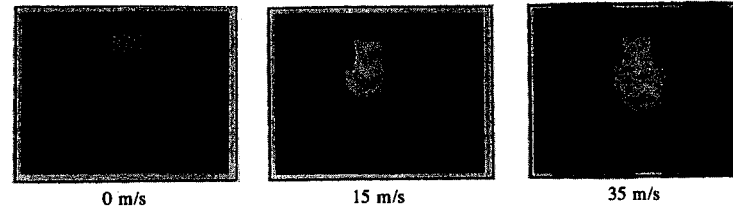


FIGURE 9-46

Photographs of single glow discharge (30 mJ, 0.77–1.5 ms) in air at 2 atm flowing perpendicular to axis of electrodes. Below 25 m/s almost no multiple discharges; above 25 m/s only multiple discharges. 1.2 mm electrode gap.<sup>56</sup>

by the flow and lengthened accordingly, as illustrated in Fig. 9-46. For velocities below 15 m/s a steady increase in discharge channel length occurs. For higher velocities, an increasing number of reignitions occur, so the discharge energy is distributed into many separate channels. As the channel lengthens, the ratio of total discharge voltage to anode plus cathode voltage drop increases substantially, and the relative importance of heat losses to the electrodes decreases. Thus more energy is transferred to the gas—the energy-transfer efficiency increases. However, as the channel is lengthened, the energy transferred is spread over a larger volume. Depending on flow velocity, and mixture and discharge conditions, increasing velocity may increase or decrease the minimum ignition energy or the lean ignition limit for a specific ignition system. Both the mean flow velocity and turbulence levels are important.<sup>53–58</sup> With a conventional coil ignition system, increasing mean flow velocity up to the point where reignitions start to occur extends the lean limit. With breakdown discharge systems, the lean ignition limit decreases as flow velocity increases.<sup>53</sup> With capacitive-discharge systems at low flow velocities, the flow has little impact; at high flow velocities the minimum ignition energy increases.<sup>59</sup>

Maly<sup>53</sup> has summarized these fundamental aspects of spark-discharge ignited flames as follows:

1. Of the total electrical energy supplied to the spark, only that fraction contained within the outer surface layer of the plasma (of thickness of the order of the inflammation zone) is available for initiating the flame propagation process. The energy density and the temperature gradient in this layer depend on the discharge mode. Highest energy densities and temperature gradients are achieved if the ignition energy is supplied in the shortest time interval.
2. A minimum radius of the spark plasma is required for inflammation of the fuel-air mixture to occur. This radius increases rapidly as the mixture is leaned out (or diluted); it decreases with increasing pressure and increasing plasma expansion velocity.
3. After inflammation, burning rates are proportional to flame surface area. Thus discharges and plasma geometries that produce the largest inflammation zone surface area, most rapidly, are advantageous.

4. The time over which the ignition energy can be used effectively for inflammation decreases as the initial flame velocity increases. Ignition energy supplied after inflammation has occurred will have only a modest impact on flame propagation.

### 9.5.2 Conventional Ignition Systems

The ignition system must provide sufficient voltage across the spark plug electrodes to set up the discharge and supply sufficient energy to the discharge to ignite the combustible mixture adjacent to the plug electrodes under all operating conditions. It must create this spark at the appropriate time during the compression stroke. Usually spark timing is set to give maximum brake torque for the specific operating condition, though this maximum torque may be constrained by emission control or knock control requirements. For a given engine design, this optimum spark timing varies as engine speed, inlet manifold pressure, and mixture composition vary. Thus, in most applications, and especially the automotive applications, the system must have means for automatically changing the spark timing as engine speed and load vary.

With an equivalence ratio best suited for ignition and with homogeneous mixture distribution, spark energies of order 1 mJ and durations of a few microseconds would suffice to initiate the combustion process. In practice, circumstances are less ideal. The air, fuel, and recycled exhaust are not uniformly distributed between cylinders; the mixture of air, fuel, recycled exhaust gas, and residual gas within each cylinder is not homogeneous. Also, the pressure, temperature, and density of the mixture between the spark plug electrodes at the time the spark is needed affect the voltage required to produce a spark. These vary significantly over the load and speed range of an engine. The spark energy and duration, therefore, has to be sufficient to initiate combustion under the most unfavorable conditions expected in the vicinity of the spark plug over the complete engine operating range. Usually if the spark energy exceeds 50 mJ and the duration is longer than 0.5 ms reliable ignition is obtained.

In addition to the spark requirements determined by mixture quality, pressure, temperature, and density, there are others determined by the state of the plugs. The erosion of the plug electrodes over extended mileage increases the gap width and requires a higher breakdown voltage. Also, spark plug fouling due to deposit buildup on the spark plug insulator can result in side-tracking of the spark. When compounds formed by the burning of fuel, lubricating oil, and their additives are deposited on the spark plug insulator, these deposits provide an alternative path for the spark current. If the resistance of the spark plug deposits is sufficiently low, the loss of electrical energy through the deposits may prevent the voltage from rising to that required to break down the gas. The influence of side-tracking on spark generation decreases with lower source impedance of the high-voltage supply, and therefore with a higher available energy.

The fundamental requirements of the high-voltage ignition source can be summarized as: (1) a high ignition voltage to break down the gap between the

plug electrodes; (2) a low source impedance or steep voltage rise; (3) a high energy storage capacity to create a spark kernel of sufficient size; (4) sufficient duration of the voltage pulse to ensure ignition. There are several commonly used concepts that partly or fully satisfy these requirements.<sup>54, 60</sup>

**COIL IGNITION SYSTEMS.** Breaker-operated inductive ignition systems have been used in automotive engines for many years. While they are being replaced with more sophisticated systems (such as transistorized coil ignition systems), they provide a useful introduction to ignition system design and operation. Figure 9-47 shows the circuit of a typical breaker ignition system. The system includes a battery, switch, resistor, coil, distributor, spark plugs, and the necessary wiring. The circuit functions as follows. If the breaker point is closed when the ignition is switched on, current flows from the battery, through the resistor, primary winding of the ignition coil, contacts, and back to the battery through ground. This current sets up a magnetic field within the iron core of the coil. When ignition is required, the breaker points are opened by the action of the distributor cam, interrupting the primary current flow. The resulting decay of magnetic flux in the coil induces a voltage in both the primary and secondary windings. The voltage induced in the secondary winding is routed by the distributor to the correct spark plug to produce the ignition spark.

The current and voltage waveforms are shown in Fig. 9-48. The primary current for any given time of contact closure  $t$  is given by

$$I_p = \frac{V_0}{R} (1 - e^{-Rt/L_p}) \quad (9.53)$$

where  $I_p$  is the primary current,  $V_0$  is the supply voltage,  $R$  is the total primary circuit resistance, and  $L_p$  is the primary circuit inductance. The primary current requires time to build up. At low speeds the time of contact closure is sufficient for the primary current to reach the maximum permitted by the circuit resistance; at high speeds the primary current may not reach its maximum. Thus, only at higher engine speeds does the term  $e^{-Rt/L_p}$  become significant. When the points open the primary current falls to zero and a voltage of order 15 kV is induced in the secondary winding. If the coil is not connected to a spark plug,

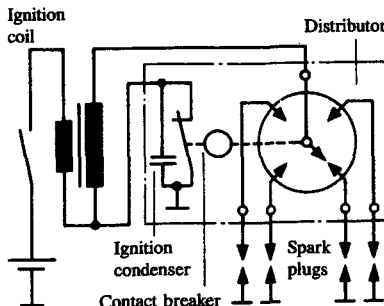


FIGURE 9-47  
Schematic of conventional coil ignition system.  
(Courtesy Robert Bosch GmbH and SAE.<sup>54</sup>)

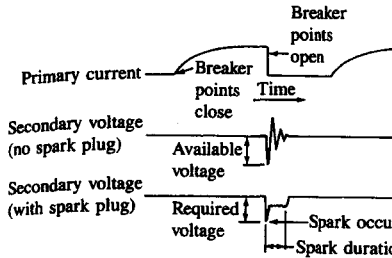


FIGURE 9-48

Current and voltage waveforms for breaker ignition system.<sup>61</sup>

this induced voltage will have a damped sinusoidal waveform, as shown in the center trace. The peak value of this voltage is the maximum voltage that can be produced by the system and is called the *available voltage*  $V_a$  of the system. The maximum energy transferred to the secondary system is given by

$$E_{s, \max} = \frac{1}{2} C_s V_a^2$$

where  $C_s$  is the total capacitance of the secondary circuit. Hence, the available voltage of the system is given by

$$V_a = \left( \frac{2E_{s, \max}}{C_s} \right)^{1/2} \quad (9.54)$$

If all the energy stored in the primary circuit of the coil,  $\frac{1}{2}L_p I_p^2$ , is transferred to the secondary,

$$V_a = I_p \left( \frac{L_p}{C_s} \right)^{1/2} \quad (9.55)$$

When the coil is connected to a spark plug, the secondary voltage will rise to the breakdown potential of the spark plug, and a discharge between the plug electrodes will occur. This alters the waveform as shown in the bottom trace of Fig. 9-48. After the spark occurs, the voltage is reduced to a lower value until all the energy is dissipated and the arc goes out. The value of this voltage which caused breakdown to occur is called the *required voltage* of the spark plug. The interval during which the spark occurs is called the *spark duration*. The available voltage of the ignition system must always exceed the required voltage of the spark plug to ensure breakdown. The spark must then possess sufficient energy and duration to initiate combustion under all conditions of operation.

The major limitations of the breaker-operated induction-coil system are the decrease in available voltage as engine speed increases due to limitations in the current switching capability of the breaker system, and the decreasing time available to build up the primary coil stored energy. Also, because of the high source impedance (about 500 kΩ) the system is sensitive to side-tracking across the spark plug insulator. A further disadvantage is that due to their high current

load, the breaker points are subject to electrical wear in addition to mechanical wear, which results in short maintenance intervals. The life of the breaker points is dependent on the current they are required to switch. Acceptable life is obtained with  $I_p \approx 4$  A; increased currents cause a rapid reduction in breaker point life and system reliability.

**TRANSISTORIZED COIL IGNITION (TCI) SYSTEMS.** In automotive applications, the need for much reduced ignition system maintenance, extended spark plug life, improved ignition of lean and dilute mixtures, and increased reliability and life has led to the use of coil ignition systems which provide a higher output voltage and which use electronic triggering to maintain the required timing without wear or adjustment (see Refs. 54 and 61). These are called transistorized coil ignition (TCI) or high-energy electronic-ignition systems. The higher output voltage is required because spark plugs are now set to wider gaps (e.g., about 1 mm) to extend the ability to ignite the fuel mixture over a wider range of engine operation, and because during the extended mileage between spark plug replacement electrode erosion further increases the gap. In automotive applications an available ignition voltage of 35 kV is now usually provided. In addition to higher voltage, longer spark duration (about 2 ms) has been found to extend the engine operating conditions over which satisfactory ignition is achieved.

Most of the solid-state ignition systems now in use operate on the same basic principle. Figure 9-49 shows the block circuit diagram of a transistorized coil ignition system. The distributor points and cam assembly of the conventional ignition system are replaced by a magnetic pulse generating system which detects the distributor shaft position and sends electrical pulses to an electronic control module. The module switches off the flow of current to the coil primary windings, inducing the high voltage in the secondary windings which is distributed to the

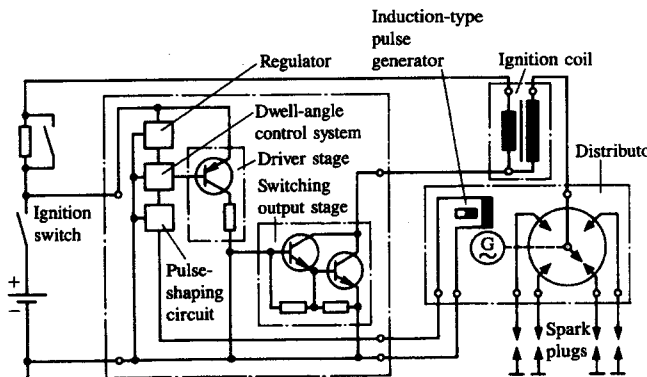


FIGURE 9-49

Schematic of transistorized coil ignition system with induction pulse generator. (Courtesy Robert Bosch GmbH and SAE.<sup>54</sup>)

spark plugs as in the conventional breaker system. The control module contains timing circuits which then close the primary circuit so that buildup of primary circuit current can occur. There are many types of pulse generators that could trigger the electronic circuit of the ignition system.<sup>60</sup> A magnetic pulse generator, where a gear-shaped iron rotor driven by the distributor shaft rotates past the stationary pole piece of the pickup, is usually used. The number of teeth on the rotor is the same as the number of cylinders. A magnetic field is provided by a permanent magnet. As each rotor tooth passes the pole piece it first increases and then decreases the magnetic field strength  $\psi$  linked with the pickup coil, producing a voltage signal proportional to  $d\psi/dt$ . The electronic module switches off the coil current to produce the spark as the rotor tooth passes through alignment and the pickup coil voltage abruptly reverses and passes through zero. The increasing portion of the voltage waveform, after this voltage reversal, is used by the electronic module to establish the point at which the primary coil current is switched on for the next ignition pulse.

**CAPACITIVE-DISCHARGE IGNITION (CDI) SYSTEMS.** With this type of system (shown schematically in Fig. 9-50) a capacitor, rather than an induction coil, is used to store the ignition energy. The capacitance and charging voltage of the capacitor determine the amount of stored energy. The ignition transformer steps up the primary voltage, generated at the time of spark by the discharge of the capacitor through the thyristor, to the high voltage required at the spark plug. The CDI trigger box contains the capacitor, thyristor power switch, charging device (to convert battery voltage to the charging voltage of 300 to 500 V by means of pulses via a voltage transformer), pulse shaping unit, and control unit.

The principal advantage of CDI is its insensitivity to electrical shunts in the high-voltage ignition circuit that result from spark plug fouling. Because of the fast capacitive discharge, the spark is strong but short (0.1 to 0.3 ms). This can lead to ignition failure at operating conditions where the mixture is very lean or dilute.<sup>54</sup>

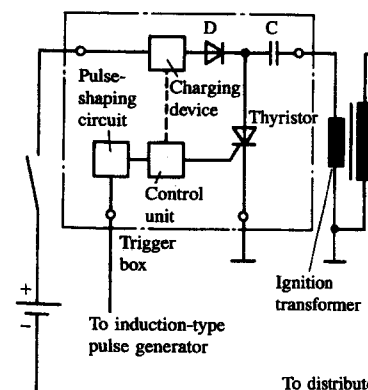
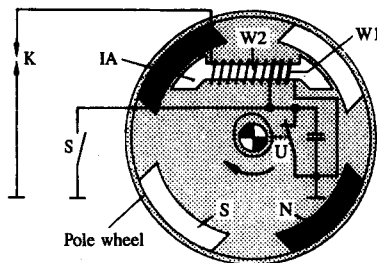


FIGURE 9-50

Schematic of capacitive-discharge system. (Courtesy Robert Bosch GmbH and SAE.<sup>54</sup>)



**FIGURE 9-51**  
Schematic of breaker-triggered magneto system with ignition armature. (Courtesy Robert Bosch GmbH and SAE.<sup>54</sup>)

**MAGNETO IGNITION.** With this type of ignition system, a magneto supplies the ignition voltage for the spark discharge independent of a battery or generator. Magneto ignition is commonly used in small four-stroke and two-stroke engines. Figure 9-51 illustrates the system and its operation. A time-varying magnetic flux  $\Phi_0$  is set up in the ignition armature (IA) as the rotating permanent magnets on the pole wheel generate a current in the closed primary winding W1. This primary current generates an additional flux  $\Phi_I$ , giving a resultant flux  $\Phi_R = \Phi_0 + \Phi_I$ . To generate the ignition voltage, the primary current flow is interrupted and the flux collapses rapidly from  $\Phi_R$  to  $\Phi_0$ , producing a high-voltage pulse in the winding which is connected to the spark plug electrode. The current can be interrupted with contact breakers (breaker-triggered magneto) or with a transistor (semiconductor magneto). Since the flux generated by the rotating pole wheel depends on engine speed, the magnitude of the ignition voltage varies with speed.<sup>54</sup>

**SPARK PLUG DESIGN.** The function of the spark plug is to provide an electrode gap across which the high-voltage discharge occurs which ignites the compressed mixture of fuel vapor and air in the combustion chamber. In addition, it must provide a gas-tight conducting path from the high-voltage wire to the electrode gap. Figure 9-52 shows a typical spark plug design. There are three principal

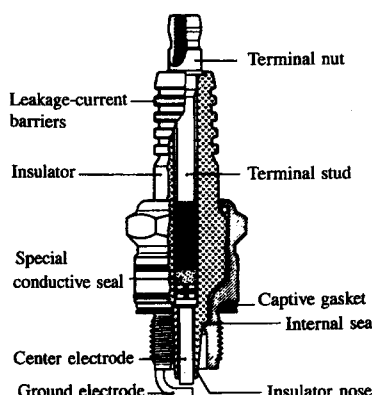


**FIGURE 9-52**  
Cutaway drawing of conventional spark plug.  
(Courtesy Robert Bosch GmbH and SAE.<sup>54</sup>)

components: an insulator, electrodes, and a shell. The insulated material must have adequate thermal shock resistance, tensile and compressive strength, and impact strength. It must also have low porosity to limit absorption of combustion gases and high resistivity to prevent leakage of high-voltage charge at both ambient temperatures and normal operating temperatures. Alumina is usually used as the insulator material.

The electrodes are normally made of high-nickel alloys to withstand the high ignition voltage, high temperatures, and corrosive gases with minimum erosion. The center-electrode surface temperatures can average 650–700°C under normal operating conditions. A wide range of electrode geometries are available.

The location of the special conductive seal within the shell affects the *heat rating* of the spark plug. For a "hot" plug, an insulator with a long conical nose is used; for a "cold" plug a short-nosed insulator is used. The length of the heat conduction path from the insulator nose to the shell is changed in this way to vary and control the temperature of the exposed part of the insulator. The spark plug insulator tip temperature increases with increasing speed. It is desirable to have the tip hotter than about 350°C to prevent fouling at low speed. High-speed high-load tip temperatures must be kept below about 950°C to prevent preignition. Normally, the gap between the center and ground electrodes is 0.7 to 0.9 mm. For extremely dilute mixtures this is usually increased to 1.2 mm. Magneto ignition systems use smaller gaps (~0.5 mm). High-compression-ratio racing engines use smaller gaps (0.3 to 0.4 mm).<sup>54</sup>

### 9.5.3 Alternative Ignition Approaches

A large number of methods for initiating combustion in spark-ignition engines with electrical discharges, in addition to those described in the previous section, have been proposed and examined. These include different designs of spark plug, use of more than one plug, use of higher power, higher energy, or longer-duration discharges, and ignition systems that initiate the main combustion process with a high-temperature reacting jet—plasma-jet and flame-jet ignition systems.<sup>62</sup> Conventional ignition systems normally ignite the unburned fuel, air, burned gas mixture within the cylinder and perform satisfactorily under conditions away from the lean or dilute engine stable operating limit. Thus, these alternative ignition approaches have the goal of extending the engine stability limit (and/or of reducing the cyclic combustion variability near the stability limit), usually by achieving a faster initial burning rate than can be obtained with conventional systems. This section describes the more interesting of these alternative ignition approaches.

**ALTERNATIVE SPARK-DISCHARGE APPROACHES.** There are many different designs of spark plugs. These use different geometry electrodes, gap widths, and gap arrangements. The effects of the major plug electrode design features on the engine's stable lean operating limit are illustrated in Fig. 9-53.<sup>63</sup> Ignition system effects are important when misfire due to the quenching effect of the spark plug

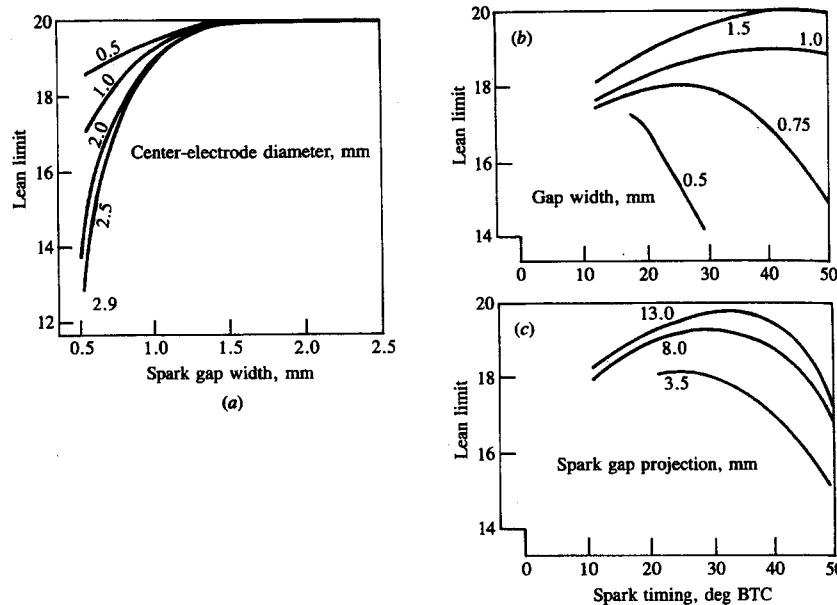


FIGURE 9-53

Effect of spark plug electrode diameter, plug gap width, and projection of gap into chamber on air/fuel ratio at engine's lean stable operating limit. Baseline conditions: 30 mJ spark energy, 3.5 mm projection, center electrode diameter 2.5 mm, gap width 0.75 mm, 40° BTC spark timing, 1600 rev/min, intake pressure 300 mmHg.<sup>63</sup>

electrodes determines the stable operating limit.<sup>†</sup> Thus, smaller spark plug center-electrode diameters (Fig. 9-53a), larger electrode gap widths (Fig. 9-53b), and higher electrode temperatures (obtained by projecting the gap further into the combustion chamber; Fig. 9-53c), all extend the lean stability limit to leaner (or more dilute) mixtures for the more advanced spark timings and smaller gap widths. For spark timing closer to TC and for larger gap widths, these data show the lean stability limit to be much less sensitive (or not sensitive at all) to plug geometry or spark energy. Multigap plugs, designed to produce a series of discharges which together form a long arc, have also been used to generate a larger initial flame kernel and thereby extend the lean limit.

Use of more than one plug, at separate locations in the combustion chamber and fired simultaneously, is also common.<sup>49</sup> The advantages are twofold. First, the effective flame area in the early stages of flame development is increased substantially (e.g., by almost a factor of two for two widely spaced plugs). Second, the variations in flow velocity and mixture composition in the vicinity of the (multiple) plugs produce less variability in the initial mixture burning rate than occurs with a single plug. Studies of heat-release rates, flame

development angle, and rapid-burning angle, and imep and torque fluctuations have defined the effects of both increasing the number of ignition sites from 1 to 12 and of changing their geometric location.<sup>64</sup> These results confirm that increasing the number of simultaneously developing flame kernels increases the initial mixture burning rate, as anticipated. It also extends the lean stable operating limit and reduces cyclic combustion variability under conditions where slow and occasional partial-burning cycles would occur with fewer spark plug gaps.

Many studies have examined the effects of higher-energy discharges on engine operation near the lean operating limit. It is useful to differentiate between higher current discharges and longer duration discharges: most high-energy (conventional-type) ignition systems have both these features. The results of these studies show that away from the lean or dilute stable operating limit, increasing the discharge current or duration has no significant effect on engine operating characteristics. The higher current does, as would be expected, result in a larger flame kernel during the inflammation process and thereby modestly reduces the spark advance required for maximum brake torque with a given combustion chamber and set of operating conditions. Figure 9-54 shows these trends for rich, stoichiometric, and slightly lean mixtures. The figure also shows that both higher

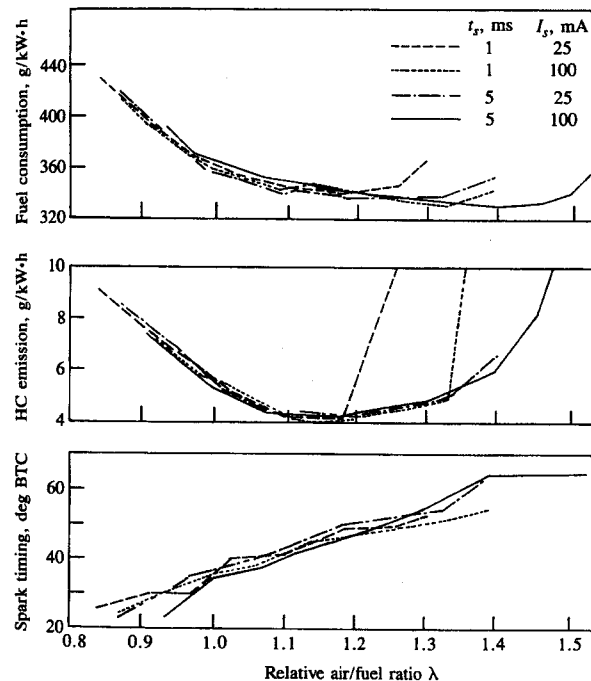


FIGURE 9-54  
Effect of higher spark currents  $I_s$  and longer spark durations  $t_s$  on fuel consumption, HC emissions, and MBT spark timing, as a function of relative air/fuel ratio  $\lambda$  ( $= 1/\phi$ ). 2000 rev/min, bmepl = 3 atm, 2.8-dm<sup>3</sup> six-cylinder engine.<sup>65</sup>

<sup>†</sup> See Sec. 9.4.3 for a detailed discussion of the stable operating limit.

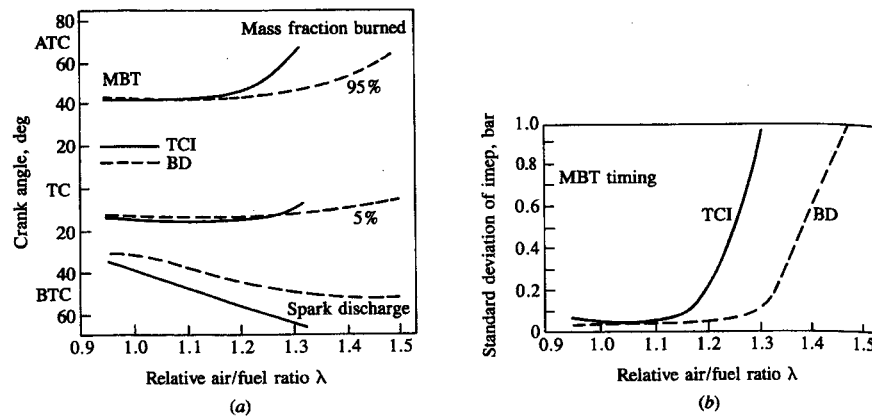


FIGURE 9-55

(a) MBT spark timing and location of 5 and 95 percent mass fraction burned points for conventional transistorized coil ignition (TCI) system (43 mJ energy, 2 ms duration) and breakdown system (BD) (43 mJ energy, ~10 ns duration) as function of relative air/fuel ratio  $\lambda$  ( $= 1/\phi$ ). (b) Standard deviation in indicated mean effective pressure as a function of relative air/fuel ratio  $\lambda$  for TCI and BD systems.<sup>66</sup>

currents and longer duration discharges do extend the lean engine stability limit [and also the dilute (with EGR) stability limit]. Note the HC emissions data, which indicate that longer discharges have a greater impact than higher currents on extending the *misfire* limit. The increase in fuel consumption as the lean operating limit is approached is due to the rapidly increasing cycle-by-cycle combustion variability.

The discussion of discharge fundamentals in Sec. 9.5.1 showed that depositing energy into the discharge during the initial short breakdown phase resulted in faster flame kernel growth than did depositing the same energy at slower rates. Ignition systems of this type have been used. In such systems, a capacitor is connected in parallel with the spark plug electrodes, and a low-impedance discharge path allows the energy stored in the capacitor to be discharged into the gap very rapidly. The anticipated effects on the engine's combustion process are observed. Away from the lean engine stability limit, the primary impact is a reduction in the flame development period due to the more rapid initial flame kernel growth. Thus MBT timing is less advanced with these breakdown systems than with conventional systems (see Fig. 9-55a). The lean limit can also be extended, and acceptable engine stability obtained (i.e., tolerable cycle-by-cycle combustion variations) for leaner or more dilute engine operation, as shown in Fig. 9-55b.<sup>66, 67</sup>

**PLASMA-JET IGNITION.** In a plasma-jet ignitor, the spark discharge is confined within a cavity that surrounds the plug electrodes, which connects with the combustion chamber via an orifice. The electrical energy supplied to the plug elec-

trodes is substantially increased above values used in normal ignition systems by allowing a capacitor to discharge at a relatively low voltage and high current through the spark generated in a conventional manner with a high-voltage low-current ignition system. Stored energies of about 1 J are typically used, and this energy is discharged in some 20  $\mu$ s. This high-power discharge creates a high-temperature plasma so rapidly that the pressure in the cavity increases substantially, causing a supersonic jet of plasma to flow from the cavity into the main combustion chamber. The plasma enters the combustion chamber as a turbulent jet, preceded by a hemispherical blast wave. The gas dynamic effects of the blast wave are dissipated by the time combustion starts, which is typically of order 1 ms after the discharge commences. Ignition in the main combustion chamber takes place in the turbulent jet; the flame starts out as a turbulent flame in contrast to the flame with conventional ignition systems, which is initially laminarlike. The penetration of the jet depends on its initial momentum; it thus depends on the amount of energy deposited, cavity size, and orifice area. If the cavity is filled prior to ignition with a hydrocarbon (or a mixture of hydrocarbons) the ignition capabilities are enhanced due to the large increase in hydrogen atoms created in the plasma.<sup>62</sup>

The effects of plasma-jet ignitors on engine combustion are similar to those of breakdown ignition systems: the flame development period is significantly shortened, and the engine's lean stable operating limit is extended. In addition, the phenomenon of misfire, which is the failure to initiate combustion in a fraction of the engine's operating cycles, no longer occurs.<sup>68</sup> The lean operating limit of the engine is, however, normally controlled by flame extinguishment.

**FLAME-JET IGNITION.** With this type of system, ignition occurs in a prechamber cavity which is physically separated from the main chamber above the piston and is connected to it via one or more orifices or nozzles. As the flame develops in this cavity the pressure of the gases in the prechamber rises, forcing gas out into the main chamber through the orifice (or orifices) as one or more turbulent burning jets. The jet or jets penetrate into the main chamber, igniting the unburned mixture in the main chamber, thereby initiating the primary combustion process. Ignition within the cavity is usually achieved with a conventional spark discharge. The function of the prechamber or cavity is to transform the initial flame around the spark plug electrodes into one or more flame jets in the main chamber, which have a substantial surface area that can ignite extremely lean or dilute mixtures in a repeatable manner. Many different systems for achieving this goal have been developed; some of these have been used in production spark-ignition engines. Examples of the three major types of flame-jet ignition systems are shown in Fig. 9-56.

Figure 9-56a shows an example of the simplest type of flame-jet ignition concept (often called a *torch cell*). The cavity has no separate valve so is unscavenged; nor is there any prechamber fuel metering system. The function of the prechamber cavity is to increase the initial growth rate of the flame immediately following spark discharge by having this flame growth take place in a

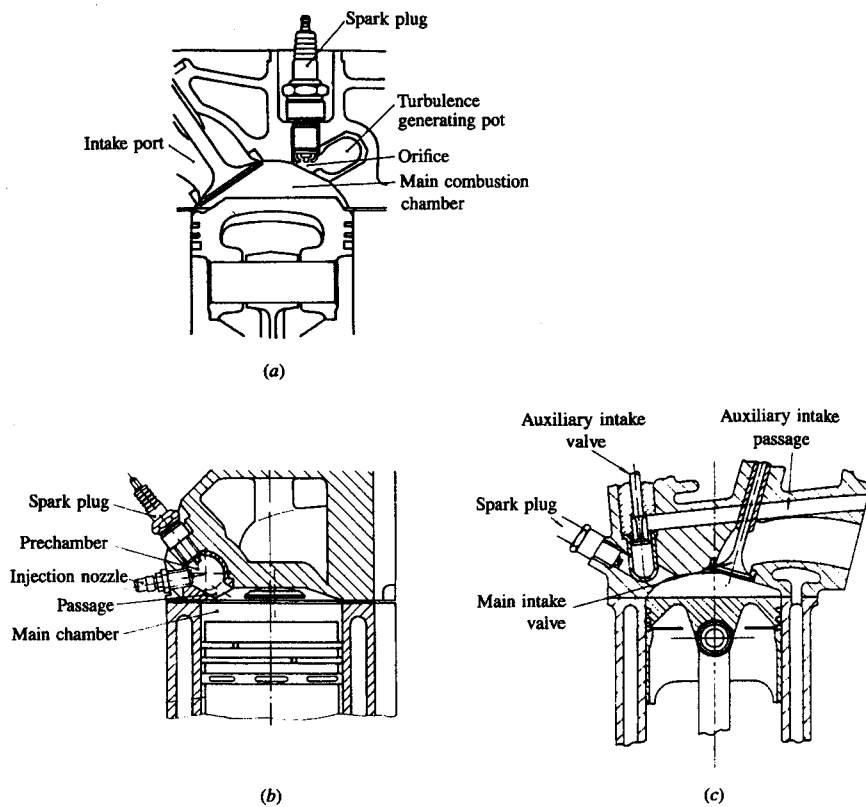


**FIGURE 9-56**  
Flame-jet ignition concepts: (a) turbulence-generating torch cell;<sup>69</sup> (b) prechamber stratified-charge engine with auxiliary fuel injector with no prechamber scavenging;<sup>70</sup> (c) prechamber stratified-charge engine with prechamber inlet valve and auxiliary carburetor.<sup>71</sup>

more turbulent region than the main combustion chamber: the flame jet or jets which then emerge from the cavity produce a large initial flame surface area in the main chamber to start the bulk charge combustion process. The prechamber system shown was called a turbulent generating pot.<sup>69</sup> Another approach is to incorporate the cavity into the spark plug. Systems with prechamber volumes varying from 20 percent of the clearance volume to less than 1 percent have been developed. The flow pattern produced within the prechamber by the flow into the cavity during compression and the location of the spark plug electrodes within the cavity and of the nozzle or orifice are critical design issues. A major problem with these systems is that the prechamber is never completely scavenged by fresh mixture between cycles, so the burned gas fraction in the unburned mixture within the prechamber is always substantially higher than the burned gas fraction in the unburned main chamber mixture.<sup>72</sup>

Figure 9-56b and c shows two *prechamber stratified-charge* engine flame-jet ignition concepts. Here the mixture in the prechamber cavity is enriched by addition of fuel so that it ends up being slightly rich-of-stoichiometric at the time of spark discharge. The initial inflammation process in the cavity then occurs more rapidly and more repeatably. The operating principle of these stratified-charge systems is described briefly in Sec. 1.9. Figure 9-56b shows a system where the prechamber is unscavenged and fuel is injected directly into the prechamber cavity (in addition to the main fuel-injection process which occurs into the fresh charge in the intake system) to enrich the mixture (which is lean overall) at the time of spark to an easily ignitable rich-of-stoichiometric composition. With this approach, the prechamber volume is usually 20 to 25 percent of the clearance volume. Figure 9-56c shows a prechamber stratified-charge flame-jet ignition system where the prechamber is scavenged between each combustion event. With this approach, a separate small intake valve feeds very rich mixture into the prechamber during the intake process, while the main fuel metering system feeds lean mixture to the main intake valve. During intake the prechamber is completely scavenged by the rich intake stream. During compression the lean mixture flowing from the main chamber to the prechamber brings the prechamber mixture equivalence ratio to slightly rich-of-stoichiometric at the time of spark discharge.<sup>71</sup>

The number and size of the orifices connecting the prechamber and the main chamber have a significant effect on the development of the main chamber burning process. Two different approaches are shown in the flame development stage in Fig. 9-57. Figure 9-57a shows the jets produced when the prechamber has more than one small nozzle which direct the burning prechamber mixture deep into the main chamber charge. A fast burning of the lean main-chamber charge results. With this approach, prechamber volumes of 2 to 3 percent of the clearance volume and nozzle area/prechamber volume ratios of  $0.03$  to  $0.04 \text{ cm}^{-1}$  are used. Figure 9-57b shows the approach used by Honda in their CVCC engine.

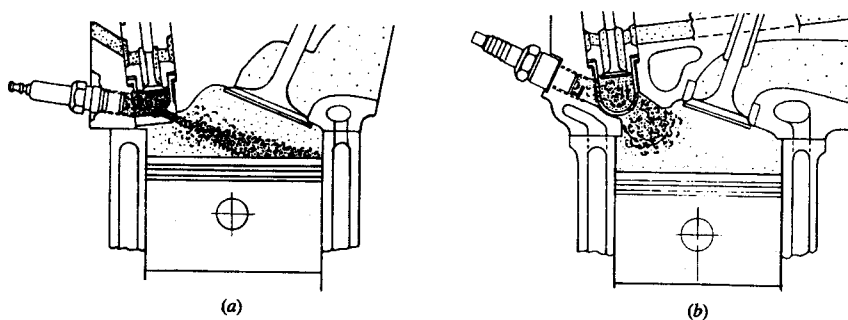


**FIGURE 9-57**  
Two different approaches to prechamber orifice design with the prechamber stratified-charge carbureted and scavenged engine: (a) one or more small orifice(s) for deep jet penetration and faster burning process; (b) large orifice for lower-velocity jet and slower burn.<sup>73</sup>

A larger prechamber (5 to 12 percent) and larger orifice (orifice area/prechamber volume ratio of 0.04 to 0.2  $\text{cm}^{-1}$ ) gives a lower velocity jet which penetrates the main chamber charge more slowly, resulting in a slower burn.

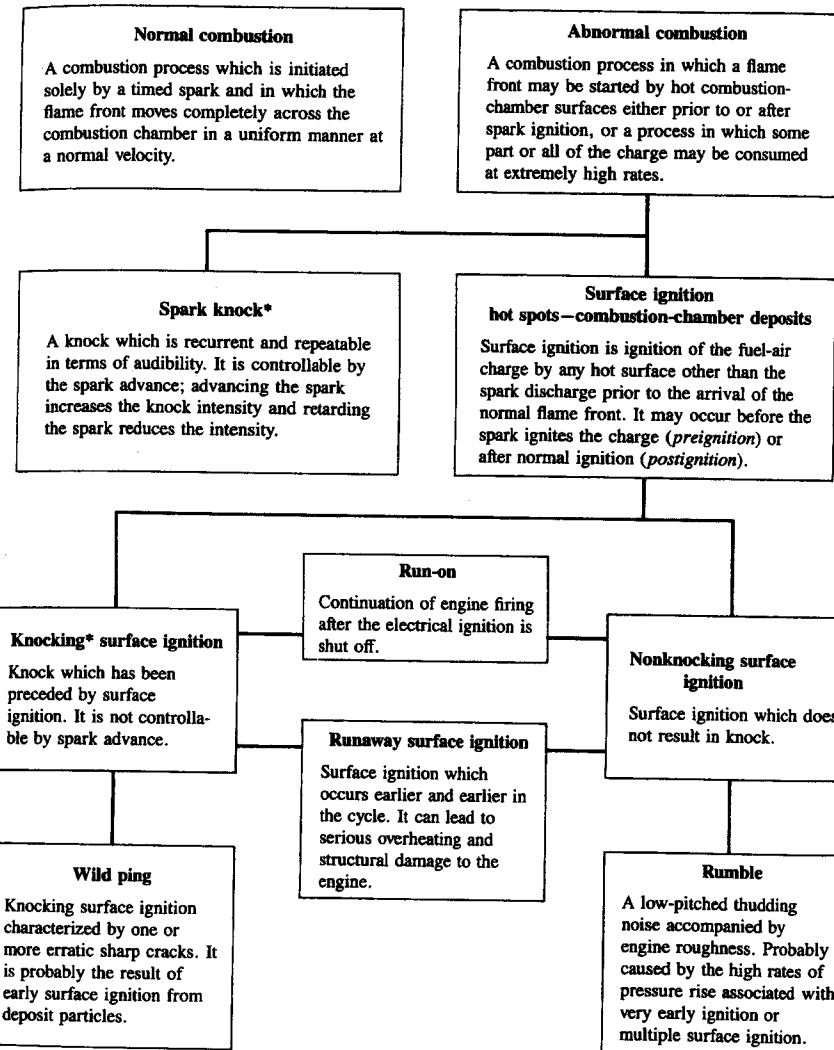
All these concepts extend the engine's lean stable operating limit, relative to equivalent conventional engines, by several air/fuel ratios. For example, the unscavenged cavity without auxiliary fueling can operate satisfactorily at part-load with air/fuel ratios of 18 (equivalence ratio  $\phi \approx 0.8$ , relative air/fuel ratio  $\lambda \approx 1.25$ ). The prechamber stratified-charge flame-jet ignition concepts can operate much leaner than this; however, the best combination of fuel consumption and emissions characteristics is obtained with  $\phi \approx 0.9 - 0.75$ ,  $\lambda \approx 1.1 - 1.3$ .<sup>70, 71</sup> One performance penalty associated with all these flame-jet ignition concepts is the additional heat losses to the prechamber walls due to increased surface area and flow velocities. The stratified-charge prechamber concepts also suffer an efficiency penalty, relative to equivalent operation with uniform air/fuel ratios, due to the presence of fuel-rich regions during the combustion process.

## 9.6 ABNORMAL COMBUSTION: KNOCK AND SURFACE IGNITION

### 9.6.1 Description of Phenomena

Abnormal combustion reveals itself in many ways. Of the various abnormal combustion processes which are important in practice, the two major phenomena are knock and surface ignition. These abnormal combustion phenomena are of concern because: (1) when severe, they can cause major engine damage; and (2) even if not severe, they are regarded as an objectionable source of noise by the engine or vehicle operator. *Knock* is the name given to the noise which is transmitted through the engine structure when essentially spontaneous ignition of a portion of the end-gas—the fuel, air, residual gas, mixture ahead of the propagating flame—occurs. When this abnormal combustion process takes place, there is an extremely rapid release of much of the chemical energy in the end-gas, causing very high local pressures and the propagation of pressure waves of substantial amplitude across the combustion chamber. *Surface ignition* is ignition of the fuel-air mixture by a hot spot on the combustion chamber walls such as an overheated valve or spark plug, or glowing combustion chamber deposit: i.e., by any means other than the normal spark discharge. It can occur before the occurrence of the spark (*preignition*) or after (*postignition*). Following surface ignition, a turbulent flame develops at each surface-ignition location and starts to propagate across the chamber in an analogous manner to what occurs with normal spark ignition.

Because the spontaneous ignition phenomenon that causes knock is governed by the temperature and pressure history of the end gas, and therefore by the phasing and rate of development of the flame, various combinations of these two phenomena—surface ignition and knock—can occur. These have been categorized as indicated in Fig. 9-58. When autoignition occurs repeatedly, during



\*Knock: The noise associated with autoignition of a portion of the fuel-air mixture ahead of the advancing flame front. Autoignition is the spontaneous ignition and the resulting very rapid reaction of a portion or all of the fuel-air mixture.

FIGURE 9-58

Definition of combustion phenomena—normal and abnormal (knock and surface ignition)—in a spark-ignition engine. (Courtesy Coordinating Research Council.)

otherwise normal combustion events, the phenomena is called *spark-knock*. Repeatedly here means occurring more than occasionally: the knock phenomenon varies substantially cycle-by-cycle, and between the cylinders of a multi-cylinder engine, and does not necessarily occur every cycle (see below). Spark-knock is controllable by the spark advance: advancing the spark increases the knock severity or intensity and retarding the spark decreases the knock. Since surface ignition usually causes a more rapid rise in end-gas pressure and temperature than occurs with normal spark ignition (because the flame either starts propagating sooner, or propagates from more than one source), knock is a likely outcome following the occurrence of surface ignition. To identify whether or not surface ignition causes knock, the terms knocking surface ignition and non-knocking surface ignition are used. Knocking surface ignition usually originates from preignition caused by glowing combustion chamber deposits: the severity of knock generally increases the earlier that preignition occurs. Knocking surface ignition cannot normally be controlled by retarding the spark timing, since the spark-ignited flame is not the cause of knock. Nonknocking surface ignition is usually associated with surface ignition that occurs late in the operating cycle.

The other abnormal combustion phenomena in Fig. 9-58, while less common, have the following identifying names. Wild ping is a variation of knocking surface ignition which produces sharp cracking sounds in bursts. It is thought to result from early ignition of the fuel-air mixture in the combustion chamber by glowing loose deposit particles. It disappears when the particles are exhausted and reappears when fresh particles break loose from the chamber surfaces. Rumble is a relatively stable low-frequency noise (600 to 1200 Hz) phenomenon associated with deposit-caused surface ignition in high-compression-ratio engines. This type of surface ignition produces very high rates of pressure rise following ignition. Rumble and knock can occur together. Run-on occurs when the fuel-air mixture within the cylinder continues to ignite after the ignition system has been switched off. During run-on, the engine usually emits knocklike noises. Run-on is probably caused by compression ignition of the fuel-air mixture, rather than surface ignition. Runaway surface ignition is surface ignition that occurs earlier and earlier in the cycle. It is usually caused by overheated spark plugs or valves or other combustion chamber surfaces. It is the most destructive type of surface ignition and can lead to serious overheating and structural damage to the engine.<sup>74</sup>

After some additional description of surface-ignition phenomena, the remainder of Sec. 9.6 will focus on knock. This is because surface ignition is a problem that can be solved by appropriate attention to engine design, and fuel and lubricant quality. In contrast, knock is an inherent constraint on engine performance and efficiency since it limits the maximum compression ratio that can be used with any given fuel.

Of all the engine surface-ignition phenomena in Fig. 9-58, preignition is potentially the most damaging. Any process that advances the start of combustion from the timing that gives maximum torque will cause higher heat rejection because of the increasing burned gas pressures and temperatures that result.

Higher heat rejection causes higher temperature components which, in turn, can advance the preignition point even further until critical components can fail. The parts which can cause preignition are those least well cooled and where deposits build up and provide additional thermal insulation: primary examples are spark plugs, exhaust valves, metal asperities such as edges of head cavities or piston bowls. Under normal conditions, using suitable heat-range spark plugs, preignition is usually initiated by an exhaust valve covered with deposits coming from the fuel and from the lubricant which penetrates into the combustion chamber. Colder running exhaust valves and reduced oil consumption usually alleviate this problem: locating the exhaust valve between the spark plug and the end-gas region avoids contact with both the hottest burned gas near the spark plug and the end-gas. Engine design features that minimize the likelihood of preignition are: appropriate heat-range spark plug, removal of asperities, radiused metal edges, well-cooled exhaust valves with sodium-cooled valves as an extreme option.<sup>75, 76</sup>

Knock primarily occurs under wide-open-throttle operating conditions. It is thus a direct constraint on engine performance. It also constrains engine efficiency, since by effectively limiting the temperature and pressure of the end-gas, it limits the engine compression ratio. The occurrence and severity of knock depend on the knock resistance of the fuel and on the antiknock characteristics of the engine. The ability of a fuel to resist knock is measured by its octane number: higher octane numbers indicate greater resistance to knock (see Sec. 9.6.3). Gasoline octane ratings can be improved by refining processes, such as catalytic cracking and reforming, which convert low-octane hydrocarbons to high-octane hydrocarbons. Also, antiknock additives such as alcohols, lead alkyls, or an organomanganese compound can be used. The octane-number requirement of an engine depends on how its design and the conditions under which it is operated affect the temperature and pressure of the end-gas ahead of the flame and the time required to burn the cylinder charge. An engine's tendency to knock, as defined by its *octane requirement*—the octane rating of the fuel required to avoid knock—is increased by factors that produce higher temperatures and pressures or lengthen the burning time. Thus knock is a constraint that depends on both the quality of available fuels and on the ability of the engine designer to achieve the desired normal combustion behavior while holding the engine's propensity to knock at a minimum.<sup>74</sup>

The pressure variation in the cylinder during knocking combustion indicates in more detail what actually occurs. Figure 9-59 shows the cylinder pressure variation in three individual engine cycles, for normal combustion, light knock, and heavy knock, respectively.<sup>77</sup> When knock occurs, high-frequency pressure fluctuations are observed whose amplitude decays with time. Figures 9-59a and b have the same operating conditions and spark advance. About one-third of the cycles in this engine at these conditions had no trace of knock and had normal, smoothly varying, cylinder pressure records as in Fig. 9-59a. Knock of varying severity occurred in the remaining cycles. With light or trace knock, knock occurs late in the burning process and the amplitude of the pressure fluctuations

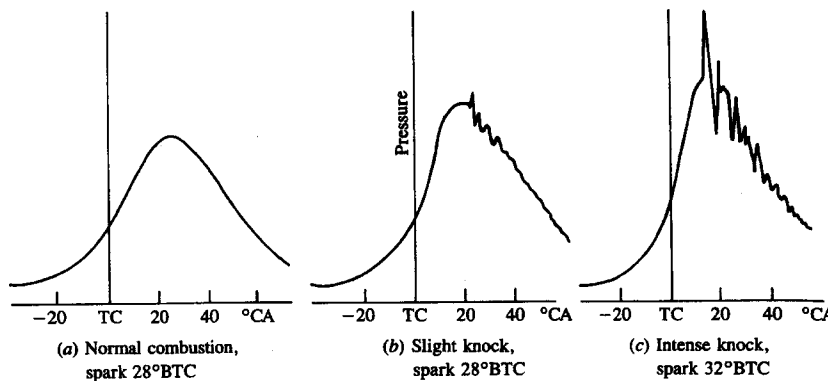


FIGURE 9-59

Cylinder pressure versus crank angle traces of cycles with (a) normal combustion, (b) light knock, and (c) heavy knock. 4000 rev/min, wide-open throttle, 381-cm<sup>3</sup> displacement single-cylinder engine.<sup>77</sup>

is small (Fig. 9-59b). With heavy knock, illustrated here with more advanced spark timing and by selecting an especially high intensity knocking cycle, knock occurs closer to top-center earlier in the combustion process and the initial amplitude of the pressure fluctuation is much larger. These pressure fluctuations produce the sharp metallic noise called "knock." They are the result of the essentially spontaneous release of much of the end-gas fuel's chemical energy. This produces a substantial *local* increase in gas pressure and temperature, thereby causing a shock wave to propagate away from the end-gas region across the combustion chamber. This shock wave, the expansion wave that accompanies it, and the reflection of these waves by the chamber walls create the oscillatory pressure versus time records shown in Fig. 9-59b and c. Note that once knock occurs, the pressure distribution across the combustion chamber is no longer uniform: transducers located at different points in the chamber will record different pressure levels at a given time until the wave propagation phenomena described above have been damped out.<sup>78</sup>

Many methods of knock detection and characterization have been used. The human ear is a surprisingly sensitive knock detector and is routinely used in determining the octane requirement of an engine—the required fuel quality the engine must have to avoid knock. Knock detectors used for knock control systems normally respond to the vibration-driven acceleration of parts of the engine block caused by knocking combustion pressure waves. A high-intensity flash is observed when knock occurs; this is accompanied by a sharp increase in ionization. Optical probes and ionization detectors have therefore been used. The spark plug can serve as an ionization detector. For more detailed studies of knock in engines, the piezoelectric pressure transducer is the most useful monitoring device. Often the transducer signal is filtered so that the pressure fluctuations caused by knock are isolated.<sup>75</sup>

The amplitude of the pressure fluctuation is a useful measure of the inten-

sity of knock because it depends on the amount of end-gas which ignites spontaneously and rapidly, and because engine damage due to knock results from the high gas pressures (and temperatures) in the end-gas region. Use of this measure of knock severity or intensity shows there is substantial variation in the extent of knock, cycle-by-cycle. Figure 9-60 shows the knock intensity in one hundred consecutive cycles in a given cylinder of a multicylinder engine operating at fixed conditions for knocking operation. The intensity varies randomly from essentially no knock to heavy knock.<sup>79</sup> Cylinder-to-cylinder variations are also substantial due to variations in compression ratio, mixture composition and conditions, burn rate, and combustion chamber cooling. One or more cylinders may not knock at all while others may be knocking heavily.<sup>80</sup>

Since the knock phenomenon produces a nonuniform state in the cylinder, and since the details of the knock process in each cycle and in each cylinder are different, a fundamental definition of knock intensity or severity is extremely difficult. The ASTM-CFR method for rating fuel octane quality (see Sec. 9.6.3) by the severity of knocking combustion uses the time derivative of pressure during the cycle. Cylinder pressure is determined with a pressure transducer. The low-frequency component of pressure change due to normal combustion is filtered out and the rate of pressure rise is averaged over many cycles during the pressure fluctuations following knock. This approach obviously provides only an average relative measure of knock intensity. The maximum rate of pressure rise has been used to quantify knock severity. An accelerometer mounted on the engine can give indications of relative knock severity provided that it is mounted in the same location for all tests. The most precise measure of knock severity is the maximum amplitude of the pressure oscillations that occur with knocking combustion. The cylinder pressure signal (from a high-frequency response pressure transducer) is filtered with a band-pass filter so that only the component of the pressure signal that corresponds to the fluctuations occurring after knock remains. The filter is set for the first transverse mode of gas vibration in the cylinder (in the 3 to 10 kHz range, depending on bore and chamber geometry). The maximum amplitude of pressure oscillation gives a good indication of the severity of knock.<sup>81</sup> The knock intensities in individual cycles shown in Fig. 9-60 were determined in

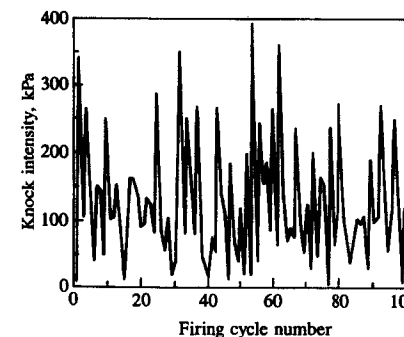


FIGURE 9-60

Knock intensity (maximum amplitude of band-pass-filtered pressure signal) in one hundred individual consecutive cycles. One cylinder of V-8 engine, 2400 rev/min, wide-open throttle.<sup>79</sup>

this manner.<sup>79</sup> Note that because the pressure fluctuations are the consequence of a wave propagation phenomenon, the location of the pressure transducer in relation to the location of the knocking end-gas and the shape of the combustion chamber will affect the magnitude of the maximum recorded pressure-fluctuation amplitude.

The impact of knock depends on its intensity and duration. Trace knock has no significant effect on engine performance or durability. Heavy knock can lead to extensive engine damage. In automobile applications, a distinction is usually made between "acceleration knock" and "constant-speed knock." Acceleration knock is primarily an annoyance, and due to its short duration is unlikely to cause damage. Constant-speed knock, however, can lead to two types of engine damage. It is especially a problem at high engine speeds where it is masked by other engine noises and is not easily detected. Heavy knock at constant speed can easily lead to:

1. Preignition, if significant deposits are present on critical combustion chamber components. This could lead to runaway preignition.<sup>†</sup>
2. Runaway knock—spark-knock occurring earlier and earlier, and therefore more and more intensely. This soon leads to severe engine damage.
3. Gradual erosion of regions of the combustion chamber, even if runaway knock does not occur.

The engine can be damaged by knock in different ways: piston ring sticking; breakage of the piston rings and lands; failure of the cylinder head gasket; cylinder head erosion; piston crown and top land erosion; piston melting and holing. Examples of component damage due to preignition and knock are shown in Fig. 9-61.<sup>82-84</sup>

The mechanisms that cause this damage are thought to be the following. Preignition damage is largely thermal as evidenced by fusion of spark plugs or pistons. When knock is very heavy, substantial additional heat is transferred to the combustion chamber walls and rapid overheating of the cylinder head and piston results. Under these conditions, knock is not stable: the overheating increases the engine's octane requirement which in turn increases the intensity of knock. It becomes heavier and heavier, and the uncontrolled running away of this phenomena can lead to engine failure in minutes. This damage is due to overheating of the engine: the piston and rings seize in the bore. The damage due to heavy knock over extended periods—erosion of piston crowns and (aluminum) cylinder heads in the end-gas region—is due primarily to the high gas pressures in this region. Extremely high pressure pulses of up to 180 atm due to heavy knock can occur locally in the end-gas region, in the 5 to 10 kHz frequency

<sup>†</sup> Note that heavy knock can also remove deposits from the combustion chamber walls, thereby decreasing the octane requirement of the engine.

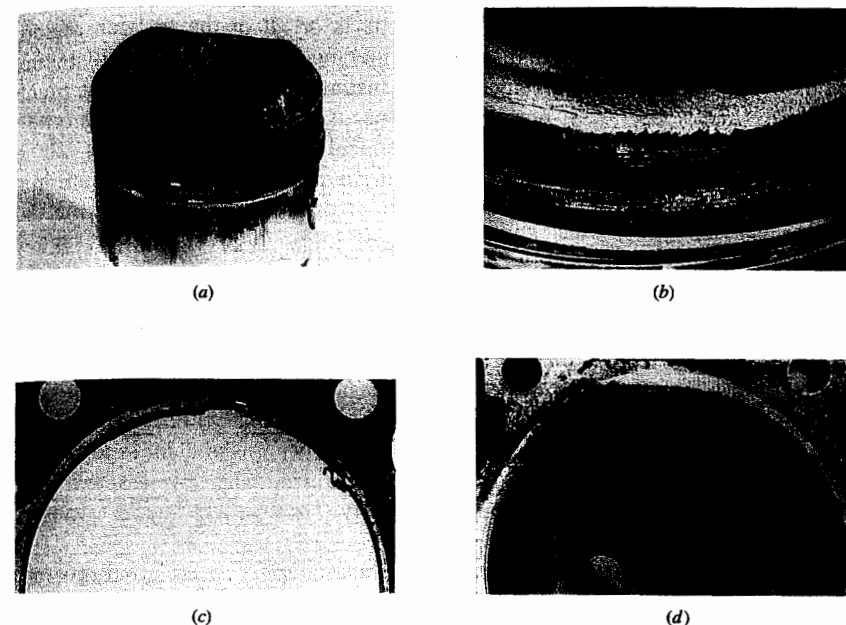


FIGURE 9-61

Examples of component damage from abnormal engine combustion. (a) Piston holing by preignition;<sup>83</sup> (b) piston crown erosion after 10 hours of high-speed knocking;<sup>82</sup> (c) cylinder head gasket splitting failure due to heavy knock;<sup>83</sup> (d) erosion of aluminum cylinder head along the top of the cylinder liner due to heavy knock.<sup>83</sup>

range. These high local pressures are combined with the higher-than-normal local surface temperatures which occur with the higher knocking heat fluxes and weaken the material. Pitting and erosion due to fatigue with these excessive mechanical stresses, and breakage of rings and lands, can then occur.<sup>78, 82-84</sup>

### 9.6.2 Knock Fundamentals

As yet, there is no complete fundamental explanation of the knock phenomenon over the full range of engine conditions at which it occurs. It is generally agreed that knock originates in the extremely rapid release of much of the energy contained in the end-gas ahead of the propagating turbulent flame, resulting in high local pressures. The nonuniform nature of this pressure distribution causes pressure waves or shock waves to propagate across the chamber, which may cause the chamber to resonate at its natural frequency. Two theories have been advanced to explain the origin of knock: the autoignition theory and the detonation theory. The former holds that when the fuel-air mixture in the end-gas region is compressed to sufficiently high pressures and temperatures, the fuel oxidation process—starting with the preflame chemistry and ending with rapid

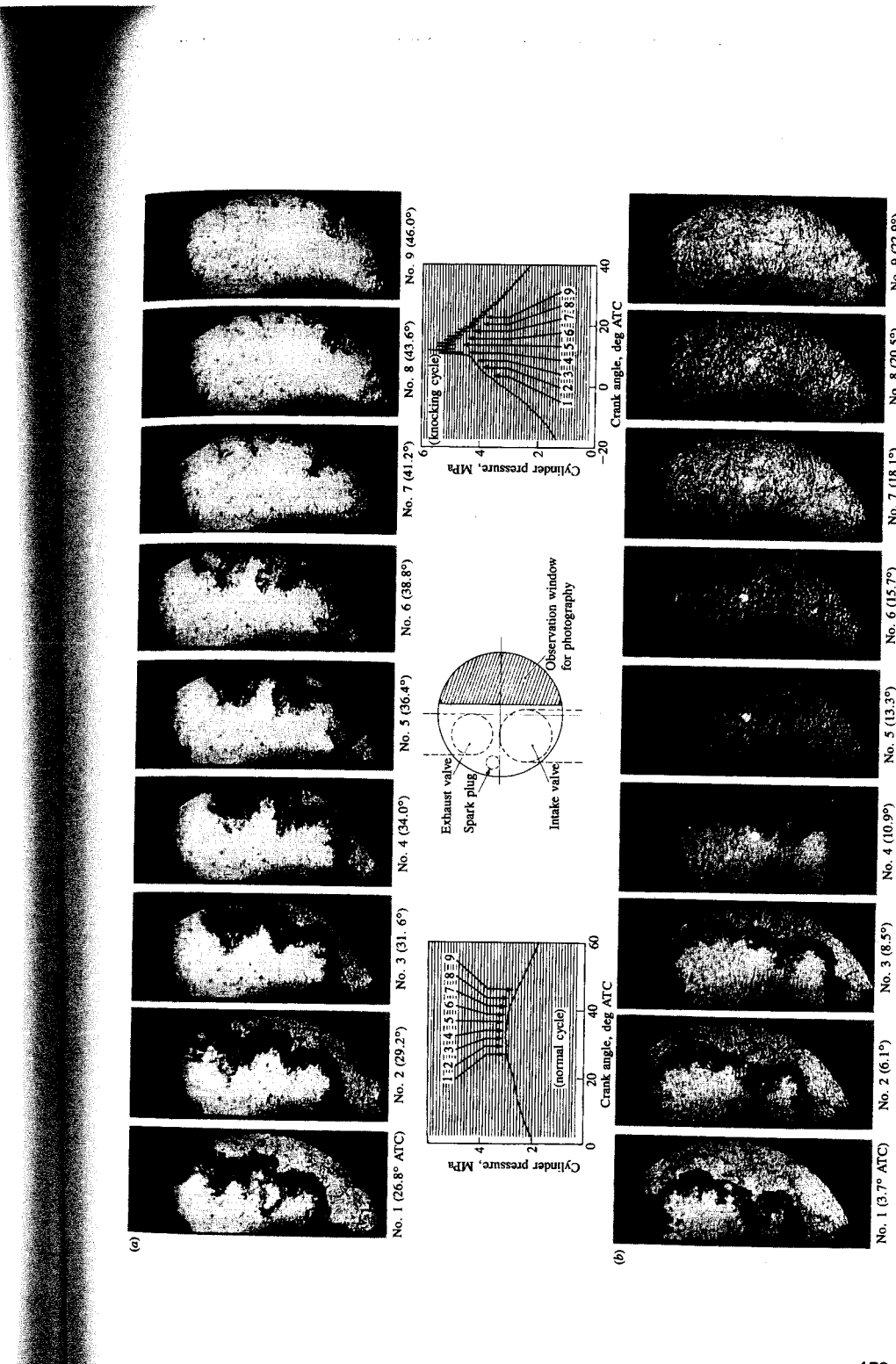
energy release—can occur spontaneously in parts or all of the end-gas region. The latter theory postulates that, under knocking conditions, the advancing flame front accelerates to sonic velocity and consumes the end-gas at a rate much faster than would occur with normal flame speeds.<sup>75</sup> These theories attempt to describe what causes the rapid release of chemical energy in the end-gas which creates very high pressures, locally, in the end-gas region. The engine phenomenon "knock" includes also the propagation of strong pressure waves across the chamber, chamber resonance, and transmission of sound through the engine structure. The detonation theory has led many to call knock "detonation." However, the more general term "knock" is preferred, since this engine phenomenon includes more than the end-gas energy release, and there is much less evidence to support the detonation theory than the autoignition theory as the initiating process. Most recent evidence indicates that knock originates with the spontaneous or autoignition of one or more local regions within the end-gas. Additional regions (some adjacent to already ignited regions and some separated from these regions) then ignite until the end-gas is essentially fully reacted. This sequence of processes can occur extremely rapidly. Thus, the autoignition theory is most widely accepted.

Photographic studies of knocking combustion have been an important source of insight into the fundamentals of the phenomenon over the past fifty years.<sup>†</sup> Figure 9-62 shows two sets of schlieren photographs, one from a cycle with normal combustion and the other from a cycle with knock.<sup>88</sup> These photographs were taken in an overhead valve engine with a disc-shaped combustion chamber, with a window which permits observation of the chamber opposite to the spark plug. A reflecting mirror on the piston crown permits use of the schlieren technique which identifies regions where changes in gas density exist. Operating conditions, except for spark advance, were the same for both cycles. In the normal combustion sequence, the turbulent flame front moves steadily through the end-gas as combustion goes to completion. The cylinder pressure varies smoothly throughout this process. When the spark is advanced by 15°, the end-gas temperature and pressure are increased significantly and knock occurs. In this sequence of photographs (b), the initial flame propagation process (photographs 1 to 3) is like that of the normal combustion sequence: then almost

<sup>†</sup> See Refs. 85 to 87 for early high-speed photographic studies. See Refs. 88 to 91 for some recent studies.

FIGURE 9-62

Schlieren photographs from high-speed movies of (a) normal flame propagation through the end gas and (b) knocking combustion (autoignition occurs in photograph 4), with corresponding cylinder pressure versus crank angle traces. Disc-shaped combustion chamber with details of window shown in insert. 1200 rev/min, 80 percent volumetric efficiency,  $(A/F) = 12.5$ ; spark timing: (a) 10° BTC, (b) 25° BTC.<sup>88</sup>



the entire region ahead of the flame appears dark (photograph 4). Between photographs 3 and 4 substantial changes in the density and temperature throughout most of the end-gas region have occurred. Examination of the cylinder pressure trace shows that this corresponds closely to the time when the pressure recorded by the pressure transducer rises rapidly. Immediately after this, pressure oscillations (at 6 to 8 kHz) are detected. In photograph 5 the flame is no longer visible: the end-gas expansion has pushed the flame back out of the field of view. Subsequent photographs are alternatively lighter and darker, indicative of changing local density fields as pressure waves propagate back and forth across the chamber.

More extensive studies of this type, which relate photographs from high-speed movies of the combustion process to the cylinder pressure development, indicate that the location or locations where ignition of one or more portions of the end-gas first occur and the subsequent rate with which the ignition process develops throughout the rest of the end-gas vary substantially cycle-by-cycle and with the intensity of the knocking process. Figure 9-63 shows five shadowgraph photographs from a knocking engine cycle in a research engine similar to that shown in Fig. 9-62.<sup>89</sup> The photographs are 33  $\mu$ s apart; the total sequence shown lasts 1°. The first photograph shows the flame front prior to onset of knock. The second photograph shows the onset of autoignition with the appearance of dark regions near the wall (two identified by arrows) where substantial density gradients resulting from local energy release exist. The third, fourth, and fifth photographs show the spread of these ignited regions with time through the remaining end-gas. The exact location where autoignition occurred was identified with a photodigitizing system which ranked regions of the photograph by their brightness or darkness. The digitized version of the second photograph is also shown in Fig. 9-63. Additional smaller regions of autoignition are evident adjacent to the wall and in the vicinity of the flame front. While the location of autoignition sites varied with engine operating conditions, the majority of occurrences in this study were in the vicinity of the cylinder wall. The rate of spread of the autoignited end-gas region also varied significantly. Under heavy knocking conditions the entire end-gas region became ignited very rapidly and high-amplitude pressure oscillations occurred. Under trace knock conditions, autoignition could occur; yet the spread of the autoignited region could be sufficiently slow for no pressure oscillations to be detected.

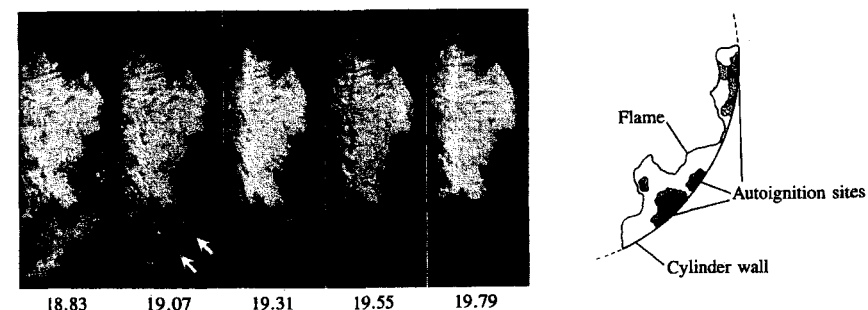


FIGURE 9-63

Five shadowgraph photographs of knocking combustion cycle identifying location of autoignition sites (arrows). Crank angle of each photo indicated: 33  $\mu$ s between frames. Operating conditions and engine details as in Fig. 9-62. Photodigitized picture of second photograph showing additional details of the autoignition sites in the end-gas region on right.<sup>89</sup>

nition sites varied with engine operating conditions, the majority of occurrences in this study were in the vicinity of the cylinder wall. The rate of spread of the autoignited end-gas region also varied significantly. Under heavy knocking conditions the entire end-gas region became ignited very rapidly and high-amplitude pressure oscillations occurred. Under trace knock conditions, autoignition could occur; yet the spread of the autoignited region could be sufficiently slow for no pressure oscillations to be detected.

When the above-described end-gas ignition process occurs rapidly, the gas pressure in the end-gas region rises substantially due to the rapid release of the end-gas fuel's chemical energy. The erosion damage that knock can produce, due to stress-induced material fatigue as described in the previous section, indicates the location of this high-pressure region. With the chamber geometry typical of most engines where the flame propagates toward the cylinder wall, the damage is confined to the thin crescent-shaped region on the opposite side of the chamber to the spark plug, where one expects the end-gas to be located. A shock wave propagates from the outer edge of this high-pressure end-gas region across the chamber at supersonic velocity, and an expansion wave propagates into the high-pressure region toward the near wall. The presence of such a shock wave has been observed photographically.<sup>90</sup> The shock wave and expansion wave reflect off the walls of the chamber, eventually producing standing waves. Usually these standing waves are due to transverse gas vibration and are of substantial amplitude. The amplitude of the pressure oscillations builds up as the standing waves are established, and then decays as the gas motion is damped out. The frequency of the pressure oscillations (normally in the 5 to 10 kHz range) decreases with time as the initially finite-amplitude supersonic pressure waves decay to small-amplitude sound waves.<sup>80</sup> Thus the pressure signal detected with a transducer during a knocking combustion cycle will depend on the details of the end-gas ignition process, the combustion chamber geometry, and the location of the transducer in relation to the end-gas region.

The pressure variation across the cylinder bore, due to knock, can be illustrated by the following example. Consider the disc-shaped combustion chamber with the spark plug located in the cylinder wall shown in Fig. 9-64a. Figure 9-64b shows the pressure and temperature distribution across the combustion chamber due to the normal flame propagation process, at the time rapid ignition of the end-gas occurs. If the end-gas ignites completely and instantaneously, its pressure and temperature will suddenly rise, as shown. A shock wave will now propagate to the right and an expansion wave to the left, as shown in the distance-time diagram in Fig. 9-64c. These waves reflect off the walls and interact. The pressures at the cylinder wall, in the end-gas region and on the opposite side of the chamber at the spark plug, develop as shown in Fig. 9-64d. Figure 9-65 shows two simultaneously recorded pressure traces with heavy knock from two transducers at the top of the cylinder liner, one located near the spark plug and one in the end-gas region. In the end-gas region the pressure rises extremely rapidly when knock occurs, to a value considerably higher than that recorded on the opposite side of the chamber where the pressure rises more gradually. Standing

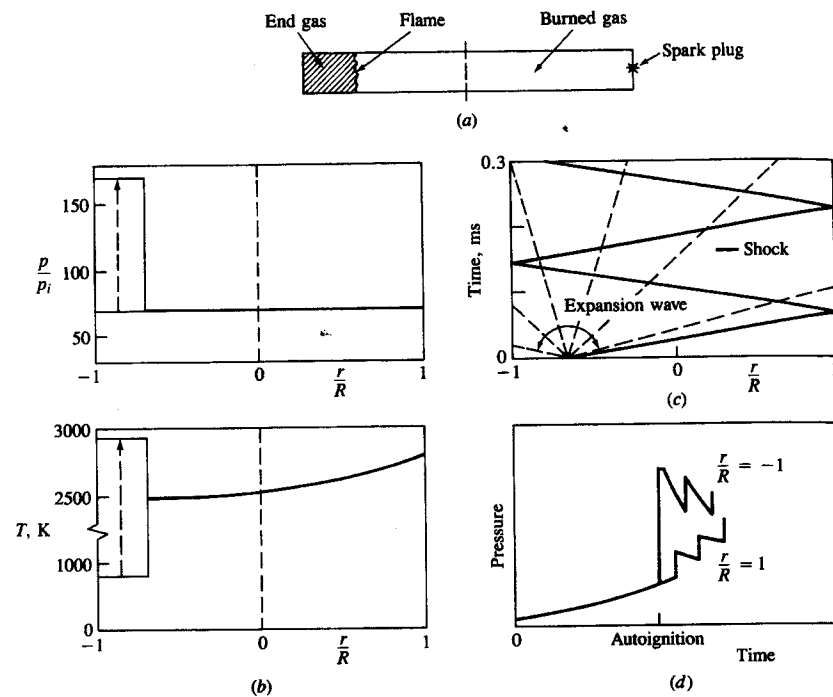


FIGURE 9-64

Illustration of how cylinder pressure distribution develops following knock. (a) Schematic of disc-shaped combustion chamber at time of knock. (b) Pressure and temperature across the diameter of a disc-shaped engine combustion chamber, before and after end-gas autoignition (assumed to occur very rapidly, at constant end-gas density). (c) Schematic of shock and expansion wave pattern following end-gas autoignition on distance-time plot. (d) Pressure variation with time at cylinder wall in the end-gas region, and at the opposite side of the cylinder.

waves are then set up and the amplitudes of the oscillations decay as the waves are damped out.<sup>78</sup>

The fundamental theories of knock are based on models for the autoignition of the fuel-air mixture in the end-gas. *Autoignition* is the term used for a rapid combustion reaction which is not initiated by any external ignition source. Often in the basic combustion literature this phenomenon is called an explosion. Before discussing the relevant theories of hydrocarbon oxidation, the necessary terminology will be defined and illustrated with the autoignition behavior of the much simpler hydrogen-oxygen system. For the hydrocarbons commonly found in practical fuels, the chemical reaction schemes by which the fuel molecules are broken down and react to form products are extremely complicated, and are as yet imperfectly understood.

The autoignition of a gaseous fuel-air mixture occurs when the energy re-

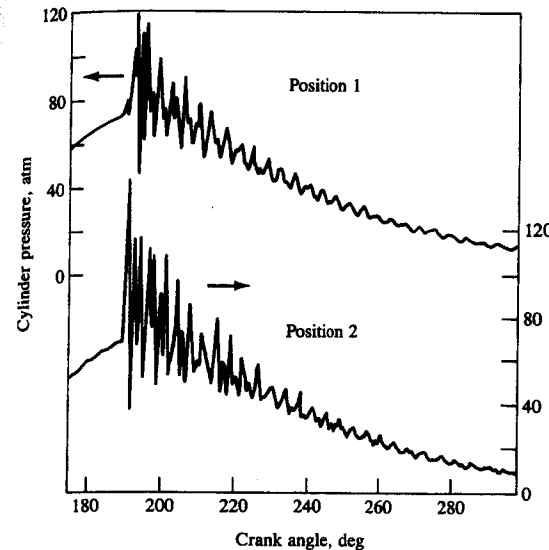


FIGURE 9-65  
 Simultaneously recorded pressure traces on opposite sides of spark-ignition engine combustion chamber in heavily knocking cycle. Position 1: at top of cylinder liner closest to spark plug. Position 2: at top of cylinder liner farthest from spark plug. 2000 rev/min, wide-open throttle, ( $A/F$ ) = 12.3, spark advance 20° BTC.<sup>78</sup>

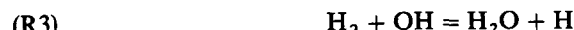
leased by the reaction as heat is larger than the heat lost to the surroundings; as a result the temperature of the mixture increases, thereby rapidly accelerating, due to their exponential temperature dependence, the rates of the reactions involved. The state at which such spontaneous ignition occurs is called the *self-ignition temperature* and the resulting self-accelerating event where the pressure and temperature increases rapidly is termed a *thermal explosion*.

In complex reacting systems such as exist in combustion, the "reaction" is not a single- or even a few-step process; the actual chemical mechanism consists of a large number of simultaneous, interdependent reactions or *chain reactions*. In such chains there is an *initiating* reaction where highly reactive intermediate species or *radicals* are produced from stable molecules (fuel and oxygen). This step is followed by *propagation* reactions where radicals react with the reactant molecules to form products and other radicals to continue the chain. The process ends with *termination* reactions where the chain propagating radicals are removed. Some propagating reactions produce two reactive radical molecules for each radical consumed. These are called *chain-branching* reactions. When, due to chain-branching, the number of radicals increases sufficiently rapidly, the reaction rate becomes extremely fast and a *chain-branching explosion* occurs. While the terms thermal and chain-branching explosions have been introduced separately, in many situations the self-accelerations in temperature and radicals occur simultaneously and the two phenomena must be combined.<sup>92, 93</sup>

The oxidation of hydrogen at high pressures and temperatures provides a good illustration of these phenomena. For stoichiometric hydrogen-oxygen mixtures, no reaction occurs below 400°C unless the mixture is ignited by an external

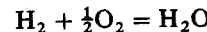
source such as a spark; above 600°C explosion occurs spontaneously at all pressures.<sup>†</sup>

The initiating steps proceed primarily through hydrogen peroxide ( $H_2O_2$ ) to form the hydroxyl radical (OH) at lower temperatures, or through dissociation of  $H_2$  at higher temperatures to form the hydrogen atom radical H. The basic radical-producing chain sequence is composed of three reactions:



The first two reactions are chain-branched; two radicals are produced for each one consumed. The third reaction is necessary to complete the chain sequence: starting with one hydrogen atom, the sequence R1 then R2 and R3 produces two H; starting with OH, the sequence R3, then R1, then R2 produces two OH. Since all three reactions are required, the multiplication factor is less than 2 but greater than 1. Repeating this sequence over and over again rapidly builds up high concentrations of radicals from low initial levels.

However, these three reactions do not correspond to the overall stoichiometry



and other reactions must become important. In flames, the chain-branched process ceases when the reverse of reactions R1-R3 become significant. A quasi equilibrium is established; while the overall process has proceeded a considerable way toward completion, a substantial amount of the available energy is still contained in the high radical concentrations. Over a longer time scale, this energy is released through three-body recombination reactions (the principal chain terminating reactions):



M refers to any available third-body species, required in these recombination reactions to remove the excess energy.<sup>92</sup>

With this introductory background let us now turn to the autoignition of hydrocarbon-air mixtures. The process by which a hydrocarbon is oxidized can exhibit four different types of behavior, or a sequential combination of them, depending on the pressure and temperature of the mixture: slow reactions; single

or multiple cool flames (slightly exothermic reactions); two-stage ignition (cool flame followed by a hot flame); single-stage ignition (hot flame). Slow reactions are a low-pressure, low-temperature (<200°C) phenomenon not normally occurring in engines. At 300 to 400°C one or more combustion waves often appear, accompanied by faint blue light emission; the reaction is quenched, however, when only a small fraction of the reactants have reacted and the temperature rise is only tens of degrees. These are called *cool flames*. Depending on conditions and the fuel, a cool flame may be followed by a "hot flame" or high-temperature explosion where the reaction accelerates rapidly after ignition. This is termed *two-stage ignition*. As the temperature of the mixture increases, a transition from two-stage to single-stage ignition occurs. While all hydrocarbons exhibit induction intervals which are followed by a very rapid reaction rate, some hydrocarbon compounds do not exhibit the cool flame or two-stage ignition behavior.

Figure 9-66 shows these ignition limits for isoctane, methane, and benzene. For isoctane, ignition in the low-temperature regions is by a two-stage process: there is a first time interval before the cool flame appears and then a second time interval from the appearance of the cool flame to the hot flame combustion process. Ignition in the high-temperature region is by a continuous one-stage process. The cool flame phenomena vary enormously with hydrocarbon structure. Normal paraffins give strong cool flames, branched-chain paraffins are more resistant. Olefins give even lower luminosity cool flames with longer induction periods. Methane shows only the high-temperature ignition limit, as indicated in Fig. 9-66. Benzene, also, does not exhibit the cool flame phenomenon and other aromatics give hardly detectable luminosity.<sup>75</sup> It is thought that some com-

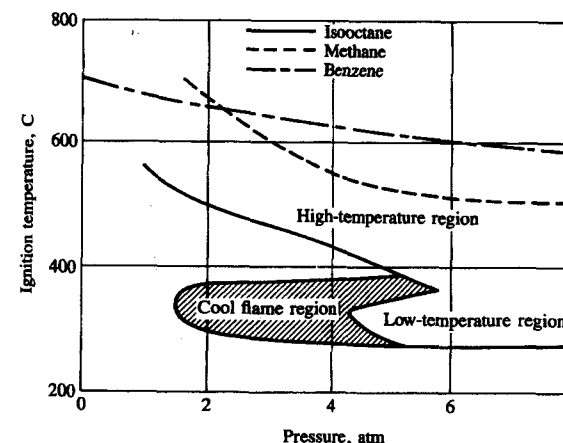


FIGURE 9-66

Ignition diagrams for isoctane, methane, and benzene. Two-stage ignition occurs in the low-temperature region; the first stage may be a cool flame. Single-stage ignition occurs in the high-temperature region.<sup>94</sup>

<sup>†</sup> In between, three separate explosion limits—pressure-temperature boundaries for specific mixture ratios of fuel and oxidizer that separate regions of slow and fast reaction—exist; these are not, however, of interest to us here.

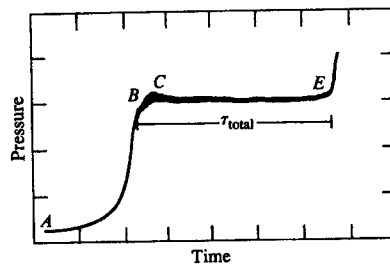
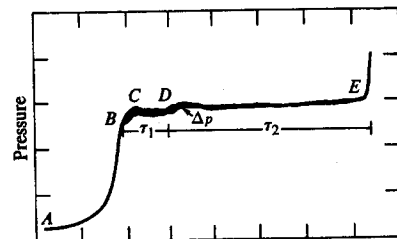


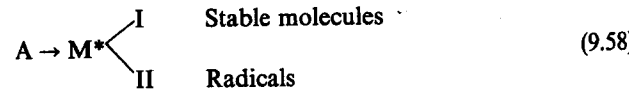
FIGURE 9-67

Pressure records of the autoignition of isoctane-air mixture ( $\phi = 0.9$ ) in a rapid compression machine.  $A \rightarrow B \rightarrow C$  is the compression process. Top: two-stage ignition (at  $D$ , then at  $E$ ) at postcompression pressure of 1.86 MPa and temperature of 686 K. Bottom: single-stage ignition at  $E$  at post-compression conditions of 2.12 MPa and 787 K. Vertical scale: 690 kPa/division. Horizontal scale: 1 ms/division.<sup>95</sup>

pounds knock by a low-temperature two-stage ignition mechanism, some via a high-temperature single-stage ignition mechanism, and for some fuels both mechanisms may play a role.

Examples of these two mechanisms in rapid-compression machine experiments, where a homogeneous isoctane-air mixture was compressed to different final conditions in a piston-cylinder apparatus and allowed to autoignite, are shown in Fig. 9-67.  $A \rightarrow B \rightarrow C$  is the piston-motion-produced compression. The top trace shows a well-defined cool flame at  $D$ , preceding hot ignition at  $E$ . The lower trace, at a higher temperature, shows a single-stage ignition process.<sup>95</sup>

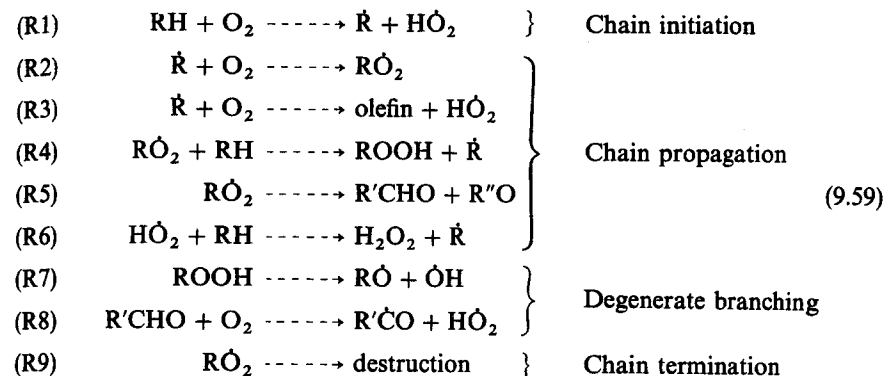
Many of the above phenomena—long induction periods, initial slow increase in reaction rate, two-stage ignition process—cannot be explained with simple mechanisms like the hydrogen oxidation process reviewed above. Although chain-branching reactions are taking place, the radical generation process must be more complex. Explanations of the long induction periods are based on the formation of unstable but long-lived intermediates. These intermediates can then either react to form stable molecules or to form active radicals, the dominance and rate of either of these paths depending on the temperature: i.e.,<sup>93</sup>



This is called a *degenerate-branching* mechanism. Hydroperoxides are an important metastable intermediate produced in the chain propagation process in the low-temperature ignition process. They have the form ROOH, where R is an

organic radical (formed by abstracting a hydrogen atom from a fuel hydrocarbon molecule). However, at higher temperatures, ROOH is no longer the major product of the chain propagation process: instead, it is hydrogen peroxide,  $H_2O_2$ . While  $H_2O_2$  is relatively stable at lower temperatures, above 500°C it decomposes into two OH radicals.

An outline of the basic hydrocarbon (RH) oxidation process due to Semenov is as follows:<sup>93</sup>



The dot denotes an active radical; each dash denotes the number of free bonds on the organic radical R.

Reaction R1 is slow and explains the induction period in hydrocarbon combustion. R2 is fast and of near-zero activation energy. R3 leads to olefins known to occur in the oxidation of saturated hydrocarbons. R4 and R5 yield the main intermediates. The degenerate branching comes about from the delay in decomposition of the reactive species in R7 and R8. As one radical is used up to form the reactants in R7 and R8, the multiple radicals do not appear until these reactants decompose.<sup>93</sup> A more extensive discussion of hydrocarbon oxidation mechanisms can be found in Benson.<sup>96</sup>

The following evidence indicates the relevance of the above mechanism to knock in engines. End-gas sampling studies have identified products of slow combustion reactions of isoctane; these principally include olefins, cyclic ethers, aldehydes (R'CHO), and ketones (R'CO).<sup>97</sup> Such studies have shown increasing concentrations of peroxides (predominantly  $H_2O_2$  with traces of organic peroxides) with isoparaffinic fuels which show two-stage ignition behavior. Higher temperature, single-stage ignition fuels such as benzene and toluene gave no detectable peroxide. Aldehydes and ketones have been measured in significant and increasing concentrations in motored engines where the peak cycle temperature was steadily increased. In motored engines, the occurrence of cool flames, the two-stage nature of the autoignition ignition process at intermediate compression temperatures, and the transition to a single-stage ignition process at very high compression ratios (i.e., motored-engine gas temperatures with a peak much higher than normal to simulate end-gas conditions in a firing engine) have also been demonstrated.<sup>75, 94</sup>

Two types of models of this autoignition process have been developed and used: (1) empirical induction-time correlations; (2) chemical mechanisms which embody many or all of the features of the "full" hydrocarbon oxidation process given in Eq. (9.59).

Induction-time correlations are derived by matching an Arrhenius function to measured data on induction or autoignition times, for given fuel-air mixtures, over the relevant mixture pressure and temperature ranges. It is then assumed that autoignition occurs when

$$\int_{t=0}^{t_i} \frac{dt}{\tau} = 1 \quad (9.60)$$

where  $\tau$  is the induction time at the instantaneous temperature and pressure for the mixture,  $t$  is the elapsed time from the start of the end-gas compression process ( $t = 0$ ), and  $t_i$  is the time of autoignition. This equation can be derived by assuming that the overall rate of production of the critical species in the induction period chemistry, for a given mixture, depends only on the gas state and that the concentration of the critical species required to initiate autoignition is fixed (i.e., independent of the gas state).<sup>98</sup>

A number of empirical relations for induction time for individual hydrocarbons and blended fuels have been developed from fundamental or engine studies of autoignition (see Ref. 99). These relations have the form

$$\tau = Ap^{-n} \exp\left(\frac{B}{T}\right) \quad (9.61)$$

where  $A$ ,  $n$ , and  $B$  are fitted parameters that depend on the fuel. The ability of these types of equations to predict the onset of knock with sufficient accuracy is unclear. The most extensively tested correlation is that proposed by Douaud and Eyzat:<sup>100</sup>

$$\tau = 17.68 \left( \frac{\text{ON}}{100} \right)^{3.402} p^{-1.7} \exp\left(\frac{3800}{T}\right) \quad (9.62)$$

where  $\tau$  is in milliseconds,  $p$  is absolute pressure in atmospheres, and  $T$  is in kelvin. ON is the appropriate octane number of the fuel (see Sec. 9.6.3). If the temperature and pressure time history of the end-gas during an individual cycle are known, Eqs. (9.60) and (9.62) together can be used to determine whether autoignition occurs before the normally propagating flame consumes the end-gas.

An important question with any model of the end-gas autoignition process is characterizing the end-gas temperature. During intake, the combustion chamber walls are hotter than the entering gases; thus, heat is transferred from the walls to the fresh mixture. During compression, the mixture temperature rises to levels substantially above the wall temperature. A thermal boundary layer will build up adjacent to the wall, as heat is now transferred to the wall. Unburned mixture away from the wall will be compressed essentially adiabatically (see Sec. 12.6.5). In addition, any unburned mixture which for some portion of time during intake and compression has been in close proximity to the exhaust valve and

piston (which run at higher temperatures than the water-cooled wall regions) could be at higher temperatures than adiabatically compressed mixture, due to substantial heat transfer to the unburned mixture. Thus, the end-gas temperature is not uniform and the distribution of temperature is extremely complex. Often, the mean unburned mixture temperature is used to characterize its state. Alternatively, the core temperature corresponding to adiabatic compression of mixture from conditions at the start of compression is used. In the absence of substantial heating by the exhaust valve and piston, the core temperature is a better representation of the maximum unburned mixture at any point in the cycle.

While more complex and complete chemical models of the autoignition process are being developed for simple paraffinic hydrocarbon fuel compounds (e.g., Refs. 91 and 101), no detailed models are yet available for use with real blended fuels in engines. However, a generalized kinetic model for hydrocarbon oxidation based on a degenerate branched-chain mechanism, known as the Shell model, has been developed and tested with some success. The model uses generic chemical entities representative of a variety of individual species which undergo a set of generalized reactions. This is justified by the broadly similar (though complex) ignition behavior of a variety of different fuel molecules and the similar kinetics exhibited by the organic radicals of the same type in the hydrocarbon oxidation process [Eq. (9.59)].<sup>95, 102</sup>

The Shell model is based on a generic eight-step degenerate chain-branching reaction scheme. The scheme involves the fuel (RH), oxygen, radicals formed from the fuel (R), products (P), intermediate product (Q), and degenerate-branching agent (B). The rate constants are either fixed at values consistent with the literature or fitted so that measured induction times (such as those illustrated in Fig. 9-67) are adequately predicted.<sup>102</sup> An example of results obtained with this scheme is shown in Fig. 9-68. It shows the calculated pressure, temperature, and species concentrations in the end-gas region of an operating spark-ignition

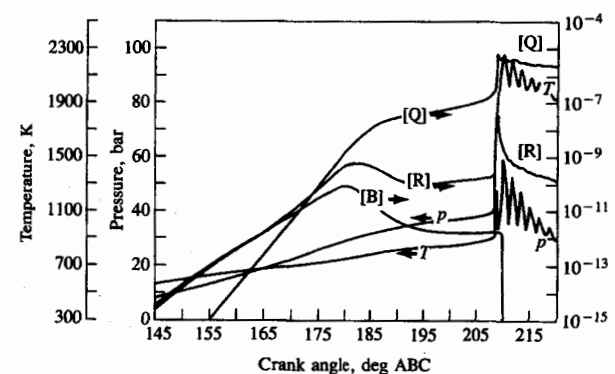


FIGURE 9-68

Pressure, temperature, and composition in the end-gas, before, during, and after autoignition, predicted by the Shell model in spark-ignition engine combustion process. B, Q, R defined in text.<sup>103</sup>

engine, leading up to knock at 209° ABC. In this example, the autoignition model has been incorporated in a multidimensional model of the flow and flame propagation processes within the combustion chamber (see Sec. 14.5).<sup>103</sup>

### 9.6.3 Fuel Factors

The tendency to knock depends on engine design and operating variables which influence end-gas temperature, pressure, and the time spent at high values of these two properties before flame arrival. Thus, for example, the tendency to knock is decreased through reductions in the end-gas temperature that follow from decreasing the inlet air temperature and retarding the spark from MBT timing. However, knock is a phenomenon that is governed by both engine and fuel factors; its presence or absence in an engine depends primarily on the anti-knock quality of the fuel.

Individual hydrocarbon compounds vary enormously in their ability to resist knock, depending on their molecular size and structure. Their tendency to knock has been measured by the *critical compression ratio* of an engine: i.e., the compression ratio at which, under specified operating conditions, the specific fuel compound will exhibit incipient knock. Knocking tendency is related to molecular structure† as follows:<sup>105, 106</sup>

#### *Paraffins*

1. Increasing the length of the carbon chain increases the knocking tendency.
2. Compacting the carbon atoms by incorporating side chains (thereby shortening the length of the basic chain) decreases the tendency to knock.
3. Adding methyl groups ( $\text{CH}_3$ ) to the side of the basic carbon chain, in the second from the end or center position, decreases the knocking tendency.

#### *Olefins*

4. The introduction of one double bond has little antiknock effect; two or three double bonds generally result in appreciably less knocking tendency.
5. Exceptions to this rule are acetylene ( $\text{C}_2\text{H}_2$ ), ethylene ( $\text{C}_2\text{H}_4$ ), and propylene ( $\text{C}_3\text{H}_6$ ), which knock much more readily than the corresponding saturated hydrocarbons.

#### *Naphthenes and aromatics*

6. Naphthenes have significantly greater knocking tendency than have the corresponding size aromatics.
7. Introducing one double bond has little antiknock effect; two and three double bonds generally reduce knocking tendency appreciably.

† See Sec. 3.3 for a review of hydrocarbon structure and its nomenclature. A more extensive discussion is given by Goodger.<sup>104</sup>

8. Lengthening the side chain attached to the basic ring structure increases the knocking tendency in both groups of fuels, whereas branching of the side chain decreases the knocking tendency.

Figure 9-69 identifies the magnitude of these trends on a plot of the critical compression ratio against the number of carbon atoms in the molecule. The strong dependence of knocking tendency on fuel molecular size and structure is apparent.

Practical fuels are blends of a large number of individual hydrocarbon compounds from all the hydrocarbon series of classes: alkanes (paraffins), cyclanes (naphthenes), alkenes (olefins), and aromatics (see Sec. 3.3). A practical measure of a fuel's resistance to knock is obviously required.<sup>107, 108</sup> This property is defined by the fuel's *octane number*. It determines whether or not a fuel will knock in a given engine under given operating conditions: the higher the octane number, the higher the resistance to knock. Octane number is not a single-valued quantity, and may vary considerably depending on engine design, operating conditions during test, ambient weather conditions during test, mechanical condition of engine, and type of oil and fuel used in past operation. The octane number (ON) scale is based on two hydrocarbons which define the ends of the scale. By definition, normal heptane ( $n\text{-C}_7\text{H}_{16}$ ) has a value of zero and isoctane ( $\text{C}_8\text{H}_{18}$ : 2,2,4-trimethylpentane) has an octane number of 100. These hydrocarbons were chosen because of the great difference in their ability to resist knock and the fact that isoctane had a higher resistance to knock than any of the gasolines available at the time the scale was established. Blends of these two hydrocarbons define the knock resistance of intermediate octane numbers: e.g., a blend of 10 percent *n*-heptane and 90 percent isoctane has an octane number of 90. A fuel's octane number is determined by measuring what blend of these two hydrocarbons matches the fuel's knock resistance.

Several octane rating methods for fuels have been developed. Two of these—the research method (ASTM D-2699)† and the motor method (ASTM D-2700)—are carried out in a standardized single-cylinder engine. In the motor method, the engine operating conditions are more severe; i.e., the conditions are more likely to produce knock. In addition, road octane rating methods have been developed to define the antiknock quality of fuels in cars operated on the road or on chassis dynamometers. The engine used in the ASTM research and motor methods is the single-cylinder engine developed under the auspices of the Cooperative Fuel Research Committee in 1931—the CFR engine.‡ This test engine is a robust four-stroke overhead-valve engine with an 82.6-mm (3.25-in) bore and 114.3-mm (4.5-in) stroke. The compression ratio can be varied from 3 to 30 while

† ASTM denotes American Society for Testing and Materials; the letter and number defines the specific testing code.

‡ The Cooperative Fuel Research Committee is now the Coordinating Research Council, Inc.